

JPL Publication 90-54

(NASA-CR-195894) PROCEEDINGS OF
THE SECOND AIRBORNE
VISIBLE/INFRARED IMAGING
SPECTROMETER (AVIRIS) WORKSHOP
(JPL) 288 p

N94-71904

Unclass

Z9/43 0005865

PROCEEDINGS OF THE SECOND AIRBORNE VISIBLE/INFRARED IMAGING Spectrometer (AVIRIS) Workshop

June 4 and 5, 1990

Robert O. Green
Editor

November 15, 1990



National Aeronautics and
Space Administration

Jet Propulsion Laboratory
California Institute of Technology
Pasadena, California

35 mm SLIDES
ATTACHED

NON-STANDARD MEDIA

Proceedings of the Second Airborne Visible/Infrared Imaging Spectrometer (AVIRIS) Workshop

June 4 and 5, 1990

Robert O. Green
Editor

November 15, 1990



National Aeronautics and
Space Administration

Jet Propulsion Laboratory
California Institute of Technology
Pasadena, California

This publication was prepared by the Jet Propulsion Laboratory, California Institute of Technology, under a contract with the National Aeronautics and Space Administration.

FOREWORD

In the text and figure captions of some of the papers, reference is made to color slides; these 35-mm slides are located in a pocket at the end of the Proceedings. They are sometimes color versions of the referenced black-and-white figures within the Proceedings.

~~iii~~

ABSTRACT

The Second Airborne Visible/Infrared Imaging Spectrometer (AVIRIS) Workshop was held on June 4th and 5th 1990 at the Jet Propulsion Laboratory, Pasadena, California. This workshop followed the successful operation of AVIRIS for acquisition of calibrated radiance data during 1989. Preceding these operations, significant instrument engineering modifications were completed to increase the radiometric precision and to improve the absolute radiometric calibration. During 1989 operations, 957 AVIRIS scenes representing 134 gigabytes of data were acquired, and of these more than 400 scenes were distributed to investigators prior to the workshop. Attendance at the workshop was in excess of 250 people with 39 presentations given during the 2-day period. These presentations highlighted the diverse disciplines to which calibrated imaging spectrometer radiance measurements are being applied. Results were presented for the fields of ecology, geology, oceanography, inland water studies, snow hydrology, atmospheric studies, calibration, and data analysis. These investigations demonstrate a growing capability to answer important earth science questions with calibrated imaging spectrometer measurements.

AVIRIS has flown successfully in 1990 for an equally diverse set of scientific investigations. Results from these data and further analyses of the 1989 data will be presented at the Third AVIRIS Science Workshop, which is planned for the first week of June 1991.

PRECEDING PAGE BLANK NOT FILMED

CONTENTS

Accuracy of the Spectral and Radiometric Laboratory Calibration of the Airborne Visible/Infrared Imaging Spectrometer (AVIRIS) Thomas G. Chrien, Robert O. Green, and Michael L. Eastwood.....	1
Determination of the In-Flight Spectral and Radiometric Characteristics of the Airborne Visible/Infrared Imaging Spectrometer (AVIRIS) Robert O. Green, James E. Conel, Veronique Carrere, Carol J. Bruegge, Jack S. Margolis, Michael Rast, and Gordon Hoover.....	15
Detection of Trace Quantities of Green Vegetation in 1989 AVIRIS Data Christopher D. Elvidge, Frederick P. Portigal, and David A. Mouat.....	35
Isolating Woody Plant Material and Senescent Vegetation From Green Vegetation in AVIRIS Data D. A. Roberts, M. O. Smith, J. B. Adams, D. E. Sabol, A. R. Gillespie, and S. C. Willis	42
Are the Spectral Shifts an Operational Concept? Critical Analysis of Theoretical and Experimental Results F. Baret, S. Jacquemoud, C. Leprieur, and G. Guyot.....	58
Potential for Determination of Leaf Chlorophyll Content Using AVIRIS J. R. Miller, J. R. Freemantle, M. J. Belanger, C. D. Elvidge, and M. G. Boyer.....	72
Application of Lowtran 7 as an Atmospheric Correction to Airborne Visible/Infrared Imaging Spectrometer (AVIRIS) Data Jeannette van den Bosch and Ron Alley.....	78
An AVIRIS Survey of Quaternary Surfaces Formed on Carbonate-Provenance Alluvium, Mojave Desert, Southern Nevada Veronique Carrere and Oliver Chadwick.....	82
Using Spectral Mixture Analysis of AVIRIS High Dimensional Data for Distinguishing Soil Chronosequences Lawrence Fox III, Arthur F. Fischer, Allen R. Gillespie, and Milton R. Smith	94
Analysis of Airborne Visible/Infrared Imaging Spectrometer (AVIRIS) Data for the Northern Death Valley Region, California/Nevada Fred A. Kruse.....	100
Analysis of Atmospheric Water Vapor Maps From AVIRIS at Salton Sea, California: Part I, Experiments, Methods, Results, and Error Budgets Veronique Carrere, James E. Conel, Robert Green, Carol Bruegge, Jack Margolis, and Ron Alley.....	107

Analysis of Atmospheric Water Vapor Maps From AVIRIS at Salton Sea, California: Part II, Surface Moisture Flux, Boundary Conditions, and Plume Measurements James E. Conel and Veronique Carrere.....	129
Cloud Identification and Optical Thickness Retrieval Using AVIRIS Data Kwo-Sen Kuo, Ronald M. Welch, Bo-Cai Gao, and Alexander F. H. Goetz.....	149
Determination of Cloud Area From AVIRIS Data Bo-Cai Gao and Alexander F. H. Goetz.....	157
Analysis of AVIRIS Data for Spectral Discrimination of Geologic Materials in the Dolly Varden Mountains, Nevada J. A. Zamudio and W. W. Atkinson, Jr.....	162
Retrieval of Reflectance from Calibrated Radiance Imagery Measured by the Airborne Visible/Infrared Imaging Spectrometer (AVIRIS) for Lithological Mapping of the Clark Mountains, California Robert O. Green.....	167
Material Absorption Band Depth Mapping of Imaging Spectrometer Data Using a Complete Band Shape Least-Squares Fit With Library Reference Spectra Roger N. Clark, Andrea J. Gallagher, and Gregg A. Swayze.....	176
AVIRIS Data for the Dolly Varden Mountains, Nevada: HIRIS Analog K. S. Kierein-Young, A. F. H. Goetz, J. A. Zamudio, and B.-C. Gao.....	187
Techniques for AVIRIS Data Normalization in Areas With Partial Vegetation Cover James K. Crowley.....	192
Mineralogic Mapping Using Airborne Visible Infrared Imaging Spectrometer (AVIRIS) Shortwave Infrared (SWIR) Data Acquired Over Cuprite, Nevada Simon J. Hook and Michael Rast.....	199
The U. S. Geological Survey, Digital Spectral Library and Analysis Software Roger N. Clark, Gregg A. Swayze, Trude V. V. King, Barry Middlebrook, Wendy M. Calvin, and Noel Gorelick.....	208
Analysis of High Spectral Resolution Data on a Personal Computer Daniel N. M. Donoghue, David W. C. Robinson, and Simon J. Hook.....	216
Investigations of Ocean Reflectance With AVRIS Data Stuart H. Pilorz and Curtiss O. Davis.....	224
Reflectance Spectra From Eutrophic Mono Lake, California, Measured With the Airborne Visible and Infrared Imaging Spectrometer (AVIRIS) John M. Melak and Stuart H. Pilorz.....	232

Interpretation of Residual Images: Spectral Mixture Analysis of AVIRIS Images, Owens Valley, California A. R. Gillespie, M. O. Smith, J. B. Adams, S. C. Willis, A. F. Fischer III, and D. E. Sabol.....	243
Evolution of the Airborne Visible/Infrared Imaging Spectrometer (AVIRIS) Flight and Ground Data Processing System Wallace M. Porter, Thomas G. Chrien, Earl G. Hansen, and Charles M. Sarture.....	271
Slide Captions.....	279

Accuracy of the Spectral and Radiometric Laboratory Calibration
of the Airborne Visible/Infrared Imaging Spectrometer (AVIRIS)

Thomas G. Chrien, Robert O. Green and
Michael L. Eastwood

Jet Propulsion Laboratory, California Institute of Technology
4800 Oak Grove Drive, Pasadena, California 91109

ABSTRACT

Current research with data collected by AVIRIS includes the disciplines of ecology, geology, oceanography, inland waters, snow hydrology, and atmospheric science. In these investigations, physical parameters are calculated from AVIRIS-measured radiance spectra. AVIRIS measures the total incident radiance in 224 channels with nominally 10-nm widths between 400 and 2450 nm in the electromagnetic spectrum. Image dimensions are 10.5 km wide by 10 to 100 km in length with nominally 20- by 20-m spatial resolution. Calibration is prerequisite for extraction of quantitative information from AVIRIS data with known accuracy and precision. The spectral channel sampling interval and spectral response functions are determined with calculated accuracy for each AVIRIS channel. AVIRIS radiometric calibration coefficients, vignetting correction, instrument stability, and noise equivalent delta radiance determinations are generated. Emphasis is placed on referencing the calibration standards, procedures, and accuracy of the calibration. Future plans for improved calibration of AVIRIS in the laboratory and for using an improved onboard calibrator are discussed.

1.0 INTRODUCTION

AVIRIS is an airborne sensor that measures high spatial resolution image data of the earth in 224 spectral channels in four spectrometers (A,B,C, and D) covering the range from 400 to 2450 nm^{1,2}. These data are spectrally and radiometrically calibrated. This paper describes the laboratory procedures, algorithms, measurements, and uncertainties associated with generation of the spectral and radiometric calibration.

Calibration of AVIRIS was initially reported in 1987 by Vane³. Since that time, improvements have been incorporated in the calibration procedure. These improvements have been primarily in the areas of increased accuracy of the transfer of calibration from standard sources, the quantification of associated accuracy, and the algorithms used to generate AVIRIS calibration files. AVIRIS system performance has been improved significantly since 1987, as reported in a companion paper by Porter⁴. These improvements, particularly with respect to stability and signal-to-noise ratio, greatly facilitate the task of instrument calibration.

Verification of the laboratory calibration is determined through an in-flight calibration experiment reported by Green et al⁵. The spectral calibration of AVIRIS agrees with the in-flight data to within 2 nm. The absolute radiometric calibration is consistent with the in-flight verification to 10 percent over the spectral range. In-flight radiometric stability, as measured by five consecutive passes over the surface calibration site, is reported to be between 3 and 5 percent. In-flight determination of AVIRIS noise equivalent delta radiance also agrees with the laboratory calibration result.

2.0 SPECTRAL CALIBRATION

The objective of the spectral calibration of AVIRIS is to determine the spectral sampling interval and spectral response function for each of the 224 channels. Variation in the spectral calibration is a consequence of the optimization of the throughput during realignment of the detector array, following a period of engineering. Realignment of the spectrometers can normally return center wavelength to within 5 nm of the previous calibration and full width at half maximum (FWHM) to within 2 nm.

The procedure for performing a spectral calibration of AVIRIS involves the following steps: (1) calibration of the laboratory monochromator from a spectral emission line source, (2) use of the monochromator to scan a narrow band source across selected AVIRIS channels while measuring the response of the channels, (3) fitting the measured responses to a Gaussian spectral response function, (4) inferring the spectral channel positions and response functions of the remaining channels, (5) quantifying and reporting the accuracy associated with these procedures.

2.1 Monochromator Calibration

The narrow band spectral calibration source consists of a Jarrell-Ash model 82-487 monochromator illuminated with a dc-stabilized lamp. The bandwidth of the monochromator is determined by the 270-mm focal length, the entrance and

exit slit widths, and the lines per millimeter grating frequency as shown in Table 1. Three monochromator configurations are used to cover the range of AVIRIS spectral channels. Each configuration uses a grating that has a blaze wavelength intended to maximize throughput. The blaze wavelengths are 0.5, 1.0, and 2.0 μm , respectively.

Table 1. Monochromator Parameters.

Spectrometer and spectral range (nm)	Grating freq. (lines/mm)	Entrance/exit slit widths (μm)	FWHM band-width (nm)
A 400 – 700	600	100	1.2
B,C 700 – 1800	600	100	1.2
D 1800 – 2500	300	50	1.2

Table 2. Effective wavelengths of mercury emission lines used for monochromator spectral calibration.

Color	Wavelength (nm)	Order	Effective Wavelength (nm)
Purple	404.656	2	809.312
		3	1213.968
		4	1618.624
		5	2023.280
		6	2427.936
Blue	435.835	2	871.670
		3	1307.505
		4	1743.340
		5	2179.175
Green	546.074	2	1092.148
		3	1638.222
		4	2184.296
Yellow1	576.959	2	1153.918
		3	1730.877
		4	2307.836
Yellow2	579.065	2	1158.130
		3	1737.195
		4	2316.260

A low-pressure mercury vapor lamp (UVP Inc. P/N 90 0012 01, S/N 243747) placed at the entrance slit is used to calibrate the monochromator. The grating drive is advanced to a position that maximizes the light throughput of a spectral emission line, as determined by visual observation. Backlash problems are avoided by always approaching a line from a shorter wavelength. Higher orders of visible lines are used to calibrate the infrared portion of the spectrum. The effective wavelength of the higher order lines is computed as shown in Table 2 by multiplying the visible wavelength times the spectral order. The counter position of each effective order is recorded at least six times and a sample variance is computed.

The monochromator calibration is computed by forming a linear fit between the effective wavelengths of observed mercury emission lines and the numeric counter. The fit uses a technique described by Bevington⁶ to compute the uncertainty of the fit parameters using the uncertainties in counter position. Uncertainties in the counter position are taken to be the larger of the sample variance or the half width at half maximum (HWHM) of the monochromator bandpass in counter units. The variance in counter position is dominant in the 400- to 700-, and 700- to 1800-nm configurations. The HWHM is the greater contribution to counter uncertainty for the 1800- to 2500-nm configuration. The stated uncertainties in the positions of the spectral lines (+ or - 0.001 nm) shown in Table 2 are negligible in comparison to the counter uncertainty.

The difference from fit is shown in Figure 1. It is apparent that a higher order polynomial might lead to a better fit. This effect is due to a slight misalignment of the sine bar mechanism that drives the grating angle. This effect can be

minimized by limiting the wavelength range of the fit. A chi-squared-per-degree freedom test is performed to confirm that the fit is valid within stated uncertainty. The resultant fitting parameters for the three monochromator calibrations are given in Table 3. The increase of uncertainty for the 1800- to 2500-nm calibration is caused, in part, by the lesser resolution of the grating (300 lines per millimeter compared to 600 lines per millimeter for the other two configurations).

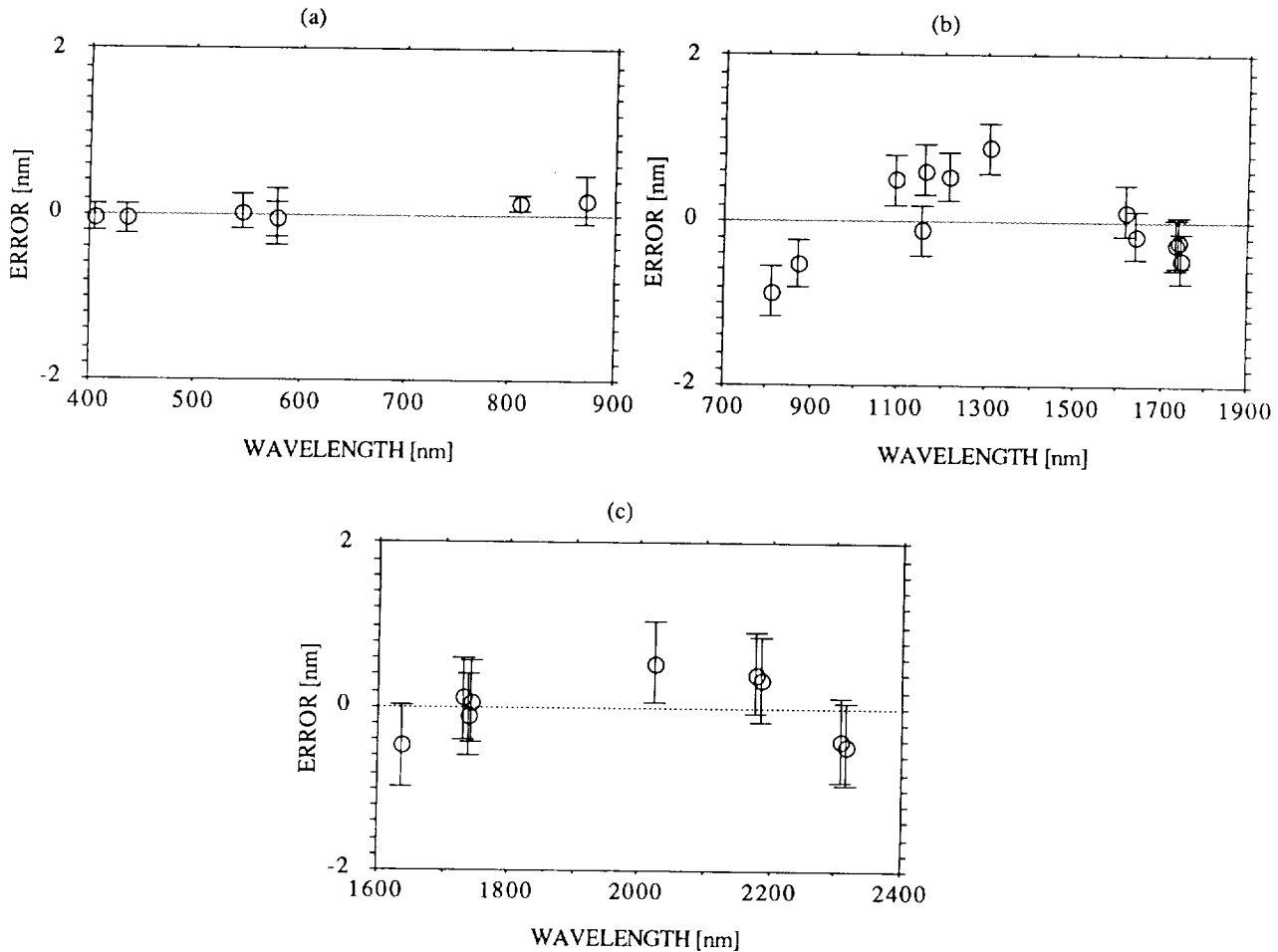


Figure 1. Difference of wavelength fit versus wavelength along with uncertainty in position for the (a) A spectrometer, (b) B and C spectrometer, and (c) D spectrometer configurations.

Table 3. Monochromator Calibration Fitting Parameters.

Spectrometer and valid spectral range (nm)	Least squares linear fit and uncertainty (nm)	Chi-squared per degree of freedom
A 400 – 700	$\lambda = (1.99 \pm 0.0005) \cdot \text{counter} - (2.9 \pm 0.2)$	0.72
B,C 700 – 1800	$\lambda = (2.00 \pm 0.0001) \cdot \text{counter} - (8.8 \pm 0.1)$	0.92
D 1800 – 2450	$\lambda = (3.99 \pm 0.0019) \cdot \text{counter} - (9.8 \pm 1.0)$	1.02

2.2 AVIRIS Spectral Calibration Procedure

The spectral calibration stimulus shown in Figure 2 consists of the monochromator, a SORL f/4, a 1-m focal length collimator, a tungsten halogen lamp, and an Oriel dc-regulated power supply, model 68735. After calibration for a given wavelength range and configuration, the monochromator is placed so that the exit slit is located in the focal place of the collimator. The lamp is imaged onto the entrance slit of the monochromator and aligned so that the grating of the monochromator is uniformly illuminated. The entire assembly is mounted in a rack with wheels so that it can be rolled under AVIRIS, which is raised on jack stands.

Alignment of the stimulus to AVIRIS is begun by setting the grating to the zero order position and removing the slits. The output beam of the stimulus is centered on the foreoptics aperture. Jack screws placed under three corners of the rack are adjusted to maximize the peak signal of a cross-track scan. This process is repeated with a series of slits of decreasing width until the optimum angular alignment is achieved with the desired slits.

The spectral response of a channel is measured by incrementing the output wavelength counter of the monochromator in steps which correspond to 2-nm intervals. The peak signal of the cross-track scan is recorded for that channel over a 40-nm range centered about the peak signal wavelength. This process is repeated for a minimum of six channels in each of the four AVIRIS spectrometers.

2.3 Results of Spectral Calibration

The spectral response function of each of the 224 AVIRIS channels has a nominal Gaussian shape⁷. A Gaussian fitting routine, written by Sobel⁸, is used to fit the response data in digitized numbers (DN) to obtain a center wavelength, full width at half maximum as shown in Figure 3. The solid line represents the best-fit Gaussian function and the squares represent measured data points. Horizontal error bars indicate the wavelength uncertainty, while the vertical error bars represent the signal response uncertainty. This is computed as the root sum square (RSS) of the product of wavelength uncertainty times the slope of the Gaussian at that point and the averaged signal variance. "Goodness" of fit is determined using chi-square-per-degree freedom analysis. The uncertainty of the fit parameters is determined by increasing the parameter until the chi-square value increases by one. In this way, computed uncertainties can be assigned to center wavelength and FWHM bandwidth. The 100 DN bias shown in the plot is due to the dark current which is not subtracted in this analysis. This bias is accounted for as one of the fitting parameters in the Gaussian routine.

Preliminary results of the chi-squared-per-degree freedom of the spectral response function curve fit show that wavelength uncertainty from the monochromator calibration is well correlated across a given spectral scan. Consequently, while the curve fit is of high precision, the absolute accuracy of the center wavelength value is limited by the monochromator calibration.

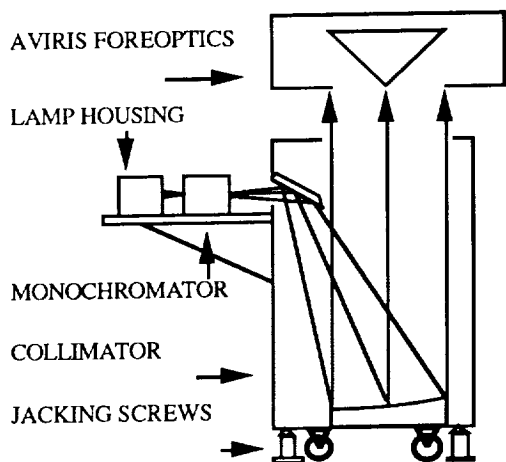


Figure 2. Spectral calibration stimulus alignment under AVIRIS.

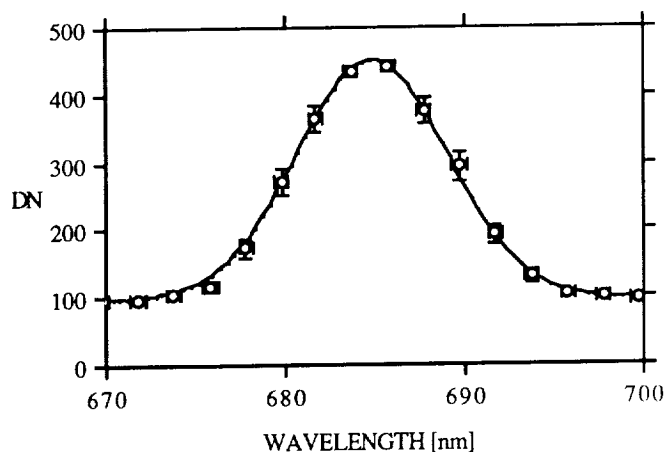


Figure 3. Spectral response function of channel A030.

AVIRIS spectral calibration is determined by computing a least squares linear fit to the measured spectral channel positions and spectral response functions. From this fit, the spectral calibration of all 224 channels is interpolated. Accuracy of the interpolated bands is computed using the procedure discussed earlier. Figure 4 shows the residual wavelength error after the linear fit is applied to the data from spectrometers A, B, C, and D. The error bars represent uncertainty in wavelength of the measured channels as limited by the monochromator calibration. The maximum residual error in the linear fit bounds the accuracy of the fit to unmeasured channels.

3.0 RADIOMETRIC CALIBRATION

Calibration parameters determined through AVIRIS radiometric calibration are: radiometric calibration coefficients, cross-track vignetting corrections, stability estimates, and noise equivalent delta radiance estimates. These calibration

parameters are calculated from AVIRIS data measured over a radiometrically and spectrally calibrated stable integrating sphere. The primary result of radiometric calibration is a file of 137,536 coefficients which calibrate AVIRIS measured DN in 224 channels to units of total spectral radiance corrected for cross-track vignetting.

Performing the radiometric calibration involves the following steps: (1) calibration of the integrating sphere with an irradiance standard, (2) measurement of the AVIRIS instrument DN from the calibrated integrating sphere, (3) computation of the calibration parameters, and (4) calculation of the accuracy.

3.1 Calibration of Integrating Sphere

The radiometric calibration stimulus is a Labsphere 100-cm-diameter integrating sphere with a 40-cm aperture. The sphere is coated internally with barium sulfate paint and illuminated with four, 500-W tungsten halogen lamps. The sphere is calibrated by establishing the ratio between the output of the sphere and a known radiance standard. The radiance standard consists of a lambertian target of known reflectance illuminated by a standard irradiance source at a fixed distance.

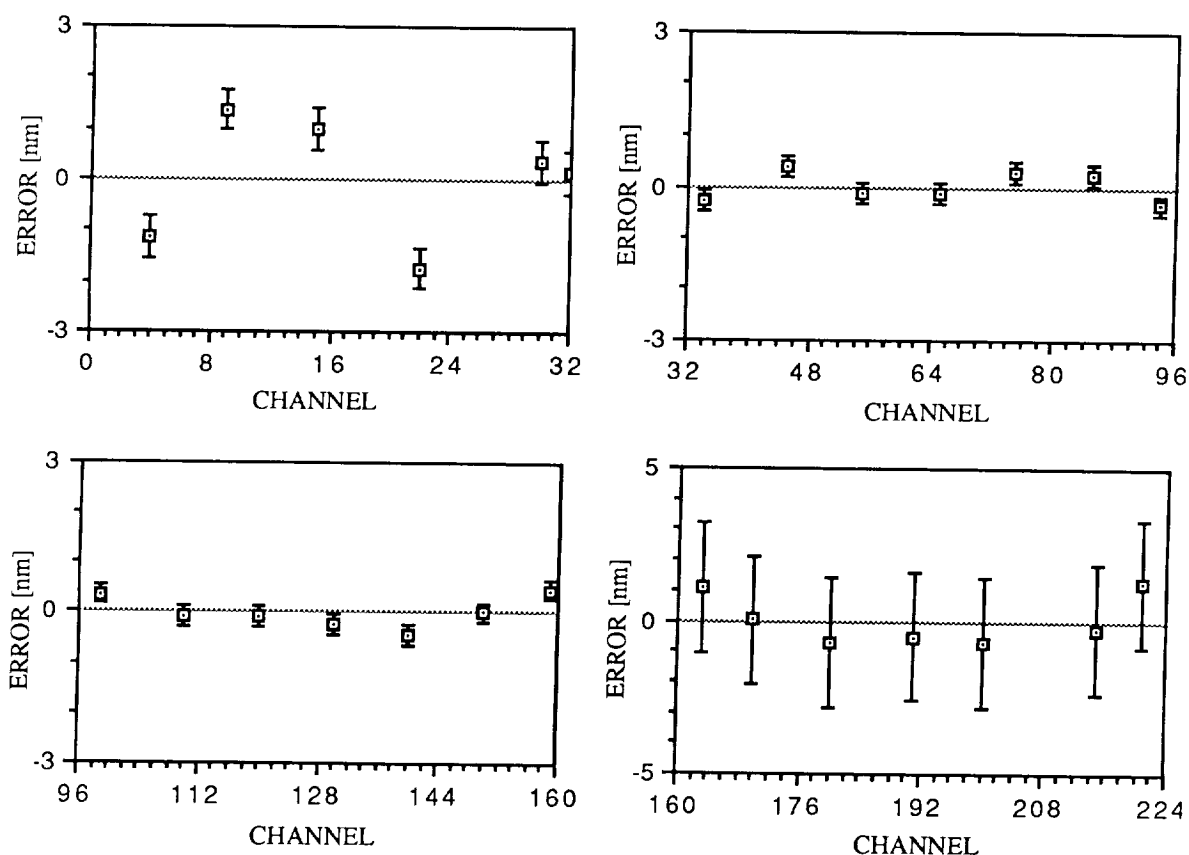


Figure 4. Plots of the residual wavelength error versus channel for the four spectrometers with error bars derived from maximum monochromator calibration uncertainty.

The irradiance standard is an Optronics model 200C, 1000-W, quartz-halogen, tungsten, coiled-coil, filament lamp (S/N S-694) powered by an Optronics model 83 constant current supply. The lamp is purchased along with a calibration report⁹ which is based on the National Bureau of Standards (NBS) 1973, 1986, and 1963 scales of spectral irradiance. Irradiance values given are interpolated to the AVIRIS channel wavelengths with a spline function as shown in Figure 5. Uncertainty in irradiance, shown in Table 4, is taken to be the RSS combination of the stated NBS uncertainty, the transfer uncertainty, and the uncertainty due to a 0.1-percent fluctuation in the 8.00-A current supplied to the lamp.

Table 4. Uncertainty of irradiance standard for various wavelengths.

Wavelength (nm)	NBS Uncertainty %	Transfer Uncertainty %	Current Uncertainty %	RSS % irradiance uncertainty
500	1.18	0.55	0.4	1.4
1000	1.34	0.5	0.35	1.5
1500	1.58	0.5	0.17	1.7
2000	3.29	0.75	0.14	3.4

The reflectance standard is a Labsphere model SRT-99-100 (S/N 2432-D) Spectralon panel. Unlike pressed halon powder, this reflectance panel is easily cleaned and maintained and may be oriented vertically with little risk. A calibration certification¹⁰ is distributed with the panel which lists the 8-deg/hemispherical spectral reflectance factor at 50-nm intervals between the range of 250 to 2500 nm, as measured using an NBS integrating sphere reflectometer. The reflectometer is calibrated using NBS standard reference material 2019a and 2021 ceramic tiles. This reflectance factor is splined to the AVIRIS wavelengths, as shown in Figure 6. Uncertainty in these measurements is given to be 0.5-percent reflectance as provided in the certification.

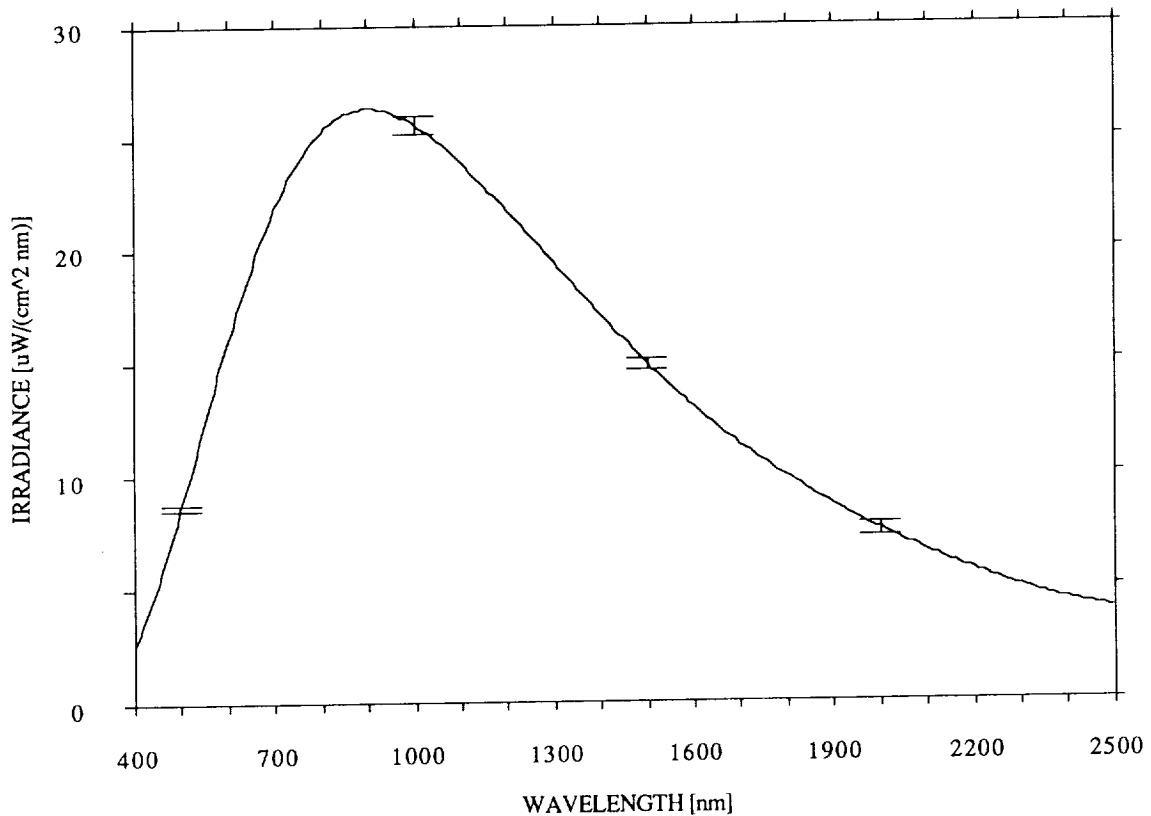


Figure 5. Spectral irradiance of standard lamp as a function of wavelength.

The radiance target geometry is shown in Figure 7. The lamp is located along a line normal to the center of the Spectralon panel at a distance of 50 ± 0.1 cm. The spectral radiance of the target is computed using Equation 1.

$$L(\lambda) = \frac{E(\lambda)R(\lambda)}{\pi} \quad (1)$$

$L(\lambda)$ is the spectral radiance as viewed by the spectroradiometer, $E(\lambda)$ is the lamp irradiance at a distance of 50 cm and $R(\lambda)$ is the reflectance of the reflectance panel. Uncertainty in the absolute radiance of the target is computed using error propagation in equation (1). These uncertainties are given in Table 5. The target spectral radiance is shown in Figure 8, along with the uncertainty in radiance.

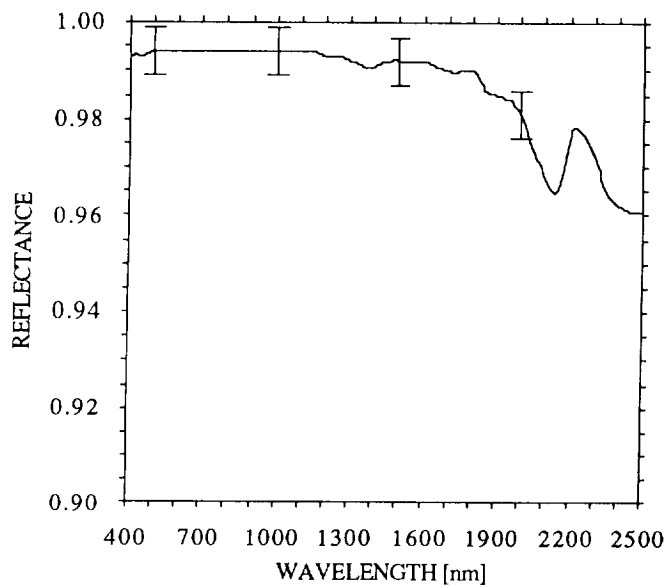


Figure 6. Spectralon 8-deg/hemispherical spectral reflectance factor.

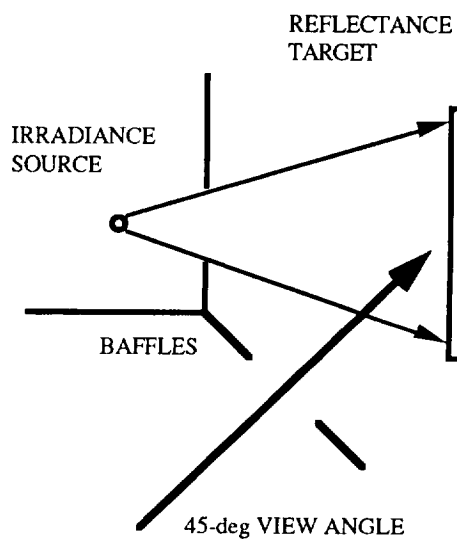


Figure 7. Radiance target geometry.

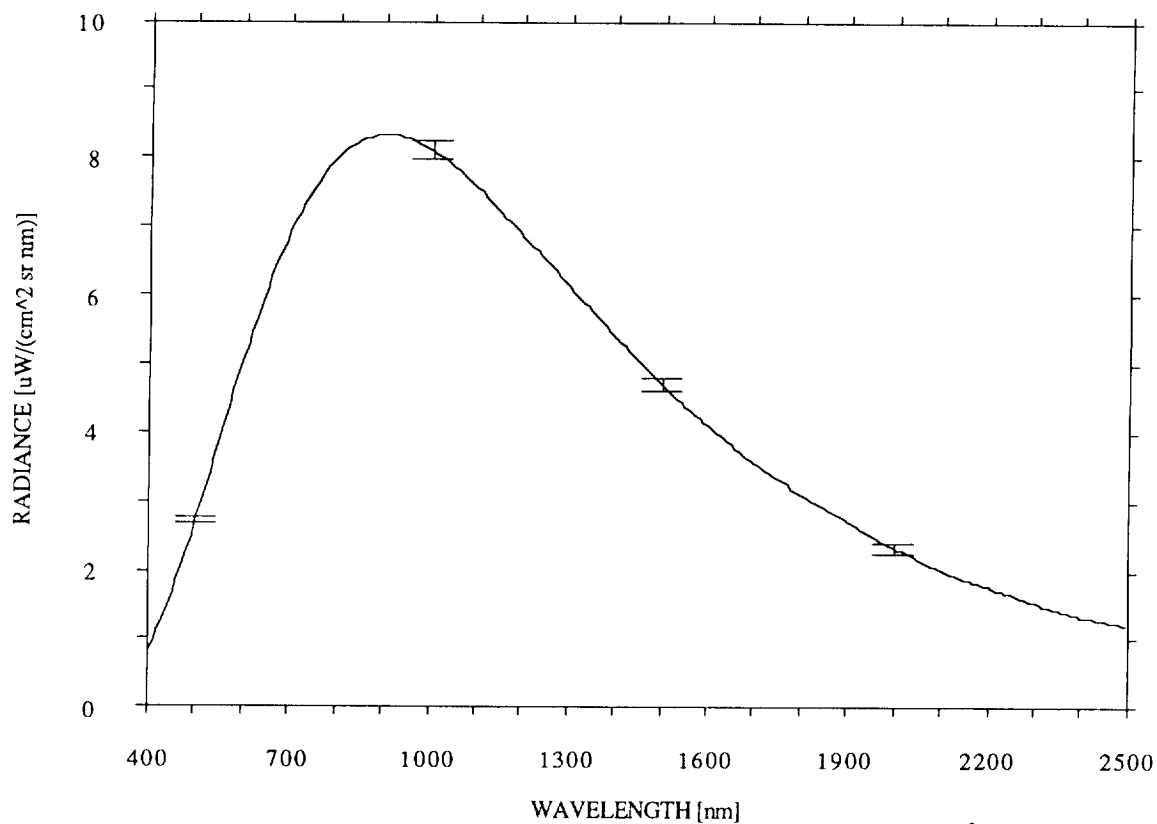


Figure 8. Radiance target spectral radiance as a function of wavelength.

Table 5. Uncertainty of radiance target for various wavelengths.

Wavelength (nm)	Irradiance uncertainty %	Reflectance uncertainty %	Distance uncertainty %	RSS uncertainty %
500	1.36	0.5	0.4	1.50
1000	1.47	0.5	0.4	1.61
1500	1.67	0.5	0.4	1.78
2000	3.38	0.5	0.4	3.44
2500	6.58	0.5	0.4	6.61

3.2 Calibration of the Integrating Sphere

Transfer of radiance calibration from the reference to the integrating sphere stimulus is accomplished using a GER IRIS single-field-of-view portable spectroradiometer¹¹ (S/N JPL-1017.) This spectroradiometer has been modified to provide improved spectral calibration repeatability, data acquisition rate, radiometric stability, and signal-to-noise ratio. For the integrating sphere calibration, the spectroradiometer alternately views the standard radiance target and the integrating sphere over a 5-minute period. The mean ratio of the signal between the two sources is splined to the AVIRIS channel wavelengths, and then multiplied by the spectral radiance of the reference target to determine the spectral radiance of the integrating sphere.

Spectral calibration of the spectroradiometer is performed by recording the spectrum of low pressure krypton emission line lamp. A third-order polynomial is fit between the krypton lines and spectroradiometer channels for each grating to provide a spectral calibration over the 400- to 2450-nm range. Consecutive spectra acquired of the krypton lamp are shown to have less than 1.0-nm spectral calibration error. Both the spectral channel sampling interval and spectral response function FWHM of the spectroradiometer are less than that of AVIRIS. Accuracy of the transfer of radiance from the standard illuminated reference panel to the integrating sphere with the spectroradiometer is shown to be 0.5 percent. This accuracy is determined as the root-mean-squared deviation divided by the mean of five consecutive integrating spheres to radiance standard ratio measurement.

The absorption features and steep slopes present in the integrating sphere as shown in Figure 9 require that this spectrum be measured at a spectral resolution better than AVIRIS. This spectrum is then convolved with the AVIRIS spectral channel positions and response functions FWHM to provide the basis for absolute radiometric calibration. The absorption features at 1400 and 1900 nm are caused by adsorbed water. To eliminate the effect of these features on the calibration, the integrating sphere is warmed up 1 hour prior to calibration. In addition, calibration data for the integrating sphere and AVIRIS illuminated by the integrating sphere are acquired concurrently.

At the time of calibration, the radiance output of the sphere is measured continuously using a broadband, stable silicon photodetector. The results of this monitoring show the sphere/detector combination is stable to better than 1 percent.

Total accuracy of the sphere radiance calibration is determined as the root sum square of the uncertainty in the radiance of the reference source, uncertainty in the transfer of calibration to the sphere including the uncertainty of the spectral calibration of the spectroradiometer, and the stability of the integrating sphere. These uncertainties are shown in Table 6.

Radiometric calibration of AVIRIS proceeds by establishing the stability, the cross-track vignetting corrections, the radiometric calibration coefficients, and the noise-equivalent delta radiance for the 224 spectral channels.

Stability is determined, following a 1-hour instrument and integrating sphere warm-up, through acquisition of 1-minute data sets every half hour over a period of 4 hours. The average of each of these 1-minute samples is formed for the central cross-track sample of each channel for 512 image lines to provide an accurate estimate of the sample mean. From these sample means, the minimum, maximum, and mean DN with dark current subtracted over the 4-hour period are determined. Figure 10 shows the laboratory stability determined as the maximum-minimum divided by the mean for the laboratory calibration. This worst-case analysis shows that most of the AVIRIS spectral channels are stable to better than 3 percent during the 4-hour laboratory calibration period.

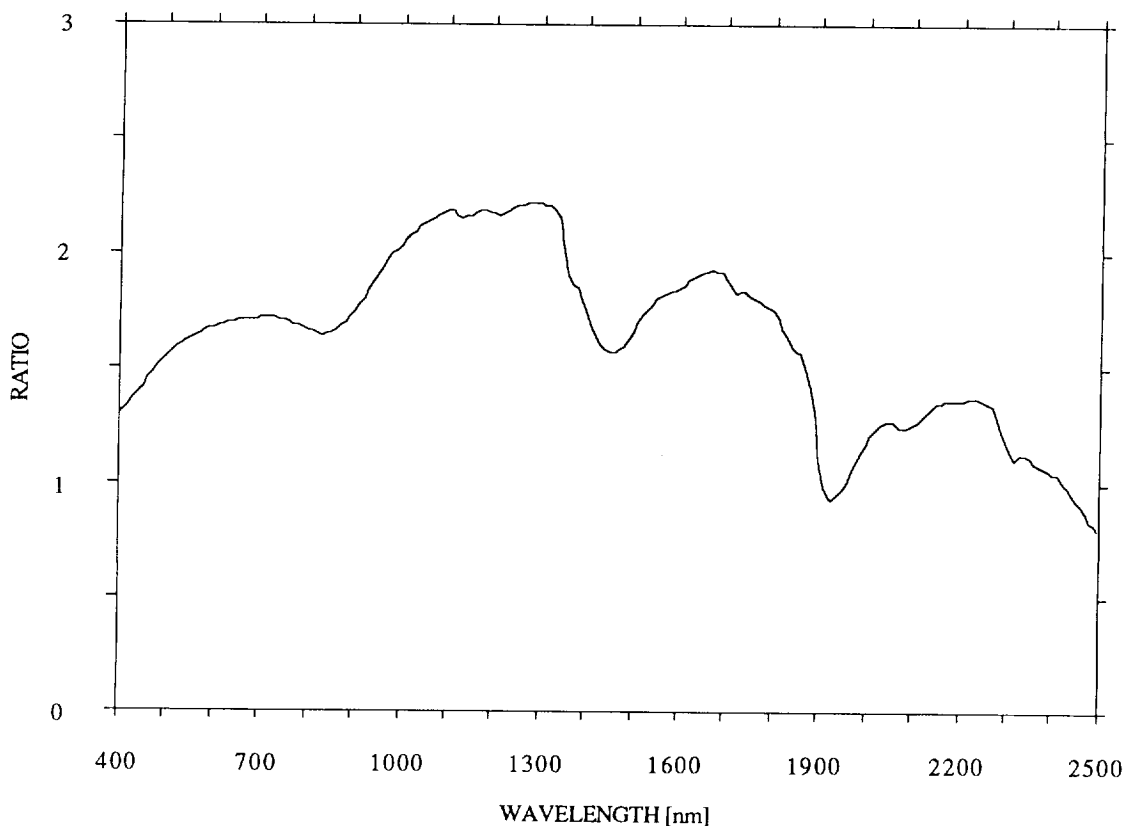


Figure 9. Ratio of the integrating sphere spectral radiance to the target as measured by the GER spectroradiometer.

Table 6. Accuracy of integrating sphere radiance.

Wavelength (nm)	Target uncertainty %	Transfer uncertainty %	Sphere stability %	RSS uncertainty %
500	1.50	0.5	1.0	1.87
1000	1.61	0.5	1.0	1.96
1500	1.78	0.5	1.0	2.10
2000	3.44	0.5	1.0	3.62

3.3 Radiometric Calibration of AVIRIS

Vignetting corrections are calculated for the 224 channels through formation of the mean for 512 lines of image for all cross-track samples. From these data, the dark current is subtracted and each cross-track sample normalized to central cross-track sample. The normalized vignetting profile for the central channel in the AVIRIS B spectrometer is given in Figure 11. Toward the edges of the field of view, vignetting accounts for roughly a 4-percent loss in signal. Calibration coefficients to compensate for vignetting are calculated as the inverse of the vignetting profile for each spectral channel.

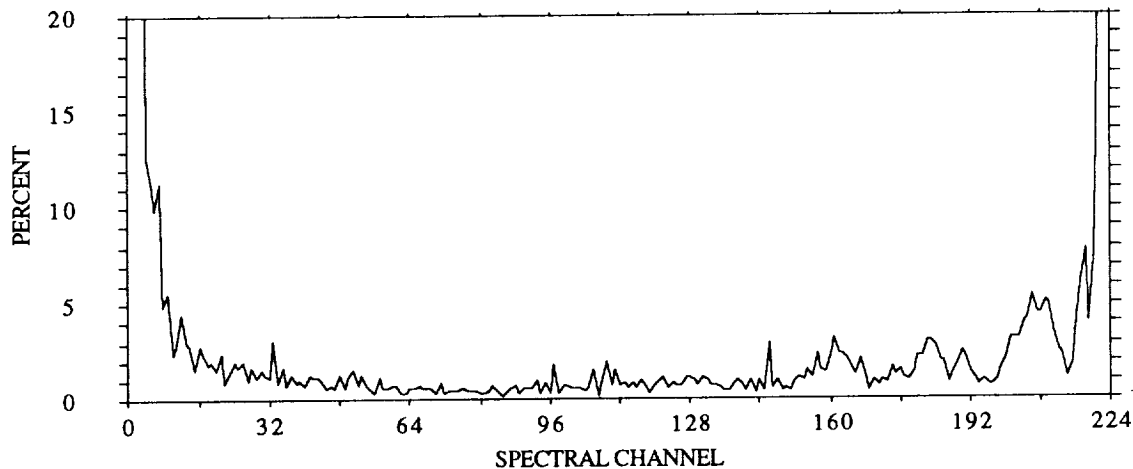


Figure 10. The percent stability of AVIRIS in the laboratory over a 4-hour period.

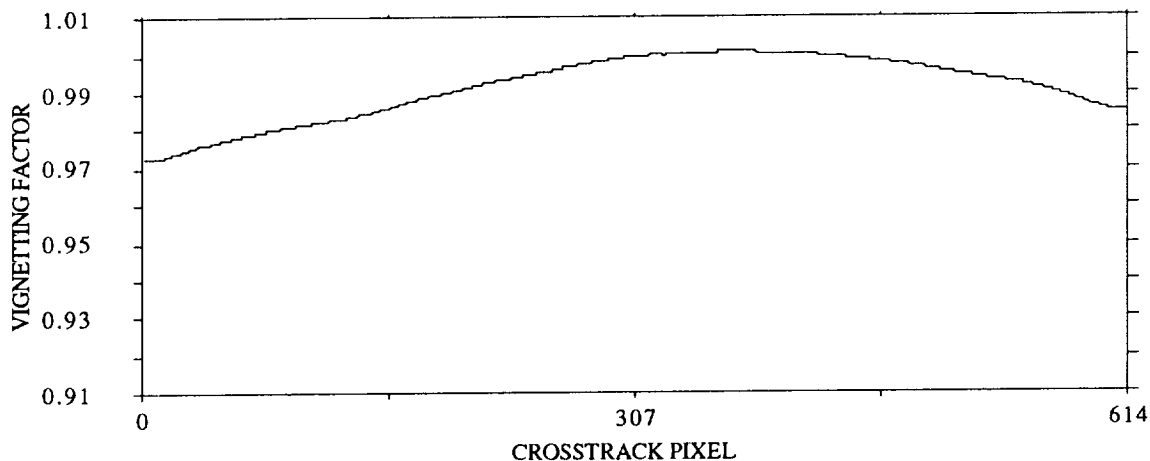


Figure 11. Cross-track vignetting for the central channel of the AVIRIS B spectrometer.

Radiometric calibration coefficients are determined by calculating the ratio of integrating sphere radiance to the mean of AVIRIS dark current subtracted DN acquired over the integrating sphere for the central cross-track sample. These coefficients calibrate AVIRIS reported DN with dark current subtracted to total spectral radiance.

In the laboratory, noise-equivalent delta radiance is calculated to place a precision calibration on AVIRIS-measured data. This quantity is calculated as the root-mean-squared deviation of 100 calibrated radiance spectra measured over the stable integrating sphere. Figure 12 presents the AVIRIS noise-equivalent radiance calculated in the laboratory. The downward-going spikes at channels 33, 97, and 161 are the first channels in spectrometers B, C, and D, respectively, and are not used. The upward-going spikes are the result of noisy detector elements in the C spectrometer array, which has subsequently been replaced.

4.0 CALIBRATION OF AVIRIS DATA

AVIRIS data are calibrated at two levels. First, the DN reported by AVIRIS are corrected for dark current, vignetting, and detector read-out-delay and calibrated to units of total spectral radiance. Second, all determined spectral, radiometric, and geometric characteristics as calculated accuracies and precisions are reported with the data or through publications.

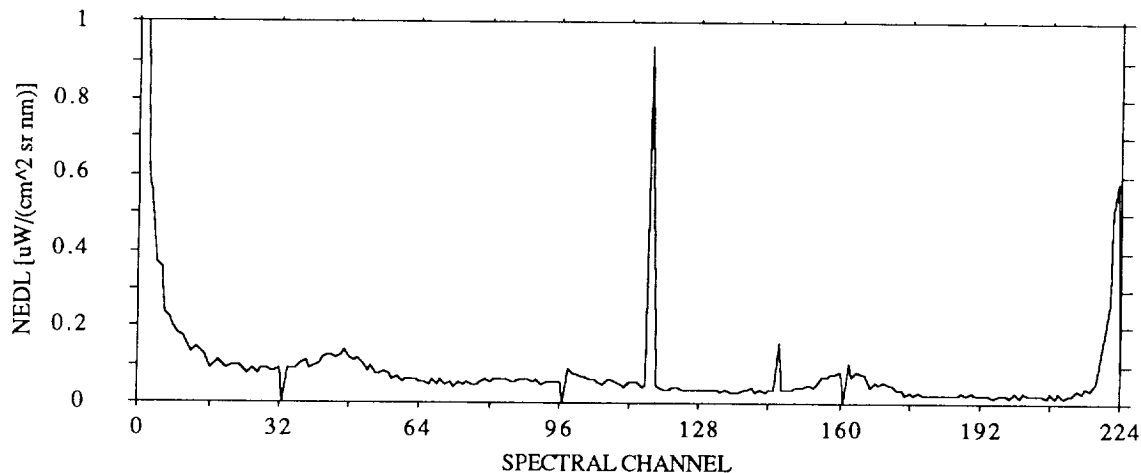


Figure 12. NE Δ L

Calibration of the measured AVIRIS data begins with subtraction of the dark current measured at the end of each image line. A mean of 101 lines of dark current is used to suppress introduction of noise present in the dark-current measurements. Following dark-current subtraction, the cross-track vignetting is compensated. Radiometric calibration coefficients are multiplied against the DN calibrating the data to units of total spectral radiance. Finally, the detector read-out-delay is compensated through a minor spatial resampling of less than one sample in the cross-track direction. These procedures were described initially by Reimer¹², and a more current description is provided by Larson¹³. The measured dark current, vignetting, and radiometric calibration coefficients are provided with each distributed AVIRIS image.

Spectral calibration is reported with each AVIRIS image as the spectral channel position, and response function FWHM for the 224 channels. Absolute radiometric accuracy, stability, and other radiometric parameters are provided in AVIRIS calibration publications. Precision is provided as the noise equivalent delta radiance determined for each AVIRIS image and included with the data. Geometric calibration of AVIRIS is provided through periodically reporting the spatial properties measured in the laboratory.

5.0 ACCURACY OF AVIRIS CALIBRATION

5.1 Accuracy of the Spectral Calibration

While the original AVIRIS functional requirements document specifies a spectral calibration accuracy of ± 5 nm, Green¹⁴ has shown that significant radiometric error is introduced with as little as ± 1 nm wavelength calibration error. This is due to the abundance of steep slopes and sharp absorption features in the terrestrial radiance spectra.

The two main sources of uncertainty in the laboratory calibration are the monochromator output wavelength versus counter position regression, and the center wavelength versus spectrometer channel regression. Table 7 shows the contribution to the maximum center wavelength accuracy for each AVIRIS spectrometer. This table can be used to bound the uncertainties in center wavelength for each of the 224 AVIRIS spectral channels.

In-flight verification of the spectral calibration uses atmospheric absorption features derived from a high-resolution LOWTRAN-7 model¹⁵ as described by Green¹⁶. This technique shows agreement with the laboratory calibration at the ± 2 -nm level.

Table 7. Spectral calibration error.

Spectrometer and spectral range (nm)	Maximum error due to monochromator calibration error (nm)	Maximum error due to spectrometer regression error (nm)
A 400 – 700	0.4	1.7
B 700 – 1200	0.9	0.3
C 1200 – 1800	0.9	0.4
D 1800 – 2450	0.6	1.3

5.2 Accuracy of the Radiometric Calibration

The absolute accuracy of the radiometric response function is estimated as the root sum square of the percent uncertainties in radiance of the integrating sphere and the system response to the integrating sphere. The integrating sphere radiance is shown in Figure 13 where the error bars indicate plus one to minus one sigma of uncertainty. The system response is shown in Figure 14 where error bars equal ± 1 standard deviations of the signal in DN during the calibration. The effects of these two uncertainty factors are RSS together to arrive at the calibration uncertainty in Table 8.

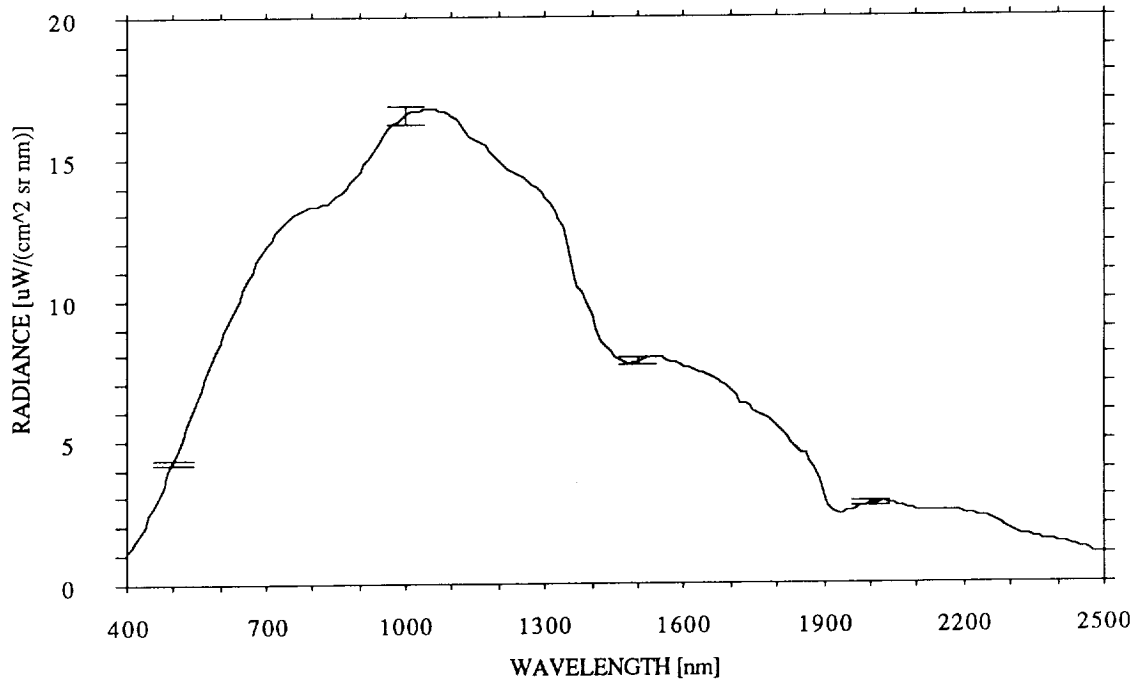


Figure 13. Integrating sphere radiance as a function of wavelength.

Table 8. Percent uncertainty of radiometric calibration.

Wavelength (nm)	Sphere Radiance (%)	Instrument Instability (%)	RSS Uncertainty (%)
500	1.50	2.87	3.24
1000	1.61	0.55	1.72
1500	1.78	0.62	1.96
2000	3.44	1.07	3.71

The percent instrument stability is bounded by the maximum minus the minimum divided by the average instrument response in DN to a constant source during a 2-hour period. Systematic changes in the instrument response between the laboratory and flight conditions are assessed using the in-flight calibration described by Green¹⁷.

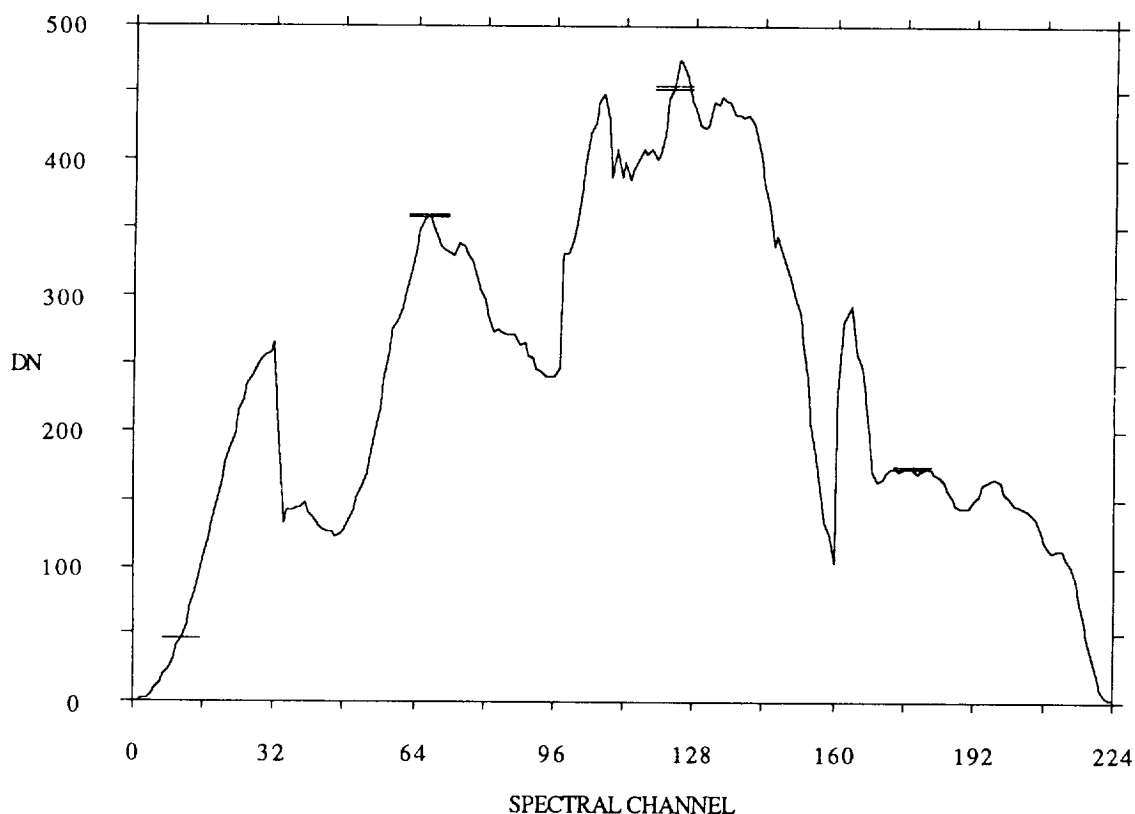


Figure 14. System response to integrating sphere as a function of spectral channel.

6.0 FUTURE PLANS

Future plans include the automation of spectral calibration in order to measure the spectral response function of all 224 channels. This will incorporate an automated monochromator calibration and a correction for intensity variations as a function of wavelength.

An investigation of the uncertainty of NIST (formerly NBS) standards of irradiance and spectral reflectance is also planned to improve the accuracy of the radiometric standards. Polarization and linearity data are currently being analyzed. Further intra- and interday stability tests are planned. A geometric performance assessment of AVIRIS will be repeated after a major refurbishment of the foreoptics and scan-drive mechanism planned for the winter of 1990.

The AVIRIS onboard calibration system, first described by Chrisp¹⁸, has been modified during the spring of 1990. The modifications include a current stabilized power supply, a brighter lamp, and a new routing of the calibration signal. The new system uses a bundle of 32 fibers to illuminate the the backside of the foreoptics shutter. This allows the calibration signal to enter the spectrometer through the data fiber. The performance of these modifications will be closely monitored during the 1990 flight season and the results reported at a later date.

7.0 ACKNOWLEDGMENTS

The authors would like to express their thanks to the many members of the AVIRIS team who have helped to design, maintain, and improve the AVIRIS instrument and ground processing facility. The AVIRIS project is greatly indebted to them for the excellence of their contributions.

The work described in this paper was carried out at the Jet Propulsion Laboratory, California Institute of Technology, under a contract with the National Aeronautics and Space Administration.

8.0 REFERENCES

1. W. M. Porter and H. T. Enmark, "A system overview of the Airborne Visible/Infrared Imaging Spectrometer (AVIRIS)," *Proc. SPIE*, 834, (1987).
2. G. Vane, M. Chrisp, H. Enmark, S. Macenka, and J. Solomon, "Airborne Visible/Infrared Imaging Spectrometer: An advanced tool for earth remote sensing," *Proc. 1984 IEEE Int'l Geoscience and Remote Sensing Symposium*, SP215, 751-757 (1984).
3. G. Vane, T. G. Chrien, E. A. Miller, and J. H. Reimer, "Spectral and radiometric calibration of the Airborne Visible/Infrared Imaging Spectrometer (AVIRIS)," *Proc. SPIE*, 834, (1987).
4. W. M. Porter, T. G. Chrien, E. H. Hansen, and C. M. Sarture, "Evolution of the Airborne Visible/Infrared Imaging Spectrometer (AVIRIS) Flight and Ground Data Processing System," *Proc. SPIE*, 1298, (1990).
5. R. O. Green, J. E. Conel, J. S. Margolis, V. Carrere, C. J. Bruegge, M. Rast, and G. Hoover, "Inflight validation and calibration of the spectral and radiometric characteristics of the Airborne Visible/Infrared Imaging Spectrometer (AVIRIS)," *Proc. SPIE*, 1298, (1990).
6. P. R. Bevington, *Data Reduction and Error Analysis for the Physical Sciences*, 169 pp., McGraw Hill, New York (1969).
7. S. A. Macenka and M. P. Chrisp, "Airborne Visible/Infrared Imaging Spectrometer (AVIRIS): Spectrometer design and performance," *Proc. SPIE*, 834, (1987).
8. H. Sobel, Gaussian fitting routine, AVIRIS design file 150 (JPL internal document).
9. Optronics irradiance standard report (Feb. 1, 1989), Optronics Laboratories, Inc., Orlando Fl.
10. Labsphere reflectance calibration certificate (June 01, 1988), Labsphere, Inc., North Hutton, NH.
11. Geophysical Environmental Research Corp., Milbrook, NY.
12. J. H. Reimer, J. R. Heyada, S. C. Carpenter, W. T. S. Deich, and M. Lee, "AVIRIS ground data-processing system," *Proc. SPIE*, 834, (1987).
13. S. Larson, E. Hansen, and R. O. Green, "The AVIRIS data facility," *Proceedings of the Second AVIRIS workshop*, JPL publication (in press), (1990).
14. *ibid* 5.
15. F. X. Kneizys, E. P. Shettle, G. P. Anderson, L. W. Abrew, J. H. Chetynd, J. E. A. Shelby, and W. O. Gallery, *Atmospheric Transmittance/Radiance; computer code LOWTRAN 7* (in press), AFGL Hanscom AFB, MA, 1989.
16. *ibid* 5.
17. *ibid* 5.
18. M. P. Chrisp, T. G. Chrien, and L. Steimle, "AVIRIS foreoptics, fiber optics, and on-board calibrator," *Proc. SPIE*, 834, (1987).

Determination of the In-Flight Spectral and Radiometric Characteristics of the Airborne Visible/Infrared Imaging Spectrometer (AVIRIS)

Robert O. Green, James E. Conel, Veronique Carrere, Carol J. Bruegge,
Jack S. Margolis, Michael Rast, and Gordon Hoover

Jet Propulsion Laboratory
California Institute of Technology

ABSTRACT

A valid spectral and radiometric calibration of radiance-measuring instruments is required for physically based analysis of the measured data and for quantitative comparison of data acquired from different sites, times, and instruments. AVIRIS is a science-research imaging spectrometer that measures radiance in 224 channels between 400 to 2450 nm in the electromagnetic spectrum. On the 20th of September 1989, a validation and calibration experiment was performed to determine the in-flight spectral and radiometric characteristics of AVIRIS. Five data sets were acquired over a calibration site on the homogeneous playa of Rogers Dry Lake, California. Surface reflectance, atmospheric optical depths, and atmospheric water-vapor measurements were acquired concurrently with the overflights. These in situ measurements were used to constrain the LOWTRAN-7 radiative-transfer code to predict the total spectral radiance incident at the AVIRIS aperture. These predicted radiances and the AVIRIS-measured radiances were analyzed to validate the in-flight characteristics. In-flight spectral channel positions and response functions over the AVIRIS spectral range were derived. Radiometric calibration coefficients were calculated for channel as well as radiometric accuracy, intraflight stability, and noise-equivalent delta radiance. These analyses both validate the laboratory-based calibration and allow direct generation of a valid spectral and radiometric calibration for AVIRIS inflight.

INTRODUCTION

AVIRIS measures total radiance in 224 spectral channels from 400 to 2450 nm in the electromagnetic spectrum. The sampling interval and spectral response function for full width at half maximum (FWHM) is nominally 10 nm over this spectral range. As an example of the spectral and radiometric properties of AVIRIS data, Figure 1 presents a high-spectral-resolution LOWTRAN-7 (Kneizys et al., 1989) spectrum for a surface of 50-percent reflectance at sea level under a 23-km midlatitude summer atmospheric model with a 23.5-degree solar zenith angle. The 10-nm spectral channels used to convolve the high-resolution spectrum to the AVIRIS spectral characteristics and the resulting modeled AVIRIS spectrum are also shown.

AVIRIS data are acquired at a flight altitude of 20 km and at a rate of 7300 spectra per second. The spatial resolution is nominally 20 by 20 m with an image area of 10.5 by up to 100 km. Spectral and radiometric properties of AVIRIS are determined in the laboratory (Chrien et al., 1990) preceding and following each period of operation.

To verify the accuracy of this laboratory calibration, an in-flight validation and calibration experiment was held on the 20th of September 1989 at Rogers Dry Lake, California. This site was selected for the homogeneity of the surface at the AVIRIS spatial scale, the access to radiosonde data acquired regularly at a nearby air force base, and the facilities available for supporting surface and atmospheric measurements. Rogers Dry Lake is located in the Mojave desert approximately 100 km north of Los Angeles, California. Measurements of the surface reflectance, the atmospheric optical depths, and atmospheric

water vapor were acquired concurrently with the AVIRIS overflights. These surface-based measurements were used in conjunction with the LOWTRAN-7 radiative-transfer code to predict at high resolution the total spectral radiance incident at AVIRIS. Through analyses with these modeled radiances and the actual measured radiances, the in-flight spectral-channel positions and spectral-response functions FWHM were determined. With these data, the radiometric accuracy, the intraflight stability, and the noise-equivalent delta radiance (NEdL) were calculated. These in-flight determinations were compared with the laboratory-derived equivalents to both validate and calibrate the AVIRIS characteristics in flight.

AVIRIS CHARACTERISTICS

AVIRIS spectral and radiometric properties were designed primarily from science investigations with the Airborne Imaging Spectrometer (AIS) and with laboratory spectrometer research. The nominal AVIRIS characteristics are given in Table 1. The spectral range of 400 to 2450 nm corresponds to a region in the electromagnetic spectrum where the atmosphere is largely transmissive. Compositional information is contained within this range for the scientific disciplines of ecology, geology, oceanography, atmospheric studies, and snow and ice hydrology. AVIRIS uses four spectrometers with the following nominal ranges: A (400 to 710 nm), B (670 to 1290 nm), C (1250 to 1870 nm), and D (1830 to 2450 nm). Over the entire range, the AVIRIS spectral-channel sampling intervals and the response functions (FWHM) for the 224 channels are nominally 10 nm. In the laboratory, these spectral properties are determined for each channel to better than 2 nm (Chrien et al., 1990).

Table 1. AVIRIS spectral and radiometric characteristics

Spectral	
Wavelength range	400 to 2450 nm
Channel sampling interval	9 to 12 nm
Channel response function	9 to 12 nm
Sampling-interval calibration	≤ 2 nm
Response-function calibration	≤ 2 nm
Radiometric	
Radiometric range	0 to maximum lambertian terrestrial radiance
Radiometric digitization	≥ 1 DN noise
Absolute calibration	$\leq 10.0\%$
Intraflight stability	$\leq 2.0\%$
Noise-equivalent delta radiance	approximately meeting spectral requirement

The radiometric range of AVIRIS is defined such that a 100-percent lambertian reflectance surface with a 0-degree solar zenith angle will not saturate the 1024 bits of digitization. Digitization is set to greater than 1 digitized number (DN) of noise within the constraint of the radiometric range requirement. Absolute radiometric, stability, and vignetting calibrations are established in the laboratory.

A radiometric precision requirement for AVIRIS was initially defined through a signal-to-noise requirement for the AVIRIS reference radiance. A spectrum of the reference radiance is given in Figure 1 and the signal-to-noise requirement in Figure 2. Figure 3 gives the corresponding AVIRIS noise-equivalent delta radiance requirement. NEdL is defined for each AVIRIS channel as the reference radiance divided by the signal-to-noise requirement as in Equation 1. NEdL unambiguously reports the precision in AVIRIS-

measured radiance for each spectral channel. To meet this precision requirement, the AVIRIS NEdL must be less than the NEdL requirement at each channel.

$$\text{NEdL}_{\text{REQ}} = L_{\text{REF}} / \text{SNR}_{\text{REQ}} \quad (1)$$

AVIRIS LABORATORY CALIBRATION

Spectral calibration in the laboratory is carried out by recording the output of a channel as calibrated monochromatic light is scanned across the spectral range of that channel. The resulting normalized curve gives the channel's position and spectral-response function. Nominally, 15 channels are measured in each spectrometer. Spectral characteristics for the entire suite of channels are generated through fitting a second-order polynomial to the measured channels for each spectrometer. The spectral response function of each AVIRIS channel may be accurately modeled by a Gaussian function with the appropriate FWHM. An example of the validity of this approximation is shown in Figure 4 by the agreement between the laboratory-measured response function and the Gaussian-modeled function for channel 150. Distribution of the AVIRIS spectral channels across the spectral range is given in Figure 5. The interpolated spectral response function FWHM for each channel is given in Figure 6. These spectral properties are not uniform across the spectral range; therefore, an accurate calibration is essential.

The importance of spectral calibration for quantitative analysis of data is shown through the retrieval of surface-reflectance spectra from AVIRIS-measured radiance. Surface reflectance is calculated from measured radiance spectra using a radiative-transfer code through constraint of atmospheric and illumination parameters. Figure 7 presents a calibration sensitivity analysis of the spectral-channel position for the recovery of a 25-percent surface reflectance spectrum from a corresponding modeled LOWTRAN-7 radiance spectrum. The reflectance is retrieved with a 0.1-, 1.0-, and 5.0-nm error in the calibration of the spectral-channel positions. As the error in knowledge of the channel position increases, the sharp features and steep slopes of radiance spectrum cause increasingly large errors in the retrieved reflectance. For the case of a 5.0-nm miscalibration, an error in reflectance of 20 percent results through failed compensation for the 1130-nm atmospheric water band. A similar analysis based on an error in calibration of the channel-spectral-response function is given in Figure 8. In the regions of strong atmospheric absorptions, for example the 760-nm oxygen band, a good spectral-response-function calibration is required to accurately retrieve reflectance from measured radiance. These analyses demonstrate the sensitivity of derived parameters, such as spectral reflectance, to the accuracy of spectral calibration.

AVIRIS is radiometrically calibrated in the laboratory by acquiring a large sample of data over an integrating sphere of known spectral radiance. For each channel, the radiance of the integrating sphere is divided by the mean dark-current-subtracted DN to generate the radiometric calibration coefficients. Figure 9 gives the laboratory-determined coefficients determined for the 20th of September 1989. Vignetting characteristics are generated by determining the change in throughput across the scan for all spectral channels. Vignetting calibration coefficients are calculated as the inverse of the scan-center normalized throughput.

Radiometric stability is determined during the laboratory calibration over a period of several hours of AVIRIS operation. Figure 10 gives the percent deviation from the mean for a set of one minute of AVIRIS data samples acquired every half hour during a 4-hour period following a 1-hour warm-up of AVIRIS and the integrating sphere. AVIRIS is stable at the 1-percent level in the laboratory over most of the spectral range. Lower

apparent stability at the short- and long-wavelength ends of the range are attributable to the extreme low intensity of the integrating sphere radiance in these spectral regions.

Noise is calculated as the root-mean-squared deviation (RMSD) of a sample of 100 spectra measured from the stabilized integrating-sphere radiance source. An equally valid method for calculating the noise is to form the RMSD of 100 samples of AVIRIS dark-current data, which represent a stable dark source. Figure 11 gives the noise calculated using both of these methods.

Radiometric precision or NE Δ L is calculated by multiplying the DN noise by the radiometric calibration coefficients. This NE Δ L is the precision-based uncertainty for AVIRIS-measured radiance. Figure 12 gives the NE Δ L calculated in the laboratory as a function of wavelength and is compared to the AVIRIS requirement. This graph shows AVIRIS to have greater precision than required over most of the spectral range.

IN-FLIGHT CALIBRATION EXPERIMENT MEASUREMENTS

To validate the laboratory calibration of AVIRIS data acquired in flight, a reflectance-based calibration experiment was performed at Rogers Dry Lake, California. A homogeneous calibration site of 200 by 20 meters, corresponding to a line of 10 AVIRIS spatial samples, was located and marked on the playa surface with large dark tarps. Surface reflectance of this site across the AVIRIS spectral range was measured at the time of the AVIRIS overflights. The field spectrometer used has a spectral-interval-sampling and response function of less than 5 nm and an approximate 10-cm circular field of view at 1 m. The mean spectral reflectance of the 80 measurements acquired bounded by the RMSD is given in Figure 13.

At a site adjacent to the playa, atmospheric measurements were acquired concurrently with the AVIRIS overflights. A stable solar radiometer with 10 discrete channels with nominal 10-nm spectral-response functions, FWHM, was used to measure solar illumination through the atmosphere. These data were acquired from sunrise to local solar noon on the day of the experiment. Using the Langley plot method (Bruegge, 1985), these data were reduced to atmospheric optical depths. The spectral-channel positions and calculated optical depths are given in Table 2. Vertical-column water vapor was calculated directly from the solar radiometer measurements using the 940-nm channel (Reagan et al., 1987 and Bruegge et al., 1990). A value of 6 mm of precipitable water vapor was derived for the time of AVIRIS overflights. This value agreed with a continuum-interpolated-band-ratio estimate derived directly from the AVIRIS radiance data. This water-vapor retrieval algorithm is described by Green, et al., 1989.

Table 2. Channel positions and derived optical depths from the solar radiometer

20 September 1989, Rogers Dry Lake, California

Channel No.	1	2	3	4	5	6	7	8	9	10
Position (nm)	370	400	440	520	610	670	780	870	940	1030
Optical Depth	.539	.398	.288	.174	.128	.082	.049	.046	.284	.028

PREDICTED AVIRIS RADIANCE

AVIRIS overpasses of the calibration site occurred at 18:28, 18:44, 18:59, 19:14, and 19:29 universal coordinated time (UCT). A LOWTRAN-7 model was used to compute the total incident radiance at the AVIRIS aperture for each overpass. These calculations were constrained by the surface reflectance, optical depth, and water vapor measured at the time the AVIRIS data were acquired. The LOWTRAN-7 code was run at the highest spectral sampling interval, which is better than that of AVIRIS in the range of 400 to 2450 nm. Model spectra were convolved to the AVIRIS spectral-sampling intervals and response function measured in the laboratory. These five LOWTRAN-7 total spectral-radiance curves are shown in Figure 14. The increase in radiance for consecutive spectra results from the decrease in the solar zenith angle as the overpass times approach local solar noon.

REPORTED AVIRIS RADIANCE

AVIRIS data acquired over the Rogers Dry Lake calibration site were calibrated to radiance by application of the laboratory calibration coefficients. The calibrated data acquired over the calibration site at Rogers Dry Lake on the 20th of September 1989 are shown in Figure 15. Excellent agreement is observed between the LOWTRAN-7-predicted and the AVIRIS-measured spectral radiances.

SPECTRAL VALIDATION AND CALIBRATION

Validation of the in-flight spectral properties of AVIRIS is based on a least-squared-error minimization algorithm operating on the high-spectral-resolution LOWTRAN-7-modeled radiance and the AVIRIS-measured radiance. The algorithm begins with a modeled high-resolution spectrum for an atmospheric absorption band and the corresponding AVIRIS-measured radiance spectrum. A least-squared-error fit is derived for the in-flight spectral characteristic that results in the best agreement between the LOWTRAN-7-modeled and AVIRIS-measured spectrum. An in-flight spectral-channel-position and response-function FWHM is returned for each atmospheric absorption band examined. This approach to in-flight spectral calibration was initially implemented graphically for AIS (Conel et al., 1987); an improved computational procedure was implemented for AVIRIS data (Green et al., 1988).

The root-mean-squared-error calculations fitting the 940-nm atmospheric water band for spectral-sampling-interval and response-function FWHM are shown in Figures 16 and 17. The in-flight spectral-sampling interval is best fit with a 0.5-nm channel shift to shorter wavelengths relative to the laboratory calibration. The in-flight spectral-response FWHM is optimized with a 0.4-nm broadening of the response function measured in the laboratory. Figure 18 shows the resulting fit between AVIRIS and LOWTRAN-7 spectra for this atmospheric-absorption band.

This algorithm was applied to 10 atmospheric absorption bands across the AVIRIS spectral range. In Table 3, the results of this validation are given as the deviation of the laboratory-calculated spectral-channel positions and response functions from the in-flight-determined spectral characteristics. Atmospheric-absorption bands were examined in each of the four AVIRIS spectrometers. For these bands, the laboratory channel-position calibration is shown to be valid to within 2 nm. The spectral-response functions determined in the laboratory also agree with those determined in flight at the 2-nm level, with exception of the 1130-nm water band. The anomalous result for this band is attributed to a discrepancy in the laboratory radiometric calibration in this spectral region and not to an actual broadening of the response function (Chrien et al., 1990). With the determination of the spectral-channel-sampling interval and response function at points across the AVIRIS

spectral range, a complete in-flight spectral calibration may be generated by fitting functions to these data over the range of each spectrometer.

Table 3. Spectral-validation results for atmospheric-absorption bands in each of the AVIRIS spectrometers. Deviation of the laboratory spectral-channel position and response function is given with respect to the in-flight determination.

20 September 1989, Rogers Dry Lake, California

AVIRIS SPECTROMETER	BAND	POSTION (nm)	POSITION (nm) DEVIATION	RESPONSE (nm) DEVIATION
A	H2O	695	+0.5	-0.5
B	H2O	725	+1.0	-0.3
B	O2	765	+0.5	+0.0
B	H2O	940	+0.5	+0.4
B	H2O	1130	+0.0	+5.9
B	O2	1265	-1.0	+0.0
C	CO2	1570	+0.0	-0.7
C	CO2	1605	+1.0	-0.7
D	CO2	2005	+0.0	-1.9
D	CO2	2055	-2.0	-1.8

RADIOMETRIC VALIDATION AND CALIBRATION

An estimate of the accuracy of the radiometric calibration is derived through a comparison of the AVIRIS radiance spectrum and the LOWTRAN-7 predicted radiance for the calibration site, accepting the LOWTRAN-7 radiance as the standard of comparison. The percent deviation of the AVIRIS-measured spectrum from the LOWTRAN-7-modeled spectrum is given in Figure 19. Across the spectral range, with exception of the regions of strong atmospheric water absorption at 1400, 1900, and 2500 nm, AVIRIS agrees to within 10% of the LOWTRAN-7 model. Disagreement in the 1100-nm regions is attributed to an error in the laboratory determination of the integrating-sphere radiance. An improved method for integrating-sphere calibration has been implemented in 1990 (Chrien et al., 1990). For data acquired in 1990, the modified onboard calibrator should provide information for a further improvement in the absolute radiometric calibration of AVIRIS. Investigations of the accuracy of LOWTRAN-7 and other radiative-transfer codes are also essential for improved validation of the in-flight accuracy of imaging spectrometer radiance spectra.

Through a ratio of the LOWTRAN-7 predicted radiance to the AVIRIS DN with dark current subtracted, the in-flight radiometric calibration coefficients were generated for each channel. These are shown in Figure 20. These radiometric calibration coefficients agree at the 10% level with those measured in the laboratory.

To establish the radiometric stability of AVIRIS in flight, variation in the measured radiance data from the five overpasses of the calibration site was analyzed. LOWTRAN-7 radiance spectra were used to normalize the data for the differing illumination and

atmospheric parameters resulting from the different times of data acquisition. The RMSD of the five AVIRIS spectra was calculated as an estimate of the variation and divided by the mean of the spectra. This provides an estimate of the intraflight radiometric uncertainty and is given in Figure 21. For the 1.5-hour period over which the data were acquired, AVIRIS was stable at the level of 2%.

In-flight NEdL was calculated as the product of the DN noise and the radiometric calibration coefficients. In-flight noise for AVIRIS is calculated both as the RMSD of the data over the homogeneous calibration site and as the RMSD of the dark-current values measured at the end of each AVIRIS image line. Noise estimates calculated by these methods are given in Figure 22. Calculation of in-flight noise from the end-of-line dark-current measurements offers a method of determining the AVIRIS noise without the presence of a large homogeneous ground target; this method avoids the influences of inhomogeneous target reflectance and atmosphere. The NEdL for this calibration experiment is given in Figure 23 along with the NEdL requirement. As in the laboratory, AVIRIS is meeting the requirement over most of the spectral range from 400 to 2450 nm.

CONCLUSION

Through an in-flight calibration experiment at Rogers Dry Lake, California, on the 20th of September 1989, the spectral and radiometric properties of AVIRIS were determined. In-flight spectral-channel positions and spectral-response functions in 10 regions of the AVIRIS spectral range, encompassing all four spectrometers, are shown to agree closely with the corresponding parameters measured in the laboratory. These results provide the basis for direct generation of an in-flight spectral calibration of AVIRIS. The radiometric calibration coefficients determined in the laboratory agree to better than 10% with the in-flight determination over most of the spectral range. Greater disagreement occurs in spectral regions of low atmospheric transmittance. The intraflight stability for the Rogers Dry Lake calibration site is better than 2% with exception of the strong atmospheric water absorptions, where the measured radiance is close to zero. This result is consistent with the laboratory determination of stability over several hours. A NEdL determination for the in-flight calibration corresponds closely to the laboratory calculation. This experiment has provided both validation of the laboratory calibration and direct generation of calibration parameters for the in-flight spectral and radiometric characteristics.

ACKNOWLEDGEMENTS

This research was carried out at the Jet Propulsion Laboratory, California Institute of Technology, under contract with the National Aeronautics and Space Administration. Thanks to Bill Tibbitts for his ongoing and extraordinary logistical support at Rogers Dry Lake, California.

REFERENCES

- Bruegge, C.J., *In-Flight Absolute Radiometric Calibration of the Landsat Thematic Mapper* (Published under Kastner), Ph.D. Dissertation, University of Arizona, 1985.
- Bruegge, C.J., J.E. Conel, J.S. Margolis, R.O. Green, G. Toon, V. Carrere, R.G. Holm, and G. Hoover, "In-situ atmospheric water-vapor retrieval in support of AVIRIS validation," *SPIE*, Vol. 1298, *Imaging Spectroscopy of the Terrestrial Environment*, 1990.

Chrien, T.G., R.O. Green, and M. Eastwood, "Laboratory spectral and radiometric calibration of the Airborne Visible/Infrared Imaging Spectrometer (AVIRIS)," *SPIE*, Vol. 1298, *Imaging Spectroscopy of the Terrestrial Environment*, 1990.

Conel, J.E., R.O. Green, G. Vane, C.J. Bruegge, and R.E. Alley, "AIS-2 radiometry and a comparison of methods for the recovery of ground reflectance," in *Proceedings of the Third Airborne Imaging Spectrometer Data Analysis Workshop*, G. Vane, Ed., JPL Publication 87-30, Jet Propulsion Laboratory, Pasadena, CA, pp. 18-47 (1987).

Green, R.O., G. Vane, and J.E. Conel, "Determination of aspects of the in-flight spectral, radiometric, spatial and signal-to-noise performance of the Airborne Visible/Infrared Imaging Spectrometer over Mountain Pass, Ca.," in *Proceedings of the Airborne Visible/Infrared Imaging Spectrometer (AVIRIS) Performance Evaluation Workshop*, JPL Publication 88-38, Jet Propulsion Laboratory, Pasadena, CA, pp. 162-184, 1988.

Green, R.O., V. Carrere and J.E. Conel, "Measurement of atmospheric water vapor using the Airborne Visible/Infrared Imaging Spectrometer," *ASPRS, Image Processing '89*, 1989.

Kneizys, F.X., E.P. Shettle, G.P. Anderson, L.W. Abrew, J.H. Chetwynd, J.E.A. Shelby, and W.O. Gallery, *Atmospheric Transmittance/Radiance; Computer Code LOWTRAN 7* (in press), AFGL Hanscom AFB, MA., 1989.

Reagan, J.A., K. Thome, B. Herman, and R. Gall, "Water vapor measurements in the 0.94 micron absorption band: calibration, measurements and data applications," *Proc. IGARSS*, Ann Arbor, pp. 18-21, May 1987.

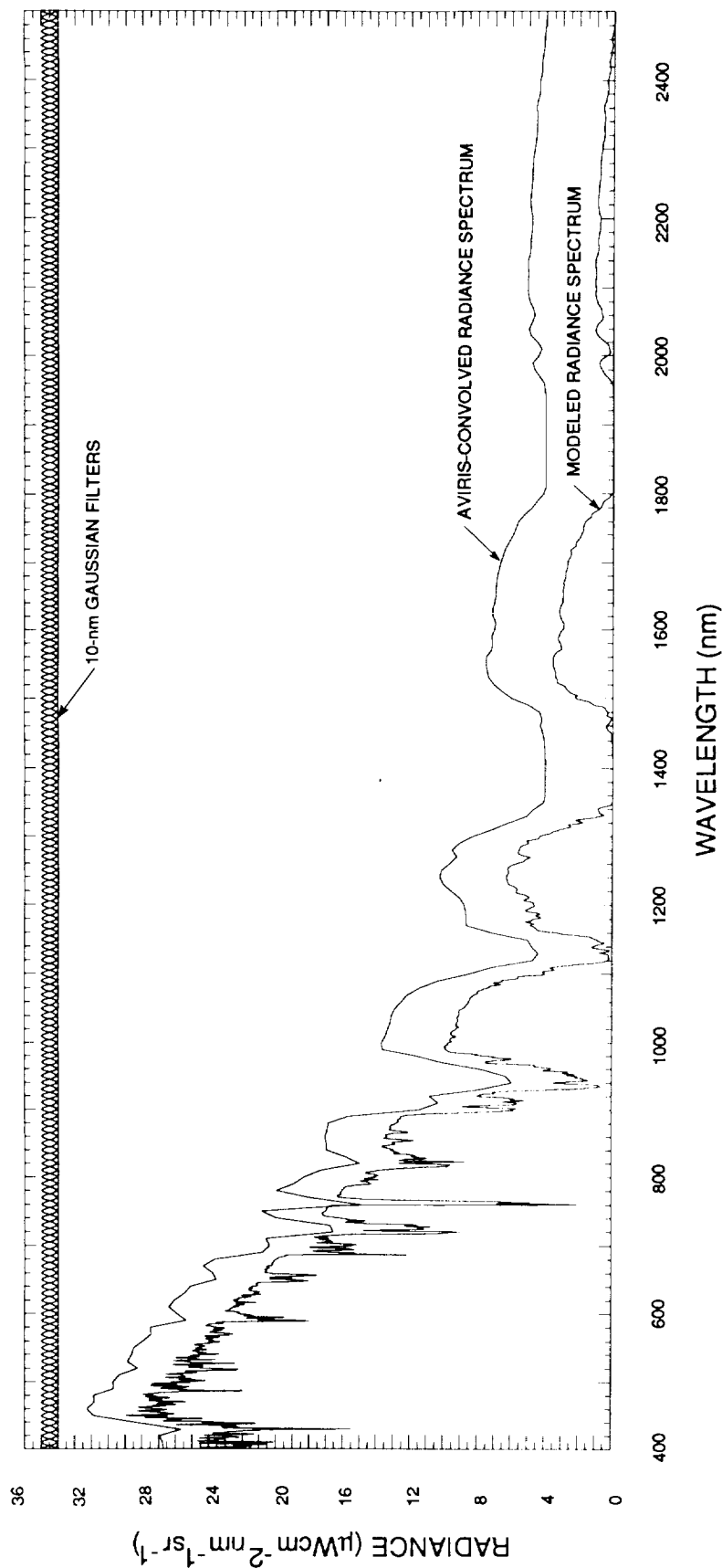


Figure 1. Full-resolution LOWTRAN-7-modeled spectrum, modeled AVIRIS nominal Gaussian filters, and the convolved AVIRIS-modeled spectrum. The AVIRIS spectrum has been offset vertically by 5 radiance units. Constraints on the LOWTRAN-7 model define the AVIRIS reference radiance. The constraints are a 50-percent-reflectance surface, under the 23-km midlatitude summer atmosphere, at local solar noon, on the summer solstice, at 45 degrees north latitude, and at sea level.

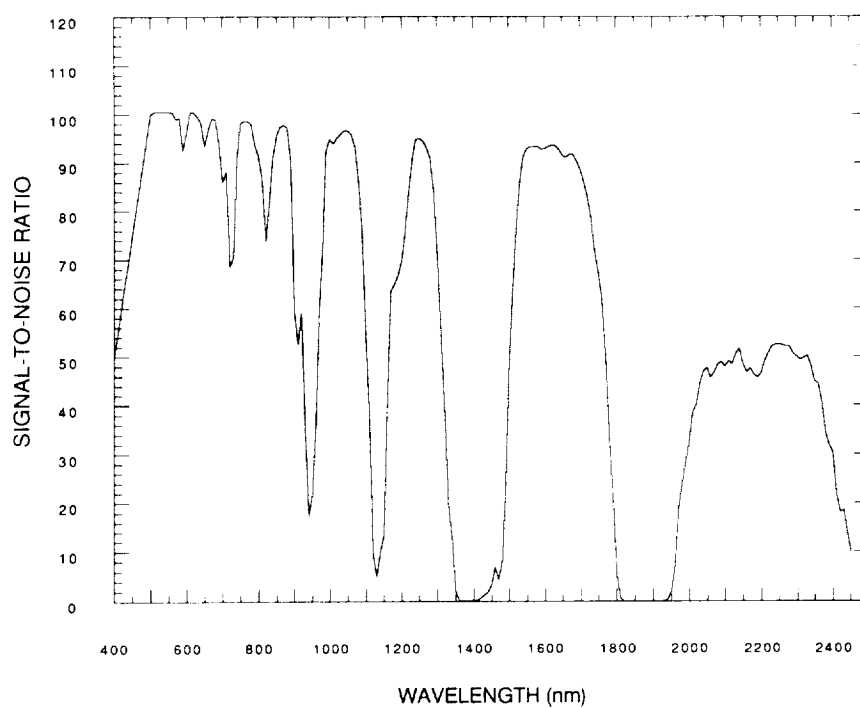


Figure 2. AVIRIS signal-to-noise requirement at the reference radiance level.

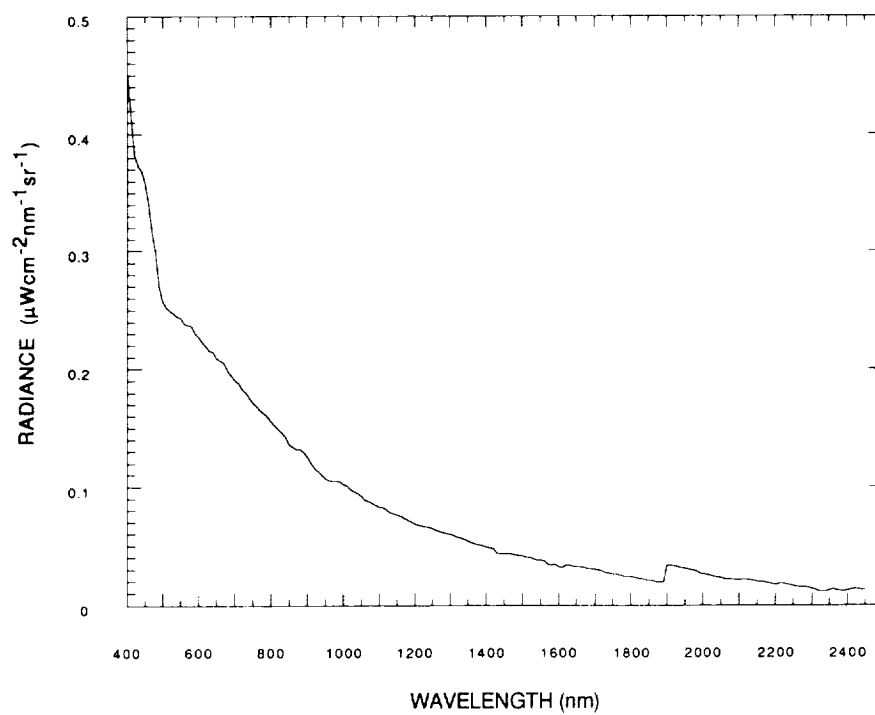


Figure 3. Noise-equivalent delta radiance requirement for AVIRIS calculated as the reference radiance divided by the signal-to-noise requirement.

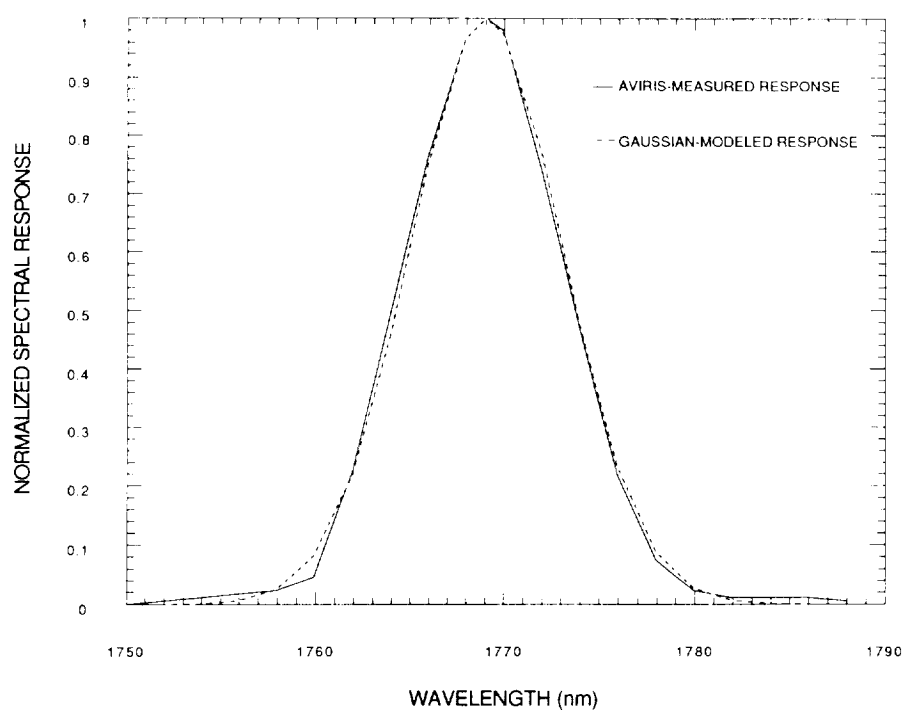


Figure 4. AVIRIS-measured and Gaussian-modeled spectral-response function FWHM for channel 150.

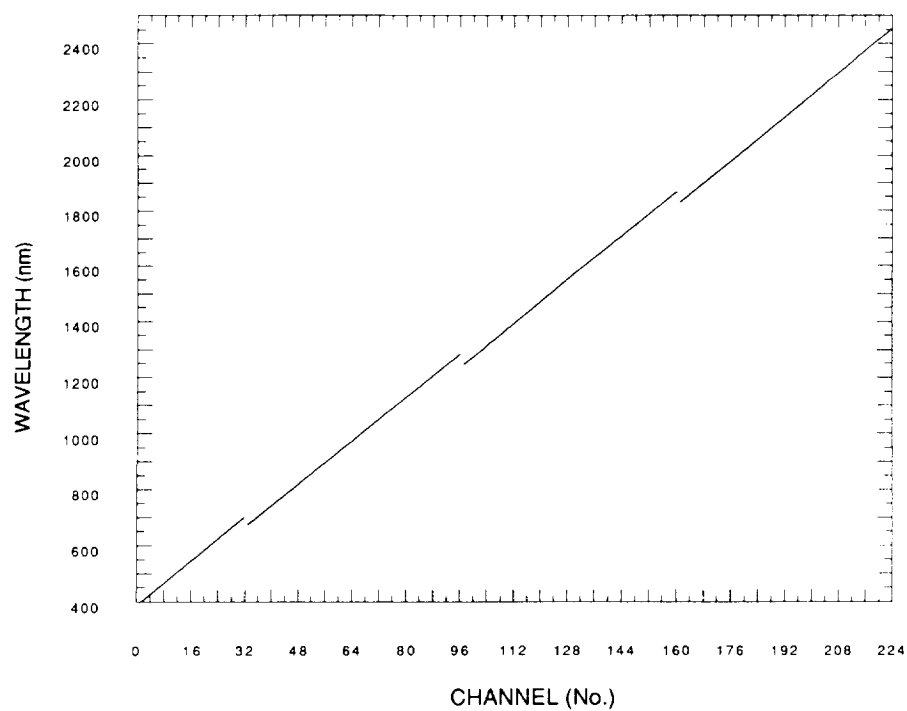


Figure 5. AVIRIS spectral-channel sampling from 400 to 2450 nm.

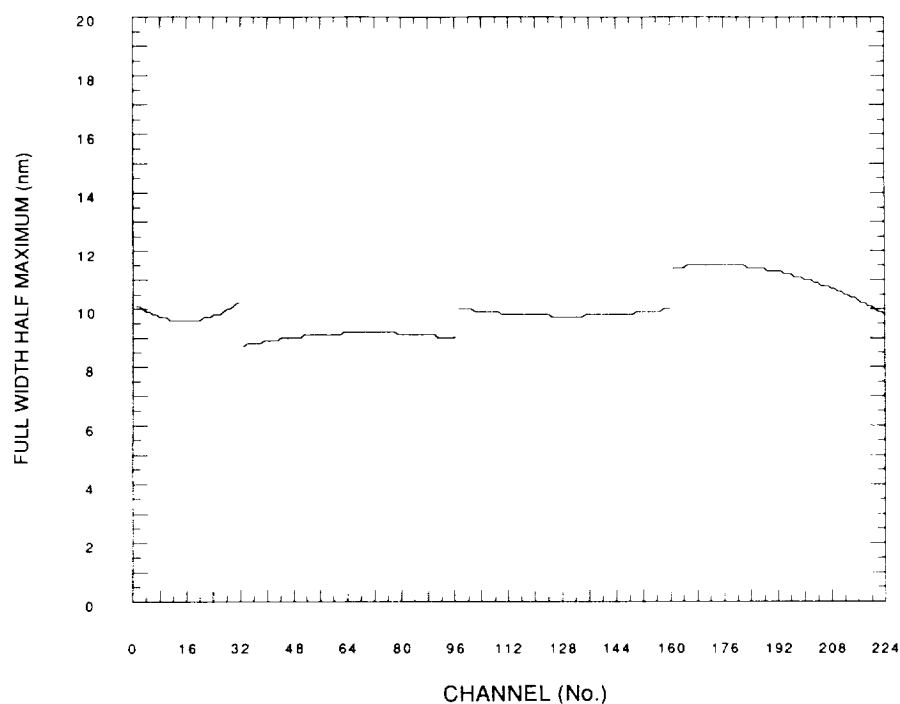


Figure 6. Spectral-channel response functions FWHM for the AVIRIS spectral range.

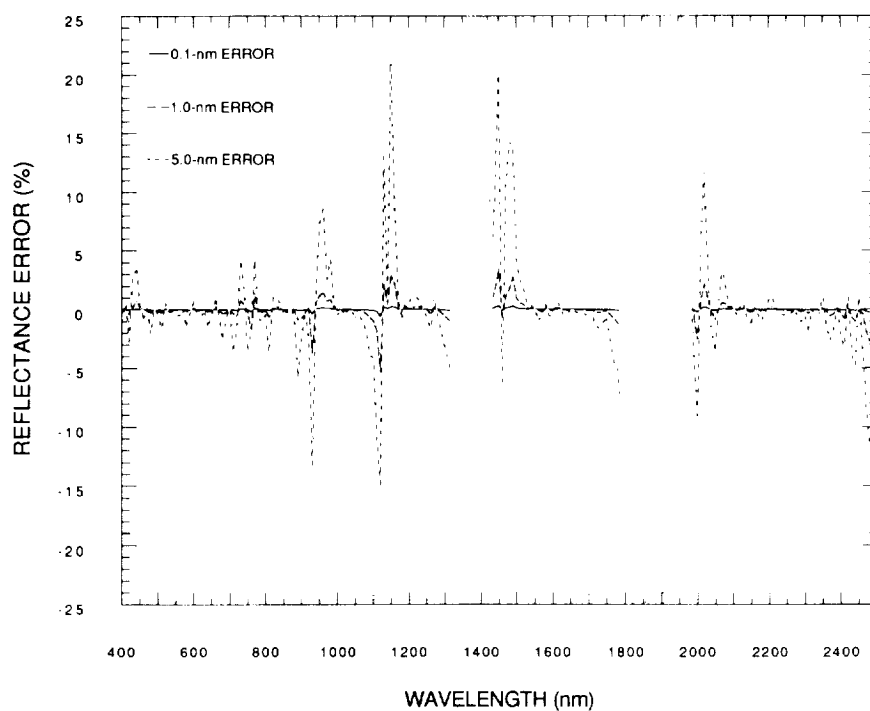


Figure 7. Sensitivity of radiative-transfer-based reflectance retrieval to spectral-channel position calibration. The analysis was based on a LOWTRAN-7 model of a lambertian, horizontal, 25-percent reflectance surface at sea level with the 23-km midlatitude summer atmosphere.

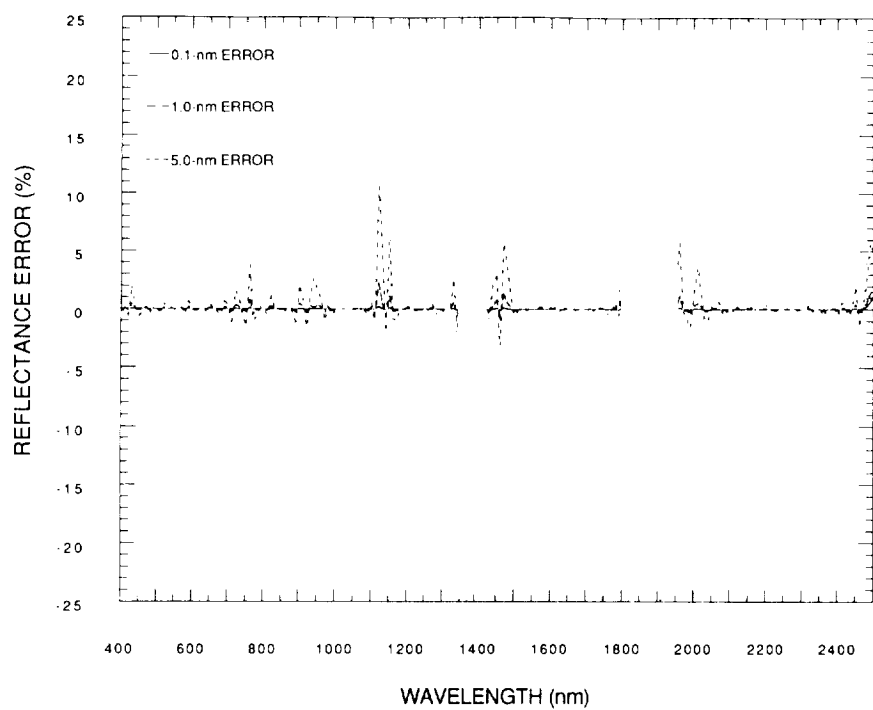


Figure 8. Sensitivity of radiative-transfer-based reflectance recovery to channel-response-function FWHM calibration.

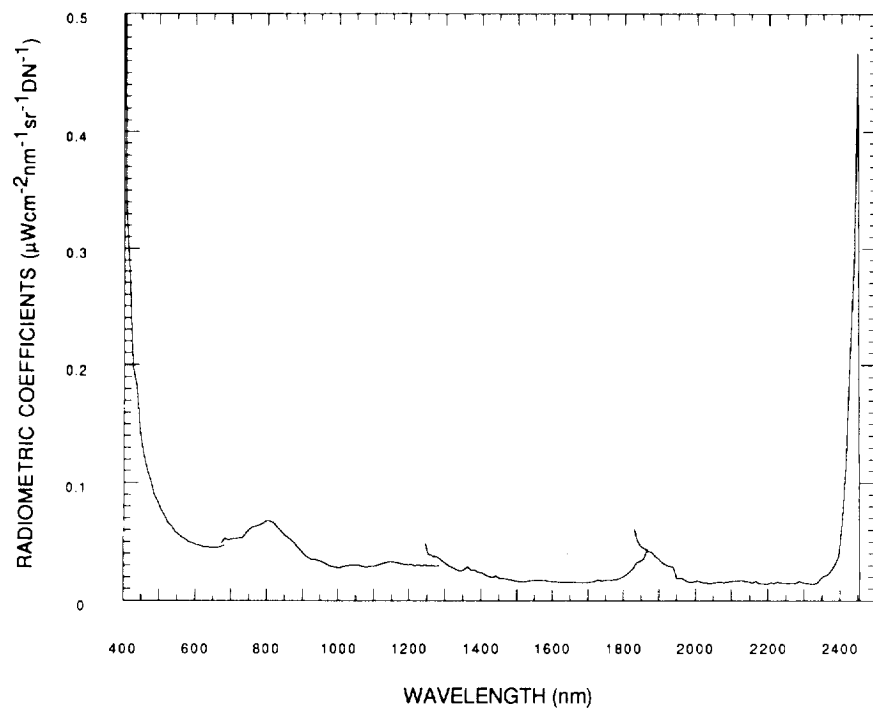


Figure 9. AVIRIS radiometric calibration coefficients determined in the laboratory for the 20th of September 1989 operational period.

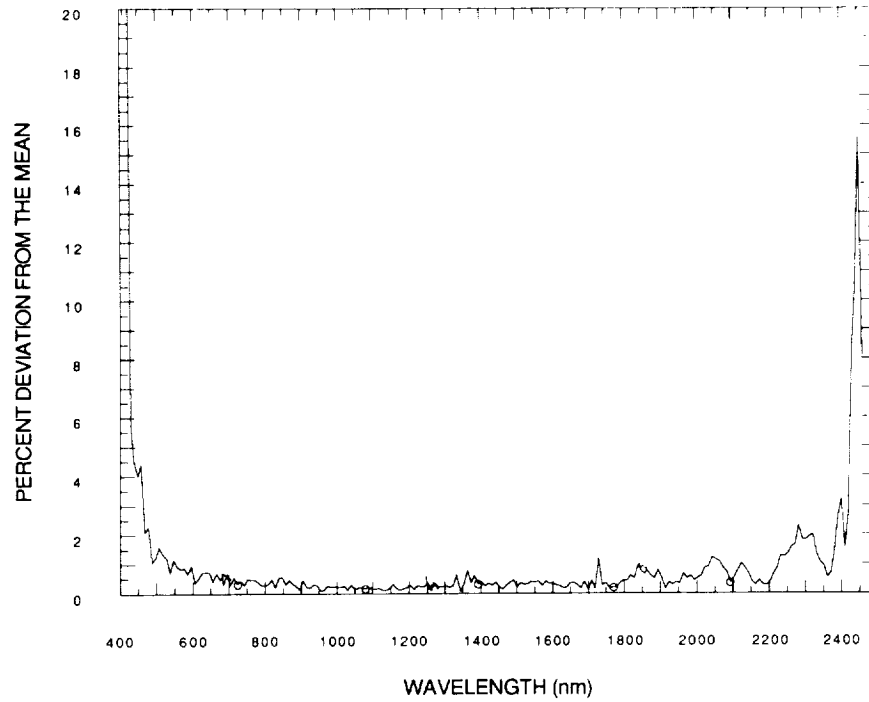


Figure 10. Radiometric stability of AVIRIS over 5 hours during the laboratory calibration.

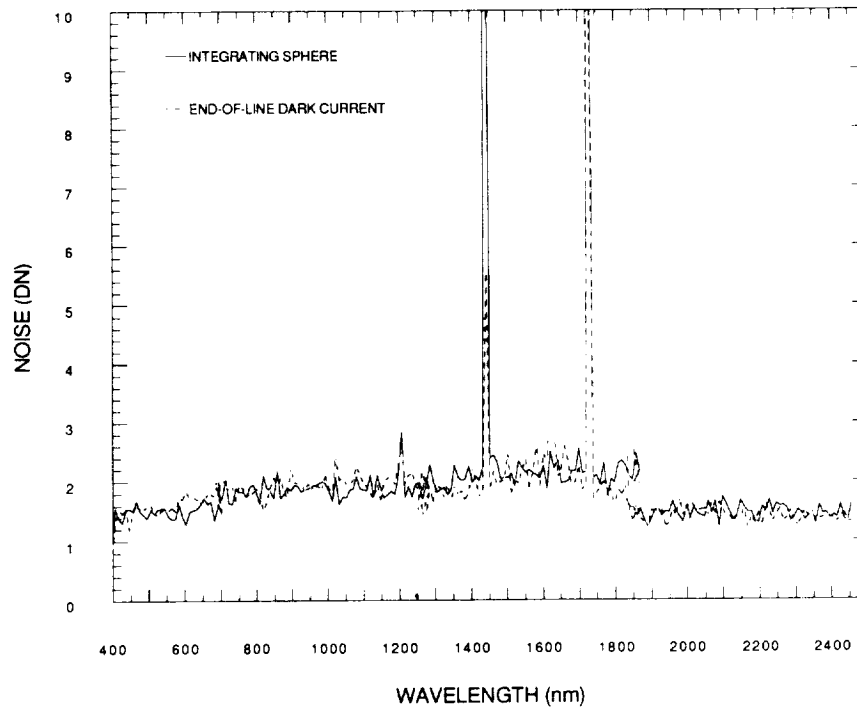


Figure 11. AVIRIS noise calculated both as the RMSD of data acquired over the laboratory integrating sphere and as the RMSD of the dark-current values measured at the end of each AVIRIS image line. In 1989, inherently noisy detector elements were present at 1442 and 1729 nm.

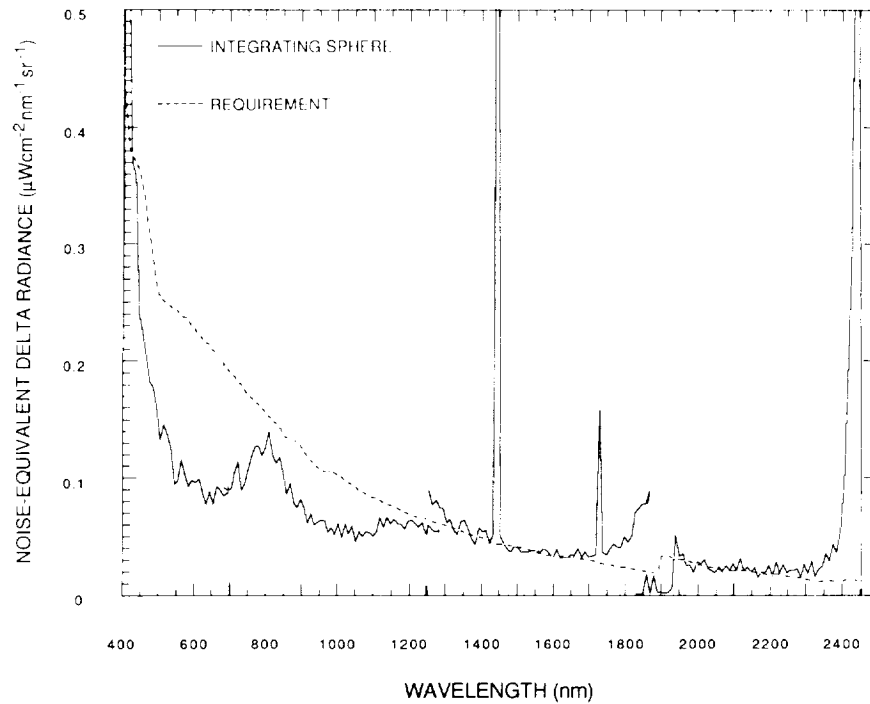


Figure 12. NEdL calculated from laboratory integrating-sphere data for the operational period beginning the 20th of September 1989 and the corresponding requirement. AVIRIS is meeting the NEdL requirement in the laboratory except in the long-wavelength regions of the C and D spectrometers.

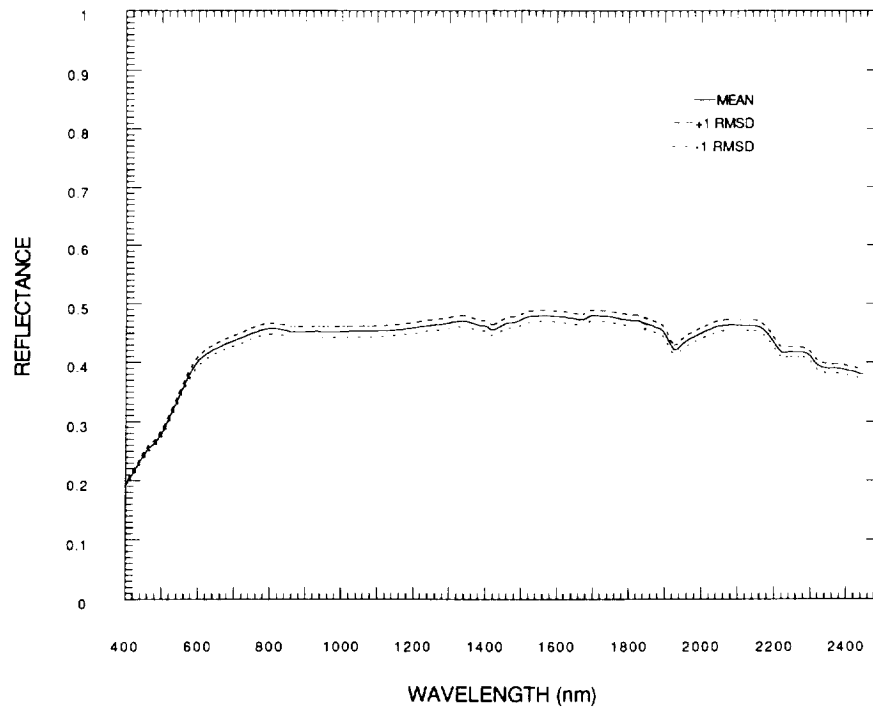


Figure 13. Mean spectral reflectance of 80 measurements of the Rogers Dry Lake calibration site concurrent with the AVIRIS data acquisition. The curve is bounded by the RMSD of these reflectance spectra.

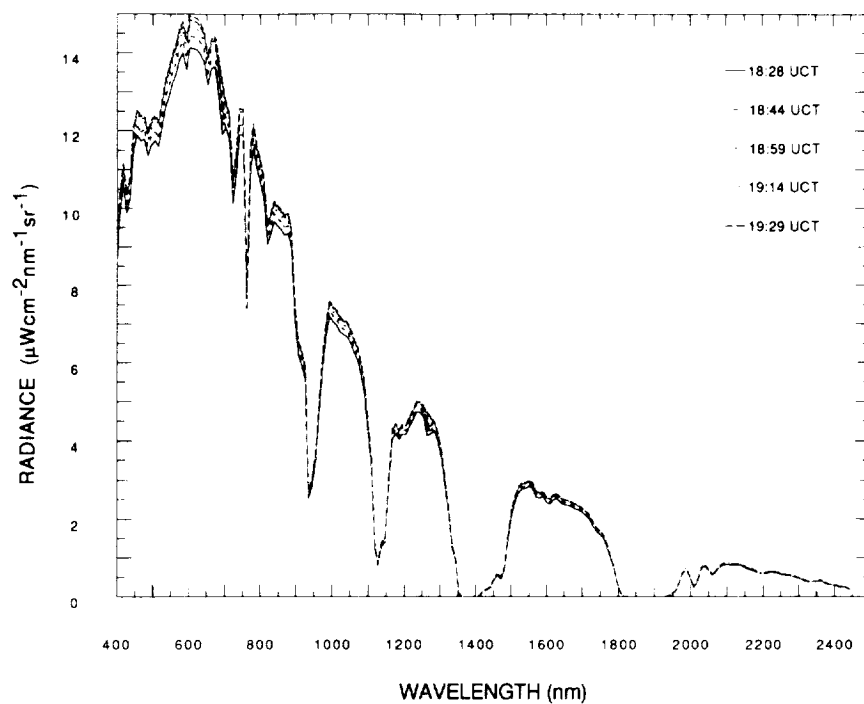


Figure 14. LOWTRAN-7-modeled total spectral radiance for the AVIRIS overflights of the Rogers Dry Lake calibration site on the 20th of September 1989.

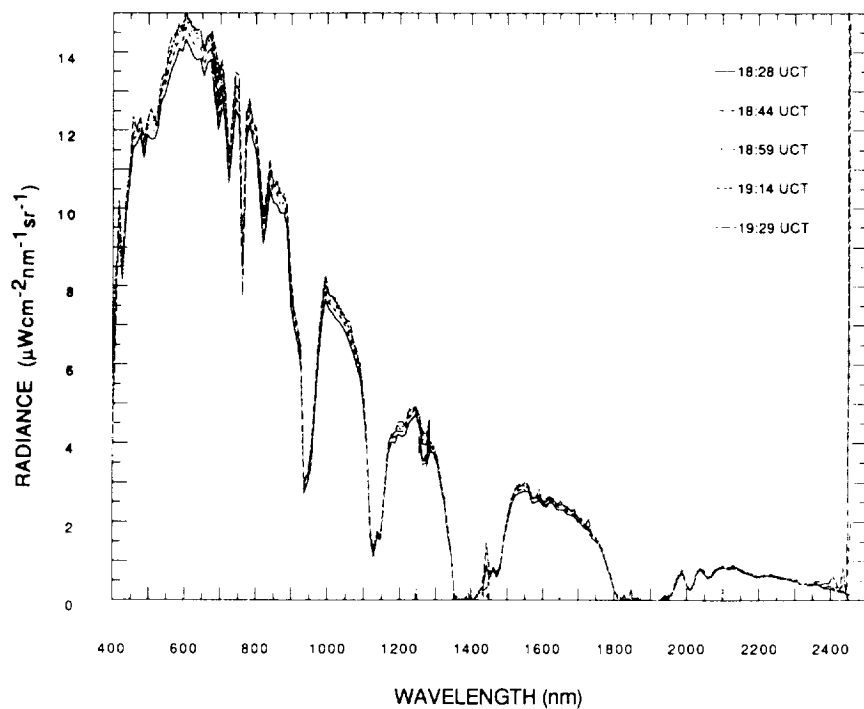


Figure 15. AVIRIS-measured radiance for the five overpasses of the Rogers Dry Lake calibration site.

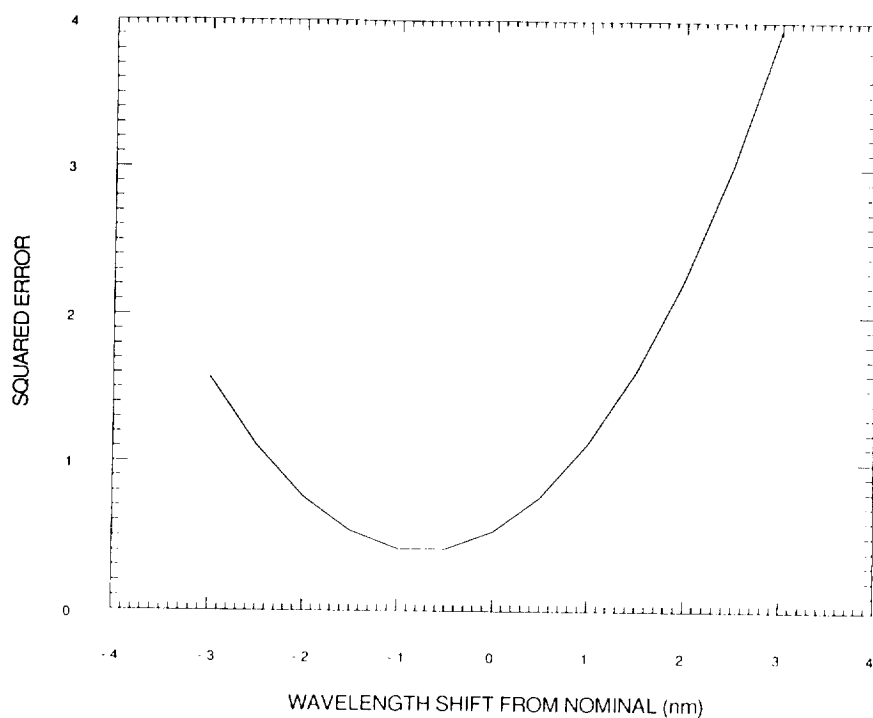


Figure 16. Calibration of spectral-channel position through error minimization between the AVIRIS-measured radiance and the LOWTRAN-7-modeled radiance for the 940-nm atmospheric water band.

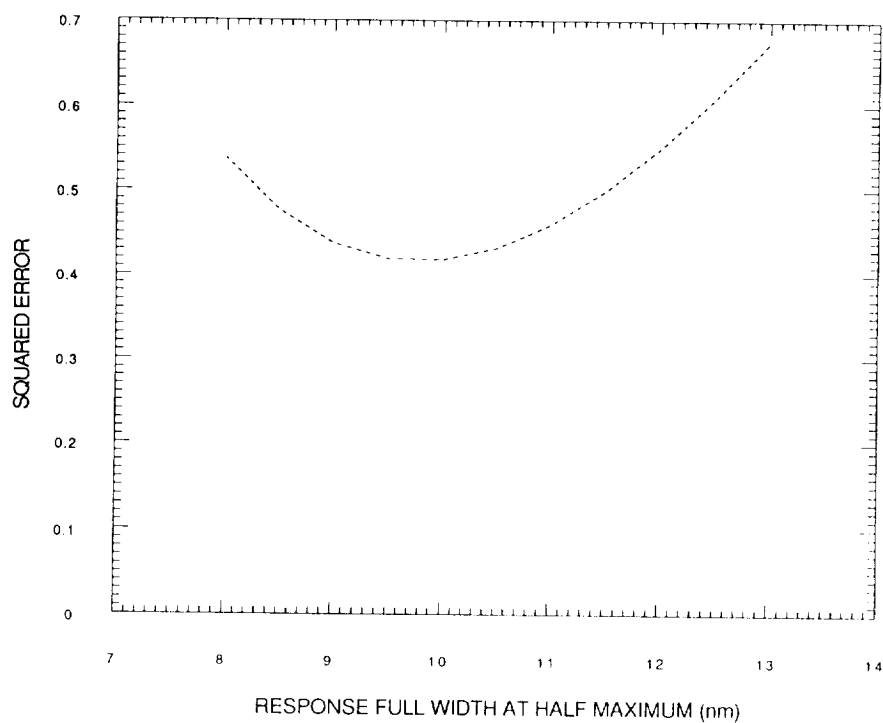


Figure 17. Calibration of spectral-channel-response-function FWHM, through error minimization between the AVIRIS-measured radiance and the LOWTRAN-7-modeled radiance for the 940-nm water band.

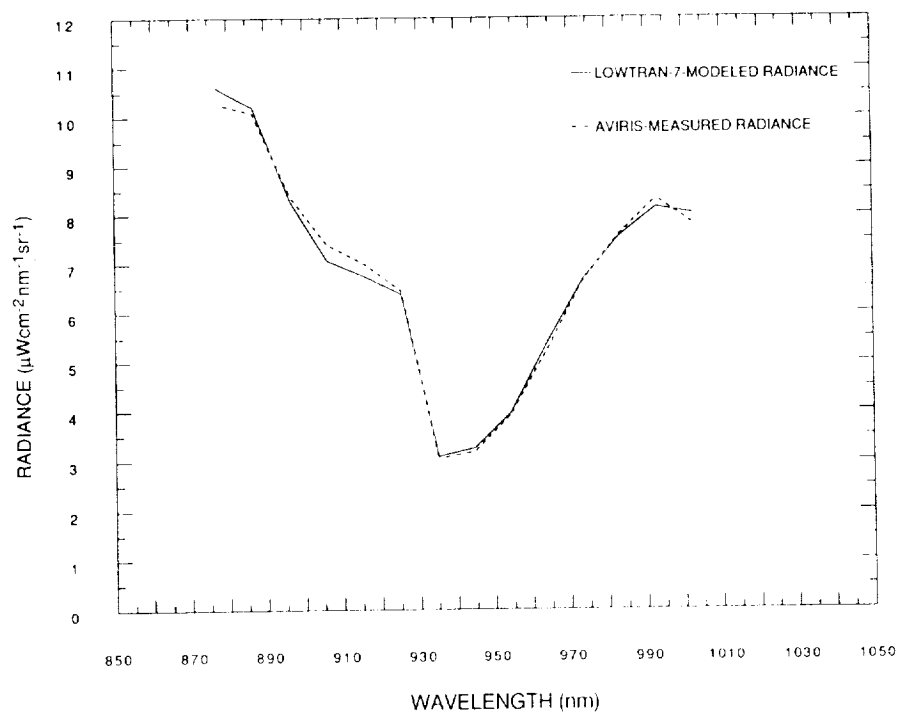


Figure 18. Best-fit result for the AVIRIS in-flight-determined spectral characteristics.

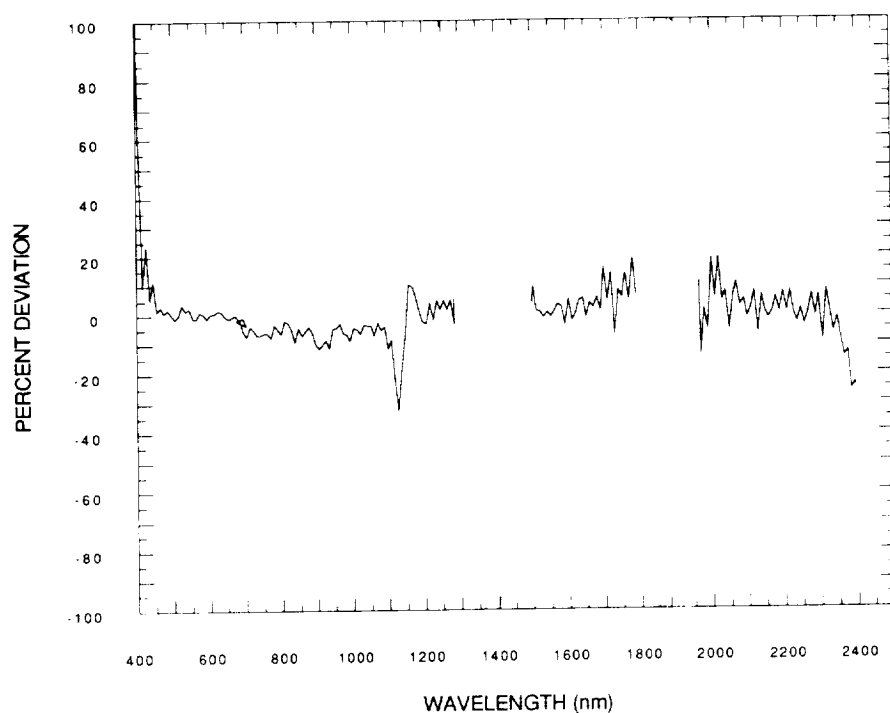


Figure 19. Absolute radiometric accuracy based on the percent deviation of the AVIRIS-measured radiance from the LOWTRAN-7-modeled radiance for the Rogers Dry Lake calibration site on the 20th of September 1989.

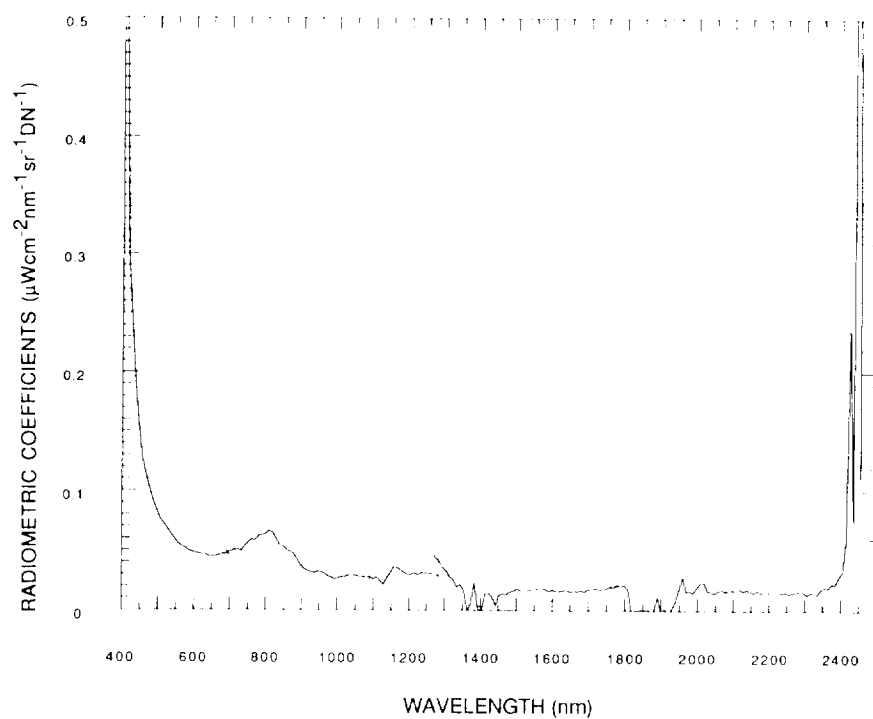


Figure 20. In-flight-determined radiometric calibration coefficients.

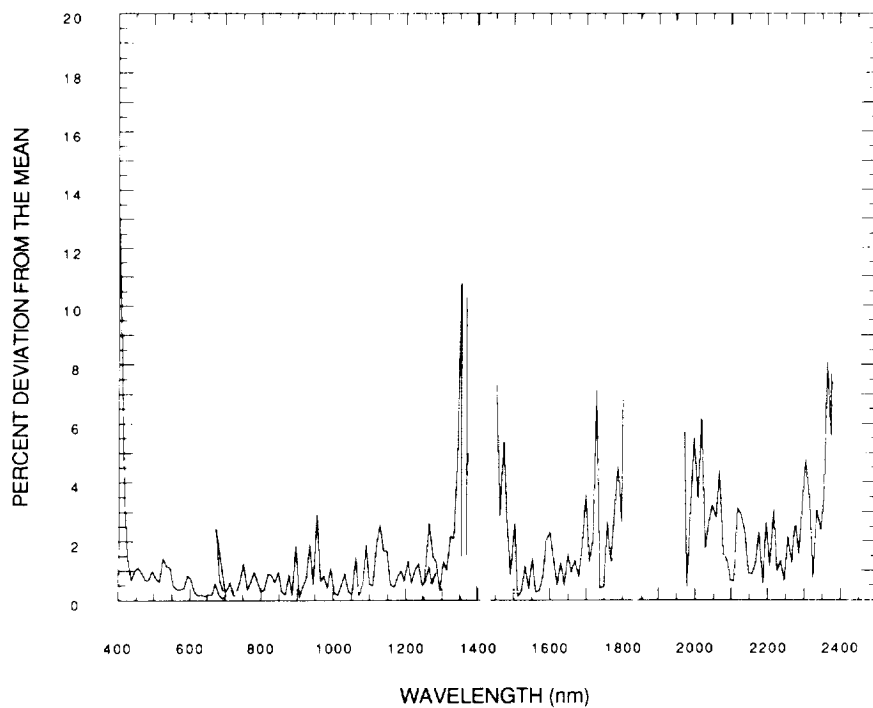


Figure 21. Intraflight radiometric stability based on the percent deviation from the mean of the illumination normalized radiances measured for the five AVIRIS overpasses.

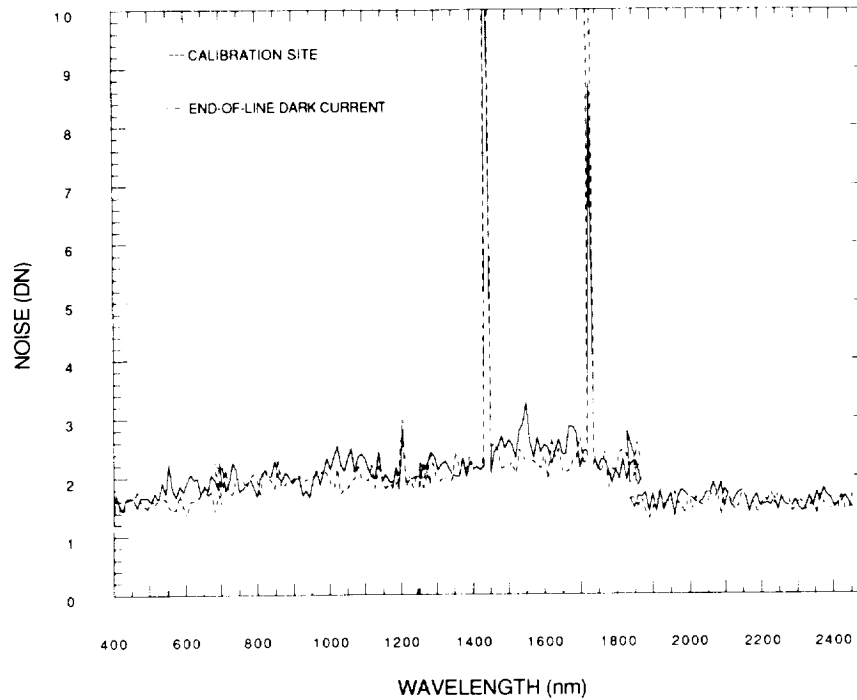


Figure 22. AVIRIS noise calculated from the homogeneous calibration site at Rogers Dry Lake and from the dark-current values measured at the end of each image line.

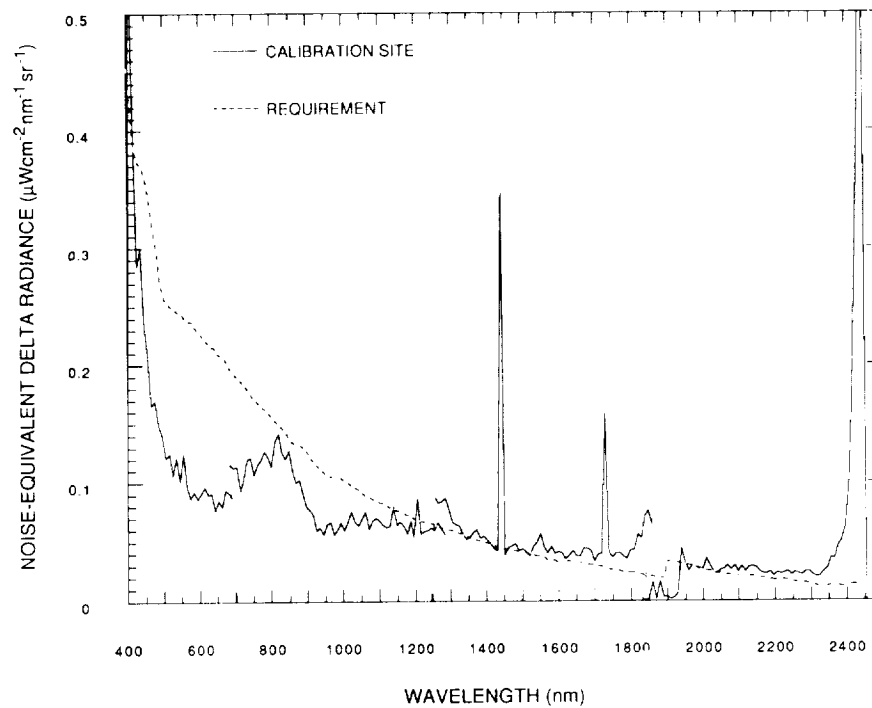


Figure 23. In-flight NEdL determined as the root-mean-squared deviation in the AVIRIS-measured radiance for the homogeneous calibration site at Rogers Dry Lake on the 20th of September 1989.

DETECTION OF TRACE QUANTITIES OF GREEN VEGETATION IN 1989 AVIRIS DATA

Christopher D. Elvidge, Desert Research Institute and Agricultural Experiment Station, University of Nevada System, Reno, Nevada 89506, U.S.A.; **Frederick P. Portigal**, Desert Research Institute and Hydrology-Hydrogeology Program, University of Nevada System, Reno; **David A. Mouat**, Desert Research Institute and CIASTA, University of Nevada System, Reno.

ABSTRACT

AVIRIS data acquired on September 20, 1989 were calibrated to ground reflectance and used to determine the detection limits for green vegetation. The chlorophyll red edge was detected in Monterey Pine plots having green vegetation covers as low as 3.8%.

INTRODUCTION

The detection of trace quantities (less than 10% cover) of green vegetation using remotely sensed data continues to be problematic. A series of red versus near infrared (NIR) vegetation indices has been used routinely on data from broadband sensors (e.g., Tucker, 1979). The red versus NIR vegetation indices operate by contrasting the chlorophyll pigment absorption in the red with the high reflectance of green leaves in the NIR. Under low green canopy cover conditions background rock and soil materials produce a range of vegetation index values, degrading the accuracy of broad band vegetation indices (Elvidge and Lyon, 1985).

The advent of high spectral resolution remote sensing opens up the possibility of extending the detection limits for green vegetation. The chlorophyll red edge (Collins, 1978), located from 700 to 780 nm is the sharpest spectral feature of green vegetation. This spectral feature is absent in rocks and soils. Our hypothesis is that the chlorophyll red edge will be the most persistent spectral feature of green vegetation at low levels of canopy cover. Elvidge and Mouat (1989) report detection limits near 2% cover using the chlorophyll red edge feature in 1988 AVIRIS data. This paper repeats the experiment described by Elvidge and Mouat (1989) using data acquired in 1989 by NASA's Airborne Visible-Infrared Imaging Spectrometer (AVIRIS).

DATA ACQUISITION AND ANALYSIS

A flight line was selected in 1987 to provide AVIRIS data of Stanford University's Jasper Ridge Biological Preserve plus a series of calibration targets. AVIRIS data for this investigation was acquired on September 20, 1989 at 1:58 PM Pacific Standard Time. Radiometrically corrected data were calibrated to ground reflectance using a set of four calibration targets of known reflectance: 1) a black rubber running track at Canada College, 2) the outer parking lot (asphalt) at Canada College, 3) Humphries Polo Field, and 4) open water from Searsville Lake. These targets cover a spread in ground reflectance from 0 to 40% over the AVIRIS bands. Linear regression was used to generate equations for converting AVIRIS digital number (DN) values into percent ground reflectance (Elvidge, 1988). The regression results are presented in Figure 1. Application of the equations removes the influence of solar illumination, most atmospheric effects (attenuation and scatter), and uncorrected band-to-band instrument response functions from the data.

The Jasper Ridge flight line covers a commercially operated Monterey Pine (*Pinus radiata*) plantation (a Christmas tree ranch) located on the strip of land between Sand Hill Road and the Stanford Linear Accelerator (SLAC). The pine trees are planted in rows and the interrow areas have been cultivated to remove unwanted plants (weeds). Various age stands are present, producing several levels of green vegetation cover. Pixels from a series of plots were extracted from the AVIRIS data and converted to units of ground reflectance. The percent green cover in each plot was determined using low altitude aerial photography. The photography was digitized and then analyzed with a supervised classification to determine the percentage of green vegetation cover. Table 1 summarizes the number of pixels and percent green vegetation cover for the five plots.

TABLE 1

	Number Of Pixels	Percent Green Cover
PLOT 1	16	21.9%
PLOT 2	12	20.0%
PLOT 3	24	12.8%
PLOT 4	20	11.6%
PLOT 5	9	9.6%
PLOT 6	32	7.8%
PLOT 7	20	5.0%
PLOT 8	16	3.8%
PLOT 9	6	2.2%
ASPHALT	42	0.0%
WET SOIL	8	0.0%

Jasper Ridge-AVIRIS Calibration

September 20, 1989

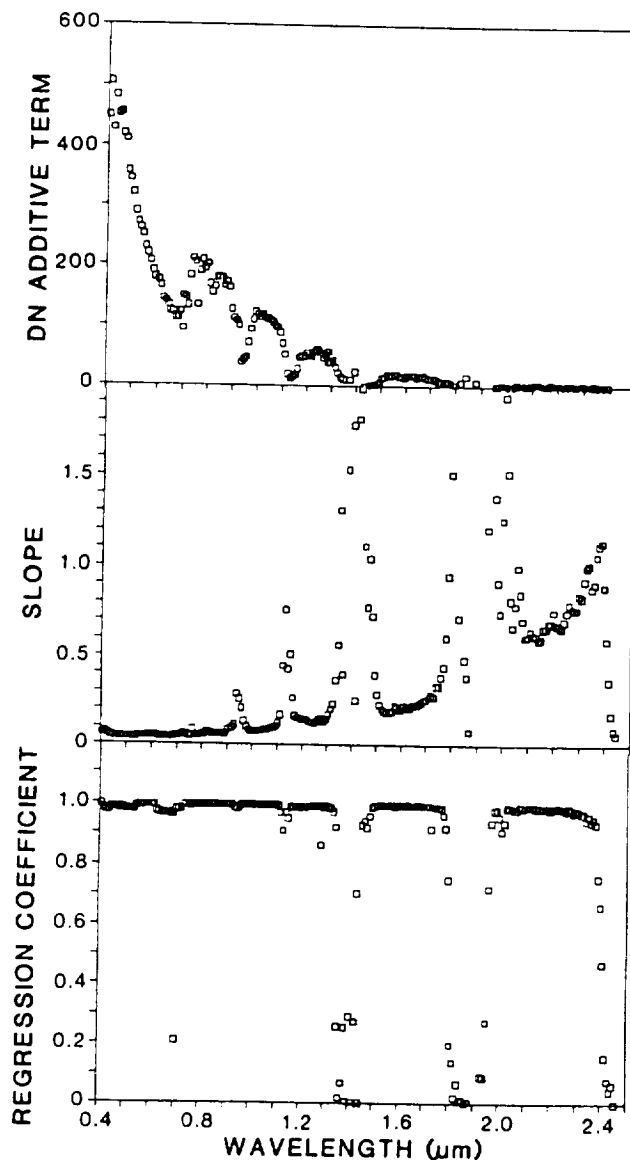


Figure 1. Results from the digital number to ground reflectance linear regressions. The regression coefficients (R^2 values) versus wavelength are presented in the lower segment. Equations were formed only for bands yielding R^2 values of 0.8 or better. The middle panel shows the slopes (B term) determined for the equation: Reflectance = $A + B \cdot \text{DN}$. The upper panel shows the "DN additive term" (DN intercept for zero reflectance) versus wavelength. The "DN additive term" encapsulates the additive factors of atmospheric path radiance and uncorrected instrument dark current.

RESULTS

The AVIRIS reflectance spectra for the Monterey Pine plots from 400 to 900 nm are shown in Figures 2 and 3. Figure 2 shows the spectra derived from plots with more than 9% green cover while Figure 3 shows the spectra for plots with 0 to 8% green cover. The curves were developed by taking the mean DN data for the group of pixels extracted from a plot and converting to ground reflectance using the equations developed in the calibration procedure. The curves for plots with 20 to 21.8% green cover exhibit recognizable spectral features of green vegetation, including chlorophyll pigment absorption in the red at 683 nm, a chlorophyll red edge from 700 to 780 nm, and high reflectance on the NIR plateau (780 to 900 nm). These features are also present, in subdued form, in the AVIRIS reflectance spectra of plots having 9.6 to 12.8% green cover on Figure 2 and plots having 7.8, 5.0, and 3.8% green cover on Figure 3. The vertical lines on Figures 2 and 3 at 683 and 723 nm mark the positions of the chlorophyll pigment absorption and red edge shoulder in the plots having less than 15% green cover. These features persist in plots having 5.0 and 3.8% green cover, but are not clearly expressed in the spectrum derived from a plot having 2.2% green cover (Figure 3). Surfaces having zero green cover (asphalt and wet soil) lack the chlorophyll pigment and red edge features.

CONCLUSION

Spectral features associated with chlorophyll pigment absorption in the red, and the chlorophyll red edge can be readily detected in AVIRIS data at green vegetation covers of greater than 10%. Traces of these spectral features persist in AVIRIS reflectance spectra down to green vegetation cover levels of 3.8%. This capability exceeds the detection limits for green vegetation obtained for broadband sensors.

There are several reasons why these two spectral features are useful for detecting trace quantities of green vegetation: 1) The chlorophyll red edge is the sharpest spectral feature of green leaves. That is to say, it is the region with the greatest change in reflectance over the smallest change in wavelength. 2) There are no other natural materials yielding an absorption edge of similar magnitude in the same spectral position. 3) There is good solar illumination from 0.7 to 0.8 μm . While the wavelength position of the chlorophyll red edge may not be measurable at low green vegetation covers, the presence and magnitude of the chlorophyll red edge may prove to be of great value in detecting and quantifying trace quantities of green vegetation.

AVIRIS REFLECTANCE DATA

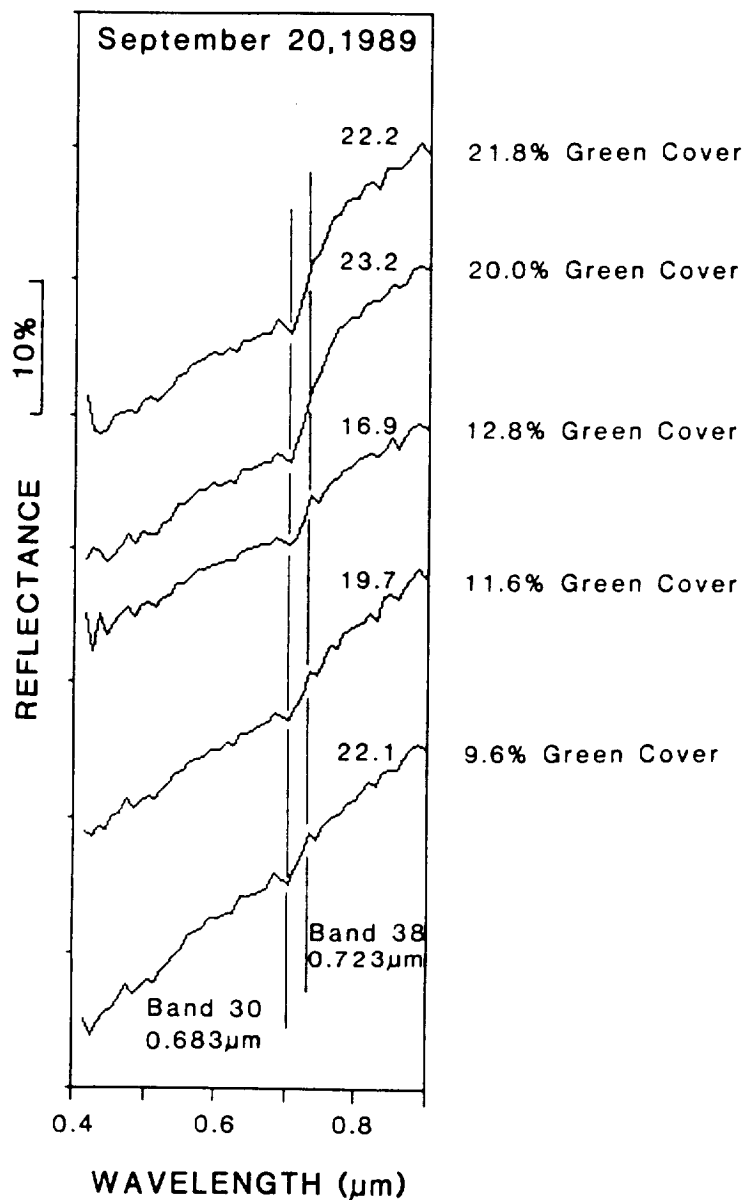


Figure 2. AVIRIS reflectance spectra for the five plots of Monterey Pine ranging from 9.6 to 21.8% green cover. The curves have been offset vertically to avoid overlap. The reflectance at 800 nm is provided for each spectrum.

AVIRIS REFLECTANCE DATA

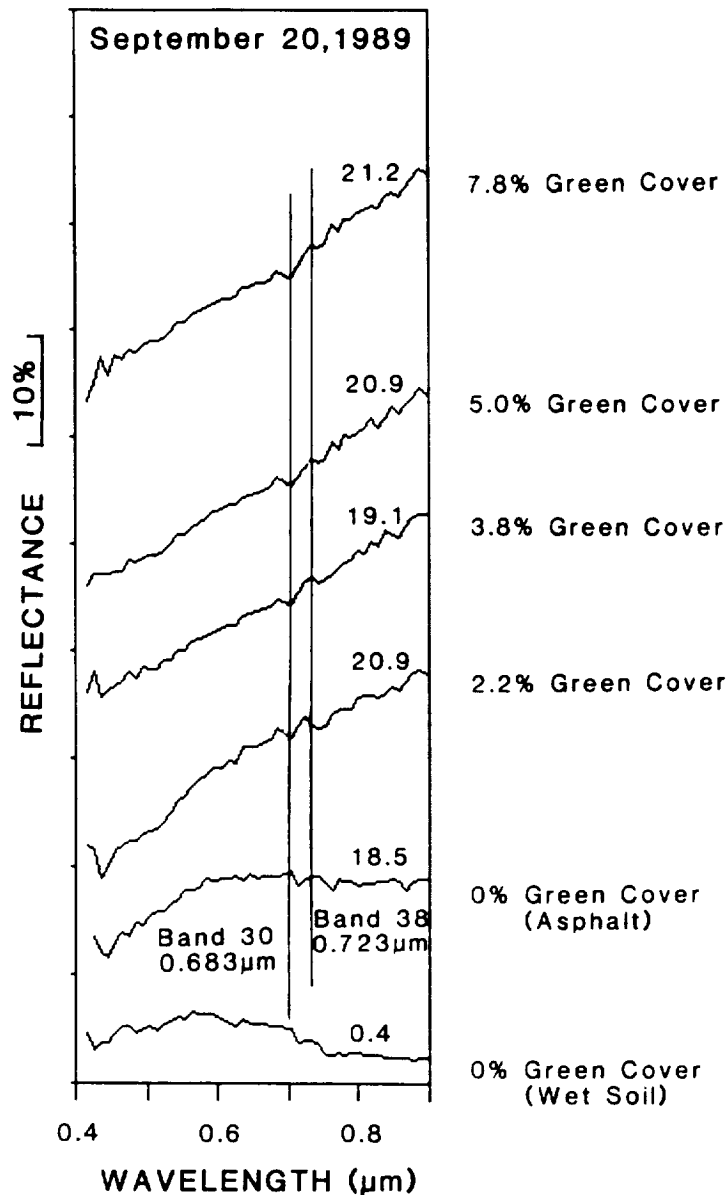


Figure 3. AVIRIS reflectance spectra for the five plots of Monterey Pine ranging from 9.6 to 21.8 % green cover. The curves have been offset vertically to avoid overlap. The reflectance at 800 nm is provided for each spectrum.

REFERENCES

- Collins, W., 1978, Remote sensing of crop type and maturity. Photogrammetric Engineering and Remote Sensing. 44:43-55.
- Elvidge, C.D. and Lyon, R.J.P., 1985, Influence of rock-soil spectral variation on the assessment of green biomass. Remote Sensing of Environment. 17:265-279.
- Elvidge, C.D., 1988, Vegetation reflectance features in AVIRIS data. International Symposium on Remote Sensing of Environment, Sixth Thematic Conference on Remote Sensing for Exploration Geology. p. 169-182.
- Elvidge, C.D. and Mouat, D.A., 1989, Analysis of green vegetation detection limits in 1988 AVIRIS data. International Symposium on Remote Sensing of Environment, Seventh Thematic Conference on Remote Sensing for Exploration Geology.
- Elvidge, C.D. and Portugal, F.P., 1990, Phenologically induced changes in vegetation reflectance derived from 1989 AVIRIS data. Twenty-Third International Symposium on Remote Sensing of Environment, In Press.
- Richardson, A.J. and Wiegand, C.L., 1977, Distinguishing vegetation from soil background information. Photogrammetric Engineering and Remote Sensing. 43:1541-1552.
- Tucker, C.J., 1979, Red and photographic infrared linear combinations for monitoring vegetation. Remote Sensing of Environment. 10:127-150.

ISOLATING WOODY PLANT MATERIAL AND SENESCENT VEGETATION FROM GREEN VEGETATION IN AVIRIS DATA

ROBERTS, D.A., SMITH, M.O., ADAMS, J.B., SABOL, D.E., GILLESPIE A.R.
and WILLIS, S.C. Department of Geological Sciences, University of Washington,
Seattle, WA 98195

ABSTRACT

Spectral linear mixture analysis was applied to Airborne Visible/Infrared Imaging Spectrometer (AVIRIS) data to calibrate the data to reflectance and distinguish senescent vegetation and woody plant material from green vegetation and soils. The linear mixing model was applied to a data set collected September 20, 1989 over the Jasper Ridge Biological Preserve. The data were successfully calibrated to reflectance resulting in reasonable reflectance spectra for vegetated and unvegetated areas within and in the vicinity of the Preserve. The data were modeled as mixtures of four endmembers: shade, green leaf, soil and a woody endmember. A senescent vegetation endmember that was spectrally distinct from soils could not be reliably modeled but could be distinguished from soils using band residuals calculated as the difference between the measured AVIRIS spectrum and a model consisting of variable fractions of the four endmembers. Positive residuals at wavelengths between 1.5 and 1.7 μm and negative residuals at 2.08 (cellulose) and 2.28 (lignin) μm distinguished senescent plant material from soils.

INTRODUCTION

Considerable research has focussed on quantifying the amount of green vegetation measured remotely. Examples include uses of vegetation indices such as the normalized difference vegetation index (NDVI) and the Perpendicular Vegetation Index (PVI) (e.g., Tucker, 1979 and Jackson, 1983). Other examples include the use of airborne spectrometer data to measure canopy biochemical constituents (Peterson et al., 1987; Goetz et al., 1990).

Considerably less research has focussed on the woody or senescent components, though these can represent a significant portion of the biomass within a canopy or a vegetation community. Huete and Jackson (1987) varied the amount of senescent material and leaf litter relative to green vegetation to determine the effects of these materials on the assessment of green vegetation using vegetation indices. Elvidge (1987) measured visible near-infrared

and thermal spectra of dry plant materials, green leaves and other organic components of California Black Oak (Quercus kelloggii) to assess the potential for the development of vegetation indices designed for the assessment of dry plant materials. Gillespie et al. (1990a) found that dry grass and shrubs, which could not be distinguished from soils using Thematic Mapper (TM) data, could be distinguished using thermal data. Recently Adams et al. (1990), using spectral mixture analysis, found that the spectral variability within TM data collected over Manaus, Brazil, could be best explained by including a wood endmember in addition to green vegetation, shade and soil.

One of the major reasons for the lack of research pertaining to wood and senescent materials is the similarity between the spectra of dry plant materials and soils (Figure 1). Dry plant materials lack the pronounced spectral contrast between near-infrared and red wavelengths that distinguish green plant materials from soils. Thus, using the broad TM bands, it is difficult to distinguish woody plant material from soils and may be impossible to distinguish senescent plant material from soils. AVIRIS, on the other hand, collects data within wavelength regions where there are cellulose and lignin absorption features that can be used to distinguish soils from senescent vegetation or wood (Elvidge, 1987). In order to investigate the applicability of AVIRIS for assessing nongreen biomass, we applied techniques similar to those of Adams et al. (1990).

METHODS

We utilized a linear-mixing approach to model radiance measured by the sensor as the sum of several "pure spectra" (endmembers), each weighted by the relative proportion of the material corresponding to each spectrum within the field of view (Equation 1).

$$DN_{ik} = g_i \sum_{j=1}^n f_j r_{ij} + o_i + \epsilon_i \quad (1)$$

where DN_{ik} is encoded radiance measured by the sensor, i is the band number, k is the pixel location, j is the endmember number, f_j is the fraction of the endmember within the field of view, r_{ij} is the laboratory reflectance for each reference endmember, g_i is an atmospheric/instrumental/solar gain term, o_i is an atmospheric/instrumental offset and ϵ_i is a residual and error term.

The gain and offset terms (g_j and o_j) used to calibrate the AVIRIS data were derived using techniques developed by Smith et al. (1987). Smith et al. used least squares regression to relate laboratory-measured reflectance to encoded radiance and solve for the gains and offsets. A regression coefficient (r^2) was generated for each band to assess the fit between encoded radiance spectra and reference endmember spectra.

An average Root Mean Squared (RMS) error was calculated using equation 2.

$$\text{RMS} = \sum_{k=1}^m \sqrt{\left(\sum_{i=1}^n (\text{DN}_{ik} - \text{DN}'_{ik})^2 / n \right) / m} \quad (2)$$

where DN_{ik} refers to modeled radiance and m is the number of pixels comprising the image. An average RMS error for the swath used in the analysis was generated to provide a measure of how much of the spectral variability was explained by the endmembers used in the analysis. An RMS error image was generated to show the spatial distribution of the error.

Fraction images for each endmember were produced. Band residuals (ϵ_j) were calculated by subtracting modeled radiance, predicted for each pixel from the fractions of the endmembers and the gains and offsets used to calibrate the data, from encoded radiance measured by the sensor ($\epsilon_j = \text{DN}_j - \text{DN}'_j$, Figure 2). A positive residual occurs when the measured spectrum has higher reflectance at a specific wavelength than the modeled spectrum, indicating that the modeled spectrum contains absorption features which were lacking in the measured spectrum. A negative band residual results when the opposite is true, indicating the presence of absorption features in the measured spectrum which were absent or less pronounced in the modeled spectrum.

Fractions of woody and senescent plant material were determined both using fraction images and by interpretation of residual images. Residual images were produced for the wavelength regions of 1.5 to 1.7 μm and 2.1 to 2.3 μm . These regions were selected because of the presence of lignin and cellulose absorption features which could potentially differentiate senescent leaf materials from soils. For more detailed descriptions of the linear-mixing approach used in this study and residual analysis techniques refer to Adams et al. (1990), Smith et al. (1990) and Gillespie et al. (1990b).

The study was conducted over Jasper Ridge, California. The Jasper Ridge Biological Preserve is located in the foothills along the

northeastern margins of the Santa Cruz Mountains, approximately 7 km west of Palo Alto (Figure 3). Elevations at the site ranged from 108 meters at Searsville Lake to 200 meters on the ridge. The 1200-acre, 4-km by 2-km preserve was chosen as a study site because it is an area in which the vegetation has been extensively mapped and because large quantities of senescent and woody plant material were present in the Preserve at the time of the overflight.

The AVIRIS data utilized in this study were collected on September 20, 1989. Calibration and analysis were restricted to a subsection of the full scene, consisting of a 112-pixel swath centered over Jasper Ridge (Figure 3). A 171-band subset of the 224 AVIRIS bands, consisting of bands outside of major atmospheric absorption features was used for analysis. (See Slide 1.)

RESULTS

Calibration

We found that most of the variability within the scene could be explained using four reference endmembers: shade, tan soil (T2HA), woody plant material ("red stems") and green leaf (PHAR on Figure 4). The resulting average RMS error was less than 3 DN (Figure 5). The image was calibrated to reflectance using a best-fit linear combination of the four endmembers and equation 1. A plot of the inverted gains used to calibrate the data roughly corresponds to a plot of the solar curve combined with atmospheric absorption (Figure 6). The inverse of the gain differed most from the solar curve at wavelengths less than 1 μm , which may reflect instrumental effects. Offsets ranged as a function of wavelength between values of 90 and 130 DN, averaging approximately 100 DN (Figure 7). An increase to approximately 130 DN at shorter wavelengths represents increased additive path radiance due to atmospheric scattering. Between 2.0 and 2.4 μm , in the wavelength range of data collected by Spectrometer D, the offset term was also high, averaging 120 DN. Across all wavelengths, the offset showed a pronounced alternating pattern between high and low values, a data characteristic that is probably instrumental in origin.

The model fit (r^2) averaged over 0.98 (Figure 8). The lowest r^2 value was 0.80, occurring approximately at 0.7 μm , at the start of the "red edge" of the vegetation spectrum. The close proximity to the red edge suggests that much of the error could be attributed to poor wavelength calibration. Instrumental wavelength calibration was tested for the September 20, 1989 data set (Green et al., 1990) and

found to be within 0.0005 μm , suggesting that a majority of the miscalibration, if present, was in the laboratory reflectance data used to calibrate the scene. Low r^2 values at 1.100, 1.400, 1.900 and >2.400 μm are probably due to changes in atmospheric water abundance with elevation across the scene (Green et al., 1989; Gao and Goetz 1990).

Overall calibration of the image to reflectance appeared to be good as judged by the shape of spectra extracted for areas containing known materials. Reflectance spectra were extracted for three areas within the scene ("lawn," "chaparral" and "drygrass," on Figure 9, labeled L, C and D on Figure 3). The overall brightness and shape of these calibrated AVIRIS spectra are close to similar materials measured in the field, though no quantitative comparison was made to evaluate the accuracy of the calibration. Spectral anomalies within the drygrass spectra at 0.7 μm are probably due to wavelength miscalibration. Spectral anomalies at 0.94 μm and 1.130 μm are probably due to differences in atmospheric water abundance. Comparison to the uncalibrated data for these same areas demonstrates a marked improvement in the interpretability of these spectra (Figure 10).

Mixture Analysis

AVIRIS spectra were modeled as mixtures of four endmembers (Figure 4). The fact that the data could be modeled using these four endmembers does not imply that these materials actually occur in the scene. For example, the spectrum T2HA corresponds to a highly reflectant soil collected in Tucson, Arizona. PHAR equals leaf reflectance of Phalaris arundinacea measured in the laboratory. What these endmembers do imply is that there are materials within the scene that have spectral properties similar to the materials used as endmembers and that all of the materials within the scene can be modeled as mixtures of these spectra. Thus, the fact that T2HA is a viable endmember suggests that the spectral properties of some of the soil in the area are similar to T2HA. Phalaris arundinacea worked well as an endmember for vegetation because of its high near-infrared/red contrast. The red stem endmember does not imply that the woody materials in the scene were red stems, only that this endmember was representative of material in the scene which is spectrally similar to wood.

Fraction images were generated for the four endmembers (Figure 11). In all of the fraction images, roads, buildings and man-made structures, such as the Stanford Linear Accelerator (SLAC), appear anomalous. These materials were not included in the model

and therefore model results for areas containing these materials are not meaningful (see also Figure 5). The highest fractions of shade were located at Searsville Lake (W in Figure 3), at several flooded quarries southeast of Jasper Ridge and on the northeast facing slope of Jasper Ridge, in an area dominated by evergreen forest (marked by arrows on Figure 11a). Shade fractions were lowest in an open field north of Jasper Ridge, in an area consisting of exposed soil and flattened, senescent grass (Elvidge, oral communication, 1990). Green leaf (Figure 11b) was highest to the extreme southeast on a well-watered golf course. A second high fraction occurred on the western edge of the Preserve, in an area containing riparian vegetation (S on Figure 3). The lowest fractions of green leaf occurred in the same region containing the flattened grass and exposed soil, along the central crest of Jasper Ridge, in an area dominated by grasslands and serpentine soils, and to the southeast in areas interpreted as grasslands. Soil fractions (Figure 11c) were highest in a series of open fields southeast of the ridge, along the central crest of the ridge and in the exposed area to the north of the preserve. The lowest soil fractions occurred on the northeast-facing evergreen forest. The fraction of the woody material endmember (Figure 11d) was low across most of the scene. Woody material fractions were highest on Jasper Ridge within the grasslands and the chaparral. According to this analysis, the endmember constituted as much as 8% of the grassland areas and 23% within the chaparral. When the shade endmember is not included in the fraction sum, the fraction of the woody endmember will be larger.

Residual Analysis

Spectral mixture analysis of the data produced coherent maps showing the fractions of these four endmembers within the Jasper Ridge scene. However, these fraction images do not effectively separate the senescent leaf material and soils. Based upon personal observations between 1983 and 1985 on the Jasper Ridge Biological Preserve, we are aware that some of the areas which are modeled as having a high soil fraction, in fact contain much higher fractions of senescent vegetation than soil. Spectral similarity between these two materials makes separating them difficult. This problem was further demonstrated during the process of mixture analysis and calibration. While initially processing and calibrating the image, the spectral library used to calibrate the image contained both dry plant material and soils. Whereas a woody material endmember was a necessary component, senescent vegetation was not. The spectrum for senescent vegetation could be modeled as some linear

combination of the woody material, green leaf, soil and shade endmembers.

Although senescent vegetation did not prove to be a viable endmember for mixture analysis, band residuals distinguished the areas containing large quantities of senescent vegetation from those containing soils (Figures 12 and 13). Figure 12 shows band residuals from 1.59 to 1.71 μm . The exposed hill north of Jasper Ridge (arrow at bottom of figure), the grassland along the crest of the ridge and areas southeast of the ridge show as positive anomalies (see also Figure 2). In the 2.04 to 2.22 μm residual image (Figure 13), these same areas are shown as prominent negative anomalies. The positive anomaly between 1.5 to 1.7 μm corresponds to a spectral region where the measured spectrum has higher reflectance than the modeled spectrum. A comparison between the reflectance spectrum of dried Phalaris arundinacea and the modeled spectrum for the area labeled as drygrass shows an overall positive anomaly with subtle spectral highs at 1.55 and 1.64 μm (Figure 14). Band residuals of the AVIRIS data between 1.588 and 1.706 μm show the highest positive residual at 1.647 μm . The negative anomaly between 2.1 and 2.3 μm corresponds to a spectral region where the measured spectrum had lower reflectance than the model. A comparison between the dried Phalaris spectrum and the modeled spectrum (Figure 14), shows two regions centered at 2.083 μm and 2.291 μm where the Phalaris spectrum contains absorption features not present in the model. The wavelength of these features suggests that the 2.08 μm absorption is due to cellulose and the 2.29 μm absorption is due to lignin (Elvidge, 1987). Using a residual approach, materials that could not readily be modeled as endmembers could be observed as residuals.

SUMMARY

The mixing model was used to successfully calibrate AVIRIS data to reflectance. An AVIRIS scene collected over Jasper Ridge on September 20, 1989 was modeled as consisting of four spectral endmembers: shade, tan soil (T2HA), green leaf (PHAR) and woody material ("red stems"). Although senescent grass could not readily be separated from soil as an endmember, residuals in the 1.5- to 1.7- μm , and 2.1- to 2.3- μm region made it possible to map regions containing high fractions of senescent plant material.

ACKNOWLEDGMENTS

This research was supported by the Land Processes Branch of the National Aeronautics and Space Administration and the W.M. Keck Foundation. We also thank the Jet Propulsion Laboratory for supplying AVIRIS data, and Dr. David Mouat for plant material supplied by him.

REFERENCES

- Adams, J.B., Kapos, V., Smith, M.O., Almeida F.R., Gillespie, A.R., and Roberts, D.A., 1990, A New Landsat View of Land use in Amazonia, Proc. of the Int. Symp. Primary Data Acquisition, Manaus, Brazil, June 24-29, 1990, pp. 177-185.
- Adams, J.B., Smith, M.O. and Gillespie, A.R., 1990, Imaging Spectroscopy: Data Analysis and Interpretation Based on Spectral Mixture Analysis, in Remote Geochemical Analysis: Elemental and Mineralogical Composition (Pieters and Englert Eds.), in press.
- Elvidge, C. D., 1987, Reflectance Characteristics of Dry Plant Material, Presented at the twenty-first International Symposium on Remote Sensing of Environment, Ann Arbor, MI, Oct. 26-30, 1987, 13 pp.
- Gao, B-C and Goetz, A.F.H., 1990, Column Atmospheric Water Vapor Retrieval from Airborne Spectrometer Data, J. Geophys. Res. - Atmos., in press.
- Gillespie, A.R., Smith, M.O., Adams, J.B., and Willis, S.C., 1990a, Spectral Mixture Analysis of Multispectral Thermal Infrared Images, Proc. Airborne Science Workshop: TIMS, Jet Propulsion Laboratory, Pasadena, CA, June 6, 1990. In this volume.
- Gillespie, A.R., Smith, M.O., Adams, J.B., Willis, S.C., Fischer, A.F. III and Sabol, D., 1990b, Interpretation of Residual Images: Spectral Mixture Analysis of AVIRIS Images, Owens Valley, CA, Proc. Airborne Science Workshop: AVIRIS, In this volume.
- Goetz, A.F.H., Gao, B-C., Wessman, C.A. and Bowman, W.D., 1990, Estimation of Biochemical Constituents from Fresh Green Leaves by Spectrum Matching Techniques, Proc. 10th Annual Int Geosci. Rem. Sens. Symp., College Park, Md, May 20-24, 1990, pp. 971-974.
- Green, R.O., Carrere, V., and Conel, J.E., 1989, Measurement of Atmospheric Water Vapor Using the Airborne Visible/Infrared Imaging Spectrometer, Proc. 12th Workshop on Image Processing, ASPRS, in press.
- Green, R.O., Conel, J.E., Bruegge, C., Carrere, V., Margolis, J., and Hoover, G., 1990, Laboratory Spectral and Radiometric Calibration of AVIRIS, Proc. Airborne Science Workshop: AVIRIS, Jet Propulsion Laboratory, Pasadena, CA, June 4-5, 1990, In this volume.
- Huete A.R. and Jackson, R.D., 1987, Suitability of Spectral Indices for Evaluating Vegetation Characteristics in Arid Rangelands, Rem. Sens. Environ., 23:213-232.
- Jackson, R.D., 1983, Spectral Indices in n-space, Rem. Sens. Environ., 13:409-421.
- Peterson, D.L., Aber, J.B., Matson, P.A., Card, D.H., Swanberg, N., Wessman, C. and Spanner, M., 1988, Remote Sensing of Forest Canopy and Leaf Biochemical Contents, Rem. Sens. Environ., 24:85-108.
- Smith, M.O., Roberts, D.A., Shipman, H.M., Adams, J.B., Willis, S.C. and Gillespie, A.R., 1987, Calibrating AIS images using the surface as a reference, Proc. 3rd Airborne Imaging Spectrometer Data Analysis Workshop, June 2 - 4, 1987, 10 p.

- Smith M.O., Ustin, S.L., Adams, J.B. and Gillespie, A.R., 1990, Vegetation in Deserts I. A Regional Measure of Abundance for Multispectral Images, *Rem. Sens. Environ.*, 31:1-26.
- Tucker, C.J., 1979, Red and Photographic Infrared Linear Combinations for Monitoring Vegetation, *Rem. Sens. Environ.*, 8:127-150.

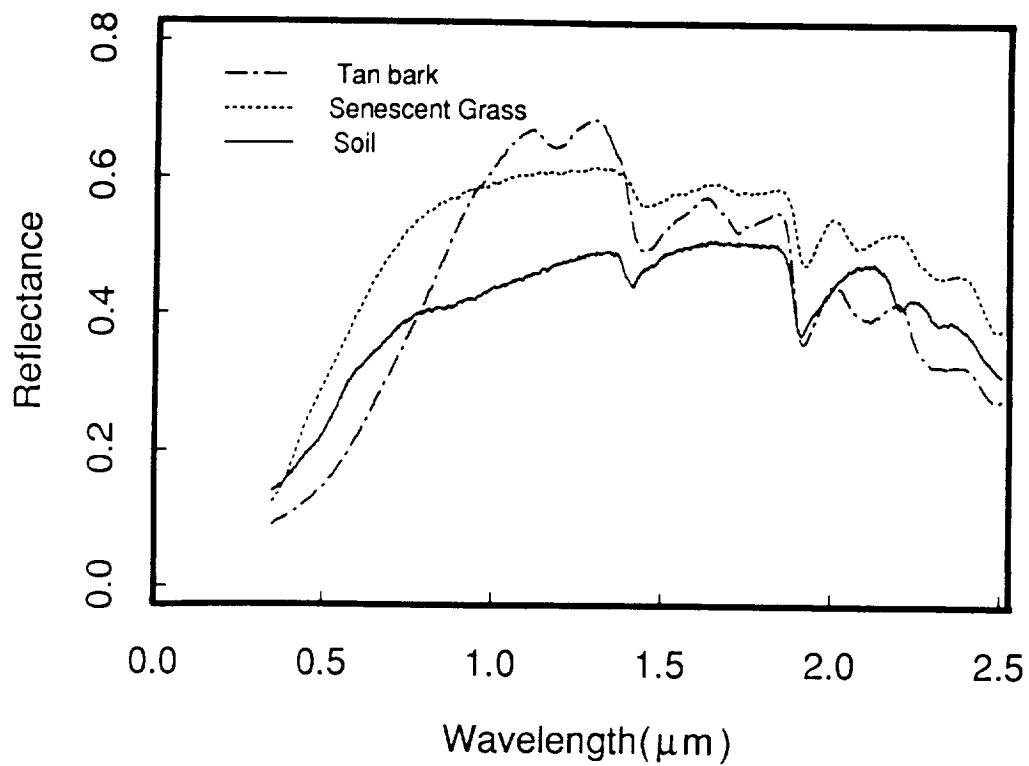


Figure 1. Reflectance spectra of tan bark (*Platanus* sp.), senescent grass (*Phalaris arundinacea*) and a soil. Note the spectral similarity, particularly between the senescent grass and the soil.

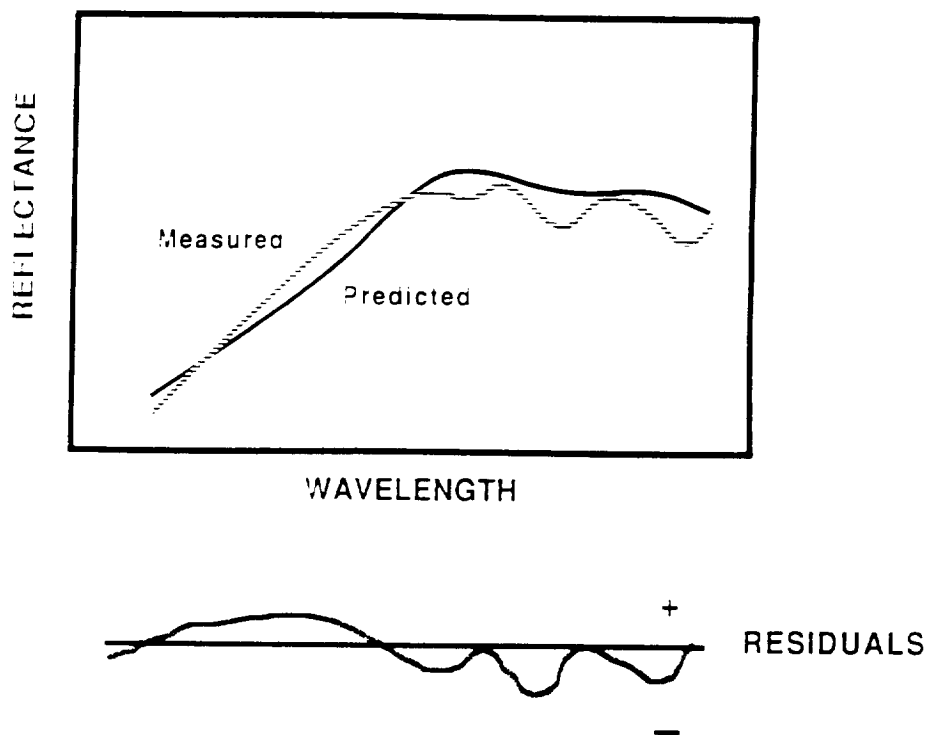


Figure 2. Comparison of measured reflectance (dashed) to modeled reflectance (solid). Subtraction of the predicted from the measured spectrum results in positive residuals when the measured value is higher than the model and negative residuals when the opposite is true.

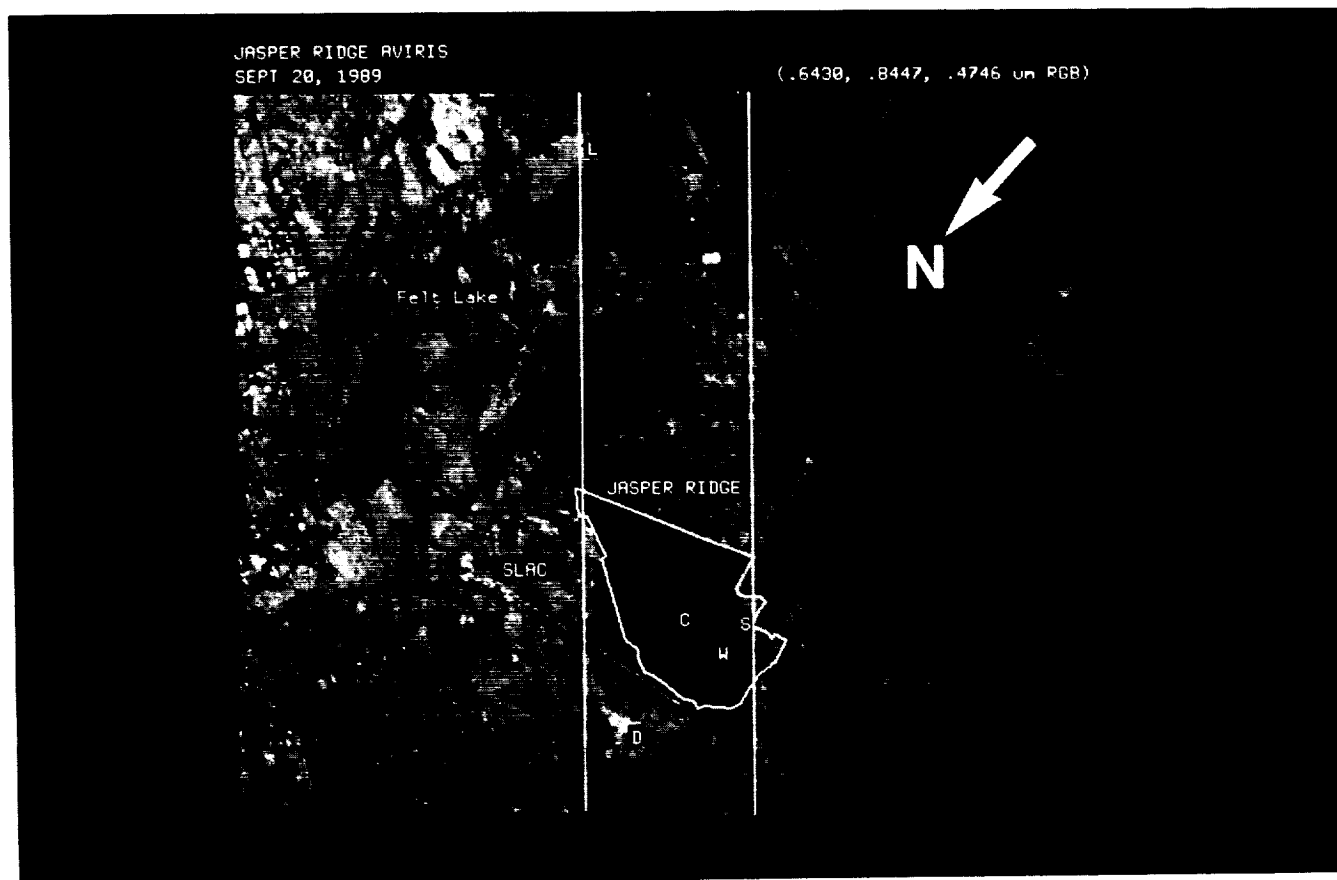


Figure 3. False color composite of AVIRIS data showing the Preserve and the 112-pixel swath. L, C and D are defined in text. S and W are swamp and water respectively.

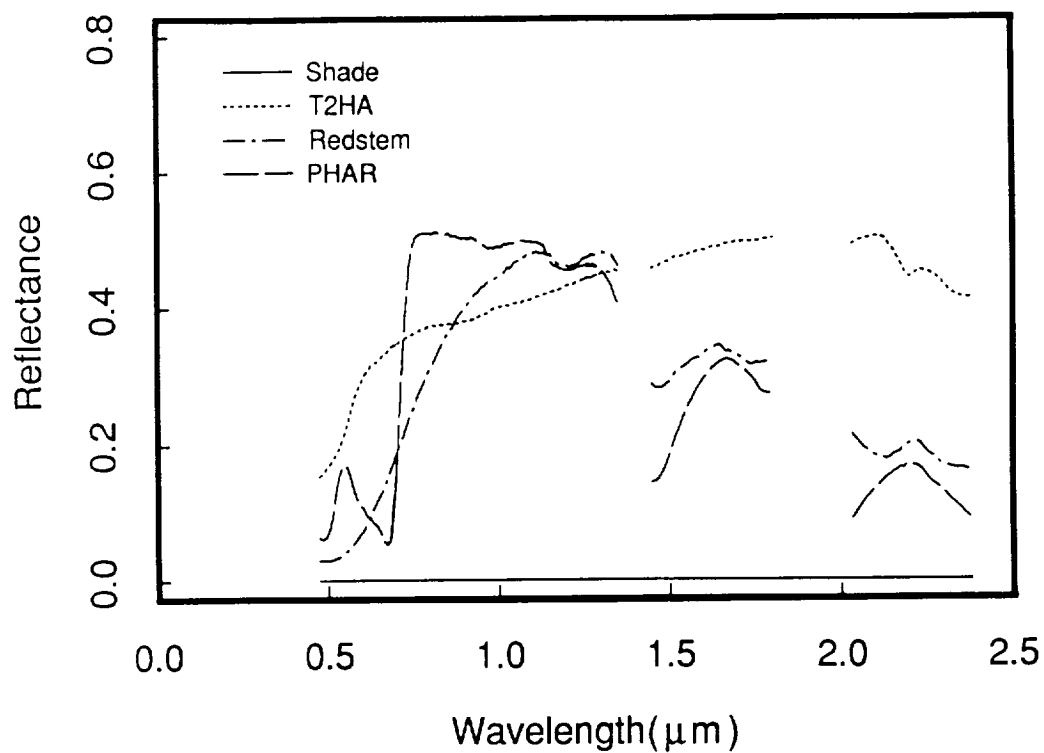


Figure 4. Reflectance spectra of the four endmembers: Shade, T2HA, Red stems and PHAR.

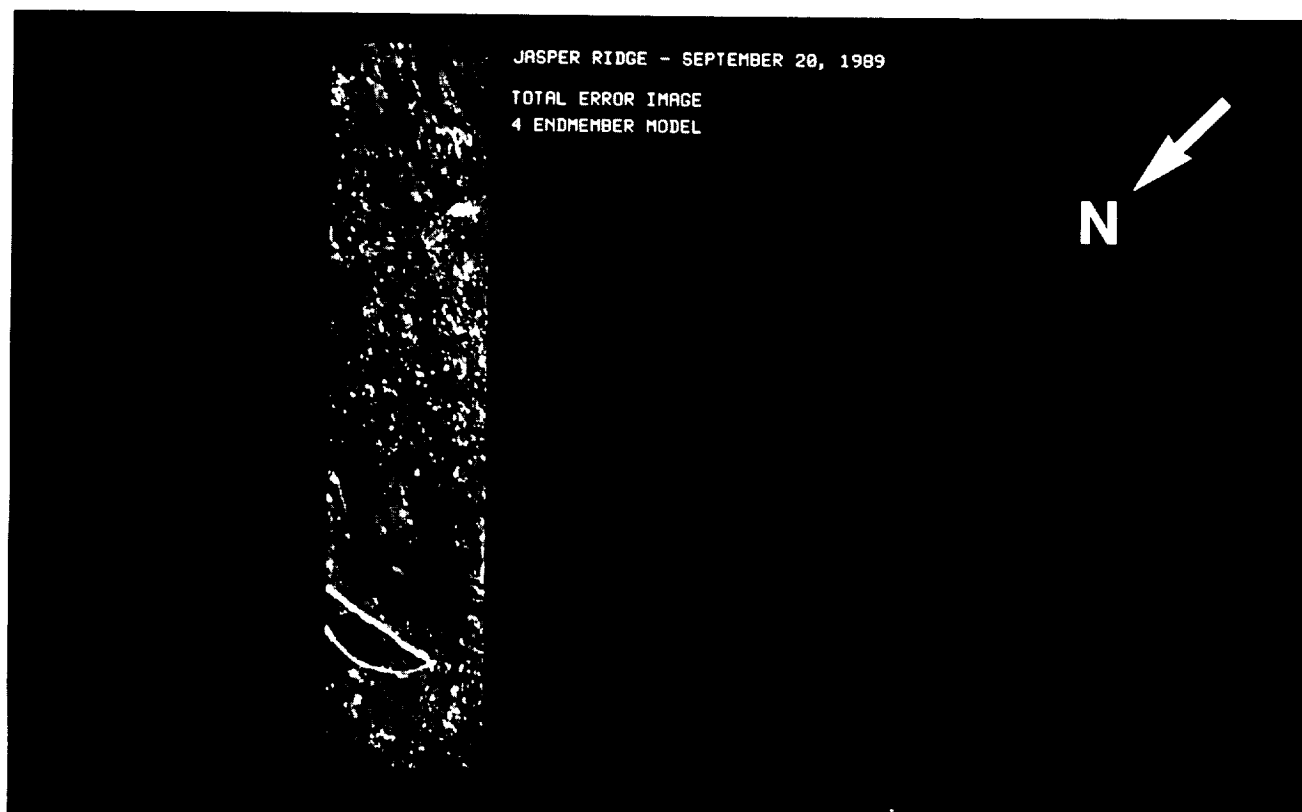


Figure 5. RMS error image. Grey areas indicate good fit of the model (< 2 DN). Light areas have $\text{RMS} > 3$ DN because they were not modeled. The average RMS was less than 3 DN.

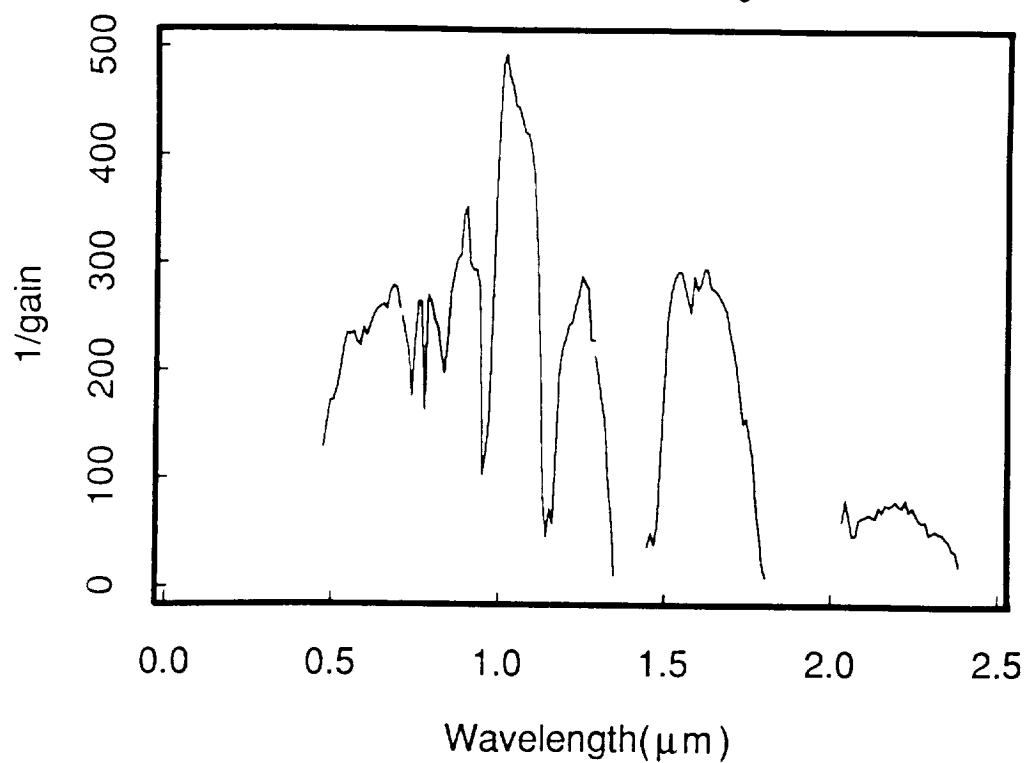


Figure 6. Inverted gains used to calibrate the data to reflectance.

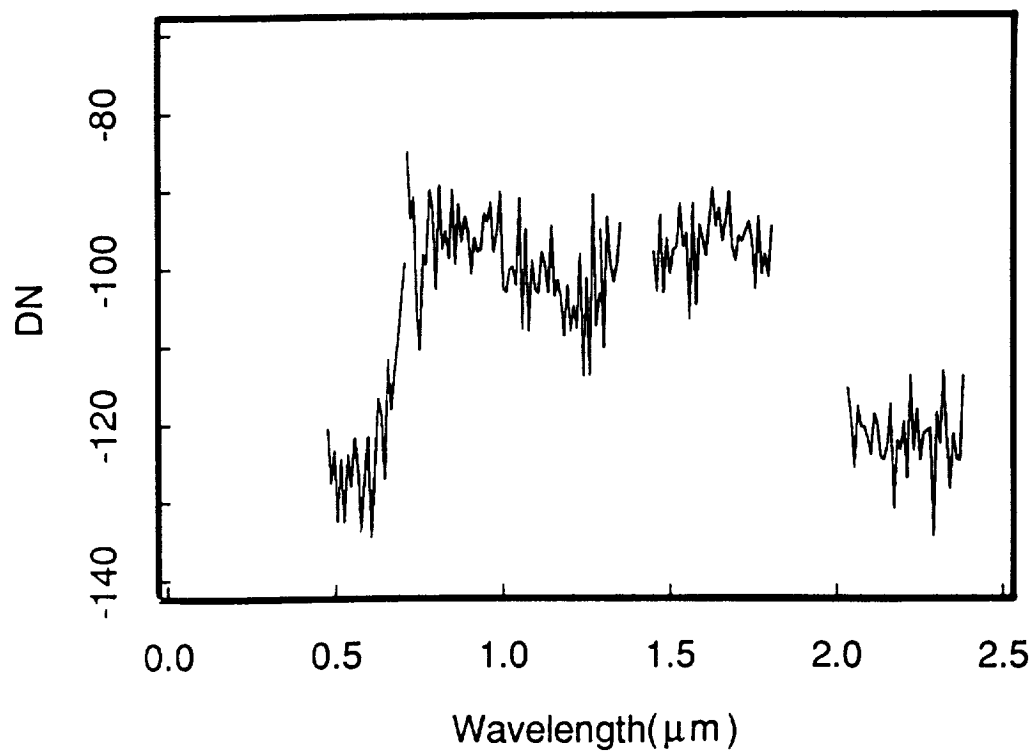


Figure 7. Offsets used to calibrate the data to reflectance.

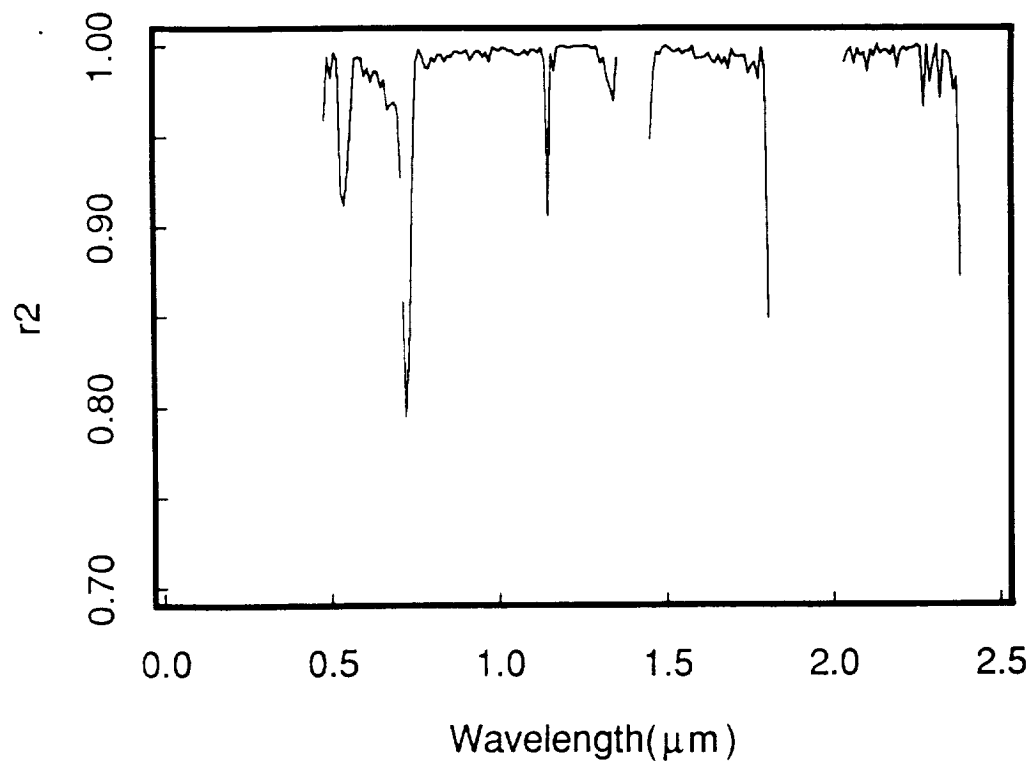


Figure 8. Regression coefficient (r^2) values plotted against wavelength.

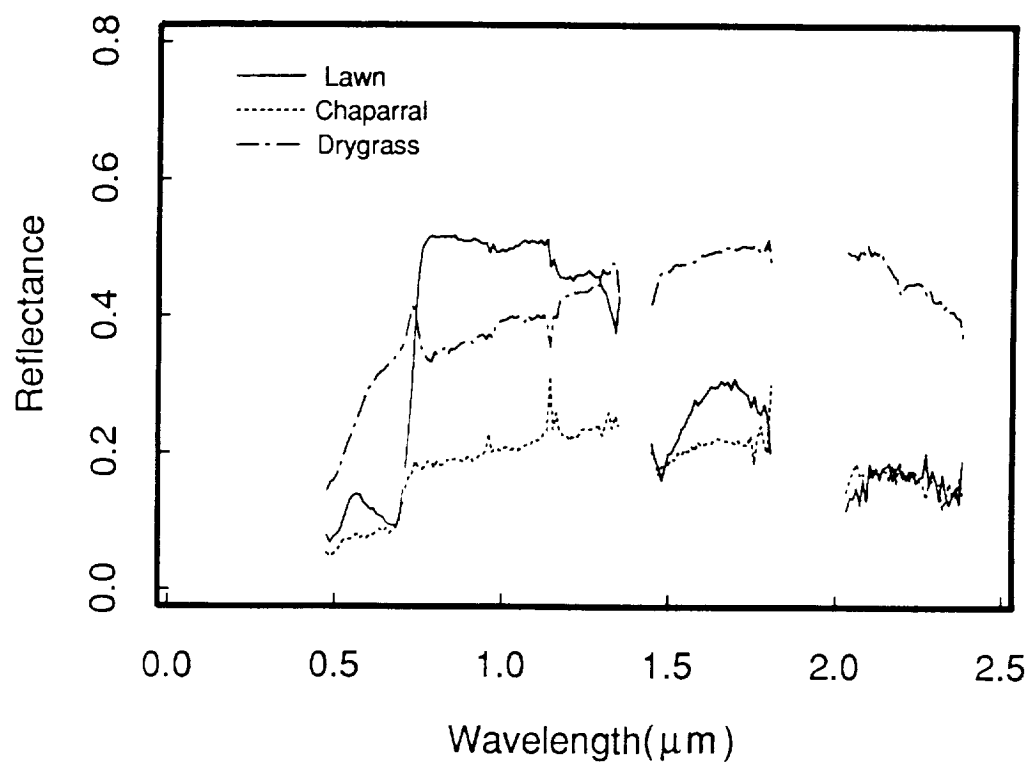


Figure 9. Reflectance spectra from calibrated AVIRIS data. The locations of lawn, chaparral and drygrass are shown on Figure 3, labeled as L, C and D respectively.

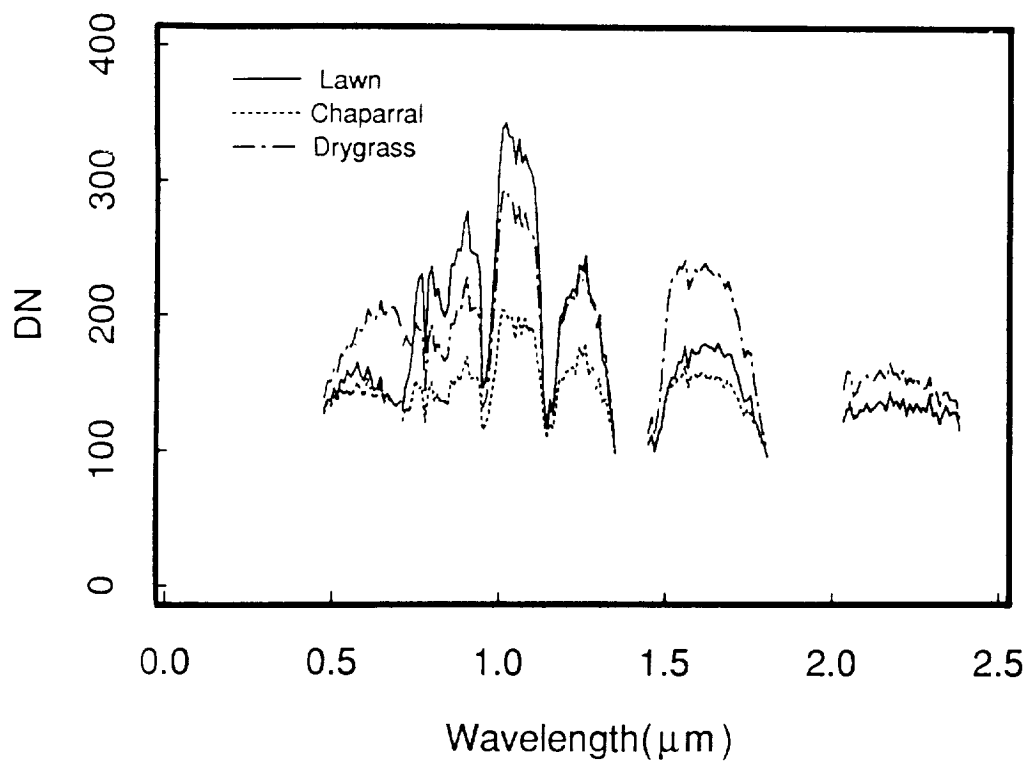


Figure 10. Uncalibrated AVIRIS data for the same areas shown in Figure 9.

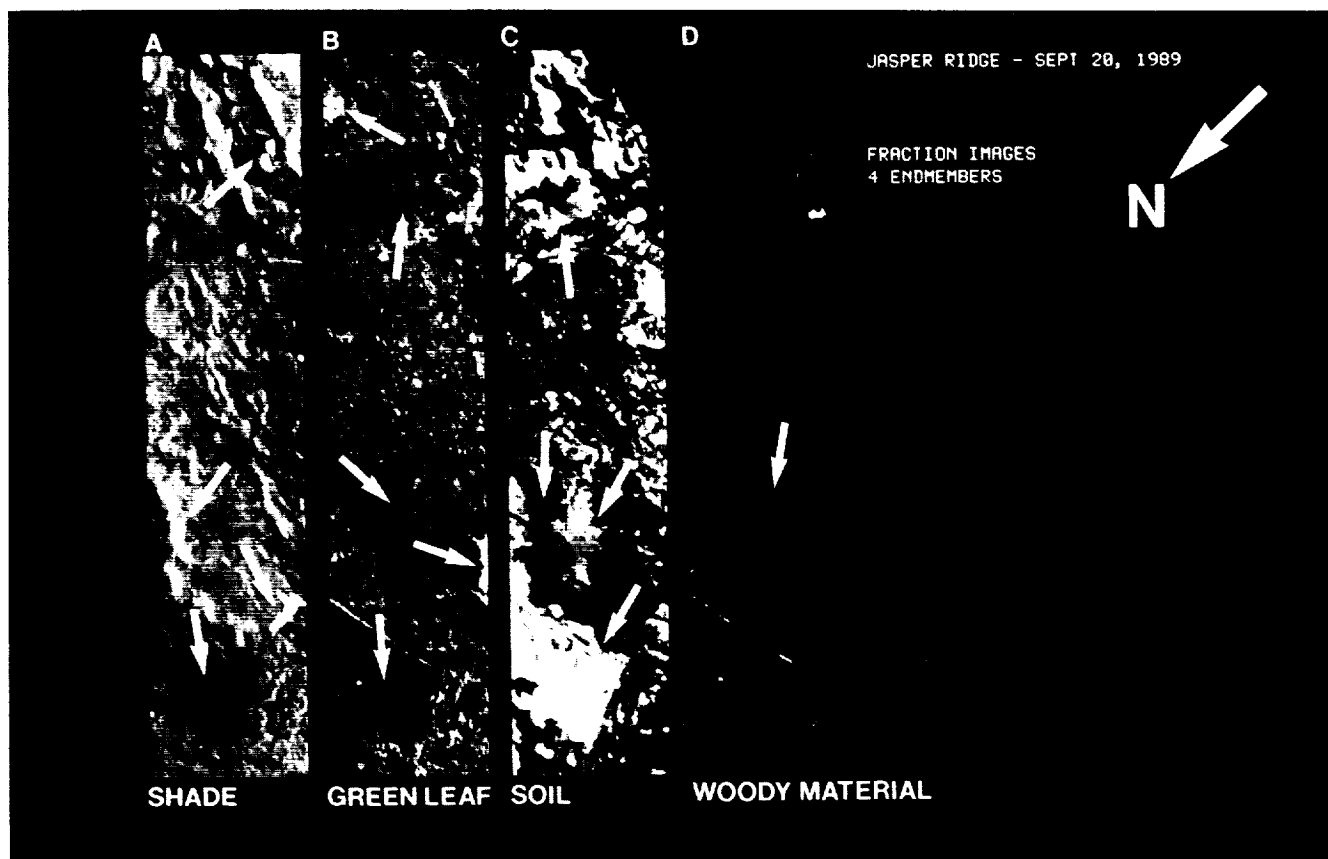


Figure 11. Fraction images of: A) shade, B) green leaf, C) soil, D) woody material.

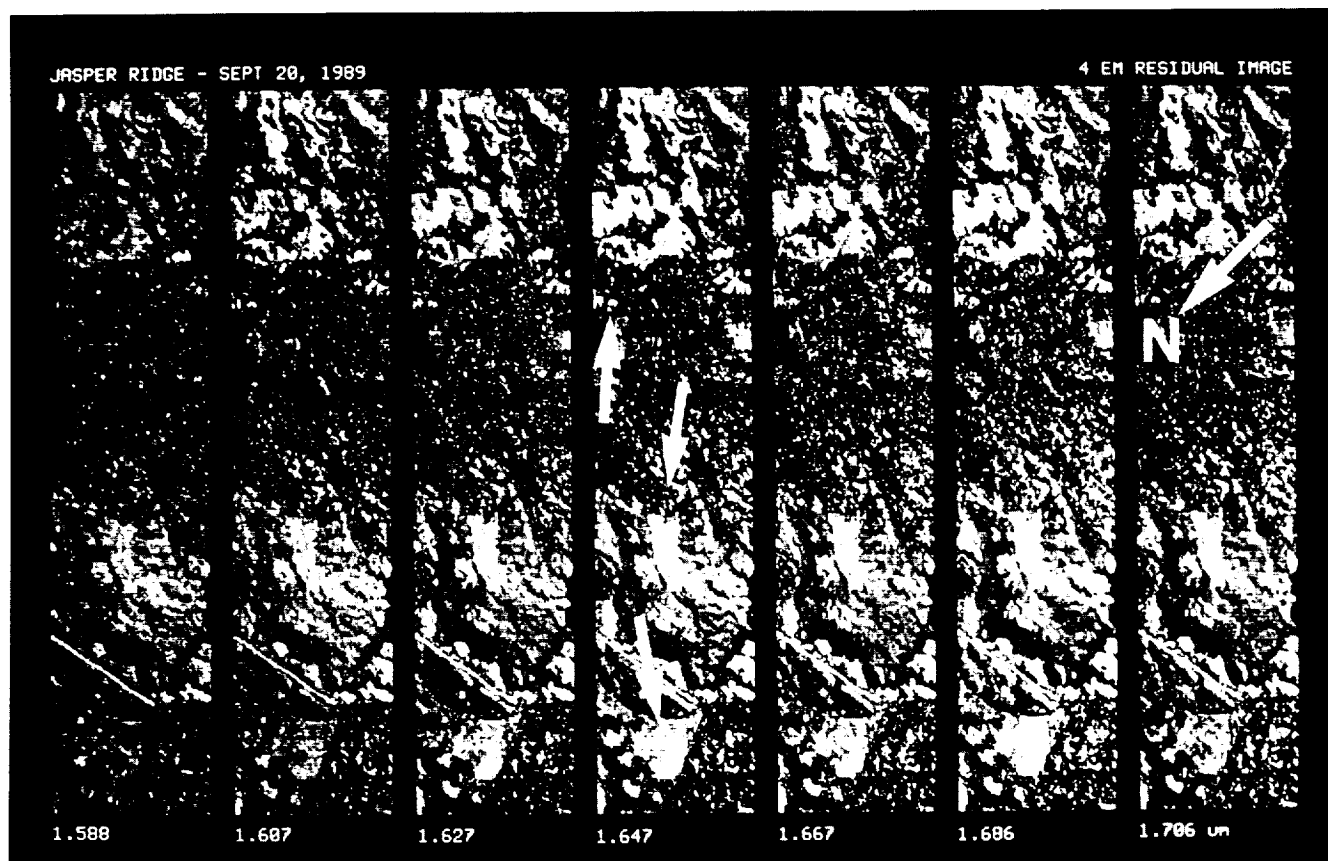


Figure 12. Band residual images for the 1.58 to 1.7 μm region. Light pixels correspond to areas in which the measured spectrum had higher reflectance than the modeled spectrum.

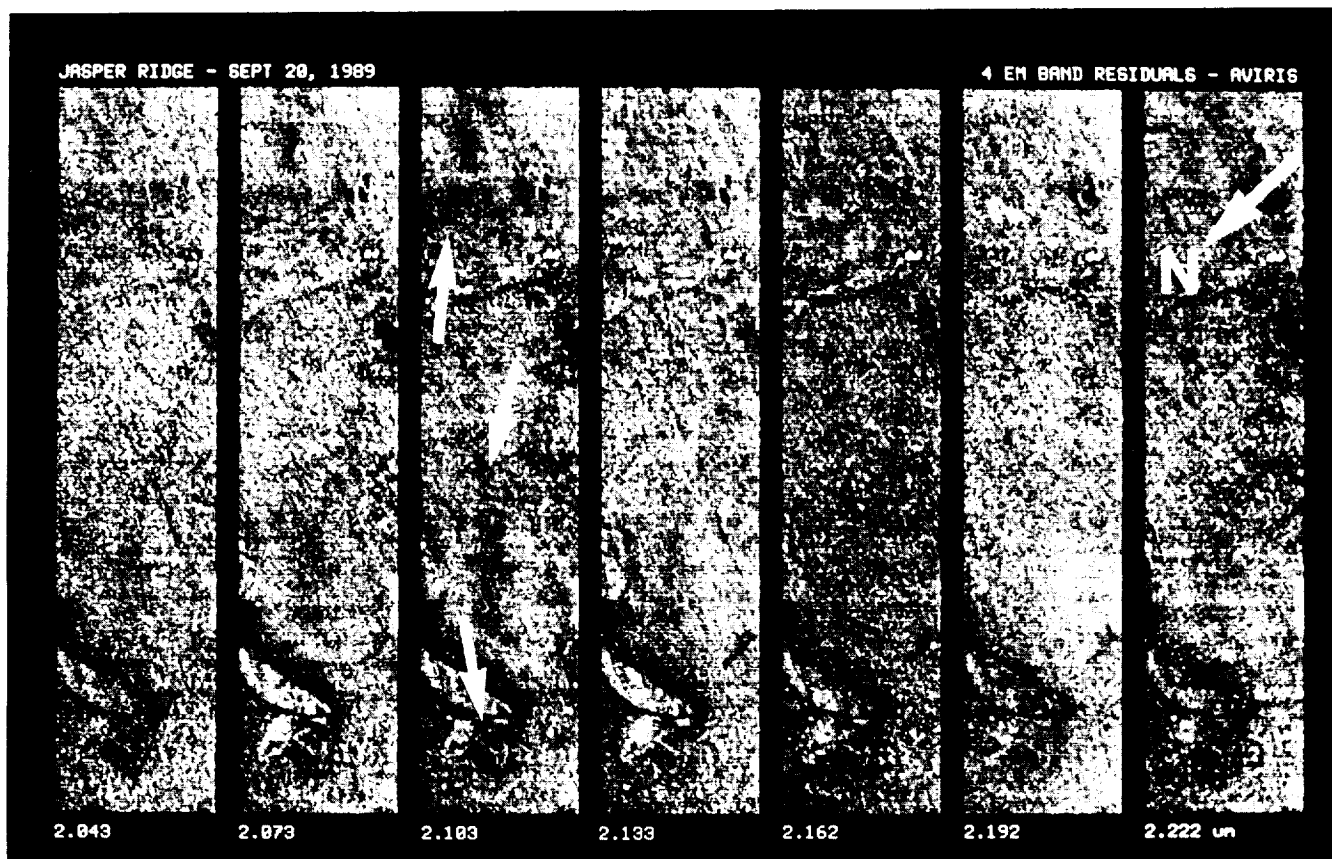


Figure 13. Band residuals for the 2.04 to 2.22 μm region. Dark areas to the north of Jasper Ridge show absorption features lacking in the modeled spectrum.

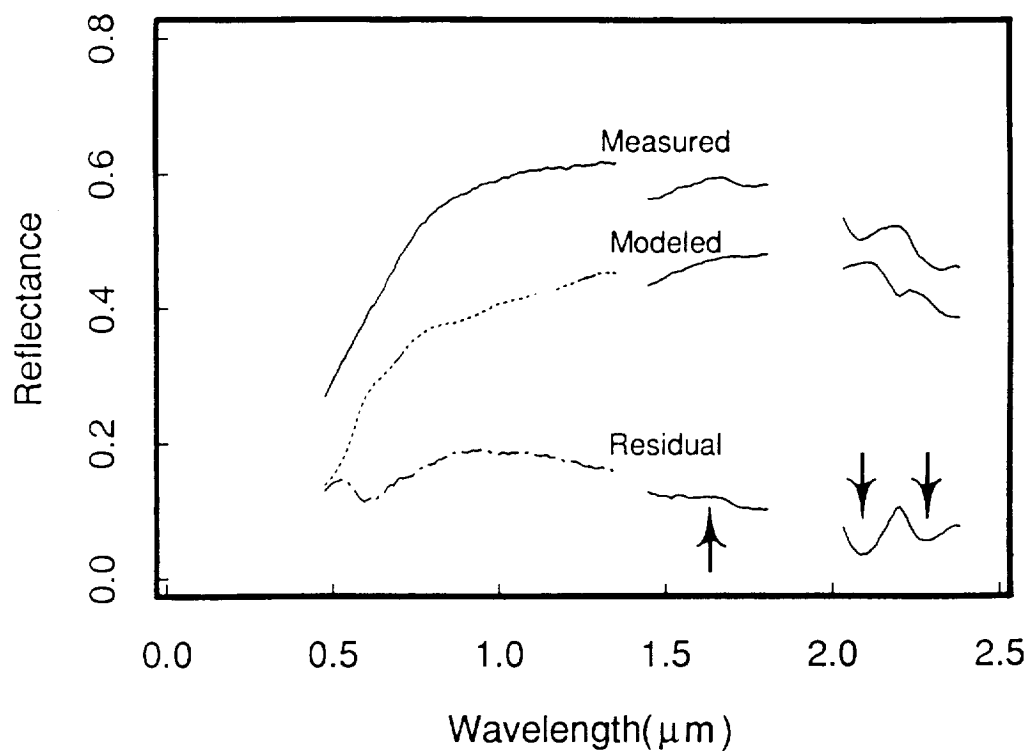


Figure 14. Comparison of measured reflectance spectrum of senescent grass (*Phalaris arundinacea*) to the linear model of drygrass. The band residual shows subtle spectral highs at 1.55 and 1.64 μm and prominent spectral lows at 2.083 and 2.29 μm (arrows on figure).

ARE THE SPECTRAL SHIFTS AN OPERATIONAL CONCEPT ?

CRITICAL ANALYSIS OF THEORETICAL AND EXPERIMENTAL RESULTS

F. BARET, S. JACQUEMOUD,* C. LEPRIEUR, G. GUYOT

INRA Bioclimatologie, BP91, 84143 Montfavet cedex, France
** LERTS, 18 Avenue E. Belin, 31400 Toulouse, France*

INTRODUCTION

With the recent development of imaging spectrometers, increasing attention has been paid to the interpretation of the new kind of information which can be obtained. Several studies have been carried out at differing scales, from the leaf to the canopy seen from space, in order to extract the vegetation biophysical characteristics from the monitored reflectance spectra. Most of the studies are focussed on the red edge, between 650 and 800 nm. This spectral domain corresponds to a sharp variation of the vegetation optical properties. A large number of studies report some spectral shifts termed blue shifts when shifting towards shorter wavelengths or red shifts when shifting towards longer wavelengths. These shifts are characterized by the wavelength of a particular point of the red edge. Authors generally refer to the inflection point the wavelength of which is termed λ_i . At leaf level, and mainly through experimental observations, λ_i is related to the chlorophyll concentrations and leaf structure (Gates, 1965; Horler *et al.*, 1983, Guyot *et al.*, 1990). The same trends are observed at canopy level, but with large scattering due to the effect of canopy geometry and external parameters such as the irradiance conditions and the viewing geometry (Collins, 1978; Chang and Collins, 1983; Collins *et al.*, 1983; Ferns *et al.*, 1984; Miller *et al.*, 1985; Gauthier and Neville, 1985; Baret *et al.*, 1987; Rock *et al.*, 1988a, 1988b; Demetriades-Shah and Steven, 1988). If all of these authors usually conclude that spectral shifts are of interest to characterize vegetation status, none has tried to rigourously demonstrate the additional information contained in the criteria derived from high spectral resolution. Furthermore, they generally agree on the complex nature of this spectral deformation, but few works explicitly quantify the λ_i sensitivity to canopy characteristics or external factors (Guyot *et al.*, 1990). The aim of this paper is to discuss the interest of λ_i in comparison with information content and signification of the classical single broad bands or vegetation indices. Finally, we will try to give an overview of the problems linked to a spatial determination of λ_i in terms of noise level and radiometric resolution capabilities. The discussion will be mainly carried out from theoretical data obtained through model simulations, but also with real AVIRIS data for the spatialization.

1. Equivalence between λ_i and single-band reflectance at leaf level

We have used the radiative transfer model elaborated by Jacquemoud and Baret (1990) to study the sensitivity of λ_i to leaf characteristics. This model requires only 2 input variables to compute, with a good accuracy, the leaf reflectance and transmittance

in the red edge domain : the Chlorophyll a and b concentration (C_{ab}) and an index related to the mesophyll structure (N). For compact leaves, N is close to one. For very thick and spongy mesophyll, N increases up to 2. It requires also three spectrally dependent parameters : the refractive index ($n(\lambda)$), the absorption coefficient of a compact leaf layer deprived of pigments and water ($k_0(\lambda)$), and the specific absorption coefficient of chlorophyll a and b ($K_{ab}(\lambda)$). $n(\lambda)$ which slowly and regularly decreases from 400 to 2500 nm has been set to its mean value ($n=1.442$). The $k_0(\lambda)$ absorption coefficient is approximated by :

$$k_0(\lambda) = 0.0114 - 4.87 \cdot 10^{-6} \cdot \lambda \quad [1]$$

$K_{ab}(\lambda)$ is described by a generalized logistic fit in the red edge. The sharp variation of K_{ab} , as seen on figure 1, is the cause of the red edge.

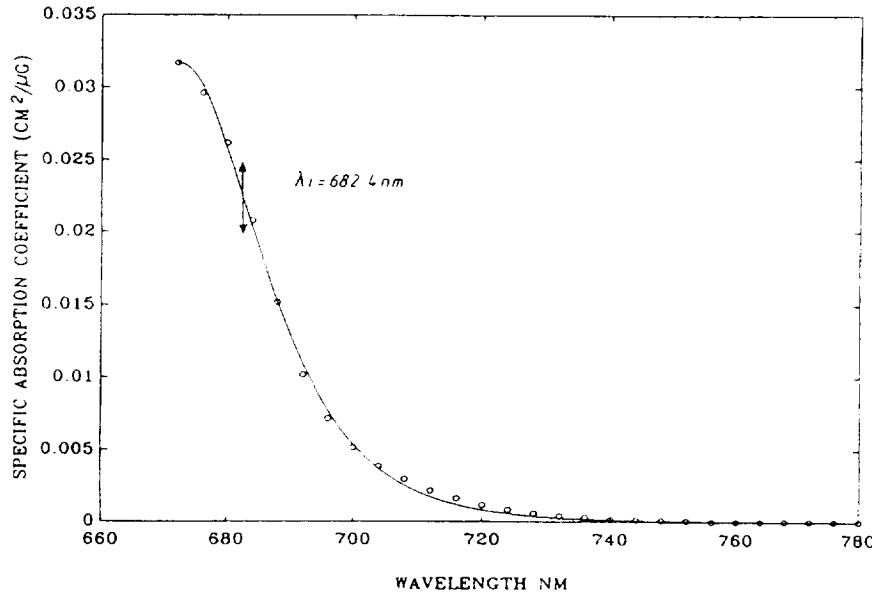


Figure 1. Specific absorption coefficient of chlorophyll a and b spectrum (from Jacquemoud and Baret, 1990). The solid line corresponds to a generalized logistic fit used in the formal derivation.

As an important remark, one can notice the dissymmetry of the specific absorption coefficient K_{ab} which probably induces a dissymmetry of the red edge. k_i is computed by formal derivation of this analytical model. Figures 2a and 2b demonstrate that λ_i mainly depends on chlorophyll concentration but also on the mesophyll structure parameter N which is in good agreement with previous results (Horler *et al.*, 1983). An increase in the chlorophyll concentration C_{ab} as well as an increase in the mesophyll structure parameter N produces a red shift. The transmittance is more sensitive to the structure parameter than the reflectance. λ_i varies from 683 nm for albino leaves deprived of pigments, to a maximum value close to 715 nm for a thick dark green leaf with a spongy mesophyll.

The question is now to demonstrate if this spectral deformation criterion provides any new information as compared with classical broad wavebands. We have plotted in a 3D space λ_i as a function of red (672 nm) and near infrared (780 nm) reflectance (respectively ρ_{672} and ρ_{780}) for a large range of variation of C_{ab} (from 1 to 70 $\text{g}\cdot\text{cm}^{-2}$ with 1 $\text{g}\cdot\text{cm}^{-2}$ step) and N (from 1.0 to 2.5 with 0.1 step). Figure 3 shows that the resulting surface is very smooth.

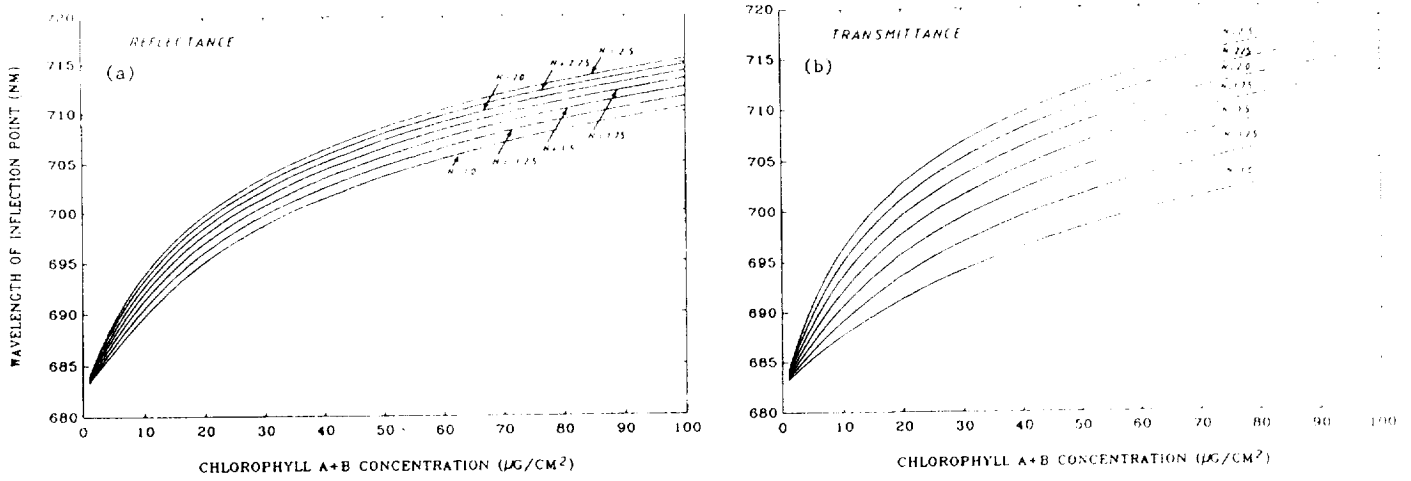


Figure 2. Effects of chlorophyll concentrations and mesophyll structure (represented by the N parameter) on reflectance (a) and transmittance (b) inflection point λ_i . Results from Jacquemoud and Baret (1990) model simulations.

It has been fitted to a 4th order polynomial surface and leads to a very low root mean square ($\text{rms}=0.73 \text{ nm}$). It can be concluded that, at leaf level, the spectral shifts observed in the red edge are equivalent to the combined red and near infrared wavebands :

$$\lambda_i = f(\rho_{672}, \rho_{780}) \quad [2]$$

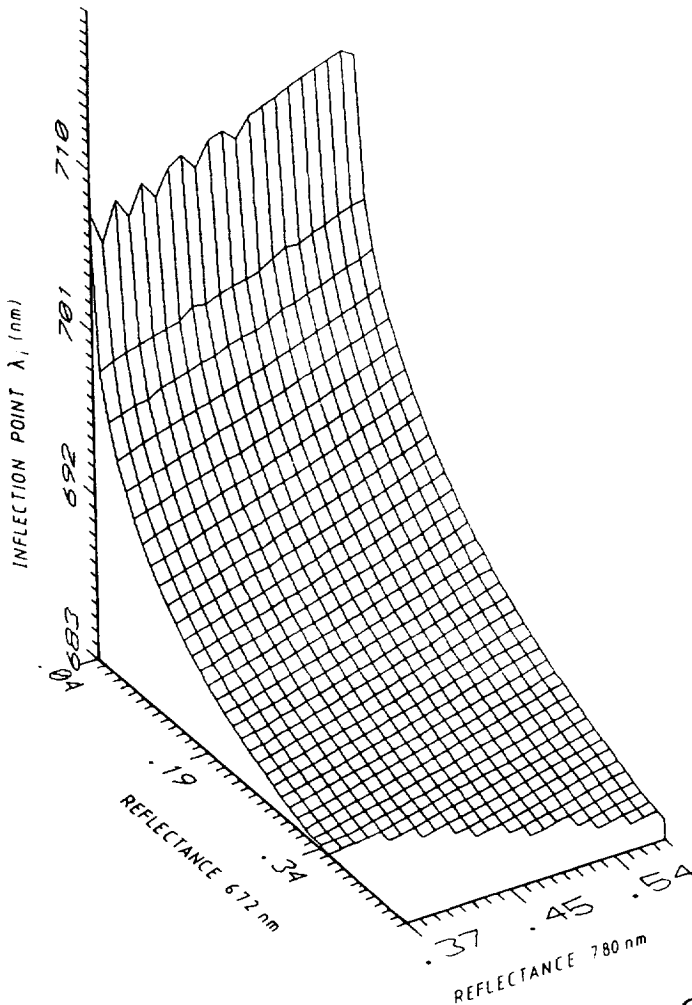


Figure 3. 3D representation of the function f relating λ_i to ρ_{672} and ρ_{780} .

This important property can be easily explained by the fact that λ_i is a function of C_{ab} and N , ρ_{780} depends on N and ρ_{672} is also determined by both N and C_{ab} :

$$\lambda_i = g(C_{ab}, N) ; \rho_{780} = h(N) ; \rho_{672} = i(C_{ab}, N)$$

$$\lambda_i = g(i^{-1}(\rho_{672}, h^{-1}(\rho_{780})), h^{-1}(\rho_{780})) = f(\rho_{672}, \rho_{780}) \quad [3]$$

Figure 2 reveals that λ_i is sensitive to changes in C_{ab} levels even for high values of C_{ab} as compared to the sensitivity of ρ_{672} which is close to the saturation level for C_{ab} close to 30 g.cm⁻² (Jacquemoud and Baret, 1990). But there is no difficulty to choose a particular wavelength in the red edge with a better sensitivity for higher C_{ab} values. Because no inflection point can be experimentally measured on spectra with a minimum of 3 data points, the determination of λ_i is no more of interest at leaf level. In the following section, we shall discuss the properties of λ_i at canopy level.

2. The nature of spectral shifts observed on canopies.

2.1. Method of λ_i computation.

To simulate canopy reflectance spectra and analyse the factors governing λ_i , we shall couple the preceding model of leaf optical properties with the SAIL (Verhoef, 1984, 1985) canopy reflectance model. This approach provides an analytical formulation of the canopy spectral reflectance ($R(\lambda)$) in the simple case of a one layer canopy with 90% directional incident radiation and 10% diffuse isotropic radiation irrespectively to the wavelength :

$$R(\lambda) = R(n(\lambda), k_o(\lambda), K_{ab}(\lambda), C_{ab}, N, LAI, \theta_o, \psi_o, \theta_s, \theta_l, \rho_s(\lambda)) \quad [4]$$

where LAI is the leaf area index, θ_o and ψ_o respectively the view zenith and azimuth angles, θ_s the solar zenith angle, θ_l the mean leaf inclination angle characterizing the leaf angle distribution function (in this case we have used ellipsoidal distributions : Campbell, 1986; Wang and Jarvis, 1986), ρ_s the soil background reflectance. In equation (4), only four terms are spectrally dependent. The first 3 are the spectral parameters of the leaf model described in the previous section. The last one, $\rho_s(\lambda)$ is assumed to be linearly wavelength dependent and verifies the soil line concept (Richardson and Wiegand, 1977) with mean values of soil line parameters (Guyot and Baret, 1990) :

$$\rho_s(780) = 1.2.\rho_s(672) + 0.04 \quad [5]$$

This leads to the following equation relating ρ_s to λ and $\rho_s(672)$ taken as a soil brightness variable :

$$\rho_s(\lambda) = \rho_s(672) + ((\lambda-672)/(780-672)).(0.2.\rho_s(672)+0.04) \quad [6]$$

The canopy spectral reflectance can then be set in the form of a function of the wavelength and a convenient notation vector of input variables which are not wavelength dependent :

$$R(\lambda) = F(\lambda, X) \text{ with } X = (C_{ab}, N, LAI, \theta_o, \psi_o, \theta_s, \theta_l, \rho_s(672)) \quad [7]$$

Henceforth, analytical derivation of F is possible. Because of the complexity of the second derivative expression which is required to compute λ_i , we have defined the implicit function $F^2(\lambda, X)$ as :

$$F^2(\lambda, X) = d^2F/d\lambda^2 \quad [8]$$

It can be mathematically demonstrated that, assuming the continuity of F^2 , and the existence and continuity of $d(F^2)/d\lambda$, the solution λ_i that equates F^2 to zero, exists and is unique. The λ_i solution is then numerically computed for each values of X input variables vector. We are now able to analyse the sensitivity of λ_i to the X values.

2.2. sensitivity analysis.

We will restrict the study to vertical viewing ($\theta_0=0$). Because the LAI is one of the main factors controlling the biophysical processes at canopy level, we shall analyse, at each step, the interaction between the LAI and any other input variable. The simulations show that the main factors governing the shifts are the chlorophyll concentration and, to a lesser extent, the leaf area index. Any increase of C_{ab} or LAI produces a red shift (figure 4a). This is in good agreement with experimental results obtained on chlorotic plants where the decrease in C_{ab} is generally linked to a decrease of the LAI (Demetriades-Shah and Steven, 1988; Rock *et al.*, 1988b). For LAI greater than 4, the amplitude of the shift when C_{ab} increases from 1 to 80 $g.cm^{-2}$ is not very different from that observed on leaf reflectance spectra (about 40 nm). For a green crop, let say C_{ab} greater than 40 $g.cm^{-2}$, the λ_i range of variation with LAI is reduced to 15 nm. But this amplitude of variation is reduced again when the canopies are more planophile (figure 4c). This effect of canopy geometry agrees with experimental results of Vanderbilt *et al.* (1988), even in the absence of simulated specular effects. The leaf mesophyll structure produces also red shifts (figure 4b) : in comparison with a compact monocotyledonous leaf ($N=1.0$), a dicotyledonous thick and spongy mesophyll leaf ($N=2.0$) shifts λ_i towards longer wavelength of about 5 nm which is not negligible if one reminds the 15 nm amplitude observed for green vegetation. Soil brightness (figure 4d) affects only slightly λ_i for intermediate LAI. Further simulations reveal the insignificant influence of irradiance conditions (sun position and diffuse/direct incoming radiation ratio) on λ_i .

From this sensitivity analysis, we have come to the conclusion that λ_i was mainly influenced by canopy parameters, particularly by the chlorophyll a and b concentration and the leaf area index. External or disturbing factors, such as soil brightness or irradiance conditions, have only little effects on λ_i . This criterion can also be of interest for high spectral resolution studies. We have to notice the small amplitude of variation which may restrict its efficiency in case of measurements performed with a relatively low accuracy. But we have still to discuss about the redundancy level with classical single wavebands.

2.3. Comparison with classical single wavebands or vegetation indices.

For a given wavelength, equation (7) states that the same set of input parameters (X vector) governs single reflectance band. As previously seen at leaf level, we will then test if the information provided by λ_i is equivalent to that contained in classical bands or in vegetation indices. We have simulated ρ_{672} , ρ_{780} , and λ_i for a large range of X vectors. The practical problem lies in the great number of arrangements if one wants to cross all of them. Hence, the input variables have been chosen at random according to

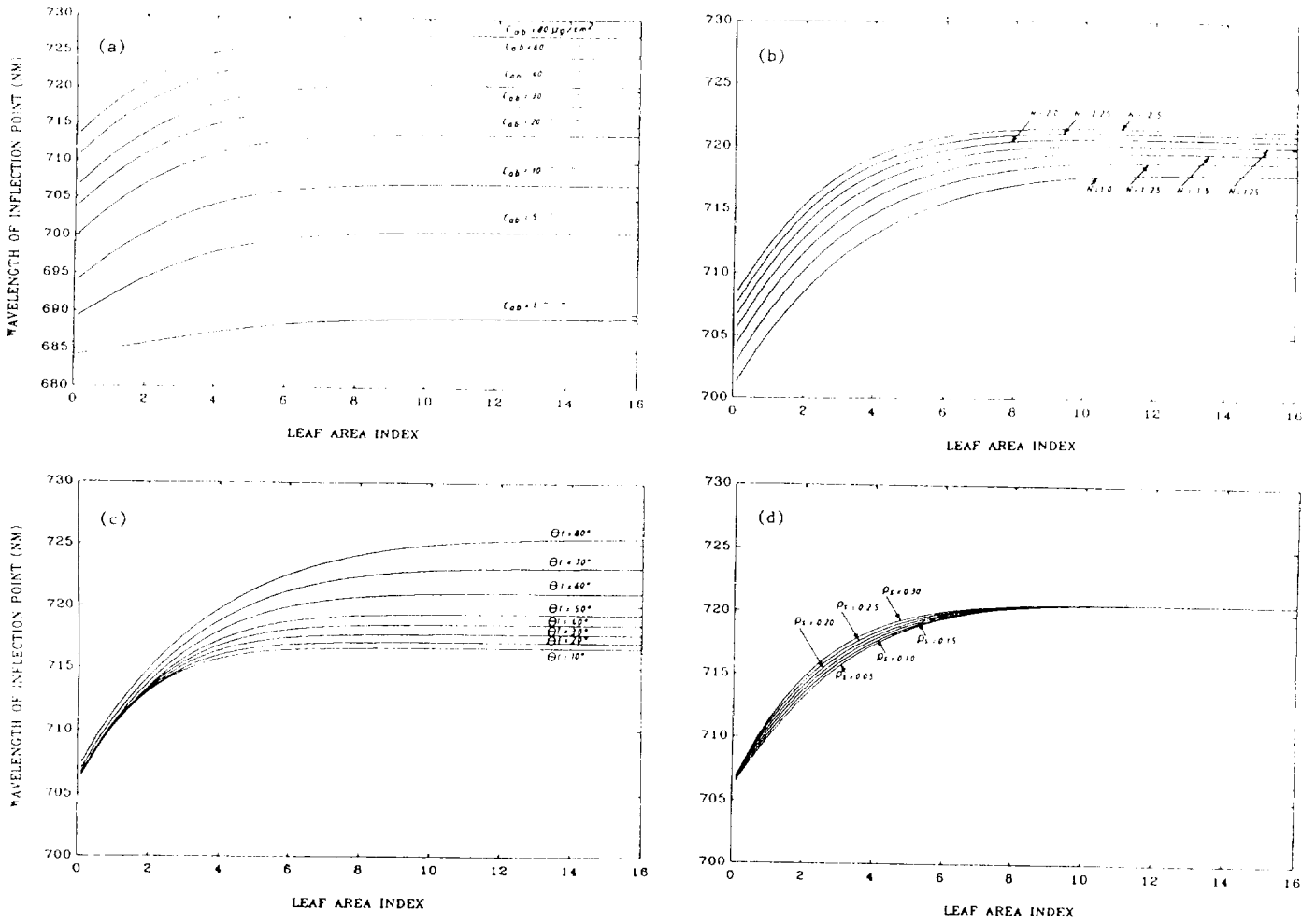


Figure 4. λ_i variations as a function of LAI for vertical viewing.
(a) : variation with C_{ab} for $X = (C_{ab}, 2, LAI, 0^\circ, 0^\circ, 40^\circ, 58^\circ, 0.15)$
(b) : variation with N for $X = (40, N, LAI, 0^\circ, 0^\circ, 40^\circ, 58^\circ, 0.15)$
(c) : variation with θ_l for $X = (40, 2, LAI, 0^\circ, 0^\circ, 40^\circ, \theta_l, 0.15)$
(d) : variation with $\rho_s(672)$ for $X = (40, 2, LAI, 0^\circ, 0^\circ, 40^\circ, 58^\circ, \rho_s(672))$

several statistical distributions : a uniform distribution for N ($1 < N < 2.5$), θ_o ($0^\circ < \theta_o < 60^\circ$), ψ_o ($0^\circ < \psi_o < 180^\circ$), θ_s ($20^\circ < \theta_s < 70^\circ$), θ_l ($20^\circ < \theta_l < 80^\circ$) and $\rho_s(672)$ ($0.05 < \rho_s(672) < 0.30$); a lognormal distribution for C_{ab} ($0.1 < C_{ab} < 80 \text{ g.cm}^{-2}$) and LAI ($0.1 < LAI < 16$). Such a choice is justified by the last analysis revealing a great sensitivity of λ_i for little values of C_{ab} and LAI. The surface corresponding to λ_i as a function of ρ_{672} and ρ_{780} is not as smooth as in the case of a leaf : it shows off some important scattering confirming the nonequivalence between λ_i and ρ_{672} and ρ_{780} and any red-near infrared vegetation index at canopy level. This is in good agreement with experimental data from Baret *et al.* (1987) and Leprieur (1989) who found that the λ_i information content was not strictly the same as the one provided by the Normalized Difference Vegetation Index (NDVI). A given set of red and near infrared reflectance (ρ_{672}, ρ_{780}) may correspond to several values of λ_i (see figure 5). The same conclusions are carried out even if we fix N , θ_o , ψ_o , θ_s or $\rho_s(672)$ which have little effect on λ_i and which can be measured or controlled (we let only C_{ab} , LAI and θ_l vary).

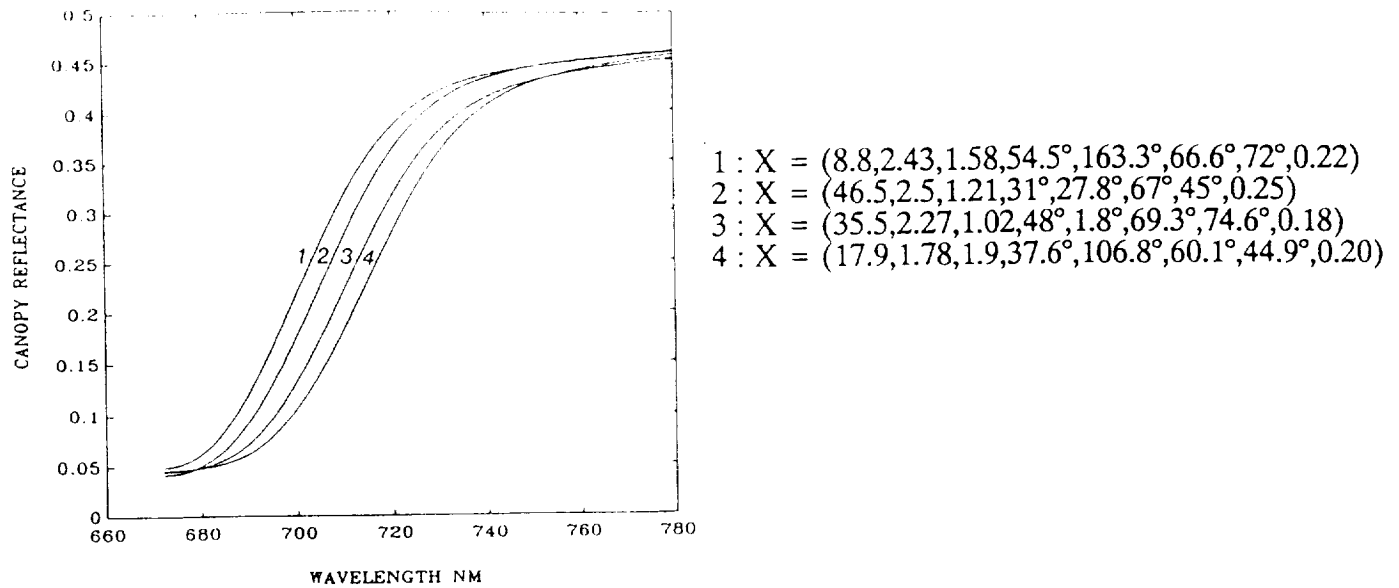


Figure 5. Demonstration of the nonequivalence between λ_i versus red and near infrared reflectances (ρ_{672} , ρ_{780}). Spectra 1 to 4 are respectively obtained for the following input variables:

Because any inflection point requires a minimum of 3 data points to be measured, we have added a new single reflectance band in order to test if this extra information significantly contributes to explain the λ_i variance. We have chosen the middle wavelength between the two red edge limits ($710\text{nm} = (780 + 740)/2$). The same set of random input variables is used to compute λ_i , ρ_{672} , ρ_{710} and ρ_{780} . Second order multivariate polynomial fitting of λ_i as a function of $(\rho_{672}, \rho_{710}, \rho_{780})$ explains more than 96% of λ_i variance. The choice of different or additional spectral bands, the use of other types than polynomial fit should explain degree of λ_i with single reflectance wavebands.

From these results, it is concluded as for the leaf level that the λ_i information is very redundant with the information contained in single reflectance wavebands because they depend on the same input variables. However, due to the important number of input variables (at least 8 if one excepts the diffuse/direct incoming radiation ratio), more single wavebands are required to get unambiguous and accurate relationships between spectral shifts and single band reflectance values. Spectral shifts could be then considered as a particular "vegetation index" of interest because of its low sensitivity to disturbing factors such as irradiance conditions or soil brightness and its high sensitivity to canopy characteristics such as chlorophyllian pigments concentration or LAI. But we have still to discuss about the way and the noise associated with the determination of λ_i monitored from space.

3. Spatial measurement of λ_i ; Evaluation of the accuracy and comparison with AVIRIS data.

This section is focussed on problems linked to the use of spectral shifts observed from space and is illustrated by AVIRIS experimental data. We will first and briefly discuss about the disturbing factors such as atmospheric effects and instrumental noise.

3.1. atmospheric effects and instrumental noise.

As it can be demonstrated (Gu, 1988), the signal measured from satellite level (S_{sat}) is related to ground level reflectance (ρ_g) through the linear relationship :

$$S_{\text{sat}}(\lambda) = a(\lambda) \cdot \rho_g(\lambda) + b(\lambda) \quad [9]$$

where $a(\lambda)$ and $b(\lambda)$ depend on the atmospheric effects if environmental effects are neglected. Molecular (Rayleigh) and aerosol (Mie) scattering are not very wavelength dependent in the red edge domain at the opposite of gaseous absorption. The 5S model (Tanre *et al.*, 1986) is used to show off the atmospheric gaseous transmittance computed for the AVIRIS spectral bands and for two differing cases (figure 6).

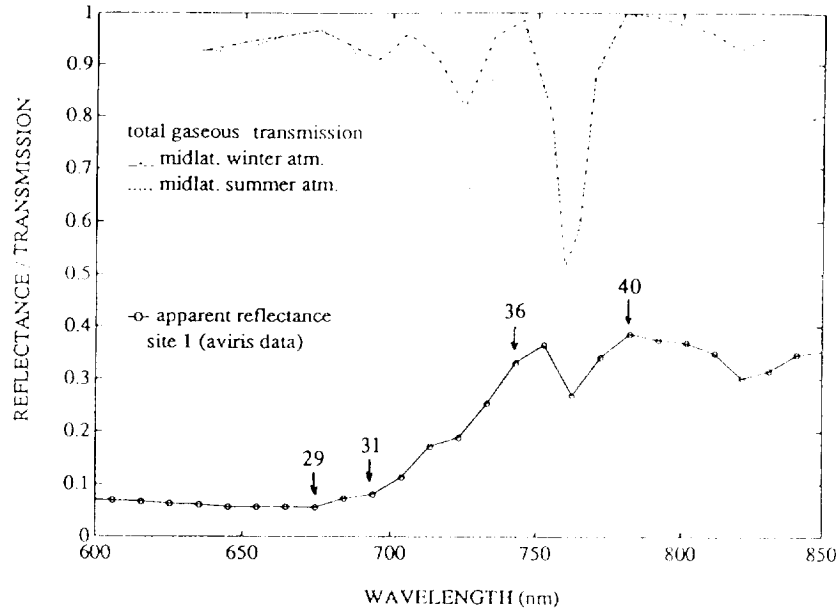


Figure 6. Gaseous transmission computed with 5S model for midlatitude winter and summer atmospheres for the AVIRIS wavebands. The effect on AVIRIS vegetation signal is represented by the bottom curve.

Gaseous absorption creates some strong disturbances on the reflectance spectra collected at satellite level. If channels strongly affected by the gaseous absorption are not used, the atmospheric effects will not affect the determination of λ_i because they just translate the whole spectrum (effect of the b parameter which is no more wavelength sensitive in this case) and transform it by an homothetic factor along the y axis (satellite signal, radiance or reflectance axis). This is one major advantage of this high spectral resolution derived criterion to remove most of the atmospherical effects as discussed previously by Guyot *et al.* (1990).

3.2. Methods of λ_i determination.

A brief review of the literature about the spectral shifts enables us to classify the methods of λ_i determination into 3 main categories :

- * derivation and spectra smoothing : These techniques are used for red edges measured with a lot of narrow spectral bands. It generally corresponds to spectra

performed at leaf or ground level (Horler et al., 1983; Demetriades-Shah and Steven, 1988 among others). Spectra are often smoothed to remove the residual high frequency noise before being derived. This smoothing technique tends to the model inversion technique when the number of parameters to adjust is reduced.

* model inversion techniques : Collins et al. (1983) used Cheybyshhev decomposition to represent the red edge and compute λ_i . But, as discussed by Gauthier and Neville (1988), this procedure still requires a too large number of spectral data points to be used with spaceborne spectroimagers. Chang and Collins (1983) and Miller et al. (1985) have used a gaussian model to fit the red edge. It requires three parameters and hence a minimum of three independent spectral bands in the red edge (including the minimum reflectance value close to 675 nm and the near infrared shoulder value reached since about 780nm) to be inverted. This procedure is time consuming and may cause problems to use it operationally on large scenes. Because it is also somewhat empirical to choose this particular gaussian model and also because exact inversion of coupled leaf optical properties and canopy reflectance models is delicate due to the number of parameters to adjust, some authors have used a more simplified assessment of λ_i .

* linear model : Because of the quasi linear pattern of the middle of the red edge (from 700 to 740 nm), Gauthier and Neville (1985) have approximated it to a straight line and have characterized the spectral shifts with its intercept at the wavelength axis. Baret et al. (1987) have later shown that the point corresponding to the mid reflectance amplitude of the red edge was a local symmetry centre very close to the true inflection point for green vegetation. Leprieur (1989) applies this definition to AVIRIS data :

$$\lambda_i = \lambda_{31} + (\lambda_{36} - \lambda_{31}) \cdot (\rho_i - \rho_{31}) / (\rho_{36} - \rho_{31}) \quad [10]$$

with $\rho_i = (\rho_{29} + \rho_{40})/2$ and the subscripts refer to the AVIRIS channels (29 = 674.4 nm; 31 = 694.0 nm; 36 = 743 nm; 40 = 782.2 nm). We will then use this simple definition of the spectral shift which requires only 4 narrow bands out of the gaseous absorption domain to discuss about the accuracy of its determination from space platforms.

3.3. Evaluation of λ_i accuracy and comparison with AVIRIS data.

The computation of the accuracy is based on the assumption that the errors on the reflectance (or radiance) measurements ($d\rho$) and on the wavelength position ($d\lambda$) of each channel are independent and have the same value ($d\rho$, $d\lambda$) for each of the four channels (Leprieur, 1990). It follows that the maximum error $d\lambda_i$ on λ_i is given by :

$$d\lambda_i = d\lambda + 2 \cdot d\rho \cdot (\lambda_{36} - \lambda_{31}) \cdot (\rho_i - \rho_{31}) / (\rho_{36} - \rho_{31})^2 \quad [11]$$

The error is computed for differing values of LAI for crop with $X = (40, 1.2, \text{LAI}, 0^\circ, 0^\circ, 30^\circ, 58^\circ, 0.15)$. It reveals (figure 7) that $d\lambda_i$ is very important for low leaf area indices and increases drastically with $d\rho$. For larger LAI, the noise level is reduced and mainly depends on $d\lambda$. The computed signal/noise ratios confirm that, even for low errors on λ and ρ , λ_i estimation should be very noisy compared to its sensitivity to LAI. The same results have been also found for the determination of the chlorophyll

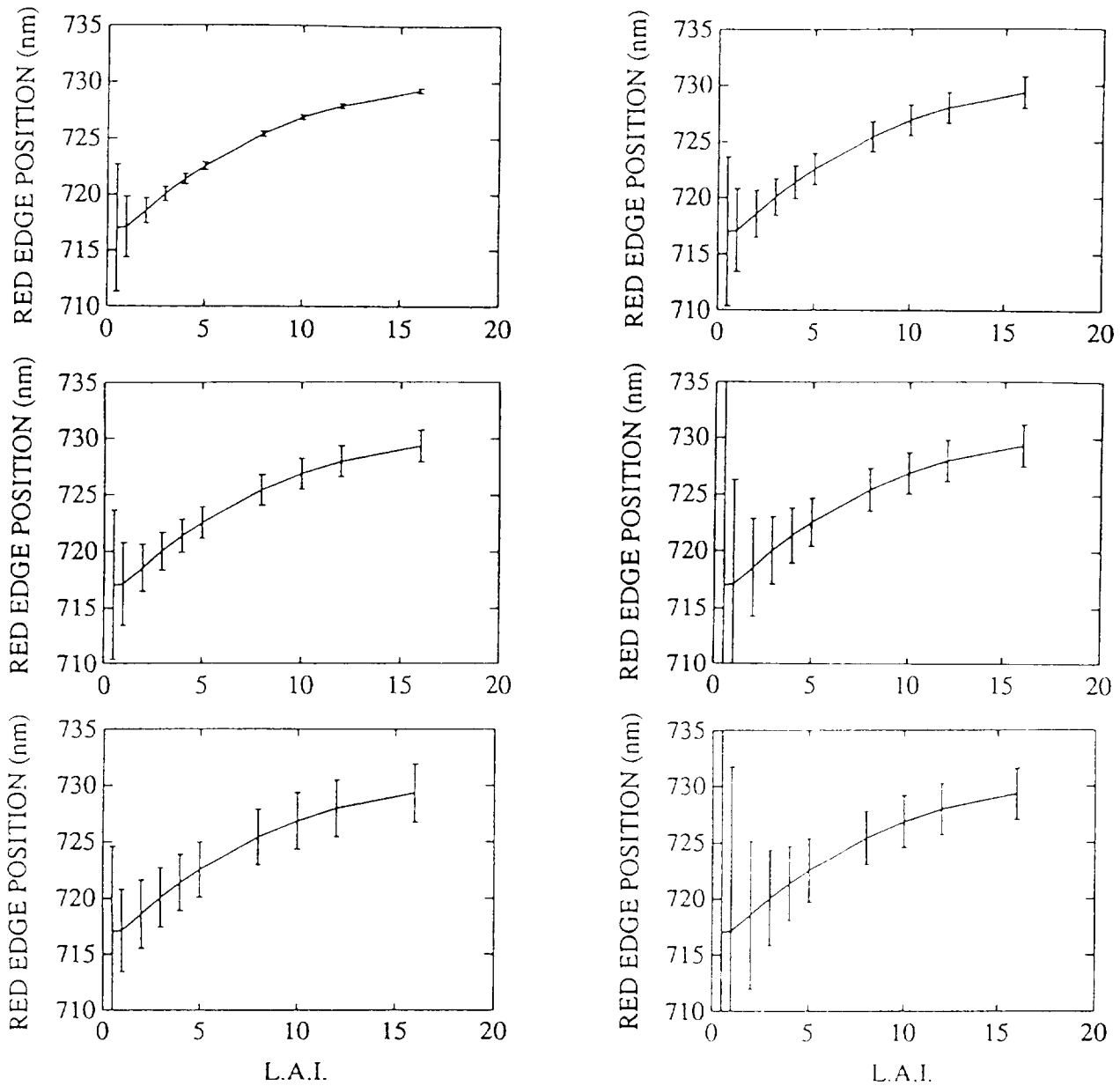


Figure 7. λ_i errors as a function of L.A.I. for differing values of $d\lambda$ and $d\rho$:

- (a): $d\rho = 0.001$; $d\lambda = 0.0$ nm
- (b): $d\rho = 0.001$; $d\lambda = 0.5$ nm
- (c): $d\rho = 0.001$; $d\lambda = 1.0$ nm
- (d): $d\rho = 0.001$; $d\lambda = 0.5$ nm
- (e): $d\rho = 0.003$; $d\lambda = 0.5$ nm
- (f): $d\rho = 0.005$; $d\lambda = 0.5$ nm

content. This evaluation of the error is performed under simplifying assumptions, and should be the maximum one. Because we have no detailed information on the error structure of the spectro-imaging systems, there is no other possibility to get an idea of the noise, except by looking at the discrimination capability on contrasted objects. This has been done on one AVIRIS scene (Moffet field test site in San Francisco Bay). It clearly appears on figure 8 that the λ_i noise is not so important as the one computed.

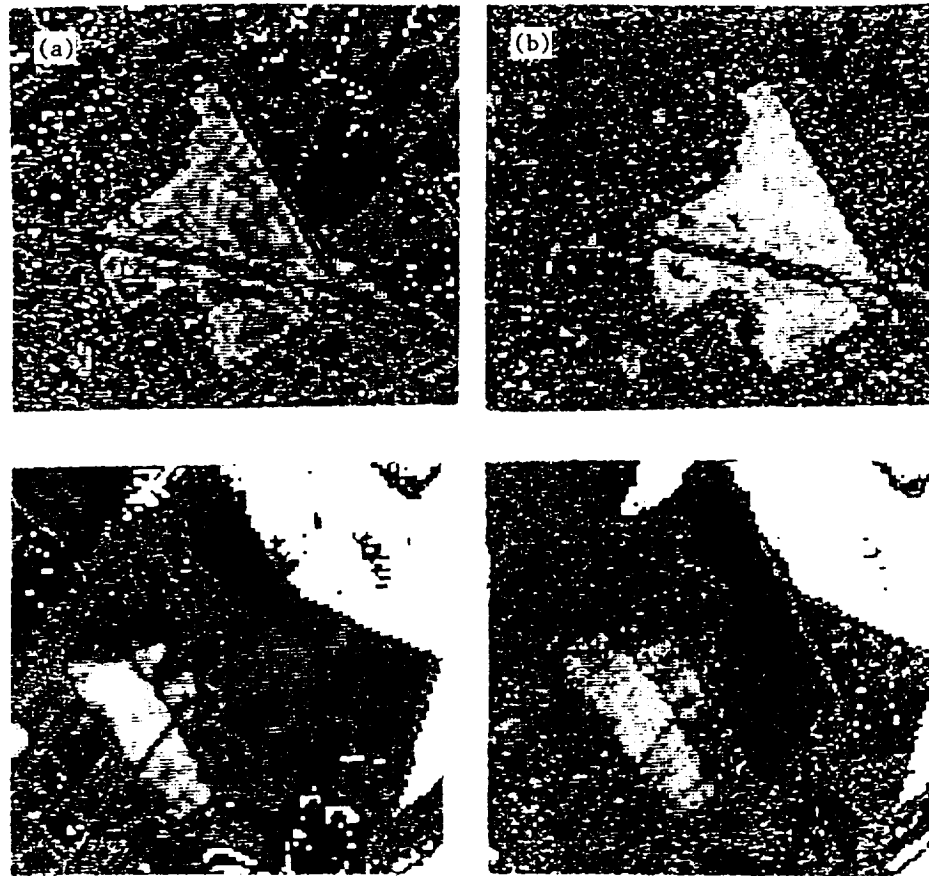
ORIGINAL PAGE
BLACK AND WHITE PHOTOGRAPH

Figure 8. Comparison between NDVI (a) and λ_i (b) observed from AVIRIS on two differing test sites.

Table 1 shows off that for 8 test sites chosen to be representative of the differing vegetation types, the root mean square decreases when green vegetation materials increase as previously expected, but remains around 1.5 nm for a 16 nm maximum range variation of the shifts. It seems to be not too bad as compared to the NDVI which has a corresponding rms close to 0.04 for a maximum range of variation of 0.043.

Site	number pixels	λ_i (nm) mean	λ_i (nm) rms	NDVI mean	NDVI rms
1	203	721.4	1.2	0.74	0.04
2	309	720.1	1.0	0.72	0.03
3	164	719.3	1.0	0.65	0.03
4	118	705.1	1.3	0.55	0.01
5	59	716.4	2.2	0.51	0.05
6	292	715.2	2.4	0.37	0.05
7	146	711.7	2.8	0.32	0.05
8	24	712.3	1.4	0.31	0.06

Table 1. Mean values and rms of λ_i and NDVI computed from 8 test sites.

This apparent contradiction between estimated values of the noise associated to λ_i and the one derived from real AVIRIS data lies in the fact that we have to improve

our knowledge about the instrumental noise structure and refine the error calculation procedure. Nevertheless, this section proves from the experiment that λ_i can be determined with an accuracy equivalent to the one associated to classical vegetation indices as NDVI, except when the vegetation is very scarce. In this case, the low slope of the red edge induces an important error on the determination of the λ_i value.

4. Conclusion.

This brief analysis shows off that the information content of the spectral shifts of the red edge is not different from the one contained in single bands reflectance or vegetation indices. At that stage of the discussion, one could say that spectral shifts are reduced to a particular vegetation index which minimizes external factors such as the irradiance conditions and soil brightness effects. It is very sensitive to the chlorophyll content and the leaf area index, and to a lesser extent, to leaf mesophyll structure and leaf orientation. All of these results obtained through model simulations are in good agreement with the literature. They should be still valid for any "edges" corresponding to a sharp variation of a specific absorption coefficient: One has just to replace the chlorophyll concentration by the corresponding absorbing material content. For example, in the middle infrared, several edges due to water absorption features exist.

When this spectral shift concept is applied at the satellite scale characterized by few wavebands and additional disturbing factors such as instrumental noise and atmospheric effects, the linear model enables getting the shift with only four wavebands. If these wavebands are chosen to be out of the gaseous absorption domain, this spectral shift should be very little dependent upon the atmospheric conditions. This important property is surely one of the main advantages of this spectral shift concept. The theoretical analysis of the noise is actually limited by the bad knowledge about the instrumental error structure. Nevertheless, from real AVIRIS data, it seems that, except for scarce vegetation, the accuracy of the spectral shift determination is close to the one observed for classical vegetation indices.

If High spectral resolution programs are developed until some years, it is certainly to try to improve our knowledge on the target from spaceborne sensors. It seems therefore somewhat restrictive to limit the high spectral resolution capabilities to build empirical indices such as the spectral shifts. The main questions which still remain unsolved are : How many and what wavebands are required to get the full spectral information of canopies ? How can we extract the pertinent characteristics of the vegetation from this spectral information ? And how can we use redundancy between differing channels to remove the atmospheric effects. Researchers have still some time to spend to struggle with these complex problems.

REFERENCES

- Baret F., Champion I., Guyot G., Podaire A., 1987, Monitoring wheat canopies with a high spectral resolution radiometer, *Remote Sens. of Environ.*, 22:367-378
- Campbell G.S., 1986, Extinction coefficients for radiation in plant canopies calculated using ellipsoidal inclination angle distribution, *Agric. & Forest Meteor.*, 36:317-321
- Chang S.H., Collins W., 1983, Confirmation of the airborne biogeophysical mineral exploration technique using laboratory methods, *Econ. Geol.*, Vol. 78, 723-736

Collins W., 1978, Remote Sensing of crop type and maturity, *Photogram. Eng. and Remote Sens.*, Vol. 44, No. 43, 43-55

Collins W., Chang S.H., Raines G., Canney F., Ashley R., 1983, Airborne biogeophysical mapping of hidden mineral deposits, *Econ. Geol.*, Vol. 78, 737-749

Demetriades-Shah T.H., Steven M.D., 1988, High spectral resolution indices for monitoring crop growth and chlorosis, in *Proc. of the 4th Int. Coll. on Spectral Signatures of Objects in Remote Sensing*, Aussois (France), 18-22 January 1988, ESA SP-287, 299-302

Ferns D.C., Zara S.J., Barber J., 1984, Application of high resolution spectroradiometry to vegetation, *Photogram. Eng. and Remote Sens.*, Vol. 50, No. 12, 1725-1735

Gates D.M., Keegan H.J., Schleter J.C., Weidner V.R., 1965, Spectral properties of plants, *Appl. Opt.*, Vol. 4, No. 1, 11-20

Gauthier R.P., Neville R.A., 1985, Narrow-band multispectral imagery of the vegetation red reflectance edge for use in geobotanical remote sensing, in *Proc. 3rd Int. Coll. on Spectral Signatures of Objects in Remote Sensing*, Les Arcs (France), 16-20 Dec., ESA SP-247, 233-236

Gu Xing-Fa, 1988, Mise en relation des luminances mesurées par SPOT avec les réflectances de surfaces agricoles mesurées au sol, Mémoire de DEA "Méthodes Physiques en Télédétection", INRA-Université Paris VII.

Guyot G., Baret F., 1990, Potentials and limits of vegetation indices, submitted for publication to *Remote Sens. Environ.*

Guyot G., Baret F., Jacquemoud S., 1990, Imaging spectroscopy for vegetation studies, in *Imaging Spectroscopy : Fundamentals and Prospective Applications*, F. Toselli and J. Bodechtel ed., Kluwer Academic Publishers (Dordrecht, The Netherlands).

Horler D.N.H., Dockray M., Barber J., 1983, The red edge of plant leaf reflectance, *Int. J. Remote Sensing*, Vol. 4, No. 2, 273-288

Jacquemoud S., Baret F., 1990, Modelling leaf optical properties, submitted for publication to *Remote Sens. Environ.*

Leprieur C.E., 1989, Preliminary evaluation of AVIRIS airborne measurements for vegetation, in *Proc. of the 9th EARSeL Symp.*, Espoo (Finland), 27 June - 1 July, 6 p

Leprieur C.E., 1990, Comparaison des ordres de grandeur des mesures et des erreurs théoriques associées en haute résolution spectrale (domaine visible et proche infrarouge), LERTS-CNES unpublished works

Miller J.R., Hare E.W., Neville R.A., Gauthier R.P., McColl D., Till S.M., 1985, Correlation of metal concentration with anomalies in narrow band multispectral imagery of the vegetation red reflectance edge, in *Proc. of the Int. Symp. on Remote Sensing of Environ.*, 4th Thematic Conference, Remote Sensing for Exploration Geology, San Francisco, April 1-4, 143-153

Richardson A.J., Wiegand C.L., 1977, Distinguishing vegetation from soil-background information, *Photogram. Eng. and Remote Sens.*, 43:1541-1542

Rock B.N., Hoshizaki T., Miller J.R., 1988a, Comparison of *in situ* and airborne spectral measurements of the blue shift associated with forest decline, *Remote Sens. Environ.*, 24:109-127

Rock B.N., Elvidge C.D., Defeo N.J., 1988b, Assessment of AVIRIS data from vegetated sites in the Owens Valley, California, In *Proc. of the Airborne Visible/Infrared Imaging Spectrometer (AVIRIS) Performance Evaluation*, Workshop June 6,7 and 8 1988, Gregg Vane Editor, NASA-JPL publication 88-38, 88-96

Tanré D., Deroo C., Dahaut P., Herman M., Morcrette J.J., Perbos J., Deschamps P.Y., 1986, Effets atmosphériques en télédétection. Logiciel de simulation du signal satellitaire dans le spectre solaire, in *Proc. 3rd Int. Coll. on Spectral Signatures of Objects in Remote Sensing*, Les Arcs (France), 16-20 Dec., ESA SP-247, 315-319.

Vanderbilt V.C., Ustin S.L., Clark J., 1988, Canopy geometry changes due to wind cause red edge spectral shift, in *Proc. of IGARSS'88 Symp.*, Edinburgh (Scotland), 13-16 Sept., ESA SP-284, 835

Verhoef W., 1984, Light scattering by leaf layers with application to canopy reflectance modeling : the SAIL model, *Remote Sens. Environ.*, 16:125-141

Verhoef W., 1985, Earth Observation modeling based on layer scattering matrices, *Remote Sens. Environ.*, 17:165-178

Wang Y.P., Jarvis P.G., 1988, Mean leaf angles for the ellipsoidal inclination angle distribution, *Agric. & Forest Meteor.*, 43:319-321

POTENTIAL FOR DETERMINATION OF LEAF CHLOROPHYLL CONTENT USING AVIRIS

J. R. MILLER, J. R. FREEMANTLE, M. J. BELANGER, Earth Observations Laboratory, Institute for Space and Terrestrial Science, York University, Toronto, Canada, C. D. ELVIDGE, Desert Research Institute, University of Nevada, Reno, Nevada, USA and M. G. BOYER, Biology Dept., York University, Toronto, Ontario, Canada.

INTRODUCTION

It is widely known that pigments play the dominant role in determining leaf reflectance in the visible to near infrared spectral region. Specifically, the reflectance amplitude at 550nm and the spectral position of the red edge have been linked to leaf chlorophyll pigment content through field and laboratory studies. The potential to transfer such results to applications in forestry and agriculture through remote sensing presents the challenge to place interpretation algorithms on a quantitative basis and to develop measurement methodologies that are amenable for practical use with modern satellite/airborne sensors. Additional important questions being explored in current research include: (i) are such relationships species-dependent, (ii) do leaf-level conclusions translate to canopy-level relationships, and (iii) what sensor configurations, in terms of spectral/spatial resolutions, permit leaf chlorophyll content to be estimated?

This paper represents a preliminary evaluation of the potential of the AVIRIS sensor to provide quantitative estimates of canopy chlorophyll through the use of laboratory/field results in interpretation algorithms applied to AVIRIS imagery. Five AVIRIS images have been acquired over Stanford University's Jasper Ridge Biological Preserve during the period July 24, 1987 to September 20, 1989, providing imagery in April, June, July, August and September spanning the vegetation seasonal cycle, albeit from different years (see Table 1). Other papers have recently reported on the seasonal variation in the AVIRIS reflectance properties of the six dominant vegetation communities at the Jasper Ridge site (Elvidge and Portigal 1990, Miller *et al.* 1990a). This paper is focussed on the potential of AVIRIS to extract leaf chlorophyll estimates from the red edge reflectance spectral region.

METHODOLOGY

Leaf Chlorophyll and Red Edge Parameters

A two-year study of the relationship between leaf spectral reflectance properties and botanical parameters (chlorophyll *a* and *b*, total chlorophyll and water content) has been recently completed, consisting of weekly samples collected of leaves of ten trees located on the campus of York University, Toronto, Canada and subsequent laboratory analyses. Joint botanical and optical data were gathered from the deciduous species: aspen (*Populus tremuloides* Michx.), bur oak (*Quercus macrocarpa* Michx.), Manitoba maple (*Acer negundo* L.), sugar maple (*Acer saccharum* Marsh.) and Norway maple (*Acer platanoides* L. var 'Crimson King'). A detailed description of the experimental methodology is presented elsewhere (Belanger 1990; Belanger *et al.* 1990, Miller *et al.* 1990b).

The pigment data was obtained from 2 cm diameter leaf discs which were ground with a mortar and pestle in acid washed sand, extracted, centrifuged and assayed in 80 percent v/v acetone distilled water. The extracts measured with a Pye Unicam SP8-500 UV/VIS spectrophotometer were used to obtain estimates of pigment concentrations on an area

basis for chlorophylls *a* and *b* and a total using the specific absorption coefficients given by MacKinney (1941).

Spectral reflectance measurements (500nm to 900nm) were made of optically thick leaf stacks, relative to BaSO₄, using a Jobin-Yvon model H-20 V-IR monochromator (4 nm spectral resolution). The leaves were consistently measured at a mid-leaf point to the right side of the main leaf vein. This target area was lightly marked, with a felt pen, and the leaves were then stored in polyethylene bags and refrigerated discs were subsequently cut from the marked leaf area for the chlorophyll analyses.

The optical parameters which are normally used to define the red edge region (680-800 nm) include: R_s (the near IR shoulder reflectance), R_o (the red edge reflectance minimum), λ_o (the wavelength corresponding to R_o), λ_{pr} (the red edge inflection point wavelength, determined from the first derivative maximum). The Inverted Gaussian model (IGM) has been fitted to the red edge (Miller *et al.* 1985, 1990c) which is defined by four parameters: R_{sg} (the Gaussian shoulder reflectance), R_{og} (the Gaussian red edge reflectance minimum), λ_{og} (the wavelength corresponding to R_{og}) and λ_{pg} (the Gaussian inflection point). The IGM parameters are thought to represent a smoothed red edge reflectance curve so that the real and IGM parameters are very similar but show important differences (Miller *et al.* 1990c). In particular, it is important to note that the specification of the red edge position from simple derivative analysis of reflectance spectra is not independent of the instrument spectral resolution because the red edge normally manifests a distinct bi-modality, or at least an asymmetry, in the first derivative curve (Boochs *et al.* 1988; Horler *et al.* 1983, Miller *et al.* 1990b). The use of the IGM curve fitting approach has been found to extract red edge spectral information that is related to the dominant controlling parameter: chlorophyll content (Belanger *et al.* 1990), independent of variations in the bi-modality in the first derivative curve.

The results of the data analysis for leaf samples from spring flush (Julian day 135) through senescence (Julian day 288) are summarized in Figure 1. These data indicate that the relationship between total chlorophyll content per unit leaf area and red edge spectral position parameters λ_{pg} and λ_{og} , obtained by curve fitting with the IG model is species independent for the 4 deciduous species studied. Although it is premature to propose a universal algorithm to determine leaf chlorophyll content from red edge spectral parameters from remote sensing sensors it does provide a quantitative basis for inference of leaf chlorophyll content from AVIRIS in the absence of field botanical/optical data from the vegetation communities at the Jasper Ridge site.

AVIRIS Red Edge Reflectance Spectra

Each of the five AVIRIS images was "calibrated" to provide scene reflectance spectra through regression analyses between AVIRIS digital numbers (raw or radiometrically-corrected values) and spectral reflectances of pseudo-invariant targets in the scene that had been previously characterized via field spectral measurements (see Elvidge 1988 for details). Two of the five data sets had been spectrally-resampled by JPL to provide 210 spectral bands with a 9.8nm spectral interval (see Table 1). For the 224 band data a spectral mask was applied to remove spectral channels that generated erroneous data (Vane *et al.* 1988) and to choose between overlapping spectral channels.

Red edge reflectance spectra from AVIRIS image pixels viewing a 50-meter-square area located in a live oak (*Q. agrifolia*) vegetation community are shown in Figure 2. For each spectrum the AVIRIS data are shown as points and the solid line though the points represents the "best fit" IGM curve. This plot represents typical AVIRIS red edge reflectance data. Systematic changes are observed in the near IR shoulder reflectance through the season with maximum values in the June imagery and the reflectance minimum near 680nm is well-defined throughout the phenological period sampled. By contrast, for the grassland communities (not shown here, see Miller *et al.* 1990a; Elvidge

and Portugal 1990) the chlorophyll pigment influence on the reflectance at 680nm is prominent in the April image but is virtually non-existent from June to September.

RESULTS

Noise and spectral resolution limit the feasibility of first derivative analysis on AVIRIS red edge spectra, as in laboratory or field spectrometers data, to obtain red edge position information. A typical red edge spectrum is shown in Figure 3 along with the IG model fitted curve. The two spectral parameters of this model, λ_{pg} and λ_{og} , provide direct quantitative measures of the red edge spectral position and are readily computed on a pixel-by-pixel basis. Such analyses have been conducted to produce images of these and other reflectance/spectral parameters (Miller *et al.* 1990a). Given the developmental state of the AVIRIS sensor over the time span being investigated, the fact that the phenological cycle is being reconstructed from imagery from 3 different years and the absence of site botanical/optical data during this period a detailed evaluation of the results obtained is not warranted. Overall, the red edge spectral position parameters show similar seasonal behavior for all vegetation communities (Miller *et al.* 1990a), except for the grassland communities as mentioned above. Variations in red edge position between species were small compared to variations with time of year.

The red edge data interpreted in terms of seasonal variation in leaf chlorophyll content for live oak (*Q. agrifolia*) are presented in Figure 4 by using the relationships between red edge position parameters and chlorophyll from Figure 1. Chlorophyll seasonal profiles derived from both λ_{pg} and λ_{og} algorithms imply relatively constant leaf chlorophyll levels followed by chlorophyll degradation after July 24. These results are generally consistent with pigment phenological patterns previously observed in other species (Belanger *et al.* 1990). The April values are unexpectedly higher than June but given the constraints on the data set already mentioned no firm conclusions are warranted about the significance of such small variations. The offset in deduced chlorophyll values between inferences from λ_{pg} and λ_{og} may be generated by the degraded spectral resolution of AVIRIS (9.8nm) compared to that of the York University study (4 nm) or may imply inadequacy of the algorithm employed for this ecosystem.

CONCLUSIONS

This preliminary evaluation of the potential of AVIRIS to map canopy chlorophyll indicates that further detailed experiments are certainly warranted. The AVIRIS red edge spectra appear amenable to curve-fitting approaches for the extraction of red edge position information. Further, when red edge position to leaf chlorophyll algorithms are applied phenological patterns in pigment content are in general agreement with optical/botanical field studies of tree leaves.

The recent research results (Belanger *et al.* 1990) which suggest that a species-independent relationship exists between certain red edge spectral parameters and leaf chlorophyll content need to be explored under a wide range of species and climate regimes. If a universal relationship does in fact exist then red edge spectral parameters from remote sensing can be used to infer mean leaf chlorophyll content per unit area in each pixel viewed. Effects of spectral mixing due to differing species with different leaf chlorophyll concentrations and due to understory effects in thin canopies would not in this case invalidate inferences of pixel mean leaf pigment content per unit area. Further, non-vegetated substrate components with spectral reflectances that vary slowly with wavelength would not be expected in the extraction of chlorophyll information from the vegetation community being viewed. Comprehensive and coordinated field and airborne experiments currently under way should permit these issues to be addressed and resolved.

ACKNOWLEDGEMENTS

This work was made possible by financial support from the Natural Sciences and Engineering Research Council of Canada (Project CRD 0038987) and the Province of Ontario through the Institute for Space and Terrestrial Science.

REFERENCES

- Belanger, M. J. (1990), *A seasonal perspective of several leaf developmental characteristics as related to the red edge of plant leaf reflectance*. M.Sc. Thesis, York University, Toronto, Canada, 110 pp.
- Belanger, M. J., Miller, J. R., Boyer, M. G. (1990), The red edge of plant reflectance as influenced by leaf phenology, submitted to *Remote Sens. Environ.* July, 1990.
- Boochs, F., Dockter, K., Kupfer, G., Kuhbauch, W. (1988), Red edge shift as a vitality indicator for plants. Presented at the *Sixteenth International Congress of Photogrammetry and Remote Sensing*, Kyoto, Japan, 8 pp.
- Elvidge, C. D., (1988), Vegetation reflectance features in AVIRIS data, *Proceedings of the International Symposium on Remote Sensing, Sixth Thematic Conference on Remote Sensing for Exploration Geology*, pp. 169 - 178, held at Houston, Texas, May 16 - 19, 1988.
- Elvidge, C. D., Portigal, F. P. (1990), Phenologically induced changes in vegetation reflectance derived from 1989 AVIRIS data. Presented at the *23rd International Symposium on Remote Sensing of the Environment*, 16p, held in Bangkok, Thailand, April 18 - 25, 1990.
- Horler, D. N. H., Dockray, M., and Barber, J. (1983), The red edge of plant leaf reflectance. *Int. J. Remote Sens.* 4:273-288.
- Mackinney, G. (1941), Absorption of light by chlorophyll solutions. *Biol. Chem.* 140:315-322.
- Miller, J. R., Hare, E. W., Neville, R. A., Gauthier, R. P., McColl, W. D., and Till, S. M. (1985), Correlation of metal concentration with anomalies in narrow band multispectral imagery of the vegetation red reflectance edge. In *International Symposium on Remote Sensing of Environment, Fourth Thematic Conference, Remote Sensing for Exploration Geology*, San Francisco, pp. 143-153.
- Miller, J. R., Elvidge, C. D., Rock, B. N., Freemantle, J. R. (1990a), An airborne perspective on vegetation phenology from the analysis of AVIRIS data sets over the Jasper Ridge Biological Preserve, *Proceedings of the 10th International Geosciences and Remote Sensing Symposium*, held at the University of Maryland, Washington, D.C. May 20 - 24, 1990, pp. 565 -568.
- Miller, J. R., Wu, J., Boyer, M. G., Belanger, M. J., and Hare, E. W. (1990b), Seasonal patterns in leaf reflectance red edge characteristics. *Int. J. Remote Sens.* (in press).
- Miller, J. R., Hare, E. W., and Wu, J. (1990c), Quantitative characterization of the vegetation red edge reflectance. 1: An Inverted-Gaussian reflectance model. *Int. J. Remote Sens.* (in press).
- Vane, G., Chrien, T. G., Riemer, J. H., Green, R. O., Conel, J. E. (1988), Comparison of laboratory calibrations of the Airborne Visible/Infrared Imaging Spectrometer (AVIRIS) at the beginning and end of the first flight season, *Proceedings of SPIE: Recent Advances in Sensors, Radiometry, and Data Processing for Remote Sensing*, Vol 924, pp. 168 - 178.

TABLE 1: AVIRIS Data Sets Over Jasper Ridge Biological Preserve

Date	Julian Day	Season	# Spectral Bands
April 13/89	103	spring	224
June 2/89	153	early summer	224
July 24/87	205	summer	210
Aug 31/88	244	late summer	210
Sept 20/89	263	early fall	224

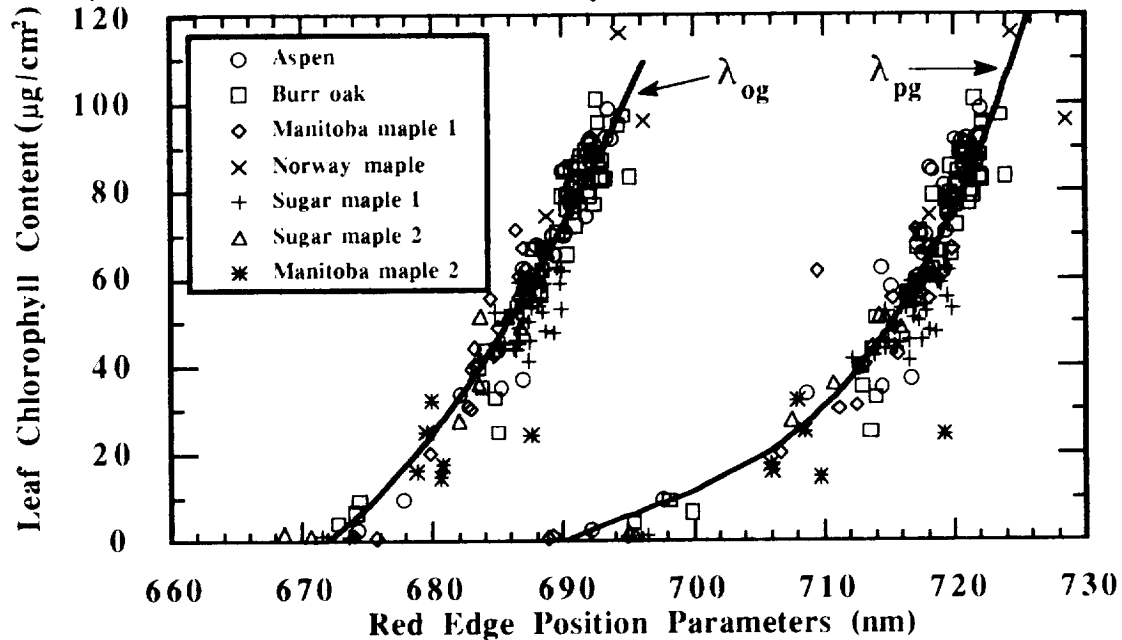


Figure 1. Relationship between the total leaf chlorophyll content per unit area and the Inverted Gaussian model red edge position parameters λ_{og} and λ_{pg} (see text) for leaves from 5 tree species sampled from spring flush through fall senescence.

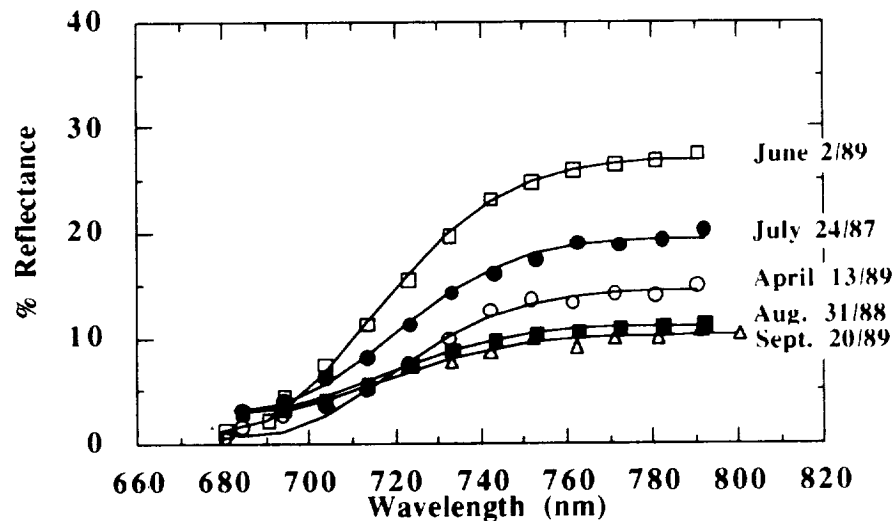


Figure 2. Seasonal variation in AVIRIS red edge spectra from live oak (*Q. agrifolia*) at the Jasper Ridge Biological Preserve. (Points - AVIRIS data; solid line - Inverted Gaussian curve fit).

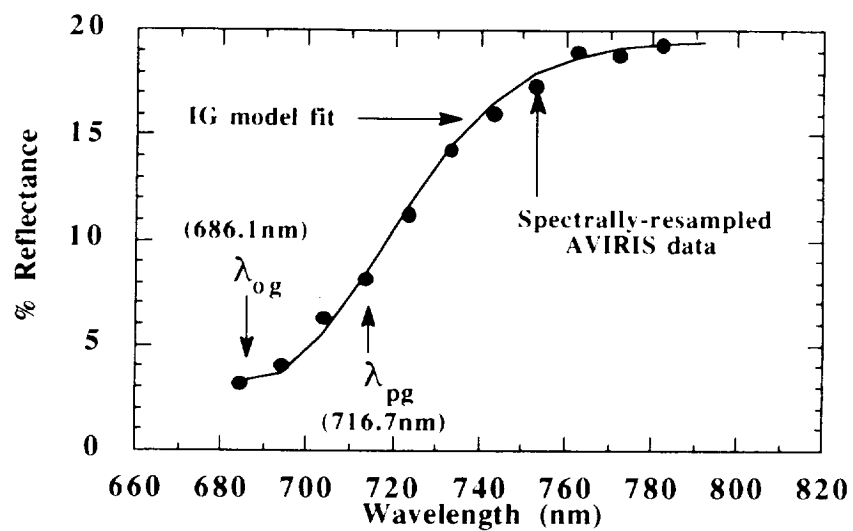


Figure 3. Detailed view of IGM curve fit for live oak (*Q. agrifolia*) red edge spectrum for July 24, 1987.

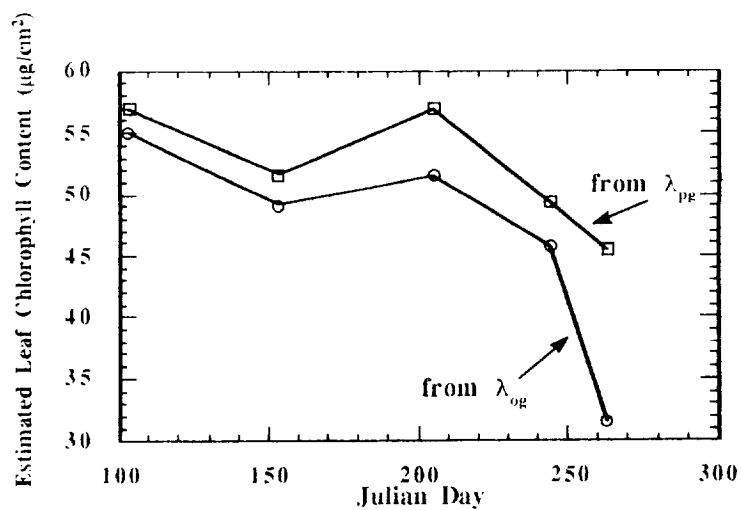


Figure 4. Estimated leaf chlorophyll concentration for live oak derived from AVIRIS red edge spectral curve fitting coupled with interpretation algorithms shown in Figure 1.

APPLICATION OF LOWTRAN 7 AS AN ATMOSPHERIC CORRECTION TO AIRBORNE VISIBLE/INFRARED IMAGING SPECTROMETER (AVIRIS) DATA

JEANNETTE van den BOSCH, Geography Department, University of California, Santa Barbara, CA 93106, USA; RON ALLEY, Jet Propulsion Laboratory/California Institute of Technology, 4800 Oak Grove Drive, Pasadena, CA 91109, USA

ABSTRACT

Previous atmospheric correction models applied to imaging spectroscopy data have included such methods as residual or scene average, internal average relative (IAR) reflectance, flat-field correction, single spectrum, and empirical line algorithm or regression method. Basic assumptions of these methods are *a priori* knowledge of the site, the existence of a spectrally neutral area with no vegetation or sparse vegetation cover, wavelength-independent average scene reflectance, or the existence of field measurements taken at the time of image acquisition. Compensation for atmosphere using LOWTRAN 7 has the potential to overcome most of the limitations imposed by the previous methods and is a versatile simulation model that has been parameterized for a variety of conditions. The application methodology is described for a 1987 AVIRIS scene of Fish Slough, a desert wetland near Bishop, California.

DESCRIPTION OF PREVIOUS ATMOSPHERIC CORRECTION MODELS

Atmospheric correction models for imaging spectroscopy have included residual or scene average method, IAR reflectance, flat-field correction, single spectrum method, and empirical line or regression method. All remove the majority of atmospheric effects: minimizing atmospheric water vapor absorption features and compensating for the solar spectral irradiance curve.

The residual (log residual, if logarithmic variables are used) or scene average method expresses scaled reflectances in terms of image-derived quantities such that the observed radiance is equal to the product of the surface reflectance and the ratio of the scene-averaged observed radiance to the scene-averaged surface reflectance. The method assumes that the path radiance is equal to zero which may not be valid in the shorter wavelengths below 1200 nm (Conel *et al.*, 1987) and may present problems with vegetated scenes where the wavelengths of interest range from the visible to the infrared. If the scene average is dominated by a particular material in the image, the resulting residual atmospheric correction will affect the scene in a multiplicative fashion.

IAR reflectance is determined by dividing each spectrum by the overall average spectrum for the whole image. Caution must be used when applying this technique as spurious features can be introduced into the converted spectra if the average spectrum contains strong absorption features related to the surface composition. Noise problems may be accentuated due to moderate vegetation cover (Kruse, 1988).

Flat-field correction relies on the existence of a neutral, homogeneous area with no absorbing minerals or vegetation, thereby assuming *a priori* knowledge of the site. The correction is applied by dividing the brightness value of each pixel in each band by the average value of the flat field in that band. The flat-field correction only removes multiplicative effects and will remove scene noise, if there is multiplicative scene noise in all channels. If noise is restricted to the flat field, noise will then be introduced into the scene. Artifacts introduced by this method include a shift in wavelength for some features (Carrere and Abrams, 1988; Rock *et al.*, 1988) and changing the intensity and/or distorting other spectral bands of interest (Clark and King, 1988).

The single spectrum method requires *a priori* knowledge to select a single spectrally well-characterized ground target, situated at about the average scene elevation. The ground target spectrum is divided by the radiometrically-corrected, but otherwise uncalibrated, image digital numbers for the same area. The resulting quotients for each wavelength channel provide a set of scalars for calibrating the image. Problems include the characterization of the field calibration target, definition of the test areas for verifying the calibration results, and determination of the proper shape of the scattering curve to subtract from the image data (Crowley *et al*, 1988).

Empirical line algorithm or regression method requires two targets of contrasting and equivalent spectral resolution for which both surface reflectance and airborne spectrometer response are known. Regression plots of the reflectance versus scanner response can be used to recover ground reflectance. A source of concern is how well the field-measured reflectances represent the standard targets (Conel *et al*, 1988).

LOWTRAN OPTIONS

LOWTRAN was developed by the Air Force Geophysics Laboratory to predict transmission losses and sky backgrounds that affect the performance of electro-optical surveillance, guidance and weapons systems. LOWTRAN has been used to simulate the 1900 nm waterband (Conel *et al*, 1986) and to verify AVIRIS channels.

LOWTRAN 7 has undergone significant improvements over previous versions with modification in the code to perform multiple scattering calculations in the visible and infrared portions of the spectrum while incorporating the effects of clouds and other atmospheric aerosols (Isaacs and Vogelmann, 1988). Different profiles—tropical, midlatitude summer, midlatitude winter, subarctic summer, subarctic winter, and U.S. standard—can be combined with any of several aerosol models: urban, rural, desert (new option in LOWTRAN 7), maritime, tropospheric, or user-designated (radiosonde data).

The input parameters for the Fish Slough scene were a midlatitude summer profile with desert aerosols along with the following information in Table 1 (*Local Climatological Data, Monthly Summary, Bishop, California, July 1987*).

Table 1. Additional Input Parameters

El	Air		Wind	
(km)	Temp	RH	Speed	Visibility
(°C)	(%)	(m/sec)	(km)	
1.329	35	9	8	48

LOWTRAN ATMOSPHERIC CORRECTION MODEL

Two basic assumptions of the LOWTRAN model are also explicit in the other atmospheric corrections previously discussed: a horizontally homogeneous atmosphere and a small elevation variation within the scene. However, the image may be subsectioned and the LOWTRAN atmospheric model may be reiteratively run with different input values for elevation to compensate for changes in elevation.

AVIRIS observed radiance can be expressed as

$$L_o = L_{ps} + L_g = L_{ps} + L_o t_1 \rho t_2 \quad (1)$$

or, rearranging

$$\rho = \frac{L_o - L_{ps}}{L_o t_1 t_2} \quad (2)$$

where L_o = observed radiance

L_{ps} = observed radiance due to path scattering

L_g = obs. radiance due to ground-reflected radiation

L_o = solar radiance

t_1, t_2 = transmittance along downward, upward paths

ρ = ground reflectance

By assuming a spectrally constant reflectance (0.1, in this case), LOWTRAN can be used to model L_{ps} and L_g for the assumed reflectance. Substituting back into Eq. 2, we get

$$\rho = \frac{L_o - L_{ps}}{\left[\frac{L_g}{0.1} \right]} = \frac{0.1}{L_g} [L_o - L_{ps}] \quad (3)$$

where L_g is now the ground reflected radiance, assuming 0.1 reflectance. Ground reflectance (ρ) values can then be computed on a channel-by-channel basis using Eq. 3.

CONCLUSIONS

Application of LOWTRAN 7 as an atmospheric correction to AVIRIS data has the potential to overcome most of the limitations imposed by previous methods. It eliminates the need for *a priori* knowledge of the scene to identify spectrally neutral areas with no absorption features in their spectra and eliminates the need for target ground measurements taken at the time of the image acquisition. In addition, LOWTRAN 7 can compensate for multiple scattering, is parameterized for a variety of atmospheric profiles, and has the option of specifying a user-designated input model (e.g., substituting radiosonde data for ground climatological data). The atmospheric correction is useful for both vegetated and geologic scenes.

ACKNOWLEDGEMENTS

The following JPL employees provided invaluable assistance in processing the AVIRIS data: Earl Hansen, Steve Carpenter, Ian Novack, Lisa Barge, and Manuel Solis.

REFERENCES

- Carrere, V. and M.J. Abrams. 1988. An Assessment of AVIRIS Data for Hydrothermal Alteration Mapping in the Goldfield Mining District, Nevada, *Proceedings of the Airborne Visible/Infrared (AVIRIS) Performance Evaluation Workshop*, JPL Publication 88-38, pp. 134-154.
- Clark, R.N. and T.V.V. King. 1988. Causes of Spurious Features in Spectral Reflectance Data, *Proceedings of the Third Airborne Imaging Spectrometer Data Analysis Workshop*, JPL Publication 87-30, pp. 134-154.
- Conel, J.E., S. Adams, R.E. Alley, G. Hoover, and S. Schultz. 1986. Analysis of AIS Radiometry with Emphasis on Determination of Atmospheric Properties and Surface Reflectance, *Proceedings of the Second Airborne Imaging Spectrometer Data Analysis Workshop*, JPL Publication 86-35, pp. 31-51.
- Conel, J.E., R.O. Green, G. Vane, C.J. Bruegge, R.E. Alley, and B.J. Curtiss. 1987. Airborne Imaging Spectrometer-2: Radiometric Spectral Characteristics and Comparison of Ways to Compensate for the Atmosphere, *Proceedings of the SPIE Conference on Imaging Spectroscopy II*, v. 834, pp. 140-157.

- Conel, J.E., S. Adams, R.E. Alley, G. Hoover, and S. Schultz. 1988. AIS Radiometry and the Problem of Contamination from Mixed Spectral Orders, *Remote Sensing of the Environment*, 24(1):179-200.
- Crowley, J., L. Rowan, M. Podwysoki, and D. Meyer. 1988. Evaluation of Airborne Visible/Infrared Imaging Spectrometer Data of the Mountain Pass, California Carbonatite Complex, *Proceedings of the Airborne Visible/Infrared (AVIRIS) Performance Evaluation Workshop*, JPL Publication 88-38, pp. 155-161.
- Isaacs, R.G. and A.M. Vogelmann. 1988. Multispectral Sensor Data Simulation Based on the Multiple Scattering LOWTRAN Code, *Remote Sensing of the Environment*, 26(10):75-99.
- Kruse, F.A. 1988. Use of Airborne Imaging Spectrometer Data to Map Minerals Associated with Hydrothermally Altered Rocks in the Northern Grapevine Mountains, Nevada, and California, *Remote Sensing of the Environment*, 24(1):31-52.
- Local Climatological Data, Monthly Summary, Bishop, California, July 1987*, National Environmental Satellite Data and Information Service.
- Rock, B.N., C.D. Elvidge, and N.J. Defeo. 1988. Assessment of AVIRIS Data from Vegetated Sites in the Owens Valley, California, *Proceedings of the Airborne Visible/Infrared (AVIRIS) Performance Evaluation Workshop*, JPL Publication 88-38, pp. 88-96.

An AVIRIS Survey of Quaternary Surfaces Formed on Carbonate-Provenance Alluvium, Mojave Desert, Southern Nevada

Veronique Carrere and Oliver Chadwick

Jet Propulsion Laboratory/California Institute of Technology
4800 Oak Grove Drive, Pasadena, California, USA

ABSTRACT

AVIRIS data acquired over Kyle Canyon (Nevada) are used in an attempt to discriminate Quaternary surfaces formed on carbonate-provenance alluvium and establish chronological sequences. Surface discrimination is based on increased albedo with age and mineralogical changes that can be inferred in great detail with AVIRIS high-spectral-resolution data. In order to do so, AVIRIS data were converted to reflectance using the radiative transfer modeling approach, combined with the extraction of total column abundance of precipitable water in the atmosphere from the AVIRIS data. Results show that the various surfaces can be easily identified and mapped in great detail on AVIRIS color composite and principal components images. All surfaces appear to present a clear carbonate absorption and the albedo seems to increase with age.

INTRODUCTION

1. Objectives

The purpose of this study is to investigate the use of high-spectral-resolution AVIRIS data for discrimination of Quaternary surfaces and attempt to establish chronological sequences based on their spectral characteristics. A previous analysis of Thematic Mapper (TM) data showed the utility of spectral information for the interpretation of Quaternary surfaces. Surface discrimination was based on increased albedo with age and mineralogical changes that were inferred from absorption differences for the TM bands. The increased spectral resolution of AVIRIS should allow detection of more subtle spectral differences between the different surfaces and within the surfaces. To extract this information, AVIRIS data need to be corrected to reflectance. A radiative transfer model approach has been used here, combined with the extraction of the total column abundance of precipitable water in the atmosphere from AVIRIS radiance data.

2. Description of the study area

The study area, Kyle Canyon, is located 25 km northwest of Las Vegas, Nevada (Figure 1). The Kyle Canyon alluvial fan is one of the largest fans flanking the east side of the Spring Mountains in southern Nevada. The bedrock of the source area consists of Cambrian to Triassic sedimentary strata, largely limestone and dolomite, with minor siltstone, sandstone, and chert.

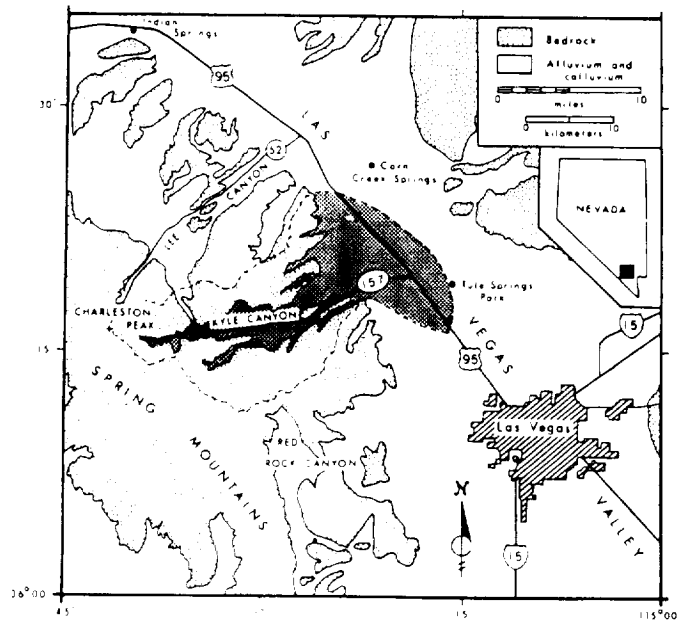


Figure 1. Location of the study area

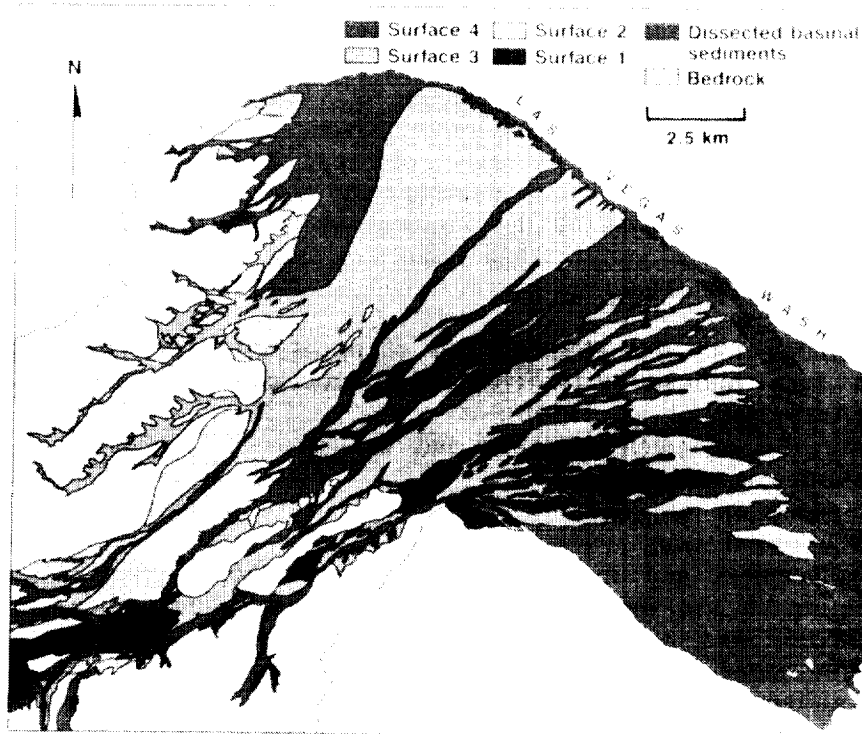


Figure 2. Simplified geomorphic map of the Kyle Canyon alluvial fan (after Chadwick et al., 1989) (see Slide 2)

Four main alluvial surfaces of different ages that can be distinguished by their surface properties and relative positions occur on the Kyle Canyon fan (Figure 2).

Surface 1, the oldest deposit, consists of rolling, dissected ballenas, and nowhere is the original depositional surface preserved. The deposit age, based on paleomagnetism of the associated pedogenic calcrete, is over 730,000 B. P., and the surface age is variable depending on erosion status (Sowers, 1985, 1986). It has a light-colored surface due to whitish calcrete fragments in the desert pavement. Desert pavement, well developed on ridge crests, is composed of extremely etched and pitted calcrete fragments and limestone clasts.

Surface 2 is moderately dissected, but remnants of the original depositional surface are preserved, giving it smooth local topography on interfluvies that are separated by many steep-sided ravines. It has been dated at about 130,000 B.P. (Amundson et al., 1989b). It also has a light-colored surface due to whitish calcrete fragments, and the presence of secondary clay in the desert pavement. The desert pavement is similar to surface 1, being composed of etched and pitted limestone clasts and calcrete fragments; however, the soil B horizons are composed of greater amounts of smectite and palygorskite. These clays are exposed at the surface by the same turbation processes that expose the calcrete, usually fossorial mammals.

Surface 3 is slightly dissected with few drainages. It has a relatively smooth appearance due to the presence of quartz and iron-rich eolian dust that fills the intergrain areas of the alluvium. Its surface is time transgressive, dated between 5000 B.P. at the toe of the fan to 75,000 B.P. near the apex (Amundson et al., 1989a). Soils have strong calcic horizons, but pedogenic carbonate is seldom exposed at the surface. It is a dark-colored surface relative to surfaces 1 and 2 because of the lack of whitish calcrete fragments, the dominance of grey limestone in the desert pavement, and the accumulation of quartz and iron-rich fines in the interpavement areas.

Surface 4 is considered the modern surface, which includes the active channel and low terraces. It is dark colored, except in recently active channels where it is light. Soil development varies from none to weak carbonate accumulation. Pavement development is weak to none. This surface is composed of loose to slightly etched limestone clasts that are well sorted, and small amounts of eolian dust.

The morphology and the physical and chemical properties of soils on the Kyle Canyon fans indicate that five major processes are involved in their pedogenesis (Amundson et al., 1989b):

- (1) formation of calcic horizons and calcrete;
- (2) additions of eolian dust;
- (3) translocation of clays;
- (4) oxidation of iron;
- (5) displacement and replacement of aluminosilicate grains, contributing to the formation of opaline or amorphous silica, palygorskite, and sepiolite.

The calcic horizons and calcrete of Kyle Canyon soils form by solution of calcite from eolian dust and the parent material and subsequent precipitation as clast coats and matrix cement.

Evolution of the carbonate-derived alluvium through a series of discrete stages of surface and soil properties suggests that we may be able to use multispectral imagery to identify significant properties at each stage. Identification of surfaces at specific evolutionary stages allows inferences

regarding stability of Quaternary deposits in specific localities and, potentially, interpretations of climatic and tectonic influences on their stability.

WHAT IS KNOWN FROM THEMATIC MAPPER (TM)

Previous analysis of TM data over the area (Chadwick et al., 1989) showed (Figure 3):

- (1) an increase in albedo as surface age increases;
- (2) Surface 1 and 2 had greater absorption in band 7 because of increased amounts of clay and/or calcite;
- (3) Surface 1 had greater iron absorption in band 4;

Those preliminary results point to the potential of AVIRIS data to:

- (1) discriminate clays from carbonates;
- (2) detect changes in depth of carbonate absorption features;
- (3) identify specific minerals such as palygorskite or sepiolite;
- (4) detect iron oxides absorption features.

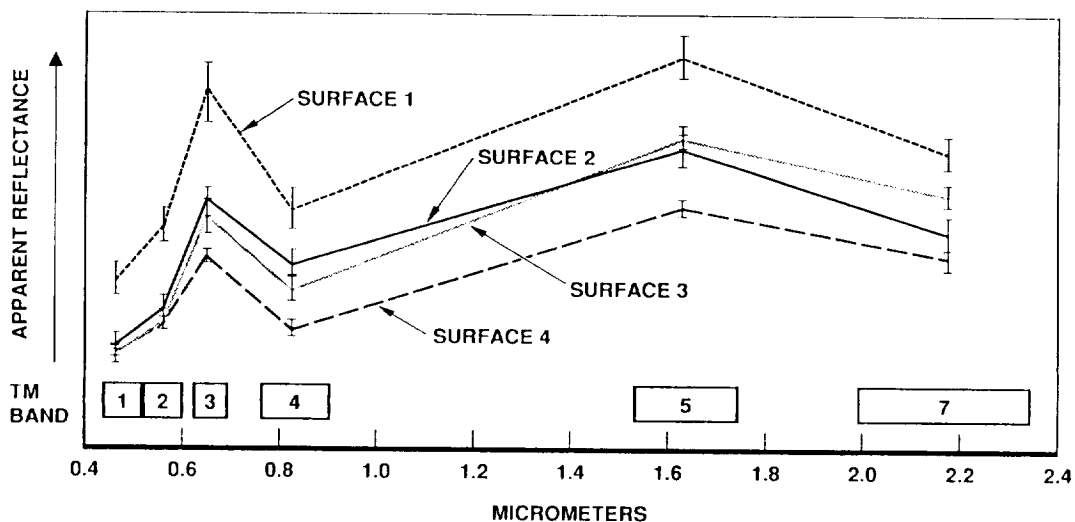


Figure 3. Thematic Mapper spectra of the various Quaternary surfaces (after Chadwick et al., 1989)

AVIRIS DATA ANALYSIS

1. Simple techniques

Color Composite interpretation

Analysis of a simple color composite (Figure 4) suggests the possibility of mapping with greater spatial detail, including possible subdivision of surfaces (e.g., Surface 3).

PCA (Figure 5)

Principal component analysis was performed on four AVIRIS bands to check the importance of spatial changes in the composition from surface-to-surface and internal to each surface. The results are similar to what was observed on the color composite.

Band ratios (Figure 6)

A simple band ratio approach was also used in an attempt to locate spatial distribution of various important minerals such as carbonates, gypsum, and clays.

Gypsum, based on a ratio to detect the 1.75-absorption feature, is detected in the paludal sediments exposed in the basin bottom at the toe of the alluvial fan.

Carbonate is spread almost evenly over the area, with the exception of surface 1 and the active part of the wash. This result is unexpected in view of the amount of calcrete exposed on surface 1.

Clays are mainly encountered on surfaces 1 and 2 and absent from surface 4.

2. Correction to reflectance

The second step in AVIRIS data analysis was to retrieve reflectance from the radiance data. The approach used to convert AVIRIS radiance data to reflectance is presented in more detail in these proceedings by van den Bosch and Alley. It consists of using the LOWTRAN 7 radiative transfer code to model the radiance at AVIRIS for the conditions of the flight and a constant background reflectance chosen by the user. This allows us to predict the atmospheric component in order to remove it to get to reflectance. The steps involved are as follows:

(1) LOWTRAN 7 is run for the conditions of flight using meteorological observations from ground stations for visibility and water from the radiosonde profile:

$$L_{\text{tot}} = L_{\text{path}} + L_{\text{ground}}$$

$$\text{with } L_{\text{ground}} = L_{\text{sun}} t_1 t_2 r$$

L_{tot} is the total radiance at AVIRIS

L_{path} is path radiance

L_{ground} is the ground reflected component with L_{sun} = solar radiance, t_1 and t_2 transmittance upward and downward and r ground reflectance as chosen by the user.



Figure 5. AVIRIS PC color composite
red: PC1; green: PC2; blue: PC3
(see Slide 4)

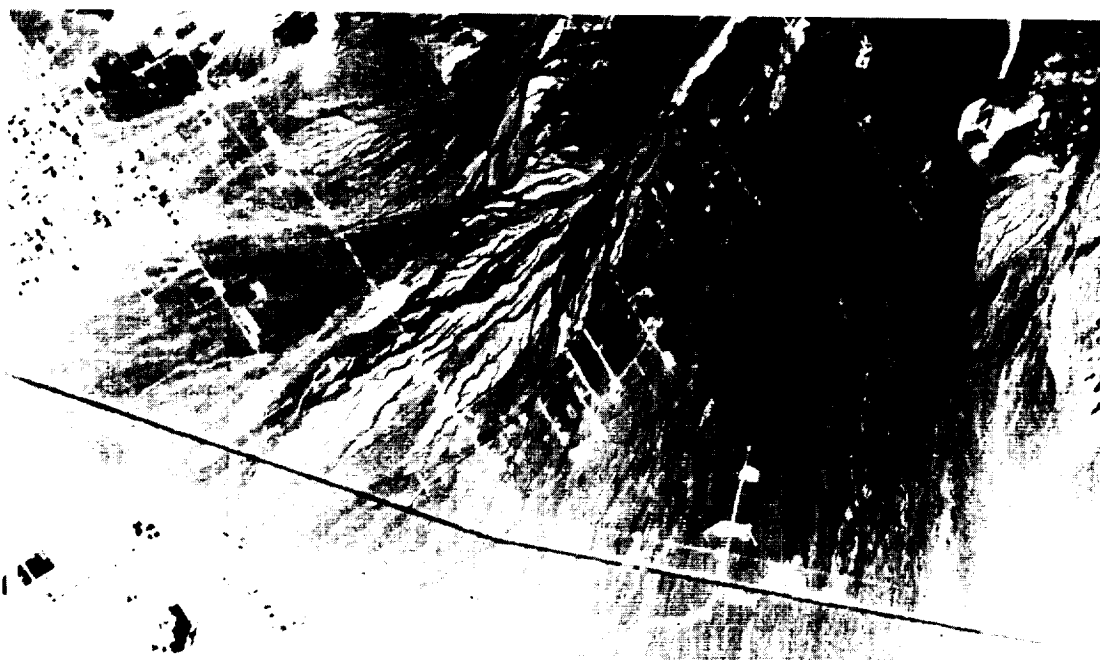


Figure 4. AVIRIS color composite
red: 2107.8 nm; green: 1022.5 nm; blue: 604.1 nm
(see Slide 3)

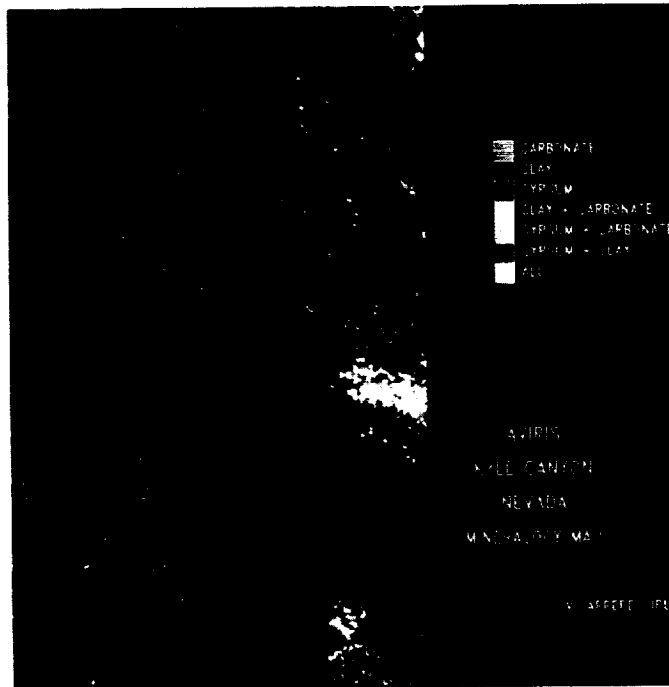


Figure 6. Mineralogy map of the Kyle Canyon fan obtained from combined band ratios (see Slide 5)

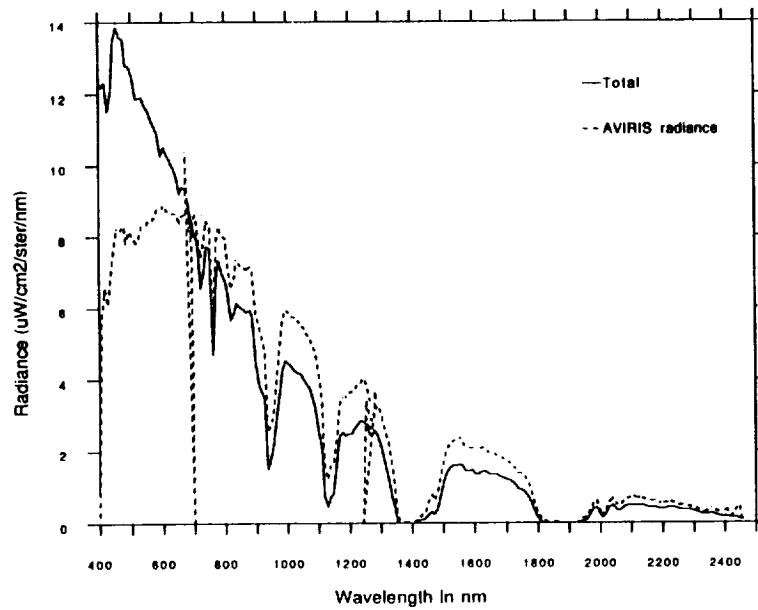


Figure 7. Radiance predicted by LOWTRAN using radiosonde data/AVIRIS radiance

$L_{sun \ t_1 \ t_2}$ is the main unknown but can be retrieved from the LOWTRAN run since the background reflectance is known:

$$L_{sun \ t_1 \ t_2} = L_{ground} / r$$

(2) Reflectance can then be extracted from AVIRIS data using the following equation:

$$R_{AVIRIS} = (rad_{AVIRIS} - L_{path}) r / L_{ground},$$

giving a gain and offset factor applicable to the entire scene (assuming the elevation does not change drastically, thus modifying the amount of water in the total column).

$$\begin{aligned} \text{gain} &= r / L_{ground} \\ \text{offset} &= - \text{gain} * L_{path} \end{aligned}$$

In the first attempt, considering we did not have any ground support simultaneous with the overflight, we used atmospheric parameters obtained from the Las Vegas airport weather station and the Desert Rock test site at Yucca Flat, Nevada, both of these being within 50 km of our study area. The visibility, as estimated from the Las Vegas data, was of 80 km, and the total column abundance of water, as observed by the radiosonde launched at the Desert Rock test site, was of 1.162 g/cm^2 .

Comparison between the AVIRIS radiance data and the radiance predicted by LOWTRAN (Figure 7) shows that the amount of water detected by the radiosonde was too large for our area. This was confirmed after correction to reflectance (Figure 8). All the atmospheric water bands were overcompensated for, appearing reversed on the spectra.

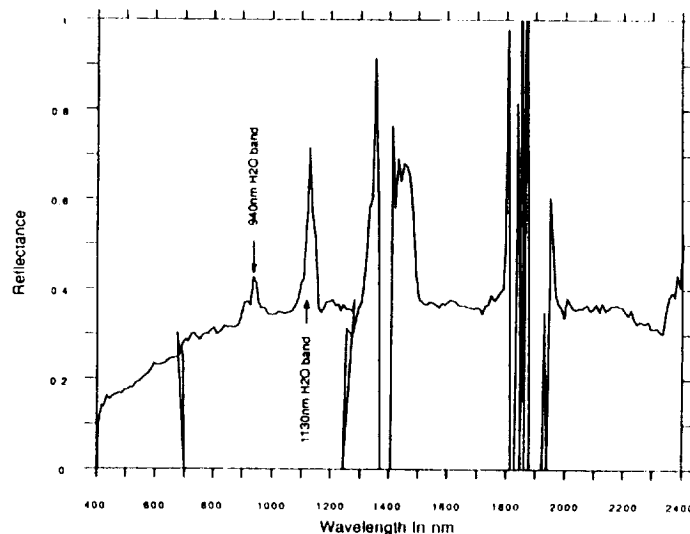


Figure 8. Reflectance obtained using radiosonde data

In a second attempt, we decided to use the information included in the AVIRIS radiance data. The technique used, known as Continuum Interpolated Band Ratio (CIBR) (Conel et al., 1988, Conel et al., 1989, Green et al., 1989), allows us to retrieve total column abundance of water using the 940-nm (or the 1130-nm) atmospheric water band (Figure 9). This estimate of the depth of the absorption feature is related to the amount of precipitable water through a curve of growth (Figure 10). This curve is obtained by running LOWTRAN 7 for the conditions of the flight, a constant background reflectance of 0.25, and increasing amounts of water ranging from 0 to 200%. The total radiances predicted by LOWTRAN are then convolved to AVIRIS bandpasses, CIBR is performed for each amount of water, and a file relating the amount of water to CIBR values is created.

Transects across and along the surfaces were extracted from this water map in order to investigate the range of changes in amount of atmospheric water over the study area. The average amount was found to be between 0.7 and 0.75 g/cm². This value was then used as input to LOWTRAN to retrieve reflectance. Figure 11 shows the result. One can notice that the atmospheric water bands are not perfectly compensated for. The 940-nm water band is undercompensated but the 1130 nm is slightly overcompensated. This points to a problem in the calibration file used to convert AVIRIS raw data to radiance, and confirms the sensitivity of this approach to selection of appropriate parameters such as radiance calibration and amount of water. The average value of 0.7 cm was kept as a best (although not perfect) estimate.

Results after correction to reflectance are shown in Figures 11 and 12. From these spectra, one can notice that:

- (1) Every surface is dominated by carbonates, as expected and shown by the ratios;
- (2) Surface 1 is the brightest because of the increased amount of pedogenic calcite;
- (3) Surface 2 is darker, possibly because of the presence of quartz-rich eolian dust, lack of calcrete at the surface, and the presence of a broader feature between 2200 and 2350 nm (possibly due to increased quantities of secondary clay minerals at the surface);
- (4) Surfaces 3 and 4 appear to have very similar spectral characteristics.

CONCLUSIONS

These preliminary results show that:

- (1) Quaternary surfaces can be easily identified and mapped in greater detail on AVIRIS color composites than with a Thematic Mapper;
- (2) Differences between surfaces derive from subtle spectral and spatial influences that are not obvious spectrally. This might be due to the fact that morphology and composition of soils on the same surface vary with elevation on the fan or a signal-to-noise ratio in the D spectrometer that is too low to allow discrimination of important mineral absorption features in the 2000- to

Figure 9: Continuum interpolated band ratio (CIBR)

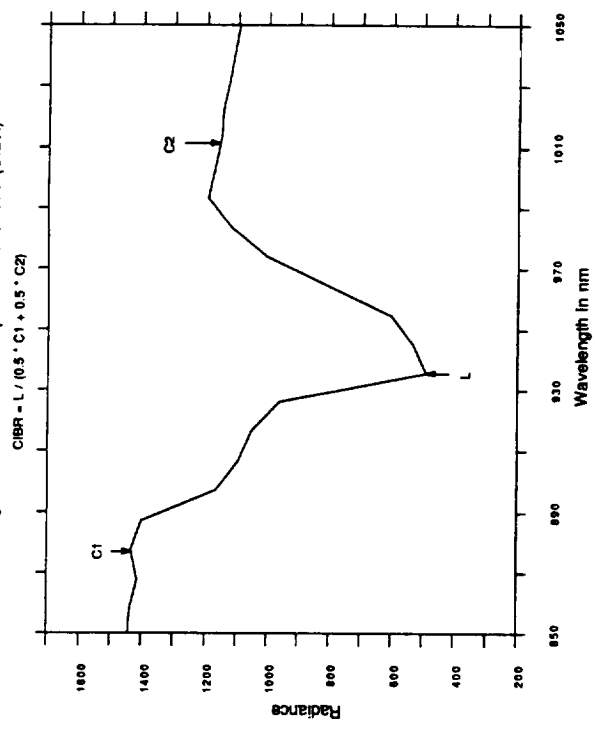


Figure 10: Curve of growth for the 940nm atmospheric water

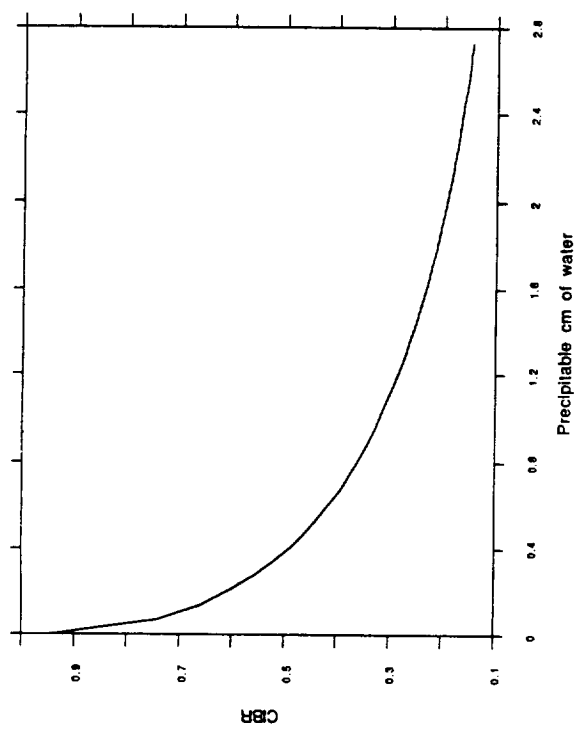


Figure 11: Average reflectance of the different surfaces

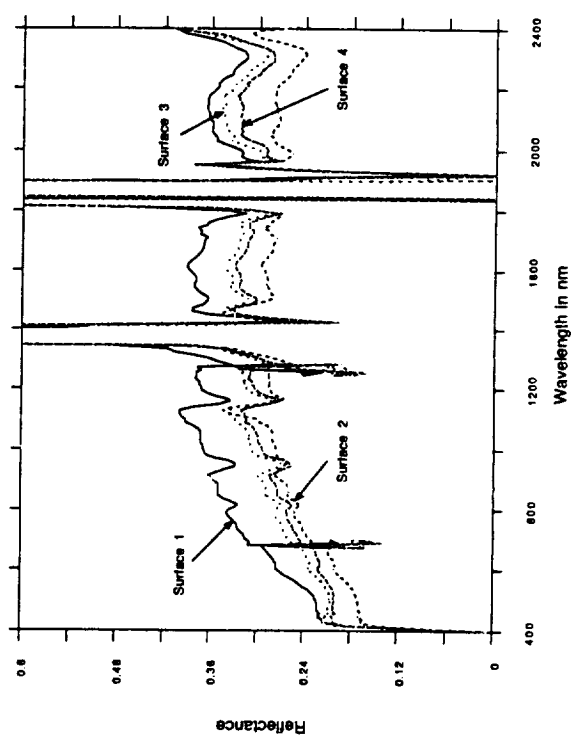
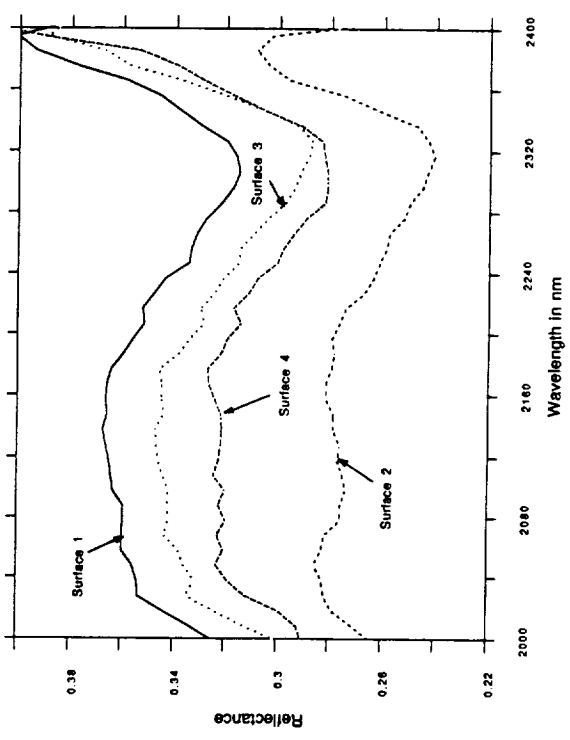


Figure 12: Average reflectance of the different surfaces between 2000 and 2400nm



2400-nm range. Poor signal to noise notwithstanding, all the surfaces appear to present a clear carbonate absorption;

(3) As observed on Thematic Mapper data, the albedo seems to increase with age;

(4) A better calibration of AVIRIS data to radiance and a very good knowledge of the amount of water in the atmosphere is indispensable to be able to correct to reflectance. The CIBR approach has proven to be an easy and accurate way to retrieve the amount of precipitable water (Conel et al., 1990a, 1990b, Bruegge et al., 1990). Its combination with the radiative transfer modeling approach allows retrieval of reflectance from AVIRIS radiance data without the necessity of ground support at the time of the overflight.

ACKNOWLEDGMENTS

The research was carried out at the Jet Propulsion Laboratory, California Institute of Technology, under contract with the National Aeronautics and Space Administration.

REFERENCES

- Amundson, R. G., O. A. Chadwick, J. M. Sowers, and H. E. Doner, 1989a, The stable isotope chemistry of pedogenic carbonates at Kyle Canyon, Nevada. *Soil Sci. Soc. Am. J.* 53: 201-210.
- Amundson, R. G., O. A. Chadwick, J. M. Sowers, and H. E. Doner, 1989b, Soil evolution along an altitudinal transect in the eastern Mojave Desert. *Geoderma* 43: 349-371.
- Bruegge, C. J., J. E. Conel, R. O. Green, J. S. Margolis, and V. Carrere, 1990, Validation and error analysis of atmospheric water abundance estimates obtained from AVIRIS. *SPIE*, Orlando, 1990.
- Chadwick, O. A., J. M. Sowers, and A. R. Gillespie, 1989, Empirically driven remote sensing interpretations of soil-geomorphic surface distribution at Kyle Canyon, Nevada. *Soil Science Society of America annual meetings*, Las Vegas.
- Conel, J. E., R. O. Green, V. Carrere, J. S. Margolis, R. E. Alley, G. Vane, C. J. Bruegge and B. L. Gary, 1988, Atmospheric water mapping with the Airborne Visible/Infrared Imaging Spectrometer (AVIRIS), Mountain Pass, California. *Proceedings of the AVIRIS Performance Evaluation Workshop*, JPL Publication 88-38, Jet Propulsion Laboratory, Pasadena, California, 134-154.
- Conel, J. E., R. O. Green, V. Carrere, J. S. Margolis, G. Vane, C. J. Bruegge, and R. E. Alley, 1989, Spectroscopic measurement of atmospheric water vapor and schemes for determination of evaporation from land and water surfaces using the Airborne Visible/Infrared Imaging Spectrometer (AVIRIS). *IGARSS'89 - 12th Canadian Symposium on Remote Sensing*, Vancouver.

- Conel, J. E., V. Carrere, C. J. Bruegge, R. O. Green, J. S. Margolis, G. Hoover and R. E. Alley, 1990a, Atmospheric water vapor: Recovery, validation, and interpretation of measurements obtained with the Airborne Visible/Infrared Imaging Spectrometer (AVIRIS). *IGARSS'90*, Greenbelt, 1990.
- Conel, J. E., V. Carrere, C. J. Bruegge, R. O. Green, and G. Hoover, 1990b, Validation of inflight recovery of atmospheric water vapor. *AVIRIS Workshop*, June 1990.
- Green, R. O., V. Carrere and J. E. Conel, 1989, Measurement of atmospheric water vapor using the Airborne Visible/Infrared Imaging Spectrometer. *Image Processing'89*, Sparks, Nevada, 31-44.
- Sowers, J. M. 1985, Pedogenic calcretes of the Kyle Canyon alluvial fan, southern Nevada - morphology and development. *Ph.D. Thesis, University of California, Berkeley*. 160 p.
- Sowers, J. M. 1986, Geomorphic map of the Kyle Canyon alluvial fan, southern Nevada. *U.S. Geological Survey Open-file Report* 86-210.

USING SPECTRAL MIXTURE ANALYSIS OF AVIRIS HIGH DIMENSIONAL DATA FOR DISTINGUISHING SOIL CHRONOSEQUENCES

Lawrence Fox III and Arthur F. Fischer, Humboldt State University, Arcata, California, USA. Allen R. Gillespie and Milton R. Smith, University of Washington, Seattle, Washington, USA.

ABSTRACT

Soil surface dating techniques are presently imprecise without expensive excavation and lab analysis. Remote sensing with airborne spectrometers offers the potential to survey large areas quickly and inexpensively. Age information from remote sensing imagery when combined with proper geomorphic interpretation may be useful for soil mapping, geologic interpretation, and ancient climate research. The study site, a glacial moraine at Pine Creek, Owens Valley, California, USA was chosen because approximate age information could be inferred from known glacial history. We used a spectral mixture analysis to compress 172 bands of AVIRIS data into five endmembers. Fraction images for well-developed soils and for undeveloped soils were compared to sites with approximate age information from soil profile development indexes and geomorphic interpretation.

Results to date indicate a good correlation ($r^2 > 0.9$) between soil profile depth and soil profile development index. Also the data suggest that differences in soil development index are related to age of the surface. Good correlations ($r^2 > 0.9$) were found between fraction image, brightness values and soil age class. Further study is required to more precisely establish the ages of tested surfaces and to relate surface age to color values in enhanced color composite imagery of three fraction images.

INTRODUCTION

Surface dating techniques are desired for soils mapping, geologic interpretation and establishment of ancient climate regimes. Geologic history can be partially interpreted from geomorphic relations, radio-isotope data and soil profile data. However, the interpretation is uncertain when carbon is not present in the soil profile and excavation of soil pits is time consuming and expensive. We have investigated the relationship of the spectral reflectance pattern of the surface with the age of the surface. If age could be estimated from surface characteristics, airborne spectroscopy holds promise for rapid survey of large areas by remote sensing from aircraft or spacecraft. Our work is based on field observations of soil surface darkening with age in arid regions. Two mechanisms are suggested for this darkening: varnishes developing on rock surfaces, and "bio-turbation" (the bringing to the surface of soil from 10 to 20 cm down in the profile by small rodents and insects burrowing in the soil).

STUDY AREA

We selected a study area in the Owens Valley, California, USA, near Pine Creek. The area is characterized by a large glacial moraine that has been formed and modified by several periods of glaciation over the past two million years (Fig. 1). This area was selected because the glacial history is relatively well known and rough age control was provided by geomorphic interpretation (Fig. 2). Three major age classes have been tentatively identified in the study area. Some of the lateral fans were formed during a glacial period occurring approximately 150 thousand years ago when the glacier extended to the nose of the current moraine. Other lateral fans were deposited later, approximately 50 to 60 thousand years ago during another period of severe glaciation. The sides of the distal fan were formed approximately 50 to 60 thousand years ago and the center portion of the distal fan was formed approximately 10 to 12 thousand years ago. All of the dates are only approximate being inferred from known glacial history and geomorphology.

METHODS

Soil Profile Development Index

Soil pits were excavated in four of the general age classes determined from air photos and geologic knowledge to provide further age control. We analyzed the soil profiles obtained from these pits using a soil profile development index (Harden and Taylor, 1983). The index is a measure of soil development from which relative age can be determined. We assumed a constant rate of soil development since climate effects should have been constant over this relatively small region bounded by mountains on the east and west sides.

Spectral Mixture Analysis

High dimensional data sets from imaging spectrometers are large enough to overwhelm existing computer systems using traditional image processing techniques. We used a spectral mixing model (Adams, et al., 1989) to tremendously reduce the dimensionality of the data set. The model is based on the theory that most pixels are mixed and the whole is equal to the sum of its parts. Each pixel was modeled to contain a mixture of spectrally pure elements ("endmembers"). The digital number (dn) of the pixel as recorded in each spectral band of AVIRIS is equal to the sum of the dn's of each endmember weighted by the fraction of the pixel occupied by that endmember. A premise of the model is that even high dimensional data sets can be reduced to four or five endmembers, thereby simplifying complex data sets such as the 224 channels of AVIRIS data.

Once the endmembers are identified, each pixel can be analyzed to determine the percentage of the pixel covered by each endmember. The

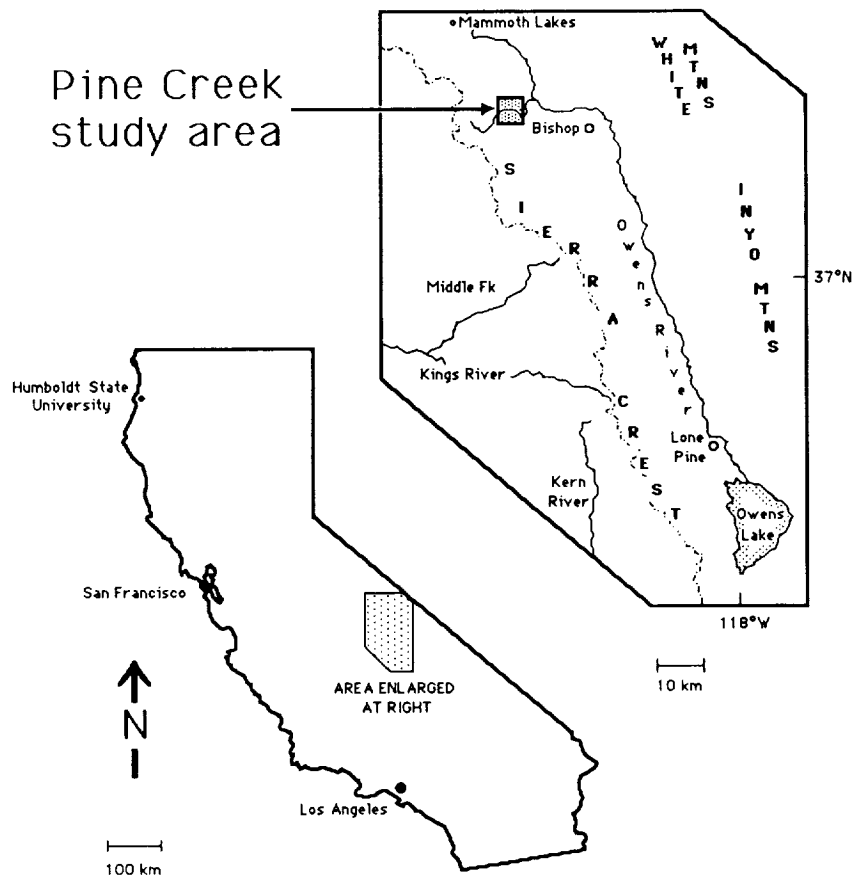


Fig. 1. Location map of the study area

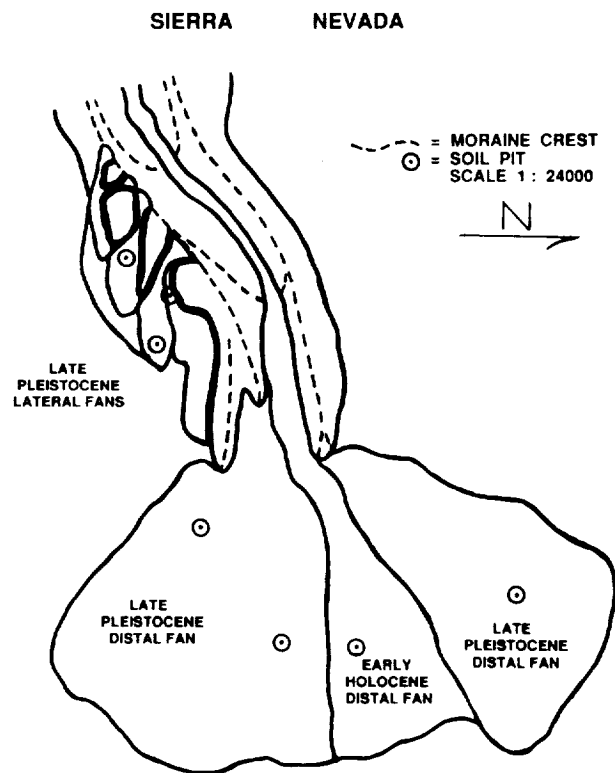


Fig. 2. A sketch map of gross morphology of the moraine made from low-altitude, color aerial photographs

analyst is able to create fraction images that display the fraction (percentage) of each pixel occupied by a given endmember as a digital number and therefore a grey level.

RESULTS

Soil Profile Development Index

We plotted the soil profile development index as a function of soil depth for three of the soil pits excavated (Fig. 3). The top curve was derived from a soil pit in an older lateral fan, approximately 65 to 70 thousand years old. The middle curve was from the side of the distal fan, approximately 65-to 70-thousand years-old and the lower curve was from the youngest part of the distal fan, approximately 10 to 12 thousand years old. A log relationship provided the best fit to the data when compared to linear regression or polynomial regression. Values of r^2 were between 0.92 and 0.95 for each of the three curves. As expected, soil development increased with depth for each soil analyzed.

Of greater interest to this study is the comparison of the three curves plotted in Fig. 3. Statistical comparison was not possible since each curve represents only one soil profile. However the data suggest that the curves are distinct and represent differences in soil age. The lowest curve was least developed and came from the youngest part of the distal fan. The middle curve was from the same age range as the upper curve yet the profile (the middle curve) suggests that the soil is younger.

Spectral Mixture Analysis

Four endmembers were selected to represent the multidimensional data cloud from AVIRIS. A darker, and therefore older, soil was chosen and named "red soil". A very light, and therefore younger soil was selected and named "white soil". These soils were selected after a general inspection of the area and the determination that various ages of soil could be represented by these two soil endmembers. Two vegetation endmembers (green and dry) and a shadow endmember were added to the model to account for the desert shrub vegetation, shadows from vegetation and terrain shadow, present in the imagery of the study area.

Dn's from the "red soil" fraction image and dn's from the white soil fraction image are displayed in Fig. 4. A large red soil dn indicates that a large percentage of the pixel was covered with red soil. From this we infer an older surface. A large white soil dn indicates that a large percentage of the pixel was covered with white soil. From this we infer a younger surface. These dn's are plotted as a function of age in Fig. 4 and we noticed a downward trend in white soil fraction and a general upward trend in red soil dn with increasing age. Linear regressions were significant ($P < 0.05$) and r^2 values were 0.92 for the red soil fraction image and 0.80 for the white soil fraction.

PDI vs. DEPTH vs. AGE

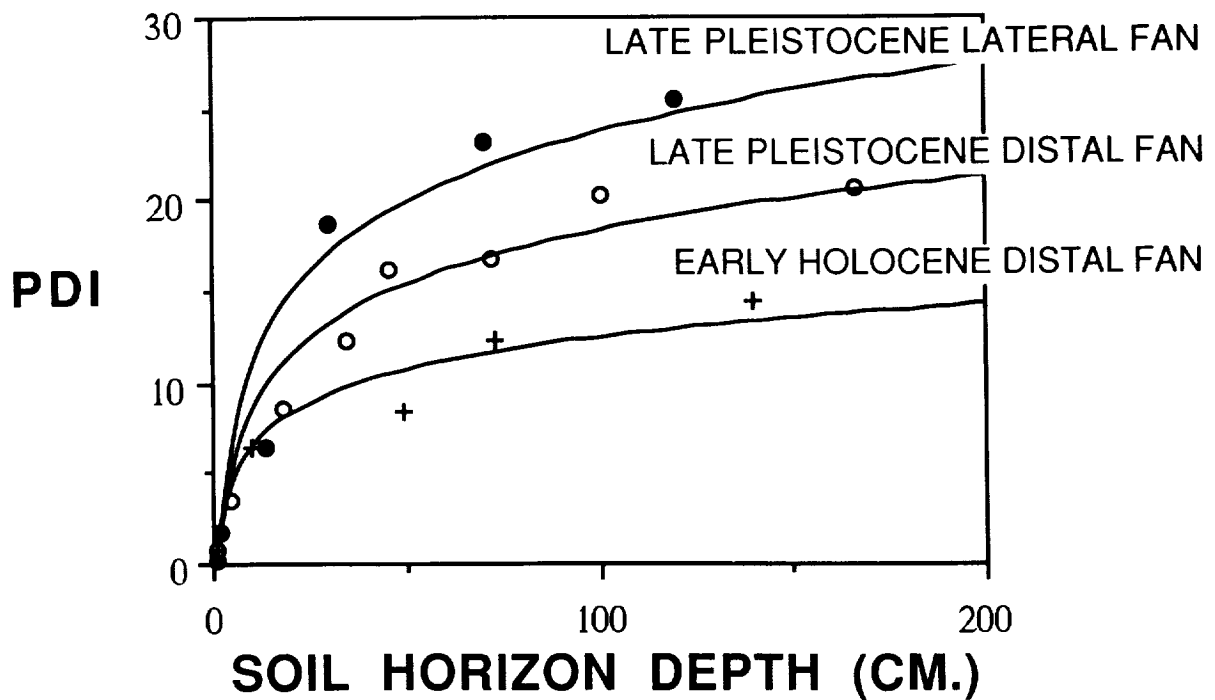


Fig. 3. A plot of the soil profile development index for three soil profiles from different parts of the study area.

RED/WHITE BRIGHTNESS COMPONENTS vs AGE

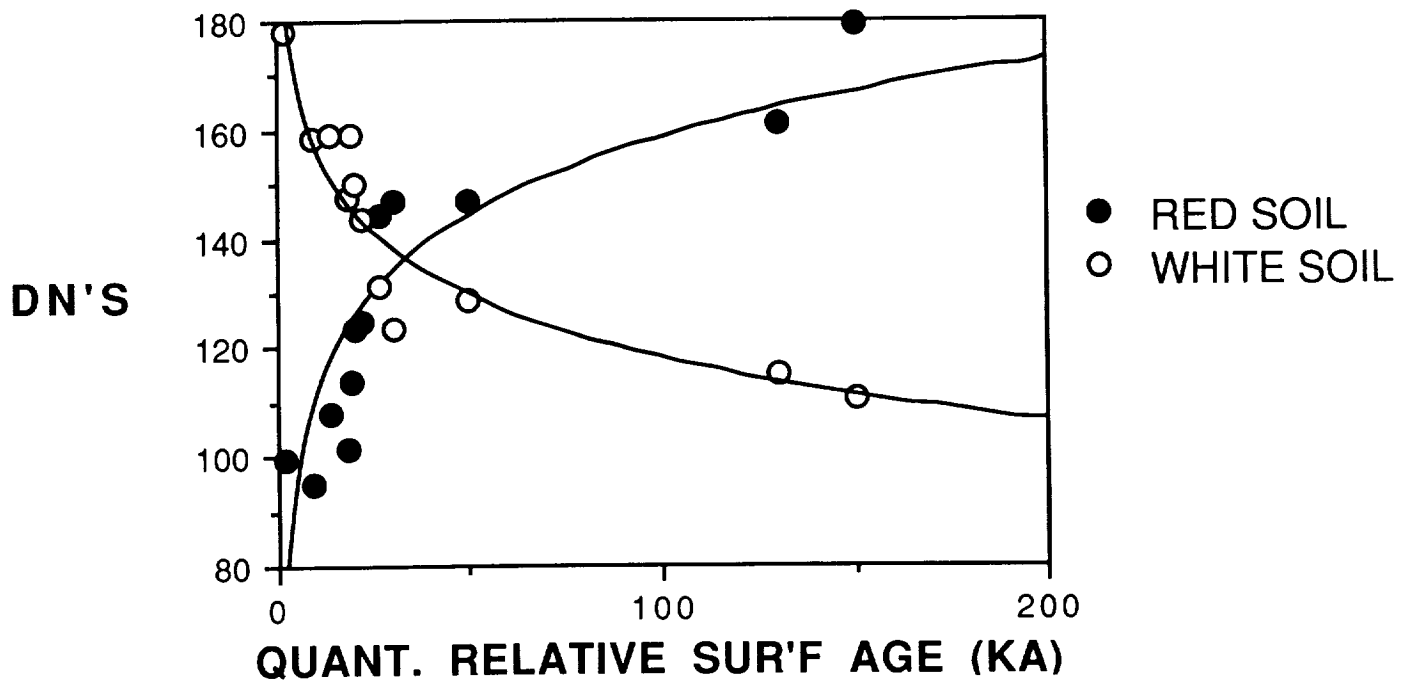


Fig. 4. A plot of the digital numbers of two fraction images for various ages of surfaces in the study area

DISCUSSION

Trends observed so far are encouraging in that surface ages seem to be well-correlated with soil development and fraction images are producing brightness values that are correlated with surface age. However, these results are tentative, due to small sample sizes and the very complex nature of the distal fan at Pine Creek. Over the next year we plan to collect additional soil profile data and further process imagery to concentrate on specific sections of the distal fans and the lateral fans.

REFERENCES CITED

- Adams, John B., M.O. Smith and A.R. Gillespie 1989. Simple models for complex natural surfaces: a strategy for the hyperspectral era of remote sensing. Proc: IGSRSS'89/12th Canadian Symposium on Remote Sensing. 1:16-21.
- Harden, J.W. and Taylor, E.M. 1983. A Quantitative Comparison of Soil Development in Four Climatic Regimes. Quaternary Research, 20:342-359.

ANALYSIS OF AIRBORNE VISIBLE/INFRARED IMAGING SPECTROMETER (AVIRIS) DATA FOR THE NORTHERN DEATH VALLEY REGION, CALIFORNIA/NEVADA**

Fred A. Kruse, Center for the Study of Earth from Space (CSES), Cooperative Institute for Research in Environmental Sciences, (CIRES), University of Colorado, Boulder, CO 80309-0449

ABSTRACT

The Airborne Visible/Infrared Imaging Spectrometer (AVIRIS), a 224-channel imaging spectrometer operating in the 0.41-2.45 μm range, was flown over portions of Death Valley during May 1989 as part of the AVIRIS evaluation program. The data were converted to reflectance using ground spectra and the "empirical line calibration" technique. Reflectance spectra were extracted from the images and compared with both field and laboratory spectra to identify the minerals sericite (fine grained muscovite), calcite, dolomite, hematite, and goethite. Binary encoding of the image spectra was used to produce an image map that showed the spatial distribution of these minerals and combinations of the iron oxides with the other minerals. The image map compared favorably with conventional geologic and alteration maps produced over several field seasons, however, it showed a few previously unmapped carbonate exposures and other areas that will require further field mapping.

INTRODUCTION

This paper summarizes recent results obtained using the Airborne Visible/Infrared Imaging Spectrometer (AVIRIS) in the northern Death Valley region, California and Nevada (Figure 1). AVIRIS is an imaging spectrometer measuring reflected light in 224 narrow (10-nm-wide) bands between approximately 0.41-2.45 μm (Porter and Enmark, 1987). Many minerals have diagnostic spectral features in this range (Hunt, 1977, 1979; Hunt and Ashley, 1979; Lee and Raines, 1984; Clark et al., 1990).

AVIRIS is flown aboard the NASA ER-2 aircraft at an altitude of 20 km, with an instantaneous field of view of 20 m and a swath width of about 10 km. It utilizes four linear arrays and four individual spectrometers to

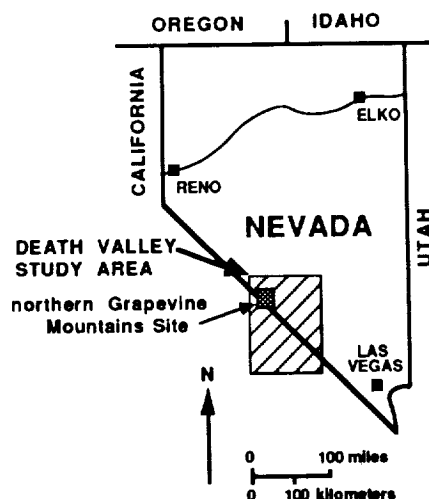


Figure 1. Location map for Death Valley Site.

** Presented at the AVIRIS Workshop, JPL, 4 June 1990.

collect data simultaneously for the 224 bands in a scanned 614-pixel-wide swath perpendicular to the aircraft direction (Porter and Enmark, 1987).

AVIRIS is one of several imaging sensors being used at the Center for the Study of Earth from Space (CSES) at the University of Colorado, Boulder, to develop a better understanding of the complex depositional and erosional processes that resulted in formation of the modern land surface in the Death Valley region (Figure 1). The spectral information derived from AVIRIS is being integrated with both thermal infrared and radar images to discriminate lithological variation and the effects of processes such as weathering, erosion, and soil development. The objectives of this research are 1) to use AVIRIS as a tool to assist in detailed lithological mapping, and 2) to evaluate the performance and utility of the AVIRIS sensor.

GEOLOGY

The extreme northern end of Death Valley (northern Grapevine Mountains) California and Nevada (Figure 1), has been studied in detail using conventional geologic mapping, geochemistry, field and laboratory reflectance spectroscopy, Landsat Multispectral Scanner (MSS), Thematic Mapper (TM), the Airborne Imaging Spectrometer (AIS) and detailed field mapping (Wrucke et al., 1984; Kruse, 1988). Precambrian bedrock in the area consists of limestones, dolomites, sandstones and their metamorphic equivalents. Mesozoic plutonic rocks include quartz syenite, a quartz monzonite porphyry stock, and quartz monzonite dikes. The Mesozoic rocks are cut by narrow north-trending mineralized shear zones containing sericite (fine-grained muscovite) and iron oxide minerals. Slightly broader northwest-trending zones of disseminated quartz, pyrite, sericite, chalcopryite, and fluorite mineralization (QSP alteration) occur in the quartz monzonite porphyry. This type of alteration is spatially associated with fine-grained quartz monzonite dikes. There are several small areas of quartz stockwork (silica flooding of the rocks) exposed at the surface in the center of the area. Skarn, composed mainly of brown andradite garnet intergrown with calcite, epidote, and tremolite, occurs around the perimeter of the quartz monzonite stock in Precambrian rocks. Tertiary volcanic rocks are abundant around the periphery of the study area (Wrucke et al., 1984). Quaternary deposits include Holocene and Pleistocene fanglomerates, pediment gravels, and alluvium.

AVIRIS ANALYSIS

AVIRIS data acquired during May 1989 were analyzed for the northern Grapevine Mountains site. Field spectra of known targets were used to calibrate the data to reflectance with the empirical line method (Roberts et al., 1985). Spectral signatures were extracted using interactive display and analysis software (Torson, 1989) allowing identification of individual minerals and mineral mixtures. Two wavelength ranges of the AVIRIS data were used to identify and map the distribution of minerals. The short-wave infrared data from 2.0 to 2.5 μm was used to identify and

map the distribution of clay minerals, muscovite (sericite), and carbonate minerals. The visible and short-wavelength, infrared portions of the spectrum (0.4-1.2 μm) allowed identification and mapping of iron oxide minerals. Figure 2a shows spectra extracted from the AVIRIS data for known occurrences of sericite, calcite, and dolomite. Comparison of the shapes and positions of the absorption features to laboratory spectra makes positive identification of the three minerals possible (Figure 2b). The AVIRIS data not only allow identification of the carbonate-group-minerals, but allow identification of the individual species (calcite and dolomite) based upon a 20-nm (2 channel) difference between the position of the main absorption feature (2.34 vs 2.32 μm , Figure 2).

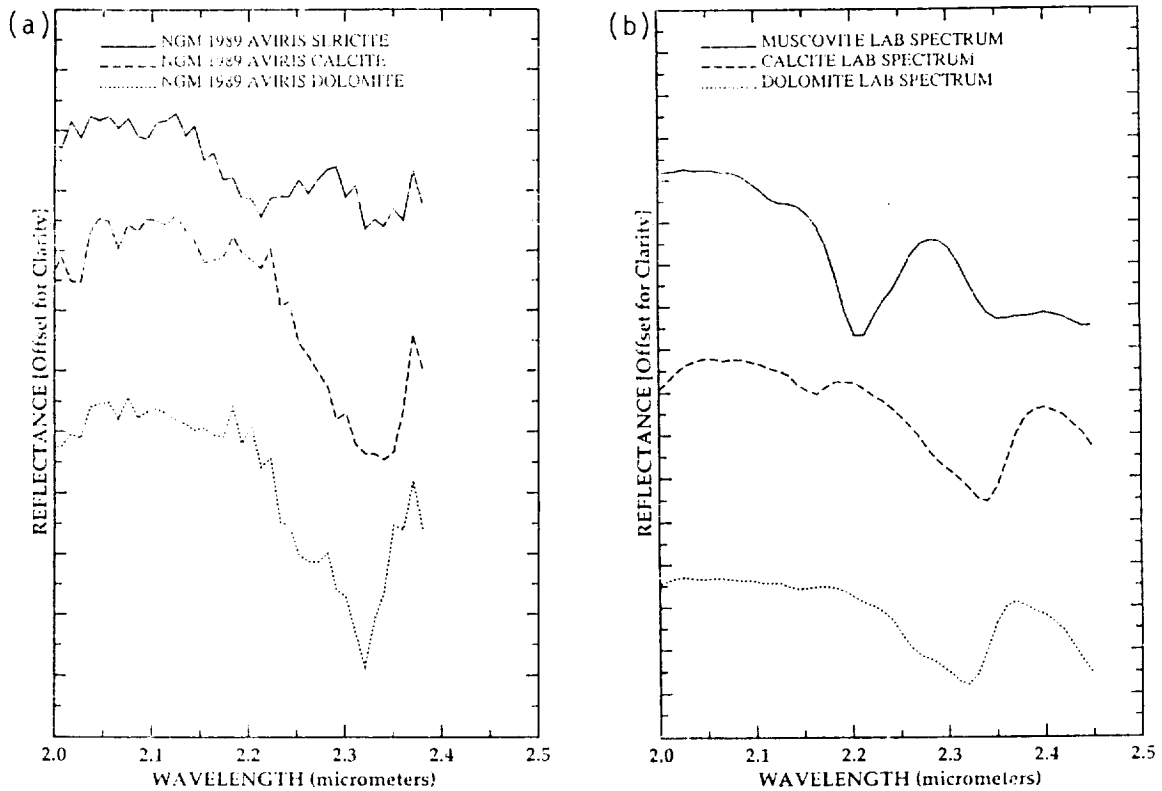
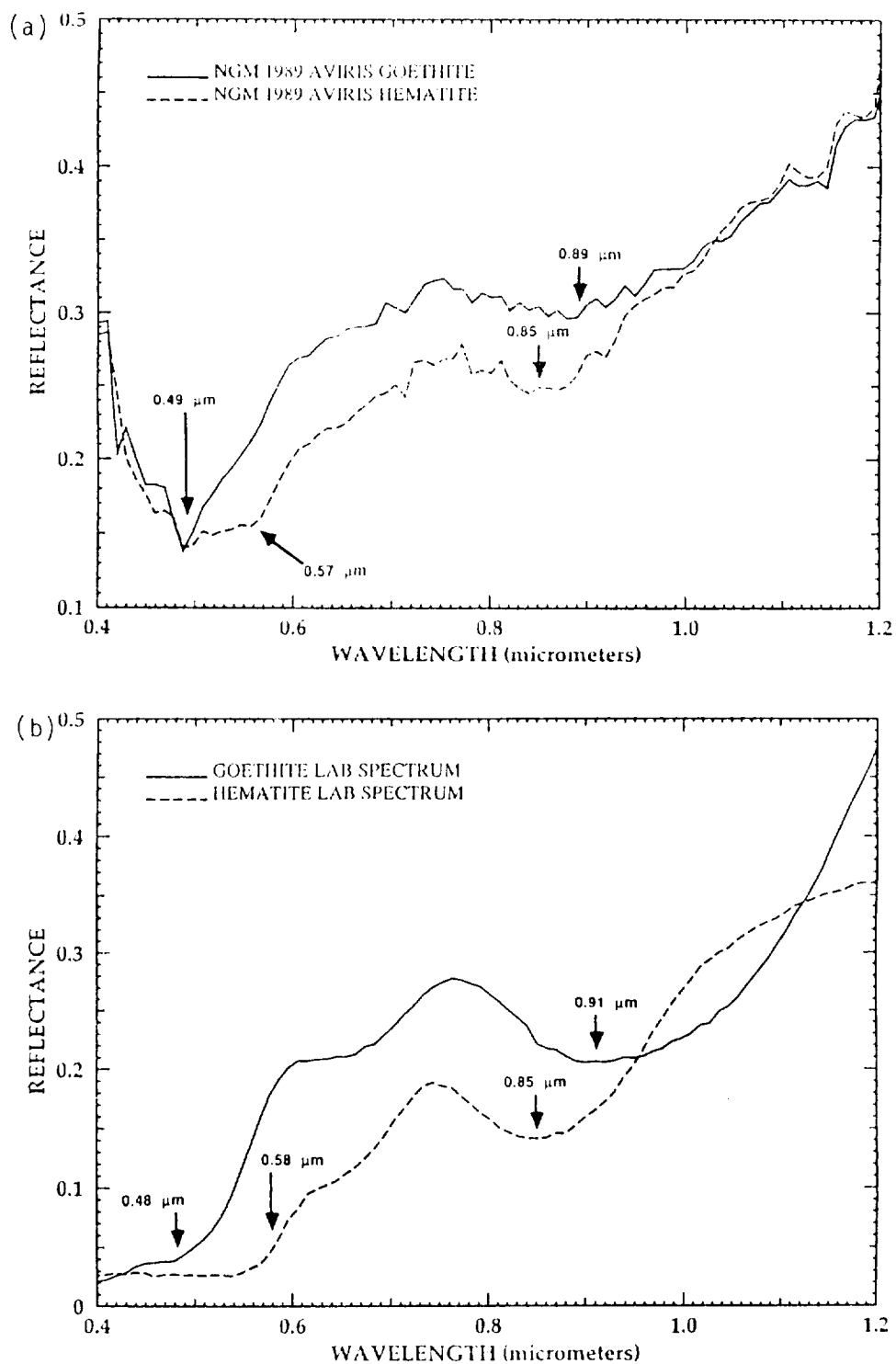


Figure 2. A. AVIRIS reflectance spectra for the minerals sericite (muscovite), calcite, and dolomite; B. Laboratory reflectance spectra convolved to AVIRIS bands for the minerals sericite (muscovite), calcite, and dolomite.

Figure 3a shows spectra extracted from the AVIRIS data for known occurrences of hematite and goethite. Comparison of these spectra to laboratory spectra for goethite and hematite permit positive identification of the two iron oxide minerals (Figure 3b). This distinction has not previously been demonstrated with imaging spectrometer data. Note the positions of the broad absorption feature near 0.9 μm for goethite and 0.85 μm for hema-

Figure 3. A. AVIRIS reflectance spectra for the minerals goethite and hematite. B. Laboratory reflectance spectra convolved to AVIRIS bands for the minerals goethite and hematite.



tite. Note also the position of the visible absorption shoulder near 0.48 μm for goethite and near 0.58 for hematite.

The final step in the analysis of the AVIRIS data was to map the spatial distribution of the minerals identified from interactive inspection of image spectra. The calcite, dolomite, sericite, goethite, and hematite spectra extracted from the image were used as a spectral library for image classification. Binary encoding of the spectrum for each pixel of the AVIRIS image was used to select those areas that closely matched the library spectra (Mazer et al., 1988). Areas that matched within specified tolerances were color coded and overlain on a gray scale image to produce a thematic image map. Mixtures were determined by identifying the individual minerals (using the SWIR to identify sericite and carbonates and the visible to identify the iron oxides) and using standard image processing techniques to combine the classifications where overlap occurred. The final thematic mineral maps provide detailed surface compositional information that can be used in developing geologic models. Color slide 6 is a color coded thematic image map showing the distribution of calcite (red) and dolomite (yellow), based upon the relative position of the $\sim 2.3 \mu\text{m}$ absorption feature ($2.32 \mu\text{m}$ for dolomite vs $2.34 \mu\text{m}$ for calcite). The basic distribution of carbonate mineralogy shown has been confirmed by field testing (acid test) and X-ray diffraction (XRD) (Kruse, 1987a, b). The lack of coherent distribution in the carbonate image is attributed to the similarity of the two mineral spectra which make the $\sim 25/1$ signal-to-noise of the AVIRIS data in the $2.3 \mu\text{m}$ region marginal for identification. Additionally, image speckle indicates that the tolerances chosen were probably slightly too high. Color slide 7 is a color coded thematic image map showing the distribution of sericite, carbonates (calcite and dolomite combined as a group), hematite, goethite, and mixtures of the iron oxides with the other minerals. Again, the basic mineralogical distribution has been confirmed by field mapping, spectral measurements, and XRD (Kruse, 1987a, b). The fracture-controlled nature of the quartz-sericite-pyrite (QSP) alteration can be seen as northwest-trending sericite (green) and sericite+goethite (yellow) in the bottom center of the image. This image also shows that goethite is mostly limited to the Jurassic-age intrusive rocks, while hematite is distributed primarily over the Tertiary volcanic rocks (Kruse, 1987a, b).

DISCUSSION

The results discussed above show the link between the physical properties of surface materials and remote sensing in the visible and infrared. Calibrated aircraft data allowed extraction of reflectance spectra that made direct compositional mapping possible. The AVIRIS data covering the $0.41\text{--}2.5 \mu\text{m}$ range permitted identification and mapping of both primary rock forming minerals (calcite and dolomite) and minerals principally associated with hydrothermal alteration (sericite, goethite, and hematite). Comparison of the AVIRIS mineral maps with conventional geologic and alteration maps showed generally good correspondence, however, the

AVIRIS data indicated several areas where further work is required. The AVIRIS analysis demonstrates that improved lithological mapping is possible even where extensive, detailed ground mapping has been completed.

The next step is to use other AVIRIS data collected during the Geologic Remote Sensing Field Experiment (GRSFE) during July 1990 to extend the analysis to a regional scale and to integrate AVIRIS with thermal infrared and radar sensors. We plan to use these data to produce detailed geologic maps that will allow development of regional geologic models for igneous processes such as emplacement of plutons, magma mixing and evolution, spatial variation of igneous phases, and hydrothermal alteration. Additional models will be developed for sediment accumulation, facies variation and migration, and shifting of sediment sources. By better understanding the nature and regional distribution of lithologies, alteration, and weathering products, a comprehensive model will be developed describing the interaction of processes that formed the modern surface in the Death Valley region.

ACKNOWLEDGMENTS

Analysis of the northern Grapevine Mountains AVIRIS data was funded by NASA grant NAGW-1143.

REFERENCES

- Clark, R. N., King, T. V. V., Klejwa, M., and Swayze, G. A., 1990, High spectral resolution spectroscopy of minerals: Journal of Geophysical Research, (in press).
- Hunt, G. R., 1977, Spectral signatures of particulate minerals in the visible and near-infrared: Geophysics, 42, 3, 501-513.
- Hunt, G. R., 1979, Near-infrared (1.3-2.4 μm) spectra of alteration minerals - potential for use in remote sensing: Geophysics, 44, 1974-1986.
- Hunt, G. R., and Ashley, R. P., 1979, Spectra of altered rocks in the visible and near infrared: Economic Geology, 74, 1613-1629.
- Kruse, F. A., 1987a, Extracting spectral information from imaging spectrometer data: A case history from the northern Grapevine Mountains, Nevada/California: in Proceedings, 31st Annual International Technical Symposium, Society of Photo-Optical Instrumentation Engineers, 834, pp. 119-128.
- Kruse, F. A., 1987b, Use of high spectral resolution remote sensing to characterize weathered surfaces of hydrothermally altered rocks:

Unpublished Ph. D. Thesis, Colorado School of Mines, Golden, Colorado, 139 p.

- Kruse, F. A., 1988, Use of Airborne Imaging Spectrometer data to map minerals associated with hydrothermally altered rocks in the northern Grapevine Mountains, Nevada and California: Remote Sensing of Environment, 24, 1, 31-51.
- Lee, K., and Raines, G. L., 1984, Reflectance spectra of some alteration minerals--a chart compiled from published data 0.4 μ m-2.5 μ m: U.S. Geological Survey Open-File Report 84-96, 6 pp., 1 chart.
- Mazer, A. S., Martin, M., Lee, M., and Solomon, J. E., 1988, Image processing software for imaging spectrometry data analysis: Remote Sensing of Environment, 24, 1, 201-210.
- Porter, W. M., and Enmark, H. T., 1987, A system overview of the Airborne Visible/Infrared Imaging Spectrometer (AVIRIS): in Proceedings, 31st Annual International Technical Symposium, Society of Photo-Optical Instrumentation Engineers, 834, pp. 22-31.
- Roberts, D. A., Yamaguchi, Y., and Lyon, R. J. P., 1985, Calibration of Airborne Imaging Spectrometer Data to percent reflectance using field spectral measurements: in Proceedings, Nineteenth International Symposium on Remote Sensing of Environment, Ann Arbor, Michigan, October 21-25, 1985.
- Torson, J. M., 1989, Interactive image cube visualization and analysis: in Proceedings, Chapel Hill Workshop on Volume Visualization, 18-19 May, 1989, University of North Carolina at Chapel Hill.
- Wrucke, C. T., Werschky, R. S., Raines, G. L., Blakely, R. J., Hoover, D. B., and Miller, M. S., 1984, Mineral resources and mineral resource potential of the Little Sand Spring Wilderness Study Area, Inyo County, California: U.S. Geological Survey Open File Report 84-557, 20 p.

ANALYSIS OF ATMOSPHERIC WATER VAPOR MAPS FROM AVIRIS AT
SALTON SEA, CALIFORNIA: PART I, EXPERIMENTS, METHODS,
RESULTS, AND ERROR BUDGETS

Veronique Carrere, James E. Conel, Robert Green, Carol Bruegge,
Jack Margolis, and Ron Alley

Jet Propulsion Laboratory
California Institute of Technology
Pasadena, California

ABSTRACT

AVIRIS data at Salton Sea were processed to yield atmospheric path precipitable water using an algorithm formed from band radiances in and adjacent to near-infrared water vapor absorption bands at wavelengths of 940 and 1130 nm. The retrieval algorithm is termed continuum interpolated band ratio (CIBR). The CIBR is formed as a ratio between an estimated continuum radiance at the absorption band center derived by linear interpolation between out-of-band continuum radiances to either side, and the actual absorption band radiance at the wavelength of maximum absorption. The CIBRs are calibrated for water abundance using the LOWTRAN 7 radiative transfer code and groundbased estimates of visibility obtained at the time of overflight. The CIBR method is easy to implement and computationally rapid in applications to AVIRIS data.

AVIRIS data over the test site were obtained around the time of solar transit in two nearly orthogonal flight lines trending NW and NE and spanning the sea and adjacent land areas. We sought to observe water vapor plume effects from the sea arising from sea-breeze conditions, as well as water emissions from cooling towers of geothermal plants near the southern seashore as means of measuring evaporation phenomena described by the theory of atmospheric diffusion. The occurrence of proximate cultivated and fallow agricultural areas in Imperial Valley underlying one line was also exploited to study possible interference of liquid water bands in vegetation on the CIBR atmospheric water vapor retrievals.

The AVIRIS-generated water maps for Imperial Valley agricultural areas show substantial variations in atmospheric moisture from place to place that appear unrelated to the background of vegetated and unvegetated fields. The column abundances retrieved using the 1130 nm band are in general 50% less than those obtained using the 940 nm band, but the spatial patterns are closely similar. Radiance measurements over the water are used to estimate the random plus coherent noise present in the AVIRIS data. These determinations with error analyses suggest precision of the measurements of about 10% or less. The differences in retrieved amounts between bands are examined from the standpoint of systematic radiometric calibration errors. The discrepancies can arise if the assumed laboratory detector responsivities are about 10% greater than those prevailing in flight. Both the choice of scattering model (e.g., rural vs marine aerosol) and departures from the assumed atmospheric visibility may contribute to uncertainties in the water retrievals.

INTRODUCTION

Atmospheric water vapor is an important reservoir in the global hydrosphere. Water vapor plays a major role in the energetics of the Earth's surface, since on the average almost half of the net local energy transport from surface to atmosphere is by evaporation of water. Water vapor has an important role in the energetics of weather and the general circulation through transport of latent heat by atmospheric motions. Water vapor is an important greenhouse gas. In addition to these major roles in global weather and climate, water vapor band and continuum absorptions provide substantial obstacles to remote sensing of the Earth's surface, especially under clear-air conditions where most surface and atmospheric sounding techniques have their greatest effectiveness. Accurate determination of the abundance and spatial variability of water vapor is therefore important for the understanding of fundamental hydrologic questions and when compensating for atmospheric effects in determination of surface properties.

We report here validation experiments on recoveries of absolute column abundances of water vapor with AVIRIS, together with new mapping applications at 20-m spatial resolution, of path precipitable water over test sites at Salton Sea, California. The validation experiments compare the water abundances retrieved by AVIRIS with abundances derived by ground-based spectroscopic techniques according to the water vapor band models incorporated in LOWTRAN 7, as well as retrievals from single spectral lines, obtained with the high-spectral-resolution Mark IV interferometer. These validation experiments also demonstrate the difficulties attending comparisons between AVIRIS and column abundances derived from radiosondes, thus emphasizing the importance of dependable radiometric calibration of the AVIRIS. The mapping experiments with AVIRIS over this test site have diverse goals, including (1) investigation of surface reflectance (background) interference on column abundance retrieval; (2) comparisons of water abundances derived from different atmospheric water bands, e.g., the 940- and 1130-nm bands, which are influenced by atmospheric scattering, background effects, and instrument calibration; (3) searches for water plume effects from geothermal power facilities as means of studying relationships between moisture source strength and distributed water abundance, as well as water vapor dispersion in the atmospheric boundary layer; (4) study from AVIRIS-derived water maps of the possible mathematical form of boundary conditions on moisture flux under steady winds near the change in surface conditions between the evaporating Salton Sea water body and adjacent dry, sparsely vegetated inland areas; (5) influences of (gentle) topographic effects on moisture distribution; and (6) the analysis of errors in the water recoveries arising from Gaussian electronic and coherent noise present in the AVIRIS data.

SALTON SEA TEST SITE

The Salton Sea is located in the Salton Trough of southeastern California, approximately 240 km (150 miles) ESE of Los Angeles (Figure 1/Slide 8). The water body is roughly 1090 km² (420 mi²) in area, with a present (stable) surface elevation of - 69.1 m (- 226.6 feet) and a maximum depth near 15 m (50 feet). The salinity is about 44,000 ppm, or 1.26 that

of ocean water. The Coachella and Imperial Valleys to the northwest and southeast in the Salton Trough (Figure 1) are well-known areas of intense agricultural activity. Six geothermal power facilities have been developed close to the southeastern shore.

EXPERIMENTAL PLAN EMPLOYING THE OVERFLIGHT PATTERN

On April 18, 1989, between approximately 10:50 and 11:05 a.m. Pacific Standard Time (1900 UT), AVIRIS overflew the Salton Trough along two flight lines oriented at nearly right angles to one another (Figure 1): (1) the first is 57 km in length and oriented N45E; (2) the second is 60 km long and oriented N40W. The two lines overlap in an approximately 11x11 km square area near the northwest end of line 2, mostly over the water. This configuration of flight lines was chosen to support the following experimental goals: (1) Flight line 1 traverses the water body and adjacent sparsely vegetated land areas to the northeast and southwest. We hoped for favorable on-shore wind conditions from sea breezes to investigate changes in atmospheric water vapor distribution across the land-water interface. Depending on the detailed nature of the boundary conditions assumed, we expected to see characteristic changes in both seaward and landward profiles of column abundances of moisture (see Conel, et al., 1988; Brutsaert, 1982; Yeh and Brutsaert, 1971). Attempting to capitalize on often hazy atmospheric conditions in the Salton Trough, the spectral and brightness contrasts between land and water areas were expected to exhibit the so-called adjacency phenomenon arising from atmospheric scattering (e.g., Diner and Martonchik, 1985).^(†) (2) Flight line 2 covered an intensely cultivated portion of the northwest Imperial Valley, presenting a checkerboard pattern of vegetated and unvegetated fields which were expected to generate background interference for the water vapor recovery algorithms employed, and possibly local abrupt changes in water column abundance from changes in evapotranspiration and soil moisture evaporation from place to place.

We expected to be able to identify water plumes from cooling evaporators and flash towers at the geothermal plants, to map the associated water distributions, possibly to relate them to theoretical models of atmospheric dispersion from approximately point sources, to compute the anomalous abundances, and to relate these to known strengths of source evaporation for the plants. Finally, we wanted to utilize the crossing portions of the two flight lines to employ water vapor distributions as tracers (Reiter, 1972), to map a kind of convective horizontal velocity-column weighted average or bulk convective velocity and relate it to near surface wind velocity determined with portable meteorological stations.

(†) The sharp contrast in surface reflectance at the shoreline between water and surface vegetation or soil cover plus moderately heavy aerosol loading was expected to generate measurable atmospheric spectral scattering effects over the water. These favorable experimental circumstances were unfortunately compromised by heavy sediment turbidity in the near shore waters, thus drastically reducing the anticipated reflectance contrast and generating considerable inhomogeneity in the water body. The AVIRIS data have consequently not been analyzed further for these effects. These atmospheric scattering experiments will be repeated at a later time, employing a different experimental arrangement together with field observations.

This paper (Part I) describes progress to date on analysis of these experimental goals employing AVIRIS data from the April 18, 1989 overflight of the Salton Sea test site. Part II describes possible applications of the water vapor imagery to several questions of importance for hydrology.

FIELD MEASUREMENTS

During the morning of the overflight and throughout the overflight period itself, ground stations were occupied to measure atmospheric optical depth using a Reagan solar photometer, the line-of-sight column abundance of water vapor with spectral hygrometers, and surface wind direction, wind speed, and atmospheric temperature with mechanical weather stations (Meteorological Research Incorporated Model 1081). The locations of these stations are shown in Figure 1.

Atmospheric optical depth. The Reagan solar photometer provides solar radiance measurements using filters at 10 wavelengths in 10-nm increments between 370 and 1030 nm. The instrument and methods of deriving optical depth via the Langley technique, both as averages over time and on an instantaneous basis, are described by Bruegge *et al.*, (1990) and in earlier references given in that paper. A single solar photometer was available to support the AVIRIS overflight on April 18, 1989. The Langley plot data and optical depths derived therefrom for that date at the western shore station are given in Figure 2. Utilizing the average 550-nm optical depth value, a visibility of 36 km was estimated from formulas given by Elterman (1970) (see Bruegge, 1985) and used to fix the aerosol loading for constraint of the scattering part of the LOWTRAN 7 (Kneizys *et al.*, 1990) radiative transfer model.

Water vapor column abundances. We made measurements of the column abundance of atmospheric water vapor at three locations on the east, west, and southwest shores of the sea, using the Reagan solar photometer 940-nm water channel, and two so-called spectral hygrometers that provide a ratio of radiances in two 10-nm channels at 880 and 935 nm. The column water abundance was derived from the aerosol-corrected radiance at 940 nm via the LOWTRAN 7 atmospheric model (Bruegge, *et al.*, 1990). The spectral hygrometers were originally calibrated using radiosonde data. The hygrometers have been recalibrated, adopting a spectroscopic scale provided by LOWTRAN 7 and using the Reagan photometer as a proxy calibration instrument. This procedure avoids problems inherent in the use of radiosonde data for calibration purposes. These questions are discussed by Bruegge, *et al.*, 1990.

Figure 3 shows the time variation of water column abundance for the LOWTRAN-7-based determinations via the Reagan sunphotometer 940-nm radiance measurement at the three Salton Sea ground stations, rectified to a vertical path.

Wind direction and speed. Using the MRI portable meteorological stations, we acquired continuous wind speed and direction measurements at sites on the western and eastern seashores; at the southern site no such instrumentation was available. Wind direction was measured approximately with a Brunton compass; speed was estimated by walking parallel to the measured direction at the perceived velocity. Winds were steady in magnitude and direction at the northern sites; calm conditions prevailed at

the southern location. The data at times of AVIRIS overflight are shown vectorially in Figure 4.

Ground measurements of surface spectral reflectance. Directional hemispherical spectral reflectance was determined over four unvegetated bright and dark targets (Figure 1) using the Portable Instantaneous Display and Analysis Spectrometer (PIDAS). We plan to use these data for in-flight radiometric calibration of AVIRIS (Green, *et al.*, 1990) and to determine surface spectral reflectance of other targets using an empirical method relating surface reflectance to scanner response (Conel, 1990; Conel, *et al.*, 1989).

ALGORITHM FOR ATMOSPHERIC WATER VAPOR RETRIEVAL

We have employed a computationally simple algorithm (Green, *et al.*, 1990), based on use of the short-wavelength infrared 940-nm and 1130-nm atmospheric water vapor absorption bands, to retrieve atmospheric moisture over land areas. Retrievals over water bodies, where the surface reflectance is zero at these wavelengths will require use of the atmospheric path radiance. The algorithm uses radiance measurements from AVIRIS at the center of an absorption band, together with values of the "continuum" radiances to either side (Figure 5). A value of the continuum radiance at the wavelength of maximum band absorption is estimated by linear interpolation between these adjacent continuum values. A ratio is formed between the interpolated continuum and band radiances, called the continuum interpolated band ratio (CIBR).

It has the form

$$\text{CIBR} = y = L_3 / (C_1 L_1 + C_2 L_2) \quad (1)$$

where C_1 and C_2 are constants, equal to 0.5 at 940 nm, where the measurement channels are equally spaced in wavelength, and 0.52 and 0.48 respectively for 1130 nm, where they are unequally spaced. To provide a calibration relationship between the CIBR as defined in Equation 1, and column water abundance w , measured in $\text{g H}_2\text{O}/\text{cm}^2$, we employed the LOWTRAN 7 radiative transfer code with the following conditions: (1) midlatitude summer; (2) surface elevation = sea level; (3) default rural aerosol model (Detailed descriptions of the aerosol scattering phase functions utilized in LOWTRAN are given by Kneizys, *et al.* (1983).); (4) 36-km visibility; (5) surface (Lambertian) spectral reflectance = 0.25; (6) altitude of AVIRIS observation = 20 km, (7) latitude = 33.2°N longitude = 115.50°W , (8) solar zenith angle = 24.9° . The resulting calibration curves are shown in Figure 6. These have the convenient and accurate functional forms

$$y = \exp(-\alpha w^\beta) \quad (2)$$

where α and β are constants. This algorithm is sensitive to the presence of water absorption bands in the surface reflectance that arise from vegetation (Figure 7), since the surface and atmospheric bands overlap one another. Accordingly, under some conditions, extraction of the surface band

contribution from the total water present will require assumption of a band model for the surface part, since the observed radiance (one observation) at wavelengths within the atmospheric band consists of contributions from both atmosphere and surface. For conditions of low visibility (e.g., a few tens of km), the algorithm is sensitive to the visibility and to the aerosol model employed. The uncertainties introduced by each of these problems are discussed below.

WATER VAPOR MAPS OVER THE NORTHWEST IMPERIAL VALLEY

Figure 8a/Slide 9 shows a three-color composite image of AVIRIS data from one segment of the northwest-southeast trending flight line. The lattice pattern of field boundaries is laid out along section lines, north being down and to the left, east up and to the left. The distance between geothermal plants U2 and U3, depicted by x's, is 0.5 mile (0.8 km). The distribution of vegetated, partially vegetated, and fallow agricultural areas for April 18, 1989 are shown in shades of green in Figure 8a. The column abundance distribution of atmospheric water vapor, calculated from the 940-nm water band, is shown in Figure 8b. These values have been rectified to a vertical path assuming local atmospheric homogeneity. It is readily apparent that superposed upon regional trending bands of variable moisture is a "residual" pattern of the fields. In Figure 9/Slide 10, the green field pattern from Figure 8b/Slide 9 has been superposed on the water image to facilitate a closer comparison. In general, there appears to be no correlation between the distribution of green fields and the total column abundance of water present. That is, the presence of green vegetation at the surface does not appear to enhance the atmospheric moisture component at the level of water vapor subdivision depicted. Nor does the presence of an unvegetated substrate generate any systematic pattern of retrieved abundance relative to the surroundings. However, the vegetation must influence the retrieved abundances. This problem is dealt with below.

COMPARISON OF RETRIEVALS FROM THE 940- AND 1130-NM BANDS

In Figure 10/Slide 11 we present a comparison of water abundances retrieved from the CIBR algorithms for the 940- and 1130-nm bands, represented on a common color scale. While the overall pattern of retrieved moisture is very similar, the derived water abundance for 1130 nm is systematically lower than that for 940 nm everywhere in the image. A similar discrepancy was found for retrievals at Salton City (Figure 2).

VALIDATION EXPERIMENTS AND PRECISION OF THE WATER VAPOR RETRIEVALS

Validation via LOWTRAN 7 and single spectral line determinations. Good agreement has been found between column abundances derived from AVIRIS, when the instrument has been calibrated in flight, and abundances measured simultaneously from the ground with the Reagan solar photometer (Bruegge, et al., 1990). Bruegge, et al. (1990) have further compared the column abundances derived from the solar photometer data based on LOWTRAN 7 with column abundances derived from analysis of eight mid-infrared single-line profile measurements obtained with a high-spectral-resolution interferometer (JPL Mark IV). The scatter of the eight interferometer determinations is $\pm 3\%$; the agreement between the LOWTRAN 7-based solar photometer retrievals and the single-line determinations is about 1%.

Estimating precision of determinations. Close inspection of the images of Figure 8 shows the presence of a grainy pattern over the water and elsewhere that represents both coherent and random electronic noise components. A coherent noise component with a frequency near 400 Hz is known in the AVIRIS data and has been traced to a power supply aboard the ER-2 aircraft. Random electronic noise, represented by dark current fluctuations measured at the end of each AVIRIS scan line, is present at the level of about ± 3 DN, equal to a noise equivalent radiance of about $0.1 \mu\text{W}/(\text{cm}^2 \text{ sr nm})$ (Chrien, *et al.*, 1990)

The fractional uncertainty in the CIBR ($= y$) σ_y/y is derived from Equation 1 as

$$\sigma_y/y = \sqrt{(y^2 C_1 \sigma_1^2 + C_2^2 \sigma_2^2 + C_1 C_2 \sigma_{12}^2 - 2y C_1 \sigma_{13}^2 - 2C_2 \sigma_{23}^2 + \sigma_3^2)/L_3} \quad (3)$$

where σ_j and σ_{ij} are diagonal and off-diagonal elements of the covariance matrix of the L_j , obtained from analysis of the radiances observed by AVIRIS over the water. σ_j and σ_{ij} contain components arising from both coherent and random noise plus possible variations in the atmospheric path radiance over the areas sampled. Also included are possible contributions from variability of the water surface, wherever the reflectance is nonzero because of suspended sediment or organic load. For the Salton Sea data of April 18, 1989, the variance-covariance matrix in terms of the radiances ($\times 100$) derived from analysis of 2500 pixels over the water is

$$\begin{bmatrix} \sigma_1^2 & & \\ \sigma_{12}^2 & \sigma_2^2 & \\ \sigma_{13}^2 & \sigma_{23}^2 & \sigma_3^2 \end{bmatrix} = \begin{bmatrix} 63.1 & & \\ 7.3 & 20.3 & \\ -7.9 & -3.6 & 25.7 \end{bmatrix}$$

for the 940-nm band, and

$$\begin{bmatrix} 33.82 & & \\ -4.3 & 40.0 & \\ 5.8 & -5.4 & 30.8 \end{bmatrix}$$

for the 1130-nm band. The fractional uncertainties in derived precipitable water values are, from Equation 2,

$$\sigma_w/w = (\sigma_y/y)/(\alpha\beta w^\beta) \quad (4)$$

Values of σ_w/w (in percent) that result from these variance-covariance data are shown in Figure 11 for four areas within the AVIRIS data segment under discussion. The values of σ_y/y for the 1130-nm band correspond closely to the values shown for σ_w/w and are not included for clarity. The notation $\sigma_{ij}^2 = 0$ corresponds to an uncertainty estimate excluding the covariances. In general, the uncertainty increases slightly when the covariances are included in the error budget, but in all cases the retrievals appear to be good to better than 10% for the present data set.

SOME SOURCES OF SYSTEMATIC ERROR

Systematic errors manifest themselves as differences in water abundances derived from the 940- and 1130-nm water bands (Figures 3, 10 and 11) amounting to about 55%. Such errors may arise from any or all of the following: (1) spectral dependence of the surface reflectance violating the constant-with-wavelength assumption, (2) calibration errors, (3) departures of the actual atmospheric visibility from that assumed in constructing the calibration curves (Equation 2) from LOWTRAN 7, (4) an incorrect assumption of the aerosol model in LOWTRAN 7 as compared to the actual conditions, or (5) incompleteness one or both of the band models employed in LOWTRAN 7. Items 1 thru 4 are discussed below. Item 5 cannot be evaluated from the AVIRIS data themselves.

Spectrally dependent background reflectance. The spectral reflectance of the Earth's surface is seldom constant with wavelength. Properly, the calibration relationship between CIBR and water abundance needs to be generated with the actual surface spectral reflectance over which the water retrieval is to be carried out. In practice this is difficult because the a priori surface reflectance is not known, so an iterative scheme has to be developed to estimate it.

The CIBR calibration curves given in Figure 6 are calculated from LOWTRAN 7 on the assumption of a constant surface spectral reflectance of 25%. We will refer to this as the standard curve. In this section we describe calculations using the LOWTRAN 7 model that explore departures from this assumption. Surface reflectance effects that are not included in the standard calibration curve introduce a systematic error into the retrieved water abundances. The magnitude of these is investigated next.

We reevaluated the CIBR calibration functions (Equation 2) employing LOWTRAN7 with the spectral reflectance of alfalfa, iron-oxide-rich soil, and the mineral gypsum as representative of possible extreme natural examples introduced by background reflectance. The reflectance data obtained with a laboratory spectrometer are shown in Figure 7. The fractional differences $(y_s - y)/y_s$ in water vapor retrieved using the standard CIBR calibration curve (y_s) and the wavelength-dependent CIBR curves (y) for these cases are given in Figure 12. The wavelength-dependent calibration functions follow from these, given the standard curve. The background reflectance changes introduce small changes in the constants α_s and β_s , $\Delta\alpha$, and $\Delta\beta$. The corresponding change in y_s is approximately

$$\Delta y_s \cong \left(\frac{\partial y_s}{\partial \alpha_s} \right) \Delta \alpha + \left(\frac{\partial y_s}{\partial \beta_s} \right) \Delta \beta \quad (5)$$

The accompanying fractional uncertainty in the water vapor recovery is

$$\frac{\Delta w}{w} \approx - \left(\frac{\Delta y_s}{y_s} \right) \frac{1}{\alpha_s \beta_s w_s^\beta} \quad (6)$$

or written out, using Equation 2

$$\frac{\Delta w}{w} \approx \frac{1}{\beta_s} \left(\frac{\Delta \alpha}{\alpha_s} \right) + \ln(w) \left(\frac{\Delta \beta}{\beta_s} \right) \quad (7)$$

The values of $\Delta \alpha / \alpha_s$ and $\Delta \beta_s / \beta$ derived from the data of Figure 12 and the standard calibration equation are listed in Table 1 for alfalfa and iron-oxide-rich soil. The case of gypsum-rich soil closely resembles that of alfalfa and is therefore not presented.

Table 1. Fractional (systematic) changes (%) in the constants α and β of Equation 2 accompanying departures of the surface reflectance from 0.25

	$\Delta \alpha / \alpha_s$	$\Delta \beta / \beta_s$
Alfalfa	2.37	2.07
Fe ₂ O ₃ soil	2.87	-1.79

The fractional (systematic) errors in water recovery implied by Equation 7 for iron-oxide-rich soil and alfalfa backgrounds are shown in Figure 13. The most extreme case is that of low atmospheric water abundance (< 0.5 cm), where it is seen that the errors grow without bound as w approaches zero. The presence of surface absorption bands increases the apparent water abundance retrieved for both cases, as expected. For typical abundances present in the Salton Sea data set (~ 1.5 to 2 g/cm²), the reported amounts would be about 5% too high for both vegetation and soil backgrounds.

Radiometric calibration uncertainty. The in-flight radiometric calibration of AVIRIS is uncertain because of changes in spectrometer configuration that may accompany (possibly time-dependent) thermal distortion of the instrument away from the steady configuration under which the laboratory calibration is carried out. These (distortion) changes introduce a systematic error Δy into the calculated CIBR values that is given by

$$\Delta y = y(\delta L_3 - y(C_1 \delta L_1 + C_2 \delta L_2) / L_3) \quad (8)$$

where the δL_j represent changes in the L_j arising from the supposed distortion. If Φ_j represents the proportionality constant between radiance and instrument output in DN for the j th channel involved in the

CIBR calculation, e.g., $L_j = \Phi_j^{-1} DN_j$, ($j = 1, 2, 3$), then $\delta L_j = L_j' - L_j = (\Phi_j'/\Phi_j - 1)L_j$, where the primes refer to flight conditions. It has not yet been possible to provide an in-flight calibration for AVIRIS from the ground-based data for the Salton Sea experiment of April 18, 1989. We can, however, estimate in-flight changes in the Φ_j that will account completely for the discrepancies, as follows. In Figure 14 the AVIRIS-derived column abundances for western and southern observation stations are compared with time histories of variation of the atmospheric water derived from analysis of Reagan sun photometer and spectral hygrometer data. Assuming the ground-based observations of water vapor abundance to be correct, the AVIRIS abundances are between 18-22% too low at 940 nm, and 46-58% low at 1130 nm. The required changes in in-flight gain factors are illustrated in Figure 11, as derived from Equations 2 and 5. To reduce the number of variables, the second term on the right-hand side of Equation 5, involving both δL_1 and δL_2 , has been treated as a single algebraic variable. Specifically, at 940 nm, a discrepancy $\delta w/w$ of - 20% could arise from a +8% change in δL_3 together with $\approx - 9\%$ in the algebraic value of $\delta L_1 + \delta L_2$. Lacking other constraints, any combination of the δL_j satisfying Equation 5 would be equally acceptable. The magnitude of these changes are in accord with those found from available analyses of in-flight AVIRIS detector responsivities (Green, *et al.*, 1990). At 1130 nm, the greater magnitude of $\delta w/w$ implies greater differences between laboratory and flight conditions than in the 940-nm region, although uncertainty in the laboratory responsivities may also be involved at 1130 nm.

Atmospheric visibility. The water calibration functions (Equation 2) depicted in Figure 5 were developed from LOWTRAN 7 under the assumptions of uniform surface reflectance of 0.25, constant visibility of 36 km, and the standard rural aerosol model contained in the LOWTRAN 7 code. Dependence of the apparent retrieved water abundance upon departures of the actual visibility from the assumed value, and upon the aerosol model assumed, are illustrated in Figure 15, where results for the rural and maritime models are compared. In either case, if the actual visibility encountered is greater than 36 km (crossover point of equal water retrieval for both bands in both scattering models), the radiances generated by LOWTRAN 7 provide lower than expected abundances for both 1130- and 940-nm retrievals with $w_{1130} > w_{940}$ by about 9%. With visibilities less than 36 km, the retrieved abundances are greater than expected, and $w_{940} > w_{1130}$. The maritime model generates higher apparent precipitable water abundances than does the rural model for visibility less than the assumed standard value, and less apparent water for visibilities that are greater than 36 km.

Rural vs maritime aerosol models. If the radiances as a function of visibility are calculated assuming a marine aerosol model in LOWTRAN 7, but the rural aerosol-based calibration curve for water vapor column abundance recovery is erroneously retained, the crossover point shifts to a visibility of 50 km, and the apparent retrieved water amounts are increased. For large visibilities the water amounts converge to the same values for each band, independent of the scattering model, as would be expected for zero scattering conditions. The difference in indicated amount between bands is about 9%.

To explain a condition of $w_{940} > w_{1130}$ retrieved from the AVIRIS observations at Salton Sea, based on assumptions about the aerosols, requires a visibility less than 36 km everywhere if either the rural or

maritime model is adopted. This includes the west shore calibration site, where the visibility estimate was established from our sun photometer data, and consequently where the two band estimates should agree. A 50% discrepancy, based on visibility or scattering model, violates the observed visibility condition and would also produce larger moisture amounts (e.g., $>> 2$ cm) than are observed over the site.

The differences in apparent water vapor amount between the rural and maritime aerosol models shown in Figure 16 suggest that the crossover water abundance for the adopted visibility may depend upon the scattering model used. This, however, is not the case. The apparent difference results from the use of radiance calculations from one aerosol (maritime) model in a water vapor calibration curve derived from another (rural) model. These differences disappear when the marine model radiances are used in a marine model calibration curve (as shown in Figure 15), although the functional dependence of retrieved water abundance on departure of visibility from the assumed standard value remains.

ACKNOWLEDGMENTS

This paper presents the results of one phase of research carried out at the Jet Propulsion Laboratory, California Institute of Technology, under a contract with the National Aeronautics and Space Administration.

REFERENCES

- Bruegge, C.J., 1985, In-flight absolute radiometric calibration of the Landsat Thematic Mapper (published under Kastner), Ph.D. Dissertation, University of Arizona, 195 pp.
- Bruegge, C.J., J.E. Conel, J.S. Margolis, R.O. Green, G. Toon, V. Carrere, R.G. Holm, and G. Hoover, 1990, In-situ atmospheric water-vapor retrieval in support of AVIRIS validation, in *Imaging Spectroscopy of the Terrestrial Environment*, SPIE Vol. 1298.
- Brutsaert, W., 1982, *Evaporation into the Atmosphere*, D. Reidel Publishing Company, Boston, 299 pp.
- Chrien, T.G., R.O. Green, and M.L. Eastwood, 1990, Accuracy of the spectral and radiometric laboratory calibration of the Airborne Visible/Infrared Imaging Spectrometer (AVIRIS), proceedings of this conference (in press).
- Conel, J.E., R.O. Green, V. Carrere, J.S. Margolis, G. Vane, C. Bruegge, and R. Alley, 1989, Spectroscopic measurement of atmospheric water vapor and schemes for determination of evaporation from land and water surfaces using the Airborne Visible/Infrared Imaging Spectrometer (AVIRIS), *IGARSS '89, 12th Canadian Symposium on Remote Sensing*, IEEE #89CH2768-0, 2658 - 2663.
- Conel, J.E., 1990, Determination of surface reflectance and estimates of atmospheric optical depth and single-scattering albedo from Landsat Thematic Mapper data, *Int. J. Remote Sensing*, 11(5), 783-828.

Diner, D.J., and J.V. Martonchik, 1985, Influence of Aerosol Scattering on Atmospheric Blurring of Surface Features, *IEEE Transactions on Geoscience and Remote Sensing*, GE-23 (5), 618-624.

Elterman, L., 1970, Vertical-attenuation model with eight surface meteorological ranges 2 to 13 kilometers, Report AFCRL-70-0200, AFCRL, Bedford, MA, 55 pp.

Green, R.O., V. Carrere, and J.E. Conel, 1990, Measurement of atmospheric water vapor using the Airborne Visible/Infrared imaging Spectrometer, *Image Processing '89*, American Society for Photogrammetry and Remote Sensing, Proceedings of a conference at Sparks, Nevada, 23 May, 1989, 31-44.

Isaacs, R.G., W.-C. Wang, R.D. Worsham, and S. Goldenberg, 1987, Multiple-scattering LOWTRAN and FASCOD models, *Appl. Optics*, 26(7), 1272-1281.

Kneizys, F.X., E.P. Shettle, W.O. Gallery, J.H. Chetwynd, L.W. Abrew, J.E.A. Selby, S.A. Clough, and R.W. Fenn, 1983, Atmospheric Transmittance/Radiance: Computer Code LOWTRAN 6, AFGRL TR-83-0187, AFGL, Hanscom AFB, MA, 193-200.

Kneizys, F.X., E.P. Shettle, G.P. Anderson, L.W. Abrew, J.H. Chetwynd, J.E.A. Selby, and W.O. Gallery, 1990, Atmospheric Transmittance/Radiance: computer Code LOWTRAN 7, (in press), AFGL Hanscom AFB, MA.

Reiter, E.R., 1971, *Atmospheric Transport Processes (Part 2: Chemical Tracers)*, U.S. Atomic Energy Commission Critical Review Series (TID-25314), 65-94.

Yeh, G.T., and W. Brutsaert, 1971, A solution for simultaneous turbulent heat and vapor transfer between a water surface and the atmosphere, *Boundary-Layer Meteorol.*, 2, 64-82.

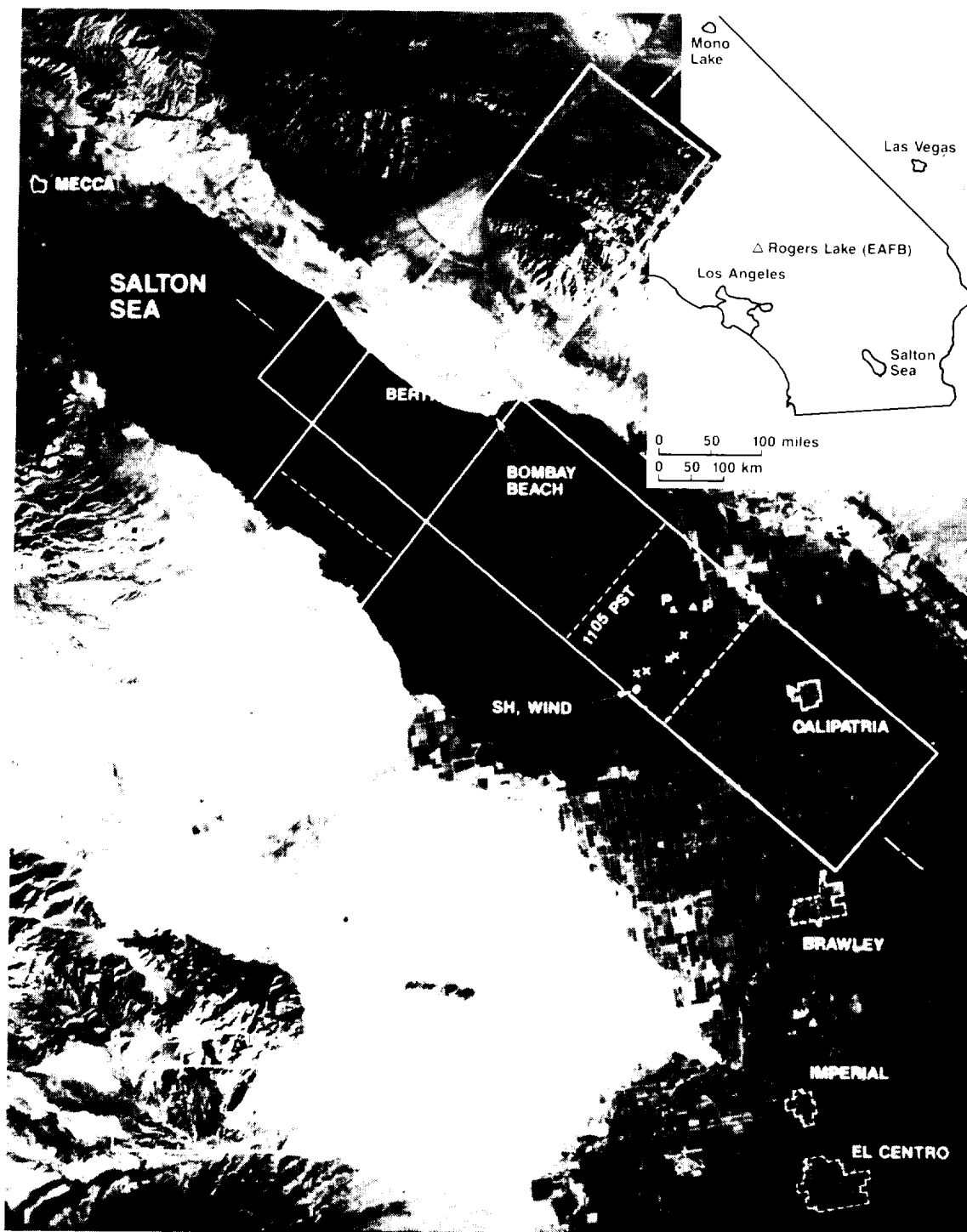


Figure 1. Location of the Salton Sea test site in southeastern California (inset). MSS image shows orientation and extent of the AVIRIS flight paths over Salton Sea, in the Salton Trough, April 18, 1989. Places mentioned in the text but not shown on this index photo include: (1) Imperial Valley - extends southeast from southeast shore of Salton Sea including agricultural areas shown in red (slide only) and the cities of Niland, Calipatria, Brawley, Imperial, and El Centro, (2) Coachella Valley - extends northwest off the image from northwest shore of Salton Sea near the town of Mecca.

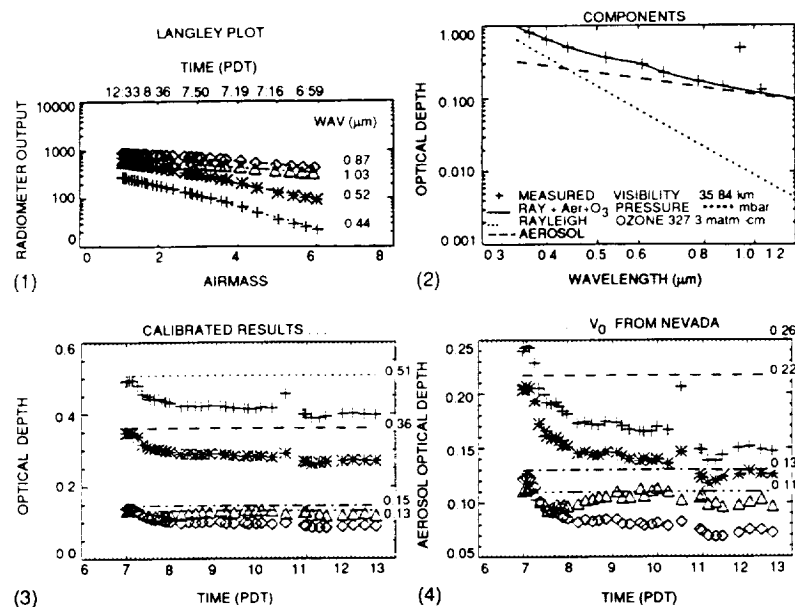


Figure 2. Atmospheric characterization via Reagan sun photometer at Salton City, 18 April 1989. (1) Langley plot - Raw radiometer output versus airmass, $1/\cos$ (solar zenith angle), (2) Components of the optical depth derived from the Langley plot data, (3) Calibrated results - instantaneous optical depths derived from two-point Langley plots using instrument calibration constants (V_0) derived from long-term-average zero-air-mass intercepts, (4) V_0 from Nevada - instantaneous aerosol optical depths derived from two-point Langley plots using V_0 values derived from high-altitude measurements at Charlton Peak, Nevada.

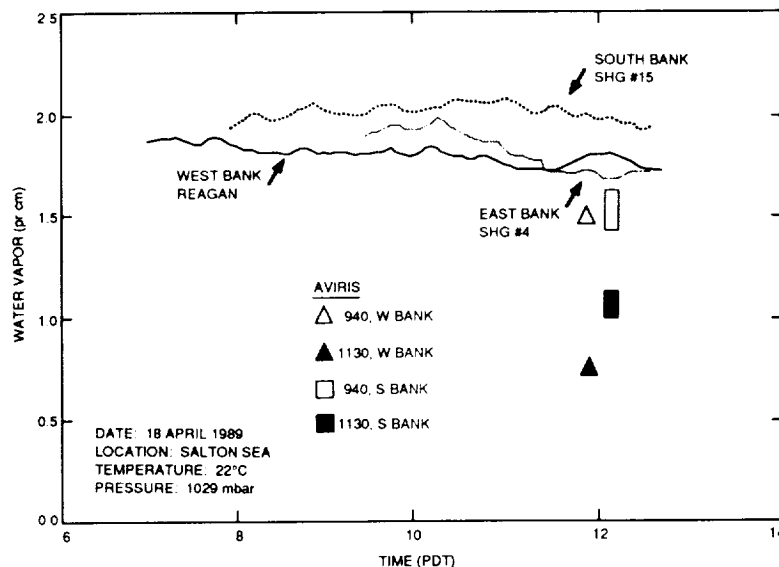


Figure 3. Instantaneous water vapor determinations from ratioing spectral hygrometer and Reagan sun photometer data at Salton City. AVIRIS determinations are via the CIBR method with LOWTRAN 7 code, using laboratory-determined responsivities to calculate inflight radiances. See text for complete explanation.

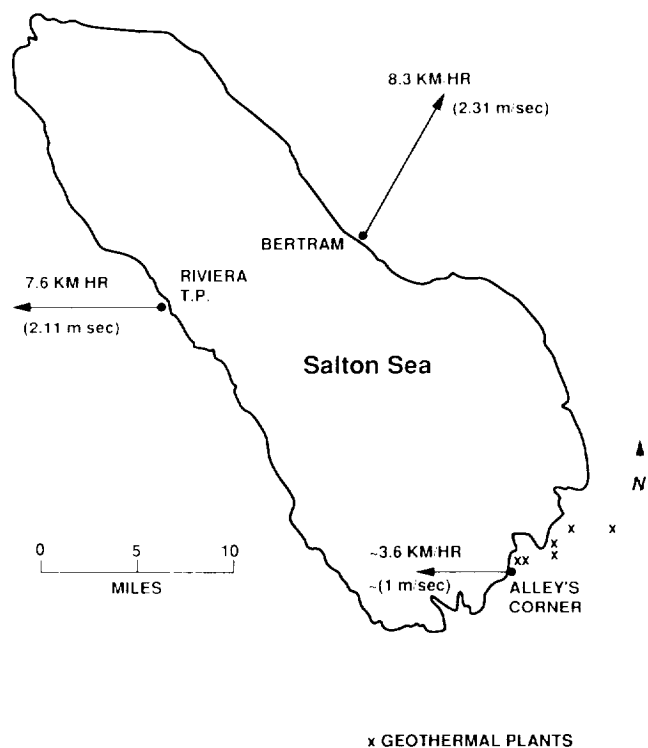


Figure 4. Wind directions and speeds at 2 meters above ground level at time of AVIRIS overpass, as measured by mechanical weather stations.

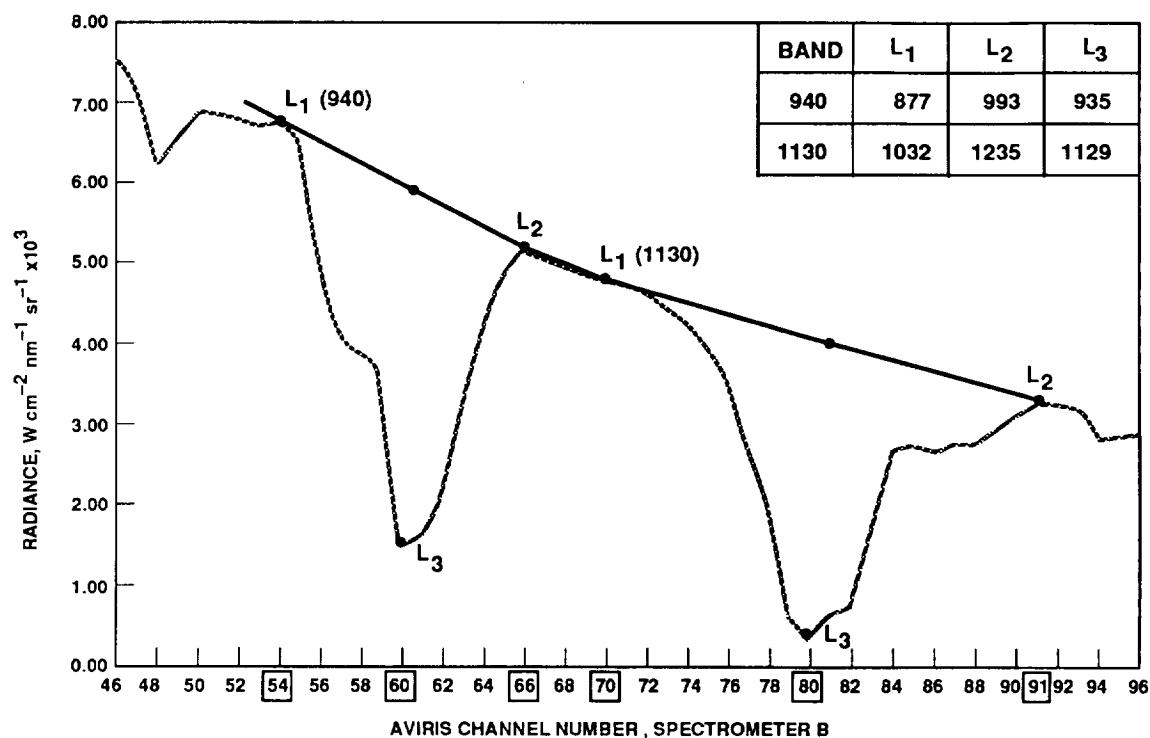


Figure 5. Wavelengths and radiance values used to calculate the *Continuum Interpolated Band Ratio (CIBR)* from AVIRIS radiance data.

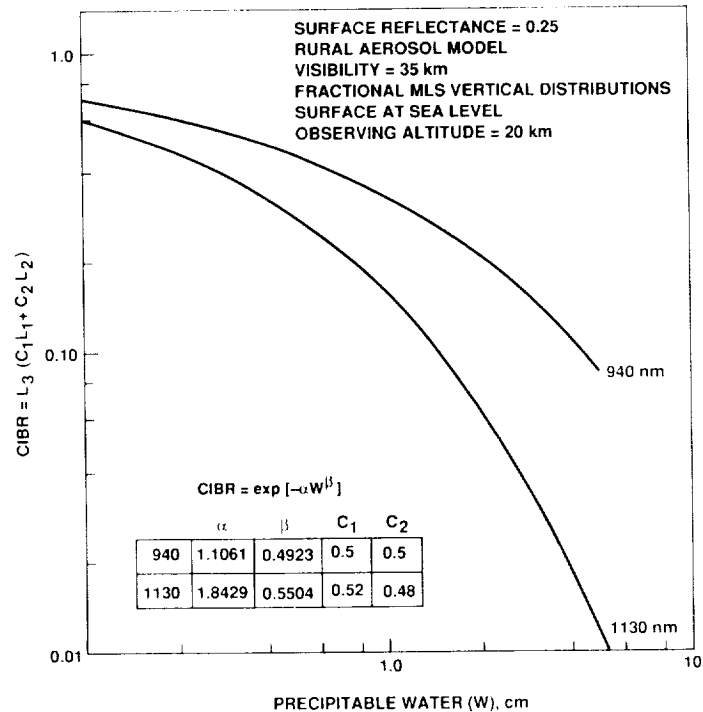


Figure 6. Calibration curves for the 940- and 1130-nm water bands using the CIBR algorithm and the LOWTRAN 7 atmospheric model.

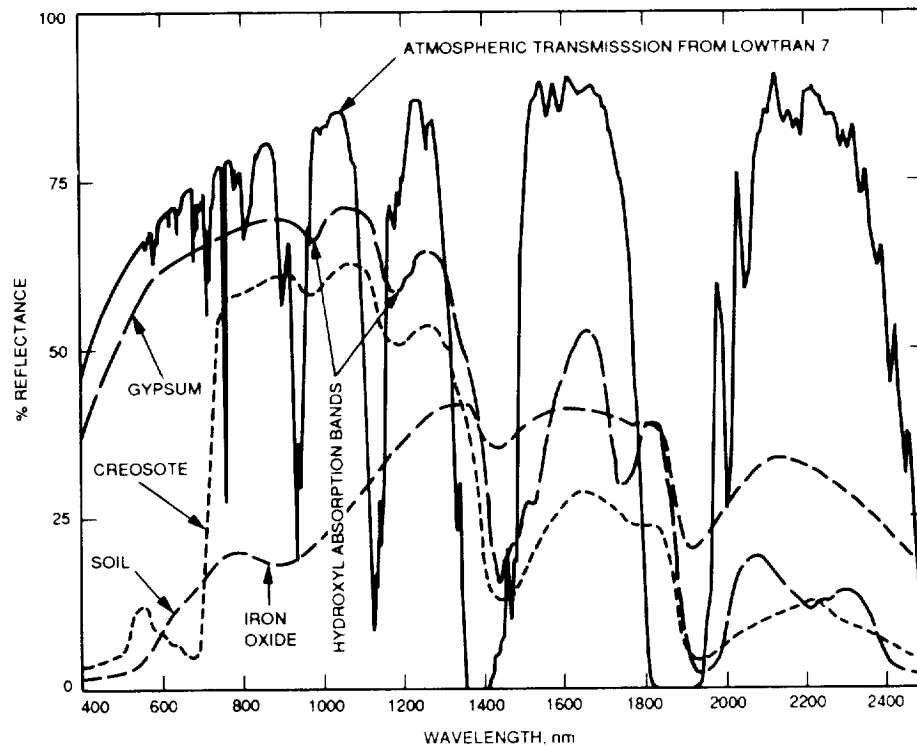
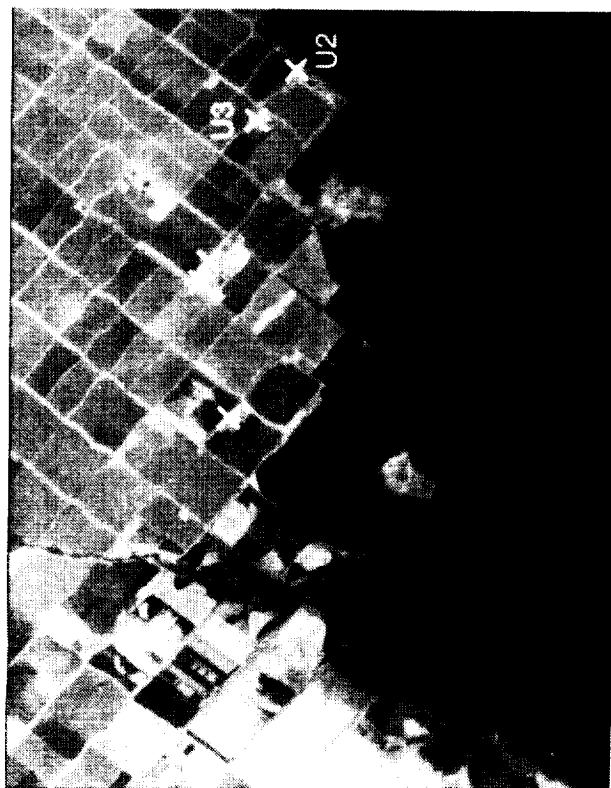


Figure 7. Atmospheric transmission from LOWTRAN 7 model compared to spectral reflectances of vegetation (creosote), iron oxide, and gypsum-bearing soils. Surface water and mineralogical absorptions impinge on retrieval of atmospheric water vapor using the CIBR method.



(a)

Red 660 6 nm Green 1012 8 nm Blue 2172 9 nm

+ GEOTHERMAL
POWER FACILITIES



(b)

Spatial distribution of water vapor
940 nm Atmospheric water band

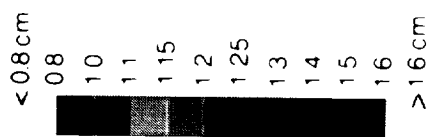


Figure 8. Left image: - three-color composite AVIRIS image of near-shore area (11:05 PST segment) in northwest Imperial Valley. Right image: - spatial distribution of atmospheric water vapor (column abundance) derived using CIBR algorithm and 940-nm water band.

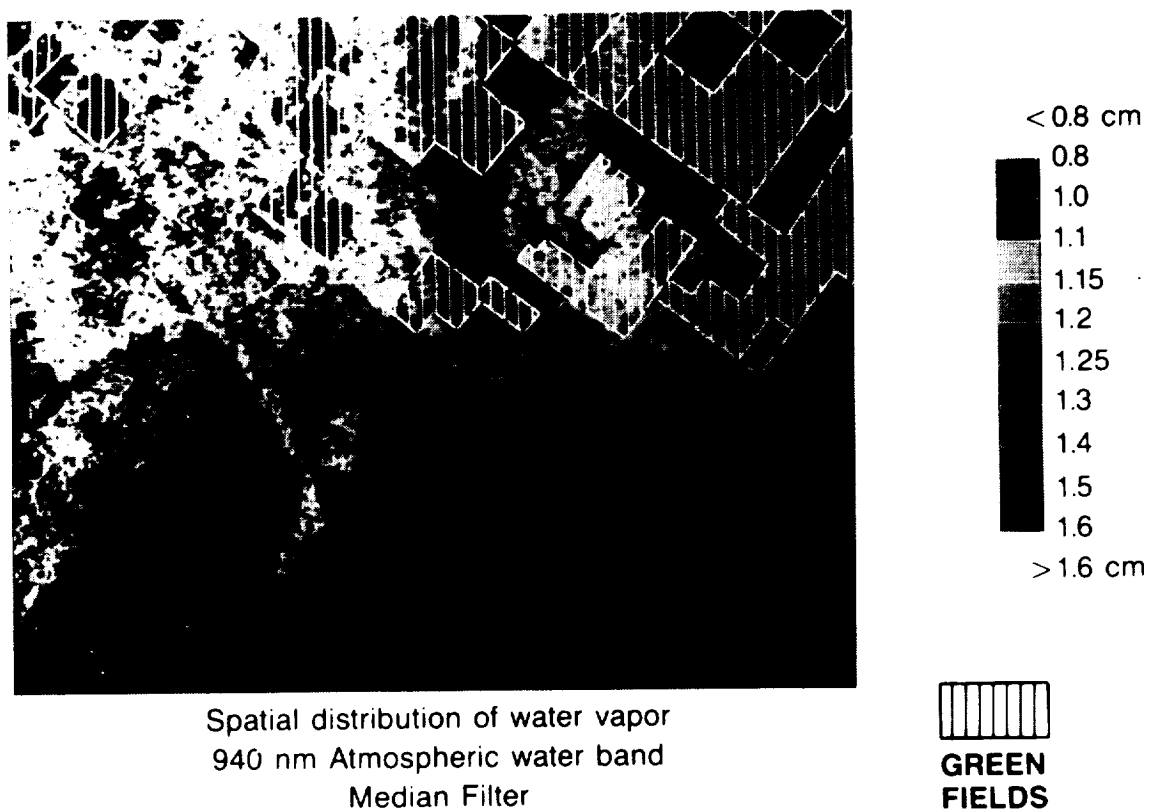


Figure 9. Spatial distribution of atmospheric moisture (column abundance) compared to the distribution of green fields as shown in left image of Figure 8. The *median filter* replaces image DN at a pixel P by the most frequent DN value in the 3×3 array of which P is the center.

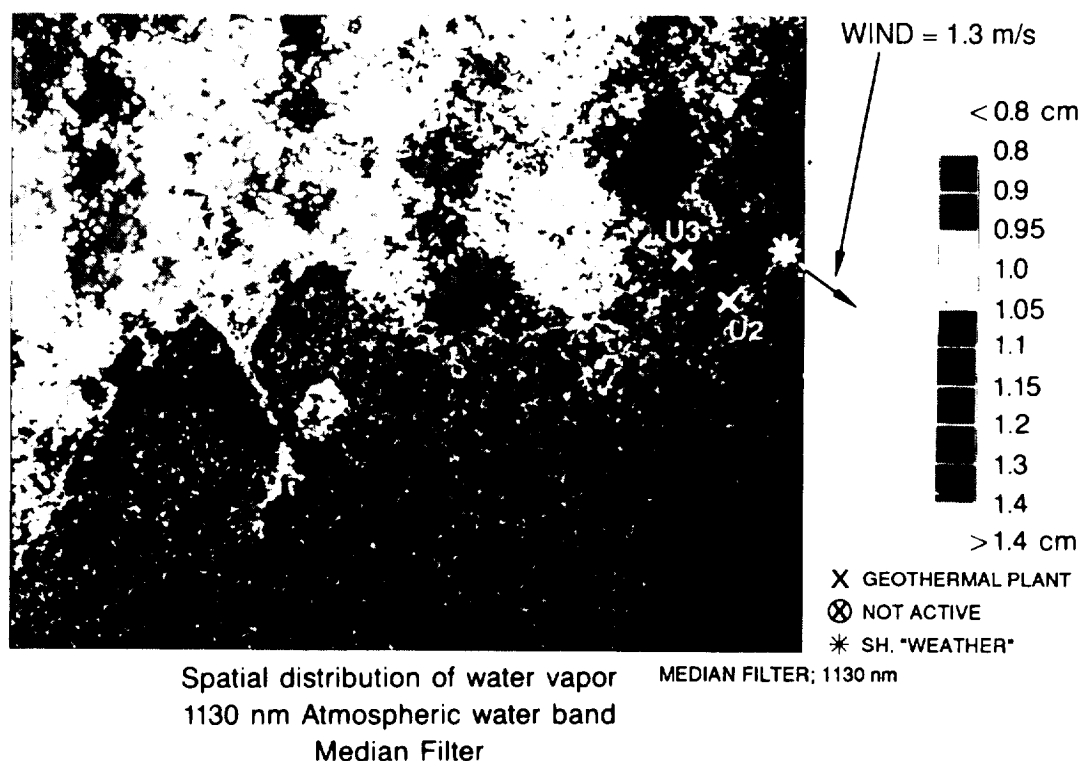
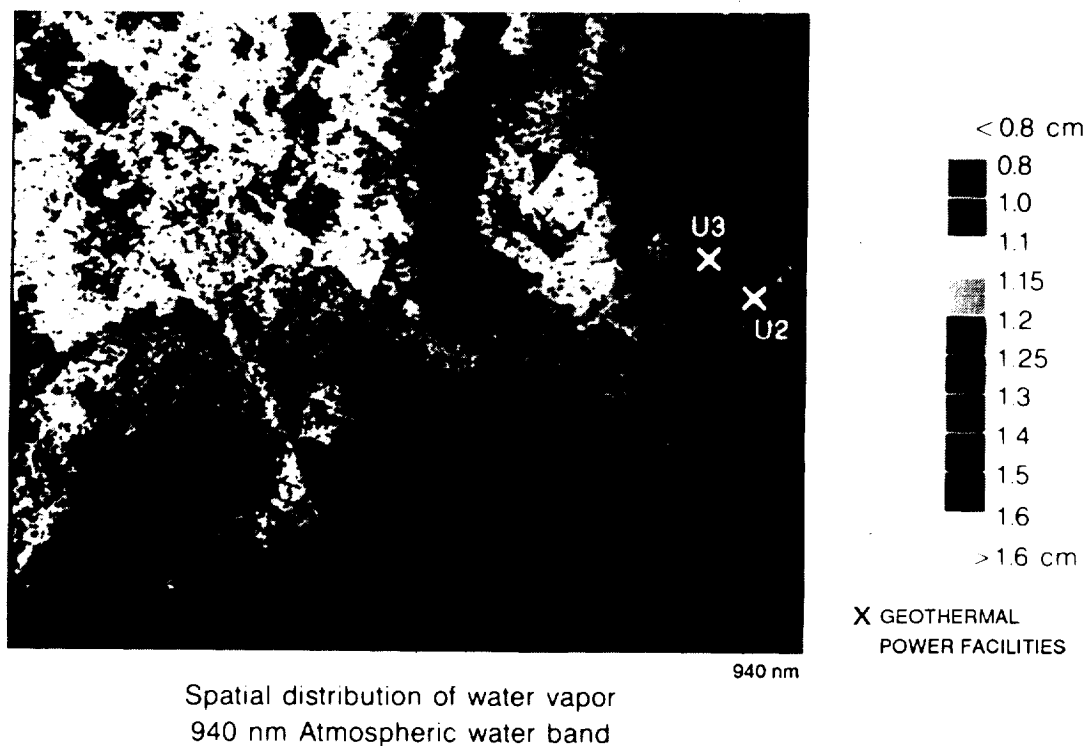


Figure 10. Spatial distribution of atmospheric water vapor (column abundance) derived by the CIBR algorithm for the 940- and 1130-nm water bands. The median filter replaces image DN at a pixel P by the most frequent DN value in the 3x3 array with center at P.

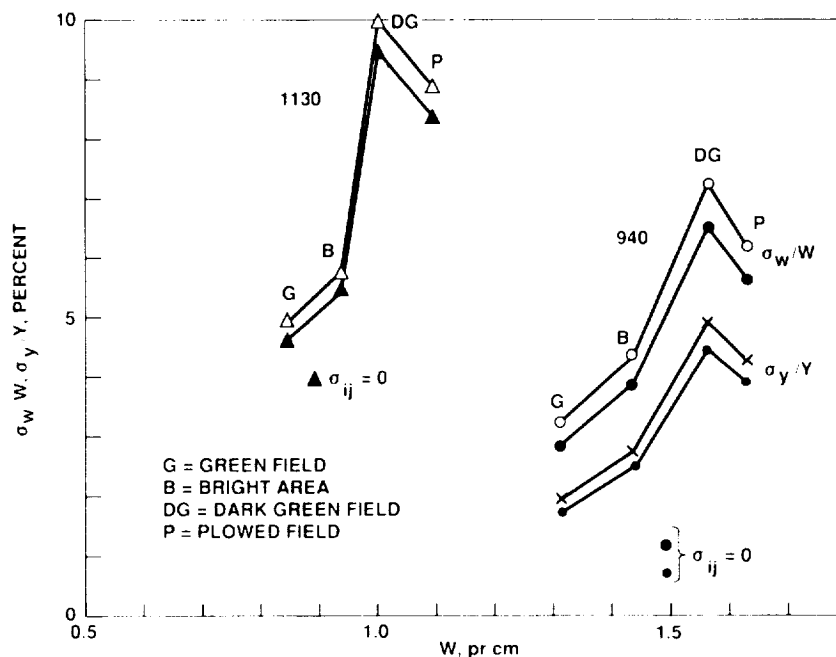


Figure 11. Fractional error in the recovered water abundance for 940- and 1130-nm bands using the CIBR algorithm over selected surface targets. Variances and covariances estimated from radiance data over a 2500-pixel area of Salton Sea northwest of the 12:05 PDT segment of the NW-SE flight line.

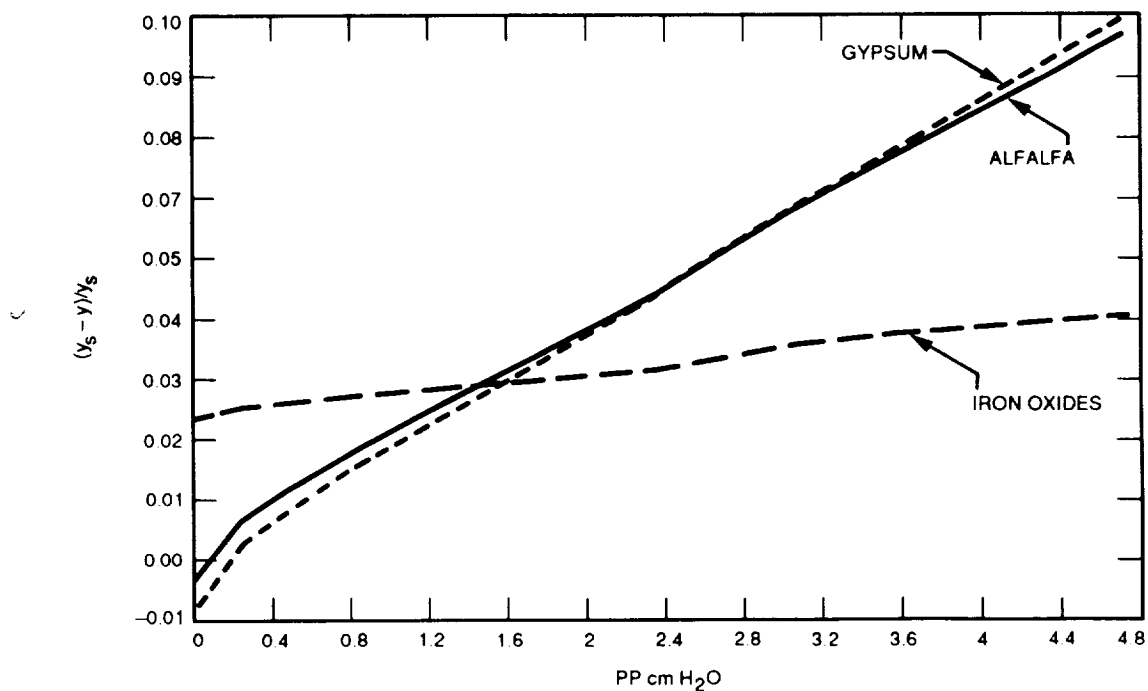


Figure 12. Normalized differences between the standard CIBR derived with constant surface reflectance of 0.25 and CIBR derived with surface reflectances of alfalfa, and iron-oxide- and gypsum-rich soils, calculated as a function of path precipitable water.

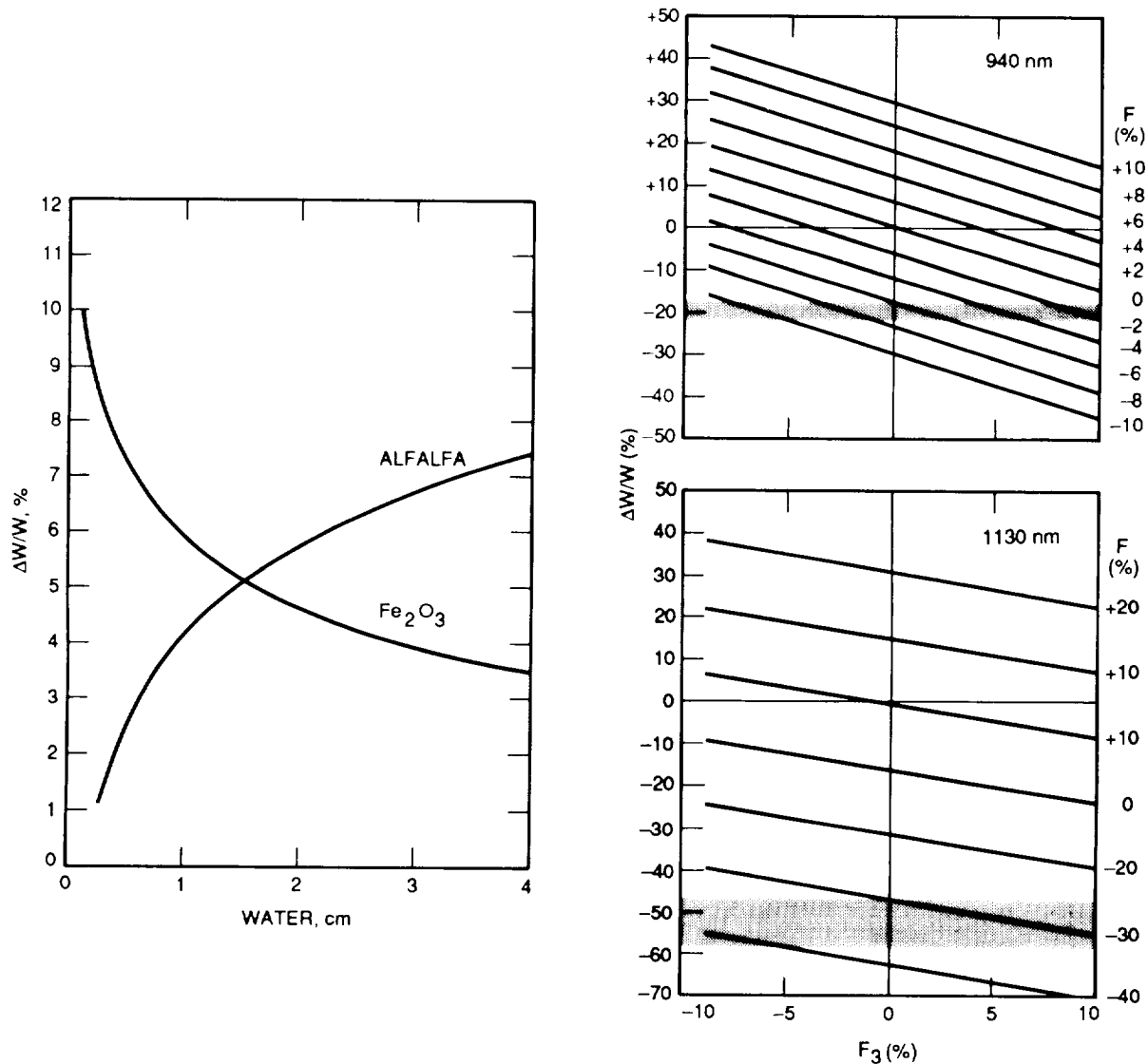


Figure 13. Fractional (systematic) error in percent of water retrieved using the standard CIBR calibration curve for background reflectance of iron- oxide-rich soil and alfalfa.

Figure 14. Fractional (systematic) uncertainty in recovered water vapor abundances for 940- and 1130-nm bands introduced by changes in radiometric calibration of AVIRIS during flight. Water abundance assumed is 1.54 g/cm^2 . The variable δL_{12} is equal to $\delta L_1 + \delta L_2$, the combined (algebraic) change in the radiances L_1 and L_2 . The horizontal axis F_3 is the percent change in the radiance L_3 . The horizontal (shaded) areas depict regions where combinations of radiance changes for L_1 , L_2 , and L_3 may lie to produce observed discrepancies between ground radiometer-based and AVIRIS-based water retrievals.

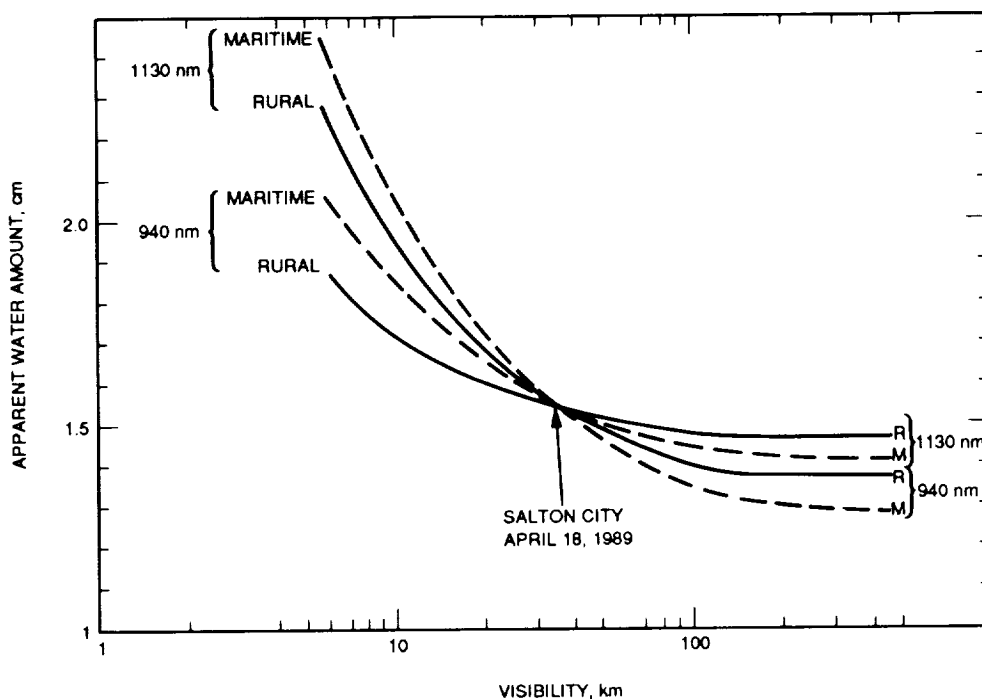


Figure 15. Dependence of apparent retrieved water vapor (column) abundance upon atmospheric visibility, calculated according to LOWTRAN 7 with a rural aerosol model.

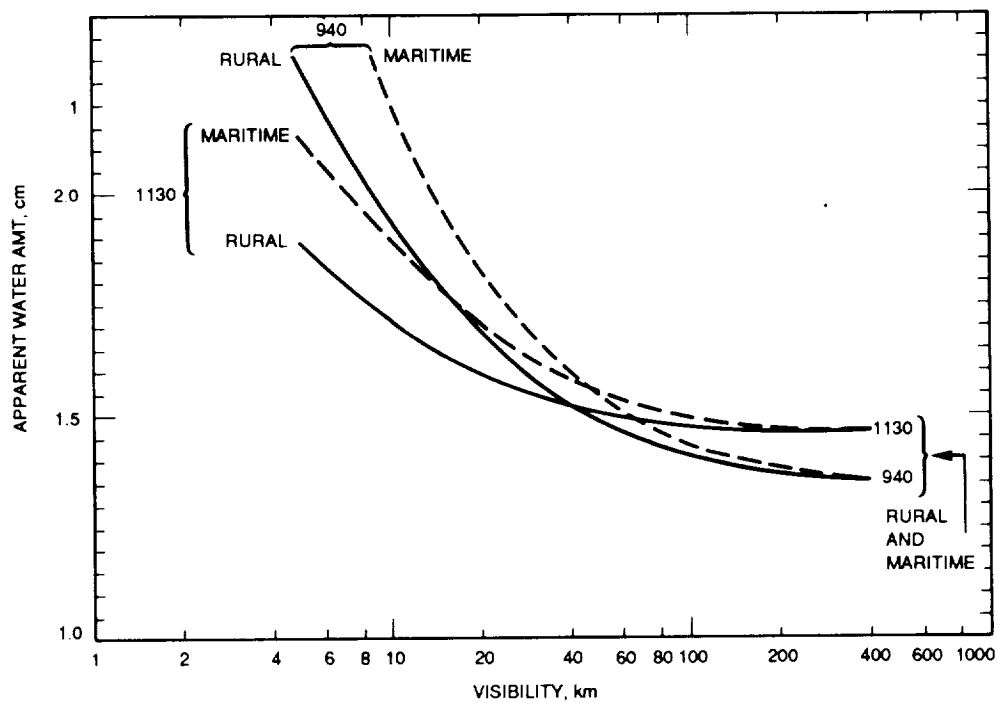


Figure 16. Dependence of apparent retrieved water vapor (column) abundance upon atmospheric visibility and the aerosol model employed, calculated according to LOWTRAN 7. Curves labeled "marine" represent apparent abundances derived from a marine aerosol model but retaining the rural aerosol-based calibration curve.

ANALYSIS OF ATMOSPHERIC WATER VAPOR MAPS FROM AVIRIS AT SALTON
SEA, CALIFORNIA: PART II, SURFACE MOISTURE FLUX, BOUNDARY
CONDITIONS, AND PLUME MEASUREMENTS

James E. Conel and Veronique Carrere

Jet Propulsion Laboratory
California Institute of Technology
Pasadena, California

ABSTRACT

Several applications of AVIRIS water vapor imagery to problems of land surface evaporation, velocity determinations in the atmospheric water vapor boundary layer, and studies of fetch requirements and boundary conditions on turbulent diffusion models are described in a preliminary way, using elementary results from atmospheric diffusion theory. A search for water vapor plumes from a geothermal power plant cooling tower is reported, together with calculations on plume dimensions expected for the atmospheric stability conditions and source strength.

INTRODUCTION

Part I of this study reported progress on application of the continuum integrated band ratio (CIBR) method to mapping of atmospheric water vapor over the Salton Sea test site. The experimental goals were described, and random and systematic errors that lead to uncertainties in the water determinations and discrepancies between amounts retrieved using different bands were enumerated. The importance of atmospheric scattering was emphasized, both from the standpoint of dependence of the calibration curves on visibility and upon choice of the scattering model, e.g., rural vs marine aerosol models, both of which among others are resident in the LOWTRAN 7 code. The dependence of retrievals upon departures of the actual surface reflectance from the wavelength-independent value assumed in construction of CIBR calibration curves was also described.

In this paper we describe some applications using elementary results of the theory of atmospheric diffusion of the AVIRIS-derived water maps. In so doing we acknowledge the probable poor accuracy of the water vapor determinations used, and instead exploit the relatively good precision. The problem of land surface evaporation is investigated from the standpoint of the atmospheric water budget method (Brutsaert, 1982). The conservation equation for atmospheric moisture can be arranged, using the divergence theorem of Gauss, to provide surface flux over a region in terms of the moisture advected normally across the enclosing vertical boundaries. This leads to tentative consideration of how to determine horizontal velocity in the water vapor boundary layer using water vapor as a tracer. A second investigation deals with fetch requirements for the observed column abundances and boundary conditions on an atmospheric turbulent diffusion model, using the onshore distribution of moisture as a result of sea-breeze circulation. Finally, we describe a search for the water vapor plume from the cooling tower of a geothermal plant located at the southern end of the Salton Sea. The amount of moisture emitted from this source is known; hence

it may form a useful example for pollution or volcanic source strength evaluation using AVIRIS images.

LAND SURFACE MOISTURE FLUXES AND SURFACE BOUNDARY CONDITIONS

Evaporation from land and water surfaces represents an important component of the hydrologic cycle and constitutes the connection between the surface water budget and the energy budget (Brutsaert, 1982, 1986). Utilization of AVIRIS spectral data allows routine mapping of column abundance distributions. Separation of the total amount thus observed into components from local evaporation or evapotranspiration sources versus components advected into a scene across the vertical boundaries surrounding it is a fundamental problem. In an earlier paper (Conel, et al., 1989) we explored models of the atmospheric moisture distribution arising across abrupt changes in surface conditions, e.g., between wet and dry areas, under steady winds (Sutton's problem, Sutton, 1953; Brutsaert, 1982). Our analyses pointed out characteristics of the spatial variation of the column abundance with respect to the assumed surface boundary condition discontinuity that might lead to identification of the nature of the surface boundary conditions and to estimation of fluxes from the surface.

Here, we explore the feasibility of using AVIRIS data for such investigations. The present discussion amplifies on use of time sequences of AVIRIS images to estimate surface evaporation. We also present an example from data over the western shore at Salton Sea that may represent a plume from the lake developed in response to a steady onshore sea breeze.

A strategy for recovery of surface moisture flux from time sequences of AVIRIS observations. The equation of conservation for atmospheric water vapor (Brutsaert, 1982) can be written, neglecting horizontal gradients of the turbulent fluxes as well as molecular diffusion,

$$\frac{\partial \bar{q}}{\partial t} + \frac{\partial}{\partial x} (\bar{u}q) + \frac{\partial}{\partial y} (\bar{v}q) + \frac{\partial}{\partial z} (\bar{w}q) = - \frac{\partial}{\partial z} (\bar{w}'q') + S_v \quad (1)$$

where \bar{q} is the specific humidity, \bar{u}, \bar{v} , and \bar{w} are mean velocities in directions x , y , and z (x , y , horizontal, and z vertical), w' is the turbulent velocity fluctuation in the z -direction, \bar{q}' is the turbulent fluctuation of specific humidity, and S_v is a source term representing the difference between vaporization and condensation at a point in grams of water per gram of moist air per unit time. AVIRIS observations provide estimates of the column abundance W of precipitable water, e.g.,

$$W = \int_0^{\infty} \bar{q} \rho dz \quad (2)$$

where ρ is the density of moist air, taken to be the mean standard value in the boundary layer. The integral extends from the surface to the top of the atmosphere, which we assume to be 20 km, the flight altitude of AVIRIS.

Integrating Equation 2 over z in this fashion, with $\bar{w}q$ equal to zero at the surface and top of the atmosphere and $\bar{w}'q'$ also zero at the top, gives

$$\frac{\partial W}{\partial t} + \nabla \cdot \int_0^\infty (U\bar{q})\rho dz = E - P \quad (3)$$

where $U = i\bar{u} + j\bar{v}$ and i and j are unit vectors in the x and y directions, respectively. In addition, $E = \rho\bar{w}'\bar{q}'$ is the evaporation flux at the surface and $P = -\int_0^\infty S_v\rho dz$ is the loss of moisture from condensation throughout the column. Forming areal averages over a scene by multiplying both sides of Equation 3 by dA/A and integrating gives

$$\frac{\partial \bar{W}}{\partial t} + \frac{1}{A} \int_0^\infty \int_S (\bar{q}U_n)\rho dS dz = \bar{E} - \bar{P} \quad (4)$$

where use has also been made of the divergence theorem to convert the volume integral of Equation 3 to a surface integral in Equation 4 extending over vertical boundaries of the volume enclosing the scene. In Equation 4, \bar{W} , \bar{E} , and \bar{P} denote spatial average values and U_n is the component of the wind normal to S , positive outward. Assuming winds $\bar{u}(z)$ parallel to the x axis blowing in the $+x$ direction, and averages over a strip $0 \leq x \leq L$ and unit width in the y direction, Equation 4 written out becomes

$$\frac{\partial \bar{W}}{\partial t} + \frac{1}{L} \left[- \int_0^\infty \bar{u}\bar{q}\rho dz \Big|_{x=0} + \int_0^\infty \bar{u}\bar{q}\rho dz \Big|_{x=L} \right] = \bar{E} - \bar{P} \quad (5)$$

In Equations 3, 4, and 5, the long-term time averages $\langle \partial W / \partial t \rangle$ and $\langle \partial \bar{W} / \partial t \rangle$ are much smaller than the other terms so averaged, and are therefore negligible (Peixoto and Oort, 1983; Kinter and Shukla, 1990). This mathematical simplification, however, does not appear to have associated practical consequences, since accumulation of the requisite AVIRIS data sets is not feasible. For example, we examined a series of 484 column precipitable water abundances (W), derived from rawinsonde observations at Edwards AFB, California for the period March 1988 through April 1989, and found a roughly cyclic variation throughout the period. An accumulation of several years of such observations would appear to be required to estimate the long-term mean and variance with any assurance. Further analysis of this problem is under way.

The further evaluation of Equation 5 leading to a determination of \bar{E} for the scene (assuming precipitation \bar{P} to be zero for the observational period) requires measurement of \bar{u} and \bar{q} with altitude along the boundaries, together with $\partial \bar{W} / \partial t$.

Aircraft measurements of moisture flux rely on limited stacks of flight lines over some boundaries, together with measurements with onboard sensors of vertical velocity and humidity fluctuations averaged over the flight paths (e.g., Betts, *et al.*, 1990; Desjardins, *et al.*, 1989). Restricted sample time and sampling length through the air impose limitations on accuracy of such flux retrievals (Lenschow and Stankov, 1986). The duration of sampling flights over Kansas during the FIFE project was on the order of two hours (Betts, *et al.*, 1990). Such aircraft measurements have led to underestimates of the sensible and latent heat fluxes at the surface compared to values from surface stations (Betts, *et al.*, 1990).

With AVIRIS, large areal sampling (swath width = 11 km) of column abundance occurs rapidly (e.g., 1/12 second per line, representing a strip 20 m in width on the ground perpendicular to the flight direction). But direct observations of wind speed and specific humidity with altitude are not available. Rather, it appears necessary to proceed indirectly by first seeking to recover average wind speed from changes in moisture patterns in time sequences of observations. Such time sequences are feasible in practice with AVIRIS at intervals of about 15 minutes.

The mean wind speed $d\bar{X}/dt$ (Pasquill and Smith, 1983, sec 3.3; also called the local convective velocity by Csanady (1973)) is given by

$$\frac{d\bar{X}}{dt} = \frac{1}{W} \int_0^\infty \bar{u}\bar{q}\rho dz \quad (6)$$

so that the integral $\int_0^\infty \bar{u}\bar{q}\rho dz$ could be estimated at a point if a value of $d\bar{X}/dt$ were available. Since \bar{X} represents the mean horizontal displacement of an ensemble of moisture "particles," it might be feasible to map changes in mean position of features in W with time, thereby employing the water vapor column abundance fluctuations as a wind tracer. An alternative and probably superior strategy would be to examine the cross correlations between time sequences of moisture profiles to determine the lag for maximum correlation between features present as a measure of displacement over the time interval between measurements. This is the method employed by Eloranta, et al. (1975) to determine wind speed in the boundary layer, using lidar, to observe drift of features in the aerosol backscatter.

Evaluation of $d\bar{X}/dt$ for power law profiles of $\bar{u}(z)$ and $K(z)$ and steady-state conditions. To get an idea of the magnitude of $d\bar{X}/dt$ and its relation to specific vertical wind $u(z)$ and eddy diffusivity $K(z)$ profiles, we work out Equation 6 for the steady-state case of evaporation from a uniformly moist surface of width L with specific humidity $\bar{q}(0)$ (at $z = 0$) = \bar{q}_0 in $0 \leq x \leq L$, surrounded by dry land areas with $q(0) = 0$, $x < 0$, and $x > L$. The wind speed and eddy diffusivity are $\bar{u}(z) = az^m$, $K(z) = bz^n$. The solution for \bar{q} in $0 < x < L$, $z > 0$ (Brutsaert, 1982, ch. 7) is

$$\bar{q}(v, \xi) = \bar{q}_0 [1 - P(v, \xi)] \quad (7)$$

where $P(v, \xi)$ is the incomplete gamma function, $v = (1 - n)/(2 + m - n)$, and

$$\xi = \frac{a}{b(2 + m - n)^2} \frac{z^{2 + m - n}}{x} \quad (8)$$

The integrals for W from Equation 2 and the product of $\bar{u}\bar{q}$ over z in Equation 6 can be evaluated (Abramowitz and Stegun, 1964) to give

$$\frac{d\bar{X}}{dt} = a \left[\left(\frac{b}{a} \right) (2 + m - n)^2 x \right]^v \left[(m + 1) \Gamma \left(\frac{2 - n}{2 + m - n} \right) \right]^{-1} \quad (9)$$

where $\Gamma(c)$ is the gamma function. Adopting the values of $m = 1/7$ and $n = 1 - m$, (e.g., Brutsaert, 1982, ch. 4) gives $d\bar{X}/dt = 0.86a(b/a)^{1/9}x^{1/9}$. Thus the apparent average speed increases with x (although weakly), even though $\bar{u}(z)$ is independent of horizontal distance. The $x^{1/9}$ dependence of $d\bar{X}/dt$ arises as a consequence of the continuity condition (Equation 8). The total

evaporative moisture crossing $x = \eta$ from advection is equal to $\int_0^\eta E(x)dx$, which is proportional to $\eta^{8/9}$. The column abundance W is proportional to $\eta^{7/9}$.

The constants a and b in Equation 14 are given by

$$a = \bar{u}_1/z_1^m \quad \text{and} \quad b \cong u_*^2/(ma) \quad (10)$$

(Brutsaert, 1982, ch. 4 and p. 160). In Equation 10, \bar{u}_1 is the mean wind speed at height z_1 above the surface, and u_* is the friction velocity, a quantity that depends upon surface roughness. Typical values for u_* range from 0.16 m/s for a smooth surface such as mud or ice to 0.63 m/s for long grass (Sutton, 1953, p. 233). Adopting $u_* = 0.3$ m/s and $\bar{u}_1 = 2$ m/s at a height of 2 m gives $d\bar{X}/dt = 1.87x^{1/9}$, where x is in meters. For example at $x = 10^4$ m, the apparent speed is 5.2 m/s as compared to an apparent speed of 1.9 m/s at $x = 1$ m.

If the wind speed and eddy diffusivity are constant with altitude, i.e., m and n equal to zero in Equation 9, $d\bar{X}/dt = a$, the assumed value of \bar{u} .

The quantity $d\bar{X}/dt$ calculated in this example cannot ordinarily be observed. The moisture distribution is steady, and no features within it move relative to the surface. Evaluation of the average speed under such conditions would require actual measurements of $\bar{u}(z)$, $K(z)$, and W . Under ordinary conditions, however, water vapor distributions can be expected to contain irregularities. An important question relates to the expected lifetime under atmospheric diffusion processes of any given irregularity, compared to the minimum observation time interval achievable with AVIRIS (about 10 minutes).

Time scale for dispersion of irregularities in the water distribution compared to minimum interval of atmospheric observations with AVIRIS. To estimate the time scale for dispersion of irregularities in the moisture distribution as observed by AVIRIS, we have used a simple puff diffusion model, the formulas for which are readily available (Seinfeld, 1986; Hanna, et al., 1982). A puff is thought of as an instantaneous release at a point, whereas any real irregularity, however it might have been generated, would presumably evolve over a finite period of time and with finite spatial dimensions. On this basis more realistic models could be evolved by evaluating the Lagrangian equation for the mean concentration (Seinfeld, 1986, p. 561), taking account of both finite source size and finite emission time; but for the present it seems adequate to provide estimates from the simpler instantaneous point-source model. The Gaussian puff formula, including total reflection of water vapor at the surface (i.e., no losses there) for a source at the point $x = y = 0$ at time $t = 0$ and integrated out over vertical distance z to correspond to the column abundance, can be derived from a formula given by Seinfeld (1986, p 570) by application of Equation 2 to give

$$W_{\text{puff}}(x,y) = \frac{S}{2\pi\sigma_x\sigma_y} \exp\left[-\frac{(x - \bar{u}t)^2}{2\sigma_x^2} - \frac{y^2}{2\sigma_y^2}\right] \quad (11)$$

where S is the source strength in grams. If the pixel size of AVIRIS is of length and width l , then the abundance over a pixel at the origin is

$$\bar{w}_{\text{puff}} = S \operatorname{erf}\left(\frac{l}{2\sqrt{(2)\sigma_y}}\right) \operatorname{erf}\left(\frac{l/2 - \bar{u}t}{2\sqrt{(2)\sigma_x}}\right) \quad (12)$$

For σ_x and σ_y ($= \sigma$), we use estimates obtained from fits of the graphical data given by Hanna, *et al.* (1982, p. 43), which yield $\sigma \approx 0.1t$, where σ is in m and t in s. Using these values, a pixel size of 20 m and an AVIRIS observation repeat time of 15 minutes yields the relative degradation in the y direction to be proportional to $\operatorname{erf}(0.094)$, or about 10% of the original puff strength. After one-half hour the relative strength is reduced to $\operatorname{erf}(0.047)$, or about 5% of the original value. Changes in the x direction could be similarly evaluated by translating the integration area with the maximum in the distribution, which is found at $x = \bar{u}t$ at any time t . The possible recurrence observation time for the relative decay of fluctuations at the 10% level is thus about equivalent to the feasible recurrence observation time interval with AVIRIS.

FETCH REQUIREMENTS AND BOUNDARY CONDITIONS

Nature of the analysis. We analyzed a segment of the northeast-southwest AVIRIS flight line over the western shore (Figure 1/Slide 12) to look for characteristic changes in atmospheric moisture distribution inland that might be identified with specific forms of the surface boundary conditions on the atmospheric turbulent diffusion problem. In this section we examine the constant-surface-humidity source model for Salton Sea and the zero-surface-humidity condition for the onshore region. Are the observed moisture abundances consistent with dimensions of the source region, and is the pattern of moisture variation onshore consistent with other physical circumstances of the problem, e.g., the implied moisture flux at the surface for maintenance of a zero surface concentration there? A difficulty with these preliminary calculations is that no satisfactory estimate of background moisture abundance is available. Therefore the amounts of water we are seeking to generate by the fetch, temperature, and wind conditions, or dispose of by the boundary conditions, or lose by topographic variation, are too great. The present calculations therefore represent extremes of variation that would probably be reduced once the background is properly assessed.

Water distribution images for the western shore segment. The atmospheric precipitable water distribution observed for the western shore segment of the NE-SW AVIRIS line at Salton Sea (see Figure 2 of paper I for location of the western shore segment), and computed using the 940-nm water band, is given in Figure 1b. It is compared there with a three-color composite image of the area, with the band color designations red = 651 nm, green = 552 nm, blue = 454 nm, as indicated in Figure 1a. The water distribution image shows a residual herringbone pattern of coherent noise, but depicts a well defined falloff in water abundance traversing inland left to right, parallel to the onshore wind direction (compare with Figure 5, paper I). The onshore profile of column moisture variation between points A and B in Figure 1b is shown in Figure 2.

Atmospheric moisture distribution for constant-specific-humidity boundary conditions. Analytically simple conditions are constant-specific humidity (m, n non zero) or constant moisture flux ($m, n = 0$). Conel *et al.* (1989) worked out expressions for column abundance changes across discontinuities in surface conditions involving wet and dry surfaces for both types of boundary conditions, assuming constant wind speed and diffusivity ($m = n = 0$) and no change in roughness between regions. Here we confine attention to the surface humidity boundary condition. Specifically, for the boundary value problem leading to Equation 7, the specific humidity \bar{q} is

$$\bar{q}(v, \xi, \xi_1) = \bar{q}_0 [P(v, \xi_1) - P(v, \xi)] \quad (x > L) \quad (13)$$

with ξ given by Equation 8 and ξ_1 by Equation 8 with x replaced by $x - L$. The corresponding column abundance W is obtained from Equation 2:

$$W(x, m, n) = \rho \bar{q}_0 \frac{\Gamma\left(\frac{2-n}{2+m-n}\right)}{\Gamma\left(\frac{1-n}{2+m-n}\right)} \left[\left(\frac{b}{a}\right) (2+m-n)^2\right]^{1/(2+m-n)} \left[x^{1/(2+m-n)} - (x-L)^{1/(2+m-n)}\right] \quad (x > L) \quad (14)$$

$$W(x, 0, 0) = \rho \bar{q}_0 \frac{2}{\sqrt{\pi}} \left(\frac{b}{a}\right)^{1/2} \left[x^{1/2} - (x-L)^{1/2}\right] \quad (x > L) \quad (15)$$

and

$$W(x, 1/7, 6/7) = \rho \bar{q}_0 \frac{\Gamma(8/9)}{\Gamma(1/9)} \left(\frac{9}{7}\right)^{14/9} \left(\frac{b}{a}\right)^{7/9} \left[x^{7/9} - (x-L)^{7/9}\right] \quad (x > L) \quad (16)$$

Fetch requirement for on-shore column abundance on the constant-surface-humidity model. Are the AVIRIS-derived column abundances for the western shore segment consistent with origin of the column moisture as evaporation and transport via horizontal advection from Salton Sea under the constant-surface-humidity model? The total column abundance $W(L, m, n)$ at the shoreline $x = L$ in Equation 13 provides an estimate of the fetch L over Salton Sea required to generate the observed total moisture present in the column at the shore. From this expression, using the notation $L(m, n)$ to designate the fetch for given indices m and n ,

$$L(0, 0) = \frac{\pi}{4} \left(\frac{a}{b}\right) \left(\frac{W(L, 0, 0)^2}{\rho^2 \bar{q}_0^2}\right) \quad (17)$$

and

$$L(1/7, 6/7) = \left(\frac{7}{9}\right)^2 \left(\frac{a}{b}\right) \left[\frac{W(L, 1/7, 6/7) \Gamma(1/9)}{\rho \bar{q}_0 \Gamma(8/9)}\right]^{9/7} \quad (18)$$

Using Equation 10, and adopting values of $a = 200$ cm/s, $z_1 = 200$ cm, $b_0 = 10^5$ cm²/s (see Seinfeld, 1986, p. 598) and $u_* = 30$ cm/s, $\rho = 1.18 \times 10^{-3}$ g/cm³ for the density of dry air at a temperature of 300K and $\bar{q}_0 = 2.16 \times 10^{-2}$ g water/g air for the saturation concentration at that temperature, gives $L(0, 0) = 65$ km and $L(1/7, 6/7) = 180$ km ($\Gamma(1/9) = 8.523$, $\Gamma(8/9) = 1.078$).

Conversely, if $L = 10$ km, with these same values, $W(L,0,0) = 0.64$ g/cm² and $W(L,1/7,6/7) = 0.172$ g/cm².

The fetches implied for the observed shoreline column abundances on these models are thus much greater than the actual dimensions of Salton Sea in the direction of the surface winds. The discrepancies may be greater when the actual wind field generated by the lake is accounted for. For example, a theoretical study of lake and land breezes generated by diurnal heating over small (circular) lakes (Neumann and Mahrer, 1975) shows the lake breezes to be strongly divergent horizontally and zero in speed at the center. Thus, in addition to violation of the constant-with-x horizontal wind speed assumption, the available fetch is only one-half the actual width of the water body. The total onshore column abundance observed at $x = L$ in the profile may therefore be comprised of a component of water surface origin that is advected by the breeze, and a resident background component that is inherited from other sources. It may be thought possible to estimate such a background component by identifying it with the moisture amount in equilibrium with the lake under zero wind conditions. However, from Equations 10 and 14, $W(x,m,n)$ is undefined with $a = 0$ in the simple diffusion model employed here.

Estimation of column abundance variation due to topography. The moisture profile given in Figure 2 contains some variation from decrease of moisture with elevation. The elevation difference is about 70 m over the 11.6-km length of the profile. The actual variation of water vapor concentration with height at the western shore site is not known. We estimated the expected falloff for the 70-m rise from the water vapor distribution resident in the LOWTRAN 7 default midlatitude summer atmospheric model. The vertical water vapor concentration $\bar{c}(z)$ (in g cm⁻² km⁻¹) over the first 10 km, which contains nearly all of the moisture present in the model, can be represented accurately by two exponential distributions of the form $\bar{c}_j(z) = A_j \exp(-\beta_j z)$, $j = 1, 2$, where $j = 1$ applies over $0 < z < 2$ km, and $j = 2$ over $2 < z < 10$ km. From the model, $A_1 = 1.372$, and $A_2 = 1.772$, and $\beta_1 = 0.54$, and $\beta_2 = 0.68$. The A_j factor can be eliminated by expressing $\bar{W}(z)$, the vertically integrated water vapor above any altitude z in terms of W_A , the observed shoreline column abundance, and by assuming continuity in the distribution at $z = 2$ km. The expression for $W(z)$ between $0 < z < 2$ km scaled in this way is

$$W(z) = W_A \left[\int_z^2 \bar{c}_1(\zeta) d\zeta + \exp(-\beta_1 \cdot 2) \int_2^{10} \bar{c}_2(\zeta) d\zeta \right] \times \left[\int_0^2 \bar{c}_1(\zeta) d\zeta + \exp(-\beta_1 \cdot 2) \int_2^{10} \bar{c}_2(\zeta) d\zeta \right]^{-1} \quad (19)$$

The observed distribution, together with the expected variation from the topographic rise calculated according to Equation 19, and the difference, or anomalous water variation, are plotted in Figure 3. The observed distribution plotted here represents a smoothed (average) version of that given in full in Figure 2.

Comparison of residual or anomalous profile with profiles expected from atmospheric diffusion models with concentration boundary conditions. The expected variation of atmospheric moisture along the inland traverse in Figure 2, according to the diffusion model with constant concentration

boundary conditions, was calculated according to the formula

$$W'(L, x', m, n) = \frac{W'(0, m, n)}{L^{1/(2+m-n)}} \left[(x' + L)^{1/(2+m-n)} - (x')^{1/(2+m-n)} \right] \quad (20)$$

($x' > L$)

where the obvious transformation $x' = x - L$ has been used. The fetch L is defined by equations 17 and 18 in terms of the observed precipitable water at $x' = 0$, the upstream ($x < L$) values of ρ and \bar{q}_0 , and adopted constants a and b (or b_0). Equation 20 is compared in Figure 4 with the anomalous distribution, i.e., that distribution obtained after correction for topography according to the LOWTRAN model.

Surface flux implied by onshore falloff in moisture on the constant-surface-humidity model. An instructive test of the zero surface-specific humidity condition is provided by the implied flux of moisture into the surface required by the falloff in anomalous atmospheric moisture abundance inland. The flux f_0 of moisture at the surface for $x > L$ is

$$f_0 = -K(z) \frac{\partial \bar{q}_0}{\partial z} \Big|_{z=0} = - \frac{b \bar{q}_0 \rho}{\Gamma(v)} \left[\left(\frac{a}{b} \right) \frac{1}{(2+m-n)^2} \right]^v \quad (21)$$

$$\times \left[\left(\frac{1}{x-L} \right)^v - \left(\frac{1}{x} \right)^v \right] (2+m-n)$$

where L is given by Equation 17 or 18 in terms of the measured column abundance at $x = L$ and the adopted values of ρ and \bar{q}_0 over $0 < x < L$. Surface fluxes for the two models $m = n = 0$ and $m = 1/7$, $n = 6/7$ are plotted in Figure 5. Maintenance of the condition $\bar{q}_0(x, 0) = 0$ requires the continuous absorption of large amounts of water by the surface, which would seemingly, sooner or later, be manifested as surface runoff. These conditions were not observed at the surface near the shore, nor elsewhere inland. Thus the observed column abundance variation depicted in Figures 1 and 2 cannot reasonably arise as a simple manifestation of the concentration boundary conditions assumed in the diffusion model.

Vertical distribution of moisture implied by column abundance variation over topography in a laterally homogeneous atmosphere. An alternative interpretation of the moisture profile variation given in Figure 2 is that the changes result dominantly from the topographic variation and therefore in some sense reflect the actual variation of atmospheric moisture vertically at the time of observation. For a laterally homogeneous atmosphere (i.e., $\bar{q}(x, z) = \bar{q}_h(z)$) without influence of advection or eddy diffusion, the column abundance $W(x)$ above any surface elevation $z_s = z_s(x)$ with $z_s = 0$ as local Salton Sea level, is

$$W(x) = \int_{z_s(x)}^{\infty} \rho \bar{q}_h(\zeta) d\zeta \quad (22)$$

Thus $dW(x)/dx = -\rho \bar{q}_h(z_s)(dz_s/dx)$, and the slope of the column abundance variation yields $\bar{q}_h(z_s)$, provided dz_s/dx is known. Conversely, for zero advection/diffusion conditions, i.e., a horizontally layered atmosphere, extraction of land surface slope based on the slope of the column abundance variation requires knowledge of the local column abundance, the density

being given. The moisture concentration $\bar{c}_h(z) = \rho \bar{q}_h(z)$ in g/cm²km, derived from dW/dx for the onshore profile, is given in Figure 6.

CONSEQUENCES OF A HORIZONTALLY VARYING ADVECTION VELOCITY

Results of the previous two sections show that the observed onshore declining column moisture abundance probably does not arise as a consequence of topographic variation and cannot arise as a consequence of a flux of moisture into the surface implied by zero-specific humidity at $z = 0$. Up to this point nothing has been said about the likely complex distribution of moisture and wind velocity over the sea and inland that would accompany the sea breeze circulation. The sea breeze associated with diurnal heating of "small" lakes (25 to 50 km in radius) and their surroundings has been investigated by Neumann and Mahrer (1974). The actual distribution of moisture in cross section in sea breeze circulation was measured considerably earlier by Craig, et al. (1945). Neumann and Mahrer (1974) calculated that the land breezes are horizontally divergent. As heating progresses, cool air penetrates landward along a front whose position is 10 to 20 km inland from the shoreline. The frontal zone is characterized by convergence of the horizontal wind at low altitude and upward motion on and immediately ahead of the front. Above a near-surface zone approximately 600 meters thick, countercirculation is present with winds blowing lakeward. Such flows and counterflows have been observed in smoke patterns along the shore of Lake Michigan at Chicago (Lyons and Olsson, 1973). The model calculations (Neumann and Mahrer, 1975) also indicate uplift of isotherms ahead of the front and downward indentation behind it that accompany the heating cycle. Similar patterns were expected in the vertical and horizontal distributions of water vapor, which, in fact, appeared in the measurements of atmospheric humidity reported by Craig et al. (1945), cited earlier here.

We want to exploit the simple, nearly constant divergence of the horizontal velocity near shore implied by these model calculations over both sea and land to compute the expected horizontal variation of the column abundance. Steady flow conditions are assumed and confined to the (x,z) plane. The topography is neglected. (See footnote (†) below for a scheme to include topography.) The horizontal velocity is taken independent of z and to vary with x according to

$$\bar{u}(x,z) = \bar{u}_0 + \alpha x \quad (23)$$

where \bar{u}_0 is the value of \bar{u} at $x = x_0$, and α is the divergence of the horizontal velocity. The condition of incompressibility yields for the vertical velocity \bar{w}

$$\bar{w}(x,z) = -\alpha z \quad (24)$$

Integrating Equation 1 vertically using Equation 2, the column abundance $W(x,z)$ obeys

$$(\bar{u}_0 + \alpha x) \frac{dW}{dx} + \alpha W = f_0 \quad (25)$$

This equation has the solution

$$W(x) = \frac{1}{\bar{u}_0 + \alpha x} \left[(\bar{u}_0 + \alpha x) W(x_0) + \int_{x_0}^x f_0(\psi) d\psi \right] \quad (26)$$

where $W(x_0)$ is the value of W at $x = x_0$. (†)

Equation 26 was fitted to the topographically corrected (anomalous) variation of W given in Figure 4 under the assumption $f_0 = 0$, with $x_0 = 10$ km, $\bar{u}_0 = 200$ cm/s and $\alpha = 2.8 \times 10^{-5} \text{ s}^{-1}$. This value of α is consistent with values obtained by Neumann and Mahrer (1974) for small lakes, i.e., 10^{-4} to 10^{-5} s^{-1} .

SEARCH FOR WATER VAPOR PLUMES

A potential application for AVIRIS's capability to provide detailed spatial (and temporal) mapping of the atmosphere is that of inventorying atmospheric constituents. Pollutant assessment and surveying volcanic effluents are two problems of current interest. The identification of plumes in the column abundance distribution would lead immediately to source emission strength by a numerical integration over plume area. We sought to carry out a material balance experiment of this kind for water vapor emission from cooling evaporators and flash towers (Figure 7/Slide 13) at a geothermal power facility located along the southern shore (UNOCAL Salton Sea Unit 3, U3 in Figure 8/Slide 11 of Part I). The total loss of water vapor from such facilities, of which there are six in the area, is monitored hourly. In principle these data, under favorable atmospheric circumstances, can be compared with total abundances derived from the AVIRIS water maps. Before attempting such an assessment, we needed to identify plumes in the AVIRIS water images. To aid this search, simple calculations were made of expected plume dimensions under the known source strength. For simplicity we have assumed in the following that emission is from a point source, although the evaporators and flash tower cover finite dimensions and are physically separated from one another.

The so-called Gaussian plume equation expresses the mean concentration of a species emitted from a continuous, elevated point source. The Gaussian plume formula under the slender plume approximation for mean concentration $\langle c(x,y,z) \rangle$ from a source at height h above the surface, total reflection at the boundary, steady horizontal mean winds $\bar{u} = (\bar{u}, 0, 0)$, and source strength Q (gm sec^{-1}) is (Seinfeld, 1986, Ch 14 and p. 571)

(†) If topographic effects were to be included in the form of a gentle uniform slope, this would introduce a vertical velocity at $z = 0$ given approximately by $\bar{w}_0(x) = \bar{u}(x)(dz_s/dx)$ [see Smith, 1979, p. 96]. With dz_s/dx unequal to zero, Equation 23 is replaced by $\bar{w} = \bar{w}_0(x) - \alpha z$. The right-hand side of Equation 25 is replaced by $f_0(x) + \bar{w}_0 \rho q(x,0)$, with the integral in Equation 26 modified accordingly. To specify $q(x,0)$ we might, as an approximation, assume the condition of zero surface flux over the land, i.e., $f_0 = 0$, $x > L$, in which case $q(x,0) = 2F_0(b/a)^{1/2} [\sqrt{x} - \sqrt{(x-L)}] / (\sqrt{(\pi)\rho b})$ (Conel, et al., 1989), where F_0 is the water vapor flux at the surface over the water body between $0 \leq x \leq L$.

$$\langle c(x,y,z) \rangle = \frac{Q}{2\pi\bar{u}\sigma_y\sigma_z} \exp\left[-\frac{y^2}{2\sigma_y^2}\right] \left[\exp\left[-\frac{(z-h)^2}{2\sigma_z^2}\right] + \exp\left[-\frac{(z+h)^2}{2\sigma_z^2}\right] \right] \quad (27)$$

where $\langle c(x,y,z) \rangle$ is in g/cm^3 . In this equation, σ_y and σ_z are the horizontal and vertical dispersion coefficients (in cm) along the y and z axes. The column abundance W is

$$W(x,y) = \frac{1}{\sqrt{2\pi}} \frac{Q}{\bar{u}\sigma_y} \exp\left[-\frac{y^2}{2\sigma_y^2}\right] \quad (28)$$

and independent of the source height and the vertical dispersion coefficient σ_z . The total evaporation rate for UNOCAL 3 over a 4-hour time period centered around the time of AVIRIS overflight is nearly steady and is given in Figure 9. (These data were generously supplied by UNOCAL, Indio, California). In addition, we took $\sigma_y(x) = \exp[I_y + J_y \ln x + K_y (\ln x)^2]$ (Seinfeld, 1986, p. 576), where the coefficients I_y , J_y , and K_y are determined by stability class, taken to be Pasquill Class A for the extant conditions of bright sun and $\sim 1 \text{ m/s}^{-1}$ wind speed. The distribution $W(x,y)$ is plotted in Figure 10, where the size of one AVIRIS pixel ($20 \times 20 \text{ m}$) is given for comparison. The anomalous water content contributed by the plume, exceeding 0.1 cm in amount, is only about four pixels in length and two in width, even for a source of the magnitude dealt with here (about 75,000 gal/hr). The actual plume dimensions might be expected to exceed this somewhat because of finite source size, but the source magnitude per unit area would correspondingly be reduced. For an AVIRIS detection sensitivity of 0.1 cm, i.e., 10% at 1 pr cm water vapor, the calculated plume area is only a few pixels in size.

Inspection of the column abundance distribution map of Figure 8 discloses no obvious oblong anomaly that might be indentified as the sought-after cloud. This may result from any or all of the following causes: (1) relatively modest detection levels possible from this particular AVIRIS data set, (2) low-speed variable wind conditions, and (3) heavy spatially variable background of water vapor from other multiple sources in the area, including the sea, transpiration from fields, and other power plant emissions. The UNOCAL 3 evaporators apparently contribute to the atmosphere amounts of water comparable to natural sources present in the area. For example, evapotranspiration of 0.65 cm (0.25 in.) of water from agricultural sources (not unreasonable for Imperial Valley conditions) yield about 1.7×10^6 gallons of water vapor per square km. This amount would be supplied to the atmosphere in about 22 hours from the UNOCAL Unit 3 source.

ACKNOWLEDGMENTS

Jack Margolis pointed out the work of Eloranta et al. (1975) and the potential usefulness of their method for measurement of wind speed in the boundary layer using water vapor instead of the aerosol distribution as a tracer. We had many valuable discussions with Carol Bruegge, Rob Green, and Gordon Hoover, all of JPL, and Prof. Fred Share of California State University Long Beach. David G. Newell, Area Production Engineer, UNOCAL Geothermal Division, Indio, California, very kindly supplied the evaporation data for the Salton Sea Unit 3 plant.

This paper presents the results of one phase of research carried out at the Jet Propulsion Laboratory, California Institute of Technology, under a contract with the National Aeronautics and Space Administration.

REFERENCES

Abramowitz, M., and I.A. Stegun, 1964, *Handbook of Mathematical Functions*, National Bureau of Standards Applied Mathematics Series, 55, p. 263.

Betts, A.K., R.L. Desjardins, J.I. MacPherson, and R.D. Kelly, 1990, Boundary-layer heat and moisture budgets from FIFE, *Boundary-Layer Meteorology*, 50, 109-137.

Brutsaert, W., 1982, *Evaporation into the Atmosphere*, D. Reidel Publishing Company, Boston, 299 pp.

Brutsaert, W., 1986, Catchment-scale evaporation and the atmospheric boundary layer, *American Geophysical Union*, Paper No. 5W0661, 39S-45S.

Conel, J.E., R.O. Green, V. Carrere, J.S. Margolis, G.Vane, C. Bruegge, and R.E. Alley, 1989, Spectroscopic measurement of atmospheric water vapor and schemes for determination of evaporation from land and water surfaces using the Airborne Visible/Infrared Imaging Spectrometer (AVIRIS), *IGARSS '89, 12th Canadian Symposium on Remote Sensing*, IEEE #89CH2768-0, 2658-2663.

Craig, R.A., I. Katz, and P.J. Harney, 1945, Sea breeze cross sections from phychrometric measurements, *Bull. Am. Meteor. Soc.*, 26, 405-410.

Csanady, G.T., 1973, *Turbulent diffusion in the environment*, D.Reidel Publishing Co., Dordrecht, 248 pp.

Desjardins, R.L., J.I. MacPherson, P.H. Schuepp, and F. Karanja, 1989, An evaluation of aircraft flux measurements of CO₂, water vapor, and sensible heat, *Boundary-Layer Meteorology*, 47, 55-69.

Eloranta, E.W., J.M. King, and J.A. Weinman, 1975, The determination of wind speed in the boundary layer by monostatic lidar, *J. Appl. Meterol.*, 14, 1485-1489.

Hanna, S.R., G.A. Briggs, and R.P. Hosker, Jr., 1982, *Handbook on Atmospheric Diffusion*, U.S. Department of Energy Document DOE/TIC - 11223, 102 pp.

Kinter, J.L., and J. Shukla, 1990, The global hydrologic and energy cycles: suggestions for studies in the pre-Global Energy and Water Cycle EXperiment (GEWEX), *Bulletin American Meteorological Society*, 71(2), 181-190.

Lenschow, D.H., and B.B. Stankov, 1986, Length scales in the convective boundary layer, *J. Atmos. Sci.*, 43(12), 1198-1209.

Lyons, W.A., and L.E. Olsson, 1973, Detailed mesometeorological studies of air pollution dispersion in the Chicago lake breeze, *Mon. Wea. Rev.*, 101(5), 387-403.

Neumann, J., and Y. Mahrer, 1975, A theoretical study of the lake and land breezes of circular lakes, *Mon. Wea. Rev.*, 103, 474-485.

Pasquill, F., and F.B. Smith, 1983, *Atmospheric Diffusion*, 3rd Ed., Ellis Horwood Limited, Chichester, 436 pp.

Peixoto, J.P., and A.H. Oort, 1983, The atmospheric branch of the hydrological cycle and climate, in *Variations in the Global Water Budget*, (A. Stree-Perrott, M. Beran, and R. Ratcliffe, eds.), D. Reidel Publishing Company, Dordrecht, 5-65.

Seinfeld, J.H., 1986, *Atmospheric physics and chemistry of air pollution*, John Wiley and Sons, New York, 738 pp.

Smith, R.B., 1979, The influence of mountains on the atmosphere, *Advances in Geophysics* (B. Saltzman, Ed.), 21, 87-230.

Sutton, O.G., 1953, *Micrometeorology*, McGraw-Hill Book Company, New York, 334.



(a) Red: 651 nm Green: 552 nm Blue: 454 nm



(b) Spatial distribution of water vapor
940 nm Atmospheric water band

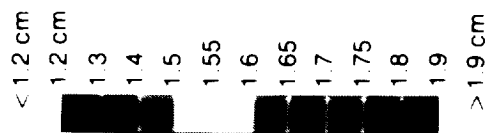


Figure 1. The 10:50 PST segment of AVIRIS data from the NE-SW flight line at Salton Sea, April 18, 1989. Left panel: three-color composite image. Right panel: distribution of water vapor retrieved for the scene using the continuum interpolated band ratio (CIBR) algorithm described in Part I. The points A and B are ends of the water vapor column abundance profile given in Figure 2. The AVIRIS image is approximately 11 km in width.

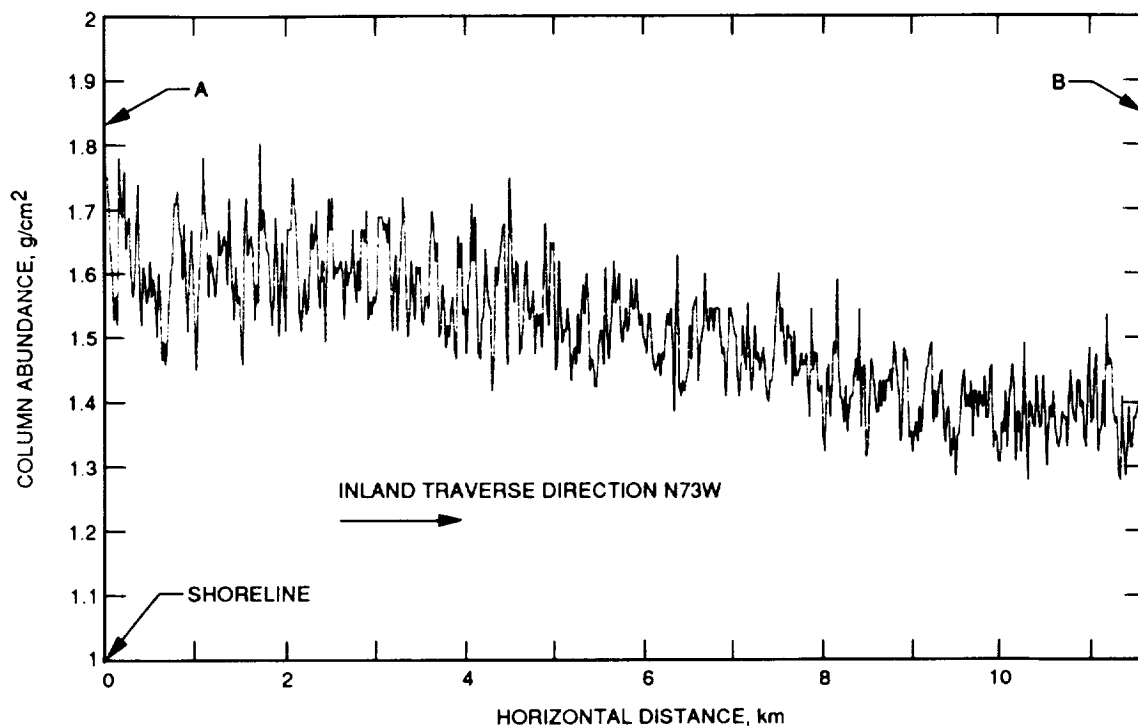


Figure 2. Variation of column moisture abundance along the profile direction AB in Figure 1.

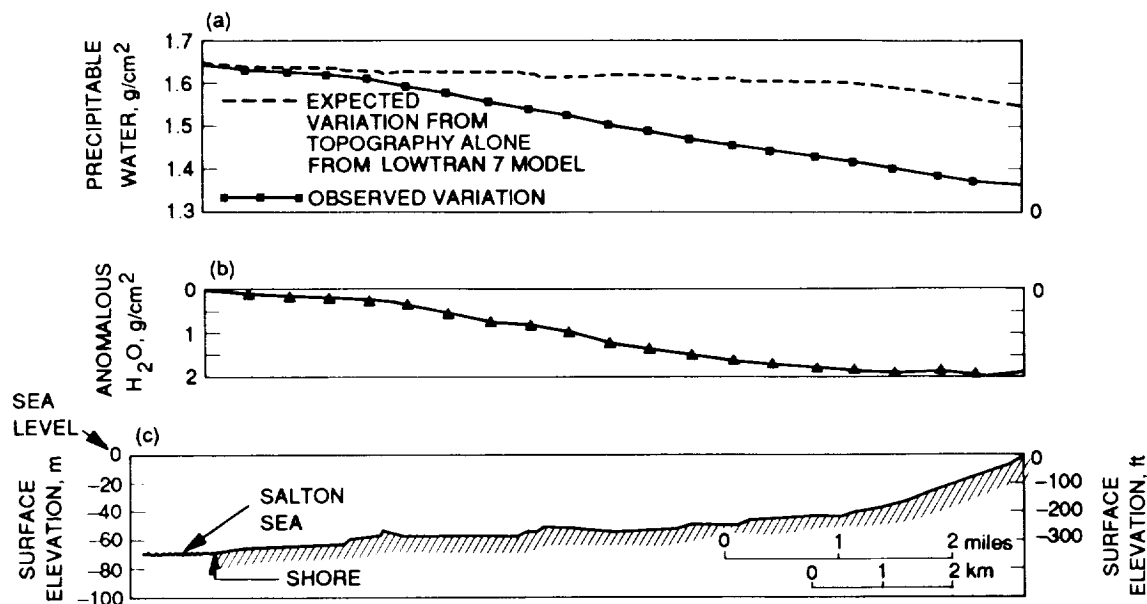


Figure 3. (a) Variation of column moisture abundance along profile AB expected from the vertical moisture concentration in the LOWTRAN 7 mid-latitude summer model together with the observed variation from Figure 2; (b) The *anomalous* column moisture variation obtained as the difference between observed and LOWTRAN 7 distributions; (c) topographic profile along AB.

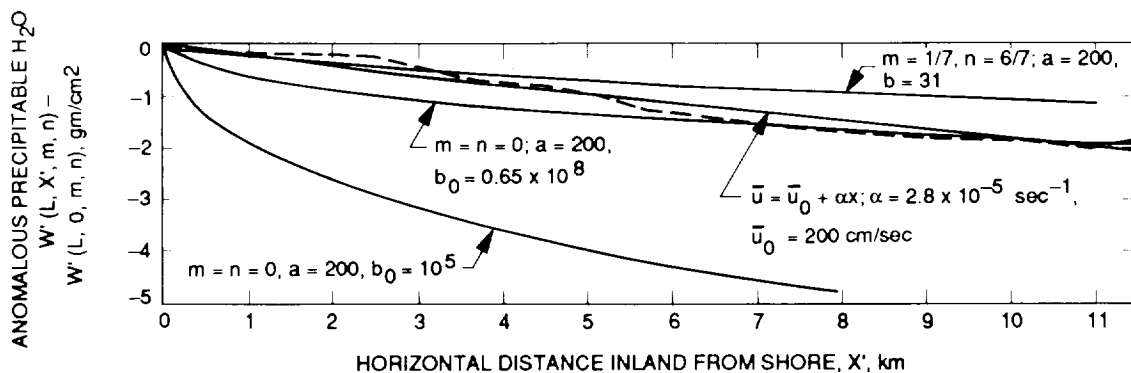


Figure 4. Anomalous moisture profile along AB compared to column abundance variations predicted by an atmospheric diffusion model. The parameters m , n , a , and b describe variation of horizontal velocity and eddy diffusivity with height according to Equation 10.

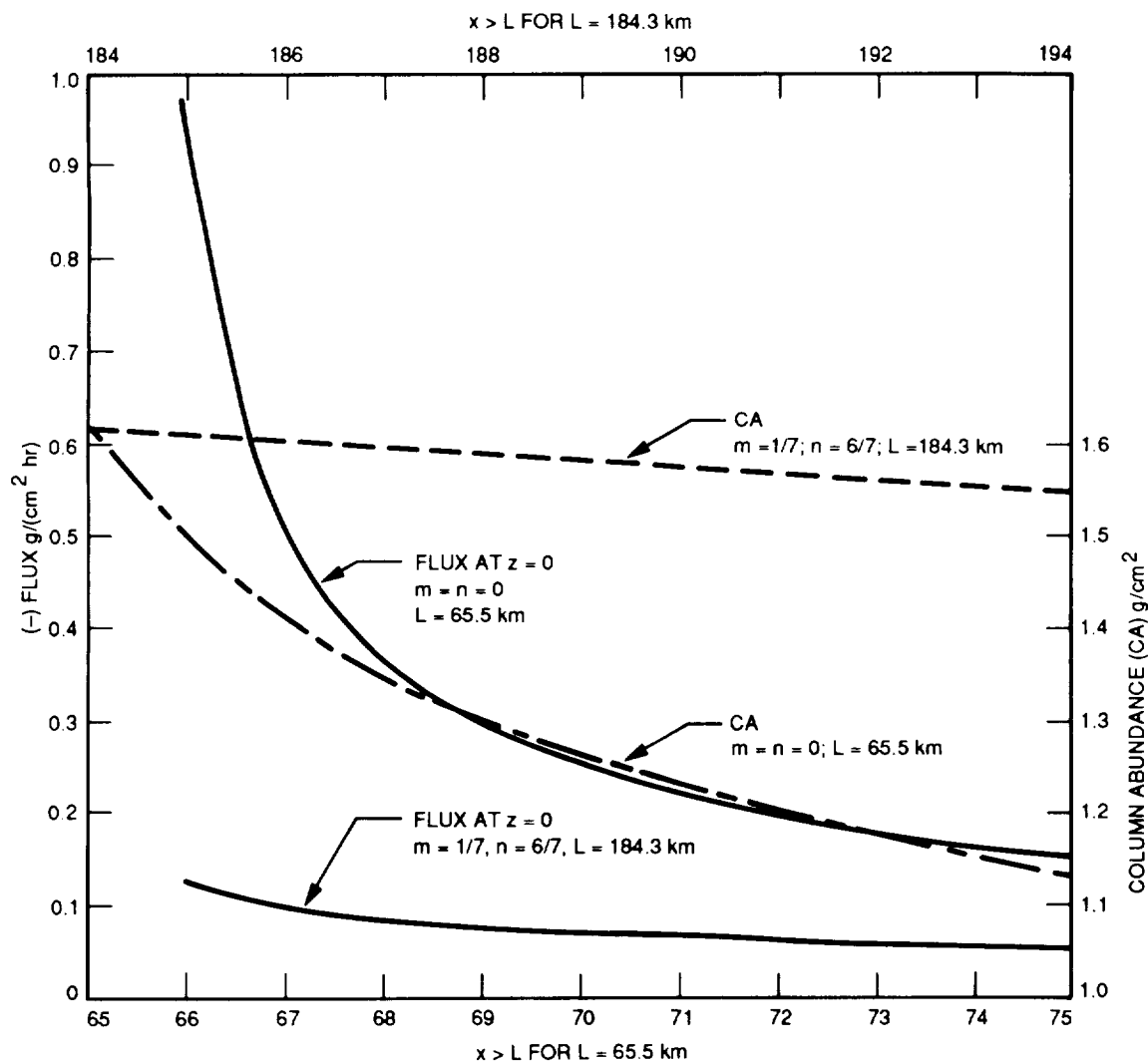


Figure 5. The moisture flux (FLUX) into the surface in $\text{g}/(\text{cm}^2 \text{hr})$ and the column abundance variation (CA) implied by the anomalous moisture variation under the inland zero surface-specific humidity boundary condition.

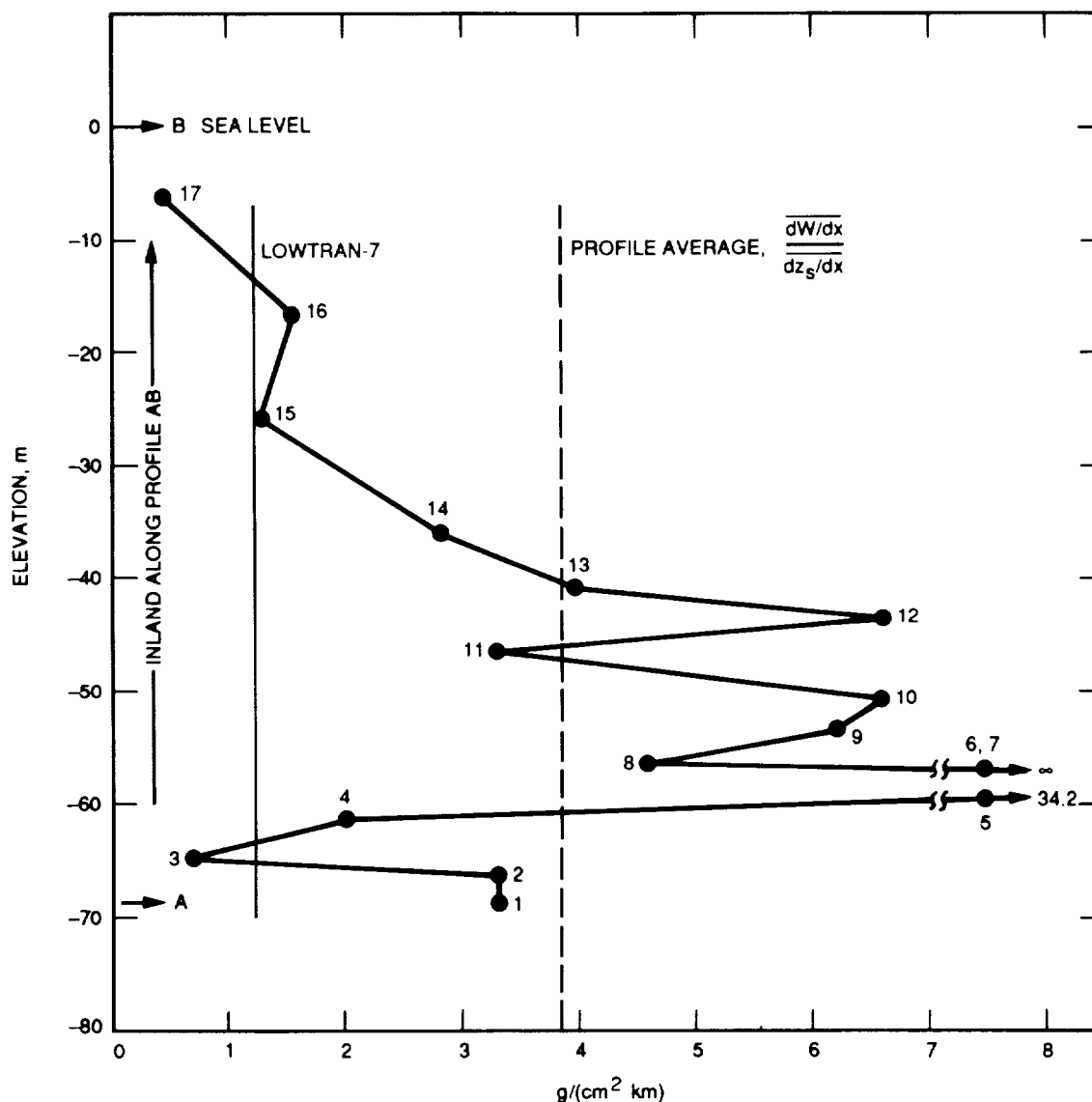


Figure 6. Vertical concentration of water vapor (in $\text{g}/(\text{cm}^2 \text{ km})$) over the western shore site implied by the horizontal gradients of moisture and topography in a horizontally stratified atmospheric model. The LOWTRAN 7 vertical distribution was scaled to give observed shoreline precipitable water. The profile average concentration was calculated by averaging derivatives for points along the profile. Numbers on points refer to successive points in the cross section.

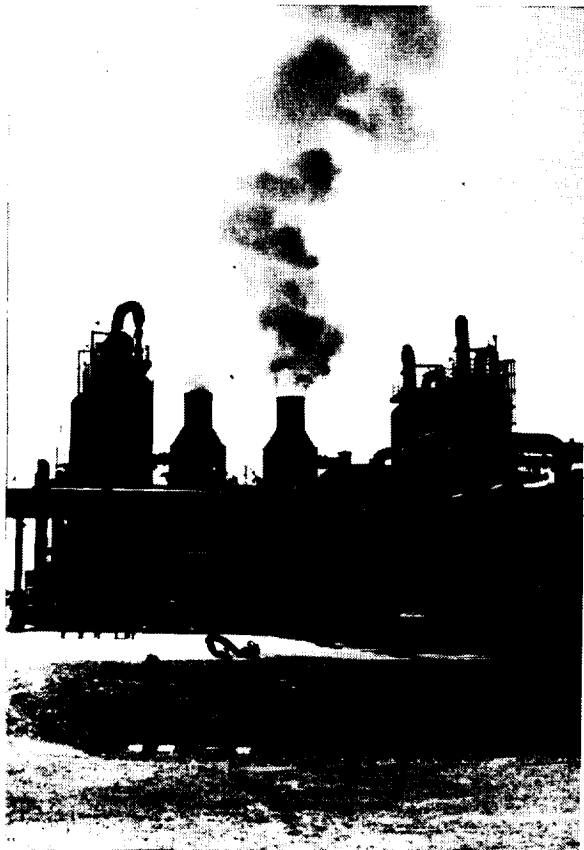
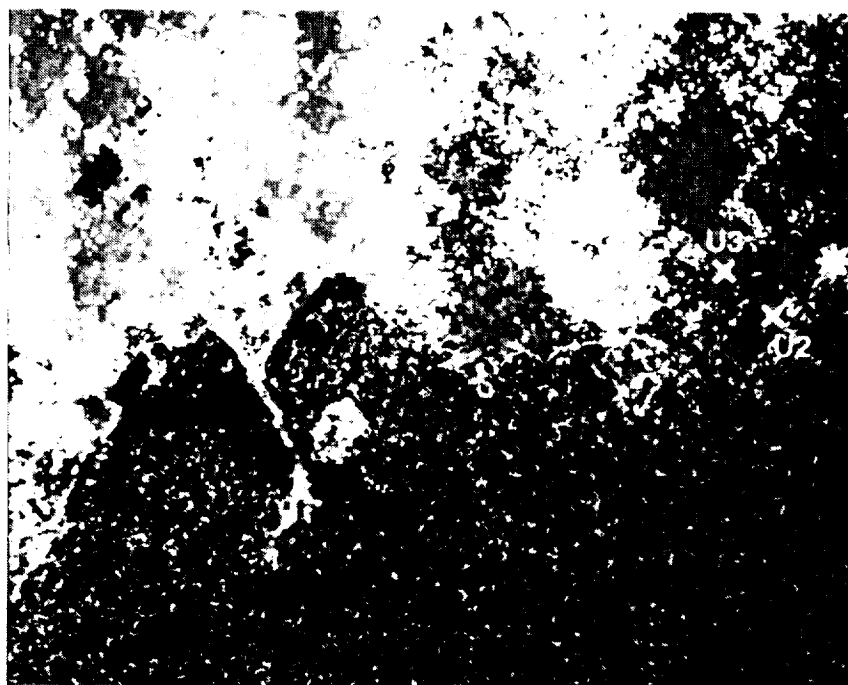
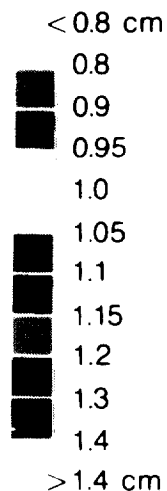


Figure 7. Flash towers at the UNOCAL Unit 3 geothermal power facility, Imperial Valley, CA.

Figure 8. Water vapor column abundance distribution over the southern shoreline and geothermal plant site calculated from the 1130-nm band. A median filter replaces the image DN value at Pixel P with the most frequent value in the 3x3 array with P at the center.



WIND = 1.3 m/s



X GEOTHERMAL PLANT
 ⊗ NOT ACTIVE
 * SH. "WEATHER"

Spatial distribution of water vapor
 1130 nm Atmospheric water band
 Median Filter

MEDIAN FILTER; 1130 nm

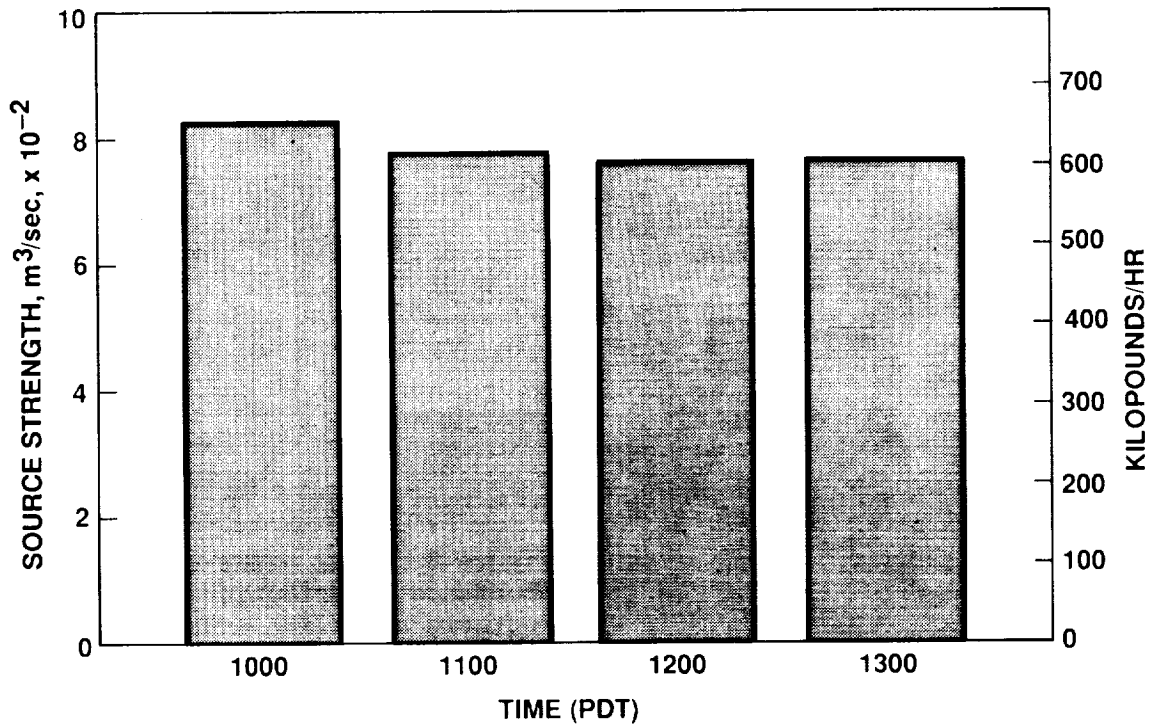


Figure 9. Rate of water loss from the UNOCAL No. 3 Unit cooling evaporators and flash towers for April 18, 1989. AVIRIS overflow the site at 12:10 PDT.

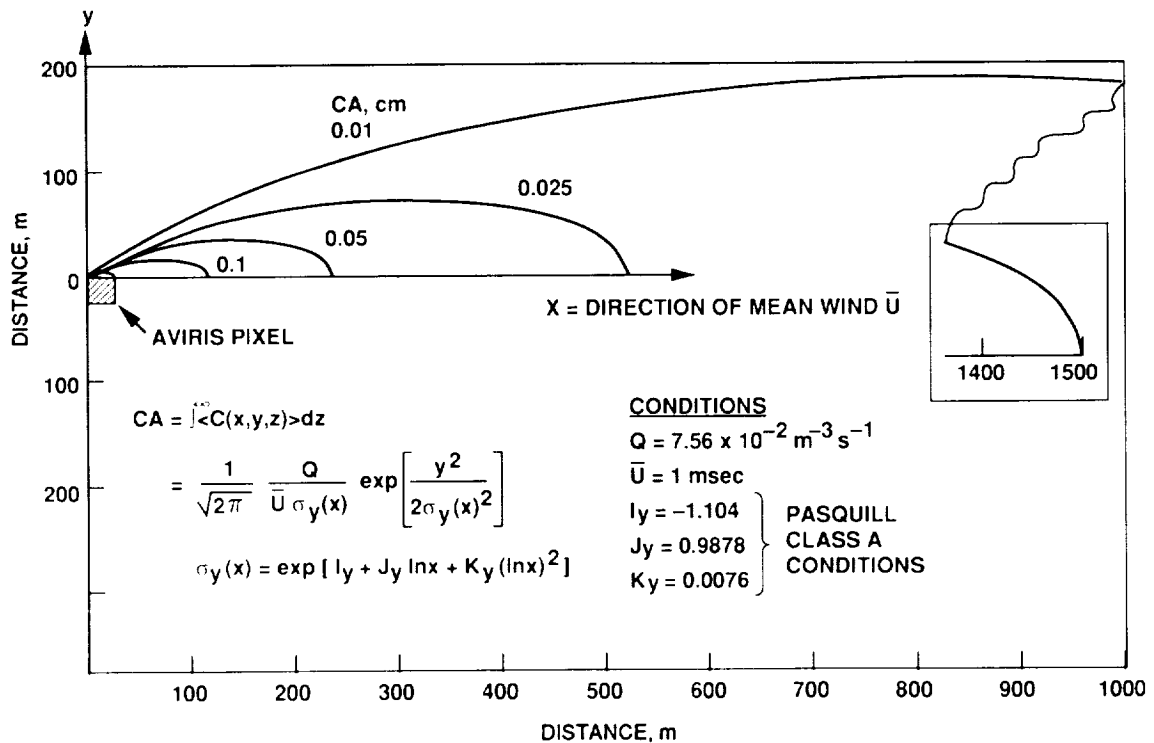


Figure 10. Contours of constant column abundance for a point source in steady horizontal wind and perfectly reflecting (zero absorption) surface. Source strength is that measured for the UNOCAL Unit 3 plant as determined from the data of Figure 9.

CLOUD IDENTIFICATION AND OPTICAL THICKNESS RETRIEVAL USING AVIRIS DATA

Kwo-Sen Kuo, Ronald M. Welch, Institute of Atmospheric Science, South Dakota School of Mines and Technology, Rapid City, South Dakota, USA; Bo-Cai Gao, Alexander F. H. Goetz, Center for the Study of Earth from Space/Cooperative Institute for Research in Environmental Sciences, University of Colorado, Boulder, Colorado, USA.

ABSTRACT

An improved ratioing technique is introduced for cloud identification. Optical thicknesses for cloudy areas are obtained using albedos calculated by a radiative transfer model at $0.752\text{ }\mu\text{m}$. A comparison of the optical thickness results from images of different resolutions is then made to demonstrate the need of high resolution data for cloud property retrievals.

INTRODUCTION

Understanding the role of clouds is among the highest priorities in the EOS (Earth Observing System) science objectives. In order to fully understand the formation and feedback processes of clouds, an accurate measurement of their microphysical properties is necessary. Remotely sensed data by satellites provide a means to monitor clouds globally, and hence the ability to assess the geographical effects on cloud formation and composition. Therefore retrieval algorithms of cloud properties using satellite data are highly in demand.

In this report we will discuss an improved technique in cloud identification and a preliminary study on retrieving cloud optical thickness using AVIRIS data.

DATA

AVIRIS is the prototype of the proposed HIRIS instrument for the EOS project. A brief description of the AVIRIS instrument and data can be found in Gao and Goetz (1990b). Each AVIRIS scene usually has 512 scan lines with 614 pixels per line and 224 channels per pixel. The pixel ground resolution is about 20×20 meters square. Each pixel is represented by a 2-byte integer on magnetic tape and is readily converted to radiance by multiplying a conversion factor. In this study we further converted radiance to albedo using solar zenith angle and solar irradiance calculated by a LOWTRAN7

model for each channel. A subset (600 x 480 pixels) of the full scene is used for the convenience of spatial degradation.

CLOUD IDENTIFICATION

The identification of clouds in an image is the first step and also a major difficulty in cloud property retrieval using remotely sensed imagery. Almost every existing cloud identification algorithm involves a choice of threshold. Such choice is often more or less subjective. Therefore the results of a cloud property analysis derived from different cloud identification algorithms can possess a large range of variability (Parker and Wielicki, 1989).

Gao and Goetz (1990a) developed a technique which enables one to make a distinction between cloud and background with greater confidence. For each AVIRIS image pixel they first take the five-channel averaged radiance over the water vapor absorption channels centered at 0.94 and 1.14 μm respectively, and over the window channels between them centered at 1.04 μm . The ratio of the sum radiance from the two averaged water vapor channels to twice the radiance of the averaged window channel is then taken for each pixel. (This process will be referred to as 3-band ratioing and the ratio obtained from this process as 3-band ratio, hereafter.) And a ratioed image is thus generated after a linear contrast stretch to put pixel ratios in integers for storage and display purposes.

In the ratioed image, clouds stand out from a rather uniform background over land. (See Gao and Goetz, 1990a, for examples.) This is because most soil ingredients have a linear spectral response in this wavelength region (Gao and Goetz, 1990b). However, where there is an uneven terrain it will show a brightness gradient on the ratioed image, because higher terrains cause shorter water absorption paths hence less water absorption and larger ratios. This effect somewhat obscures the distinction between cloud and background and makes the choice of threshold more difficult than on an even terrain. It is desirable to be able to improve this technique in this regard.

Figure 1 shows the histograms from the three averaged channels of AVIRIS scene AS0628. The three-maximum characteristics of the histograms are very typical for an image composed of shadows cast by clouds, background features, and a good portion of clouds. These histograms can be viewed as composites of the distributions of three classes of pixels (Fig. 2) with the maximum of the lowest albedo corresponding to the distribution of shadow pixels, and similarly the second maximum to the background pixels and the third to cloudy pixels.

With closer examination we found that water vapor absorption poses two effects to the histograms: (1) narrowing the distribution of each class, and (2)

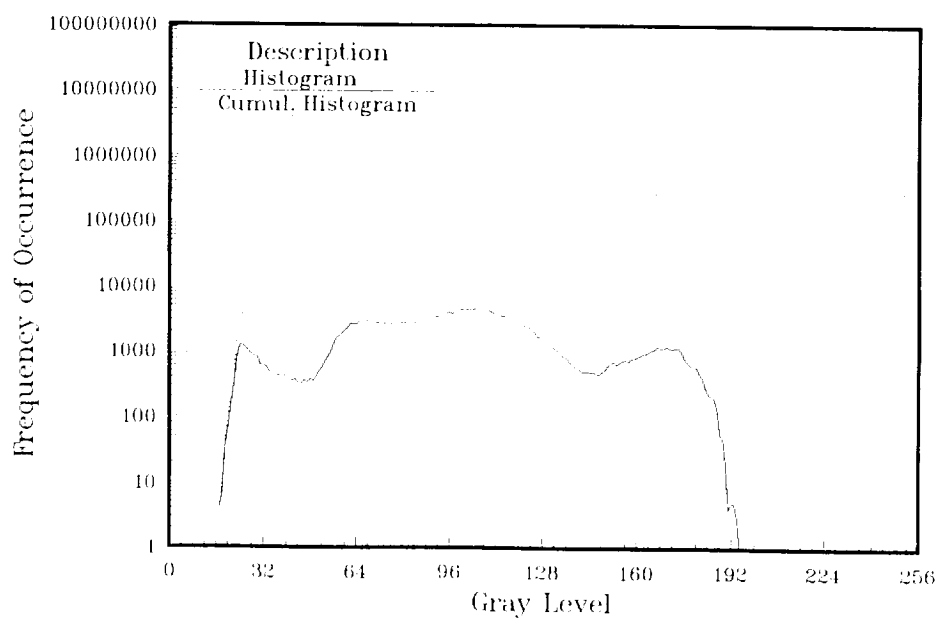


Figure 1a. Window channel centered at 1.04 μm .

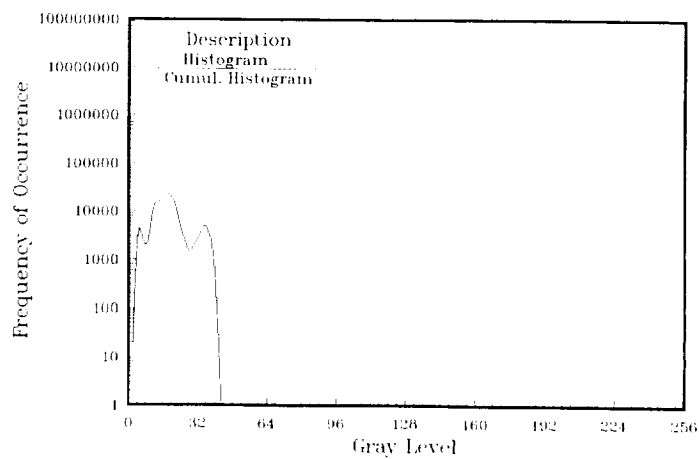
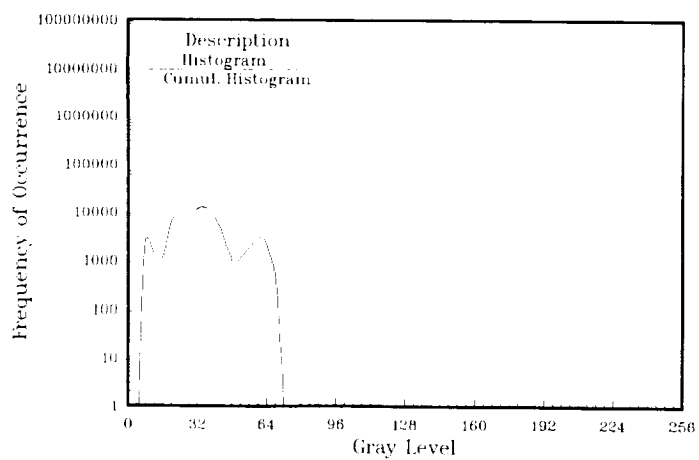


Figure 1b. Water vapor absorption channels at 0.94 μm and 1.14 μm .

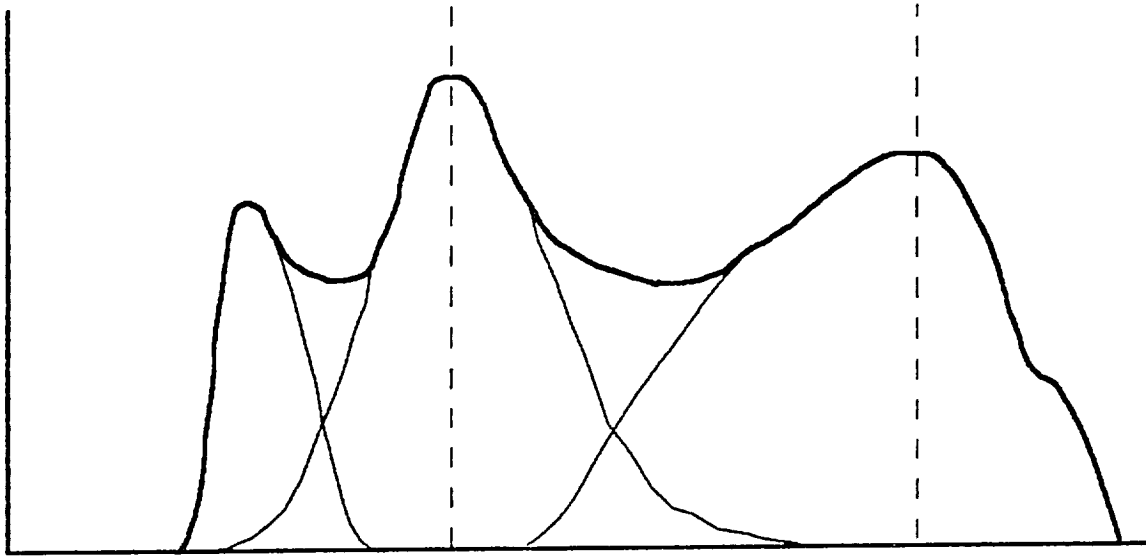


Figure 2. Typical histogram for an AVIRIS scene.

the composite envelope distribution being shifted to the lower albedo end. However, it is observed that the distribution of different classes is shifted by a different degree. These effects can be explained by the attenuation of radiation by water vapor. Since clouds are higher objects and the upper atmosphere has substantially lower humidity, the attenuation of the radiation reflected by clouds is much less than that reflected by background. Table 1 shows the 3-band ratios of the second and third maxima for scene AS0628. The 3-band ratio of the first maximum is not compared since this distribution is likely to be heavily contaminated by the left tail of the second distribution (Fig. 2).

Table 1. Ratios at the 2nd and 3rd maxima of the histograms for different scenes.

Scene	Ratio at Maximum		Cloud Cover %
	second	third	
AS0526	0.32	0.39	30.9
AS0590	0.51	*	17.8
AS0628	0.25	0.29	33.1
AS0630	0.37	*	5.1

*No third maximum for the scene due to low cloud cover

After the observation and reasoning made above, we use the 3-band ratio of the background maximum as the lower limit in the 3-band process. The range of the 3-band ratios is thus reduced and the resulting image is further enhanced. The improvement can be seen in Figure 3 for scene AS0590. (Detail may be lost in reproduction.) We can therefore choose a threshold on this image with ease and filter out background before we color code the optical depths of clouds. Using the cutoff ratio, a cloud cover of 17.8% is found, which is higher than the 15+% obtained by the original method (Gao and Goetz, 1990a). Therefore more cloudy area is preserved.

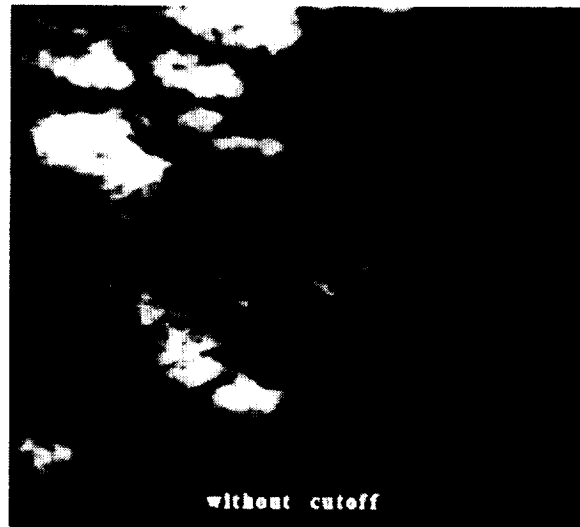


Figure 3a. Ratioed image for AS0590 without a cutoff ratio.



Figure 3b. Ratioed image for AS0590 with a cutoff ratio.

OPTICAL DEPTH RETRIEVAL

Model Description

A discrete ordinate radiative transfer model (Stamnes and Dale, 1981) is used to simulate the albedos being observed by the instrument under the same radiometry. In this preliminary study a uniform layer of cloud with certain optical depth is put in between two vacuum spaces. In other words there is no water vapor absorption or Rayleigh scattering effect simulated in the model. At the bottom of the lower space is a Lambertian surface with an albedo obtained by analyzing the histogram of the scene (i.e., the albedo corresponding to the background maximum). Figure 4 is a schematic diagram for the model setup.

Procedure and Results

Nakajima and King (1990) showed that at $0.752\text{ }\mu\text{m}$ the albedo is sensitive to optical thickness and insensitive to the droplet size distribution of the cloud. Therefore we chose to use the C1 size distribution from Diermendjian (1969) and ran a Mie scattering calculation at $0.752\text{ }\mu\text{m}$ to get the Lengendra polynomial expansion of the phase function, which is then fed to the radiative transfer model to calculate albedos for a set of optical thicknesses. We then used the calculated albedos to contour the optical thicknesses of the given scene. Then the scene was spatially degraded by averaging 24×24 pixels

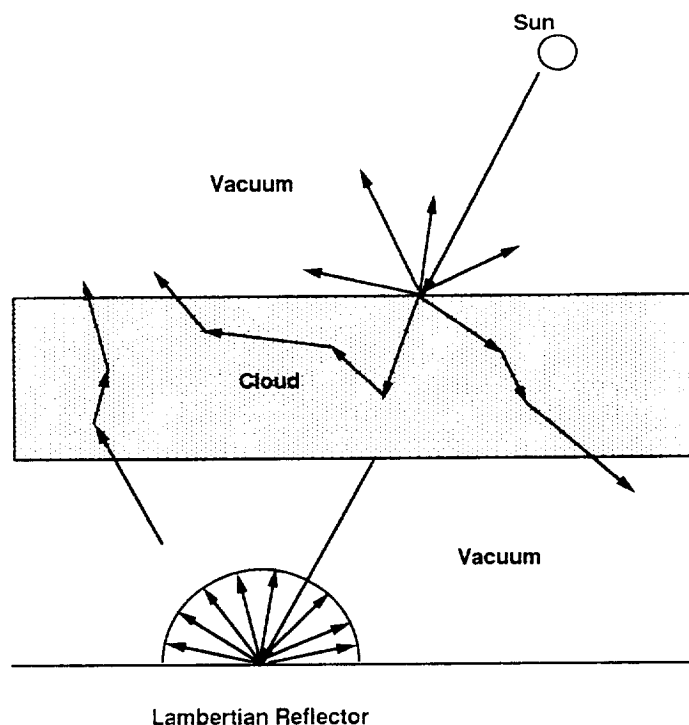


Figure 4. Schematic diagram of model setup.

(480 m x 480 m) on the original image to simulate the best resolution of MODIS-N (MODerate resolution Imaging Spectrometer-Nadir, another EOS facility instrument) data. A comparison of scene AS0526 is shown in Figure 5.



Figure 5a. Cloud optical thickness result with original resolution.

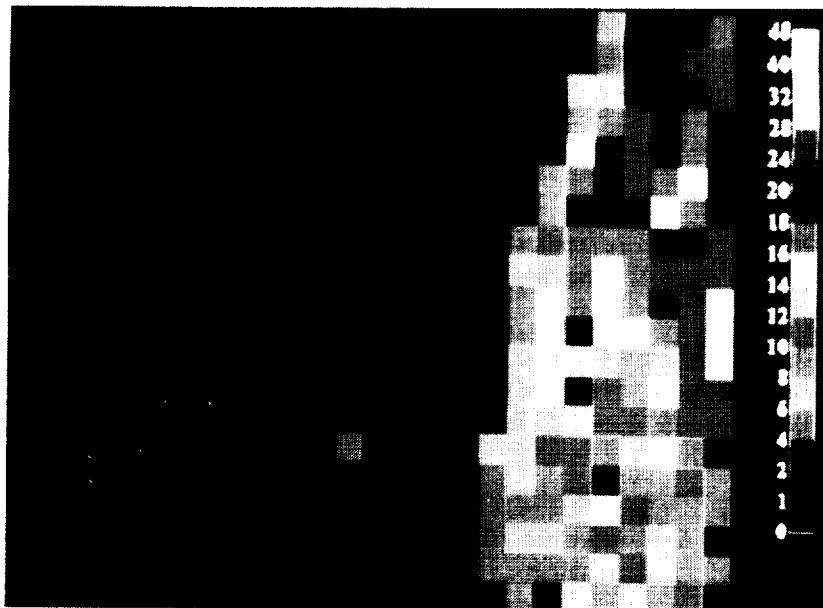


Figure 5b. Cloud optical thickness result with coarse resolution.
(480 m x 480 m)

It can be seen that much of the detail of the fine distribution of the optical thickness is lost in the image with coarser resolution. Smaller clouds and optically thinner pixels disappeared in the averaging process which results in a decrease of cloud cover from 33.1% to 30.8%.

CONCLUSION

The original Gao and Goetz (1990a) technique in identifying cloudy areas is improved by using a lower limit of the ratio suggested by the background albedos in the 3-band ratioing process. A threshold can then be chosen without ambiguity to single out clouds from background. Then the images are contoured with varying optical thickness according to albedos resulting from radiative transfer model calculations. A comparison is made between images with original resolution and a 24 times lower resolution. A great loss in detail of the optical thickness distribution can be seen along with a lower cloud cover. Therefore it is concluded that a higher resolution data set is necessary to validate the lower resolution data which has the advantage of global coverage.

REFERENCE

- Diermendjian, D., 1969. *Electromagnetic scattering on spherical polydispersions*. American Elsevier Publishing Company, New York, 260pp.
- Gao, B.-C., and A. F. H. Goetz, 1990a. Determination of cloud area from AVIRIS data. *Proceedings of 2nd AVIRIS workshop* (this JPL publication).
- Gao, B.-C., and A. F. H. Goetz, 1990b. Column atmospheric water vapor and vegetation liquid water retrievals from airborne imaging spectrometer data *J. Geophys. Res.*, vol. 90, No. D4, 3549–3564.
- Nakajima, N., and M. D. King, 1990. Determination of the optical thickness and effective particle radius of clouds from reflected solar radiation measurements. Part 1: theory. *J. Atmos. Sci.* (in press).
- Parker, L., and B. A. Wielicki, 1989. Comparison of satellite-based cloud retrieval methods for cirrus and stratocumulus. FIRE Science Meeting, Monterey, California, U.S.A., July 10–14, pp 219–223.
- Stamnes, K., and H. Dale, 1981. New look at the discrete ordinate method for radiative transfer calculations in anisotropically scattering atmospheres. Part 2: intensity computations. *J. Atmos. Sci.*, vol. 38, No. 12, 2696–2706.

Determination of cloud area from AVIRIS data

Bo-Cai Gao and Alexander F. H. Goetz

Center for the Study of Earth From Space/Cooperative Institute for Research in Environmental Sciences
University of Colorado, Boulder, Colorado 80309-0449

ABSTRACT

Fractional cloud area is derived from spectral images collected by the Airborne Visible/Infrared Imaging Spectrometer (AVIRIS). The derivation is made by ratioing radiances near the 0.94- and the 1.14- μm water vapor band centers against those in the intermediate atmospheric window regions. The derivation makes use of the facts that (1) the reflectances of most ground targets vary approximately linearly with wavelength in the absorption region of the 2 water vapor bands, and (2) atmospheric water vapor concentration decreases rapidly with altitude. The band ratioing technique effectively discriminates among clouds and surface areas having similar reflectance values. It is expected that the use of water vapor channels in the near infrared region in future satellites will improve the ability to determine cloud cover over land.

1. INTRODUCTION

Clouds reflect and absorb solar radiation in the visible and near-infrared (VNIR) region, absorb infrared (IR) radiation originating from the earth's surface, and emit IR radiation to space. Consequently, clouds strongly influence the radiative transfer processes in the atmosphere. In order to improve the understanding of the nature of cloud-radiation feedbacks, global cloud parameters, including cloud cover fraction and cloud optical properties, must be monitored reliably.

Meteorological satellites make possible the global monitoring of clouds on a daily basis. The data typically have fields of view that are 1 to 8 km in diameter on the ground, while the sizes of many clouds can range from approximately 30 m to a few km or even larger. Consequently, a typical satellite image may contain many pixels that are partially filled by clouds. Accurate determination of fractional cloud area from low spatial resolution (1 km or larger) data requires the proper treatment of partially cloud-filled pixels [Shenk and Salomonson, 1972]. Arking and Childs [1985] developed a technique, that used a "maximal clustering" scheme to treat the partial cloud filling problem, for deriving cloud parameters from the Advanced Very High Resolution Radiometer (AVHRR) data. They found that, when a pixel was considered to be partially cloud-filled, there was a wide range in the combination of cloud amount, height, and optical thickness that matched the observed radiances. This demonstrates that the information content of AVHRR data on cloud parameters is limited.

Shenk and Salomonson [1972] predicted theoretically that sufficiently high spatial resolution data would minimize the partial cloud filling problem discussed above and allow the accurate determination of cloud cover with a simple radiance threshold method. However, Wielicki and Welch [1986] studied high spatial resolution (79 m) Landsat Multispectral Scanner (MSS) data and found that the derived fractional cloud cover strongly depended on the assumed threshold because large portions of clouds had reflectances comparable to or smaller than the surface.

In this paper we present results from an improved cloud detection technique using imaging spectrometry data from AVIRIS [Vane, 1987]. Total column atmospheric water vapor amounts are used to separate cloudy and clear areas. This method may be applicable to future imaging spectrometer data from the earth observation system (Eos) mission [Butler et al., 1987].

2. IMAGING SPECTROMETRY

Imaging spectrometers are being developed for remote sensing of the earth from aircraft and from space [Goetz et al., 1989]. The most recent imaging spectrometer under development is AVIRIS [Vane, 1987]. This instrument images the earth's surface in 224 spectral bands approximately 10 nm wide, covering the spectral region from 0.4 to 2.5 μm , from an ER-2 aircraft at an altitude of 20 km, with a swath width of 12 km. The ground instantaneous field of view (GIFOV) is 20x20 m. Complete descriptions of the AVIRIS instrument, including radiometric calibration and data processing, are given by Vane [1987]. Figure 1 shows an example of an AVIRIS spectrum. The main water vapor features centered at approximately 0.94, 1.14, 1.35, and 1.87 μm are clearly observed. A method for quantitative retrievals of column atmospheric water vapor from AVIRIS data with a spectral curve fitting technique has been described by Gao and Goetz [1990]. This technique has high precision (~3%) and can be used to map elevation differences of approximately 100 m based on changes in column water vapor amounts.

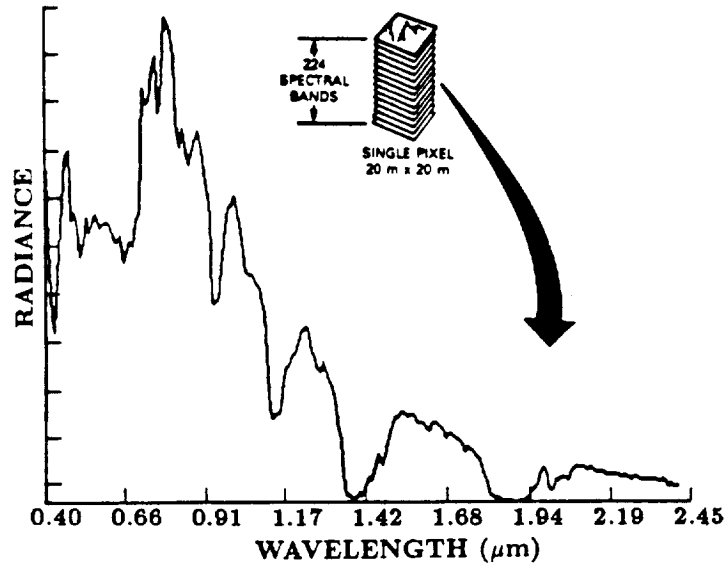


Fig. 1 An AVIRIS spectrum from single pixel (from Vane, 1987).

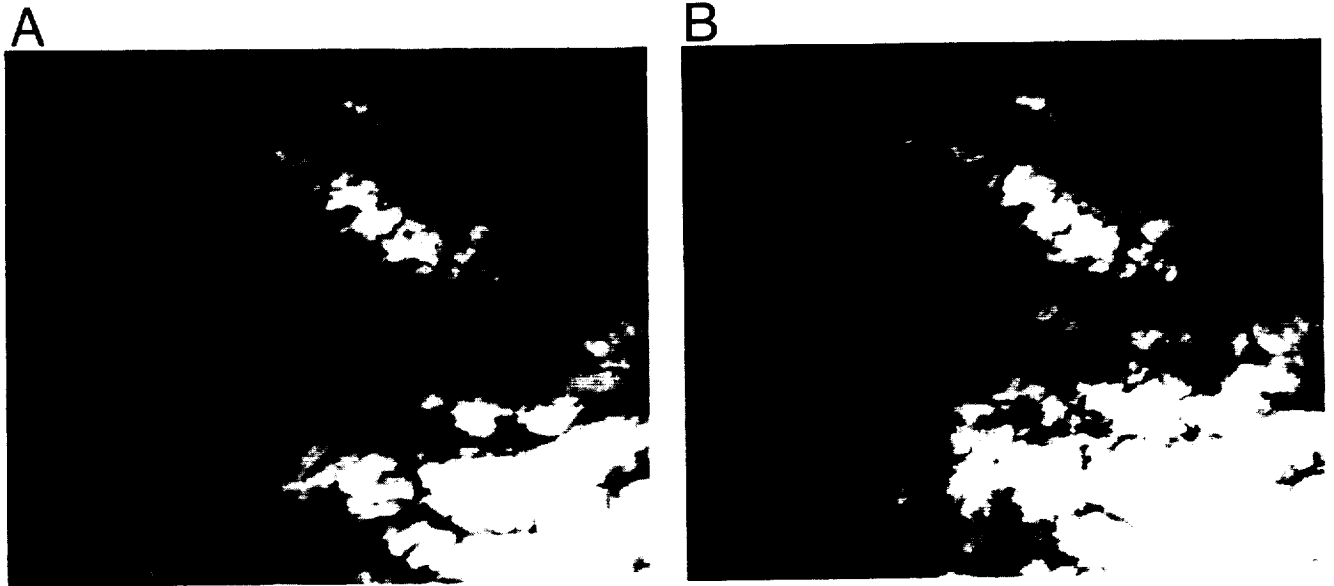


Fig. 2 (a): An AVIRIS image ($0.704 \mu\text{m}$) of Rogers Dry Lake, CA. The data were collected on a partly cloudy day on September 1, 1988. Some dark portions are the low-reflectance cloud areas. (b): An image processed from band ratios.

3. BAND RATIOING

For the sake of simplicity, we describe the band ratioing method for cloud area determination by means of examples.

AVIRIS data taken over Rogers Dry Lake in California on September 1, 1988 and over northern Death Valley in California on May 31, 1989 are used in our cloud cover studies. Figure 2a shows a $0.704 \mu\text{m}$ Rogers Dry Lake image. The image contains 614×512 pixels, corresponding to a ground area of approximately $12 \times 10 \text{ km}$. The variation of surface elevation over the entire scene is less than 50 m. The bright portions of the image are clouds. The dark portions can not all be classified as

cloud shadows, because their shapes are very different from those of bright clouds. A road traverses the image from the upper left to the middle right.

Figure 3 shows a continuous histogram of the radiances at 0.704 μm for the entire scene. The distribution shows no clusters at large or small radiances. It is difficult to select a radiance threshold that separates clouds from clear areas. A large threshold results in misclassification of the low-reflectance clouds as clear surface areas, and a small threshold results in misclassification of high-reflectance surface areas as clouds. If a threshold is placed at the position marked in the figure, then the fractional cloudy area of the scene is 25%. In this situation, the atmospheric water vapor absorption features are useful in cloud area determination.

Figure 4 shows reduced and normalized AVIRIS spectra over a cloudy pixel with the cloud top height approximately 2 km above ground, and a spectrum over a clear pixel. The reduction was performed by dividing the AVIRIS radiances by a solar radiance curve above the atmosphere [Iqbal, 1983] in order to remove the effects of the variation of solar radiance with wavelength. The resulting reduced spectra are referred to as the "apparent reflectance spectra". The normalization was made at 1.01 μm in the atmospheric "window" region. The peak absorptions, relative to the window, of the 0.94 and 1.14 μm water vapor bands over the cloudy pixel are significantly smaller than those over the clear pixel, because the atmospheric water vapor concentrations decrease rapidly with increasing altitudes. The differences in water vapor absorption features above clouds and above clear areas allow the delineation between cloudy pixels and clear pixels.

The AVIRIS radiances are also functions of surface reflectance. After studying a variety of surface target reflectances [Bowker et al., 1985], Gao and Goetz [1990] concluded that reflectances of most common surfaces vary approximately linearly with wavelength in the 0.9- to 1.3- μm region, except for iron-rich soils and minerals, which have broad electronic bands centered near 0.9 μm . The deviations from linearity for most surface targets are typically on the order of 1%. Because of this linearity in common surface reflectances, a band ratio (BR),

$$\text{BR} = (R(0.94 \mu\text{m}) + R(1.14 \mu\text{m})) / (2 \times R(1.04 \mu\text{m})) \quad (1)$$

will essentially eliminate effects associated with differing surface spectral reflectances. In Eq. (1), R represents the apparent reflectance described above. The error, associated with the removal of the linear surface reflectance effect using Eq. (1), is estimated to be 0 - 2% for common surfaces and atmospheric conditions.

4. RESULTS

Figure 2b shows an image processed from the band ratios that were calculated according to Eq. (1). In order to increase the S/N ratios, apparent reflectances of five AVIRIS channels around 0.94 μm were first averaged to give a mean apparent reflectance at 0.94 μm . The same arithmetic operations were carried out for the channels around 1.14 and 1.04 μm before the ratio based on Eq. (1) was made. There are several salient features in Figure 2b. For example, the road is hardly visible. This indicates that the band ratio does remove the surface reflectance effects. Many dark portions in Figure 2a are now shown as clouds. Also, the bright areas in Figure 2b have cloud morphologies.

Figure 5 shows the brightness distribution of the entire ratioed scene. The ratios were multiplied by 1000 for computational purposes. The continuous distribution curve also makes it difficult to select a threshold above which pixels can be classified as cloudy. However, we propose that the cloud area fraction can be derived quantitatively from the distribution curve with procedures described below.

The terrain within the Rogers Dry Lake scene, as shown in Figure 2a, is flat. Therefore, the amounts of water vapor over clear pixels on a partly cloudy day should be within 3% of the same value [Gao and Goetz, 1990]. The band ratios of clear pixels, calculated according to Eq. (1), should also be the same. However, because of the presence of instrument noise, the band ratios for clear pixels will exhibit a gaussian distribution. The clear area fraction is derived by fitting all points in Figure 5 with pixel values less than 260 with a gaussian function by using a non-linear least squares method. The resulting fitted curve is also shown in Figure 5. The normalized area below the gaussian curve is 44 on a scale of 100 with the area uncertainty of approximately 1, based on the uncertainties of the derived gaussian parameters. This means that the clear surface area fraction is 44%. The remaining 56% is attributed to the cloudy area fraction.

The ratio method was applied to a more complex area containing significant elevation differences. Band ratios were calculated with Eq.(1) from AVIRIS data measured over northern Death Valley. The surface elevation differences within the AVIRIS scene were approximately 1 km. The fitting technique described above is not applicable for the derivation of clear area fraction over this scene, because the band ratios are sensitive to elevation differences. Several other techniques were used

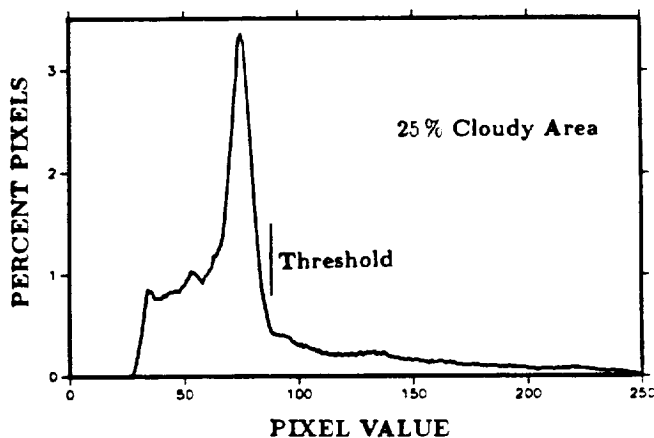


Fig. 3 Distribution of radiances corresponding to the image in Fig. 2a.

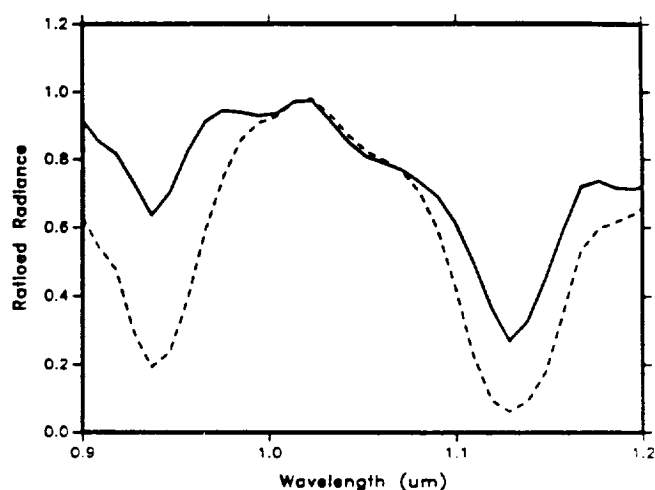
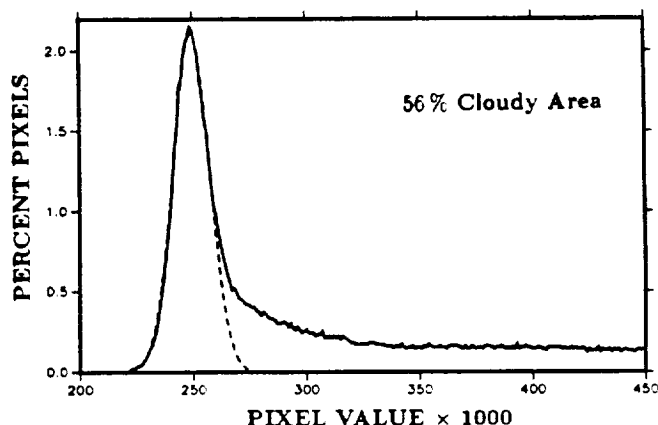


Fig. 4 Examples of AVIRIS spectra over a thick cloud (solid line) with top height of approximately 2 km above the ground, and over a clear pixel (dotted line). The measurements were made in Rogers Dry Lake, CA on September 1, 1988. The spectra were obtained by dividing the observed radiances by a solar radiance curve above the atmosphere (Iqbal, 1983) and then normalizing at 1.03 μm . The water vapor peak absorptions at 0.94 and 1.14 μm over the cloudy pixel are smaller than those over the clear pixel.

Fig. 5 Distribution (solid curve) of band ratios corresponding to the image in Fig. 2b and a gaussian function curve (dotted curve) which approximates the distribution of band ratios from clear pixels.

to estimate the cloud area coverage from the ratioed image. The estimated cloud area coverage from the band ratioed image is 15.4% with an error of less than 2%. For comparison, thresholding techniques were also applied to original AVIRIS images for determining cloud area fractions. Threshold values were selected with the method described by Wielicki and Welch [1986] for land areas. The resulting cloud area fractions for 11 AVIRIS band-images in the 0.7-0.8 μm region, the bandpass of MSS channel 6, were between 4.9 and 7.0% with the average being 6.2% (R. Welch and K. S. Kuo, personal communication, 1990). This demonstrates that significant underestimation of cloud area over land can occur with simple radiance thresholding techniques.

5. DISCUSSION

Our observations indicate that clouds with top altitudes of 500 m have significantly smaller water vapor absorption depths than clear surface pixels. Therefore, the band ratioing method can be used to detect clouds with top altitudes of at least 500 m or greater. The peak absorptions of the 0.94 and 1.14 μm water vapor bands over a cloudy pixel depend not only on the amount of water vapor above the cloud top, but also on the absorption and scattering properties of particles (solid and liquid) and water vapor within the cloud. Theoretical studies by Arking et al. [1987] have demonstrated the importance of water vapor absorption within clouds. It is possible that the very low level clouds (or fog) with cloud top altitudes of approximately 300 m or less may give ratios (see Eq. (1)) comparable to the ratios over clear surface areas, and the band ratioing method may not be able to detect the low level clouds. Because of these concerns, we have not claimed the accuracy with which the cloud area fraction can be determined using our band ratioing method. Theoretical and experimental studies of absorption and scattering properties of very low level clouds are required in order to resolve the accuracy issue.

6. SUMMARY AND CONCLUSIONS

Over high-reflectance land areas the simple radiance threshold method for cloud area determination does not allow the discrimination between low-reflectance clouds and high-reflectance surface areas. Because the atmospheric water vapor concentration decreases rapidly with height, the depths of water vapor absorption bands above clouds are usually smaller than those above clear surface areas. The band ratios, calculated with Eq. (1) by using radiances from narrow spectral channels located at the 0.94 and 1.14 μm water vapor band centers and at the atmospheric window near 1 μm , eliminate the surface reflectance variation effects and allow the separation between clouds and clear surface areas.

In the mid-1990s, NASA expects to carry, among others, two imaging spectrometers, the Moderate Resolution Imaging Spectrometer (MODIS) [Salomonson et al., 1989] and the High Resolution Imaging Spectrometer (HIRIS) [Goetz and Herring, 1989] aboard the Earth Observing System (Eos) Polar Platform. Because HIRIS has spectral channels and a spatial resolution similar to that of AVIRIS, our method is directly applicable to cloud area determination from HIRIS. Also, the results from HIRIS data analysis may be useful in refining algorithms for retrieving cloud parameters from data measured by MODIS, which has a pixel size of approximately 0.5 km and has the capability of global coverage.

7. ACKNOWLEDGMENTS

The authors are grateful to R. O. Green and G. Vane of the Jet Propulsion Laboratory for providing the AVIRIS spectral image data. This work was partially supported by the Jet Propulsion Laboratory, California Institute of Technology under contract 958039.

8. REFERENCES

- Arking, A., and J. D. Childs, Retrieval of cloud cover parameters from multispectral satellite images, *J. Clim. Appl. Meteorol.*, 24, 322-333, 1985.
- Arking, A., J. D. Childs, and J. Merritt, Remote sensing of cloud cover parameters, *Atmospheric Radiation Progress and Prospects, Proceedings of the Beijing International Radiation Symposium*, edited by K.-N. Liou and Z. Xiuji, 473-488, Science Press, Beijing, 1987.
- Bowker, D. E., R. E. Davis, D. L. Myrick, K. Stacy, and W. T. Jones, *Spectral Reflectances of Natural Targets for Use in Remote Sensing Studies, NASA Reference Publication 1139*, 1985.
- Butler, D. M., et al., *From Pattern to Process: The Strategy of the Earth Observing System, NASA Earth Observing System*, Vol. II, 1987.
- Gao, B. C., and A. F. H. Goetz, Column atmospheric water vapor and vegetation liquid water retrievals from airborne imaging spectrometer data, *J. Geophys. Res.*, 95, 3549-3564, 1990.
- Goetz, A. F. H., and M. Herring, The High Resolution Imaging Spectrometer (HIRIS) for Eos, *IEEE Transactions on Geoscience and Remote Sensing*, 27, 136-144, 1989.
- Iqbal, M., *An Introduction to Solar Radiation, Academic Press*, 43-95, 1983.
- Shenk, W. E., and V. V. Salomonson, A simulation study exploring the effects of sensor spatial resolution on estimates of cloud cover from satellites, *J. Appl. Meteorol.*, 11, 214-220, 1972.
- Salomonson, V. V., W. L. Barnes, P. W. Maymon, H. E. Montgomery, and H. Ostrow, MODIS: Advanced Facility Instrument for Studies of the Earth as a System, *IEEE Transactions on Geoscience and Remote Sensing*, 27, 145, 1989.
- Vane, G., Ed., *Airborne Visible/Infrared Imaging Spectrometer (AVIRIS), JPL Publication 87-38*, 1987.
- Wielicki, B. A., and R. H. Welch, Cumulus cloud properties derived using Landsat data, *J. Clim. Appl. Meteorol.*, 25, 261-276, 1986.

ANALYSIS OF AVIRIS DATA FOR SPECTRAL DISCRIMINATION OF GEOLOGIC MATERIALS IN THE DOLLY VARDEN MOUNTAINS, NEVADA

J.A. Zamudio^{1,2} and W.W. Atkinson Jr.²

¹Center for the Study of Earth from Space/CIRES

²Department of Geological Sciences
University of Colorado
Campus Box 449
Boulder, CO 80309-0449
tel. (303) 492-5051
fax (303) 492-5070

ABSTRACT

Airborne Visible/Infrared Imaging Spectrometer (AVIRIS) data were collected over the Dolly Varden Mountains and Currie Hills in northeastern Nevada in June of 1989. The study area contains a variety of sedimentary, plutonic and volcanic rock types as well as a contact metamorphic aureole around a large intrusion. The internal average relative (IAR) reflectance calibration method is compared with the empirical line calibration method. A binary encoding routine was used to match selected spectra and produce thematic scenes. These scenes provide geologists with evidence of previously unmapped faults and folds in the area.

INTRODUCTION

Five flight lines of Airborne Visible/Infrared Imaging Spectrometer (AVIRIS) data were collected on June 2, 1989 over the Dolly Varden Mountains-Currie Hills area in northeast Nevada. AVIRIS collects radiance data in 224 bands using four spectrometers to cover a wavelength region from 0.4 to 2.45 μm . These data were collected to assist in our goal of determining the style of structural deformation prevalent in this region during Mesozoic time. Geologic mapping is essential in delineating structural elements such as faults and folds. Spectral signature mapping using imaging spectrometer data assists in correlating geologic units and helps identify places where rocks have been folded or faulted. It is then left to the geologist to measure the structures in the field. By studying information derived from imaging spectrometer data, time spent mapping in the field is reduced as the geologist is directed to specific areas where faults and folds may occur.

The Dolly Varden Mountains and Currie Hills are located in the semi-arid environment of the northeastern Great Basin. The area ranges in elevation from 1750 to 2600 meters. Other than some high relief areas of bare outcrop, vegetation cover typically ranges from about 20% to 50%. In some places along drainages and on high, north-facing slopes, vegetation cover approaches 100%. Sagebrush is present at lower elevations and piñon pine and juniper are prevalent at higher elevations from about 2000 meters.

GEOLOGY

The study area contains a variety of geologic materials exposed at the surface. A sequence of Late Paleozoic and Triassic sedimentary rocks includes limestone, dolomite, sandstone, siltstone and shale. Igneous rocks in the area include a two-phase monzogranite and quartz monzonite intrusion and volcanic rocks with compositions ranging from andesite to quartz latite to rhyolite. The igneous intrusion produced a calc-silicate contact metamorphic aureole in the sedimentary section. Minerals such as andradite, diopside, tremolite, epidote, serpentine, sepiolite and saponite resulted from this metamorphism.

DATA CHARACTERISTICS

The detectors on AVIRIS have an instantaneous field of view (IFOV) of 0.95 mrad (Vane et al., 1988). When flown on the ER-2 aircraft at 20,000 m, the pixel size at sea level would be 19 m. In the Dolly Varden area, using the median altitude of 2200 m, the pixel size would be 17 m. However, AVIRIS spatially oversamples by 17% (Vane et al., 1988) so that the actual pixel size should be 14.1 m at an elevation of 2200 m. Sections of road in the AVIRIS scenes were measured and scaled to maps, and pixel size at an elevation of 2200 m was found to be about 14.4 m in both cross-track and along-track directions. Over the whole area, where the relief is about 800 m, pixel size should vary by less than a meter. The measured flight line swath width at about 2200 m is approximately 9.5 km.

Signal-to-noise ratios were calculated for the AVIRIS data by dividing the average radiance of 9 pixels over homogeneous targets by the standard deviation of the radiance. A bright playa and a dark andesite flow were used to calculate signal-to-noise. Four spectrometers (A-D) sample wavelength intervals from 0.4-0.7, 0.68-1.28, 1.24-1.86 and 1.83-2.45 μm . Signal-to-noise ratio values for dark and light targets respectively are 50 and 180 for spectrometer A, 60 and 150 for B, 35 and 100 for C, and 15 and 45 for D (Table 1). The assumption of homogeneity of these targets is perhaps a generous one, so these values are probably somewhat lower than the actual signal-to-noise ratio. It can be assumed that signal-to-noise values over other materials in the area fall between the values obtained for these dark and bright targets.

Table 1. AVIRIS signal-to-noise over the Dolly Varden Mountains

midday June 2, 1989 latitude=40°22'				
spectrometer	A	B	C	D
bright target Albedo=0.53	180	150	100	45
dark target Albedo=0.24	50	60	35	15

CALIBRATION

Preprocessing of the data was done to convert the radiance values to reflectance. Two methods were used, the internal average relative (IAR) reflectance method (Kruse, 1988) and the empirical line method (Conel et al., 1987). The first step followed in each calibration method was to normalize the data to equal energy by calculating a multiplier for each pixel to scale the data to a total image average. By shifting each spectrum to the same relative level of brightness, this step removes albedo variations and topographic effects.

The conversion to IAR reflectance was done by dividing each pixel's spectrum by the average spectrum for that flight line segment. This method produces relative reflectance spectra that show features not common throughout the flight line segment. Thus, atmospheric absorption features common throughout are removed. The IAR conversion has an advantage in that no *a priori* knowledge of the geology of the area is required. However, this method can introduce peaks in reflectance if the average spectrum for the scene contains an absorption feature that some pixels do not have. For example, in a scene where vegetation coverage is sufficient to produce a chlorophyll absorption feature in the average spectrum, pixels that do not contain vegetation will show an "anti-vegetation" peak in their reflectance spectra that mirrors the absorption feature in the average spectrum (Figure 1). Consequently, if one is interested in features within that wavelength region, this calibration method might not prove satisfactory.

The empirical line method for conversion to reflectance involves calculating gain and offset values for each band based upon reflectance measurements taken from bright and dark targets under the same illumination conditions as the AVIRIS data. Radiance values from AVIRIS data are plotted against field reflectance measurements and a linear regression is performed to find the intercept and slope (offset and gain) for each band. These values are then used to convert the radiance spectra to reflectance spectra (Conel et al., 1987). This method corrects for the multiplicative effects of solar irradiance, atmospheric attenuation and instrument response, and the additive factor of path radiance. For this study, a dark andesite flow and a bright playa adjacent to the Dolly Varden Mountains were chosen as calibration targets. A Geophysical Environmental Research, Corp. Single FOV Infrared Intelligent Spectrometer (SIRIS) was used to take reflectance spectra of these targets concurrent with the AVIRIS flyover.

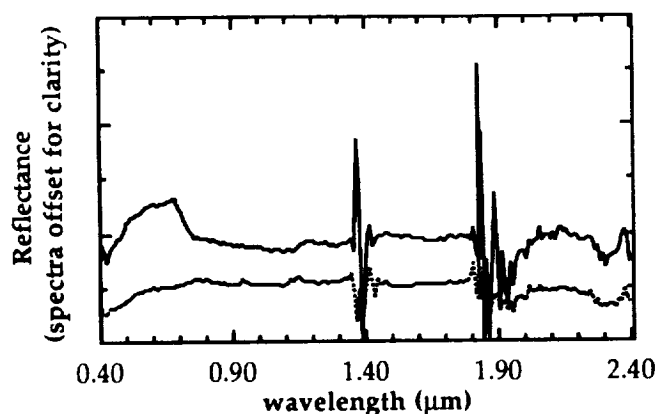


Figure 1. Comparison of the IAR reflectance calibration method (solid line) with the empirical line method (dashed line) for the same pixel.

Figure 1 compares reflectance spectra from the same pixel using the two calibration methods. Nonvegetated outcrops of a carbonate formation are exposed in this pixel, thus, the presence of an "anti-vegetation" peak at $0.68\ \mu\text{m}$ in the IAR spectrum for reasons discussed previously. Both spectra show noise-dominated H_2O bands about 1.4 and $1.9\ \mu\text{m}$ and both show the dominant CO_3 feature around $2.33\ \mu\text{m}$. A relatively noisy D spectrometer is evident in both spectra. The empirical line calibrated spectrum has two small peaks around 0.94 and $1.13\ \mu\text{m}$ that are due to overcorrection for atmospheric H_2O vapor. This overcorrection results from the calibration targets being located about $500\ \text{m}$ lower in elevation than the pixel sampled in figure 1. When using calibration targets over which there is greater atmospheric attenuation than over a particular pixel, the conversion to reflectance produces peaks in the spectrum at the atmospheric bands.

DATA ANALYSIS

Reflectance spectra for the same area taken from the AVIRIS data and the SIRIS field instrument are compared in figure 2. The AVIRIS spectrum is noisier and displays the same over-corrected atmospheric H_2O peaks as in figure 1. Both spectra show the dominant CO_3 feature at about $2.31\ \mu\text{m}$. This area also contains some iron oxide alteration. It is likely that AVIRIS sampled more of this alteration, as iron absorption bands are more pronounced in the AVIRIS spectrum.

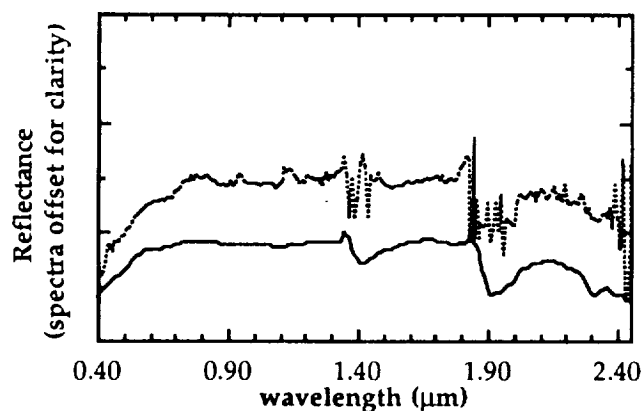


Figure 2. Comparison of an AVIRIS spectrum (dashed line) with a SIRIS field spectrum (solid line) over the same ground target.

The reflectance data were analyzed using the QL3 software developed by the U.S. Geological Survey at Flagstaff, Arizona and enhanced by the Center for the Study of Earth from Space at the University of Colorado. This software package enables the user to interactively examine a three-dimensional cube of imaging spectrometer data (two spatial and one spectral dimension) (Kieffer et al., 1988). QL3 can handle three million voxels (volume elements) at one time.

Pixels with spectra characteristics of various geologic materials were selected from the AVIRIS reflectance data and then, using a binary encoding algorithm, other pixels whose spectra matched closely were selected and color coded. These thematic images were then studied to locate geologic structures. On the east slope of the Dolly Varden Mountains, thematic images show lateral separation of a tuff-vitrophyre volcanic sequence. It is evident that faulting

has offset the sequence. Recent field mapping has also provided clues to the existence of these faults which do not appear on a previous geologic map of the area (Snow, 1964). Unmapped folds and faults located on the southwest side of the range are also apparent in the AVIRIS data.

CONCLUSIONS AND FUTURE WORK

AVIRIS data are of sufficient quality to detect mineral absorption features. This study demonstrates the usefulness of imaging spectrometer data in helping to identify and map minerals and rock types. These data enable us to concentrate our field efforts to specific areas of faulting and folding. Future field work will involve the measurement of geologic structures detected in the AVIRIS data. Finally, a tectonic history of the area will be proposed and correlated to other ranges in the region.

ACKNOWLEDGEMENTS

This study is funded under NASA grant NAGW-1293.

REFERENCES

- Conel, J.E., Green, R.O., Vane, G., Bruegge, C.J., Alley, R.E. and Curtiss, B.J. 1987. Airborne Imaging Spectrometer-2: Radiometric Spectral Characteristics and Comparison of Ways to Compensate for the Atmosphere. In Imaging Spectroscopy II, Proceedings of SPIE-Society of Photo-Optical Instrumentation Engineers, vol. 834, pp. 140-157.
- Kieffer, H.H., Eliason, E.M., Mullins, K.F., Soderblom, L.A. and Torson, J.M. 1988. Radiometric Performance of AVIRIS: Assessment for an Arid Region Geologic Target. In Proceedings of the Airborne Visible/Infrared Imaging Spectrometer (AVIRIS) Performance Evaluation Workshop. JPL Publication 88-38, pp. 30-35.
- Kruse, F.A. 1988. Use of Airborne Imaging Spectrometer Data to Map Minerals Associated with Hydrothermally Altered Rocks in the Northern Grapevine Mtns., Nevada and California. Remote Sensing of Environment, Special Imaging Spectrometer Issue. vol. 24, no. 1, pp. 31-51.
- Snow, G.G. 1964. Mineralogy and Geology of the Dolly Varden Mountains Elko County, Nevada, unpublished Ph.D. thesis, University of Utah, 153 pp.
- Vane, G., Porter, W.M., Reimer, J.H., Chrien, T.G., and Green, R.B. 1988. AVIRIS Performance During the 1987 Flight Season: An AVIRIS Project Assessment and Summary of the NASA-Sponsored Performance Evaluation. Proceedings of the Airborne Visible/Infrared Imaging Spectrometer (AVIRIS) Performance Evaluation Workshop. JPL Publication 88-38, pp. 1-20.

Retrieval of Reflectance from Calibrated Radiance Imagery Measured by the Airborne Visible/Infrared Imaging Spectrometer (AVIRIS) for Lithological Mapping of the Clark Mountains, California

Robert O. Green

Jet Propulsion Laboratory
California Institute of Technology,
Pasadena, California 91109

ABSTRACT

Spectral radiance images measured by the Airborne Visible/Infrared Imaging Spectrometer (AVIRIS) are reduced to reflectance through compensation for atmospheric scattering, water-vapor absorption, absorption of the well-mixed gases, solar irradiance, and the solar zenith angle. The LOWTRAN-7 radiative-transfer code forms the basis for this retrieval. LOWTRAN 7 is constrained with water-vapor determinations from the AVIRIS radiance data through an algorithm operating on the 940-nm atmospheric water band for every spatial element. In situ measurements of atmospheric optical depths are used to constrain the LOWTRAN-7 aerosol models. Accuracy of the retrieved reflectance spectra is evaluated with respect to surface spectra measured at the time of the overflight. The mineral bastnaesite is identified in the analysis of the retrieved reflectance imagery. These reflectance data provide a means to map the subtle mineral gradients in the Precambrian block of the Clark Mountain range in southeastern California.

1.0 INTRODUCTION

AVIRIS measures the incident total spectral radiance with 224 channels from 400 to 2450 nm in the electromagnetic spectrum. The spectral sampling interval is nominally 10 nm, which corresponds to the spectral response function for full-width-at-half-maximum (FWHM) throughput. Image data are acquired with a width of 10.5 km and a length ranging from 10 to 100 km with nominally 20- by 20-m spatial resolution for all spectral channels. These data are provided in units of radiance, and the spectral position and response function of each channel is given.

The Clark Mountain Precambrian block is selected for the spectrally distinct surface mineralogy, the potential for rock-unit separation in previously undifferentiated metamorphosed Precambrian terrain, and the occurrence of a preexisting AVIRIS data set. The study site is located in southeastern California adjacent to the Nevada border and south of Las Vegas, Nevada. The region covered by the AVIRIS data and the location of the asphalt parking lot and gravel pit targets are given in Figure 1.

Reduction of AVIRIS-measured radiance to surface spectral reflectance offers the potential to quantitatively map the distribution of surface constituents based on physically determined spectral absorption features.

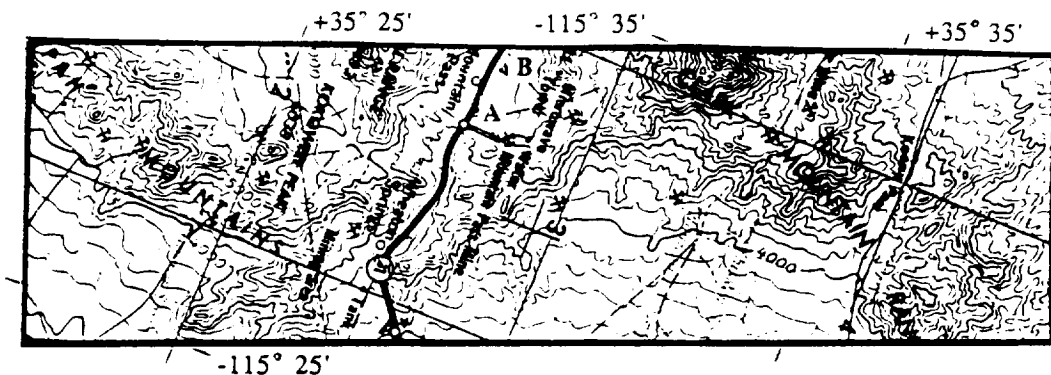


Figure 1. Location of the study area in the Clark Mountains of California. Target A is an asphalt parking lot. Target B is a gravel pit.

2.0 AVIRIS DATA

AVIRIS data were acquired over the Clark Mountain Precambrian block on the 28th of April 1989 at 12:05 p.m. These data were acquired in conjunction with an in-flight calibration experiment for verification of AVIRIS in-flight spectral characteristics. The mineral bastnaesite, which contains rare earth elements, has 12 strong absorption features over the AVIRIS spectral range. These features are used to validate the in-flight spectral calibration. The spatial coverage of the AVIRIS data set is 10.5 by 40 km trending northwest on the eastern flank of the Clark Mountains. These data are provided in units of total radiance with complete spectral calibration parameters for each channel (Chrien et al. 1990). Figure 2 gives the calibrated AVIRIS radiance for a gravel pit and asphalt parking lot targets located within the data set.

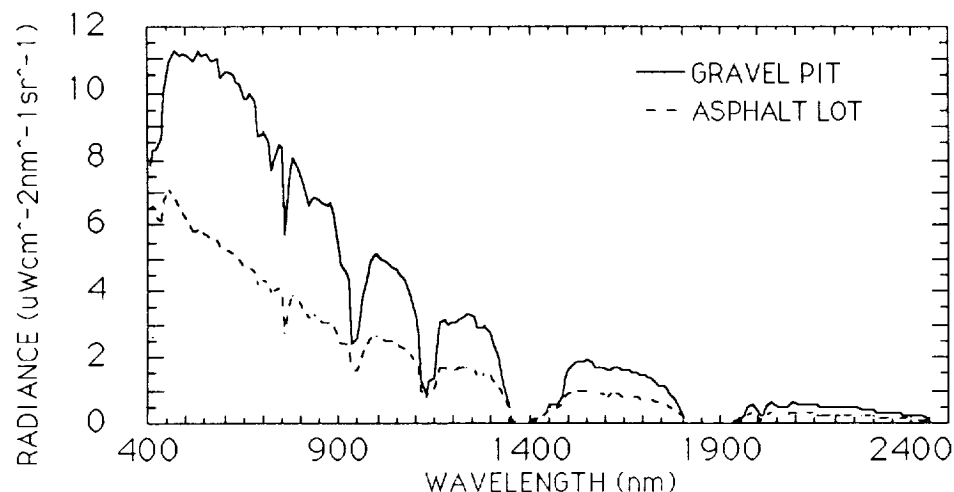


Figure 2. AVIRIS radiance spectrum for the asphalt parking lot (target A) and the gravel pit (target B).

3.0 FIELD MEASUREMENTS

In support of this experiment, measurements of the atmospheric optical depth and surface reflectance were acquired. On the day of the AVIRIS overflight, solar illumination measurements were acquired with a radiometer from sunrise to local solar noon. The instrument used has 10 discrete spectral channels with 10-nm response function FWHM in the region from 370 to 1030 nm. These data were reduced to atmospheric optical depth with the Langley plot method (Bruegge 1985). Figure 3 gives the reduced optical depths and the corresponding LOWTRAN-7 (Kneizys et al. 1989) optical depths that are used over the entire AVIRIS spectral range. These measured and modeled optical depths show good agreement in the region of overlap where aerosol scattering dominates. The LOWTRAN-7 visibility corresponding to these optical depths was 260 km.

Reflectance spectra for two surface targets were acquired in conjunction with this data set. These spectra were measured with a field spectrometer (Goetz 1987), which has a spectral channel sampling interval and response function FWHM that are less than half that of AVIRIS. Sets of 16 surface reflectance measurements, distributed evenly over the asphalt and gravel targets, were averaged and are given in Figure 4. These spectra are convolved to the AVIRIS spectral characteristic at the time of data acquisition.

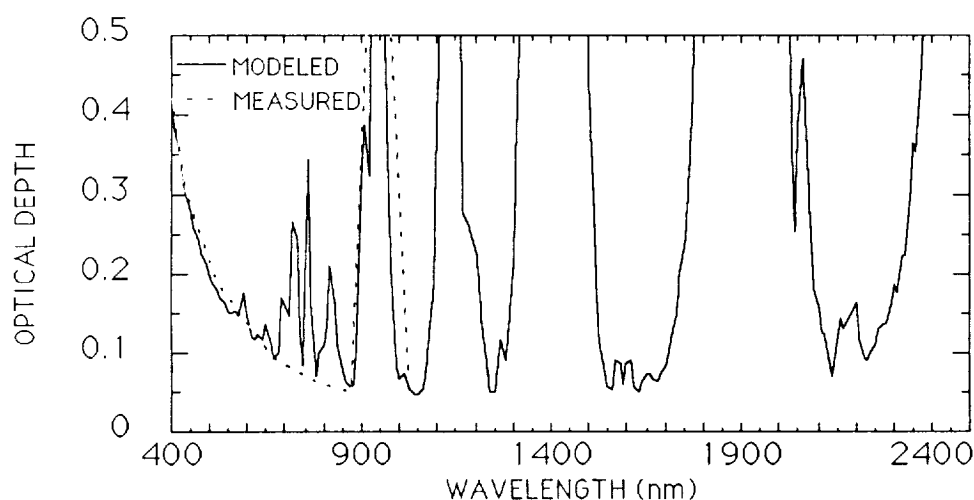


Figure 3. Atmospheric optical depths measured concurrently with the acquisition of AVIRIS data. Also given are the corresponding LOWTRAN-7 optical depths used to constrain the atmospheric model over the range of 400 to 2450 nm.

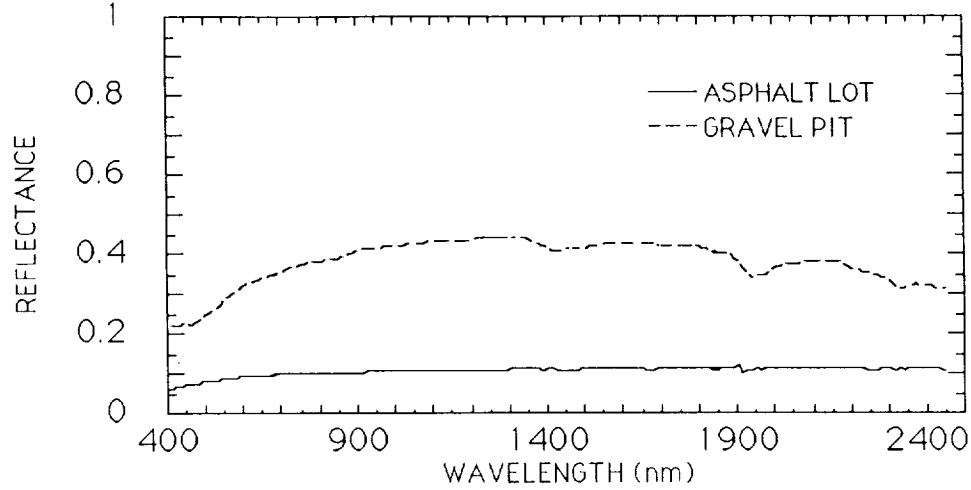


Figure 4. Measured surface reflectance for asphalt parking lot and gravel pit target.

4.0 REDUCTION OF AVIRIS DATA TO REFLECTANCE

An algorithm to retrieve reflectance directly from imaging spectrometer-measured radiance using a radiative-transfer code was originally developed for data acquired from the Airborne Imaging Spectrometer (AIS) (Conel et al. 1987). This reflectance-retrieval algorithm compensates for atmospheric scattering and absorption as well as solar illumination geometry; however, the surface incident and emergent angles and the bidirectional reflectance function remain uncompensated. Currently, aerosol and well-mixed gas variations with topography are approximated by the mean elevation. In the future, with the use of a topographic elevation data set, these parameters may be more accurately accounted for.

This algorithm treats AVIRIS-measured, total spectral radiance as the linear combination of radiance that has been reflected from the surface and radiance that is derived solely from atmospheric path scattering, as in Equation 1. Radiance scattered along the atmospheric path to AVIRIS without reflecting from the surface is given as L_p . L_r is the component of the AVIRIS radiance reflected by the surface. The total radiance measured by AVIRIS is given as L_t . The reflected radiance (L_r) is given in Equation 2 as the solar irradiance E_s multiplied by the cosine of the solar zenith angle over pi steradians and multiplied by the downward atmospheric transmittance (T_d), surface reflectance (ρ), and upward atmospheric transmittance (T_u).

$$L_t = L_r + L_p \quad (1)$$

$$L_r = (E_s \cos \theta / \pi) T_d \rho T_u \quad (2)$$

$$L_r = L_t - L_p \quad (3)$$

$$L_r / L_{r25} = (E_s \cos \theta / \pi) T_d \rho T_u / (E_s \cos \theta / \pi) T_d \rho_{25} T_u \quad (4)$$

$$\rho = (L_r / L_{r25}) \rho_{25} \quad (5)$$

Path radiance may be calculated with LOWTRAN 7 for the conditions of data acquisition leading to Equation 3, where the product L_r is isolated. With LOWTRAN 7, the reflected radiance (L_{r25}) for a 25-percent reflectance surface (p_{25}) may be modeled as in the denominator of Equation 4. AVIRIS reflectance may then be solved for as in Equation 5. This approach to deriving reflectance through modeling a known reflectance requires only minimal modification of an existing radiative-transfer code, such as LOWTRAN 7, and is easily adapted to other codes.

This radiative, transfer-based algorithm is sensitive to the absolute radiometric calibration of the AVIRIS data. Errors in calibration propagate directly to errors in retrieved reflectance. Calculations involving AVIRIS-measured radiance spectra and LOWTRAN-7-modeled spectra require the modeled data to be convolved to the exact in-flight spectral characteristics of AVIRIS. These calculations are highly sensitive to the spectral channel sampling interval and response-function calibration.

To constrain LOWTRAN 7 for calculation of the path and reflected radiance, atmospheric parameters were determined. AVIRIS-measured radiance is dominantly affected by atmospheric water vapor, as shown with a series of LOWTRAN-7 models for differing water in Figure 5. As the amount of water vapor varies from 0.0 to 23.56 precipitable mm, absorption features increase in depth across most of the spectral range from 400 to 2450 nm. In addition, a continuum absorption from water vapor affects the entire range. Over terrestrial surfaces, wide ranges of water vapor amounts are encountered. In regions with topographic relief, precipitable water vapor is modulated by changes in atmospheric path length through the vertical water-vapor distribution. Lateral and vertical heterogeneities of water vapor in the terrestrial atmosphere are also caused by local sources and sinks of water.

To show the importance of accurately constraining atmospheric water vapor, a sensitivity analysis for radiative, transfer-based reflectance retrievals, with respect to error in the knowledge of water vapor, is given in Figure 6. The error in retrieved reflectance is shown for an underestimate of the actual water vapor present by 1, 10, and 30 percent. At a 10-percent error in knowledge of water vapor, significant reflectance errors occur in the spectral regions of strong absorption, particularly the 940-, 1130-, 1400-, 1900-, and 2500-nm bands.

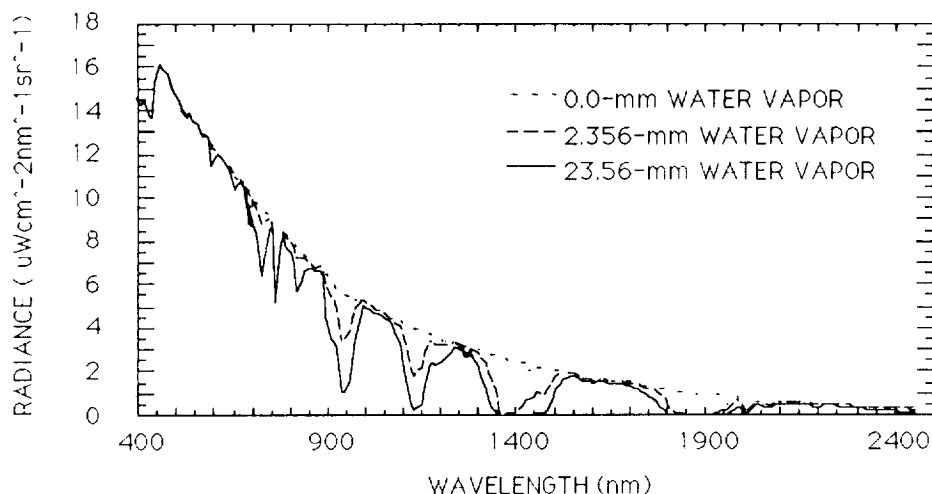


Figure 5. Modeled AVIRIS radiance for a constant 25-percent reflectance surface for differing amounts of atmospheric water vapor.

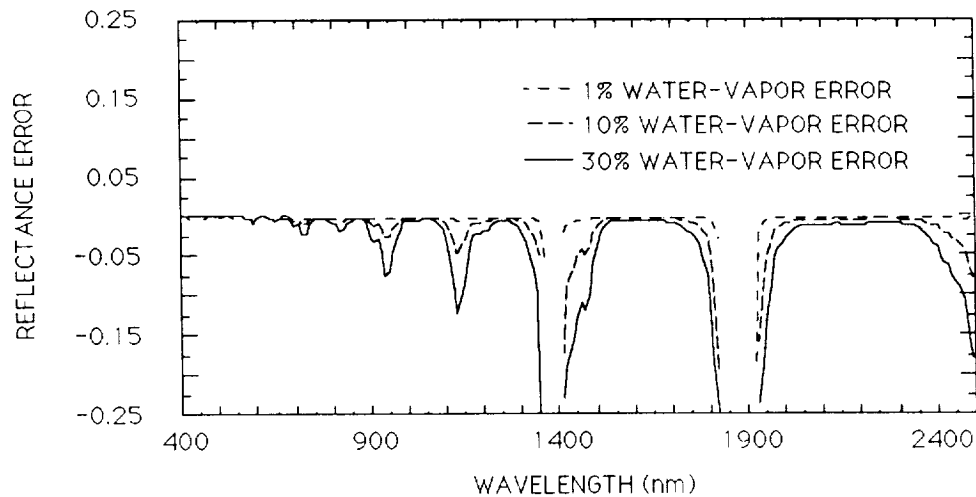


Figure 6. Sensitivity of reflectance recovery to total column atmospheric water vapor. Inaccuracies in knowledge of atmospheric water vapor result in errors in retrieved reflectance in regions of water absorption.

Sensitivity of the absorption depth in the 940- and 1130-nm atmospheric water band to the amount of water offers an approach to recovery of water vapor directly from the radiance data. A ratio-based algorithm was originally developed for recovery of total column water vapor from AVIRIS data (Conel et al. 1988, and Conel et al. 1989). The sensitivity of this technique to background surface reflectance prompted the development of the continuum-interpolated band ratio (CIBR) (Green et al. 1989 and Bruegge et al. 1990). For the 940-nm water band, the CIBR is calculated as the interpolated continuum from AVIRIS channels on either side of the water band ratioed to the channel in the band center. The CIBR is then calibrated to the vertical column equivalent of water vapor, using LOWTRAN 7 for the conditions of observation.

To constrain the radiative, transfer-based reflectance retrieval of the Clark Mountain data set, the CIBR algorithm is used to recover estimates of the total water vapor for each spatial element. Over this data set, water-vapor retrieval ranged from 7 to 18 precipitable mm. This wide range confirms the need to estimate the water vapor for each spatial element. With these water estimates, a 25-percent reflectance LOWTRAN-7 path and reflected-radiance spectrum library is developed for each tenth of a millimeter variation in water vapor in the data set. Measured optical depths, mean topographic elevation, and solar-illumination geometry at the time of data acquisition are used to further constrain LOWTRAN 7. Reflectance is solved from the AVIRIS-calibrated radiance data for each spatial element, with the correct water-vapor-constrained library spectrum. Figure 7 gives the AVIRIS radiance spectrum for the gravel target, with the LOWTRAN 7 library spectra for path and reflected radiance. Figure 8 is the retrieved reflectance for the asphalt and gravel targets. Good agreement is seen between the field measurement given in Figure 4 and these AVIRIS-retrieved reflectance spectra.

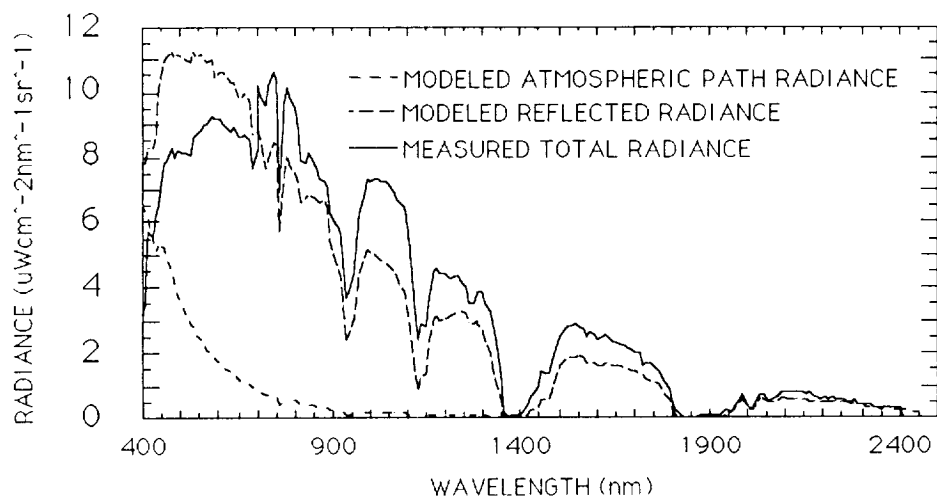


Figure 7. AVIRIS-calibrated radiance spectrum for the asphalt parking lot. The modeled LOWTRAN-7 path and reflected radiance for the observations are given for a 25-percent reflectance surface under solar illumination, atmospheric aerosols, and calculated water vapor.

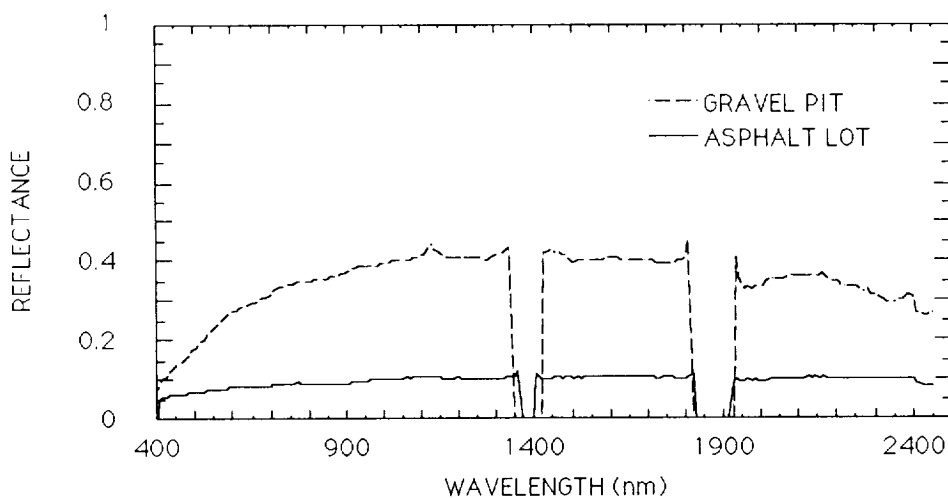


Figure 8. Radiative transfer-based retrieval of reflectance for the asphalt and gravel targets.

In the future, to more accurately constrain the radiative-transfer code, the aerosol estimate will be derived directly from the AVIRIS data through an iterative algorithm based on the differential effect of scattering on the 940- and 1130-nm water bands in AVIRIS data (Green et al. 1989). A CIBR assessment of the depth of the atmospheric oxygen band at 760 nm will be used to estimate the pressure altitude to constrain LOWTRAN-7 aerosol and well-mixed gas absorption parameters for variation in surface topography and pressure.

5.0 COMPOSITIONAL MAPPING

With the AVIRIS data in units of reflectance, physically based compositional identification may be determined for the surface. An example of a retrieved reflectance spectrum for the mineral bastnaesite and a laboratory spectrum of the same mineral are given in Figure 9. The unique combination of spectral absorptions allows unambiguous identification of this mineral. An unmixing algorithm (Adams et al. 1986) offers an approach to quantitatively explaining the entire AVIRIS reflectance data in terms of a suite of mineral endmembers. This and other approaches to spatial mapping the distribution of minerals in this data set will be investigated and confirmed in the field.

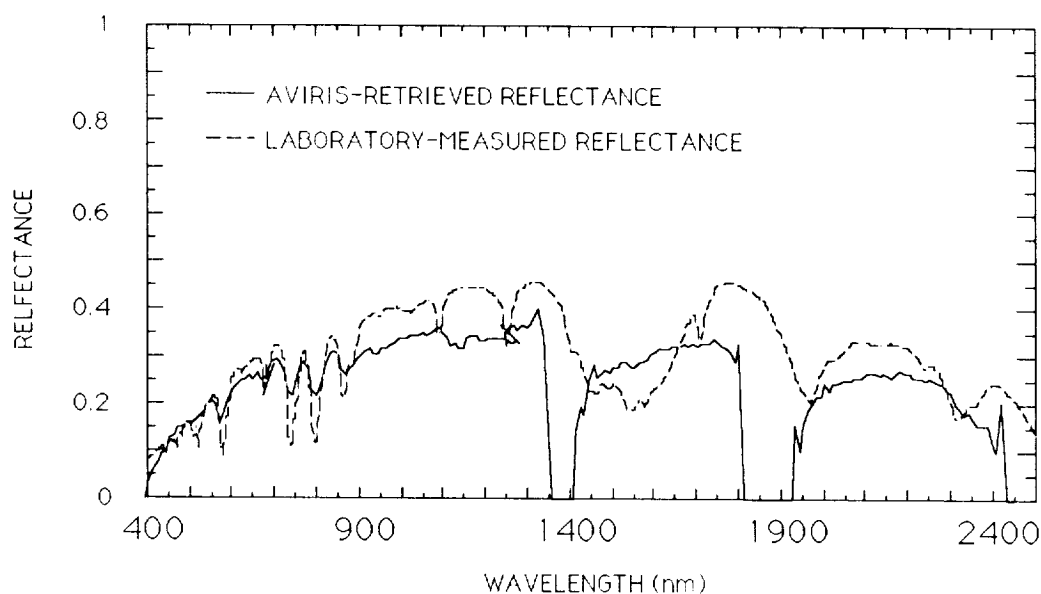


Figure 9. Retrieved reflectance for exposed bastnaesite associated with the Mountain Pass mine and laboratory-measured spectrum.

6.0 CONCLUSION

Reflectance spectra have been retrieved from AVIRIS radiance data using a radiative-transfer-code-based algorithm. In this instance, LOWTRAN 7 was used. To constrain the code, atmospheric water-vapor estimates were derived directly from the AVIRIS radiance data for every spatial element of the imagery. Aerosols, measured at the time of the overflight and the solar-illumination geometry were used to further constrain the code. Algorithms retrieving aerosols and pressure altitude from AVIRIS radiance data at known accuracy and precision are being developed to improve this radiative-transfer-based reflectance recovery in the future. The retrieved reflectances agree with measurement of targets in the field. Accuracy of this retrieval is a function of both the radiative-transfer code and constraints as well as the accuracy of AVIRIS spectral and radiometric calibration. Calculated AVIRIS surface reflectance data offer a quantitative approach to regional geological analysis through determinations of surface mineralogy and lithology at known accuracies and precisions.

7.0 ACKNOWLEDGMENTS

Thanks are due Carol Bruegge who acquired and reduced the atmospherical optical depth data. This research was carried out at the Jet Propulsion Laboratory, California Institute of Technology, under contract with the National Aeronautics and Space Administration.

8.0 REFERENCES

Adams, J.B., M.O. Smith, and P.E. Johnson, Spectral mixture modeling: a new analysis of rock and soil types at the Viking Lander 1 site, *J. Geophys. Res.* 91, 1986.

Bruegge, C.J., In-flight absolute radiometric calibration of the Landsat Thematic Mapper (Published under Kastner), Ph.D. Dissertation, University of Arizona, 1985.

Bruegge, C.J., J.E. Conel, J.S. Margolis, R.O. Green, G. Toon, V. Carrere, R.G. Holm, and G. Hoover, In-situ atmospheric water-vapor retrieval in support of AVIRIS validation, *SPIE Vol. 1298, Imaging Spectroscopy of the Terrestrial Environment*, in press, 1990.

Chrien, T.G., R.O. Green, and M. Eastwood, Laboratory spectral and radiometric calibration of the Airborne Visible/Infrared Imaging Spectrometer (AVIRIS), *SPIE Vol. 1298, Imaging Spectroscopy of the Terrestrial Environment*, in press, 1990.

Conel, J.E., R.O. Green, G. Vane, C.J. Bruegge, R.E. Alley, and B.J. Curtiss, AIS-2 Radiometry and a comparison of methods for the recovery of ground reflectance, in *Proceeding of the Third Airborne Imaging Spectrometer Data Analysis Workshop* (G. Vane, ed.), JPL Publication 87-30, Jet Propulsion Laboratory, Pasadena, CA, 1987.

Conel, J.E., R.O. Green, V. Carrere, J.S. Margolis, R.E. Alley, G. Vane, C.J. Bruegee, and B.L. Gary, Atmospheric water mapping with the Airborne Visible/Infrared Imaging Spectrometer (AVIRIS), Mountain Pass, CA., in *Proceedings of the AVIRIS Performance Evaluation Workshop* (G. Vane, ed.), JPL Pub. 88-38, 21-26, 1988.

Conel, J.E., R.O. Green, V. Carrere, J.S. Margolis, R.E. Alley, G. Vane, C.J. Bruegee, and R.E. Alley, Spectroscopic measurement of atmospheric water vapor and determination of evaporation from land and water surfaces using the AVIRIS, *IGARSS'89 12th Canadian Symposium on Remote Sensing*, 4, 2658-2663, 1989.

Goetz, A.F.H., The Portable Instantaneous Display and Analysis Spectrometer (PIDAS), *Proceedings of the Third Airborne Imaging Spectrometer Data Analysis Workshop* (G. Vane, ed.), JPL Publication 87-30, Jet Propulsion Laboratory, Pasadena, CA, 1987.

Green, R.O., V. Carrere, and J.E. Conel, Measurement of atmospheric water vapor using the Airborne Visible/Infrared Imaging Spectrometer, *ASPRS, Image Processing '89*, 1989.

Kneizys, F.X., E.P. Shettle, G.P. Anderson, L.W. Abrew, J.H. Chetwynd, J.E.A. Shelby, and W.O. Gallery, Atmospheric Transmittance/Radiance; computer Code LOWTRAN 7, AFGL, Hanscom AFB, MA, 1989.

**MATERIAL ABSORPTION BAND DEPTH MAPPING OF IMAGING SPECTROMETER DATA
USING A COMPLETE BAND SHAPE LEAST-SQUARES FIT
WITH LIBRARY REFERENCE SPECTRA**

ROGER N. CLARK,
ANDREA J. GALLAGHER, and GREGG A. SWAYZE
U.S. Geological Survey, MS 964
Box 25046 Federal Center
Denver, CO 80225-0046
(303) 236-1332

ABSTRACT

Mapping of mineral and vegetation absorption features in imaging spectrometer data is demonstrated using a least-squares solution of the total band shape of a reference library spectrum to spectra from the imaging data set. The method removes a continuum from the observed and reference spectra and expands and compresses the reference absorption profile to best fit the observed data. The advantage of the method is that it can map complicated band shapes, like a kaolinite doublet, and fits to all data points comprising the feature. The algorithm computes the band depth for a particular absorption feature, a goodness of fit, and the reflectance level of the continuum at the band center. Images of the band depth and goodness of fit are maps of a specific species. The images from this method show species distribution in significantly better detail and with less noise than simpler methods such as band ratios or band-depth images computed from two continuum and one band center channels. Combinations of mineral absorption features may be used to map geologic units.

INTRODUCTION

Imaging spectroscopy instruments such as AVIRIS have narrow bandwidths in many contiguous spectral channels to accurately define absorption features from a variety of materials. However, such data sets must be analyzed in a spectroscopic sense rather than an imaging sense to derive mineralogic information. Spectroscopists generally analyze individual absorption features in a spectrum, not simply ratios at particular wavelengths. In an effort to develop tools to map species, including minerals, vegetation, or environmental materials, we have developed an algorithm to map any complex absorption feature in a spectrum, given a suitable reference spectrum.

The band ratio is a simple analysis of a spectrum that has been common for at least two decades. The band ratio is sensitive to the relative absorption in a spectrum at two wavelengths. In imaging spectrometer data sets, the wavelengths can be chosen close together such that the ratio is particularly sensitive to a given absorption band.

However, it is also sensitive to sloping spectra, so a ratio is not a foolproof indicator of the presence of an absorption band.

BAND-DEPTH ANALYSIS

A band-depth analysis using three spectral channels with imaging spectrometer data was shown by Clark *et al.* (1988). In that case, the absorption band depth, D , was defined relative to its continuum:

$$D = 1 - R_b/R_c \quad (\text{eqn 1})$$

where R_c is the reflectance of the continuum at the band center, and R_b is the reflectance at the band center. The definition originates from Clark and Roush, (1984).

The band depth images from Clark *et al.*, 1988 were quite noisy, mostly due to the noisy AVIRIS data during the 1987 flight season. However, the method still is inherently susceptible to noise, because only three channels are used, and only one at (or near) the band center.

In practice most absorption features consist of many spectral channels. For example, the hematite 0.9- μm absorption extends from ~ 0.75 to $\sim 1.3 \mu\text{m}$, or about 56 AVIRIS channels. The kaolinite doublet covers about 13 AVIRIS channels in the 2.2- μm region. Mapping an absorption feature at say 2.2 μm using only three channels (two continuum and one channel at 2.2 μm) is insensitive to either a kaolinite doublet or the singlet montmorillonite feature (and other similar absorptions). Examining all channels comprising the feature for the proper shape would more accurately map the absorption.

In practice, absorption band shapes, such as the kaolinite doublet, are well recognized. The process of absorption band analysis is to first remove a continuum (Figure 1, and see Clark and Roush, 1984; Clark *et al.*, 1988). Once the continuum is removed, a band can be characterized by determining how well the feature matched a reference library spectrum.

A typical spectrum from an imaging spectrometer data set will include other materials in the scene, either in an areal mixture (e.g. vegetation) or in an intimate mixture (e.g. mineral grains in a rock or soil). Commonly, although not always, the pure mineral reference spectrum will have absorption features stronger than observed in flight data. Figure 1 shows a comparison between reference spectra and flight data of kaolinite. Any comparison between the reference and flight data must be able to change the spectral contrast of one of the spectra in order to match the other. The most accurate way to do this would be using a radiative transfer model like that from Hapke (1981), but it is also the most compute intensive.

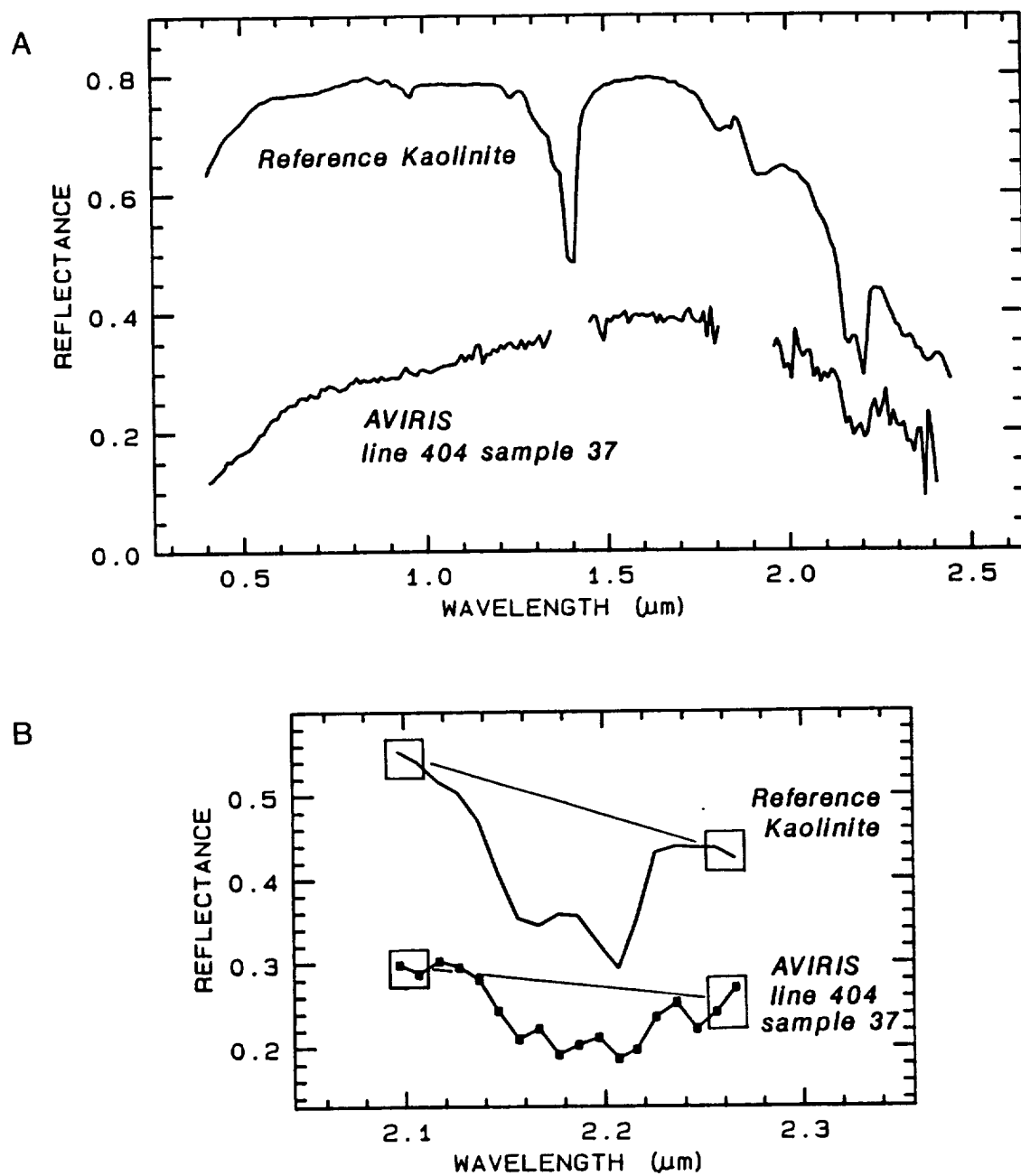


Figure 1. A spectrum from the Canon City AVIRIS flight data is compared to a library reference kaolinite spectrum. The kaolinite spectrum has been convolved to the spectral resolution and sampling interval of the 1989 AVIRIS flight data. A) the full spectrum. B) the isolated kaolinite 2.2- μm doublet is shown with the continua chosen for each spectrum. In this Figure, the absorptions in the reference spectrum are stronger than in the flight data.

A simpler model to change a continuum-removed-absorption feature's contrast is by a constant added to the data at all wavelengths. In this case, the feature would not be represented properly if the band saturation changed significantly, from say a major change in grain size between the reference and observed spectra. The algorithm presented here uses the simple case of an additive component because it is computationally fast compared to a full radiative transfer model. The method can easily be adapted to the full model however, or even a method that examines the band depth and chooses an appropriately saturated absorption feature from a library of materials at several grain sizes.

The algorithm, which we call the Band Mapping Algorithm, Version 1 (BMA1) first removes a straight line continuum from the library reference spectrum using channels on each side of the absorption feature that is to be mapped (e.g. Figure 1b). The continuum is removed from the observed spectrum in the flight image using the same method and spectral channels. The user may select several channels on each side of the band so that noise in the continuum is averaged. The continuum is removed by division:

$$L_c(\lambda) = \frac{L(\lambda)}{C_l(\lambda)} \quad \text{and} \quad O_c(\lambda) = \frac{O(\lambda)}{C_o(\lambda)}, \quad (\text{eqn 2 a and b})$$

where $L(\lambda)$ is the library spectrum as a function of wavelength, λ , O is the observed spectrum, C_l is the continuum for the library spectrum, C_o is the continuum for the observed spectrum, L_c is the continuum removed library spectrum, and O_c is the continuum removed observed spectrum.

The contrast in the reference library spectrum absorption feature is modified by a simple additive constant, k :

$$L_c' = \frac{L_c + k}{1.0 + k}, \quad (\text{eqn 3})$$

where L_c' is the modified continuum removed spectrum that best matches the observed spectrum. This equation can be rewritten in the form:

$$L_c' = a + bL_c, \quad (\text{eqn 4})$$

where

$$\begin{aligned} a &= k / (1.0 + k), \text{ and} \\ b &= 1.0 / (1.0 + k). \end{aligned} \quad (\text{eqn 5})$$

In Equation 4 we want to find the a and b that gives a best fit to the observed spectrum O_c . The solution is done using standard least squares:

$$a = (\sum O_c - b \sum L_c) / n,$$

$$b = \frac{\sum O_c L_c - \sum O_c \sum L_c / n}{\sum L_c^2 - (\sum L_c)^2 / n},$$

and

$$k = (1-b)/b,$$

(eqn 6)

where n is the number of spectral channels in the fit.

Figure 2 shows an example reference kaolinite spectrum and the observed spectrum from Figure 1, where the continua have been removed and the library spectrum fitted to the observed spectrum by the above method. By fitting a library reference spectrum to each spectrum in an imaging spectrometer data set, a map of the material can be produced. The algorithm produces a band depth, indicating its spectral abundance in the image, and a goodness of fit which gives a measure of confidence of the accuracy of the resulting map.

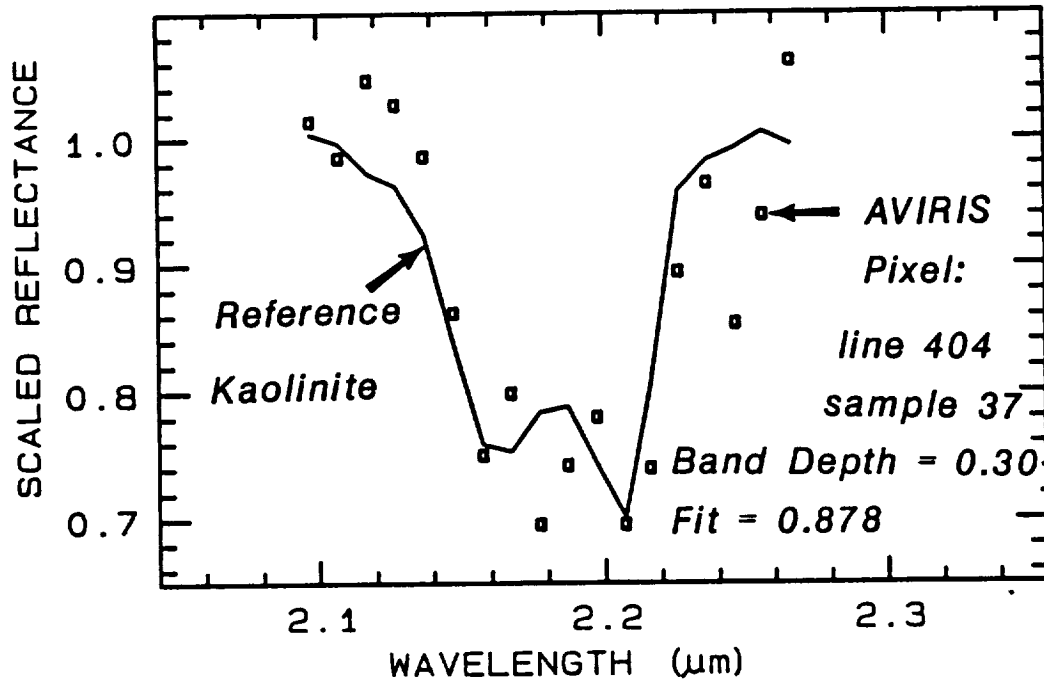


Figure 2: The kaolinite spectra from Figure 1b have had continuum removed and the library spectrum fitted to the observed AVIRIS spectrum. While a single spectrum may not show the kaolinite doublet structure well, an average of several pixels from this region does.

MINERAL MAPPING

Absorption Band Mapping was applied to the AVIRIS image taken over Canon City, Colorado using the U. S. Geological Survey digital spectral library. The AVIRIS data were obtained on September 24, 1989 at 1 p.m. MDT, so the sun angle was relatively high. The radiance data were corrected to ground reflectance using large uniform areas on the ground as calibration targets. The ground sites were calibrated using hand samples and the same spectrometer that was used to measure the spectral library samples.

To properly fit a reference spectrum to the flight data, the data sets must be sampled at the same wavelengths and resolution. The USGS spectral library was spectrally convolved to the resolution of the flight data and sampling values as supplied by the JPL AVIRIS investigators (Green, private communication).

The images processed cover an area of 11 km wide by about 14 km long (Figure 3a and Slide 14; in the images, north is to the upper left). In the lower portion of the image, Phanerozoic dolomite, limestone, arkose, sandstone and shale rock units form gently southwest dipping hogbacks on the east limb of a broad syncline. These rock units are truncated by northwest trending faults which juxtapose them against Proterozoic meta-igneous and gneiss rock units in the upper right part of the image.

Example mineral maps using three different techniques are shown in Figure 3. The fastest method, a ratio of 2 channels, used to map kaolinite, appears rather noisy (Figure 3b), as does the 3-channel band-depth computation (Figure 3c). The least-squares method shows less noise and more detail (Figure 3d).

DISCUSSION

Many materials can be mapped with the algorithm. For example, Figure 4 shows maps of dolomite, calcite, green vegetation and goethite. Maps of three materials can easily be combined to produce color images. Clark et al. (1988) called such images Color-Composite-Band-Depth Images (CCBDI). Slides 15 through 18 illustrate such maps. The mapped minerals correlate very well with geologic maps of the region.

For example, this method is so sensitive to absorption band position and geometry, that it can distinguish between dolomite and calcite which have nearly identical absorption bands shifted from each other by only 20 nanometers at AVIRIS spectral resolution. Figure 5 shows an averaged AVIRIS spectrum of the dolomite unit compared to laboratory spectra for dolomite and a field sample of the dolomite unit. Note the presence of a strong 2.3- μm region absorption in the AVIRIS data that matches well with the laboratory spectra. Figure 4a and red in Slide 15 highlight flatirons and erosional outliers of dolomite overlying basement in the upper right portion of the image. Figure 4b and green in Slide 15 show a thin sinuous outcrop of limestone trending across the lower central portion of the image. Although the dolomite image also

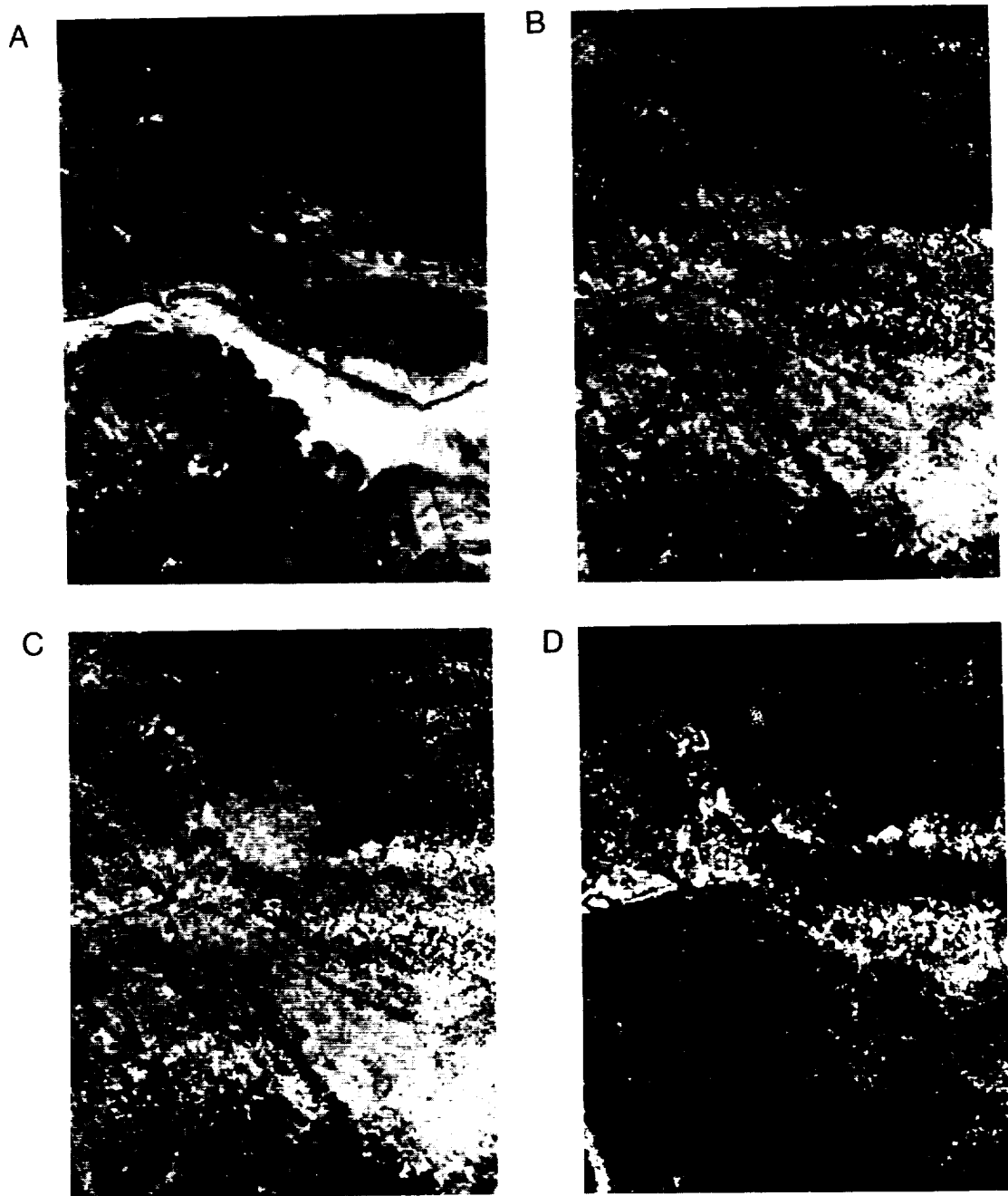


Figure 3: A) A single band image of the Canon City scene. Canon City is at the lower part of the image. North is to the upper left. B) A simple band ratio image ($2.25/2.205 \mu\text{m}$) shows some detail related to kaolinite occurrence. C) A simple three-point band-depth image (continuum points at 2.12 and $2.25 \mu\text{m}$ and band center at $2.205 \mu\text{m}$) shows detail similar to the ratio method. D) The least-squares band map image method is shown. The image is the band-depth times the goodness of fit. The least-squares method isolates very well the kaolinite exposures. In B, C and D, white corresponds to stronger kaolinite signature.

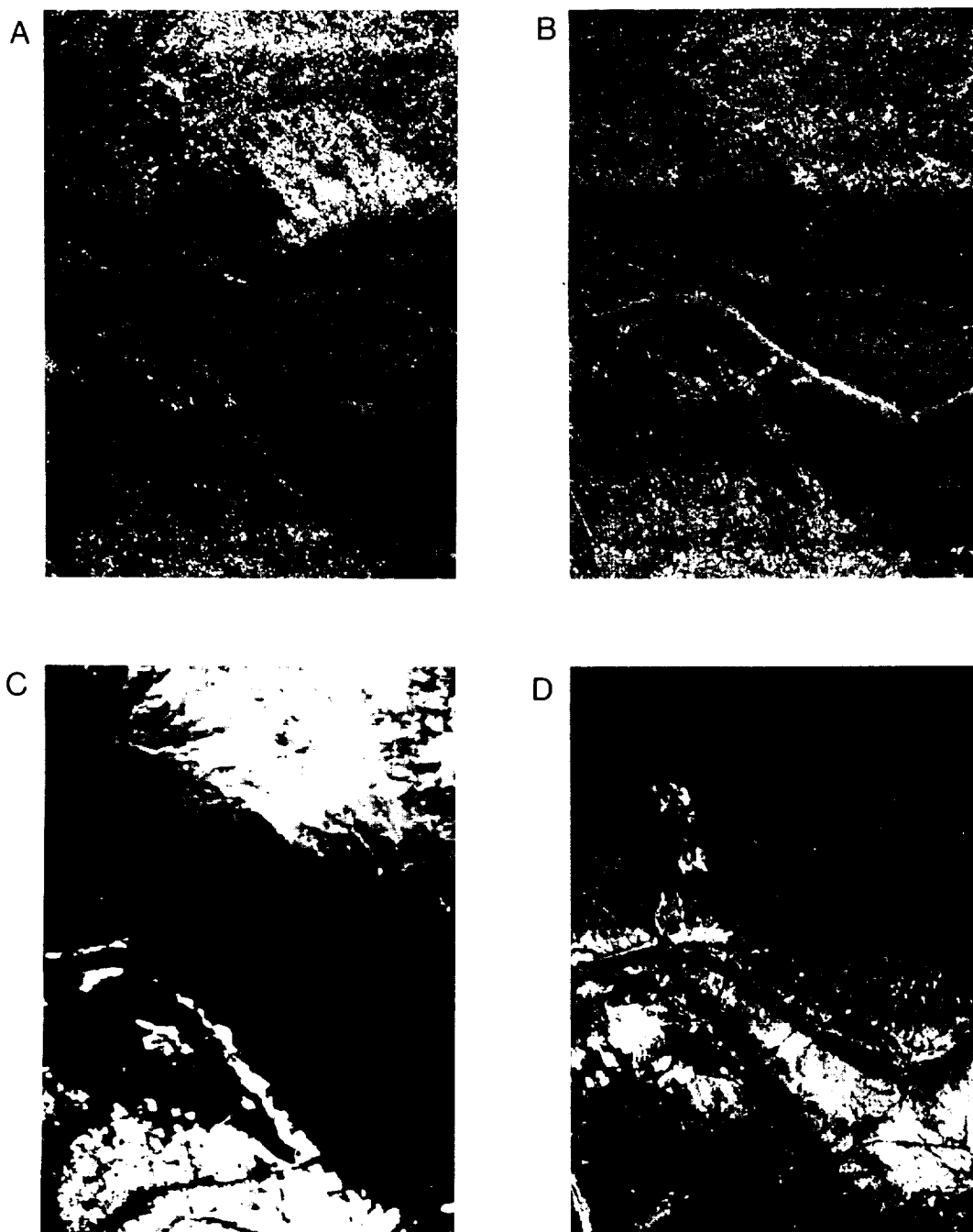


Figure 4: Band maps for 4 materials are shown. Each image is the band-depth times the goodness of fit, and white corresponds to greater signature. A) Dolomite. B) Calcite. C) Green vegetation. D) Goethite. Note that the band-depth maps separated dolomite (upper right of center) from calcite (thin line below center from left to right). In addition, note that the region of dolomite exposure shows no kaolinite (compare to Figure 3d). Also see the color slides.

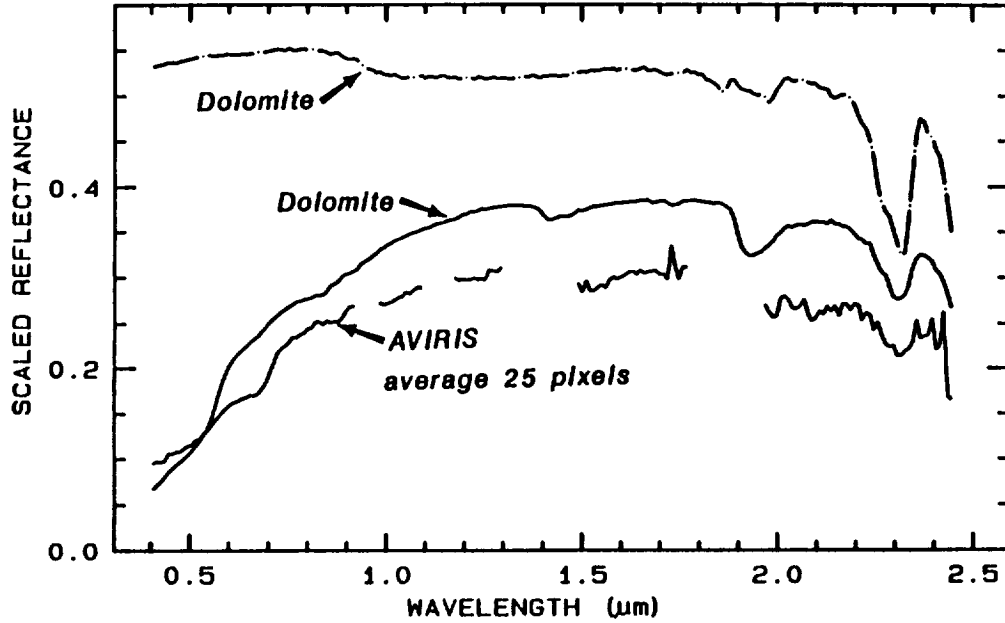


Figure 5: An average spectrum of 25 pixels from the Canon City AVIRIS image (bottom curve) compared to a reference library spectrum of dolomite (dashed-dotted curve, top) and a spectrum of a rock sample from the dolomite rock unit seen in Figure 4a. Spectral regions of atmospheric absorption have been deleted for clarity in the averaged AVIRIS spectrum. The rock unit and AVIRIS spectra both show a dolomite absorption band at $2.3 \mu\text{m}$.

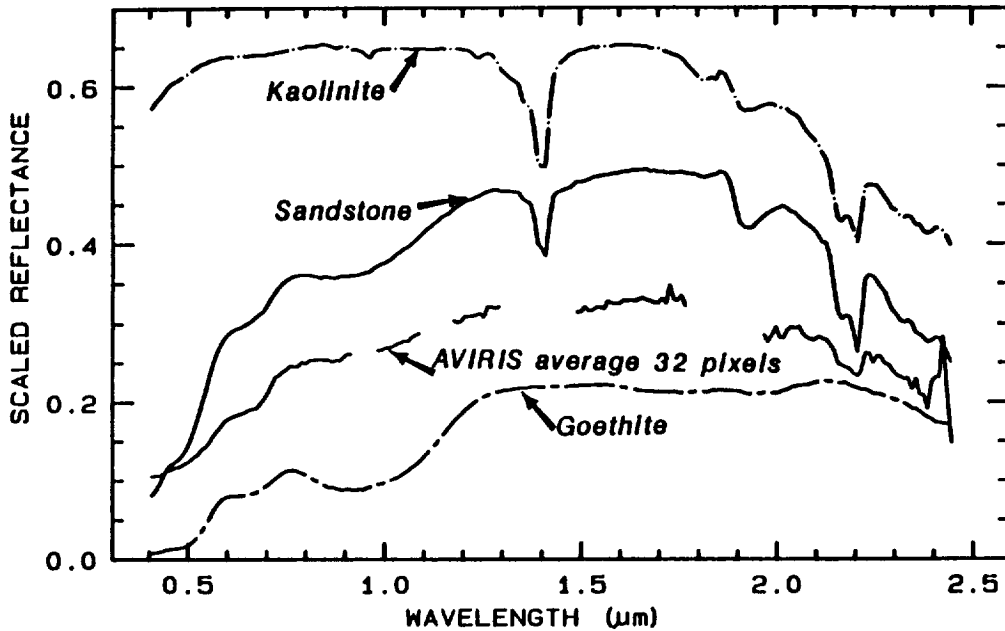


Figure 6: An average spectrum of 32 pixels from the Canon City AVIRIS image compared to reference library spectra of kaolinite and goethite (dashed-dotted curves) and a spectrum of a rock sample from the sandstone unit seen in Figure 3d. Spectral regions of atmospheric absorption have been deleted for clarity in the averaged AVIRIS spectrum.

shows this limestone unit because of noise in the signal, it does so with less intensity and can be adequately differentiated by the goodness of fit.

Because the program can fit complex absorption bands like the kaolinite doublet, it can differentiate this mineral from montmorillonite, illite, and other clay minerals having single absorptions in the 2.2- μm region. Figure 6 shows an averaged AVIRIS spectrum of the sandstone unit compared to laboratory spectra of kaolinite, goethite, and a field sample of the sandstone unit. Figure 3d and the blue in Slides 15, 16, and 18 show the presence of kaolinite in the sandstone and arkose units where feldspars have been altered. In Slide 18, montmorillonite (red) and illite (green) highlight and differentiate several shale units. This suggests the possibility of mapping subtle compositional variations within individual rock units.

This method of mapping mineral absorptions is much less sensitive to noise in individual channels. For instance, the kaolinite spectrum in Figure 2 has the strongest feature in the Canon City image, yet the noise in the spectrum is quite high. In general, the Canon City AVIRIS data have a signal to noise of about 30 for a reference reflectance of 0.5 in the 2.2- μm region (Figure 7). The typical albedo in the image is about 0.25 or less, so the signal to noise to map the kaolinite doublet is only about 15. Examining regions of the image where significant kaolinite is mapped, the band-depth of about 4% is mapped. A signal to noise of only 15 in the spectrum corresponds to mapping the absorption band when the feature strength is about one-half the signal to noise of a single channel. The method is able to map the feature because many channels are used, effectively increasing the signal to noise for feature detection.

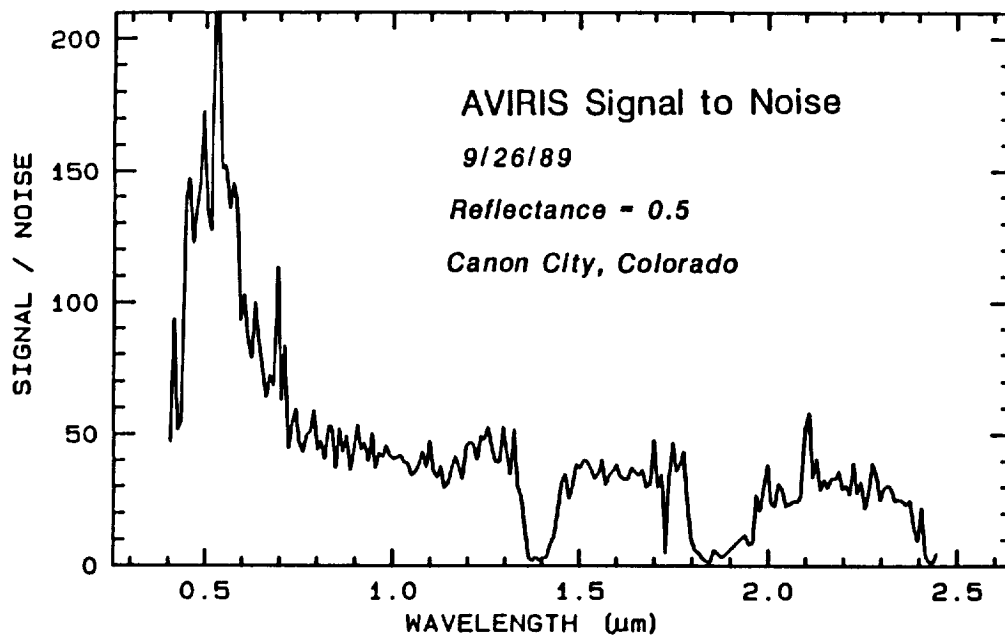


Figure 7: The signal to noise of AVIRIS on September 26, 1989 for a reference reflectance of 0.5.

The method is sensitive enough to map different regions as a kaolinite versus a halloysite-like feature. Although such subtle spectral differences have yet to be confirmed by field work, it illustrates the power of fitting to an entire spectral feature compared to more simple band minima and width methods.

CONCLUSIONS

We have developed a new method of image processing which can map absorbing materials using a least-squares linear regression between imaging data and a reference spectrum. This method requires a reference spectrum of the material that is accurately convolved to the spectral resolution and sampling of the flight instrument. Our analyses have shown that this method gives substantially improved results over simpler techniques like band ratios or 3-point band-depths. It should be pointed out that this technique can be used to map any material, not just minerals, as long as there are diagnostic absorption bands in the spectral region covered by the imaging instrument.

REFERENCES

- Clark, R.N. and T.L. Roush, 1984. Reflectance Spectroscopy: Quantitative Analysis Techniques for Remote Sensing Applications, *J. Geophys. Res.*, **89**, 6329-6340.
- Clark, R.N., B.J. Middlebrook, G.A. Swayze, K.E. Livo, D.H. Knepper, T.V.V. King, and K. Lee, 1988. Calibration and Evaluation of AVIRIS Data: Cripple Creek in October 1987, *Fourth Airborne Imaging Spectrometer Workshop Proceedings*, JPL Publication 88-38.
- Hapke, B., 1981. Bidirectional reflectance spectroscopy 1. Theory, *J. Geophys. Res.*, **86**, 3039-3054.

SLIDE CAPTIONS

- Slide No. 14. A false-color-infrared composite of the Canon City AVIRIS scene.
- Slide No. 15. A Color-Composite-Band-Depth Image (CCBDI) for Canon City: blue is kaolinite, green is calcite, and red is dolomite.
- Slide No. 16. A Color-Composite-Band-Depth Image (CCBDI) for Canon City: blue is kaolinite, green is montmorillonite, and red is goethite.
- Slide No. 17. A Color-Composite-Band-Depth Image (CCBDI) for Canon City: blue is montmorillonite, green is goethite, and red is hematite.
- Slide No. 18. A Color-Composite-Band-Depth Image (CCBDI) for Canon City: blue is kaolinite, green is illite, and red is montmorillonite.

AVIRIS DATA FOR THE DOLLY VARDEN MOUNTAINS, NEVADA: HIRIS ANALOG

K. S. KIEREIN-YOUNG, A. F. H. GOETZ, J. A. ZAMUDIO, and B.-C. GAO

Center for the Study of Earth from Space/CIRES and Geological Sciences,

University of Colorado, Boulder, CO 80309

ABSTRACT

A HIRIS analog data set is being produced from Dolly Varden, Nevada AVIRIS data. HIRIS parameters will be simulated and the data will be used to investigate handling and analysis of HIRIS data. The Dolly Varden area contains interesting geology, vegetation and topographic features which will allow use in a variety of disciplines. The first simulation of a HIRIS data set was produced by calibrating and registering three overlapping AVIRIS flight lines. Problems were encountered because the three flight lines were obtained at different sun angles and atmospheric conditions. Each flight line showed a 10-15% variation in radiance across track. This variation was dominated by shadowing effects resulting from the scan angle of AVIRIS. Rayleigh scattering and vignetting also contribute to the radiance differences, but not by more than 1% each. Once the radiance differences are removed, the resulting HIRIS analog data set will allow for scientific and equipment preparations.

INTRODUCTION

A HIRIS analog data set is being produced for use in a variety of disciplines. The data will simulate as best as possible HIRIS coverage, spectral resolution, spatial resolution and signal-to-noise ratio. It will be used to gain experience in data handling and analysis of a data set the size of a HIRIS scene. Both hardware and software requirements can be determined using these data. Each scene requires approximately 290 Mbytes of disk space plus additional space for analysis. The HIRIS analog data set will be available for distribution to the scientific community.

The High Resolution Imaging Spectrometer, HIRIS, will be flown on the EOS platform slated for launch in 1997. It has a ground instantaneous field of view of 30 meters and a swath width of 24 km. It has a spectral range of .4-2.5 μm , with an average spectral sampling interval of 10 nm. The data encoding for HIRIS is 12 bits instead of the 10 bits of AVIRIS to account for its higher signal-to-noise ratio (Goetz and Herring, 1989).

The Dolly Varden AVIRIS data were chosen for the creation of the HIRIS analog because it was the only data set currently available with a large enough swath coverage to simulate HIRIS. The Dolly Varden area also contains interesting geology, a variety of vegetation coverage, and has a large elevation variation. The three AVIRIS flight lines shown in Figure 1 were used to create the HIRIS swath. They were flown from south to north, and overlap by approximately one kilometer. The AVIRIS data were obtained June 2, 1989 within a period of one hour, before solar noon, and the sun was in the southeast quadrant.

SETTING

The Dolly Varden Mountains and Currie Hills are located in the semi-arid environment of the northeastern Great Basin. The area ranges in elevation from 1750 to 2600 meters. Other than some high relief areas of bare outcrop, vegetation cover typically ranges from 20% to 50%.

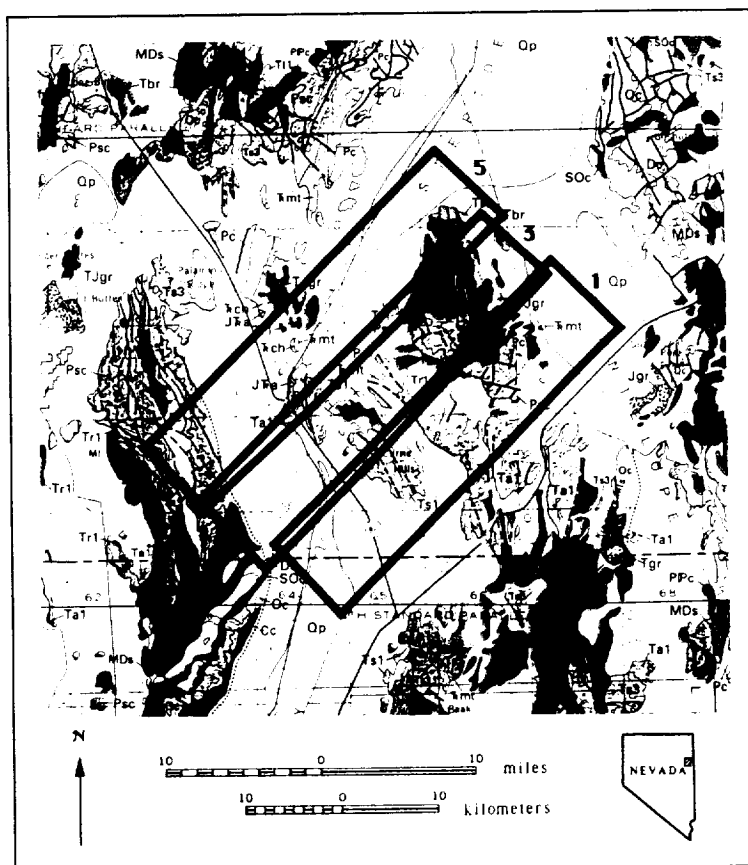


Figure 1. Location and geologic map of the Dolly Varden AVIRIS flight lines.

In some places along drainages and on high, north-facing slopes, vegetation cover approaches 100%. Sagebrush is present at lower elevations and piñon pine and juniper are prevalent at elevations above 2000 meters. Also, some deciduous vegetation is present around springs in the area.

The study area contains a variety of geologic materials exposed at the surface. A sequence of Late Paleozoic through early Jurassic sedimentary rocks includes limestone, dolomite, sandstone, siltstone and shale (Coats, 1987). Igneous rocks in the area include a two-phase monzogranite and quartz monzonite intrusion and volcanic rocks with compositions ranging from andesite to quartz latite to rhyolite. The igneous intrusion produced a calc-silicate contact metamorphic aureole in the sedimentary section. Minerals such as andradite, diopside, tremolite, epidote, serpentine, sepiolite and saponite resulted from this metamorphism. Alluvial fans slope down from the ranges to the relatively flat valley floors. Cenozoic lacustrine deposits occur locally, especially to the northeast of the Dolly Varden Mountains. A playa lies along a generally dry stream bed to the northwest of the range.

CALIBRATION

The first step in producing the HIRIS analog data set was to reduce the 15-meter AVIRIS pixels to 30-meter HIRIS resolution. A HIRIS pixel was created by averaging four pixels in the AVIRIS data. Next, five AVIRIS segments were appended to produce three long flight lines of data, which then were registered together. A problem encountered in trying to produce the HIRIS data set was that the three runs were obtained at different times of day and different sun angles. Therefore, the three runs could not be registered together without some kind of calibration that would account for the differences in atmospheric scattering and shadowing. As a first approximation, areas in the overlapping parts of the images were used to calibrate the outer two runs, Run 1 and Run 5, to the center run, Run 3, using gains and offsets. The gains and offsets were calculated using a method similar to the empirical line method used for

conversion to reflectance. Areas in the center run were used as the reference spectra and the other runs were calibrated by applying gains and offsets. The offsets that were applied to the outer runs are shown in Figure 2. These curves look like solar radiance curves indicating that the calibration is adding or subtracting radiance. This is due to differential Rayleigh scattering because of differences in the solar zenith angles between the three runs. Table 1 shows the values for the solar zenith angles for the three runs calculated based on the latitude, longitude, date and time.

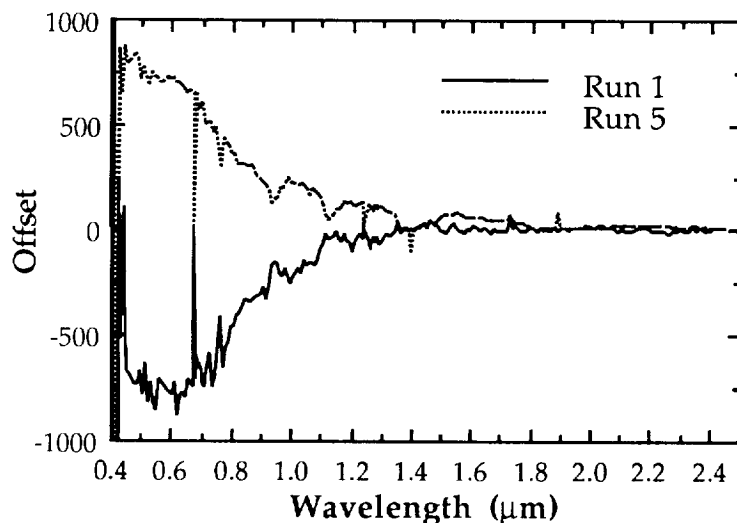


Table 1. Solar zenith angles.

Run 1	21.94°
Run 3	19.73°
Run 5	18.27°

Figure 2. Offsets for calibration to Run 3.

Once the three runs were calibrated for atmospheric differences, the empirical line method was used to convert the data to reflectance (Conel et al., 1987). This involves calculating gain and offset values for each band based upon reflectance measurements taken from bright and dark targets under the same illumination conditions as the AVIRIS data. For this study, a dark andesite flow just to the southeast of the range and a bright playa to the northwest of the range were used as calibration targets. Several field spectra were taken for each target and then averaged and used in the calibration. The calibrated reflectance flight lines were registered together, producing a HIRIS image of 800x800 pixels (see Slide 19). The seams between the three flight lines were smoothed by averaging 10 pixels with a ramp function.

COMPARISON OF SPECTRA

Figure 3 compares reflectance spectra from the same area taken by a Geophysical and Environmental Research field spectrometer, from AVIRIS and from the HIRIS analog. The spectra have been vertically offset for clarity and the 1.4 and 1.9 μm water bands have been omitted. A CO_3 absorption feature around 2.31 μm is apparent in all spectra as are Fe absorption features shortwards of .7 μm . The AVIRIS pixel apparently included relatively more iron oxide as the Fe features in its spectrum are deeper. The AVIRIS and HIRIS spectra have two peaks around 0.94 and 1.13 μm that are due to over-correction for atmospheric H_2O vapor. This over-correction results from the calibration targets being located about 500 m lower in elevation than the pixel sampled in Figure 3. When using calibration targets over which there is greater atmospheric attenuation than over a particular pixel, the conversion to reflectance produces peaks in the spectrum at the atmospheric bands.

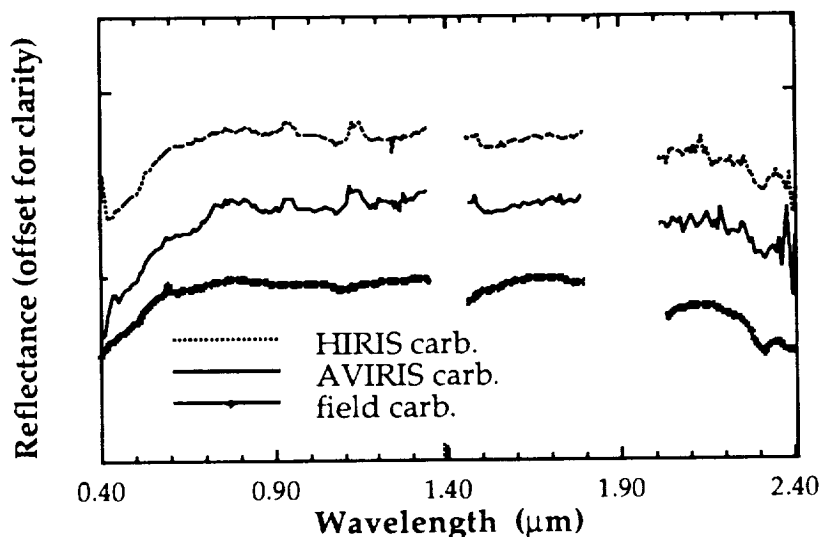


Figure 3. HIRIS analog, AVIRIS, and field spectra for a carbonate rock.

ATMOSPHERIC EFFECTS

Because the field of view of HIRIS is 1.8° while AVIRIS is 30° , atmospheric effects which exist across an AVIRIS scene will not greatly affect the HIRIS data. Therefore, the atmospheric effects in the AVIRIS data must be removed in order to simulate a HIRIS scene. Column averages every 30 pixels were obtained for each AVIRIS flight line to investigate the radiance changes across the flight lines. The column averages across each run show a 10-15% change in radiance from one side of the flight line to the other. Vignetting causes a reduction in radiance at the edges of the images, but is only a 1-2% effect. Figure 4 shows the column averages for Run 3.

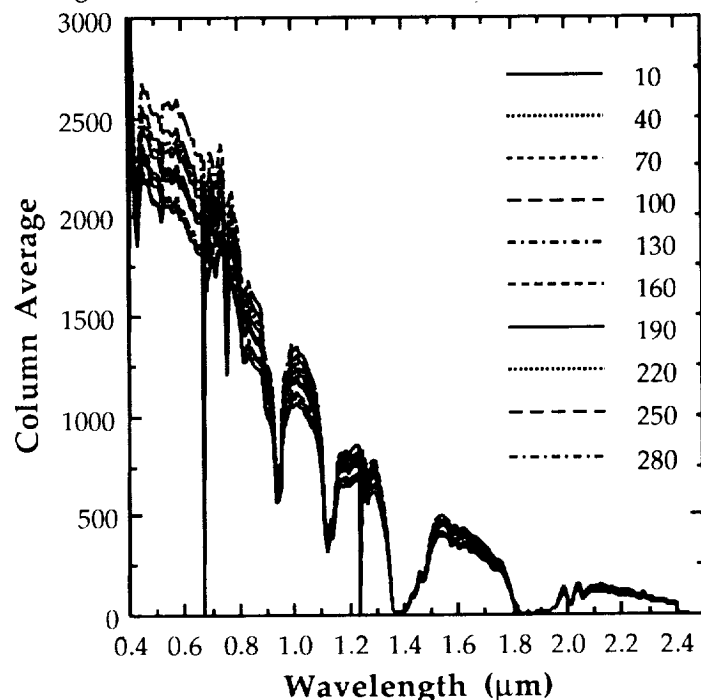


Figure 4. Column averages across Run 3.

LOWTRAN7 was used to estimate the contribution of Rayleigh and aerosol scattering to the radiance variations across the scenes. Path length changes due to scan angle causes changes in Rayleigh and aerosol scattering. LOWTRAN7 was used to simulate radiances at the 20 km AVIRIS altitude by assuming that the solar zenith angle was 20 degrees, the ground elevation was 1.8 km, and the relative azimuthal angle between the solar and the observational directions was 90 degrees. Two observational geometries were used: nadir and off-nadir by 15

degrees. In two case studies, a rural aerosol model with a visibility of 23 km and Lambertian surface reflectances of 0.1 and .3 were assumed. Two other case studies assumed the same surface reflectance values but no aerosol. The calculated radiances in the 0.4-1.0 μm spectral region at the off-nadir viewing geometry were greater than the corresponding nadir geometry by less than 1% in all four cases. These results indicate that the observed radiance differences in the AVIRIS flight lines are not caused by atmospheric path radiance effects only.

Due to the orientation of the AVIRIS flight lines, the instrument looked either into or away from the sun during its scanning. When AVIRIS scanned toward the sun, it received a lower radiance because it was viewing shadows. When it scanned away from the sun, AVIRIS received a higher radiance because it did not view as many shadows. The changing viewing angles caused different amounts of shadow to be seen, and therefore, different radiance values are obtained across a scene. Also, because of the differing solar zenith angles, the overall radiances for each flight line are different. The run with the largest solar zenith angle has the most shadows in its data and the lowest radiance. The run with the smallest zenith angle has the highest radiance due to the least amount of shadows. It was concluded that the observed radiance differences across individual runs and between runs were dominated by shadowing effects.

DISCUSSION

This has been the first attempt at creating a HIRIS analog data set. Currently, methods for removing the atmospheric effects are being worked on to allow for a better simulation of a HIRIS scene. An attempt to correct each pixel for radiance variations due to the differing sun angles and scanning effects is in progress. A problem exists in trying to simulate the signal-to-noise ratio of HIRIS with AVIRIS data because HIRIS has 30 times the integration time per pixel than AVIRIS. The expected signal-to-noise ratio for HIRIS ranges between 150-400 for .5 reflectance. From the AVIRIS derived HIRIS data, the signal-to-noise ratio calculated for a playa with .5 reflectance ranges from 50-200. Therefore, the HIRIS signal-to-noise cannot be exactly simulated. This HIRIS analog data set will allow for experience in data handling and analysis of such a large amount of data and will be distributed to the scientific community.

REFERENCES

- Coats, R.R., 1987. Geology of Elko County, Nevada. Nevada Bureau of Mines and Geology Bulletin 101.
- Conel, J.E., R.O. Green, G. Vane, C.J. Bruegge, R.E. Alley, and B.J. Curtiss, 1987. Airborne Imaging Spectrometer-2: Radiometric Spectral Characteristics and Comparison of Ways to Compensate for the Atmosphere. Imaging Spectroscopy II, Proceedings of SPIE-Society of Photo-Optical Instrumentation Engineers, vol. 834, pp. 140-157.
- Goetz, A.F.H. and M. Herring, 1989. The High Resolution Imaging Spectrometer (HIRIS) for EOS. IEEE Transactions of Geoscience and Remote Sensing, vol. 27, pp. 136-144.
- Kneizys, F.X., E.P. Shettle, L.W. Abreu, J.H. Chetwynd, G.P. Anderson, W.O. Gallery, J.E.A. Selby, and S.A. Clough, 1988. Users Guide to LOWTRAN 7. AFGL-TR-88-0177.

TECHNIQUES FOR AVIRIS DATA NORMALIZATION IN AREAS WITH PARTIAL VEGETATION COVER

JAMES K. CROWLEY, U.S. Geological Survey, MS 927, Reston, Virginia 22092

ABSTRACT

Several normalization procedures were developed to aid in analyzing AVIRIS data of the Iron Hill, Colorado carbonatite complex. The procedures include 1) a flat field correction suitable for use in areas with moderate vegetation cover, 2) a method for approximate calibration to percent reflectance based on the flat field normalization spectrum, and 3) a first order vegetation "removal" strategy. Each procedure uses relative absorption band depth images to provide a basis for correcting the AVIRIS data without a priori knowledge of surface targets.

INTRODUCTION

Semiarid areas with moderate to heavy vegetation cover present special problems for airborne imaging spectrometer data analysis. Available ground targets for use in spectral calibration commonly are very small or contain patchy vegetation that is difficult to characterize. Moreover, few image pixels have an "average" amount of vegetation cover so that simple first order corrections (e.g. Kruse, 1988) to remove atmospheric and solar components in radiance measurements generally cause serious distortions in the spectral curve shapes.

This paper describes several methods of data analysis applied to Airborne Visible/Infrared Imaging Spectrometer (AVIRIS) data of the Iron Hill carbonatite complex in southwestern Colorado. The Iron Hill carbonatite is dolomitic and has relatively low rare-earth element (REE) content on the order of 100-500 ppm (Nash, 1972). Associated alkaline igneous rocks include pyroxenite, uncomphagrite, nepheline syenite, ijolite and fenitized granite. Visible and near-infrared spectra of samples from the carbonatite display CO₂ absorption bands centered near 2.32 μm , reflecting the dolomitic composition, an intense, broad Fe²⁺ doublet in the 1.25 μm region, and weak Nd³⁺ features located between 0.7 and 0.9 μm . Where exposed, the alkaline rocks exhibit Mg-OH features in the 2.3-2.4 μm region (Rowan and others, 1986). More commonly, however, the alkaline rocks are marked by dark micaceous soils that have weak Mg-OH absorption features which are further diluted by partial vegetation cover. The vegetation in the area is highly variable in amount, with

sagebrush and grasses typically comprising about 30-80 percent of most upland surfaces. Dense coniferous tree cover occurs on the highest elevations, and the presence of a broad absorption band near 2.31 μm in the sagebrush and conifer spectra presents a significant problem for discerning the CO_2 features of the carbonatite.

Three full segments and one partial segment of AVIRIS data were acquired over Iron Hill in September, 1989. The data were radiometrically corrected using laboratory calibration measurements (Vane and others, 1987) and provided in the JPL unresampled spectral format. The data analysis procedures described below consist of a series of FORTRAN programs within the REMAPP image processing software system developed at the U.S. Geological Survey.

FLAT FIELD CORRECTION

Flat field correction refers to a data normalization technique in which the radiance spectrum of a ground target is divided through an entire data set to remove the atmospheric and solar radiance components. Previous flat field corrections have typically involved the selection of a ground target that is 1) situated near the average scene elevation, and 2) relatively free of mineral and vegetation absorption features. An additional consideration is the size of the flat field target, as the use of targets which are too small can diminish the effective signal to noise of the data. An alternative to the use of a single ground target that avoids the signal to noise problem is the use of an average spectrum of the entire data set (Kruse, 1988).

For the Iron Hill study area a classification technique using relative band depth (RBD) images (Crowley and others, 1989) was developed to identify pixels that exhibit both low vegetation cover and low mineral absorption intensity. The technique locates and utilizes individual pixels distributed over the entire image, hence it has been termed a "distributed" flat field (DFF) correction. It avoids the necessity for large uniform ground targets, and incorporates a sufficient number of pixels to avoid signal to noise degradation.

To perform the distributed flat field correction for the Iron Hill study area, an RBD image was constructed by using AVIRIS channels 18+40/29 to provide an index of green vegetation cover. Similarly, RBD index images were generated to map 2.20 μm absorption (channels 192+206/199), characteristic of many clays and other Al-OH-bearing minerals, and 2.315 μm absorption (channels 203+217/210), commonly associated with dolomitic carbonate rocks and Mg-OH-bearing minerals. The classification procedure first examined the vegetation index RBD image to identify pixels that have low vegetation cover. Corresponding pixels that have low DN values in both the 2.20 and 2.315 RBD images (i.e., weak or absent mineral absorption) were then averaged to produce a normalization spectrum for use in the DFF correction. In principle any number of

RBD images can be combined in the procedure. In the Iron Hill study area, approximately 200 pixels were identified in the DFF classification procedure, which was a substantially greater number than could be obtained from any single usable ground target. Figure 1 shows three AVIRIS spectra extracted from the DFF corrected data set, including an area within the carbonatite stock, and two different exposures of clay-rich soils. Notice that the DFF correction permits kaolinitic clays to be distinguished from illite/smectite clays, a separation which was not possible using an ordinary flat field correction based on a single discrete ground target.

CALIBRATION TO REFLECTANCE USING THE DFF SPECTRUM

Airborne imaging spectrometer data have been successfully calibrated to percent reflectance by using ground spectral measurements of bright and dark calibration targets (Roberts and others, 1985). To perform this type of calibration, DN's of the target areas are regressed against the known ground reflectance values, providing a gain and offset correction for each spectral channel. Problems with the method include the difficulty in locating suitable ground targets and the practical problem of measuring targets in situ for every dataset.

An attempt was made to circumvent these problems by using the distributed flat field normalization spectrum obtained from the entire image as described above. If this spectrum is taken to represent a spectrally flat target having some estimated brightness, an approximate calibration to reflectance can be performed. Experience indicates that the actual brightness of most soil/vegetation mixtures is probably in the range of about 25-50 percent reflectance. Thus, if an intermediate brightness level is selected, for example 35 percent, a scalar can be calculated for each AVIRIS channel by dividing this assumed reflectance by the actual DFF spectrum DN. The scalars may then be applied channel by channel to calibrate the radiance data to reflectance. Figure 2 compares spectra for a 10 by 10 pixel area within the carbonatite stock calibrated by using three different assumed DFF reflectance levels.

FIRST ORDER VEGETATION REMOVAL

A series of programs were developed to perform a second normalization to the flat field corrected data set with the goal of compensating for the vegetation spectral component in each pixel. At the center of the procedure are two assumptions: The first is that the vegetation consists of a single major cover type. At Iron Hill this assumption appears to be reasonable as mixed sagebrush and grass is the principal cover type in nearly all areas with significant

soil and rock exposures. The second assumption is that a linear relationship exists between digital numbers in the vegetation index RBD image and the percent vegetation cover, at least over some portion of the total index DN range.

To perform the normalization, a target area was selected that contained approximately 100 percent sagebrush and grass cover (Table 1). This selection was based on an examination of the vegetation index image in conjunction with aerial photography. The target area's mean DN value in the vegetation index image was used to calculate the equation of a line defining the relation between index DN's and percent cover. The AVIRIS spectrum of the 100 percent vegetation area was subsequently scaled according to the estimated amount of vegetation in each image pixel, and then subtracted from the spectrum for the pixel. At this stage the spectra represent (ideally) only the exposed minerals within each pixel, the vegetation having been "removed." The final step in the procedure is a correction for the dilution of the mineral spectra due to the original vegetation component. This involves a second application of the vegetation index, in which the mineral spectrum is multiplied by a factor that is the reciprocal of the percent exposure (the complement of the percent vegetation). The individual steps in the vegetation correction procedure are summarized in Table 1. Figure 3 shows two pairs of spectra that illustrate the effects of the procedure.

DISCUSSION AND CONCLUSIONS

Several AVIRIS data normalization and calibration procedures have been described that have particular relevance to moderately vegetated study areas. A "distributed" flat field (DFF) correction makes use of selected pixels within an image that have optimum characteristics of low vegetation cover and low mineral absorption. At the Iron Hill locality this correction produced much better results than other flat field corrections involving an average spectrum of the entire dataset, or the spectrum of a single discrete ground target.

The DFF normalization spectrum can also be used to calibrate imaging spectrometer data to percent reflectance by assuming that the spectrum represents a spectrally flat target of intermediate brightness. Preliminary results at Iron Hill indicate that this calibration method can yield a good first order calibration to percent reflectance, particularly when the image data have already been corrected for channel to channel radiometric offsets related to detector sensitivity variations. This ability to obtain an approximate calibration without reliance on ground spectral measurements should provide a very useful starting point for more accurate calibration efforts, such as those based on linear modeling of mixtures of field spectra.

A third procedure was designed to provide a first order "defoliant" for AVIRIS data. The principal objective of the

procedure is to generate image products in which characteristic spectral attributes of different lithologic units (such as 2.20 μm band intensity) are enhanced and the complicating effects of variable vegetation cover suppressed. The procedure does not require a priori assumptions about the mineral absorption characteristics of an area and is much less demanding computationally than algorithms that "unmix" numerous spectral components within individual pixels. On the other hand, the resulting spectral signatures are only approximate, and most useful in parts of an image that contain the single vegetation cover type around which the procedure is designed.

REFERENCES

- Crowley, James K., Brickey, David W., and Rowan, Lawrence C., 1989, Airborne Imaging Spectrometer data of the Ruby Mountains, Montana: Mineral discrimination using relative absorption band-depth images: *Remote Sensing of Environment*, v. 29, p. 121-134.
- Kruse, Fred A., 1988, Use of Airborne Imaging Spectrometer data to map minerals associated with hydrothermally altered rocks in the northern Grapevine Mountains, Nevada and California: *Remote Sensing of Environment*, v. 24, p. 31-51.
- Nash, W.P., 1972, Mineralogy and petrology of the Iron Hill carbonatite complex, Colorado: *Geological Society of America Bulletin*, v. 83, p. 1361-1382.
- Roberts, D.A., Yamaguchi, Y., and Lyon, R.J.P., 1985, Calibration of Airborne Imaging Spectrometer data to percent reflectance using field spectral measurements, in *Proceedings of the Nineteenth International Symposium on Remote Sensing of Environment*, Ann Arbor, Michigan, p. 21-25.
- Rowan, Lawrence C., Kingston, Marguerite J., and Crowley, James K., 1986, Spectral reflectance of carbonatites and related alkalic igneous rocks: Selected samples from four North American localities, *Economic Geology*, v. 81, p. 857-871.
- Vane, Greg, Chrien, Thomas G., Miller, Edward A., and Reimer, John H., 1987, Spectral and radiometric calibration of the Airborne Visible/Infrared Imaging Spectrometer: in G. Vane, Editor, *Airborne Visible/Infrared Imaging Spectrometer (AVIRIS), A Description of the Sensor, Ground Data Processing Facility, Laboratory Calibration, and First Results*, Jet Propulsion Laboratory Publication 87-38, p. 73-87.

Fig. 1. (Next Page) Spectra of three 10 x 10 pixel ground targets in the Iron Hill study area extracted after the Distributed Flat Field correction. Note the characteristic 2.17 μm feature in kaolinite, which was not apparent in spectra produced by standard flat field normalization techniques. Y axis shows digital numbers. The spectra are offset for clarity.

Fig. 2. (Next Page) Three spectral plots showing the effects of different assumed brightness levels of the DFF spectrum when used to perform an approximate calibration to percent reflectance. The upper curve represents a carbonate-rich exposure in the Iron Hill study area and an assumed DFF brightness of 45 percent. The lower two curves are for the same target using assumed brightnesses of 35 and 25 percent, respectively. Y axis is in reflectance units.

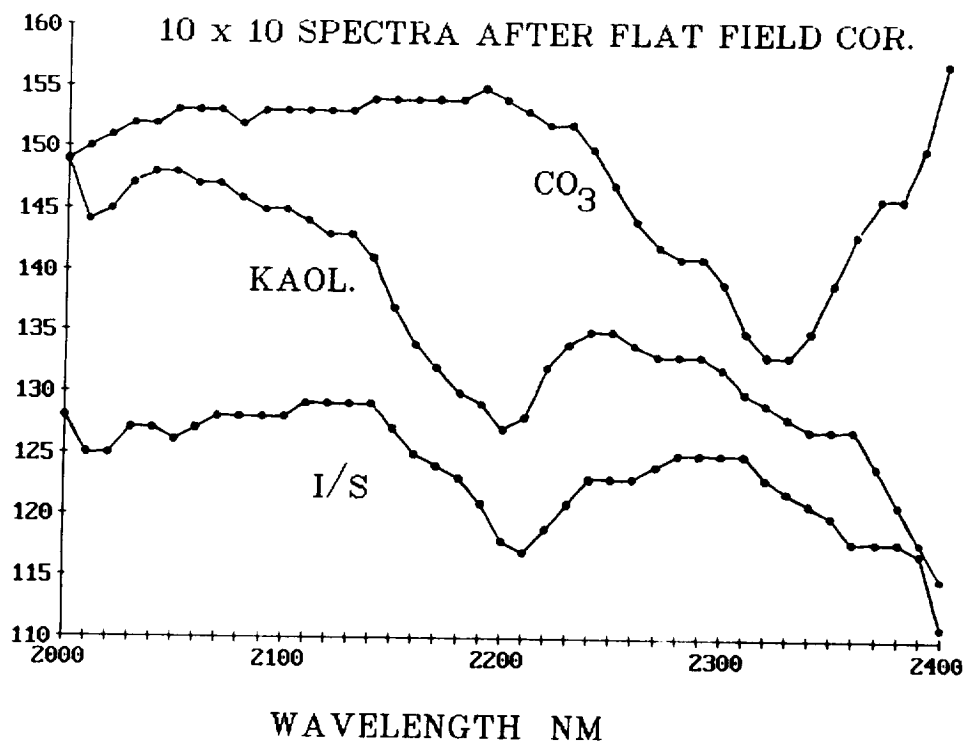


FIGURE 1.

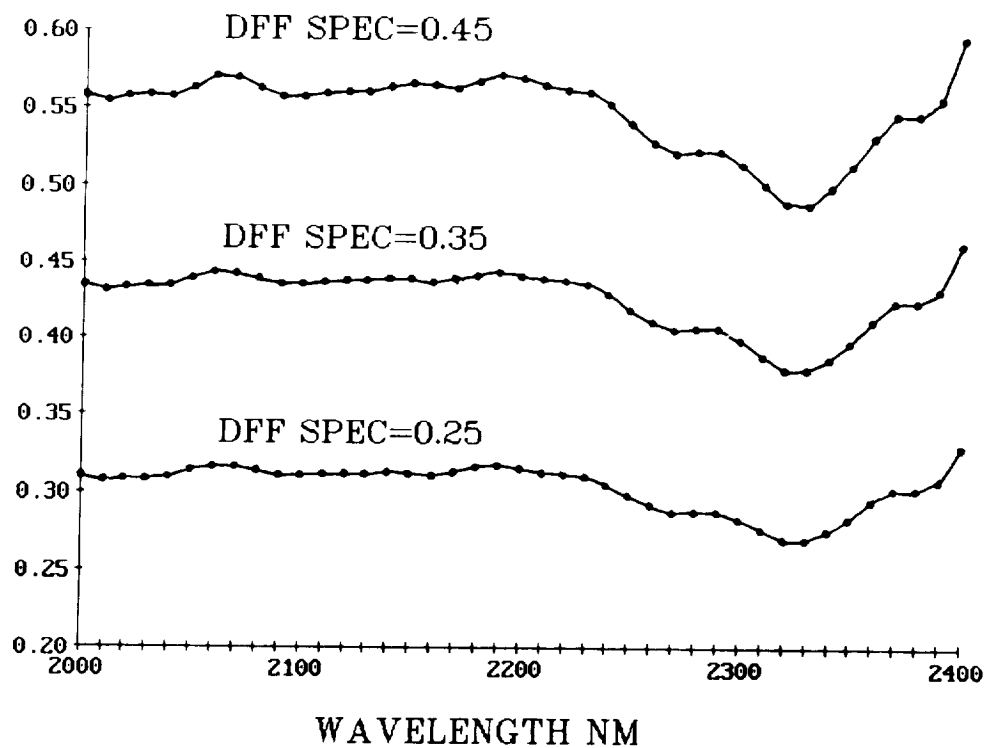


FIGURE 2.

Table 1. Steps in Vegetation Removal Procedure.

- 1). Construction of vegetation index image; identification of 100% vegetation covered target area. Calculation of linear relation between index DN's and percent cover.
- 2). Distributed flat field correction followed by equal energy normalization (See Kruse, 1988).
- 3). For every pixel, scale the 100% vegetation spectrum by the percent vegetation in that pixel as determined by the equation in step (1).
- 4). Correct the equal-energy data set produced in (2) pixel by pixel by subtracting the scaled vegetation spectrum for each pixel.
- 5). Rescale the data set produced in (4) by the reciprocal of the percent exposure in each pixel (vegetation dilution correction).

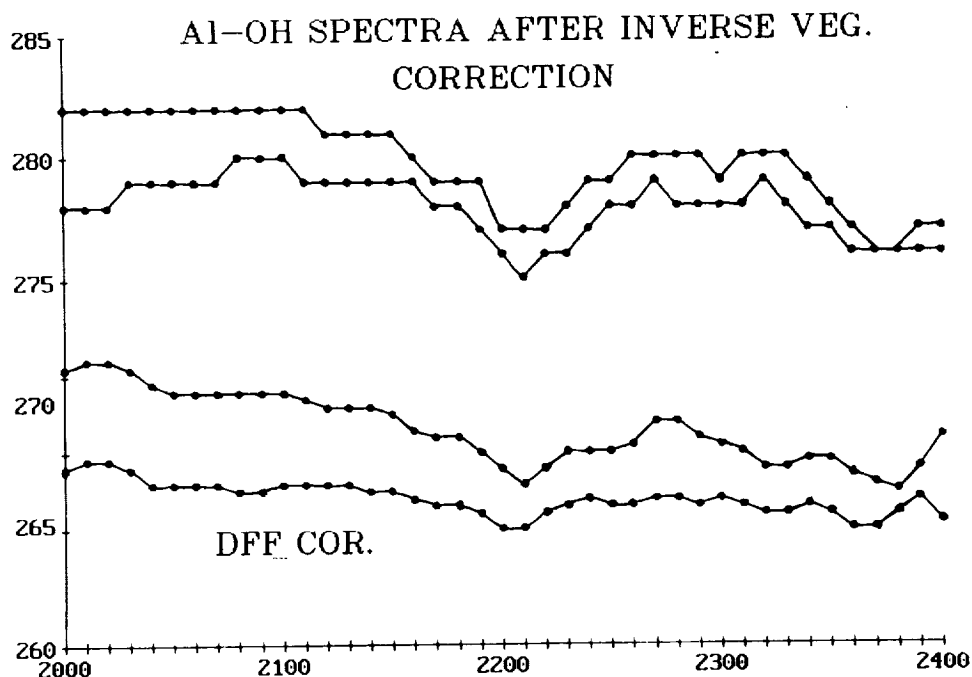


Fig. 3. Spectra of two partially vegetated targets within the same lithologic unit showing Al-OH absorption features before and after the first order vegetation correction. Prior to the correction (bottom curves), the two targets exhibit different 2.20 μm absorption intensities associated with different amounts of vegetation cover. Removal of the variable vegetation component has "equalized" the absorption intensities in the postcorrection (upper) spectra. Y axis is in digital numbers; X axis shows wavelength in nanometers. The spectra are offset for clarity.

MINERALOGIC MAPPING USING AIRBORNE VISIBLE INFRARED IMAGING SPECTROMETER (AVIRIS) SHORTWAVE INFRARED (SWIR) DATA ACQUIRED OVER CUPRITE, NEVADA

SIMON J. HOOK, Jet Propulsion Laboratory, California Institute of Technology, Pasadena, California, and
MICHAEL RAST, European Space Agency, Noorwijk, The Netherlands.

ABSTRACT

This paper evaluates the use of AVIRIS SWIR data acquired in 1989 for discriminating and identifying alteration minerals at Cuprite, Nevada.

Initially, the AVIRIS data were processed by a variety of scene-based techniques in order to determine the optimum methodology for identifying several areas of known mineralogy on the basis of the location of diagnostic spectral absorption features. These techniques included the decorrelation stretch, log residuals, flat-field correction, hull quotients/differences, and wavelength-depth, full-width-half-maximum (WDW) images. Of these, the decorrelation stretch, log residual, and WDW images proved most effective for delineating the areas of known alteration mineralogy. These data were used to produce a mineralogic map of the area that divided the alteration into zones dominated by the minerals alunite, kaolinite, buddingtonite, and silica, respectively. This map was checked by comparison with existing geologic maps, field mapping and X-Ray Diffraction (XRD), and laboratory spectral analysis of field samples.

In general, the mineralogic map concurred with an existing alteration map that had divided the alteration into argillised, opalised, and silicified zones. The area covered by the combined alunite and kaolinite zones corresponded to area covered by the argillised and opalised zones. The silicified zone of the mineralogic map matched the silicified zone of the alteration map and was divided further into an outer and inner silicified zone.

INTRODUCTION

The wavelength region between 2000 and 2400 nm in the SWIR is particularly useful for mineralogic mapping studies, because it contains a large number of absorption features diagnostic of the presence of certain hydroxyl- and carbonate-bearing minerals or mineral groups (Goetz et al. 1983).

In this paper we evaluate the mineral discrimination and identification capabilities of the 1989 AVIRIS data covering the 2000- to 2400-nm wavelength range. The approach used for this evaluation involved processing the AVIRIS data with several scene-based techniques developed to enhance the diagnostic absorption features of a variety of alteration minerals.

These included the decorrelation stretch, flat-field correction, log residuals, hull quotients/differences, and WDW. These procedures were selected because they do not require external data such as reflectance spectra of calibration targets or estimates of incoming solar irradiances.

STUDY SITE

The Cuprite area is located on the western edge of Esmeralda County, Nevada, about 25 kilometers south of the town of Goldfield. The study area is divided in half by U.S. Highway 95 (Figure 1). On the west side of the highway the

geology exposed consists of Cambrian sediments and metasediments, Tertiary volcanics, and Quaternary alluvium. On the eastern side of the highway only the Tertiary volcanics and Quaternary alluvium have been mapped (Figure 1).

Sections of the Tertiary volcanics on both sides of the highway were intensively altered in mid- to late-Miocene times. Ashley and Abrams (1980) divided the alteration into three field-mappable zones; silicified rocks, opalized rocks, and argillised rocks (Figure 2). The alteration on the east side of the highway has a bullseye pattern, with the silicified zone forming a circular core surrounded by opalised then argillised rocks (Figure 2). The minerals identified in these alteration zones by Ashley and Abrams (1980) include quartz, opaline silica, alunite, kaolinite, and calcite.

The distribution of these alteration assemblages is typical of a fossilised hot-spring deposit (e.g. Buchanan et al. 1981). The recognition of such deposits is particularly important for mineral exploration since they frequently contain economic gold mineralisation.

In addition to the minerals described, buddingtonite (an ammonium feldspar) has been identified at Cuprite using high spectral resolution data from the 2000- to 2400-nm wavelength range in a study by Goetz and Srivastava (1985). This mineral has also been shown to be associated with gold-bearing fossilised hot-spring deposits (Krohn and Altaner, 1987).

The wealth of alteration minerals present at Cuprite coupled with the excellent exposure, limited soil development and sparse vegetation cover (0 to 10%) has led to Cuprite becoming a major testing area for evaluating the mineralogic mapping capabilities of airborne and spaceborne sensors. These include studies using data from the first airborne imaging spectrometer (Goetz and Srivastava 1985) and more recently data from the Geophysical Environmental Research Imaging Spectrometer (Kruse et al. 1990).

DATA PROCESSING AND INTERPRETATION

Initially, three bands were selected from the AVIRIS data which, based on known mineral absorption features, would separate the minerals alunite, buddingtonite, and kaolinite. These were AVIRIS bands 187 (2088 nm), 192 (2134 nm), and 198 (2217 nm). These three bands were processed with the decorrelation stretch algorithm and then displayed as red, green and blue, respectively, to form a false-color composite (Figure 3/Slide 20). The decorrelation stretch technique is described in Gillespie et al. (1986), and enhances reflectance variations whilst retaining topographic information useful for spatial orientation.

This false-color composite permits discrimination of many of the mapped lithologies and also alteration types (Figure 3/Slide 20, Figures 1 and 2). Areas of alunite appear magenta; buddingtonite, deep blue; and kaolinite, yellow. The area mapped as the silicified zone varies in color from an inner core, light blue in color, to an outer rim, green in color. For applications where the composition of the ground is known at selected locations, a product similar to that shown in Slide 20 provides an excellent tool for discriminating lithologies and alteration zones. However, in order to fully utilize all the channels of data available, a series of systematic effects unrelated to the composition of the terrain surface need to be removed: in particular, the solar irradiance curve, atmospheric attenuation/scatter, and topographically induced illumination differences. These effects often mask subtle absorption features that can be used to identify certain alteration minerals through comparison with laboratory spectra of known minerals. A variety of techniques have been developed to remove some or all of these effects.

They include flat-field correction (Roberts et al. 1986), internal average reflectance (Kruse et al. 1988), log residuals, and hull quotients/differences (Green and Craig 1985).

The techniques examined in this study were the flat-field correction, log residuals, and hull quotients/differences. Of these, log residuals proved the most effective method, on the basis that it recovered the spectral shapes for several areas of known mineralogy and introduced the least number of artifacts into the data. Five spectra were extracted from the log residual data, which illustrate some of the absorption features of the alteration minerals present at this site (Figure 4). These spectra are mean spectra calculated from a box of pixels that appeared the same color on the decorrelation stretch images. The size of the extracted boxes depends on how large the area with a distinct color appeared on the image. For example, the largest box extracted was from the alunite area (312 pixels) and the smallest box extracted was from the buddingtonite area (12 pixels). The location of these boxes is shown on Figure 3/Slide 20 and numbered 1 through 5. The dashed lines either side of the mean spectra are the mean \pm 1 standard deviation. Also shown, are laboratory spectra from the weathered surfaces of field samples collected from these five areas. The laboratory spectra were obtained with a Beckman UV-5240 Spectrophotometer equipped with an integrating sphere. The Beckman has bands every 4 nm in 2000- to 2400-nm wavelength region with bandwidths from 20 to 28 nm.

The location and shape of absorption features in the laboratory spectra closely match those in the corresponding image log residual spectra. Particularly noteworthy in the image spectra is the detection of the kaolinite doublet between 2160 nm and 2250 nm (Figure 4). The mineral dickite has a similar doublet with a slightly different shape. The ability to detect this doublet may enable separation of areas dominated by kaolinite from those dominated by dickite. This is particularly important for mineral exploration since kaolinite can result from weathering by authigenesis in sediments or by hydrothermal processes, whereas dickite typically results from hydrothermal processes (Murray, 1988). The asymmetry in the alunite laboratory spectrum around 2200 nm is less apparent in the log residual spectrum from the same area. Isolated pixels were located in which the doublet was well defined; the loss of this feature in the mean spectrum from the larger area may result from spectral mixing with other alteration minerals.

The image spectra from the silicified zone exhibit a strong absorption feature around 2250 nm. An absorption feature at this wavelength has been noted in hydrothermal silica collected from Nevada and Utah (Podwyssocki et al. 1985). These workers attribute this absorption to "gel effects", or noncrystalline silica. This absorption may also result, in part, from the log residual calculation, which involves subtracting off the log mean of each band from the log of each pixel in that band. If this mean is dominated by an absorption feature around 2200 nm, then any spectra not containing an absorption feature at this wavelength would be artificially elevated giving the appearance of a drop-off at longer wavelengths. The color difference between the inner and outer silicified zone appears to relate to the steepness of the slope from shorter wavelengths to the absorption at 2250 nm.

Using this approach, of taking an area of uniform color in the decorrelation stretch image and extracting an average log residual spectrum, it was possible to begin to produce a simplified alteration map of the area. However, numerous ambiguities arose where it was difficult to assign an area to a dominant alteration mineral. Therefore, a further technique was developed that involved examining the wavelength, depth, and full width half maximum (WDW) of the deepest absorption feature. Prior to searching for this feature, it is necessary to remove any atmospheric absorptions, otherwise the deepest absorption feature detected will frequently relate to the atmosphere rather than the composition of the surface. In addition, the solar atmospheric curve needs to be removed, otherwise the lowest value in the 2000- to 2400-nm region will occur at the longest wavelength. To correct for these effects, the hull quotient technique was applied to log residual data. Both these techniques are described in Green and Craig (1985). The wavelength, depth full width half maximum of the deepest feature, was then extracted from the hull quotients of the log residual data. The wavelength of the deepest feature was displayed as a gray level (dark - short wavelengths; light - long wavelengths). The depth of this feature was also displayed as a gray level (dark, deep feature; light, shallow feature). Wavelength and depth images for the study area are shown in Figure 5/Slide 21. The wavelength image is particularly useful for separating the alteration types. The area mapped as buddingtonite appears dark having an absorption feature at the shortest wavelengths (2120 nm). The area mapped as alunite appears slightly lighter since its deepest absorption feature is around 2170 nm. The kaolinite area appears lighter still, its deepest absorption feature occurring around 2209 nm. The silicified area appears lightest, its deepest absorption feature occurring around 2250 nm.

Using the decorrelation stretch, log residual, and WDW images, it was possible to produce an mineralogic map of the area (Figure 6). It should be realised that this map is only a first attempt; nonetheless, it does improve on certain aspects of the existing alteration map. For example, the silicified area has been separated into an outer and inner silicified zone. The opalised and argillised zones, which are often difficult to separate on the ground, have been divided according to the dominant alteration mineral present, either alunite, buddingtonite, or kaolinite.

SUMMARY AND CONCLUSIONS

The 1989 AVIRIS data are capable of differentiating areas rich in the alteration minerals alunite, buddingtonite, kaolinite, and silica at Cuprite, Nevada. This can be achieved using a color composite generated from a decorrelation stretch of three AVIRIS channels selected to maximise differences in the spectral shapes of these minerals. However, in order to identify a particular mineral by matching the absorption features in the AVIRIS spectrum with those in the laboratory spectrum of a pure mineral, further processing is required to remove a series of systematic effects superimposed on the spectrum of the surface material. These relate to the solar irradiance curve, atmospheric absorption/scatter, and topographically induced illumination differences. These can be adequately removed using the log residual calculation. After removal of these effects, spectra from five areas in the image clearly matched laboratory spectra obtained from field samples collected from those areas. Particularly noteworthy was the well-defined kaolinite doublet in the AVIRIS spectra. The ability to resolve this doublet may permit the separation of areas of kaolinite from dickite,

which can be distinguished in laboratory spectra in this wavelength region by a subtle difference in the shape of this doublet.

A further technique that proved particularly useful for identifying the dominant alteration mineral in an area involved searching for the wavelength, depth and full width half maximum of the deepest absorption feature and displaying these three pieces of information as separate gray-scale images.

Using the decorrelation stretch, log residual, and WDW data, it was possible to produce a mineralogic map of the area that was then compared to an existing alteration map. The mineralogic map concurred with the existing alteration map and permitted greater separation of certain units. For example, the previously mapped silicified zone was separated into an outer and inner silicified zone.

ACKNOWLEDGMENTS

The research described in this paper was carried out whilst the first author held a National Research Council, Resident Research Associateship at the Jet Propulsion Laboratory, California Institute of Technology.

REFERENCES

- Abrams, M. J., Ashley, R. P. 1980. *Alteration Mapping Using Multispectral Images - Cuprite Mining District, Esmeralda County, Nevada*. U.S. Geological Survey Open File Report 80-367.
- Buchanan, L. J., 1981. Precious Metal Deposits Associated With Volcanic Environments in the Southwest. In *Relations of Tectonics to Ore Deposits in the Southern Cordillera*, eds. W. R. Dickinson and W. D. Payne (Arizona Geological Society Digest, v. 24), pp. 237-262.
- Gillespie, A. R., Kahle, A. B., Walker, R. R., 1986. Color Enhancement of Highly Correlated Images: I Decorrelation and HSI Contrast Stretches. *Remote Sensing of Environment*. v. 20, pp. 209-235.
- Goetz, A. F. H. and Srivastava, V., 1985. Mineralogic Mapping in the Cuprite Mining District. *Proceedings of the First AIS Workshop*. Publication 85-41, Jet Propulsion Laboratory, Pasadena, California.
- Goetz, A. F. H., Rock, B. N., Rowan, L. C., 1983. Remote Sensing for Exploration: An Overview. *Economic Geology*, 78, pp. 573-590.
- Green, A. A., and Craig M. D., 1985. Analysis of Aircraft Spectrometer Data With Logarithmic Residuals. *Proceedings of the First AIS Workshop*. Publication 85-41, Jet Propulsion Laboratory, Pasadena, California.
- Krohn, M. D. and Altaner, S. P., 1987. Near-Infrared Detection of Ammonium Minerals. *Geophysics*. v. 52, pp. 924-930.
- Kruse, F. A., Calvin, W. M., Seznec, O., 1988. Automated Extraction of Absorption Features From Airborne Visible/Infrared Imaging Spectrometer (AVIRIS) and Geophysical and Environmental Research Imaging Spectrometer (GERIS) Data. *Proceedings of the AVIRIS Performance Evaluation Workshop*. Publication 88-38, Jet Propulsion Laboratory, Pasadena, California, pp.62-75.
- Kruse, F. A., Kierein-Young, K. S., Boardman, J. W., 1990. Mineral Mapping at Cuprite, Nevada With a 63-Channel Imaging Spectrometer. *Photogrammetric Engineering and Remote Sensing*. v. 56, pp. 83-92.

- Murray, H. H., 1988. Kaolin Minerals: Their Genesis and Occurrences. In *Hydrous Phyllosilicates*, ed. S. W. Bailey (*Reviews in Mineralogy*, Mineralogical Society of America v. 19), pp. 69.
- Podwysocki, M. H., Salisbury, J. W., and Vergo, N., 1985. Use of Near-Infrared Spectra to Distinguish Between Sedimentary Cherts and Hydrothermal Silica Associated With Disseminated Gold Deposits. Geological Society of America, Abstract.
- Roberts, D. A., Yamaguchi, Y., Lyon, R. J. P., 1985. Comparison of Various Techniques for Calibration of AIS Data. *Proceedings of the Second AIS Data Analysis Workshop*. Publication 86-35, Jet Propulsion Laboratory, Pasadena, California, pp. 21-30.

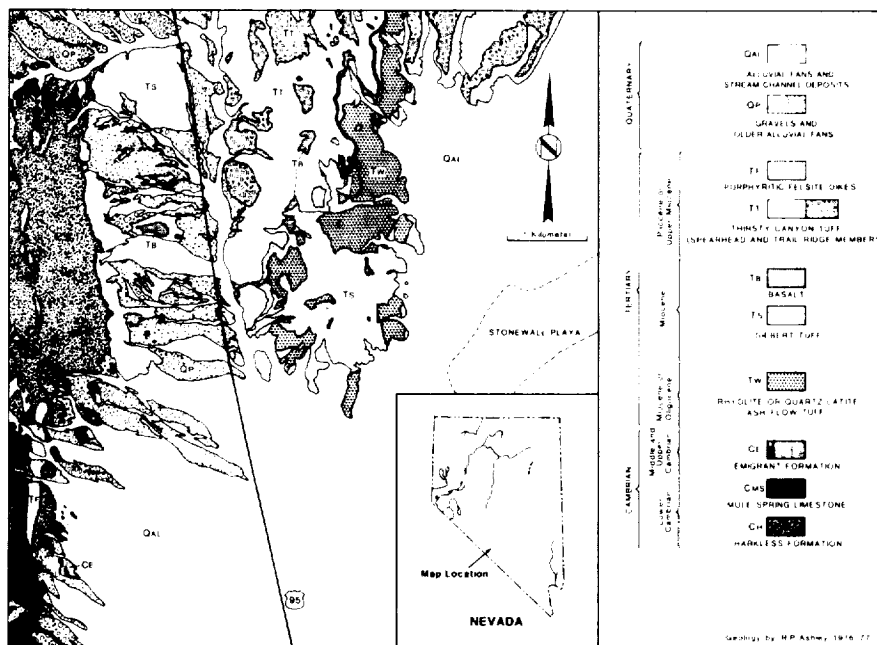


Figure 1. Geologic map of the Cuprite, Nevada study site. Redrawn from Ashley and Abrams (1980).

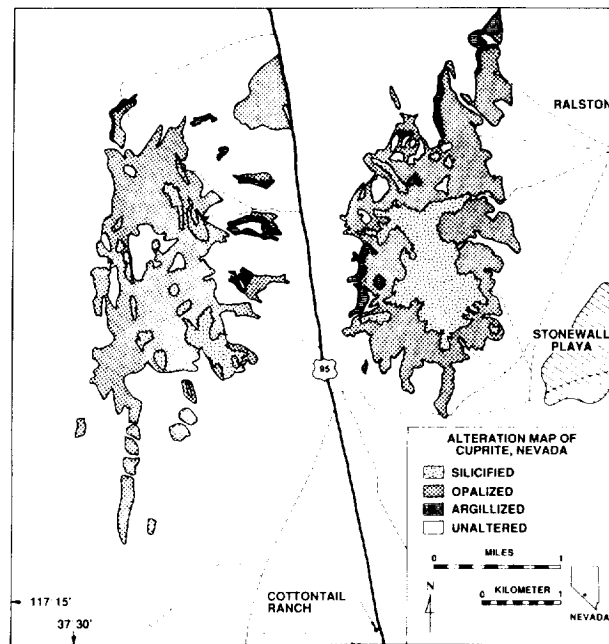


Figure 2. Alteration map of the Cuprite, Nevada study site. Redrawn from Ashley and Abrams (1980).



Figure 3. Color composite image produced from a decorrelation stretch of AVIRIS bands 187 (2088 nm), 192 (2134 nm), and 198 (2217 nm) displayed as red, green, and blue, respectively.

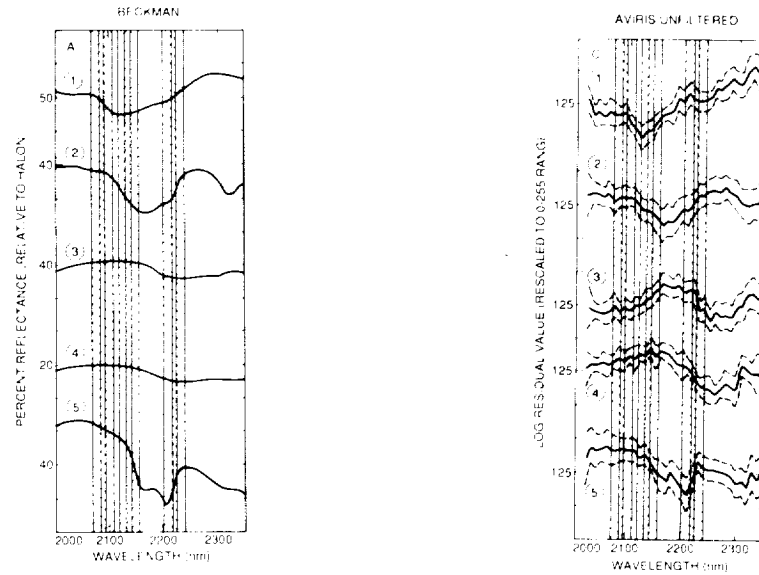


Figure 4. Laboratory and AVIRIS SWIR spectra for five sites at Cuprite. The AVIRIS spectra are the result of a log residual algorithm applied to the entire flight line. The spectra are offset for clarity; 1=Buddingtonite Zone, 2=Alunite Zone, 3=Silicified Zone edge, 4=Silicified Zone center, 5=Kaolinite Zone.

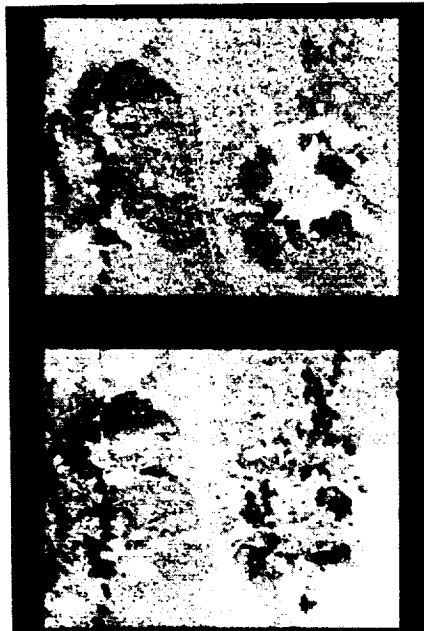


Figure 5. Wavelength and depth of deepest absorption feature in each pixel in hull quotients of log residual AVIRIS data from 2000 to 2350 nm wavelength range displayed as gray scale images. Wavelength - top; depth - bottom.

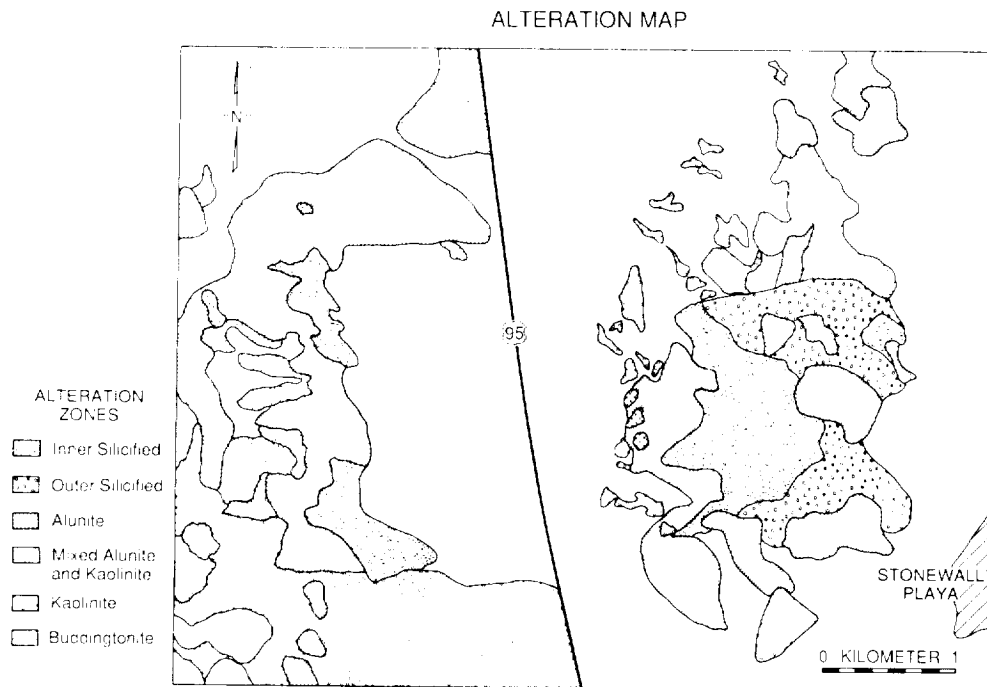


Figure 6. Simplified alteration map of the Cuprite, Nevada study site from analysis of AVIRIS SWIR data.

THE U. S. GEOLOGICAL SURVEY, DIGITAL SPECTRAL LIBRARY AND ANALYSIS SOFTWARE

ROGER N. CLARK, GREGG A. SWAYZE, TRUDE V.V. KING,
BARRY MIDDLEBROOK, WENDY M. CALVIN, and NOEL GORELICK
U.S. Geological Survey, MS 964
Box 25046 Federal Center
Denver, CO 80225-0046
(303) 236-1332

ABSTRACT

The U. S. Geological Survey, Denver Spectroscopy Laboratory has developed a digital spectral library, library management software, and spectral analysis software. The software and library will be ready for general release in the summer of 1990. The library will include approximately 410 spectra measured from 0.2 to 3.0 μm with sample documentation. The library search software will enable a user to search on documentation parameters as well as spectral features. The analysis system includes general spectral analysis routines, plotting packages, radiative transfer software for computing intimate mixtures, routines to derive optical constants from reflectance spectra, tools to analyze spectral features, and the capability to access imaging spectrometer data cubes for spectral analysis. The laboratory spectral library will also be convolved to flight instrument spectral resolution and spectral sampling. Users may build customized libraries for their own instruments/flight conditions using software tools and command files. Absorption coefficients will be derived from all spectra so that the radiative transfer routines can be used to compute mineral mixtures.

INTRODUCTION

Imaging spectroscopy instruments such as AVIRIS have narrow band widths in many contiguous spectral channels that permit accurate definition of absorption features from a variety of materials. Identification of materials from such data requires a knowledge base: a spectral library of minerals, vegetation, man-made materials, and other subjects in the scene. Acquiring spectral measurements and sample characterizations for this library has taken several years. The first release will contain approximately 410 spectra and software to manage the library and provide scientific analysis capability.

THE SPECTRAL LIBRARY

The spectral library contains spectra of approximately 180 minerals (Table 1). In some cases, several spectra were measured to

span a solid solution series and/or a grain size series.

All spectra were run on a modified Beckman 5270 spectrometer (Clark *et al.*, 1990) from 0.2 to 3.0 μm and corrected to absolute reflectance. (Any use of trade names is for descriptive purposes only and does not imply endorsement by the U.S. Geological Survey.) Each sample has a documentation entry to describe the mineral, its composition, formula, and pointers to corresponding spectra in the library (an example is shown in Table 2). Each spectrum has a pointer to the documentation, so that all related data are properly cross-referenced.

The sample documentation includes extensive analyses such as X-ray diffraction, electron microprobe, X-ray fluorescence, and petrographic microscope examination. Not all analyses have been completed for all samples, but all samples have at least one analysis. These analyses are expensive and time consuming and limited funding has precluded complete analysis of all samples for this release of the library. Sample analysis will continue and the sample documentation will be updated in future releases of the library.

The intent of the spectral library is to serve as a knowledge base for spectral analysis. Comparison of spectral data is best done when the spectral resolutions of the knowledge base and the spectra undergoing analysis are identical. The spectral analysis software has tools for convolving the spectral library to the resolution and sampling interval of any instrument. The native (laboratory) spectral library is also convolved to nominal AVIRIS, HIRIS, GERIS, and TM resolution and sampling (e.g. Figure 1) for the terrestrial instruments, and to NIMS and VIMS for the planetary imaging spectrometer instruments. The convolution to any other instrument (laboratory, or flight) is a simple matter of changing pointers in a command file to the custom resolution and sampling data sets and running the command file with the spectral analysis system.

The spectral feature analysis tools and search facilities included with the library allow users to find entries based on selected parameters, such as those in the sample documentation as well as spectral features. For example, one might search for all minerals with an SiO_2 content of 10 to 30% and containing a 2.2- μm feature.

For computing intimate mineral mixtures (e.g. rock or soil) radiative transfer algorithms using the Hapke reflectance model (Hapke, 1981) are available. To compute mixture or pure end-member spectra, a set of optical constants is required as a function of wavelength. The algorithms use the model at the optical constant level so spectra can be calculated as a function of grain size, abundance in the mixture, and viewing geometry. Grain size distributions can also be simulated by computing a mixture of the same mineral (or even several minerals) at several grain sizes. A future release of the library will include optical constants for the spectra in the library. Optical constant libraries will also be computed for the same flight instrument spectral resolutions and wavelengths as the convolutions to the native spectral library. We anticipate the optical constant libraries to be completed this fall.

Table 1

Minerals in the Spectral Library, Version 1

1 Acmite	1 Clinozoisite	4 Illite	3 Pyrophyllite
5 Actinolite	1 Cobaltite	1 Ilmenite	9 Pyroxene
1 Adularia	3 Cookeite	1 Jadeite	1 Pyrrotite
3 Albite	1 Copiapite	3 Jarosite	4 Quartz
1 Allanite	1 Coquimbite	7 Kaolinite	1 Rectorite
5 Almandine	1 Cordierite	1 Kerogen	2 Rhodochrosite
2 Alunite	1 Corrensite	1 Kyanite	3 Rhodonite
1 Amphibole	1 Corundum	2 Labradorite	2 Richterite
1 Analcime	1 Covellite	1 Laumontite	2 Riebeckite
2 Andalusite	1 Cronstedtite	1 Lazurite	3 Ripidolite
1 Andesine	1 Cuprite	3 Lepidolite	1 Roscoelite
5 Andradite	2 Datolite	1 Limonite	2 Rutile
1 Anhydrite	1 Diaspore	4 Lizardite	1 Samarium Oxide
2 Annite	7 Diopside	1 Magnesite	2 Sanidine
3 Anorthite	1 Dolomite	2 Magnetite	2 Saponite
2 Anorthoclase	1 Dumortierite	1 Malachite	9 Scapolite
1 Anthophyllite	3 Elbaite	1 Manganite	1 Scolecite
7 Antigorite	1 Endellite	3 Marialite	4 Sepiolite
1 Apatite	2 Enstatite	2 Mascagnite	2 Serpentine
1 Arsenopyrite	4 Epidote	4 Meionite	1 Siderite
1 Attapulgit	1 Erionite	1 Mesolite	1 Sillimanite
1 Augite	1 Europium Oxide	5 Microcline	1 Smaragdite
1 Axinite	1 Fassaite	1 Monazite	4 Spessartine
1 Barite	1 Ferric Oxide	1 Monticellite	7 Sphalerite
2 Beryl	1 Fibroferrite	15 Montmorillonite	1 Sphene
1 Biotite	2 Forsterite	1 Mordenite	1 Spodumene
1 Bronzite	8 Galena	2 Muscovite	1 Staurolite
1 Brookite	3 Gibbsite	2 Natrolite	1 Stilbite
1 Brucite	1 Glaucosite	1 Neodymium Oxide	1 Strontianite
1 Buddingtonite	1 Glaucophane	1 Nepheline	1 Sylvite
1 Bytownite	4 Goethite	1 Nephrite	4 Talc
2 Calcite	1 Granite	3 Nontronite	1 Tephroite
1 Carbon	3 Grossular	2 Oligoclase	4 Thuringite
1 Carphosiderite	2 Grossularite	16 Olivine	18 Topaz
1 Cassiterite	1 Gypsum	4 Orthoclase	1 Tosudite
1 Celsian	1 Halite	2 Paragonite	1 Tourmaline
1 Chabazite	5 Halloysite	2 Pectolite	2 Tremolite
2 Chalcopyrite	2 Hectorite	1 Perthite	1 Uralite
7 Chlorite	1 Hedenbergite	5 Phlogopite	1 Uvarovite
1 Chromite	9 Hematite	1 Pigeonite	6 Vermiculite
1 Chrysoberyl	1 Heulandite	1 Praseodymium Ox.	1 Witherite
1 Chrysocolla	1 Holmquistite	3 Prochlorite	1 Wollastonite
1 Chrysotile	3 Hornblende	1 Psilomelane	1 Zincite
1 Cinnabar	1 Hydrogrossular	5 Pyrite	1 Zircon
1 Clinocllore	1 Hypersthene	2 Pyrope	1 Zoisite
1 Clinoptilolite	1 Idocrase		

Total: 414 spectra of 182 different minerals.

Table 2

Sample Documentation Example

TITLE: Kaolinite CM9 DESCRIPT

DOCUMENTATION_FORMAT: MINERAL

SAMPLE_ID: CM9

MINERAL_TYPE: Phyllosilicate

MINERAL: Kaolinite, a clay mineral of the Kaolinite-Serpentine group.

FORMULA: Al₂Si₂O₅(OH)₄

FORMULA_NROFF: Al₂Si₂O₅(OH)₄

COLLECTION_LOCALITY: Mesa Alta, New Mexico

ORIGINAL_DONOR: Clay Mineral Standard from Wards Natural Science Inc.

CURRENT_SAMPLE_LOCATION: USGS Denver Spectroscopy Lab

ULTIMATE_SAMPLE_LOCATION: USGS Denver Spectroscopy Lab

SAMPLE_DESCRIPTION:

A spectrum for this sample was published by:
Clark, R.N., T.V.V. King, M. Klejwa, G. Swayze, and N. Vergo, 1990, High
spectral resolution reflectance spectroscopy of minerals:
J. Geophys Res., in press, 96pp,
who noted that it was spectrally pure.

END_SAMPLE_DESCRIPTION.

XRD_ANALYSIS:

Analysis by Norma Vergo indicates the sample is well ordered kaolinite.
The <2μm cut is kaolinite + small amount of quartz.

END_XRD_ANALYSIS.

COMPOSITIONAL_ANALYSIS_TYPE: XRF # XRF, EM(WDS), ICP(Trace), WChem

COMPOSITION:	SiO2:	47.1	wt%	NROFF: SiO ₂
COMPOSITION:	TiO2:	0.46	wt%	NROFF: TiO ₂
COMPOSITION:	Al2O3:	37.4	wt%	NROFF: Al ₂ O ₃
COMPOSITION:	Cr2O3:		wt%	NROFF: Cr ₂ O ₃
COMPOSITION:	V2O3:		wt%	NROFF: V ₂ O ₃

continued...

Table 2 Continued

```

COMPOSITION:      Fe2O3:      0.47 wt%      NROFF: Fe2O3
COMPOSITION:      FeO:         wt%         NROFF: FeO
COMPOSITION:      NiO:         wt%         NROFF: NiO
COMPOSITION:      MnO:      <0.02 wt%      NROFF: MnO
COMPOSITION:      MgO:      0.16 wt%      NROFF: MgO
COMPOSITION:      SrO:         wt%         NROFF: SrO
COMPOSITION:      ZnO:         wt%         NROFF: ZnO
COMPOSITION:      BaO:         wt%         NROFF: BaO
COMPOSITION:      CaO:      0.05 wt%      NROFF: CaO
COMPOSITION:      Li2O:         wt%         NROFF: Li2O
COMPOSITION:      Na2O:      <0.15 wt%      NROFF: Na2O
COMPOSITION:      K2O:      0.08 wt%      NROFF: K2O
COMPOSITION:      P2O5:      <0.05 wt%      NROFF: P2O5
COMPOSITION:      Cl:         wt%         NROFF: Cl
COMPOSITION:      F:         wt%         NROFF: F
COMPOSITION:      S:         wt%         NROFF: S
COMPOSITION:      SO3:         wt%         NROFF: SO3
COMPOSITION:      CO2:         wt%         NROFF: CO2
COMPOSITION:      H2O+:         wt%         NROFF: H2O+
COMPOSITION:      H2O-:         wt%         NROFF: H2O-
COMPOSITION:      H2O:         wt%         NROFF: H2O
COMPOSITION:      LOI:      14.1 wt%      NROFF: LOI
COMPOSITION: -----
COMPOSITION:      Total:      100.04 wt%
COMPOSITION:      O=Cl,F,S:         wt%      #correction for Cl, F, S
COMPOSITION:      New Total:         wt%

```

COMPOSITION_TRACE:

COMPOSITION_DISCUSSION:

XRF Analysis by Branch of Analytical Chemistry, USGS, Denver.

END_COMPOSITION_DISCUSSION.

MICROSCOPIC_EXAMINATION:

END_MICROSCOPIC_EXAMINATION.

DOCUMENTED_BY: wcalvin@speclab (Wendy M. Calvin)

LIB_SPECTRA_HED: where Wave Range Av_Rs_Pwr Comment

LIB_SPECTRA: splib00_r_____ 0.2-3.0μm 200 g.s.=

Notes: The last line contains the file identification and record number for the spectral data entry and is blank until the final assembly of the library.

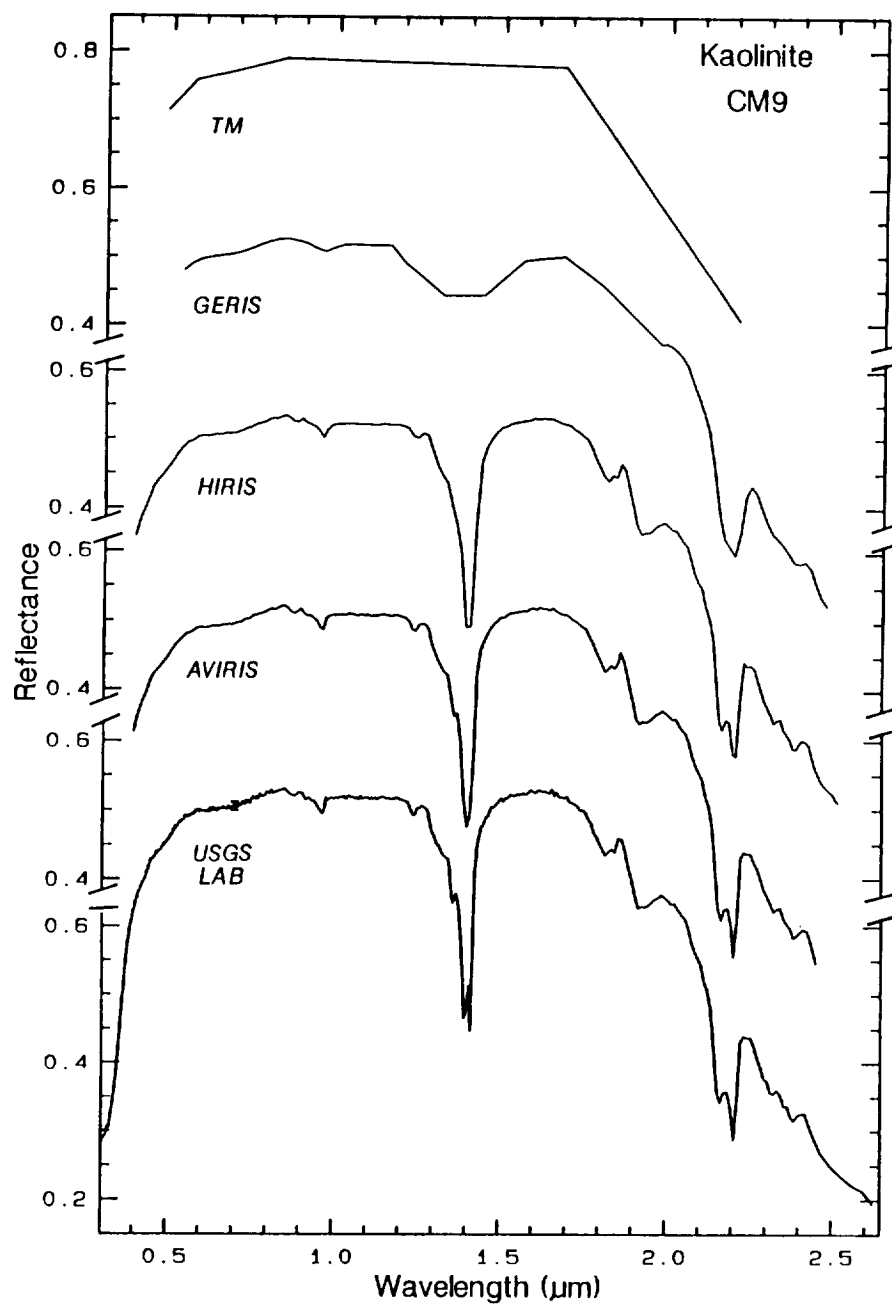


Figure 1. Sample spectra for kaolinite sample CM9 is shown at the native spectral library resolution (labeled USGS Lab), and for AVIRIS, HIRIS, GERIS, and TM.

SPECTRAL ANALYSIS SOFTWARE

With the spectral library, version 3.0 the SPECTrum Processing Routines (SPECPR), an integrated program for analysis of spectral data is available. Specpr is an interactive system for detailed processing of a few to many (meaning thousands) spectra and permits the user to be intimately involved with each spectrum and analysis step. Specpr is also a general x-y paired data processing system, where x and y can be many things (like reflectance versus wavelength, band intensity versus grain size, water content versus time, etc.). Specpr also has facilities for managing the spectral library. It is currently in use by several research groups around the country and an earlier version (version 1.0) was described in Clark (1980).

Specpr version 3.0 includes access to imaging spectrometer data sets in BIL, BIP and BSQ formats. It has routines for manipulating spectra (addition, subtraction, multiplication, division, logs, trigonometric functions, powers, etc.), plotting spectra on graphics terminals, and analyzing absorption bands for depth, position, shape, asymmetry. Specpr also has many special functions such as smoothing, spectral feature analysis, Planck black body generation, continuum removal, and many more.

HARDWARE REQUIREMENTS

The software consists of 50,000 lines of code and runs on Unix computers. The programs currently run on HP Unix machines, Sun Microsystems workstations, and DEC VAXes under Berkeley 4.3 Unix, Ultrix, and Wolongong's Eunice (Unix under VMS). To install the software, about 25 megabytes of disk space are required. The executable programs total about 3 megabytes.

The graphics requirement for the system needs either an HP-compatible graphics terminal (or a PC running an HP-graphics terminal emulator), or a Tektronix Plot-10 compatible graphics terminal. However, some interactive graphics routines are not supported on Tektronix Plot-10 terminals simply because those terminals do not have the needed graphics capability. X-Windows support is currently under development and will be available by the fall of 1990.

The spectral libraries will require about 50 megabytes of disk space, not including the optical constant libraries (which will require another 50 megabytes). Selected libraries, such as the AVIRIS library will be on the order of 5 megabytes, and each can be loaded separately.

AVAILABILITY

The software and spectral libraries will be published as USGS Open File Reports. They will be submitted for review in July and will be available for public release as soon as the review cycle is complete.

Contact any of the authors at the above address, or send electronic mail to:

```
rclark&speclab.uucp@csm9a.mines.colorado.edu      # Internet
STAR::"rclark&speclab.uucp@csm9a.mines.colorado.edu"  # SPAN
```

or

r.clark on NASAMAIL

for information on how to acquire the software and libraries.

FUTURE PLANS

The senior author (RNC) is a team member on the EOS HIRIS flight investigation team and is developing spectral libraries for the team. He is also a team member on Mars Observer Thermal Emission spectrometer, Mars 94 VIMS, and CRAF VIMS. To satisfy the requirements of all these missions, the mineral spectral library will be extended to cover the spectral range 0.2 to 200 μm and include many more minerals. For the HIRIS team, spectral libraries will be developed for all disciplines represented by team members.

REFERENCES

- Clark, R.N., 1980. A Large Scale Interactive One Dimensional Array Processing System, *Pub. Astron. Soc. Pac.*, **92**, 221-224.
- Clark, R.N., T.V.V. King, M. Klejwa, G. Swayze, and N. Vergo, 1990. High Spectral Resolution Reflectance Spectroscopy of Minerals: *J. Geophys. Res.* in press.
- Hapke, B., 1981. Bidirectional reflectance spectroscopy 1. Theory, *J. Geophys. Res.* **86**, 3039-3054.

ANALYSIS OF HIGH SPECTRAL RESOLUTION DATA ON A PERSONAL COMPUTER

DANIEL N.M. DONOGHUE, DAVID W.C. ROBINSON, Department of Geography, University of Durham, Durham, DH1 3LE, United Kingdom and **SIMON J. HOOK**, Mail-Stop 183-501, Jet Propulsion Laboratory, California Institute of Technology, Pasadena, California 91109.

ABSTRACT

This paper describes the specifications of a personal computer-based software package suitable for the analysis of high spectral resolution data sets such as Airborne Imaging Spectrometer (AIS) and Airborne Visible/InfraRed Imaging Spectrometer (AVIRIS). The software has been designed to allow imaging spectrometer (or any other spectral) data to be analysed in numerical, graphical and image form. Particular features of note include: flexible data entry, support for integer and real data types, wavelength indexing of spectra and spectral curve extraction.

INTRODUCTION

There are a growing number of remotely sensed data sets which have the ability to highlight both the spectral and spatial properties of a target area. Unfortunately there has been very little concurrent software development to aid the analysis of such data sets. One notable exception is the Spectral Analysis Manager developed by the Jet Propulsion Laboratory (Mazer et. al. 1988). However, this software was developed specifically for AIS data and problems were encountered when processing AVIRIS data. In addition, adding to SPAM's spectral library can be difficult and until recently the software only operated under the VAX/VMS environment. This led the authors to develop a system for analysis of high spectral resolution data, termed T-Spectra. The software is designed to process image data with an almost infinite number of spectral channels from either laboratory or airborne/spaceborne sensors and is built around a data reading engine intimately tied to wavelength information.

The advent of spectrometer data demands a new approach in image processing; changing functionality away from display and enhancement towards techniques for spectral processing. A number of researchers have identified priority areas for software improvement for dealing with data generated by the EOS programme (Warton and Newcomer 1989, Halem 1989).

Current research using imaging spectrometer data shows

that there is a need for rapid evaluation, calibration, and pre-processing before substantive interpretation is possible. Therefore, software needs to be orientated towards spectral and numerical functions. Equally important, data should be easily entered, displayed, and saved in a form that preserves the history of the procedures applied to it. At the core of spectral analysis are qualitative and quantitative methods for comparing spectra. Therefore, it is important to retain a quantitative description of essential data such as wavelength position, spectral sampling, and statistical properties of the data to avoid confusion and aid later analysis.

The software described in this paper specifically addresses the computational and graphical requirements of high spectral resolution data. It has been implemented to run on a standard IBM Personal Computer and has been successfully applied to analyse AVIRIS data from NASA's 1989 Airborne campaign, providing a simple and effective tool for integrating laboratory and image-based spectral data.

SOFTWARE DESIGN

The software has been developed with the following principal objectives:

1. Software must read image or laboratory data from a wide range of data types.
2. There should be no limit to the spectral dimension of the data cube.
3. The data should be structured and processed according to the wavelength start and stop position of each data channel.
4. The code should be structured and where possible conform to ANSI standards to ensure portability and maintenance.

Thus far, a system is available for IBM PCs with VGA (or EGA) graphics. It contains certain fundamental image processing functions such as spatial filters and image enhancement routines as well as the following spectral analysis capabilities (see figure 1):

1. The data entry and conversion functions can handle any combination of Bands, Samples, and Lines and convert among these.
2. Spectral plots are directly tied to image coordinates and can be compared visually with library spectra.
3. Scatter plots are mapped to image coordinates; thus the location of each point on the plot may be found in the image. This is of particular value for identifying likely spectral end-members.
4. The software has a menu-led interface.

Figure 1. The structure of the T-SPECTRA software showing its major functions.

User Interface				
(Forms)				
File structure				
(Data types, header structure)				
Arithmetic	Statistics	Filters	Graphics	Spectra
-Single band	-Whole image	-Stat	-Hist	-Pixel
-Multi band	-Sub area	-Spatial	-Scatter	-Lib
-Strips				
Display				
-Window				
-Zoom				
-Sub-sample				

User interface

The interface has two screens; a text screen with sliding bar menus is used for displaying information such as commands, responses, help, statistics, and file management tasks (see figure 2); a graphics screen is used to display images, graphs and spectral plots (see figure 3).

A series of pull-down menus on the graphics screen allow the user to set area and statistical parameters for spectral curve extraction and plotting. One feature of the interface is its ability to remember the parameter settings used to generate spectra. Therefore, it is possible to reload a saved spectrum and the file structure will retain its spatial and statistical properties.

Screen forms are provided to assist with the description of the format of data to be entered into the system. The user is presented with an appropriate template from which to choose or specify image or spectral file details. Details on the form not known to the user or the system are calculated automatically without need to exit the form. In the future the interface will supply the necessary menus for users to spawn their own functions, supplied as executable programs.

In addition, the MS-DOS system may be accessed directly or simply called to generate directory listings.

File structure

The file structures are a novel feature of the T-SPECTRA software. Our approach has been to define three separate but interrelated header structures for images, spectra, and graphical plots. For example, the image header structure contains essential information about the data type, format, and wavelength position for each data channel. The corresponding structure for a spectrum contains details of its genesis (eg. image position and statistical processing), wavelength range

Input form (01)	Input form (02)	Output form (03)
Desc. file:	Desc. file:	Desc. file:
Format to use:	Format to use:	Format to use:
Start at sample:	Start at sample:	Start at sample:
Stop at sample:	Stop at sample:	Stop at sample:
Start at line:	Start at line:	Start at line:

Format to use

Format to use

Start at sample 336

Start at line 9

Start at line 264

Sample resample 1

Line resample 1

Format to use 38

Press ESC when finished.

Barocis N/A

Shouess N/A

Figure 2. (See Slide 22) The T-SPECTRA menu interface showing interactive selection of input image format.

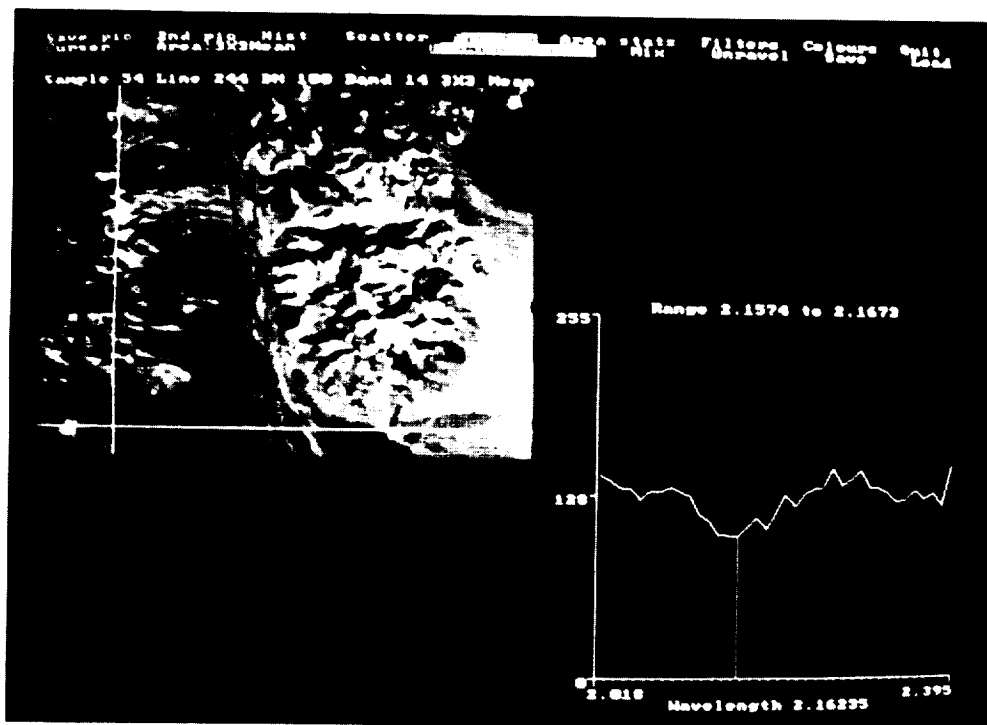


Figure 3. (See Slide 23) The graphics interface showing an albedo image from AVIRIS SWIR data processed with the log residual technique. Spectra from a 3*3 area have been interactively extracted and these correspond closely with the minerals kaolinite and alunite.

and bit fields for recording information about the shape of the spectral curve.

The image structure supports a wide range of data types, and, where necessary, will process data in 8-byte double precision arithmetic (table 1). These types are supported by a memory manager which loads the function for the appropriate data type and so it is possible to provide optimal support for any data type.

Table 1. Data types supported	bytes
unsigned char	1
signed int	2
float	4
double	8

The user defines the system's file structure with reference to a 'look up' file which tells the system how the data is formatted and where to find it. This file can be viewed and edited in ASCII format with any text editor. This approach gives enormous flexibility and negates much of the need for file conversions.

All arithmetic calculations are processed in double precision since many data sets produce absolute numerical reduction to physical values. Separate data files can be processed in an operation regardless of data type or file format (BSL, SBL etc.).

The file handling procedures are designed to be freely read in order to facilitate data exchange and integration.

SPECTRAL ANALYSIS

There are two methods of analysis for spectral data. First, spectra may be generated interactively from multi-channel imagery from a screen which displays both a spectral plot and a single channel reference image simultaneously. An exact position is selected by moving a mouse or cursor keys and the program then plots the raw data from disk as a spectral plot. Figure 3 shows an example of spectra being generated from SWIR AVIRIS 1989 data from Cuprite mining district, Nevada. Results from the analysis of these data are presented in Hook and Rast (1990) in this volume. In figure 3 the spectra represent the mean of a 3 by 3 kernel with no threshold defined. Up to sixteen spectra may be loaded (any number may be viewed) and interrogated using the **examine curves** option. This allows a moving cursor to range along the wavelength axis and display the FWHM positions for each AVIRIS channel for interpretation. Loaded spectra may be saved to a spectral library or simply as an ASCII file for export.

Spectra may also be displayed as a full screen plot or extracted from a graphical plot (see next section). In full screen mode, as with the image mode, both saved image and

laboratory spectra may be plotted and processed. In this mode functions are available for calculating hull quotients, spectral feature wavelength positions, and additive linear mixtures.

GRAPHICAL CAPABILITY

The system can produce spectral (or wavelength) plots, histograms and scatter plots. These may be saved or printed and are designed to relate directly to image data through the tying together of their coordinate systems.

Spectral plots

Any number of spectral channels may be plotted; however, the plot may be resampled spectrally depending upon the screen mode chosen. It is possible to re-scale both the intensity and the wavelength axes in order to view data at full spectral resolution or to compare spectra with differing spectral bandpasses. Multiple spectra may be plotted for any given wavelength range and each spectrum is resampled to that range. Each spectrum has a descriptive structure which contains its wavelength file and 16 bit fields are used to store information about its shape. Currently we are evaluating new methods for describing spectral shape for feature recognition purposes. Features include:

- plot tied to image coordinate system
- graphical display of multiple spectra
- linear mixing of n number of spectra
- save spectrum and re-display on same axis
- define spatial kernel for spectral data extraction
- print spectrum or spectra

Spectral extraction from scatterplots

It is possible to extract spectra directly from scatter plots.

This function takes advantage of the file system to locate image coordinates from plot coordinates. Where image locations are superimposed in plot space the coordinates are displayed and the user can either plot the spectrum or skip to the next location. Spectra can also be saved for later analysis.

Since image coordinates are stored during scatter plot generation it is possible to mark or mask the image location(s) of any plotted point.

Features include:

- Locate any plot coordinate on image
- Locate any image coordinate and locate on plot
- Set density slice (colours) for either band on plot
- View data in scaled or unscaled form
- Save and output to printer

BASIC IMAGE PROCESSING

There are a number of general purpose image processing functions incorporated into the software. These allow arithmetic and statistical manipulation of the data. For example, the system will allow the following arithmetic functions to be performed on images and on parts of images, defined as strips of rows or columns.

- log10, loge, sine, cos, tan, arcsine, arccos, arctan, sqrt
- linear equations, [+,-,*,/,constant]
- multiple ratio, average
- Strips (user defined rows or columns in the data)
- [+,-,*,/], sum, average, min, max

Statistics may be calculated on any number of selected bands or any area within the data cube (samples, lines, bands). Basic statistics are held in the header structure for image scaling for display purposes or can be calculated when required.

- min, max, mean, median, mode, variance, stdev

Filters

Filters are an important component of spectral analysis software, both for noise reduction and image enhancement purposes.

All image filtering is carried out in the spatial domain using convolutions defined by kernels. These are divided into mathematical and statistical transformations.

1. Mathematical

The following operations may be defined by a kernel of n^2 where $n > 1$ and is an odd number.

- Laplacian, Sobel, Inverse laplacian, Directional (edges)
- definable, Roberts (only applied as 2 by 2 kernel)

2. Statistical: -mean, median, mode, min, max, range, stdev
Several of the functions have been implemented as rapid screen enhancement routines in the spectral analysis mode.

CONCLUDING REMARKS

T-SPECTRA does not duplicate existing image processing software, instead it provides a data processing and development tool for high spectral resolution data. The software allows the user considerable flexibility for integrating and processing spectral data.

It differs from most image analysis systems developed for broad band multi-spectral data such as LANDSAT TM in that it processes data according to wavelength position. It is therefore possible to integrate both imaging spectrometer and laboratory spectroradiometer data easily with wavelength referenced plots.

The data reading engine has been written to allow flexibility of data format and data type as well as lifting restrictions on the number of spectral channels which may be processed.

Finally the program will run on **any** IBM (or strictly compatible) Personal Computer. It requires a VGA graphics card for the display, a minimum of 256k of RAM, a MS-Mouse, and a reasonably sized fixed disk drive to store the data. The software functions with or without a math co-processor and MS-mouse, and will run on any IBM PC platform operating under MS-DOS 3.3 or above.

For additional information please contact any of the authors at the addresses listed at the beginning of this paper.

REFERENCES

- Halem, M., (1989) Scientific Computing Challenges Arising From Space-Borne Observations. **Proceedings of the IEEE**, 77(7):1061-1091.
- Kruse, F.A., K.S. Kierein-Young, and J.W. Boardman. (1990) Mineral Mapping at Cuprite, Nevada with a 63-Channel Imaging Spectrometer. **Photogrammetric Engineering and Remote Sensing**, 56(1):83-92.
- Mazer, A., M. Lee, M.Martin, J.E.Sullivan, W. Lawton, G.T. Cooper. (1988) SPAM SPECTral Analysis Manager, Jet Propulsion Laboratory, California Institute of Technology, Pasadena, California.
- Warton, S.W. and J.A. Newcomer (1989) Land Image Data Processing Requirements for the EOS Era **IEEE Trans. Geoscience and Remote Sensing**, 27(2):236-242.

INVESTIGATIONS OF OCEAN REFLECTANCE WITH AVIRIS DATA

STUART H. PILORZ and CURTISS O. DAVIS
Jet Propulsion Laboratory, California Institute of Technology
M/S 300-323, 4800 Oak Grove Dr., Pasadena, California, 91109, USA

ABSTRACT

Multispectral imagery with the resolution of the Airborne Visible/Infrared Imaging Spectrometer (AVIRIS) offers the possibility for retrieving concentrations of in-water constituents in turbid and coastal waters inaccessible to instruments of low spectral and spatial resolution. The oceanography group at the Jet Propulsion Laboratory (JPL) is involved in an ongoing experiment at Monterey Bay, California, coupling AVIRIS overflights with in-situ data for development of spectral unmixing algorithms suitable for AVIRIS and the High Resolution Imaging Spectrometer (HIRIS). Given the low signal emitted by water, a large portion of the developmental work has centered on defining signal-to-noise characteristics necessary for separation of spectral endmembers. Although AVIRIS was not originally designed for ocean viewing, several improvements have been made in the data processing and acquisition, as well as to the instrument itself, which put AVIRIS on the borderline of detection requirements for estimation of chlorophyll concentrations. Further modifications have been proposed which would increase the S/N by a factor of 2 to 4 in the blue regions of the spectrum enabling use of the instrument for spectral unmixing of pigments, chlorophyll, and suspended sediments. This paper documents the present capabilities of AVIRIS for ocean studies and quantifies the need for improved S/N in the visible part of the spectrum.

INTRODUCTION

Quantitative evaluation of the concentrations of constituents within a body of water has many uses, ranging from analysis of pollutants and eutrophication in lakes and estuaries to estimation of carbon production in the ocean [JGOFS, 1988]. The dominant factor affecting the remote sensing reflectance of waters of slight to moderate turbidity is the bulk absorption of the water column. For the open ocean, surface chlorophyll concentrations have been regressed against ratios of reflected radiance taken for pairs of frequencies, but the larger number of absorbers in coastal waters (Figure 1) make this method unreliable in that environment. Specifically, with only a few bands and limited S/N, it becomes impossible even to deconvolve the effects of suspended sediment from those of chlorophyll on the reflected radiance. Also, differences in the carbon fixing capabilities of different phytoplankton groups relative to their chlorophyll content make it desirable to discriminate between them, or at least to discriminate between the concentration of chlorophyll itself and that of related pigments.

Analysis of in-water constituents that utilize the capabilities of an instrument such as AVIRIS hinges upon the development of a wavelength-dependent model expressing the reflected radiance as a function of the optical properties of the water column. This entails modelling the effects of the optical properties of individual particles or classes of particles upon the bulk absorption and scattering properties of the water column. Significant literature exists involving application of radiative transfer methods to hydrologic optics [Preisendorfer, 1976; Kirk, 1983], as well as dealing with Monte Carlo simulation of water optical properties [Gordon et al, 1975; Kirk, 1981]. A model consistent with both of the above expresses the water reflectance as being proportional to the bulk backscattering and

inversely proportional to the absorption properties of the water column [Morel and Prieur, 1977] :

$$R = k \cdot b_b / (b_b + a) \quad (1)$$

Here R represents the reflectance at a wavelength, b_b the bulk backscattering, and a the bulk absorption of the water column at that wavelength. The constant k has been empirically evaluated at 0.33. Expressing this equation at all wavelengths, and assuming that Beer's law holds for absorption, leads to a matrix equation for spectral reflectance as a function of concentrations of spectral endmembers [Pilorz and Davis, 1990]:

$$R_M(Ac + b) = kb \quad (2a)$$

$$\text{or} \quad c = (A^T A)^{-1} A^T (R_M^{-1} - I) kb \quad (2b)$$

R_M in equations 2a and b is a square matrix with reflectances at observed wavelengths as the diagonal entries, A is a column matrix of specific absorption coefficients at those wavelengths for some number of endmembers, c is a vector of concentrations for the endmembers represented in A , and b is a column vector of backscattering coefficients at each wavelength. Clearly, accurate evaluation of c from this expression must involve simultaneous estimation of the concentration vector and spectral backscattering, although that will not be discussed in the present text.

Use of the above expression with remotely sensed data requires additional formulae for propagation of flux across the water surface and expression of the upwelled radiance in terms of the reflectance. In the following expression [Gordon and Clark, 1981; Austin, 1974], L_u represents the upwelled radiance just above the surface, ρ and ρ_b represent the fresnel transmittances of the surface from above and below, n is the index of refraction of water, and Q is roughly equal to the inverse of the average upwelling cosine, used for conversion to radiance units:

$$L_u = E_d (1 - \rho)(1 - \rho_b)R / Qn^2 \quad (3)$$

METHODS AND DATA

The purpose of our investigation is to examine the feasibility of applying equations (1) through (3) to spectral decomposition through in-situ determination of the magnitudes and variances of individual terms as well as empirical testing of the reflectance model itself.

On 19 October 1989 in-water optical measurements were made on the R/V Shana Rae as part of an experiment in Monterey Bay in conjunction with an AVIRIS overflight taken the previous day. The research area is shown in Figure 2, where the overlaid boxes correspond to the scenes used in this analysis. Optical data were collected with a Bio-Optical Profiling System (BOPS), an updated version of the BOPS developed by Smith et al. [Smith et al., 1984]. The heart of the BOPS is a Biospherical Instruments MER-1048 Spectroradiometer which measures upwelling and downwelling spectral irradiance and upwelling spectral radiance. The MER-1048 also has sensors for Photosynthetically Available Radiation (PAR), depth, tilt, and roll. In addition, chlorophyll fluorescence was measured with a Sea-Tech fluorometer and beam transmission with a Sea-Tech 25-cm transmissometer. The BOPS data were filtered to remove obvious data spikes and then binned into one-meter averages over depth.

These data were used for calculation of optical parameters as well as chlorophyll concentrations for use in checking equations (1) through (3). Figure 3 shows plots of R ,

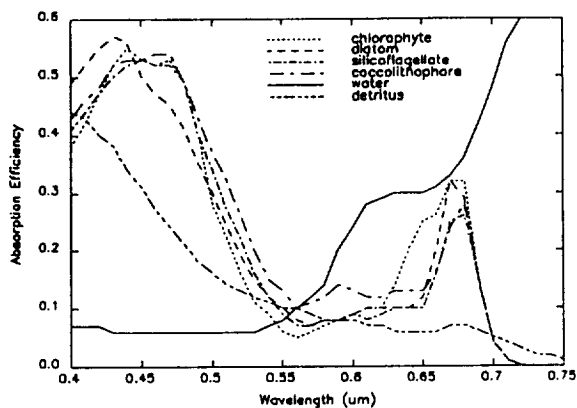


Fig. 1. Absorption efficiencies plotted versus wavelength for some classes of in-water constituents.

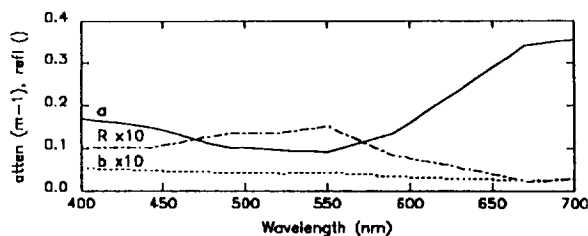


Fig. 3. Spectral absorption (a), reflectance (R), and backscattering (b) plotted versus wavelength. Reflectance is relatively smaller than absorption and inversely proportional to it.

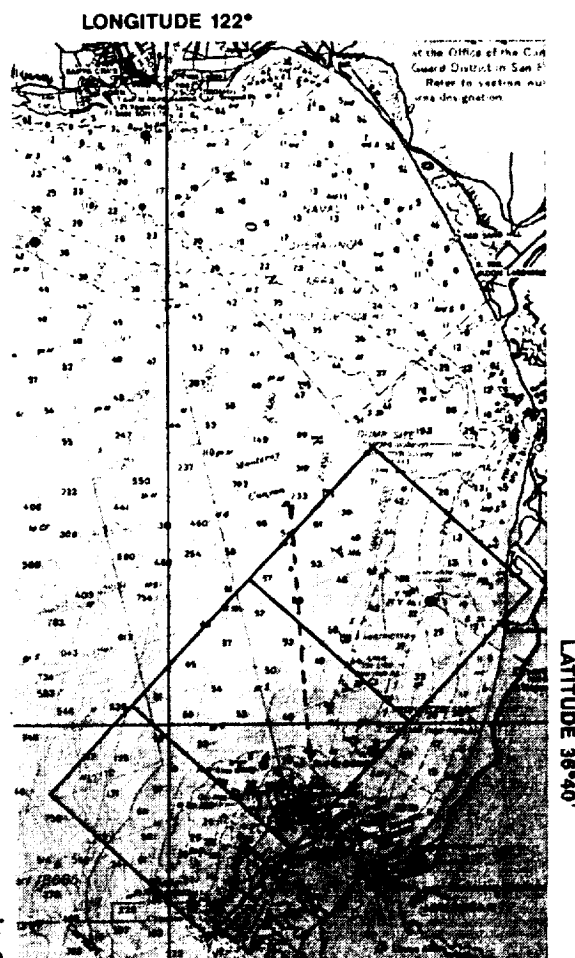


Fig. 2. Monterey Bay, California. Boxes correspond to AVIRIS scenes taken on 18 October, 1989. Dotted line shows transect plotted in figure 5.

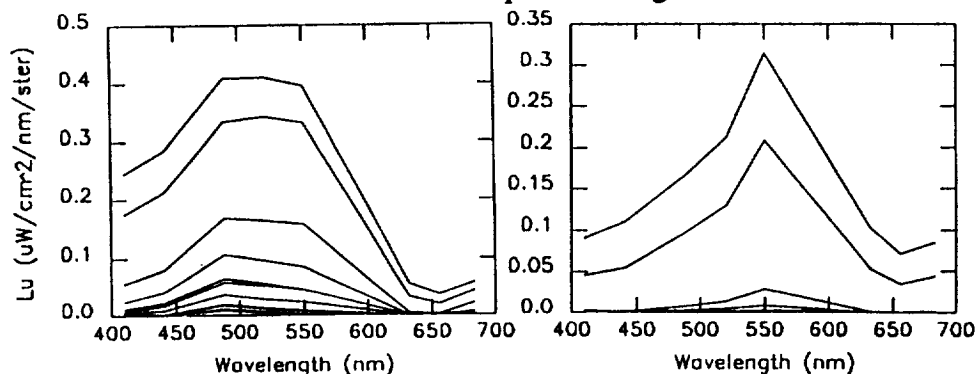


Fig. 4. (a) Upwelling radiance plotted versus wavelength from the station at 36°39.1'N, 121°55.8'W. Separate lines correspond to 5 m increments in depth. (b) Same as in (a) except for the station at 36°47.8'N, 121°50.8'W.

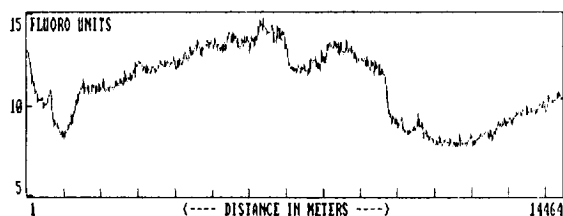


Fig. 5. Surface fluorometer measurements taken from the transect marked in figure (2).

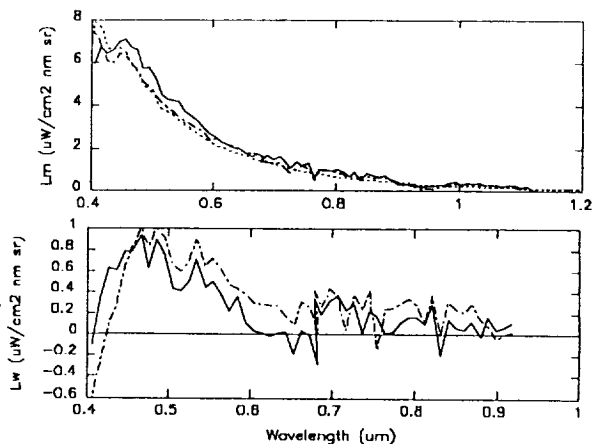


Fig. 6. (a) Spectrum from the scene plotted versus wavelength (solid), and path radiances calculated from LOWTRAN 7 and a single scattering model (dotted). (b) Difference between the received radiance and the calculated path radiances.

b, and a as functions of wavelength, evaluated at a station off Monterey, California, at $36^{\circ} 39.1' \text{ N}$ and $121^{\circ} 55.8' \text{ W}$. This shows the general inverse dependence of R upon a, as well as the small magnitude and spectrally flat properties of the backscattering spectrum, b.

Figures 4a and 4b show upwelling radiances below the surface from low and high chlorophyll stations, in which the effect of increased chlorophyll can be clearly seen as a depression of the reflectance in the 400 to 450 nm region in Figure 4b. The surface pigment levels correspond to approximately 2.5 and 6.5 mg chlorophyll + phaeopigment/ m^3 for figures (a) and (b) respectively, and even though the absorption was due to different phytoplankton groups at each station, the magnitude of the signal is characteristic of that which we would need to discriminate. A difference of $0.17 \mu\text{W}/\text{cm}^2 \text{ nm sr}$ at 450 nm for a chlorophyll variation of 3 or 4 mg/m^3 implies that we would need to distinguish signals on the order of $0.05 \mu\text{W}/\text{cm}^2 \text{ nm sr}$ in order to determine chlorophyll fluctuations on the order of 1 mg/m^3 .

Figure 5 is included to give an idea of the spatial structure of the chlorophyll field, taken along a 14 km transect running diagonally across the image (Figure 2). The fluorometry is a linear function of chlorophyll, where the peaks of 15 fluoro units correspond to approximately 2.7 mg chlorophyll/ m^3 (3.5 mg chlorophyll + pigment/ m^3) and the low of 7.5 fluoro units corresponds to approximately 1.3 mg chlorophyll/ m^3 (1.9 mg chlorophyll + phaeopigments/ m^3).

The AVIRIS data from the scene were taken at a solar zenith angle of approximately 48° , hence, they have an unfavorably small S/N. Figure 6 shows a sample spectrum from near the middle of the scene with path radiances calculated using LOWTRAN 7 and a single scattering model. The residual signal (Figure 6b) ranges from 2 to 15% of that received at the sensor, hence has a S/N ranging of 0.1 to 0.02 times that of the received signal.

Suppose that the S/N was 90:1 at 500 nm, then the standard deviation on a signal of $6 \mu\text{W}/\text{cm}^2 \text{ nm sr}$ would be about $0.075 \mu\text{W}/\text{cm}^2 \text{ nm sr}$, or roughly one DN. In actuality, from factors due mostly to aircraft-induced periodicities, we observe a standard deviation of roughly $0.26 \mu\text{W}/\text{cm}^2 \text{ nm sr}$, or about 3.5 DN (S/N of about 25:1), as compared to an atmospherically corrected signal on the order of $0.8 \mu\text{W}/\text{cm}^2 \text{ nm sr}$. This gives an effective S/N of slightly better than 3:1 for the signal, implying that discernment of a $0.05 \mu\text{W}/\text{cm}^2 \text{ nm sr}$ signal would require binning to a spatial resolution of 100 m, or 5×5 pixels, in the absence of correlation effects within the noise.

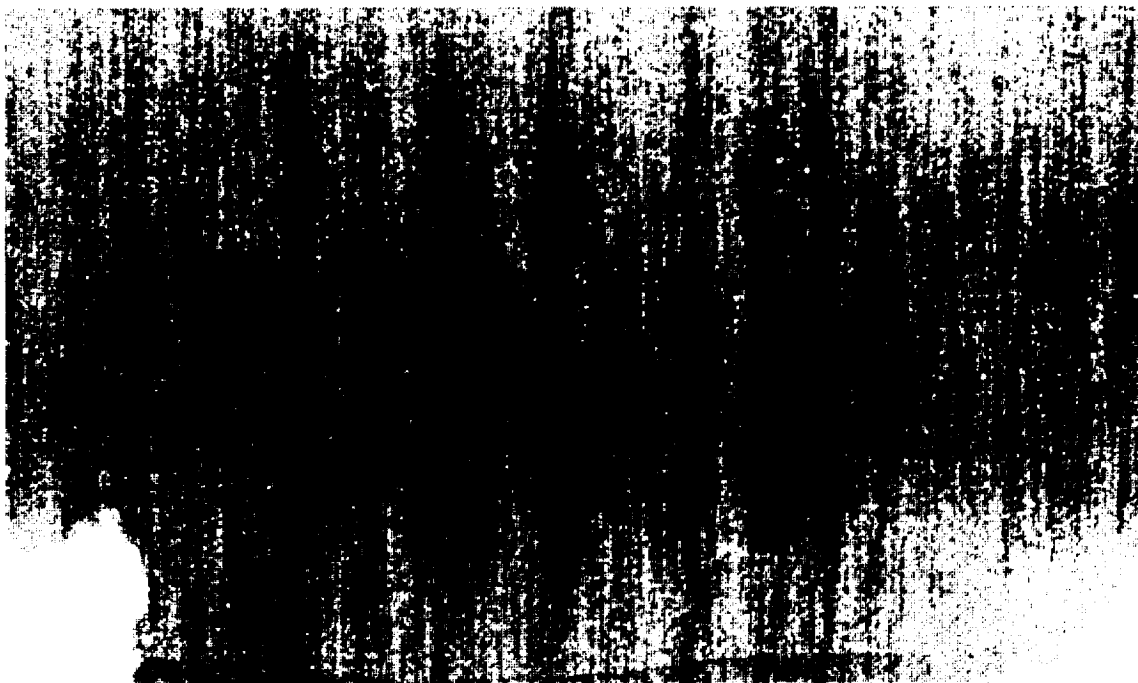


Fig. 7. Data from the calibrated AVIRIS scene corresponding to the Eastern two boxes in Figure 1. Band 12 is shown stretched linearly two standard deviations about the mean. Linear grey scale is used for this and other images.

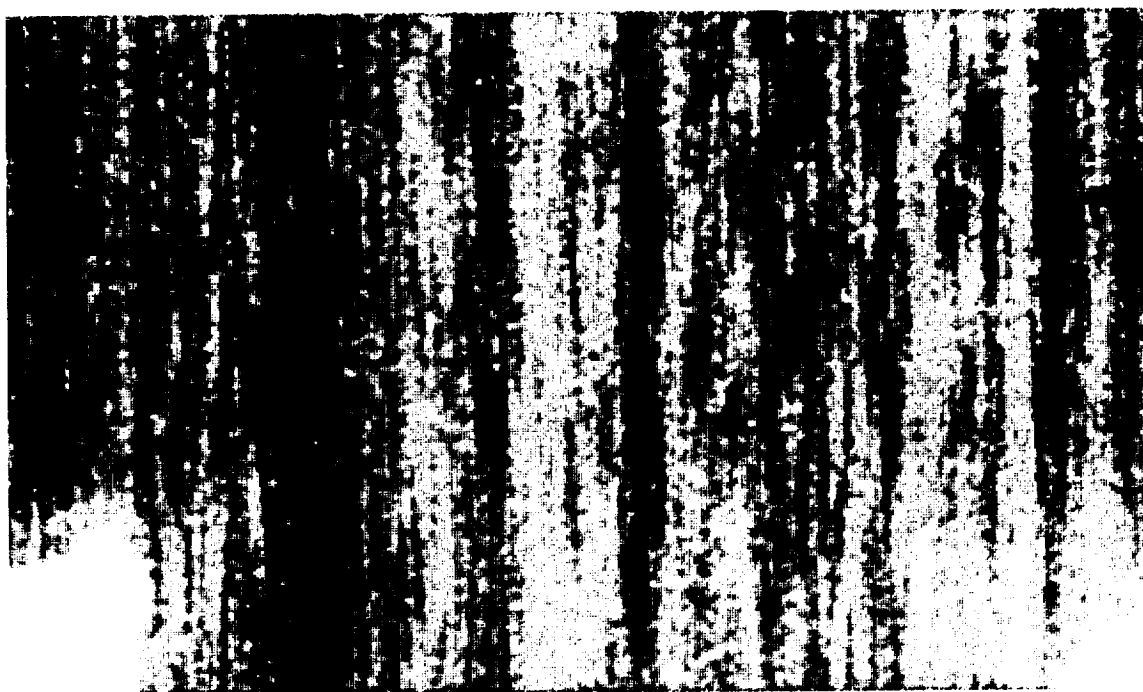


Fig. 8. Ratio of bands 15 to 12 from the AVIRIS scene, stretched linearly 2 standard deviations about the mean. This should give some idea of chlorophyll concentrations, as band 12 is more sensitive to chlorophyll than band 15.

Examination of the calibrated data, Figure 7, shows a vignetting effect of approximately $0.15 \mu\text{W}/\text{cm}^2 \text{ sr nm}$ in the cross-track direction. This resulted from the use of a single vignetting profile to correct all of the bands in spectrometer A, whereas in this region the vignetting is spectrally dependent. New vignetting profiles at each band have since been generated from integrating sphere data, and in the future these will be used routinely during data processing.

Application of a chlorophyll ratio algorithm using bands 15 and 12 (Figure 8) decreases the vignetting effect. Large features are apparent in this image; however, they are obfuscated by wide vertical striping not present in the raw data. This is due to subtraction of a dark current from each line during processing which was not representative of the actual dark current during the data acquisition for that line. This small effect is significant for dark scenes. Its appearance in this data has lead to changing the size of the boxcar filter applied to the dark current prior to its removal during data calibration, as well as to the investigation of modifications to the instrument which would allow collection of more dark current data during the scan flyback.

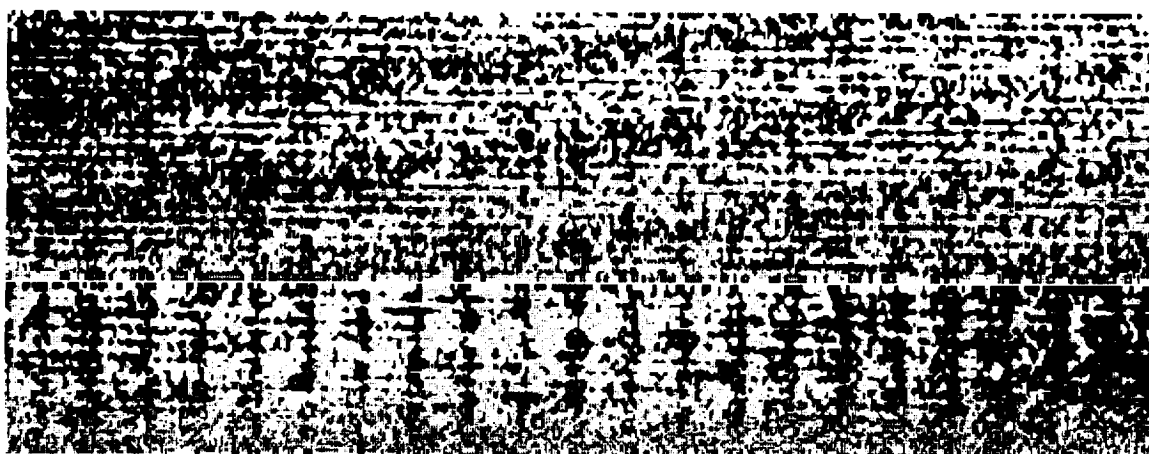


Fig. 9. One line of data from the AVIRIS scene. Bands 1 to 80 are along the vertical scale, with 614 cross-track samples along the horizontal. Data are smoothed by 3 pixels cross track and by 2 bands spectrally. Each band (row) has had the mean subtracted and is divided by its standard deviation.

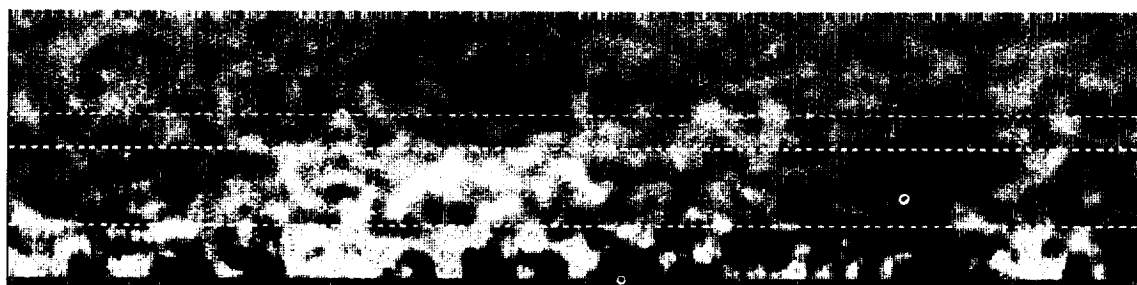
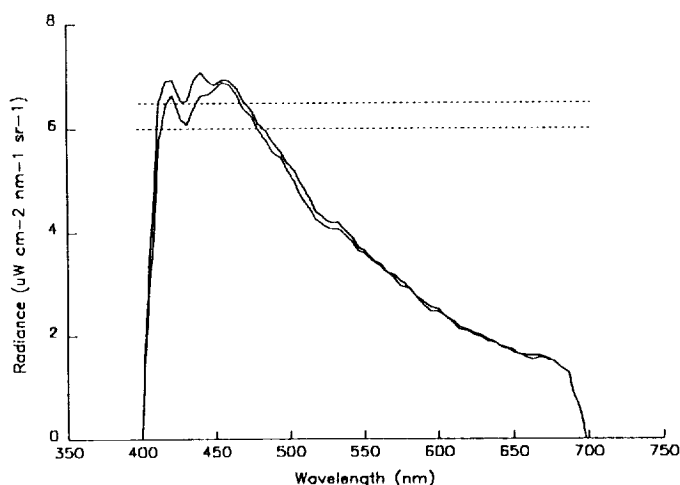


Fig. 10. Along track nadir transect from the AVIRIS scenes with bands 1 to 80 along the vertical axis and 1024 lines along the horizontal axis. Each row has had its mean subtracted and been divided by its standard deviation. Dotted lines correspond to bands 5, 12, and 15. Large features between bands 5 and 12 correspond to chlorophyll low and high, respectively, moving from left to right.

Fig. 11. Sample spectra from low and high chlorophyll areas within the scene, binned by 100 pixels (10 x 10) spatially. Dotted lines are at 6.0 and 6.5 $\mu\text{W}/\text{cm}^2 \text{ nm sr}$, and are intended to show the magnitude of the chlorophyll signature.



Viewing of a dark target has proven useful in finding periodicities in the signal as well. Figure 9 shows one line of data with spectral bands 1 to 80, in which multiple periodicities are apparent as vertical and diagonal striping. The signals causing these are both time sequential (diagonal bands) as well as scan related (vertical bands) and have individual amplitudes of up to more than 2 DN. Comparison with integrating sphere data has shown that most of this coherent noise is due to aircraft operation. The problems are twofold for viewing dark targets, in that the periodicities increase the standard deviation of the data (reducing the S/N), as well as preclude the use of binning to beat down the S/N. Also, due to the large number of frequencies and the mixing of some of these features with the vignetting profile, notch filtering was not possible with this data set.

Examination of a smoothed along track transect (Figure 10) shows the spectral variation from West to East across the scene. Patches of high chlorophyll would be seen at this resolution as relative lows in bands 1 to 12, with higher bands remaining relatively stable. Such a large high and low are evident moving across the scene from West to East (left to right). The issue of dark current effect, however, as well as a slight diagonal skew to the high pixels, suggests the possibility that this is at least partially an artifact due to periodic noise. Thus, caution is required in interpretation of this feature as being chlorophyll induced. Smoothed spectra taken from these areas, also along this transect, are shown in Figure 11, demonstrating that a signal may be extracted from the data.

CONCLUSIONS

AVIRIS and HIRIS data will undoubtedly be extremely useful for the study of the ocean's role in the world carbon cycle, as well as in understanding coastal waters whose complex reflectances elude the capability of low resolution instruments. In-situ studies as well as modelling indicate that the use of this data in the manner desired will require a Noise Equivalent Delta Radiance (NEDR) on the order of 0.05 $\mu\text{W}/\text{cm}^2 \text{ nm sr}$, well below the present stated requirements for AVIRIS. This study has shown that, nonetheless, AVIRIS is presently on the borderline for meeting the S/N requirements for ocean viewing.

Typical ocean albedos of 1 to 2% lead to a path radiance contribution of usually 90% to the radiance received at the sensor. Calibration sensitivities for this study ranged from 0.4 to 0.05 $\mu\text{W}/\text{cm}^2 \text{ nm sr}$ in the blue spectrum, with a NEDR ranging from 0.8 to 0.1. The net result is that without substantial data binning, the desired signal is sufficiently less than the noise in the signal, and care must be taken to limit coherent noise as much as possible.

Substantial contributions to the NEDR from aircraft operation were apparent in this data, as well as patterns due to spectrally dependent vignetting and dark current filtering. These problems are especially bothersome in that they will not be removed by binning, and

are not always obvious in themselves. The steps which have been taken to remedy these problems are increased shielding on instrument cables, routine application of spectrally dependent vignetting profiles, and modification of the filter size applied to the dark current during processing. In addition, the AVIRIS engineering team has suggested several relatively inexpensive modifications to the instrument which, if implemented, could produce a factor of 2 to 4 increase in S/N in the blue spectral region by the 1991 or 1992 season. These include modifying the blaze on the diffraction grating for spectrometer A, changing some spectrally dependent optical coatings in the foreoptics, and replacing the line array for spectrometer A with one of higher efficiency. The results of this study suggest that such improvements would be extremely beneficial for future oceanographic studies.

ACKNOWLEDGMENTS

The authors would like to thank the AVIRIS engineering team in general and Rob Green in particular for their many invaluable suggestions and keen interest in increasing the performance capabilities of the instrument. The research described in this paper was carried out at the Jet Propulsion Laboratory, California Institute of Technology, and was funded by NASA grant FY-413-18-00-06-45 to C.O. Davis and the HIRIS project.

REFERENCES

- Austin, R. "The Remote Sensing of Spectral Radiance from below the Ocean Surface," Optical Aspects of Oceanography, N.G. Jerlov and E.S. Nielsen [eds.], pp. 314-344, Academic, 1974.
- Gordon, H. and D. Clark, "Clear Water Radiances for Atmospheric Correction of Coastal Zone Color Scanner Imagery," Applied Optics, Vol. 20, No. 24, pp. 4175-4180, 1981.
- Gordon, H. et al., "Computed Relationships between the Inherent and Apparent Properties of a Flat Homogeneous Ocean," Applied Optics, Vol. 14, No. 2, pp. 417-427, 1975.
- Kirk, J., "Monte Carlo Study of the Nature of the Underwater Light Field in, and the Relationships between Optical Properties of Turbid Yellow Waters," Aust. J. Mar. Freshwater Res., Vol. 32, pp. 517-532, 1981.
- Kirk, J., Light and Photosynthesis in Aquatic Ecosystems, Cambridge Press, NY, 1983.
- Morel, A. and L. Prieur, "Analysis of Variations in Ocean Color," Limnol. Oceanogr., Vol. 22, No. 4, pp. 709-722, 1977.
- Pilorz, S. and C. Davis, "Spectral Decomposition of Sea Surface Reflected Radiance," Proc. IGARSS 1990, Vol. 1, pp. 345-348, IEEE, 1990.
- Preisendorfer, R., Hydrologic Optics, U.S. Dept of Commerce NOAA publ. (6 volumes), 1976.
- Scientific Committee on Oceanic Research, "The Joint Global Ocean Flux Study, Report of the First Session of the SCOR Committee for JGOFS," Miami, FL, January 25-28, 1988.

Reflectance spectra from eutrophic Mono Lake, California,
measured with the Airborne Visible and Infrared Imaging Spectrometer (AVIRIS)

John M. Melack

Department of Biological Sciences and Marine Science Institute
University of California, Santa Barbara, CA 93106

Stuart H. Pilon

Jet Propulsion Laboratory, California Institute of Technology
4800 Oak Grove Drive, Pasadena, CA 91109

ABSTRACT

An AVIRIS image was obtained for Mono Lake, California, on 26 May 1989, a day with excellent visibility. Atmospherically-corrected reflectance spectra derived from the image indicate a spectral signature for chlorophyll *a*, the dominant photosynthetic pigment in the phytoplankton of the lake. Chlorophyll *a* concentrations in the lake were about 22 mg m⁻³, and the upwelling radiance was low with a peak reflectance at about 570 nm of about 5%. Coherent noise appeared in the image as regular variations of 0.1 to 0.2 $\mu\text{W cm}^{-2} \text{sr}^{-1}$ oriented diagonally to the flight line. A simple ratio of two spectral bands removed the conspicuous undulations, but modifications of the shielding within the instrument are needed to improve the signal, especially over dark targets such as lakes.

1. INTRODUCTION

Lakes have several distinctive characteristics which require for their study by remote sensing the spatial and spectral resolution offered by imaging spectrometers such as the Airborne Visible and Infrared Imaging Spectrometer (AVIRIS). In particular, most lakes are moderate to small-sized, have long interfaces with land and often have strong horizontal gradients in biological and physicochemical conditions. Furthermore, a very wide range of optical conditions occurs among lakes.

Recent satellite-borne sensors have permitted some success in the examination of lakes. While identification of open water and sediment-laden water is straightforward^{1,2,3}, quantitative detection of chlorophyll by the Landsat Multispectral Scanner and Thematic Mapper has had only modest results^{4,5,6,7,8}. While the Coastal Zone Color Scanner (CZCS)⁹ has proven valuable in mapping chlorophyll distributions in oceanic environments^{10,11,12,13}, its application to large lakes has been less common and less successful¹⁴ and its application to small or moderate-sized lakes is precluded by its pixel size.

Accurate measurement of primary productivity is a major scientific problem in lakes and is amenable to significant improvement with application of imaging spectrometry. Primary productivity is generally estimated from measurements of the quantity of photosynthesizing material and the rate of carbon fixation per unit biomass. Much of the variance in such estimates is owed to temporal and spatial variability in the distribution of the photosynthetic organisms^{8,15}. Synoptic coverage provided by remote sensing offers a considerable reduction in errors associated with spatial heterogeneity. Furthermore, phytoplankton species vary in pigment composition as a function of taxonomic group and nutritional status. Hence, additional improvements in estimates of primary productivity are possible if spectral signatures are obtained that permit discrimination of taxa or nutritional condition. Recent bio-optical modeling of oceanic primary productivity^{16,17} shows promise for use in lakes when combined with data obtained from imaging spectrometers.

The principal problem with application of airborne imaging spectrometers to lakes is the weak upwelling signal, especially when narrow spectral bands with high spatial resolution are sought. Furthermore, atmospheric path radiance dominates the signal received from dark targets such as lakes. An additional potential concern is the adjacency effect¹⁸, i.e. diffuse radiation scattered into the line-of-sight of the sensor from neighboring, bright terrain. Once atmospheric effects have been removed from the radiance received at the sensor, semi-empirical relationships can be developed to extract information about phytoplankton pigment concentrations for different underwater optical conditions^{19,20,21,22}. In lakes where concentrations of dissolved organics and suspended detritus may not co-vary with phytoplankton pigments, the many spectral channels of an imaging spectrometer such as AVIRIS are likely to be required to distinguish the various aquasols.

AVIRIS utilizes silicon and indium antimonide line array detectors to cover the spectral region from 0.395 μm to 2.45 μm with 224 contiguous, 10-nm wide bands²³. When flying at an altitude of 20 km aboard NASA's ER-2 aircraft, the instrument images a 614-pixel swath with ground instantaneous field-of-view of 20 m and a swath about 10 km wide. Ten-bit data are recorded onto 14-track high-density digital tapes at a rate of 17 Mbit s⁻¹. Signal-to-noise specifications for a surface albedo of 0.5 viewed through a standard LOWTRAN atmosphere with 23-km visibility are 100 to 1 at 0.7 μm . The electronics are packaged by major function in an attempt to isolate signal chains from other noisier circuitry.

The objectives of this paper are three fold: (1) To present reflectance spectra with the atmospheric path radiance removed for a lake with moderate phytoplankton abundance; (2) To estimate the chlorophyll content of the lake by applying CZCS-type algorithms to AVIRIS data; (3) To examine the spatial variability of reflectances from the lake. These objectives are prerequisites to an application of AVIRIS data for modeling of primary productivity in lakes.

2. METHODS

2.1. Study site

Mono Lake is a large (150 km²), moderately deep (mean depth, 17 m), hypersaline (total dissolved solids, ca. 90 g L⁻¹) lake lying in the North American Great Basin just east of the Sierra Nevada, California (38°N, 119°W; elevation ca. 1942 m above sea level)²⁴. A decade-long, ongoing limnological study has included examination of spatial variability of the plankton^{5,25} and primary productivity²⁶. The phytoplankton is dominated by very small (2-3 μm diameter) coccoid cells that vary in abundance from <1 to ca. 60 mg chlorophyll a m⁻³. The offshore waters are largely uncontaminated by suspended particles from inflows.

2.2. Sampling and measurements

Two flight lines were flown over Mono Lake on 26 May 1989. Only the flight segment that covered the western and southern portions of the lake was used in the analyses reported here because the field sampling was limited to this region. The five segments acquired combine to include most of the lake.

Twenty locations (Figure 1) were sampled for phytoplankton on 26 May 1989. Integrated samples of the top 2 m were collected with a plastic tube at each location. The material was kept cool and in the dark during transport to the field laboratory, where the water was filtered onto 47 mm Gelman A/E glass fiber filters or 47 mm Whatman GF/F glass fiber filters; the filters were kept frozen (ca. -40°C) until pigments were analyzed. The filters were homogenized in 90% acetone, and the pigments extracted at room temperature in the dark for about 30 minutes. Following clarification by centrifugation, absorption was measured at 750, 665, 663, 645, 630, 570 and 480 nm. The samples were then acidified (0.1 ml of 0.1 N HCl per 3 ml of extract) in the spectrophotometer cuvette, and absorption was determined at 750 and 665 nm. Absorbances were converted to chlorophyll a, b and c and carotenoid concentrations²⁷ and to phaeophytin-corrected chlorophyll a concentrations²⁸. At four locations underwater attenuation of photosynthetically available irradiance (PAR, 400 nm-700 nm) was measured with a submersible LiCor quantum sensor.

Mono Lake

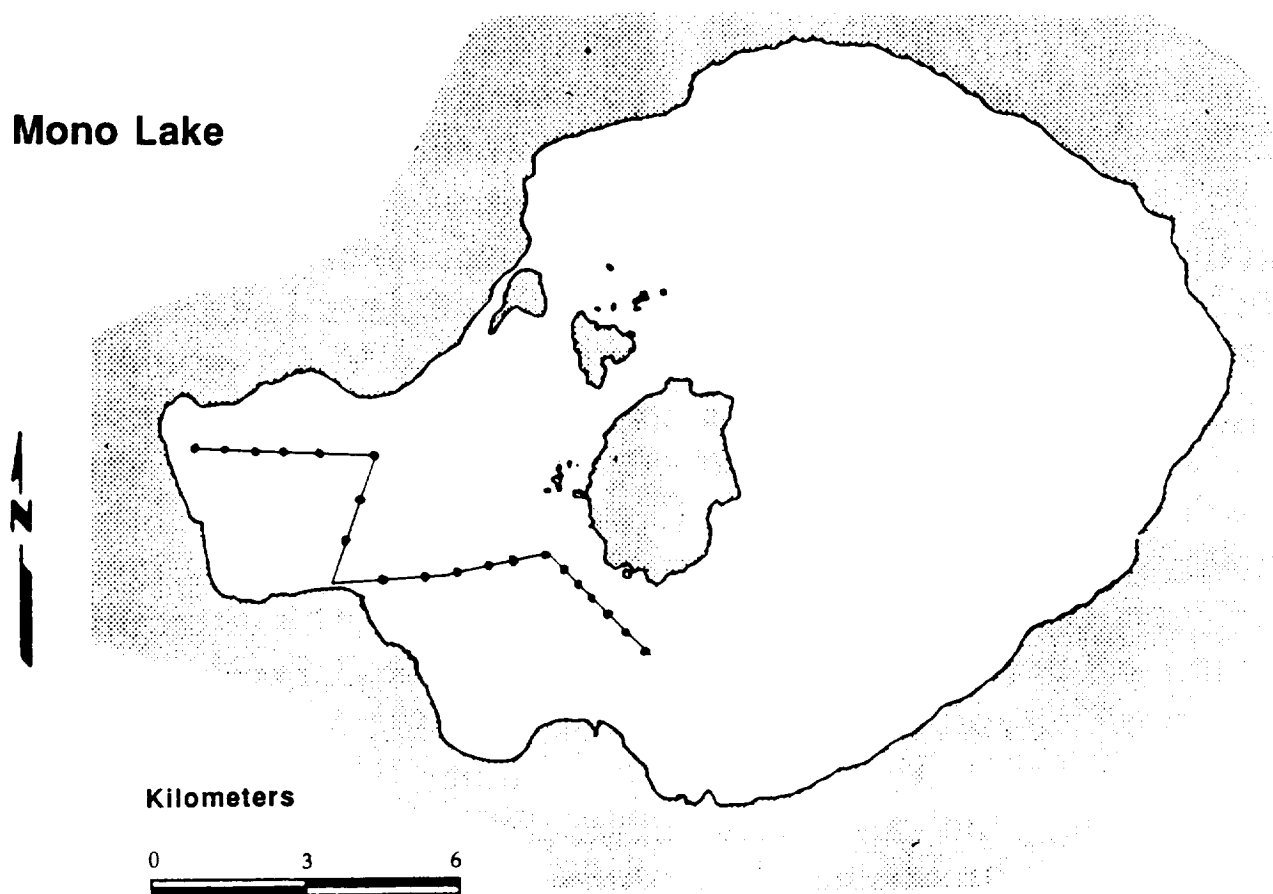


Figure 1 Mono Lake shoreline at lake level of 1945 m above sea level. Stippling is land. Line with dots is sampling transect; station numbers are consecutive from west (1) to east (20) along line.

On 26 May 1989, measurements were made with a Reagan radiometer of atmospheric conditions, and measurements of the spectral reflectance of dark, volcanic debris and bright deposits were made with the Portable Instant Display and Analysis Spectrometer (PIDAS)²⁹. These measurements were used to calculate atmospheric corrections of the spectral imagery with LOWTRAN 7³⁰ and the empirical line algorithm³¹.

3. RESULTS AND DISCUSSION

Visibility, as measured with the Reagan radiometer, was excellent on 26 May 1989; hence, conditions were ideal for imaging Mono Lake with AVIRIS.

Attenuation of PAR was 0.84 m^{-1} ; hence the 10% light level was 2.7 m and the 1% light level was 5.5 m. Chlorophyll concentrations in Mono Lake were moderate (Figure 2, Table 1) compared to the seasonal range in Mono Lake. As expected, chlorophyll a is the dominant photosynthetic pigment in the phytoplankton. The minor amounts of chlorophyll b indicate the presence of chlorophytes, and the chlorophyll c indicates diatoms and/or chrysophytes.

Table 1. Pigment concentrations in Mono Lake, 26 May 1989; Mean \pm 1 standard deviation (SD) for 20 stations from Gelman A/E filters. Chlorophyll a concentrations determined from Whatman GF/F filters are about 10% higher. All but the first chlorophyll values are calculated according to Strickland and Parsons²⁷.

Pigment	Mean \pm SD mg m ⁻³
Chlorophyll a ²⁸	22.3 \pm 3.4
Chlorophyll a	21.6 \pm 3.1
Chlorophyll b	5.3 \pm 1.3
Chlorophyll c	5.7 \pm 2.2
Carotenoid 1	10.5 \pm 2.5
Carotenoid 2	8.4 \pm 1.9

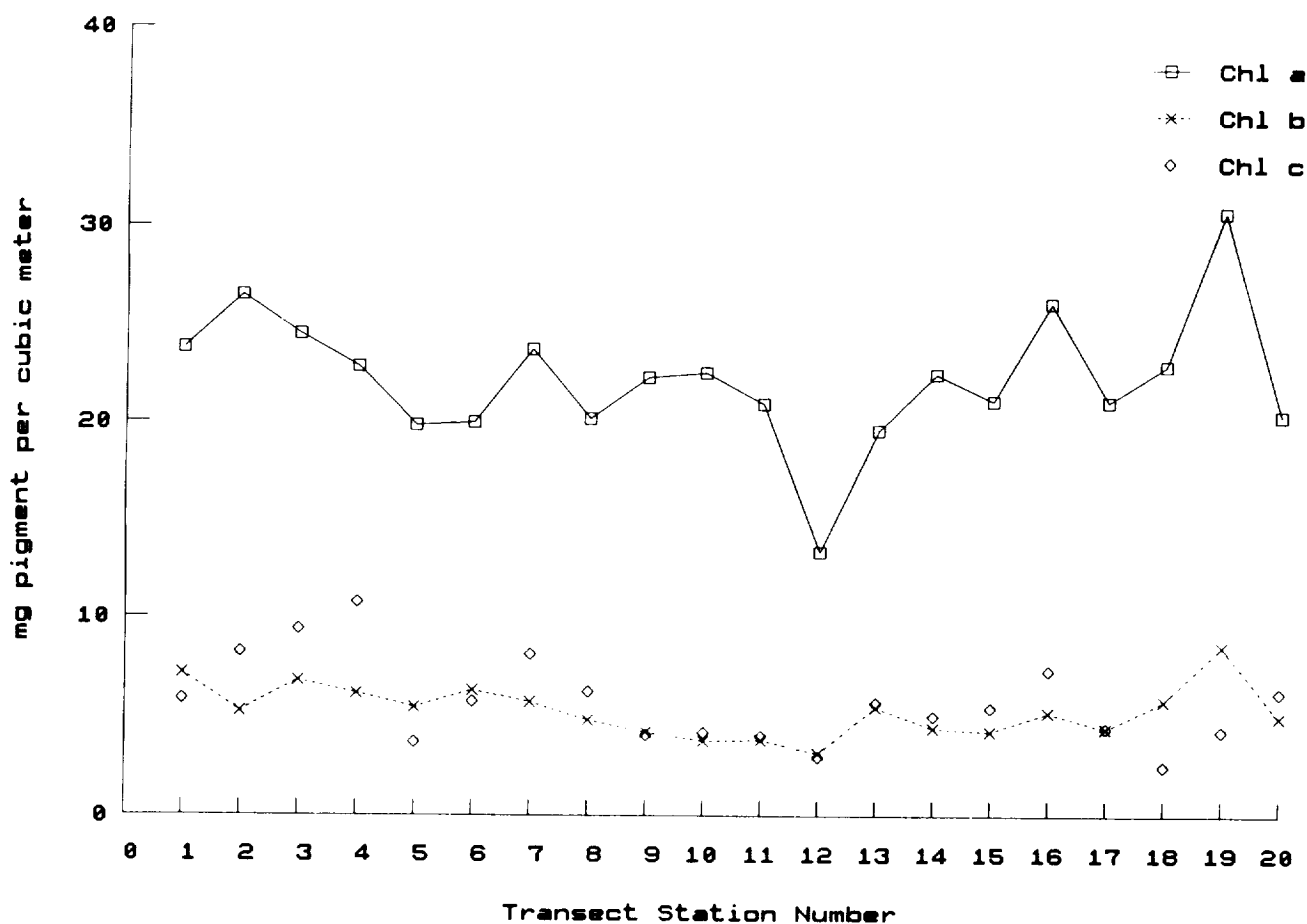


Figure 2 Chlorophyll (chl) a, b, c concentrations at 20 stations in Mono Lake, 26 May 1989. Chl a is phaeophytin corrected using the method of Golterman²⁸; chl b and chl c are calculated using the method of Strickland and Parsons²⁷.

As an initial attempt to calculate chlorophyll concentrations in Mono Lake from AVIRIS data, the CZCS algorithm developed for oceanic waters with about 1 mg chlorophyll m⁻³ was applied. CZCS spectral bands at 520 and 550 nm were simulated by a weighted summation of the four AVIRIS bands closest to each of the two CZCS bands. The weighting factors were derived from applying a normal distribution to the 20 nm full width-at-half maximum locations of the two CZCS bands. The chlorophyll concentration was calculated using the equation:

$$\log_{10} \text{chl}a = 0.522 + 2.44 (\log_{10} (L_w^{550}/L_w^{520})) \quad (1)$$

where L_w^{550} and L_w^{520} are the upwelling radiances at 550 nm and 520 nm. This algorithm produced chlorophyll values of about 10-12 mg m⁻³. These values are about half those measured in the lake (Table 1). However, the actual values in Mono Lake exceeded by about an order of magnitude the values used to develop the CZCS algorithm. Moreover, the lake probably contains other aquasols that behave different optically from those typically found in offshore oceans. Further research, now in progress, will utilize more of the spectral information from AVIRIS to develop new algorithms appropriate for inland waters.

Atmospherically-corrected reflectance spectra from Mono Lake indicate a signature of chlorophyll a (Figures 3 and 4). Both the empirical line method and LOWTRAN served well for atmospheric correction as judged by visual inspection; further comparison is warranted. Maximal reflectance broadly peaked at about 570 nm; a secondary peak occurred between 400 and 450 nm. Reflectance minimum occurred at about 680 nm and 480 nm, the regions of chlorophyll absorbance peaks. These reflectance spectra are among the first good spectra obtained for inland waters with AVIRIS.

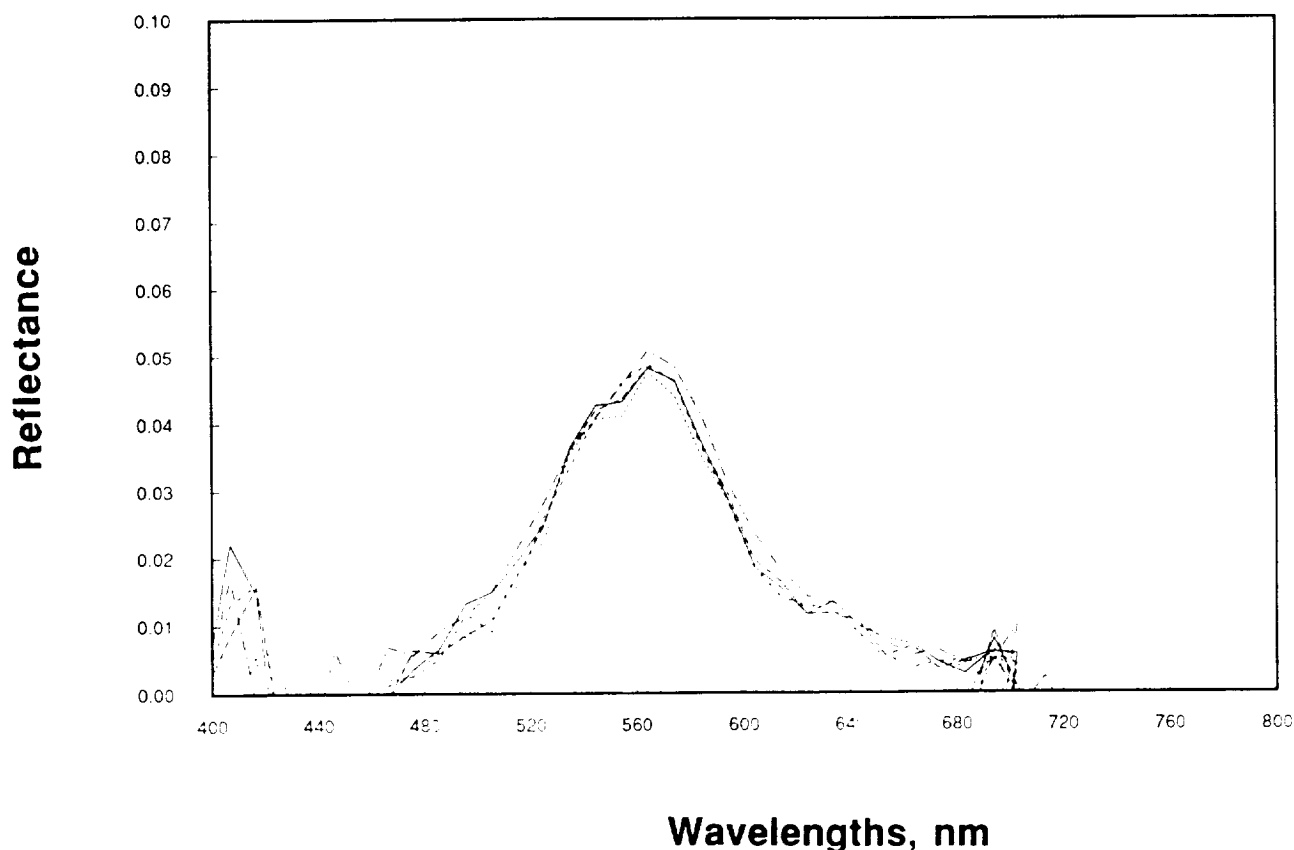


Figure 3 Reflectance spectra, atmospherically corrected with empirical line method³⁰, for five pixels in south-central Mono Lake, 26 May 1989.

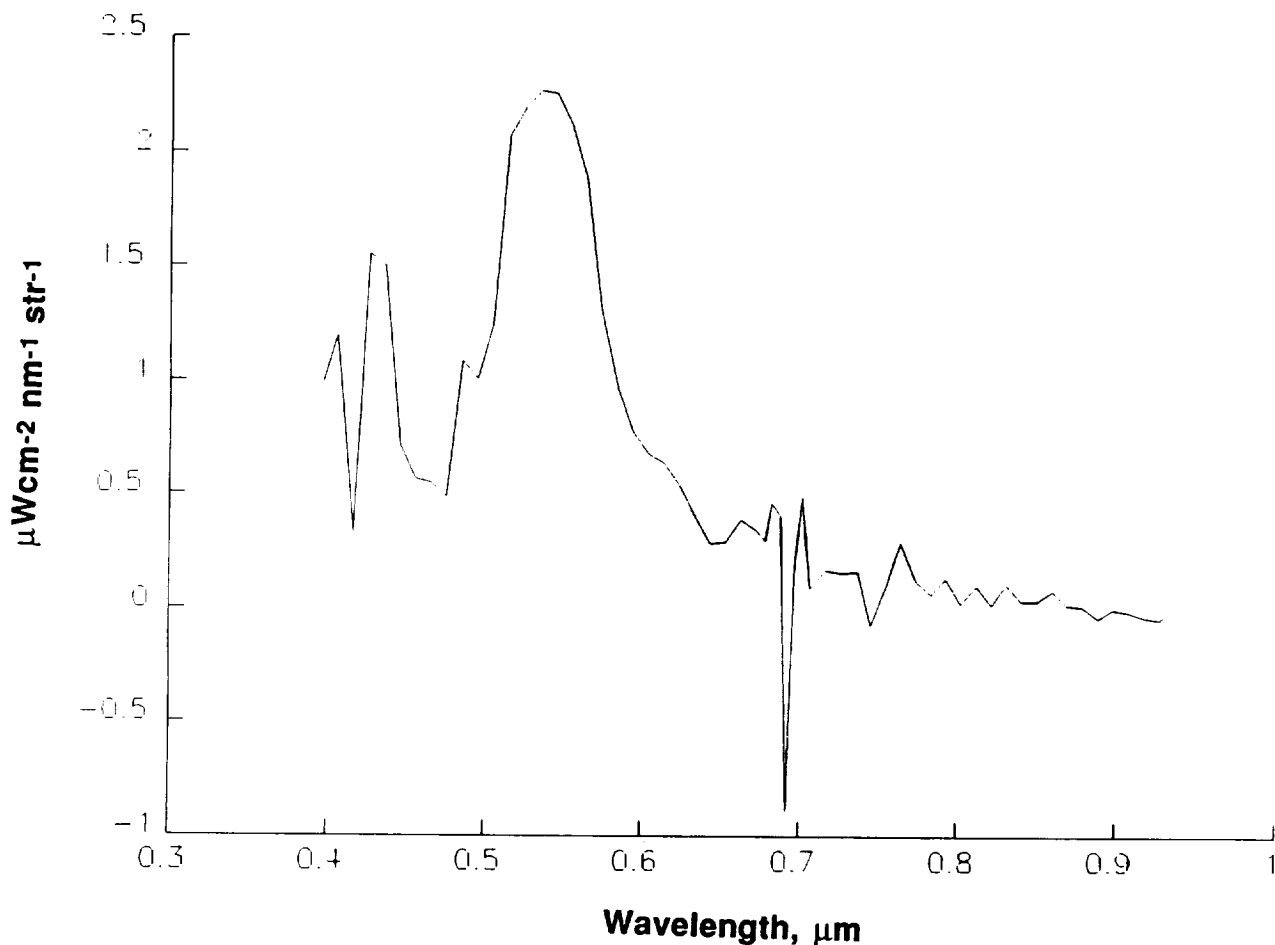


Figure 4 Reflectance spectrum, atmospherically corrected with LOWTRAN 7, for a 15 x 15 pixel averaged region in west-central Mono Lake, 26 May 1989. Spike at about 0.69 μm is an artifact of switch from spectrometer A to B.

As expected for a dark target such as an eutrophic lake, the reflectances are low. Maximal values are about 5%, and the low upwelling radiances (0.5 to 2.5 $\mu\text{W cm}^{-2} \text{ nm}^{-1} \text{ str}^{-1}$) impose high signal to noise requirements on the instrument. During the period in which these data were taken, the instrument detection capability varied from approximately 0.35 to 0.1 $\mu\text{W cm}^{-2} \text{ nm}^{-1} \text{ str}^{-1}$ over the wavelengths from 410 to 550 nm. In addition, coherent noise was evident in the imagery (Figure 5). The largest of these effects appears in the form of 0.1 to 0.2 $\mu\text{W cm}^{-2} \text{ nm}^{-1} \text{ str}^{-1}$ undulations oriented diagonally to the flight line (Figure 6).

Deciphering spectral signatures of even broad classes of absorbers such as chlorophyll, phaeopigments, and suspended sediments, will require the ability to distinguish 0.1 to 0.05 $\mu\text{W cm}^{-2} \text{ nm}^{-1} \text{ str}^{-1}$ differences in upwelling radiance. In order to obtain this goal it will be necessary to remove a large portion of the coherent noise patterns and make use of spatial, and possibly spectral, data binning. Most of the coherent noise is now known to be due to aircraft operation, which may be improved by planned modifications to the shielding of the instrument.

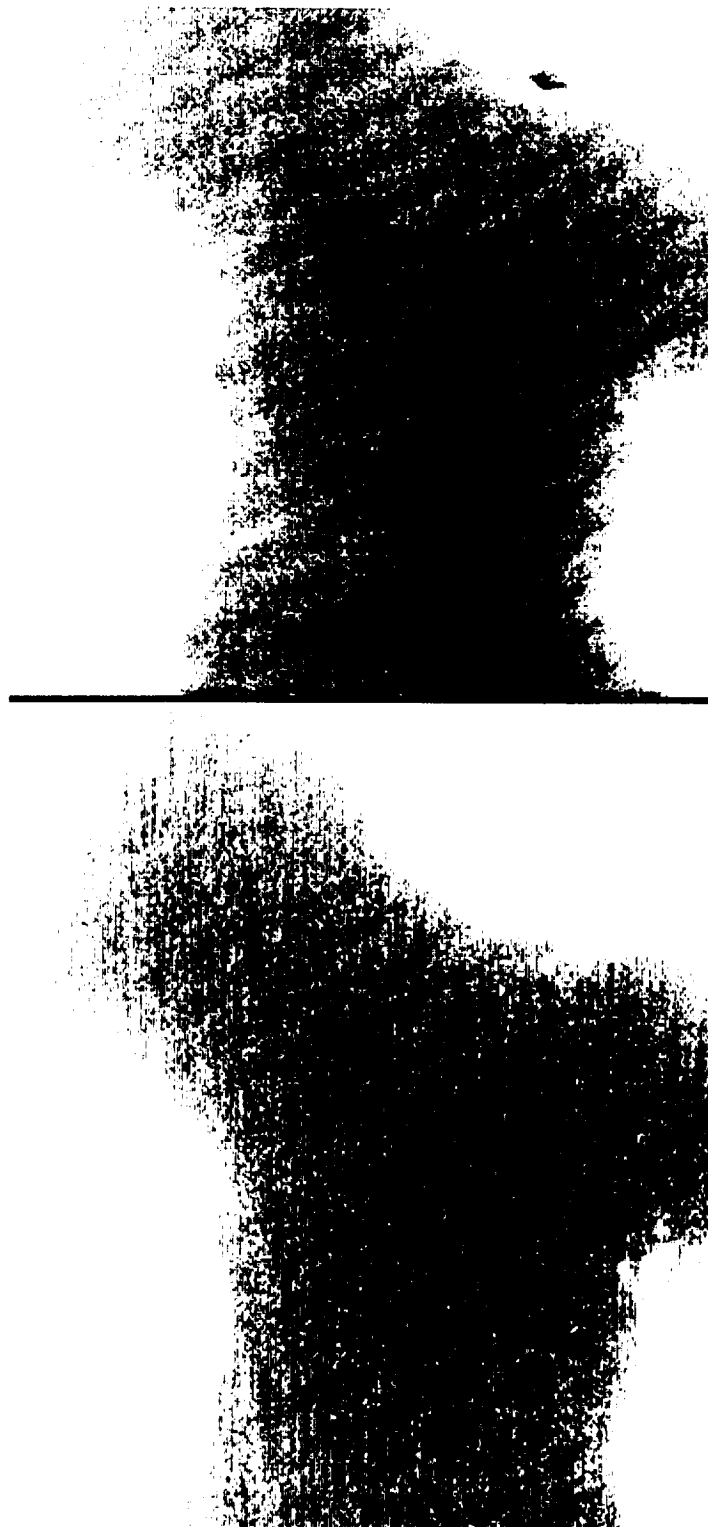


Figure 5

AVIRIS images (26 May 1989, flight 5, run 3, segment 4) of western and southern Mono Lake. Top panel is 937 nm-centered band and bottom panel is 535 nm-centered band. Images are masked to remove land and stretched to ± 2 standard deviations of within lake reflectances.

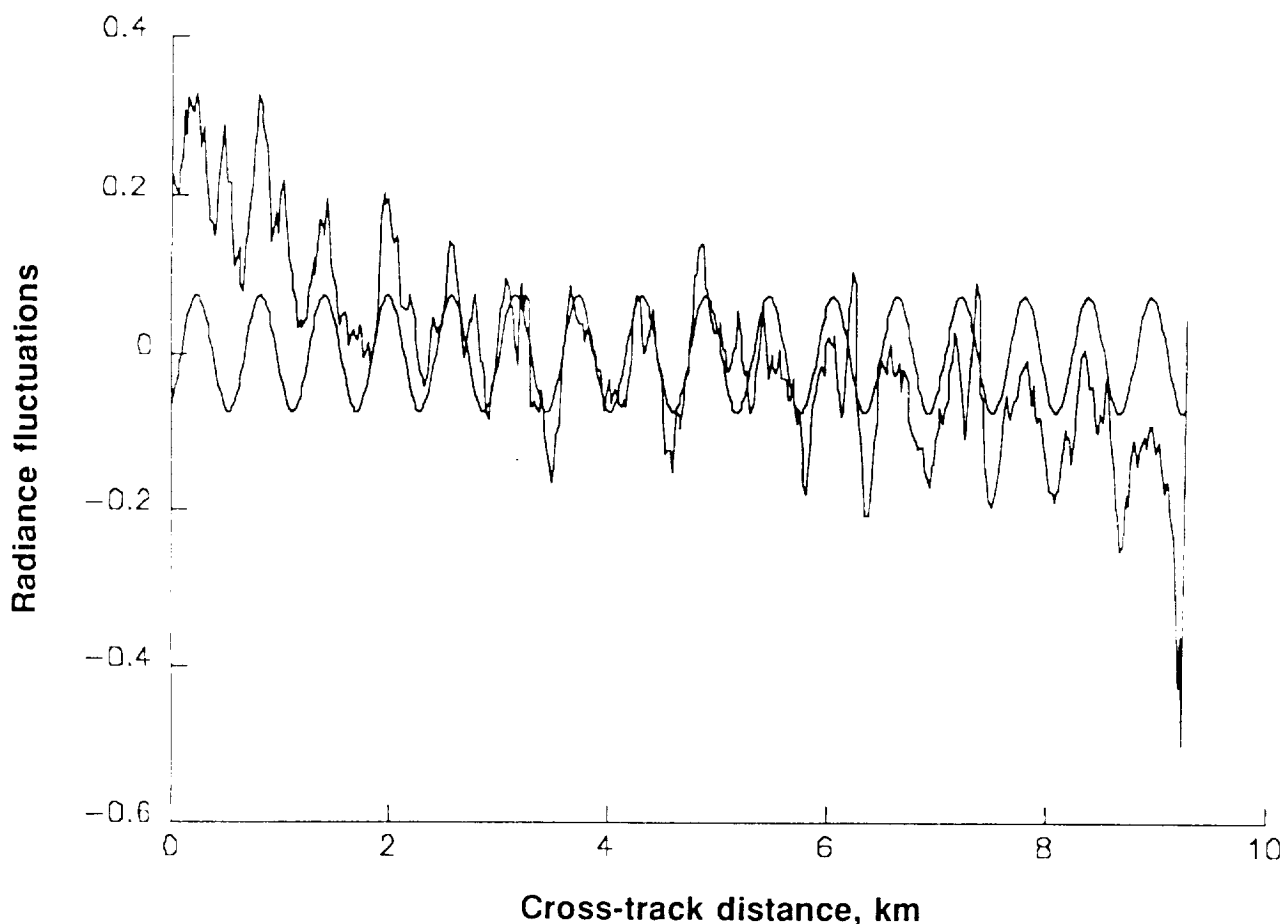


Figure 6 Transect of averaged radiance fluctuations ($\mu\text{Wcm}^{-2} \text{ nm}^{-1} \text{ str}^{-1}$) from east to west across the scene shown in Figure 5, plotted together with the inverse Fourier transform of the most significant peak from the power spectrum. The data represent an average over bands 2 to 29 (415 to 682 nm), and part of the large scale slope is probably due to faulty vignetting correction.

To remove the coherent noise a simple ratio of two spectral bands was calculated after confirming that the undulations were in the same location in the different spectral bands. AVIRIS channels with midpoints of 515 and 545 nm were ratioed because these are approximately the bands used with the CZCS algorithm. After calculating ratios, masking the land using the AVIRIS channel centered at 937 nm, stretching the image and averaging 5×5 pixels, an across lake variation was evident. Slightly brighter regions one half to one km wide appeared around the perimeter of the lake. These regions are not caused by vignetting because the lake shore was not on the edge of the image, and are unlikely to be an adjacency effect because of the extreme clarity of the atmosphere on the day of the overflight. The underwater attenuation of light was too great for the bottom to be influencing the signal. Hence, the pattern may indicate differences in phytoplankton abundance, but limnological sampling was insufficient to test this possibility.

To further examine spatial variability in the image, an unfiltered fast Fourier transform was performed on the deviations from the mean of the ratio of the reflectances at 545 and 515 nm for an east to west transect of 360 pixels (Figure 7). While this preliminary analysis must be considered cautiously, a conspicuous minimum in variance occurred at a spatial scale of 240 m and maxima in variance occurred at 80 m and 1500 m and perhaps at 50 m and 360 m. Interpretation of these features is premature until further filtering of the coherent noise and additional analysis of the spatial patterns in variance are performed.

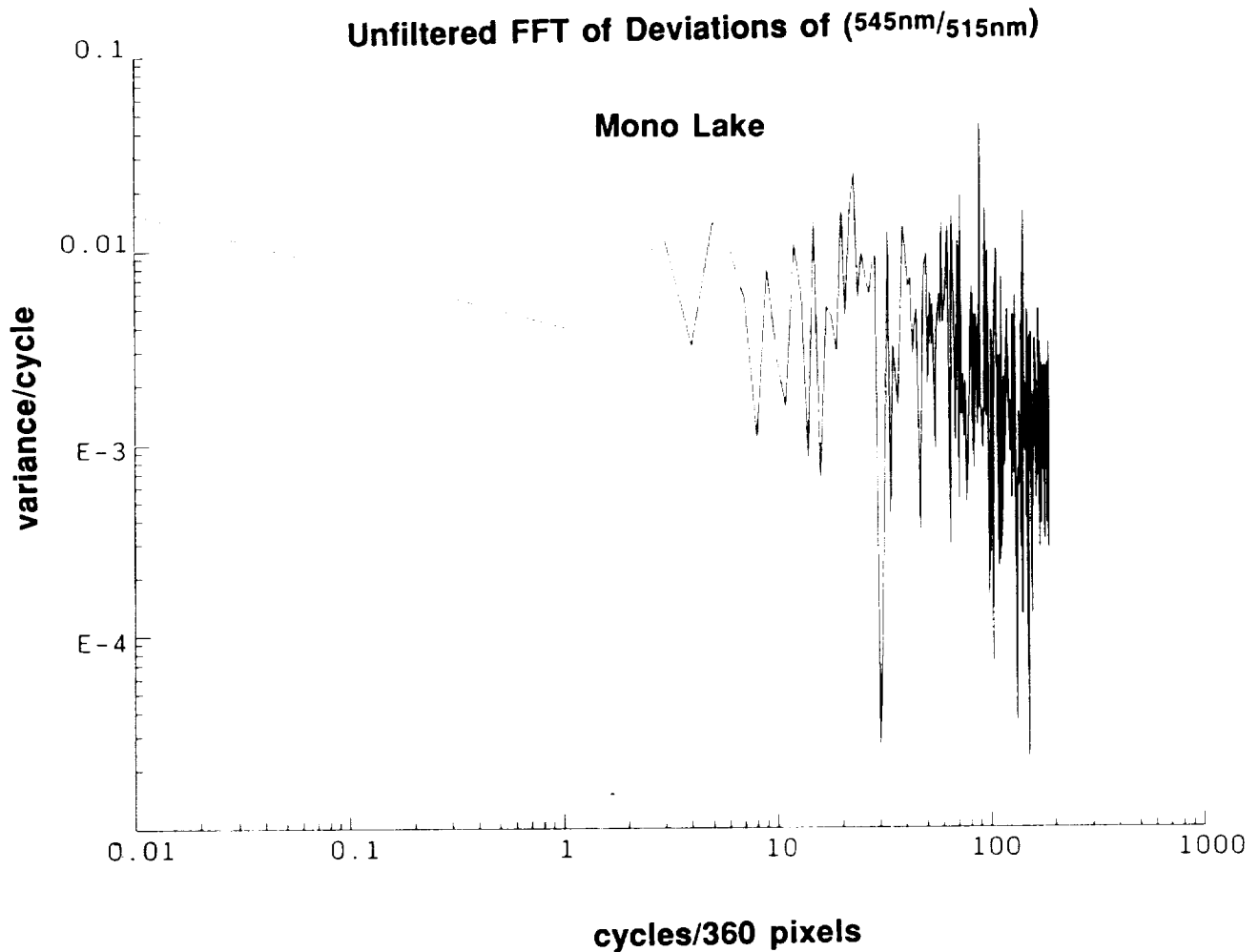


Figure 7 Unfiltered fast Fourier transform (FFT) of deviations from mean of ratios of upwelling radiance at 545 nm and 515 nm; E-3 is 0.001; E-4 is 0.0001.

During 1990, AVIRIS imagery will be obtained from Mono Lake during two seasons and from neighboring lakes with different optical properties. If the coherent noise can be reduced, which is likely, this imagery promises to permit ecological interpretation of spatial patterns in upwelling radiances. Improvements in the algorithms to calculate chlorophyll concentrations, which utilize more of the spectral signature provided by AVIRIS, will permit examination of phytoplankton distribution and better estimates of primary productivity.

4. ACKNOWLEDGEMENTS

Partial funding for field sampling was provided by the Los Angeles Department of Water and Power and partial support for data analysis was obtained from the National Aeronautics and Space Administration. We thank G. Dana, L. Dyer and R. Jellison for the limnological data. V. Carrere applied the empirical line correction to the AVIRIS data using PIDAS measurements that she made. C. Bruegge made available Reagan radiometer measurements.

5. REFERENCES

1. Boland, D.H.P., D.S. Schaeffer, D.F. Sefton, R.P. Clarke and R.J. Blackwell, Trophic Classification of Selected Illinois Water Bodies, EPA-600/3-79-123, 1979.
2. Holyer, R.J., "Toward universal multispectral suspended sediment algorithms," *Remote Sens. Environ.*, 7, 323-338, 1978.
3. Curran, P.J. and E.M.M. Novo, "The relationship between suspended sediment concentration and remotely sensed spectral radiance: a review," *J. Coastal Res.*, 4, 351-368, 1988.
4. Lindell, L.T., "Experiences from correlations of Landsat data versus transmission of light and chlorophyll a," *Verh. Int. Ver. Limnol.*, 21, 438-441, 1981.
5. Almanza, E. and J.M. Melack, "Chlorophyll differences in Mono Lake (California) observable on Landsat imagery," *Hydrobiologia* 122, 13-17, 1985.
6. Lathrop, R.G. and T.M. Lillesand, "Use of thematic mapper data to assess water quality in Green Bay and central Lake Michigan," *Photogram. Eng. Remote Sens.*, 52, 671-680, 1986.
7. Dwivedi, R.M. and A. Narain, "Remote sensing of phytoplankton - an attempt from the Landsat Thematic Mapper," *Int. J. Remote Sensing*, 8, 1563-1569, 1988.
8. Galat, D.L. and J.P. Verdin, "Patchiness, collapse and succession of a cyanobacterial bloom evaluated by synoptic sampling and remote sensing," *J. Plankt. Res.*, 11, 925-948, 1989.
9. Hovis, W.A. and others, "Nimbus 7 Coastal Zone Color Scanner: System description and initial imagery," *Science*, 210, 60-63, 1980.
10. Smith, R.C. and K.S. Baker, "Oceanic chlorophyll concentrations as determined using Nimbus 7 Coastal Zone Color Scanner imagery," *J. Mar. Biol.*, 66, 269-279, 1982.
11. Abbott, M.R. and P.M. Zion, "Satellite observations of phytoplankton variability during an upwelling event," *Cont. Shelf Res.*, 4, 661-680, 1985.
12. Brown, O.B. and others, "Phytoplanktonic blooming off the U.S. east coast: A satellite description," *Science* 229, 163-167, 1985.
13. Pan, D., J.F.R. Gower and G.A. Borstad, "Seasonal variation of surface chlorophyll distribution along the British Columbia coast as shown by CZCS satellite imagery," *Limnol. Oceanogr.*, 33, 227-244, 1988.
14. Mortimer, C.H., "Discoveries and testable hypotheses arising from Coastal Zone Color Scanner imagery of southern Lake Michigan," *Limnol. Oceanogr.*, 33, 203-226, 1988.
15. Abbott, M.R., T.M. Powell and P.J. Richerson, "The relationship of environmental variability to the spatial patterns of phytoplankton in Lake Tahoe," *J. Plankt. Res.*, 4, 927-941, 1982.
16. Bidigare, R.R., R.C. Smith, K.S. Baker and J. Marra, "Oceanic primary production estimates from measurements of spectral irradiance and pigment concentration," *Global Biogeochem. Cycles*, 1, 171-186, 1987.

17. Platt, T. and S. Sathyendranath, "Oceanic primary production: estimation by remote sensing at local and regional scales," *Science*, 241, 1613-1620, 1988.
18. Diner, D.J., and J.V. Martonchik, "Influence of aerosol scattering on atmosphere blurring of surface features," *IEEE Trans. Geosci. Remote Sensing*, GE23, 618-625, 1985.
19. Morel, A. and L. Prieur, "Analysis of variations in ocean color," *Limnol. Oceanogr.*, 22, 709-722, 1977.
20. Carder, K.L. and R.G. Steward, "A remote-sensing reflectance model of a red-tide dinoflagellate off west Florida," *Limnol. Oceanogr.* 30, 286-298, 1985.
21. Carder, K.L., R.G. Steward, J.H. Paul and G.A. Vargo, "Relationships between chlorophyll and ocean color constituents as they affect remote-sensing reflectance models," *Limnol. Oceanogr.*, 31, 403-412, 1986.
22. Carder, K.L., R.G. Steward, G.R. Harvey and P.B. Ortner, "Marine humic and fulvic acids: their effects on remote sensing of ocean chlorophyll," *Limnol. Oceanogr.* 34, 68-81, 1989.
23. Vane, G. (ed), Airborne Visible/Infrared Imaging Spectrometer (AVIRIS), JPL Publication 87-38, Pasadena, California, 1987.
24. Melack, J.M., "Large, deep salt lakes: a comparative limnological analysis," *Hydrobiologia*, 105, 223-230, 1983.
25. Lenz, P.H., S.D. Cooper, J.M. Melack and D.W. Winkler, "Spatial and temporal distribution patterns of three trophic levels in a saline lake," *J. Plankt. Res.*, 8, 1051-1064, 1986.
26. Jellison, R. and J.M. Melack, "Photosynthetic activity of phytoplankton and its relation to environmental factors in hypersaline Mono Lake," *Hydrobiologia*, 158, 69-88, 1988.
27. Strickland, D. and T. Parsons, A Practical Manual of Seawater Analysis, Fish Res. Bd. Canada Bull., 167, 1972.
28. Golterman, H.L. (ed.), Methods for Chemical Analysis of Fresh Waters, IBP Handbook No. 8, Blackwell Scientific Publications, Oxford, England, 1969.
29. Goetz, A.F.H., "The portable instant display and analysis spectrometer (PIDAS)," Proc. Third Airborne Imaging Spectrometer Data Analysis Workshop, G. Vane (ed.), JPL Publ. 87-30, pp. 8-17, Pasadena, California, 1987.
30. Kneizys, F.X. and others. Users Guide to LOWTRAN 7, AFGL-TR-88-0177, ERP No. 1010, Air Force Geophysics Laboratory, Hanscom Air Force Base, Massachusetts, 1988.
31. Conel, J.E., S. Adams, R.E. Alley, G. Hoover and S. Schultz, "Analysis of AIS radiometry with emphasis on determination of atmospheric properties and surface reflectance," Proc. Second Airborne Imaging Spectrometer Data Analysis Workshop, G. Vane and A. Goetz (eds.), JPL Publ. 86-35, pp. 31-51, Pasadena, California, 1986.

INTERPRETATION OF RESIDUAL IMAGES: SPECTRAL MIXTURE ANALYSIS OF AVIRIS IMAGES, OWENS VALLEY, CALIFORNIA

GILLESPIE, A. R.¹, SMITH, M. O.¹, ADAMS, J. B.¹, WILLIS, S. C.¹, FISCHER, A. F. III², and SABOL, D. E.¹

1. Dept. of Geological Sciences, University of Washington, Seattle, WA 98195, USA.

2. Dept. of Natural Resources, Humboldt State University, Arcata, CA 95521, USA.

ABSTRACT

Hyperspectral AVIRIS images may be expressed in terms of mixtures of a small number of spectral endmembers, each of which corresponds to a significant scene constituent. Although the continuum spectra may be well described as mixtures of the spectra of these endmembers, discrete spectral features due to unrecognized or rare scene constituents may not be. In special mixture analysis, the abundances of the endmembers are collected in fraction images. The anomalies are collected in residual images, which are the spectral differences between the modeled and measured data. Root-mean-square residual images, averaged across the spectrum, are sensitive to errors in the continuum model spectrum, but are insensitive to unmodeled narrow absorption features. These are best seen in images of the residuals in each image channel. Detection of unusual scene constituents is enhanced by spectral mixture analysis, but is still limited by sensor sensitivity and the number and width of spectral channels. Mixture analysis has application to remote soil characterization, because of the importance of clay mineralogy, distinguished by weak, narrow absorption bands.

INTRODUCTION

AVIRIS was designed with 224 10-nm channels in order to resolve discrete absorption bands characteristic of many mineral spectra, and to resolve fine structure in vegetation spectra [Goetz *et al.*, 1985]. Much early research with AVIRIS data has focused on this aspect. However, the high dimensionality of the data also offers an unparalleled opportunity to characterize well the continuum spectrum - the major part of the spectrum that lies between small discrete absorption bands. The continuum spectrum offers a store of information about the scene [e.g., Adams *et al.*, 1990b]. Normal concentrations of minerals such as clays or rare earths that may cause local absorption in the spectrum can only be detected and identified against the continuum background, and with a knowledge of what that background signifies in the scene [Shipman and Adams, 1987; Adams *et al.*, 1989; 1990b].

In conventional analyses, the scene is ordinarily taken to consist of pixel-sized elements or tessera of identifiable composition, and a meaningful reflectance spectrum is assumed to exist for each pixel. If the tessera happens to contain multiple components, then it is commonly assumed that a unique mixed spectrum exists for each pixel. If the assumptions are correct, important components may be identified from discrete spectral features in these spectra.

However, a different view of the world is possible, in which a scene is composed of mixtures of a only few components: Aristotle [ca. 335 BC], for example, proposed a set of four such endmembers, although not on the basis of their spectral properties. Many natural scenes do appear to be mixtures of a limited number of basic constituents, and the radiant energy from such scenes, measured and displayed as an image, is likewise mixed from energy radiated from these components. It is thus appropriate to analyze images in terms of mixtures; indeed, many images can only be analyzed as mixtures, for the pixel sizes of 5 m or more currently attainable.

In spectral mixture analysis, most of the scene is taken to consist of a few spectrally unique components, the number and identity of which depend upon the spatial scale, spectral resolution, and number of bands of the image [Adams *et al.*, 1989, 1990b; Smith *et al.*, 1990a]. There exists a set of rules governing the spectral mixing of the components. For each pixel, a set of component fractions may be deduced. Each unique pixel spectrum may be estimated from the spectra of the components (endmembers) and their fractions or abundances.

AVIRIS is capable of resolving far more spectral endmembers than is required to reproduce or model the continuum spectrum. If the scene does contain more constituents than is required to reproduce the continuum spectrum, then either these cannot be resolved (ambiguous) or they introduce deviations from the well modeled behavior at only a few wavelengths, as is the case for many minerals with strong absorption bands. These locally absorbing constituents could be regarded as additional endmembers, especially if a second level of analysis was invoked covering only those few bands where they deviated most strongly from the well modeled continuum. However, it is precisely in these absorption regions that linear mixing models function least well [e.g., Shipman and Adams, 1987]. Therefore, we regard the AVIRIS spectrum as consisting of two parts: a well modeled continuum, and a residual spectrum - the observed data minus the estimation [Smith *et al.*, 1988b] - in which information about unusual or unmodeled components may be concentrated. This strategy is best suited for detecting scene constituents having no well-defined absorption features, and low concentrations of scene constituents that do have them. Both these categories of constituents *can only be identified against the continuum background*.

In this paper the general case for linear analysis is investigated. Two AVIRIS images of Owens Valley, California, are analyzed in terms of their spectral mixtures, and the endmember fraction and residual images are constructed. The images were chosen because they depicted previously studied local outcrops of strongly colored epidote-bearing metavolcanic rocks with distinct absorption features, and widespread argillic soils containing small amounts of montmorillonite and kaolinite clays.

Previous Work

The systematics of mixture analysis have been well elaborated in a number of disciplines such as isotopic geochemistry and petrology: for example, Reid *et al.* [1973] used linear mass-balance equations to relate chemical compositions of minerals to chemical composition of lunar samples. The significance of mixtures in multispectral images was recognized at the very beginning of the Landsat era [Horwitz *et al.*, 1971; Detechmendi and Pace, 1972; Hallum, 1972; Nalepka and Hyde, 1972; Sacco, 1972].

Pace and Detechmendi [1973] and Horwitz *et al.* [1975] used linear mixture analysis to estimate proportions of components in mixed pixels, and Richardson *et al.* [1975] developed linear regression models to describe relative amounts of vegetation, soil, and shadow for Landsat MSS data. Ranson [1975] recognized the impact of mixtures on image classification, and Heimes [1977] studied the effects of substrate proportions on spectral reflectance in forests. Kauth and Thomas [1976] considered the changes in spectral mixtures in multitemporal data, and Crist and Cicone [1984] extended this "tasselled cap" analysis to Landsat TM data. Chittmeni [1981] estimated mixture proportions through their region characterization. Adams and Adams [1984] used linear unmixing of MSS images to estimate natural vegetation cover. Much of the agricultural research has been directed towards creating vegetation indexes only, disregarding the compositional differences in the "substrate." However, Huete *et al.* [1985] and Huete [1986] explicitly focused attention on the complex nature of the soil components, and Adams *et al.* [1990a] used spectral mixture analysis of TM images to

differentiate among different types of vegetation in Amazonia. Roberts *et al.* [1990] further explore spectral unmixing to differentiate senescent and woody plant material.

The geologic surface has also received attention. Singer and McCord [1979] proposed unmixing spectroscopic measurements of Mars. Marsh *et al.* [1980] used linear discriminant analysis to estimate constituent proportions in mixed pixels. Dozier [1981] extracted proportions of snow and substrate from multichannel thermal images. Conel and Alley [1984] explored spectral mixture analysis of arid steppe to isolate soil and desert scrub. Smith and Adams [1985a,b] developed an unmixing strategy and applied it to imaging spectrometer data. Pieters *et al.* [1985] showed that spectral mixtures were required to explain lunar images. Adams *et al.* [1986] applied linear mixture analysis to Viking images of Mars. Smith *et al.* [1985] and Mustard and Pieters [1986] estimated abundances from mixed spectra, and Mustard and Pieters [1987] applied these techniques to terrestrial images. Gillespie *et al.* [1986] used linear unmixing of TM images to characterize a desert soil chronosequence. Smith *et al.* [1988a, b] demonstrated that imaging spectrometer calibration could be refined by spectral mixture analysis, requiring only a library of reference spectra. Recently, Boardman [1989] used singular value decomposition and mixing analysis to characterize the spatial scales of spectral variance, and Goetz and Boardman [1989] have suggested spectral unmixing studies as a way to predict the ideal number of channels in hyperspectral images. Gillespie *et al.* [1990] extended spectral mixture analysis to multispectral thermal infrared images.

Spectral data have been treated both as linear and nonlinear mixtures. Linear models are widely, but not universally, applicable to terrestrial satellite images. For example, individual rock types are intimate mixtures of small mineral grains, and their reflectance spectra are nonlinear functions of the spectra of the pure constituents [Adams and McCord, 1972; Nash and Conel, 1974; Johnson *et al.*, 1983, 1990; Pieters *et al.*, 1985; Mustard and Pieters, 1986, 1987; Shipman and Adams, 1987]. Similarly, multiple scattering and transmission in plant canopies produce nonlinear spectral responses [Suits, 1972]. Sasaki *et al.* [1983] used a constrained nonlinear method for estimating endmember proportions. However, intimate mixtures can be treated linearly by converting reflectance to single-scattering albedo [Hapke, 1981; Johnson *et al.*, 1983; 1990]. Additionally, in complex scenes both individual lithologies and plant communities have been regarded as entities having characteristic spectra, which may mix additively with other constituent spectra (references cited above).

During the past decade, we have attempted to formulate a systematic treatment for the general mixing problem - one that is applicable to a wide range of data types and scientific goals [e.g., Adams *et al.*, 1989, 1990b; Possollo *et al.*, 1990; Smith *et al.*, 1990a,b; Gillespie *et al.*, 1990]. Although linear mixing models adequately describe many low-dimensional data such as from Landsat TM, the relation of spectral contrast in absorption bands to abundance of the absorbing material is inherently nonlinear, and more complex modeling is required for many hyperspectral images. To address this issue, Smith *et al.* [1988b] treated AIS (precursor to AVIRIS) hyperspectral data as linear mixtures of endmembers and a residual spectrum, which contained the unmodeled data.

Current Research

In the present paper, we employ a two-stage analysis for AVIRIS images: modeling of the continuum as linear mixtures of the constituents that comprise the bulk of the scene, and isolation of the discrete absorption bands as unmodeled residuals, suitable for later analysis by spectral-matching and band-shape techniques [e.g., Clark *et al.*, 1990]. This analysis differs from previous discussions of spectral mixing by Horwitz *et al.* [1975], Jackson [1983], Conel and Alley [1984], Huete *et*

al. [1985], and Pech *et al.* [1986] in that the approach is directed at using a simple mixture model to link reflectances measured by field and/or laboratory instruments with image relative-radiance measurements acquired by AVIRIS. Although previous studies have discussed the importance of spectral mixtures, they do not provide the methodology to determine the combined atmosphere and instrument calibration at the time of image acquisition, to remove variations in lighting geometry caused by topographic and other factors, and to separate spectral mixtures.

Mathematical Framework

The radiant energy from a scene element, R , is integrated over wavelength band i and linearly encoded as $DN = g R + o$ in an image. Parameters g and o are the calibration coefficients for AVIRIS, and are generally determined by imaging known targets before and during flight [e.g., Chrien *et al.*, 1990; Green *et al.*, 1990]. The measured gray level for each pixel may be described as:

$$DN_i = \sum_{k=1}^n f_k DN_{ik} + \epsilon_i \quad [1a]$$

or, in matrix notation:

$$\vec{D}_m = \vec{f}_n [\mathbf{L}]^T_{m,n} + \vec{\epsilon}_m \quad [1b]$$

where k denotes each of n endmembers comprising the scene, fraction f is the abundance of each endmember, m is the number of image channels, ϵ is the remainder between the measured and modeled encoded radiance, \vec{D} is the vector of measured radiances (DN), and $[\mathbf{L}]$ is the matrix of endmember DN vectors, each referred to as an *image endmember*. The fractional abundances f must all sum to unity:

$$\sum_{k=1}^n f_k = 1 \quad [2]$$

The measured spectra may be described as mixtures of $m+1$ endmembers. Generally, fewer endmembers will be used, so that equation 1 is overdetermined. At least one degree of freedom is retained for ϵ . For low-dimensional systems, n may be estimated by the number of eigenvalues for the covariance matrix that exceeds the system noise level.

The radiance from a scene is temporally variable, responding to lighting and viewing geometry and to atmospheric conditions. The radiance also depends upon the scene topography and roughness, as well as the reflectivity. Of the above parameters, only reflectivity is directly related to composition, and as such it is frequently the parameter of greatest interest in interpreting AVIRIS data. For purposes of this discussion, it is assumed that radiance (R_i) and reflectance (r_i) are linearly related as $R_i = a_i r_i + b_i$ [cf. Hapke, 1981; Diner and Martonchik, 1984]. The coefficient a_i includes atmospheric absorption as well as geometric and irradiance terms, and b_i is an atmospheric path radiance term. It is further assumed for simplicity that atmospheric effects are invariant over the scene, although this clearly is an approximation [e.g., Green *et al.*, 1989; Conel *et al.*, 1990; Gao and Goetz, 1990].

Given the above qualifications, the image DN may be related to scene reflectivity and the image endmembers may be expressed as mixtures of more fundamental reflectance spectra:

$$DN_i = (g_i a_i) r_i + (g_i b_i + o_i) \quad [3a]$$

$$DN_{ik} = g'_i \sum_{j=1}^n f_{jk} r_{ij} + o'_i + \epsilon_{ik} \quad [3b]$$

where $g'_i = (g_i a_i)$ and $o'_i = (g_i b_i + o_i)$; or, in matrix notation:

$$[\mathbf{D}]_{m,n} = \left[\sum_{i=1}^m g'_i \hat{i} \right] [\mathbf{R}]_{m,n} [\mathbf{f}]_{n,n} + \left[\sum_{i=1}^m o'_i \hat{i} \right] + [\mathbf{E}]_{m,n} \quad [3c]$$

where \hat{i} is the unit vector for the i th band, and $[\mathbf{R}]$ is the matrix of n reflectance spectra r , known as *reference* endmember spectra. Equation 3 relates the image endmembers to global coefficients g'_i and o'_i , plus $[\mathbf{R}]$. Using equation 3, g'_i and o'_i may be found from the image itself [Smith *et al.*, 1988a,b], with no ground measurements other than those from a generalized spectral library [e.g., Clark *et al.*, 1990]. For real data with measurement errors, equation 3 may not have a unique solution. Gillespie *et al.* [1990] and Smith *et al.* [1990c] describe an indirect method of finding the solution that is most appropriate in terms of the field scientist's observations.

Once the calibrating coefficients and n are known, it is possible to describe the image DN for each pixel, not just the image endmembers, in terms of mixtures of the chosen set of reference endmember spectra:

$$DN_i = g'_i \sum_{j=1}^n f_j r_{ij} + o'_i + \epsilon_i \quad [4a]$$

or, in matrix notation:

$$\vec{D}_m = \vec{g}'_m [\vec{f}_n [\mathbf{R}]^T_{m,n}] + \vec{o}'_m + \vec{\epsilon}_m \quad [4b]$$

The goal of subsequent analysis is to find the endmember fractions f_j for each pixel of the image. It should be clear from equation 3 that this is possible by inversion. For example, given the case with two image channels and three endmembers,

$$\begin{aligned} f_1 &= \frac{\{ (D_1 - r_{13}) (r_{22} - r_{23}) - (D_2 - r_{23}) (r_{12} - r_{13}) \}}{\{ (r_{11} - r_{13}) (r_{22} - r_{23}) - (r_{21} - r_{23}) (r_{12} - r_{13}) \}} + \\ f_2 &= \frac{\{ (D_2 - r_{23}) - f_1 (r_{21} - r_{23}) \}}{\{ r_{22} - r_{23} \}} \\ f_3 &= 1 - (f_1 + f_2) \end{aligned} \quad [5]$$

where $D_i = (DN_i - o_i) / g_i$ and, because this particular solution is exactly determined, $\varepsilon_i = 0$. The explicit expression for the endmember fractions is more complicated for more channels and endmembers than used for equation 5. In general, equation 4 will be overdetermined, and may be solved by least-squares methods.

The products of spectral mixture analysis are thus sets of n reference spectra and fraction images depicting their abundances in the scene, and m residual images containing the difference between the modeled and measured data.

METHODOLOGY

Image Endmembers

The first step in analyzing the AVIRIS images is to determine the number and identity of the image endmembers that are necessary to model the continuum spectrum. The image endmembers - the DN vectors on the right-hand side of equation 1 - are generally extracted from the image itself, not from a reference spectral library, and as such they typically do not represent "pure" scene constituents, but are themselves mixed from more basic reference spectra.

The number of endmembers is one more than the number of dimensions required to explain the data variance, or the number of channels actually required to describe the spectral constituents of the scene. This number, the *intrinsic dimensionality* of the data [Possollo *et al.*, 1990], may vary from image to image. Spectral data are typically redundant [e.g., Adams *et al.*, 1989; 1990b] and the intrinsic dimensionality may be much smaller than the number of channels of data acquired by AVIRIS.

The intrinsic dimensionality is determined from analysis of the image, where possible after nominal calibration to radiance using preflight data [e.g., Otterman *et al.*, 1980; Chrien *et al.*, 1990] and atmospheric corrections [e.g., van den Bosch and Alley, 1990]. For low-dimensional data, it is approximated by the number of eigenvalues of the covariance matrix that exceeds the noise variance of the system. This estimate is refined by inspection of data spaces in which selected transects from the image are displayed [e.g., Buja and Asimov, 1985]. For AVIRIS data, inverting the entire covariance matrix to find the eigenvalues is impractical, and we make an initial estimate from the number of eigenvalues for a subset of grouped channels, which together span the AVIRIS spectrum. In this way, the dimensionality of the continuum spectrum - but not of the entire spectrum containing sharp absorption features - is approximated. Scene constituents spectrally distinguished only by local departures from the continuum (low concentrations, sharp absorption features) are not treated as endmembers, but are concentrated in a residual spectrum, discussed below.

Principal-component analysis permits approximation of the intrinsic dimensionality, but it provides little information on which endmembers are important and with which other endmembers they mix. Inspection of data clusters is necessary to determine which endmembers mix together, to identify "extreme" pixels that consist dominantly of a single endmember, and to identify which endmembers comprise the bulk of the data. During inspection of the data clusters, the binary mixing lines connecting the tangible endmembers with shade also are identified, and their intersection is found in order to estimate the shade endmember, as discussed below. In contrast to the principal axes, the endmember vectors generally are not orthogonal in the original data space. Sabol *et al.* [1990] discuss the consequences of nonorthogonality on fraction resolution and endmember detectability.

Once a list of candidate image endmembers has been made, a final estimate of \mathbf{n} is made by tentative solutions of equation 1 using successively greater values of \mathbf{n} until the root-mean-square (rms) residual $((\mathbf{m}^{-1}\Sigma(\epsilon_i^2))^{1/2})$ is reduced to the noise level (i.e., 1-2 DN). The first iteration uses only the two or three best-defined image endmembers. The rms residual image is inspected to determine how well the image is fit by the selected endmembers and, equally important, where the fit is worst. DN vectors from the worst-fit areas are compared to the list of unused image endmembers, and - one by one - new endmembers are used in solving equation 1 until the entire rms image (or at least the part of interest to the analyst) has a DN level comparable to image noise. From our experience, this will generally be at a level of $\text{DN} < 2$ for AVIRIS. Equally important, when the image is properly modeled it will generally not be possible to see much structure other than microphonic noise in the rms residual image.

In the above strategy, the image endmembers are selected by meeting the formal requirements sequentially, not in one step. This approach conforms with that of both Possolo *et al.* [1990] and Huete [1986].

Finding Shade

Topographic shadows and photometric shading differ from the atmospheric and global irradiance terms that influence measured radiance in that they are spatially variable at the pixel scale. Thus they cannot be described by the coefficients \mathbf{g}'_j and \mathbf{o}'_j . In a calibrated image, topographic shadows and photometric shading together act as a zero-reflectance endmember that we refer to as "shade" [Adams *et al.*, 1986; Smith *et al.*, 1990a]. From a single AVIRIS image, it is difficult to distinguish the darkening due to photographic (Lambertian) shading from darkening caused by discrete subpixel shadows. The shade endmember is spatially and temporally variable and contrasts conceptually with the other, "tangible" endmembers that correspond to physical scene constituents that change slowly if at all.

In a single image of a scene it may not be possible to distinguish shade from darkening due to low albedo. Resolution of inherently dark surfaces is possible using multitemporal data, which is beyond the scope of the present discussion.

A satisfactory image endmember for shade [Richardson *et al.*, 1975; Adams *et al.*, 1986; Ranson and Daugherty, 1987; Smith *et al.*, 1990a; Roberts *et al.*, 1990] requires that multipixel shadows on a black surface exist somewhere in the image. Although in the first stages of analysis the "darkest pixel" is sometimes used as the shade vector, the darkest pixel generally contains contributions from illuminated as well as from shaded or shadowed scene constituents, and in any case the reflectance is greater than zero. Consequently, for refined analysis, in most images the shade image endmember must be estimated from the distribution of the image data in the DN space.

The strategy is to find a group of pixels comprising only one or two tangible endmembers, but a range of illumination geometries. In DN space, these data will be distributed along one or two binary mixing lines connecting the lightest and darkest scene elements. If different mixing lines are present, they will converge towards a common small (dark) DN vector, although the intersection will not itself be observed. The locus may be found graphically, a tedious procedure for AVIRIS data, or it may be estimated from the closest approach of lines regressed to two or more binary mixing clusters. In general, shade will lie close to the principal axis of the data, so that it may be approximated well even if the DN value for only a single channel is found by triangulation. In finding shade, it is important to note that shadows cast by leafy vegetation contain green and near-infrared light transmitted through the leaves, and are not described by the same vector as shadows from opaque objects [Roberts *et al.*, 1990].

Reference Endmembers

Transforming the AVIRIS image to fractions of image endmembers is useful, but does not realize the full power of spectral mixture analysis. This is because the image endmembers themselves may be mixtures of still more basic or spectrally extreme scene constituents. The image endmembers are derived from the image itself, and if no "pure" pixels are encountered, the endmembers will be impure also.

The next step in analysis is to select a subset of spectra from a reference library that, in the experience of the analyst, is likely to be encountered as scene constituents. The choice of individual spectra is not too important, provided a sufficiently wide range is represented. It is better to include too many than too few reference spectra. In our experience with Landsat TM, the preliminary list of reference endmembers may include 60 - 100 spectra. Because AVIRIS spectra have more detail, more reference spectra may be useful. However, this is not a foregone conclusion: because of the way in which we divide the spectrum into a continuum and residual part, the number of endmembers is not necessarily related to the number of image channels, and the number actually chosen is likely to be on the order of ten.

After selecting a pertinent subset of the reference library, the reference spectra are grouped by scene constituent: e.g., riparian vegetation, carbonate rocks, and so forth. These groups include those needed to describe the image endmembers. The library is sampled again, this time into a large number of subsets of n spectra each, where n is the number of image endmembers. Each spectrum in each sample is drawn from a different group; the same groups may be represented in each sample.

The n image endmembers (DN) are modeled as mixtures of the n reference spectra (reflectance) in each sample, first using a method of successive approximation to solve equation 3 for the calibration coefficients, g' and o' [e.g., Gillespie *et al.*, 1990]. Because of system noise, direct inversion of equation 3 to solve for the calibration coefficients and endmember fractions simultaneously may not be feasible: there may be multiple apparent solutions. The first approximation is to assume values for the reference endmember fractions f_j , based on any available information, including ground measurements and observations, photointerpretation and past experience. For reasonable subsets of reflectance spectra, the calibration coefficients will cluster about central values. Because the AVIRIS data have already been nominally calibrated, the remaining calibration basically corrects for atmospheric effects, plus minor changes in AVIRIS sensitivity during flight. Thus the values of the calibration coefficients determined above may be predicted fairly closely. Subsets requiring greatly different coefficients are rejected, and the list of candidates is narrowed.

The second approximation is to assume the value of the calibration coefficients, generally the mode or mean of the found values. Equation 3 is solved again for the remaining subsets of reference spectra. This time f values are tabulated, and the list of spectra is winnowed further.

The next steps involve successively closer approximation to the "correct" values of g' , o' and f , and further winnowing. At this level of analysis, it is likely that many values for the calibration coefficients and endmember fractions will cluster tightly, such that it is not obvious which reference spectra fit the image endmembers best. New criteria are invoked to proceed with the winnowing process: the sets that are retained are the ones for which the rms residuals are smallest. Ultimately, it is possible to narrow the choice to at most three or four sets of similar spectra.

It is next useful to solve equation 4 for fractions and residuals for the remaining sets of reference spectra. This step differs from the previous ones in that it is the image, not the set of image endmembers, that is recast in terms of the reference spectra. Final refinement of the calibration coefficients and the choice of endmembers is made in light of spatial patterns in the residual and fraction images. This is a

powerful advantage that may not be evident at first glance, because it brings into play the considerable range of skills and experience of the photointerpreter and field scientist. This step in the analysis involves inspecting fraction images for large out-of-bounds areas ($0 \leq f_k \leq 1$). Strictly, subzero or superunitary fractions mean only that the endmembers have less spectral contrast than the data; mathematically, the solution may be satisfactory. Nevertheless, it may be desirable to choose more extreme spectra from the same groups.

An rms residual image calculated for the chosen reference endmembers is inspected for areas of high DN and spatial structure pertinent to the scene rather than to image noise. The fraction images themselves are then studied for conformity to what is known about the scene: i.e., areas of known vegetation should have high f -values in the vegetation image. Finally, band-residual images (p_i) are constructed for each channel, and studied for areas that are not well modeled. It may be necessary to return to solving equation 3 in light of the experience gained with the image data; but, if this is the case, it will be with a much narrower range of reference spectra and a refined concept of the range of valid calibration coefficients and endmember fractions.

Many of the ambiguities in choosing reference spectra arise because there is little difference between the candidates: either would suffice as an endmember. It is necessary to recall that for the fractions to have quantitative significance in terms of scene constituents, they must be calibrated to field measurements [e.g., Smith *et al.*, 1990a]. If the "wrong" endmember is selected, in general the main effect will be an adjustment of the calibration relating the endmember fractions to field measurements of scene constituents. The fit of the model to the data may also be affected, and in this case there may be a change in the rms residual image. Finally, if one of the ambiguous endmembers has more local spectral contrast or structure than the other, the individual band-residual images may differ. It is important to emphasize this trade-off, because it may happen that there is no obviously "correct" endmember.

Band Residuals

Band residual images are calculated by subtracting the continuum model from the observed data, band by band. They differ from the rms residual image, which is averaged across the spectrum. Positive anomalies occur when an absorption feature in the endmembers is not found in the data; negative anomalies occur when the data contain such a band, but not the endmembers.

The continuum model is based on a small number of endmembers, and spectral information describing all the other scene constituents resolvable by AVIRIS will be concentrated in the residual spectra. The information contained in the residual spectrum may be studied by further mixture analysis, or by other approaches that focus on specific band locations and depths [e.g., Clark *et al.*, 1990]. Band residual images differ from the rms residual image in that the rms data describe the fit of the model in a general sense, over the entire spectrum, whereas the band residual data refer to a single wavelength or image channel only.

It is advantageous before analysis of specific absorption features to remove the continuum spectra defined by the handful of endmembers that together comprise most of the spectral variance of the scene. In part this is because the interference of different features is reduced. For example, the spectrum of vegetation is convex near the 2.2- μ m absorption bands in clays [e.g., Roberts *et al.*, 1990]; inspection of the mixed spectrum from vegetation and clays might lead to a bad estimate of the band depth, or in noisy data the clay bands might be obscured entirely. The amount of vegetation present is estimated from the entire spectrum, however, not just from a small suspect window, and the vegetation fraction may be determined precisely. Thus the correction of the spectrum near 2.2 μ m for vegetation is also precise, and the residual spectrum contains only information from the clay-rich substrate.

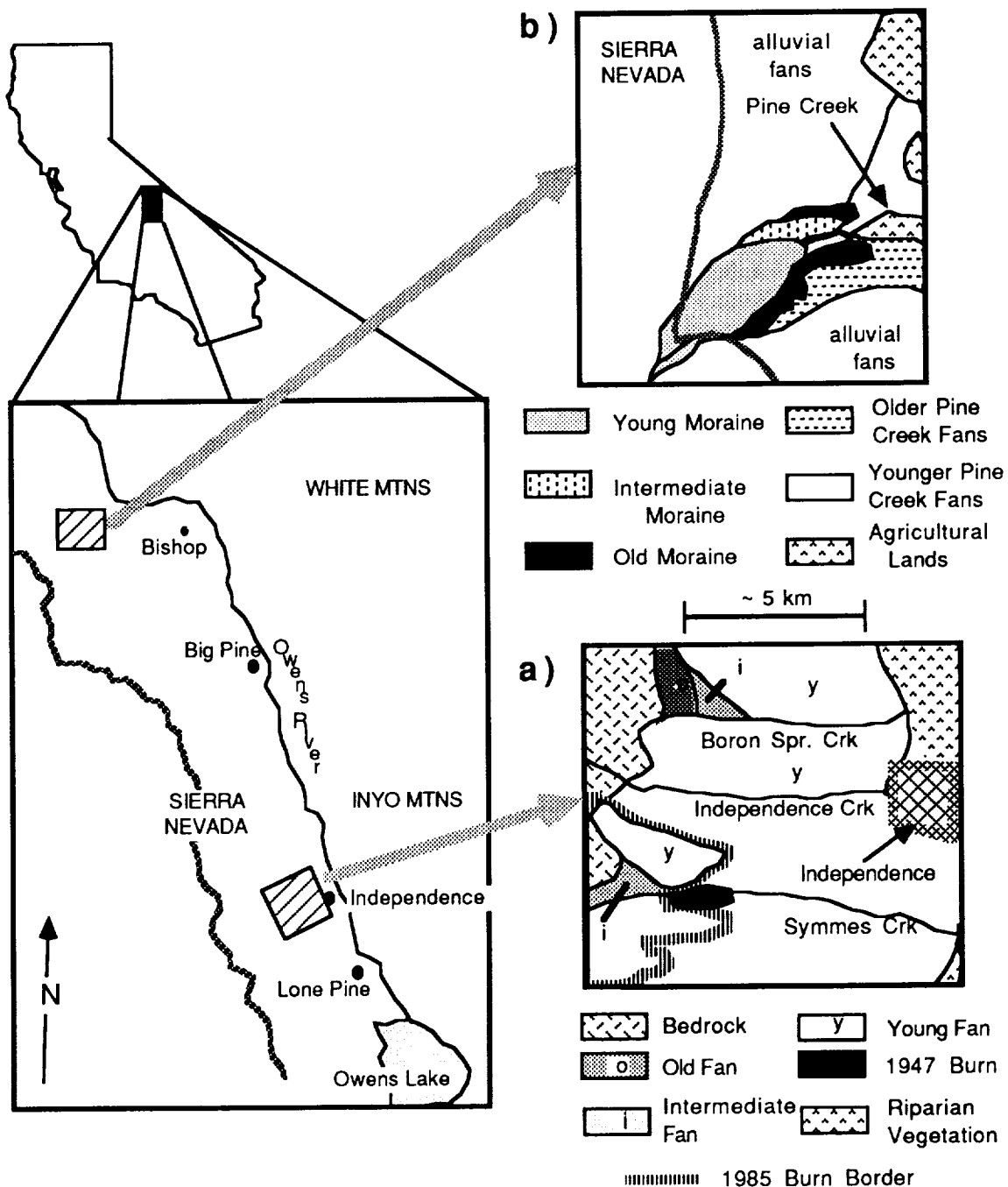


Figure 1. Index and interpretive maps of California showing AVIRIS study areas in Owens Valley. a) Independence Creek. b) Pine Creek.

Band residual data are displayed to good advantage in image format. This is because localized concentrations of unusual, unmodeled endmembers stand out well when the images are scanned sequentially, in order of wavelength. Where the measured spectrum is well modeled, scene detail will be lacking in residual images, but at

wavelengths where the fit is not as good, structural information will be evident. Once an anomalous area is identified in the residual images, it is possible to display the data for that region as a spectrum, devoid of spatial context, for conventional analysis [e.g., Goetz *et al.*, 1982; Vane and Goetz, 1988].

APPLICATION

We applied spectral mixture analysis to two AVIRIS images of different scenes in Owens Valley, California: Independence Creek, west of the town of Independence, and Pine Creek, northwest of the town of Bishop (Fig. 1). Both were acquired at ~18:15 GMT, shortly before local noon, 14 June 1989. Both scenes contained examples of minerals - especially epidote and clays - with strong absorption bands, present in minor amounts. These minerals might be expected to affect residual images, but not endmember fraction images. We expect the minerals sought for in this example to be difficult to identify in conventional approaches, because they are present only in low concentrations.

Desert scrub of the Great Basin sage community (*Artemisia*, *Coleogyne*, *Purshia*, *Ephedra*) covered both study areas ~20-50%. The alluvial fans of the Independence area were previously modeled using the six-channel Landsat TM data and a four-endmember model [Smith *et al.*, 1990a]. Certain critical scene constituents were ambiguous to TM: for example, argillic soils could be modeled as mixtures of vegetation, and different ferrihydrite-rich soils, and wood, bark and vegetation litter masqueraded as weakly developed soil. AVIRIS offers the possibility of making these and other important distinctions directly. However, our results will show that AVIRIS required no more endmembers than TM to model the continuum spectra accurately. The remaining information lies in the residual data. Figure 1 provides geologic sketches of the two study areas, discussed in their respective sections below.

The AVIRIS data, before spectral resampling, were analyzed using WISP, an interactive image analysis system developed and implemented in LISP on Symbolics computers at the University of Washington [Shippert *et al.*, 1988]. A Pixar is peripheral to one of the Symbolics, and permits the rapid processing of large amounts of data. The Pixar was used to scroll through a spatial subset of the AVIRIS images, channel by channel, to select the bands for spectral mixture analysis. Images channels were rejected if they were obviously noisy or if they were in atmospheric water-absorption bands (~1.4 and 1.9 μm). Very few channels outside of the water bands were unuseable, and 171 channels were accepted. Using the Pixar, data from all these channels were unmixed simultaneously, rather than hierarchically, in different steps for each spectrometer or spectral region within the AVIRIS window. Reference endmembers were chosen from a preliminary list of 96 reflectance spectra.

Spectra of Epidote and Clay-Bearing Soils

Figure 2 shows that reflectance spectra for both epidote and a sieved sample (~100- μm grain size) from the surface of a desert soil have similar overall convex shapes in the spectral region 0.4 - 2.5 μm . In each case, the rising slope of the spectrum at wavelengths <1 μm is due to absorption by Fe^{3+} , and the falling slope beyond 2 μm is due to OH^- . The overall reflectance is also influenced by particle size.

Ionic absorptions are also responsible for deviations from the continuum spectra. A broad, weak Fe^{++} is seen in the soil spectrum near 1 μm (arrow), and a narrower feature near 2.2 μm (arrow) is attributed to OH^- in clay. There is a hint of a $\text{CO}_3^{=}$ band near 2.3 μm . The Fe^{++} is probably due to unweathered mafic minerals, and will only weaken with further soil development. The OH^- is attributable to clay

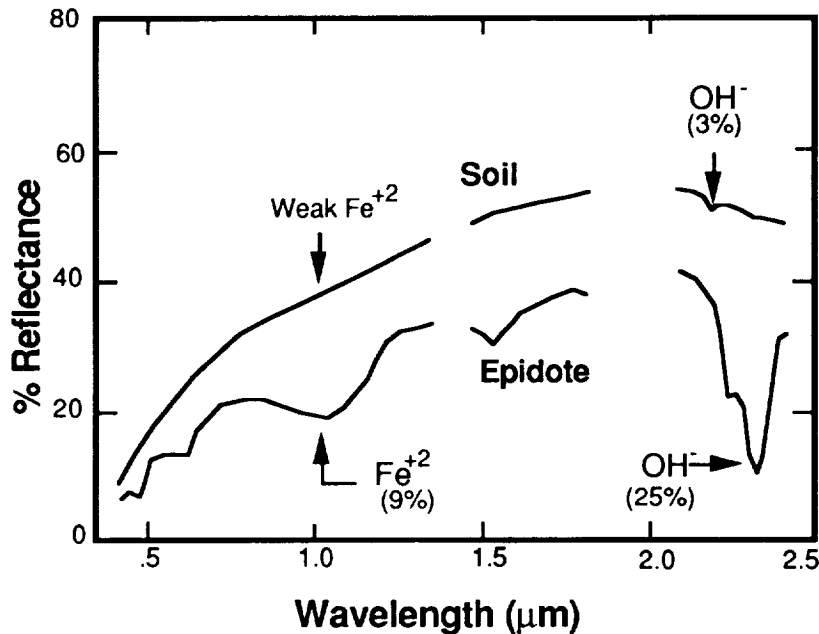


Figure 2. Laboratory reflectance spectra for a clay-bearing soil and for epidote in metavolcanic rocks, Independence Creek. The spectra have been convolved with the 171 AVIRIS bands used in the mixture analysis; gaps near 1.4 and 1.9 μm are the locations of major atmospheric water absorption bands. Selected absorption features and band depths are indicated.

coatings on sand grains [Burke *et al.*, 1986]. Although the soil is well developed for eastern California, the spectral contrast is only 0.03 reflectance units. This band depth is close to the resolution limit of AVIRIS spectrometer D (~ 0.02).

The epidote spectrum shows several deep discrete bands due to Fe^{3+} and Fe^{++} at wavelengths $< 1.4 \mu\text{m}$. However, the most prominent feature, near $2.3 \mu\text{m}$, is due to OH^- and has a depth of 0.25 reflectance units.

The epidote spectrum shows stronger discrete absorption features than the soil spectrum, at least at the scale of the laboratory spectrometer measurement (2 cm). However, at the scale of AVIRIS measurement ($\sim 10 \text{ m}$) epidote is present in much lower concentrations, and the spectral features will be proportionately weaker, whereas the soil spectrum is representative of even larger areas.

The major absorptions that determine the overall shape of the spectra will be described by mixtures of endmembers during mixture analysis. The goal of the present investigation is to recognize the discrete absorption features in the band-residual images over soils of Owens Valley and epidote-bearing rocks along Independence Creek.

Independence Creek

The Independence Creek study area was chosen because it encompassed both an outcrop of metavolcanic rocks containing epidote, and a soil chronosequence developed on granitic alluvial fans containing montmorillonite and kaolinite clays. Figure 1 gives a geologic interpretation of the study area. Most of it falls on the bajada, here consisting of the alluvial fans of Independence Creek and adjacent drainages. The image spans the fans, from their heads on the Sierra Nevada range front to their toes in the fluvial sediments of Owens River. The fans are of different ages, ranging from $\sim 10^4$ to 5×10^5 years. Because deposition was episodic, corresponding to major glaciations, there are large areas of uniform soil development, proportional to age. The soils are non-calcic, and the chief weathering products are ferrihydrite and montmorillonite clays on the younger fans, with the addition of kaolinite on better developed soils. Discrete areas of different development are seen on the fans north of Independence Creek, near the Sierra Nevada range front.

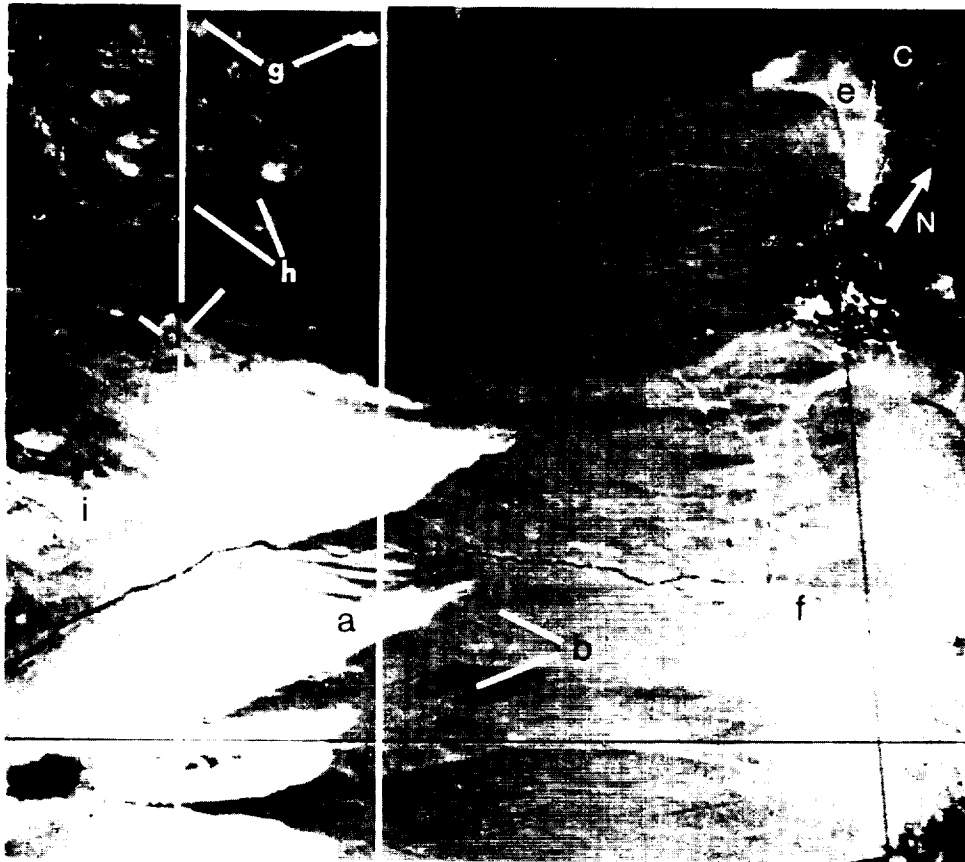


Figure 3. Single band ($0.554 \mu\text{m}$) of the AVIRIS image of Independence Creek. Scene is approximately 9 km across. Image strip for which band residuals were calculated is outlined. Letters a - i denote areas discussed in the text.

The fans are covered uniformly with 30-50% desert scrub [Smith *et al.*, 1990a]. Along Independence Creek and on the valley floor are more densely vegetated areas, generally dominated by oak and cottonwood trees, or agricultural fields. Along the contact between fans and fluvial sediments is a zone of dry grasses and brush, including Russian thistle.

The fans and valley floor are subject to range fires, and a major recent (1985) fire at Symmes Creek has denuded the upper reaches of the alluvial fans south of Independence Creek (Fig. 1). At the time of AVIRIS image acquisition (1989), only a fraction of the bushes had recovered, but dry annuals and grasses were common. Along Symmes Creek itself, a smaller older (1947) burn scar is also visible. The fires covered areas of different degrees of soil development: west of the 1947 scar, visibly reddish soils ($\sim 150 \text{ ka}$) are exposed in contact with a range of less-developed soils to the north. The strong winds that accompany the fires can mobilize the upper few cm of the soils, moving silt and clays great distances and creating low-amplitude dunes of sand and pea-gravel [Bierman and Gillespie, 1990]. The burn scars are interesting in terms of spectral mixing because they provide views of the same soils with different patterns and density of vegetation.

The bedrock lithologies of the Sierra Nevada range front are dominantly granitic, with scattered metamorphic pendants. The granitic rocks spall during range fires and shed grus as they weather, providing an unstable surface for the growth of

lichens and coating by desert varnish. Exposed metavolcanic rocks do not become grusy, but they do spall and shatter. Epidote is a widespread alteration product in the metavolcanic rocks and, disseminated in microcrystalline form, it is probably ubiquitous. Local concentrations also occur, in which some coarser epidote crystals up to 1 mm in diameter are also found. Some of these concentrations are in cm-thick veins, but others are in patches or vein aggregates ranging upwards in diameter to ~100 m. Nevertheless, abundance rarely exceeds a few percent.

The AVIRIS image of Independence Creek (Fig. 3) shows the bajada as uniformly gray, with subtle tone differences due to variation in lithology and, especially, in vegetation density. The fire scars are the most prominent aspect of the image (a). Soil development differences on the bajada are subtle (b). Riparian vegetation on the valley floor and along the streams is dark (c,d), but the dry vegetation at the toes of the fans does not stand out (e). Light-colored patches there are sandy areas, in part along aquifer recharge canals south of Independence Creek (f). Granitic bedrock (g) is light, whereas the metavolcanic outcrops (h) are very dark. Where granitic bedrock is exposed in the fire scars (i) it is even lighter. This is a measure of the extent of darkening of the unburned surface due to vegetation and rock varnish.

The AVIRIS data for the bajada were found to have an intrinsic dimensionality of only three. Smith *et al.* [1990c] give an extended discussion of the choice of endmembers and the range of candidates. Four reference endmembers corresponding to moderately developed reddish and weakly developed sandy soils on granitic alluvium, desert scrub vegetation (*Coleogyne*) and shade were selected. Riparian vegetation and dry grass were equally valid candidates, but were not present in large amounts on the bajada and were not used.

Fraction images for two of the reference endmembers are presented in Fig. 4. Figure 4a shows the fractions for the moderately developed reddish soil. The chief patterns in the image are the low fractions over the recent fire scar (a), especially over the less developed soils on the younger fans (b). Along Symmes Creek near the range front, old fans within the scar (c) have the same fractions as across the boundary (d). The rest of the bajada (e) appears as mottled gray, with patterns delineating fan units according to age, as verified in the field. In general, bedrock outcrops have high fractions, and so do some - but not all - heavily vegetated areas. This phenomenon is best observed along Independence Creek (f) and at the distal ends of the fans (g). Lastly, a zone extending beyond the perimeter of the recent fire scar is locally light in the fraction image, always on the southeast side of the scar (h).

Figure 4b shows the fractions for the sandy soil. It is in many respects the complement of Fig. 4a. However, over all heavily vegetated areas (i,j) the soil fractions are both low. Were there additional soil endmembers, the complementary fractions would be less common.

The four continuum reference endmembers together accounted for all except 1-4 DN of rms residual data, over all bands (Fig. 5). Over most of the bajada and foothills of the Sierra Nevada, the rms residual was about 1 DN. This low value is close to the noise level of AVIRIS; nevertheless, the rms image does show scene detail that would not be evident in a TM residual image at 1 DN. This increased resolution we attribute to the large number of bands in AVIRIS.

The greatest rms residuals occurred in the riparian vegetation (a), metavolcanic rocks (b), and south-facing slopes of granitic bedrock in the burned areas (c). The riparian vegetation and the metavolcanic rocks were not represented by an endmember in the analysis, but the granitic rocks were spectrally similar to the sandy soil endmember. The metavolcanic rocks were of low albedo, and were not assigned an additional endmember because it would be so similar to shade that the two fraction images would appear "noisy."

Figure 6 shows band residuals for three selected spectral windows predicted from the spectra of epidote and/or soils (Fig. 2) to have absorption features. Every

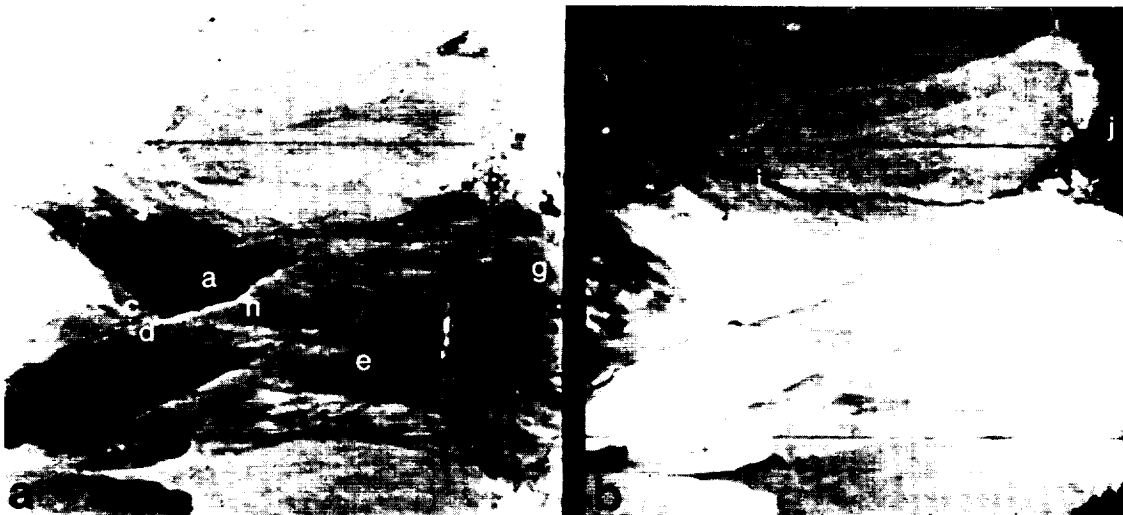


Figure 4. Two reference endmember fraction images, Independence Creek (light = high; dark = low). **a)** Well developed oxidized and argillic granitic soil. **b)** Weakly developed sandy granitic soil. Letters **a - g** denote areas discussed in the text.

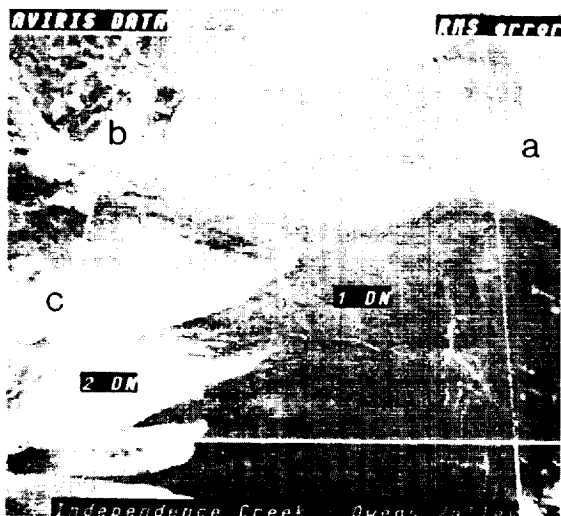


Figure 5. RMS residual image of Independence Creek. The image has been strongly stretched to reveal detail. The original data range was 0 - 4 DN. Lettered features are explained in the text.

third 10-nm band within each window is displayed, although all were calculated and inspected. The residuals were uniformly contrast-stretched for display such that the total range was ± 3 DN, with negative values dark and positive values light. The residuals were calculated for the vertical image strip outlined in Fig. 3.

Figure 6a shows the residual data for a 21-band span in the visible spectrum. These residual images superficially resemble the radiance data (e.g., Fig. 3), but upon close inspection differences are evident. The positive spectral contrast between the burned (a) and unburned sandy alluvium (dark) peaks at $0.554 \mu\text{m}$; the unmodeled residual in either case is quite small at shorter wavelengths, and the contrast lessens at longer wavelengths. This lessening of contrast is not as pronounced for the older alluvium in the fire scar (b). The unburned fan at (c) shows an interesting reversal

of contrast between residuals for the reddish and sandy soils. At wavelengths ≤ 0.554 μm , the reddish soil appears neutral, whereas the sandy soil appears light. At 0.613 μm the residuals are both moderately high, and above 0.643 μm the reddish soil is the lighter. The quartz monzonite bedrock (d) has a residual peak near 0.584 μm , and an epidote-rich zone (e) within the metavolcanics has a residual minimum centered near 0.6 μm . The peak for the quartz monzonite is most prominent on south-facing slopes, and it is therefore tempting to attribute it to an error in the shade vector, but were this the case the sunlit/shaded contrast would persist across a wide range of wavelengths, and it does not.

Figure 6b shows the residual strips from 0.931 to 1.183 μm , spanning the minimum of a major Fe^{++} absorption in epidote. The residual images have enhanced contrast from 0.989 to 1.076 μm , with the sense of the residuals similar to Fig. 6a, for many of the same features. The burned areas and granitic bedrock are light, and the metavolcanics are dark. The sunlit/shaded slopes appear anomalous in the same way as before. However, the fans at (c) are not associated with any positive or negative residuals, and the contact cannot be detected in Fig. 6b. The southeastern margin of the 1985 fire scar just north of Symmes Creek (f), appearing to have a high fraction of reddish soil in Fig. 4, shows a higher positive anomaly than the scar itself from 1.076 to 1.134 μm . Lastly, trees bordering Independence Creek (g) have a positive anomaly from 1.076 to 1.185 μm .

Figure 6c shows residuals in the 2.2 - μm region, where both clays and epidote have absorption bands. Excess montmorillonite that is not accounted for by the reddish soil endmember should show as a narrow negative anomaly centered at 2.2 μm ; epidote should show a wider negative anomaly deepening with wavelength, because the center of the absorption band is > 2.252 μm (Fig. 2). However, these patterns are not observed, and across the entire window the continuum model appears to fit the data well, within the noise limits imposed by spectrometer D (~ 0.02 reflectance units).

Figure 6 is effective in showing spatial characteristics of relative anomalies in band-residual data, but less well suited for showing the shape or actual magnitude of

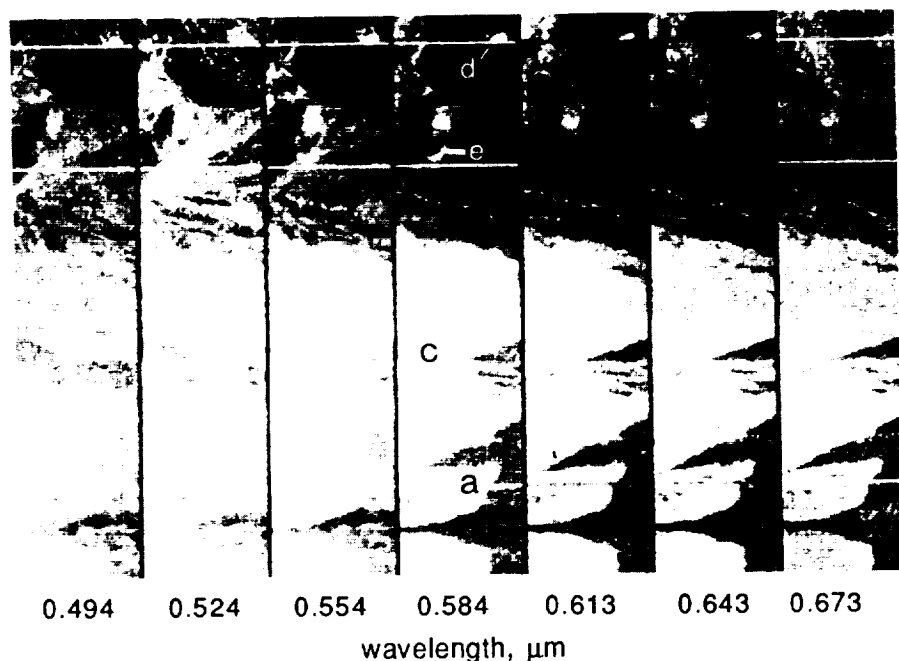
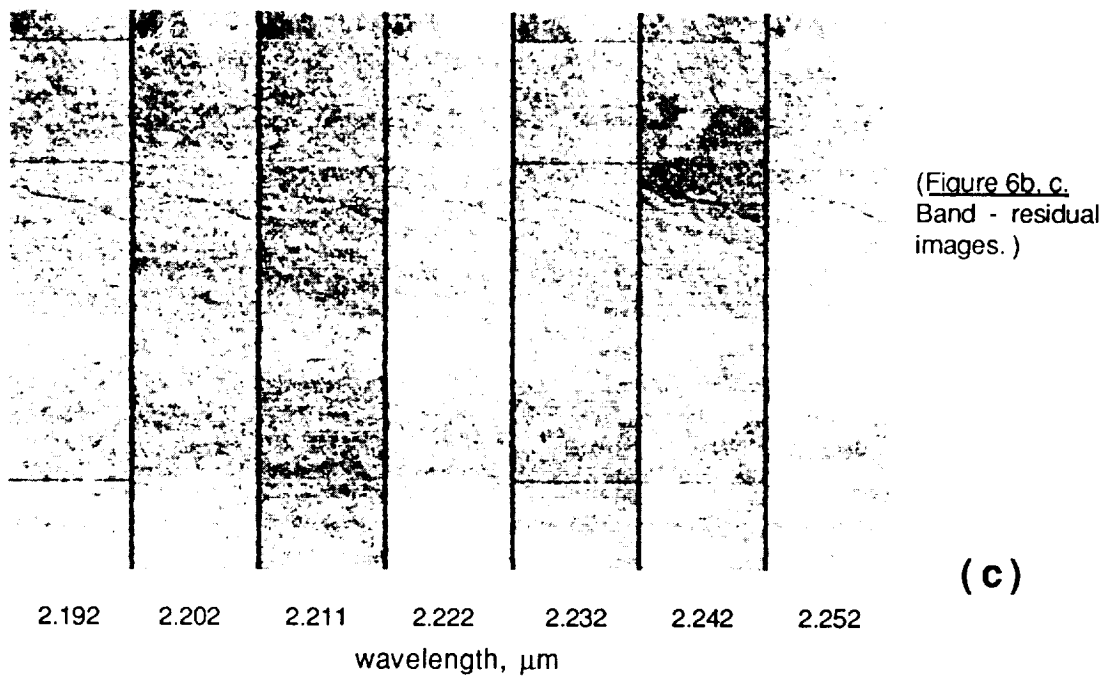
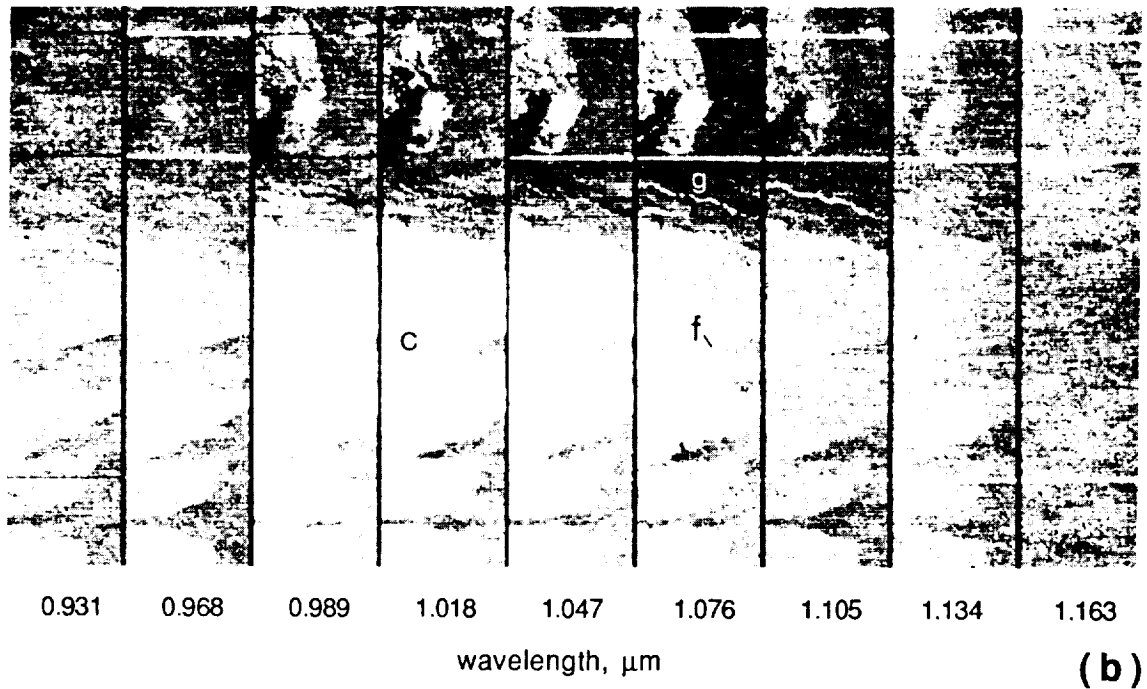
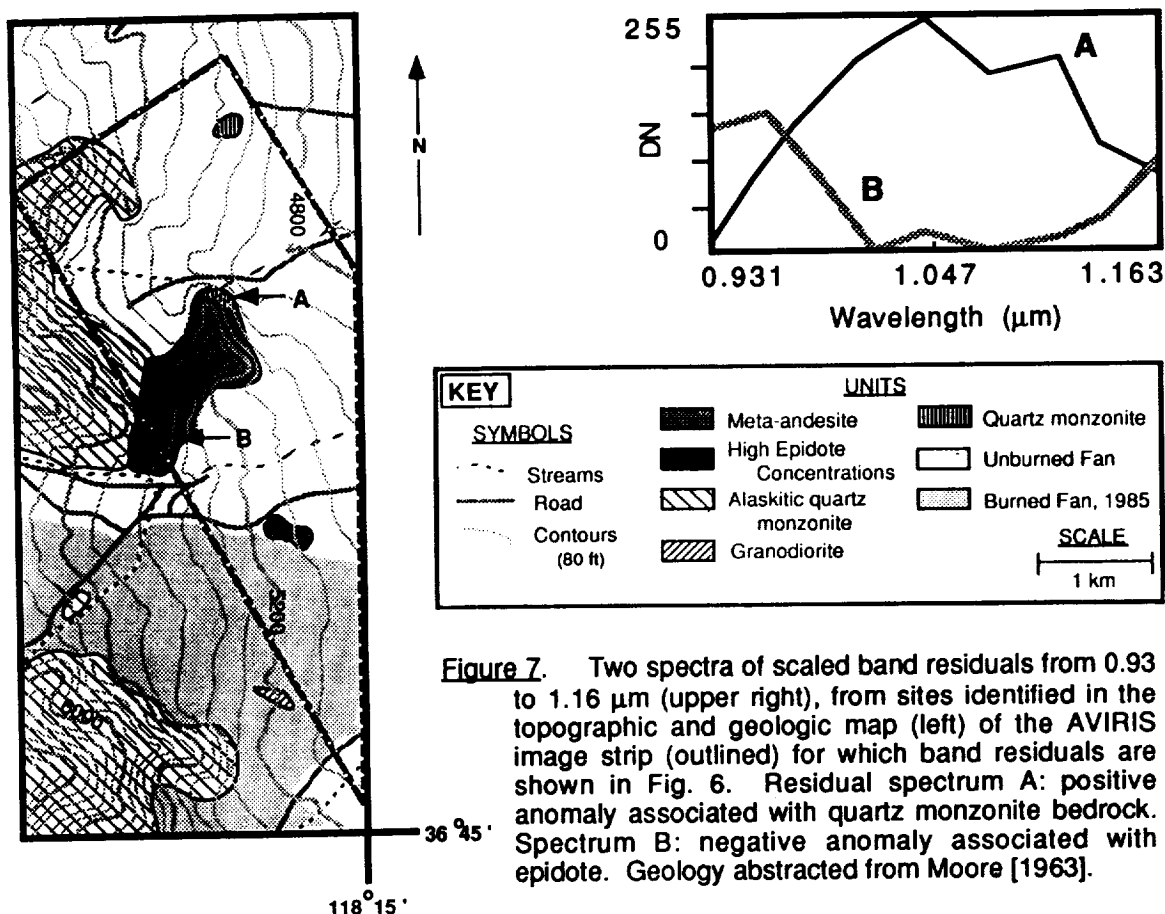


Figure 6. Band-residual image strips, for three spectral regions. The strips are from the image area outlined in Figure 3. Letters denote areas explained in text. a) Visible ($0.49 - 0.67$ μm). b) Near-infrared ($0.93 - 1.16$ μm). c) Near-infrared ($2.19 - 2.25$ μm).

(a)



the anomalies. In Figure 7, spectra from two of the anomalous areas from Fig. 6 are graphed, for the middle spectral window ($\sim 1 \mu\text{m}$). Feature A has a broad positive anomaly, roughly 0.03 reflectance units in height. It is associated with the quartz monzonite bedrock, the spectrum being taken from an outcrop at the northern end of the same meta-andesite ridge that had the highest concentrations of epidote. Residual



spectrum B, from the south end of the ridge, is from one of the epidote-rich areas. Spectrum B shows a broad negative anomaly.

Pine Creek

The Pine Creek [Fox *et al.*, 1990] and Independence Creek areas are similar geologically. In both, lithologies are dominated by the granitic rocks of the Sierra Nevada, but metasedimentary rocks - especially marble - crop out near Pine Creek instead of the meta-andesite. As seen in Fig. 1, the AVIRIS image of Pine Creek was centered over the bajada, which here is dominated by a large moraine complex left by the Pleistocene glaciers of Pine Creek. Downstream from the terminus of the moraines are largely young gravelly sediments, covered locally by grassy meadows with denser stands of trees along distributaries of the creek. Especially south of the moraines, older deposits of bouldery debris flows are preserved.

The glaciations have controlled the alluviation history of the Pine Creek fan. Of chief interest in this study is the preservation of fan units of a broad range of ages and degrees of soil development. Fox *et al.* [1990] have characterized the volumetric clay concentrations in each unit of the chronosequence, and we seek to find associated anomalies near 2.2- μm in the residual spectrum. These are anticipated if no endmember accounts for clay alone, or if the depths of the clay OH^- bands are not proportional to the fraction of the clay-rich endmember.

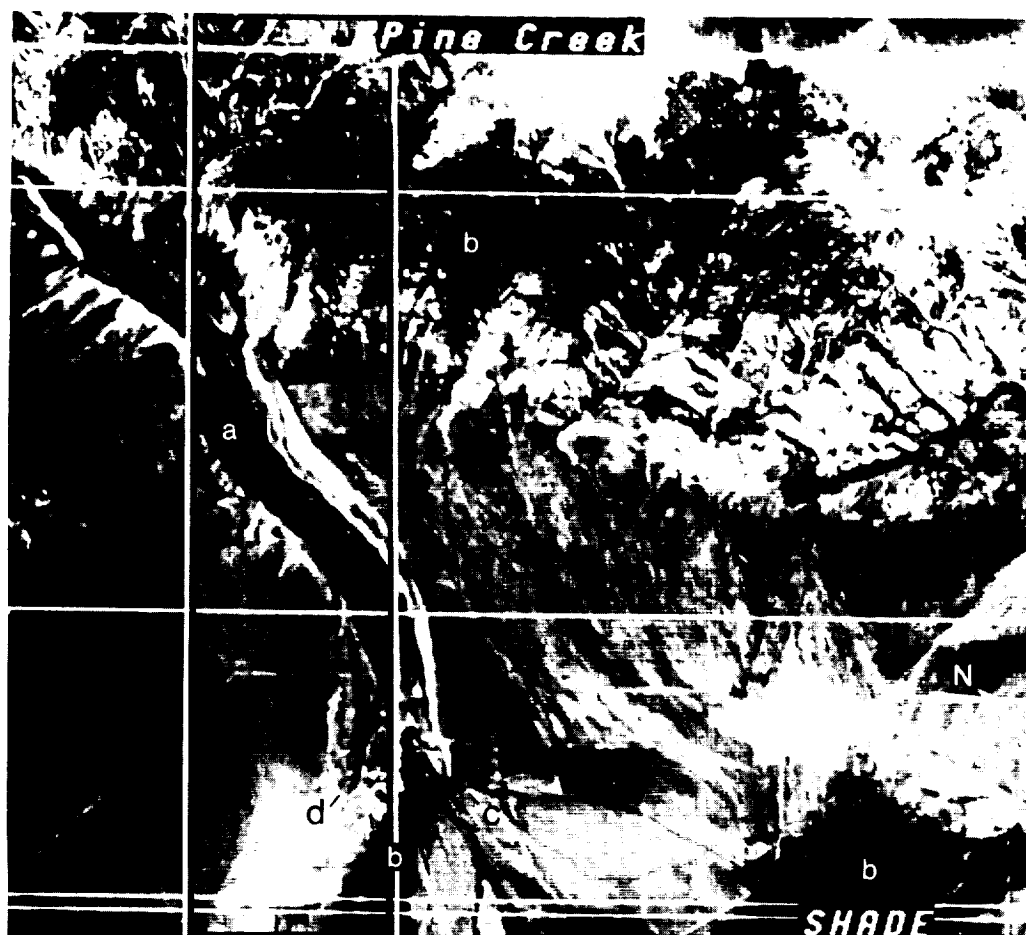


Figure 8. Shade fraction image, Pine Creek. Image has been inverted (complemented) such that high shade fractions are dark instead of light. Scene is ~8.5 km across. Rectangle shows the area for which band residuals were calculated. Letters *a* - *d* denote areas discussed in text.

The mixture model that was used was the same as for Independence Creek. However, alfalfa was used instead of *Coleogyne* for the vegetation endmember. The shade endmember fraction image is shown in Fig. 8, inverted to resemble a radiance image. The highest shade fractions (dark) are associated with north slopes (*a*) and dense stands of vegetation (*b*), especially below the terminus of the moraines (*c*, *d*).

Figure 9 shows seven residual images for the 2.2- μ m window of Fig. 6c. The data were taken from the area outlined in Fig. 8. At Independence Creek, the continuum model accounted for all the spectral variance. At Pine Creek, more information is evident. The strongest anomaly is positive (light), associated with riparian vegetation along the stream (*a*). The positive residual is not directly correlated with a high fraction of shade. In the meadow area, both light and dark patterns are seen in all the images of Fig. 9 (*b*, *c*). Much of the alluvial fan south of Pine Creek (*d*) is dark in Fig. 9, again for all seven bands. This large region of negative anomaly contrasts with the mountain area (*e*), which has a neutral residual and was well modeled.

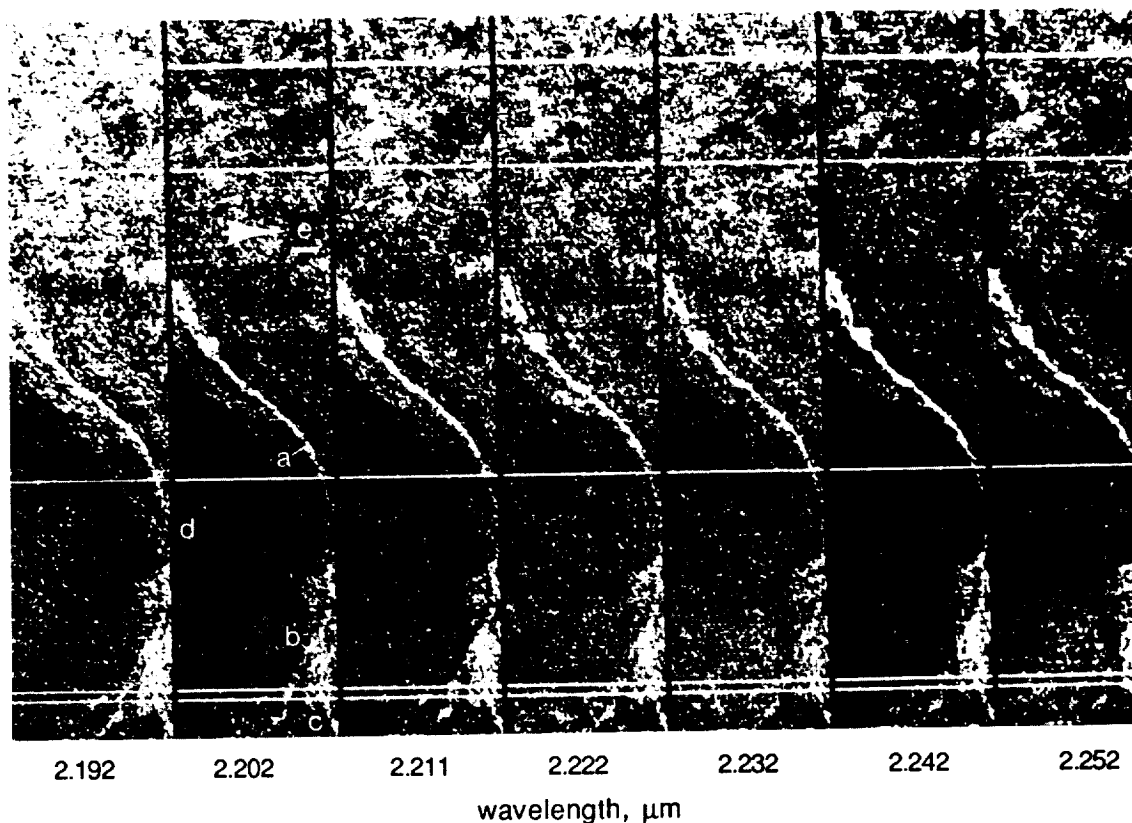


Figure 9. Strongly stretched band-residual images of Pine Creek, 2.19 - 2.25 μm . Letters a - e denote areas mentioned in text.

DISCUSSION

Although absorption features are always reflectance minima, anomalies in the residual spectrum can be higher or lower than the model continuum spectra. Negative residuals occur where there are absorption bands in the data not modeled by the endmembers. Positive residuals occur where the endmember spectra contain absorption features stronger than found in the data.

Areas of high rms residual either are deviant from the continuum model over much of the spectrum, or they must exhibit extremely strong deviations in a few bands. The correct explanation may be found by inspecting the band-residual images: global deviance will be expressed as light or dark anomalies over many or most of the band residuals, whereas local absorption features will appear in only a few bands. However, subtle local deviations of a few percent will not appear in the rms residual, even though they may be detected in the appropriate band residuals. It is these subtle local effects that we anticipate in the band-residual images for scenes such as Owens Valley.

The residual images we calculated resembled the radiance images: the light revegetated areas of the fire scars were associated with positive anomalies; the dark meta-andesite is associated with a negative residual; sunlit slopes are positive, and so forth. However, the residuals are not simply proportional to reflectance or radiance. For example, the correspondence of the residuals to the radiance data is not evident at

all wavelengths. Figures 6 and 9 show only three spectral windows for which there were strong residuals. Across the rest of the spectrum, they were much weaker. Even within the windows, close inspection shows that the supposed correspondence varies from unit to unit in the scene: the positive anomalies on the southeast perimeter of the fire scars appear in all three windows, whereas the stronger anomalies associated with the scars themselves are not evident in the $\sim 2.2\text{-}\mu\text{m}$ residuals. Anomalies associated with trees along Independence Creek have different signs in the different windows: they are positive in the visible and $1\text{-}\mu\text{m}$ regions, but negative at $2.2\text{ }\mu\text{m}$. Yet in the radiance images, vegetation is relatively dark in the visible and light at $1\text{ }\mu\text{m}$. Finally, the centers and widths of the anomalies differ for the various units: the positive anomaly near $0.6\text{ }\mu\text{m}$ for the old alluvial fan west of the 1947 fire scar on Symmes Creek is greater at $0.643\text{ }\mu\text{m}$ than for the young fan to the north, yet they are the same at $0.613\text{ }\mu\text{m}$, and the sense is reversed at lower wavelengths. The conclusion is inescapable that the correspondence between residual and radiance is spurious.

Figure 7 shows that near $1\text{ }\mu\text{m}$ the anomalies over the meta-andesite and quartz monzonite at Independence Creek are equal in magnitude and bandwidth, yet opposite in sign. The meta-andesite has a negative anomaly because there was no endmember with strong Fe^{++} absorption, but why are the burn scars and quartz monzonite positive? A plausible explanation is that the endmember that spectrally most resembles granitic bedrock and soil exposed by the fire was sandy soil, which was actually sampled from an adjacent drainage containing more numerous mafic rocks, and hence more Fe^{++} . On the fire scars the top few cm of soil were removed by wind, and the granitic bedrock shed grus. Both processes expose unweathered soil or rock, and decrease the dilution of the granitic spectrum by vegetation, lichen, and weathering products. As a result, the spectrum is dominated by the Fe^{++} -poor quartz monzonite, with less absorption than the endmember. Hence, the residual spectrum is positive in the Fe^{++} absorption region.

According to this interpretation, the similar magnitudes of the anomalies are coincidental, but the similar bandwidths and centers are unexplained. The anomalies for the same sites, but at $\sim 0.6\text{ }\mu\text{m}$, are at different band centers and have different bandwidths, showing that the anomalies are not linked at all wavelengths. The differential effects observed for different soils may arise because the weathered horizons of the soils extend to different depths, but the æolian stripping is constant across different units.

Anomalies over sunlit (positive) and shaded (negative) slopes of the same material pose an interpretive challenge. In part, the pattern may be explained by a small error in the shade vector, such that the larger rms residual results simply from the high radiance. However, the burned fans also have a moderately high rms residual ($\sim 2\text{ DN}$): twice that of the adjacent unburned fans. Because these fans are not a factor of two darker than the sunlit granite (Fig. 3), the residual must also represent a real difference between the spectra of the granite bedrock in the burned area and the reference sandy alluvium, as discussed above.

Some residuals appear to be related to patterns in vegetation abundance or type. The unburned fans near Boron Springs Creek had detectable negative residuals at red, but not green, wavelengths. This is explainable by increased leaf area, compared to the *Coleogyne* endmember; however supporting field observations have not been made. The anomaly along Independence Creek, especially near $1\text{ }\mu\text{m}$, could be related to the concentration of trees there, yet the bandwidth is too narrow to correspond to the near-infrared plateau of vegetation. The positive anomaly along the fire-scar perimeter appears to be similar, but may be stronger: it is evident at $2.2\text{ }\mu\text{m}$ as well. Field observations suggest that this anomaly corresponds to a zone of dead shrubs, killed by the 1985 fire. There are no leaves, and the wood is much more reflective than the dark stems and bark of the *Coleogyne*. Hence, high positive anomalies are

likely over the reflective plateaus of the wood spectrum. We have not inspected the entire residual spectrum to establish this correlation.

Dry grass and brush were not modeled as endmembers, but where they occurred - at the distal ends of the fans - they were expressed as high fractions of the old, reddish soil endmember. Although the spectra are similar [Roberts *et al.*, 1990] they are not identical, and high residuals are expected, especially near the sharp OH⁻ bands near 2.2 μm . However, this area was outside of the residual image strips we computed.

At Pine Creek, alfalfa instead of *Coleogyne* was used as an endmember. Despite this, trees and meadows along the creek have positive residuals near 2.2 μm . The endmember was defined from irrigated fields; a suggested explanation is that the natural vegetation is water-stressed at this time of year, and less absorptive at 2.2 μm .

Spectral Discrimination and the Number of Endmembers

We anticipated that many more endmembers would be required for AVIRIS than for Landsat TM, but such was not the case. Why are there no more than four or five required for AVIRIS with 171 bands, when four are needed for TM with six? Generally, when less discrimination is achieved than expected, the problem is attributed to low sensitivity, or to a low signal/noise ratio (SNR). Without a high SNR, only strong spectral differences would be apparent, and few endmembers could be

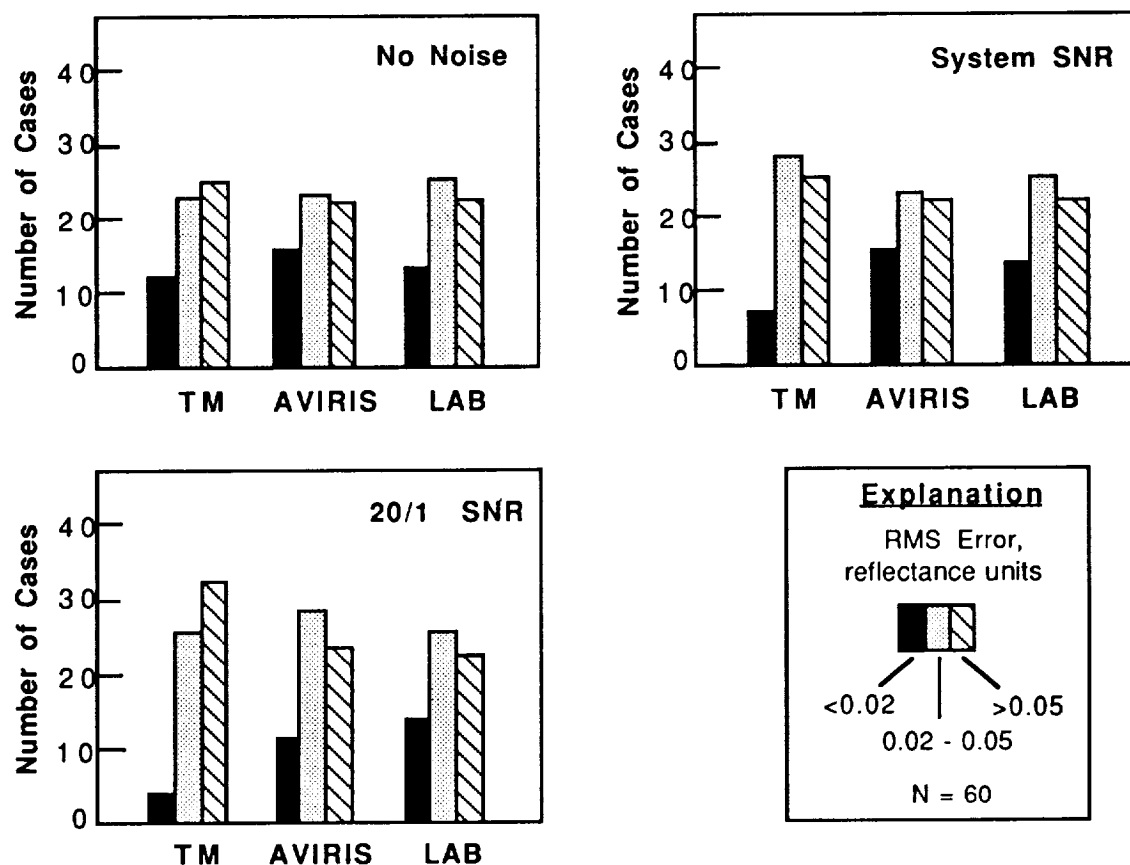


Figure 10. Spectrometer discrimination among 60 reference spectra. Well-modeled spectra have residuals of <0.02 reflectance units.

resolved. But important aspects of the continuum spectrum could be resolved using many measurements, even with lower SNR. Thus, the number of bands is a factor in discrimination also. Low noise is required primarily to resolve narrow absorption features—that is, for the residual spectrum, not the continuum.

We explored the interplay of SNR and band number in spectral discrimination experimentally. One measure of spectral resolution or discrimination is the number of spectra that cannot be differentiated under a given set of sensor characteristics. We took the four endmember spectra used for the Independence Creek image and attempted to express 60 other reflectance spectra from the reference library as mixtures of these four. The finer the discrimination, the fewer spectra should be expressed well as mixtures. The particular spectra used did not matter, because the test was comparative. In this experiment, we simulated different SNR levels by adding random noise to the reflectance spectra. We sampled the spectra using three different sets of bands: the six bands of TM, the 171 of AVIRIS used in this study, and the 512 of our laboratory data (which covered the 1.4- and 1.9- μm windows excluded from the AVIRIS bands). We considered three cases: SNR = 0, SNR = 20, and SNR set to the instrument specifications: variable for AVIRIS, from 20 to 100; 90 for TM; and = 100 for the laboratory spectra. The first two cases bracketed the actual case. The spectra were modeled using equation 3, and the degree of fit was assessed using the rms-residual term. A fit was defined as "good" if the residual was < 0.02 reflectance units.

The results are tabulated in Figure 10, for three ranges of the rms residual. For the noiseless case and AVIRIS bands, 15 reference spectra were fit by mixtures of the four reference spectra with an rms residual of <2%, whereas for TM and the laboratory spectra, 12 and 13 spectra respectively were modeled at that level. For the second, pessimistic case (SNR = 20), the number of well-fit laboratory spectra was unchanged, whereas the number for AVIRIS was reduced by four and the number for TM was reduced by eight. For laboratory spectra, the number in the intermediate and poorly fit categories was unchanged; for AVIRIS, the number in the intermediate category increased; and for TM, the number of poorly fit spectra increased.

For the realistic case ("system SNR"), the number of spectra in all three categories was unchanged, for both laboratory and AVIRIS data. For TM, the number of well-fit spectra was reduced by seven, and the number in the intermediate category was increased by the same amount; the number of poorly fit spectra was unchanged.

Clearly, addition of noise to the spectra reduced discrimination most for the systems with the fewest bands. The SNR of AVIRIS does not seem to be the factor limiting discriminability, at least for continuum spectra, and AVIRIS data were nominally equal to laboratory data in this test. It follows that noise in AVIRIS data serves primarily to reduce the detectability of discrete absorption features, where the degradation of signal cannot be overcome by multiple measurements in nearby bands.

CONCLUSIONS

We found that, for desert surfaces of Owens Valley, the background spectra measured by AVIRIS could be described as linear mixtures of weakly and moderately weathered soils, vegetation, and shade. A fifth endmember, representing a second type of vegetation, would have been locally useful on the valley floor. The clay OH⁻ band in the weathered soil endmember spectrum near 2.2 μm , 0.03 reflectance units deep, was evidently sufficient to describe all the clay absorption in the scene, at the AVIRIS spectrometer D sensitivity and SNR levels. We did not detect the strong OH⁻ epidote bands near 2.3 μm , from which we infer that the area covered by epidote was nowhere more than ~15%.

At shorter wavelengths, AVIRIS is more sensitive, and shallower bands are thus detectable. We were able to see Fe⁺⁺ features at 1 μ m, for which the residual band depth was 0.03, too great to be explained by epidote alone. It seems likely that other ferrous minerals in the meta-andesite host rock must have contributed to this measured band depth.

Evidently, the continuum may be described by a small number of spectral endmembers and their fractions. This is a signal advantage of endmember analysis. The continuum spectra, containing most of the information in the 171 bands of AVIRIS data, may be described by four or five fraction images. This number appears to be inherent to the scene: doubling the number of bands does not increase it, and the dimensionality of TM, with only six bands, is roughly the same as of AVIRIS.

Endmember-fraction images have the advantage that they are thematically meaningful; that is, they depict proportions of spectrally distinct scene constituents as defined by the field scientist, not just radiant fluxes in a particular spectral band. The endmember fractions may be empirically quantifiable as proportions of scene constituents [e.g., Smith et al., 1990b]. Not only is there strong data compression, but the remaining data are rendered more digestible by the image interpreter.

Although hyperspectral data do not appear to be necessary to determine the continuum endmembers, they do define the model spectra with great precision, enabling fine distinctions to be made using the residual spectra. The removal of the continuum or background spectrum is a necessary precursor to analysis, or even recognition, of the absorption features in the residual spectrum. For example, near 2.2- μ m woody plant material has a reflectance peak, at the same wavelengths at which OH⁻ in clays absorbs [e.g., Roberts et al., 1990]. By estimating the fraction of wood based on a large number of bands, the residual spectrum may be corrected for wood near 2.2 μ m, resulting in a more accurate representation of the depth of the clay feature. Without characterization of the background, detection and identification of absorption bands may be uncertain.

Spectral mixture analysis is a means of calibrating AVIRIS data for instrumental, atmospheric and geometric effects such as sun elevation. This approach does not depend on simultaneous field spectra or preflight AVIRIS measurements, even though such data are useful [e.g., Smith et al., 1988a]. Another result of mixture analysis is the partitioning of scene radiance into "tangible" and ephemeral sources: namely, physical scene constituents and photometric shading and shadowing, respectively. The shade fraction image is dominated by topographic information. It has not yet been possible to separate low radiance due to "shade" from low radiance due to dark surfaces using only VNIR data; nevertheless, removal of shade has led to more time-invariant fractions for the tangible endmembers [Adams et al., 1990a].

We find linear spectral mixture analysis to be an effective tool in the analysis and interpretation of AVIRIS data. It is a productive strategy to consider spectra measured by AVIRIS as consisting of a continuum, which describes the general background shape, and a residual, which contains spectral contributions from unusual scene constituents and nonlinear effects, especially concentrated in narrow absorption bands.

Research reported herein was supported in part by the Land Processes Branch of the National Aeronautics and Space Administration.

REFERENCES

- Adams, J. B., and Adams, J. 1984. Geologic mapping using Landsat MSS and TM images: Removing vegetation by modeling spectral mixtures. Third Thematic Conf. Remote Sens. for Expl. Geol., ERIM 2:615-622.

- Adams, J. B., Kapos, V., Smith, M. O., Filho, R. A., Gillespie, A. R., and Roberts, D. A. 1990a. A new Landsat view of land use in Amazonia. Intl. Symp. on Primary Data Acquisition '90, ISPRS, submitted, Manaus, Brazil (June).
- Adams, J. B., and McCord, T. B. 1972. Spectral reflectivity: Optical properties of mineral separates, glass and anorthositic fragments from Apollo Mare samples. Proc. Apollo 12 Lunar Sci. Conf. 3, 2183-219. MIT Press.
- Adams, J. B., Smith, M. O., and Gillespie, A. R. 1989. Simple models for complex natural surfaces: A strategy for the hyperspectral era of remote sensing. Proc. IEEE Intl. Geosci. and Remote Sens. Symp. '89 1:16-21.
- Adams, J. B., Smith, M. O., and Gillespie, A. R. 1990b. Imaging spectroscopy: Data analysis and interpretation based on spectral mixture analysis. In Pieters, C. M., and Englert, P. J., eds., Remote Geochemical Analysis: Elemental and Mineralogical Composition, Lunar and Planetary Institute, Houston, TX, *in press*.
- Adams, J. B., Smith, M. O., and Johnson, P. E. 1986. Spectral mixture modeling: A new analysis of rock and soil types at the Viking Lander 1 site. J. Geophys. Res. 91:8098-8122.
- Aristotle, ca. 335 BC. Metaphysics, Book Alpha 3-4. R. Hope, *translator*. U. Michigan Press, Ann Arbor, 394 p.
- Bierman, P. R., and Gillespie, A. R. 1990. Range fires: A significant factor in the dating and evolution of geomorphic surfaces. Geology, submitted.
- Boardman, J. W. 1989. Inversion of imaging spectrometry data using singular value decomposition. Proc. IEEE Intl. Geosci. and Remote Sens. Symp. '89 pp. 2069-2072.
- Buja, A., and Asimov, D. 1985. Grand Tour methods, an outline. Proc. 17th Symp. on the Interface, Computing Science and Statistics.
- Burke, R.M., Lunstrom, S., Harden, J., Gillespie, A.R., and Berry, M. 1986. Soil chronosequence on eastern Sierra Nevada fans, CA, supports remote sensing studies. Geol. Soc. Am. Abstr. with Program 18(6):553.
- Chittmeni, C. B. 1981. Estimation of proportions in mixed pixels through their region characterization. Proc. Machine Processing of Remote Sens. Data Symp., Purdue Univ., West Lafayette, IN, p. 292-303.
- Chrien, T. G., Green, R. O., and Eastwood, M. 1990. Laboratory spectral and radiometric calibration of AVIRIS. Proc. Airborne Sci. Workshop: AVIRIS, Jet Propulsion Laboratory, Pasadena, CA., 4-5 June. *This volume*.
- Clark, R. N., Middlebrook, B., Livo, E., and Gallagher, A. 1990. Material absorption band depth mapping of imaging spectrometer data using a complete band shape least-squares fit with library reference spectra. Proc. Airborne Sci. Workshop: AVIRIS, Jet Propulsion Laboratory, Pasadena, CA., 4-5 June. *This volume*.
- Conel, J. E., and Alley, R. A. 1984. Lisbon Valley, Utah, uranium test site report. In The Joint NASA/Geosat Test Case Project Final Report, Part 2, Vol. 1, Sec 8 (Paley, H. N., ed.), AAPG Bookstore, Tulsa, OK, pp. 1-101.
- Conel, J. E., Breugge, C., Carrere, V., Green, R. O., and Hoover, G. 1990. Validation of in-flight recovery of atmospheric water vapor. Proc. Airborne Sci. Workshop: AVIRIS, Jet Propulsion Laboratory, Pasadena, CA., 4-5 June. *This volume*.
- Crist, E. P., and Cicone, R. C. 1984. A physically-based transformation of Thematic Mapper data - the TM tasseled cap. IEEE Trans. Geosci. Remote Sens. (3) GE-22:256-263.
- Detechmendy, D. M., and Pace, W. H. 1972. A model for spectral signature variability for mixtures. Remote Sens. Earth Resources, Vol. 1., F. Shahrokhi, ed., Tullahoma, TN, p. 596-620.
- Diner, D. J., and Martonchik, J. V. 1984. Atmospheric transfer of radiation above an inhomogeneous non-Lambertian reflective ground - I. Theory. J. Quant. Spectros. Rad. Transf. 31:97-125.
- Dozier, J. 1981. A method of satellite identification of surface temperature fields of subpixel resolution. Remote Sens. Environ. 11:221-229.
- Fox, L. III, Fischer, A. F. III, Gillespie, A. R., and Smith, M. O. 1990. Investigation of AVIRIS imagery for application in differentiating soil chronosequences. Proc. Airborne Sci. Workshop: AVIRIS, Jet Propulsion Laboratory, Pasadena, CA., 4-5 June. *This volume*.

- Gao, B-C, and Goetz, A. F. H. 1990. Column atmospheric water vapor retrieval from airborne spectrometer data. J. Geophys. Res., *in press*.
- Gillespie, A. R., Abbott, E. A., and Hoover, G. 1986. Spectral basis for relative dating of granitic alluvial fans, Owens Valley, CA (abs.). Geol. Soc. Am. Abstr. with Program 18:614.
- Gillespie, A. R., Smith, M. O., Adams, J. B., and Willis, S. C. 1990. Spectral mixture analysis of multispectral thermal infrared images. Proc. Airborne Sci. Workshop: TIMS, JPL Publication 90-55, Jet Propulsion Laboratory, Pasadena, CA., 6 June 1990.
- Goetz, A. F. H., and Boardman, J. W. 1989. Quantitative determination of imaging spectrometer specifications based on spectral mixing models. Proc. IEEE Intl. Geosci. and Remote Sens. Symp. '89 pp. 1036-1039.
- Goetz, A. F. H., Rowan, L. C., and Kingston, M. J. 1982. Mineral identification from orbit: Initial results from the shuttle multispectral infrared radiometer. Science 218, 1020-1024.
- Goetz, A. F. H., Vane, G., Solomon, J. E., and Rock, B. N. 1985. Imaging spectrometry for earth remote sensing. Science 228:1147-1153.
- Green, R. O., Carrere, V., and Conel, J. E. 1989. Measurement of atmospheric water vapor using the Airborne Visible/Infrared Imaging Spectrometer. Proc. 12th Workshop on Image Processing, Am. Soc. Photogramm. Remote Sens., *in press*.
- Green, R. O., Conel, J. E., Bruegge, C., Carrere, V., Margolis, J., and Hoover, G. 1990. Laboratory spectral and radiometric calibration of AVIRIS. Proc. Airborne Sci. Workshop: AVIRIS, Jet Propulsion Laboratory, Pasadena, CA., 4-5 June. *This volume*.
- Hallum, C. R. 1972. On a model for optimal proportions estimation for category mixtures. Proc. Eighth Int'l Symp. Remote Sens. Environ., Ann Arbor, MI, p. 951-958.
- Hapke, B. 1981. Bidirectional reflectance spectroscopy. 1. Theory. J. Geophys. Res. 89:6329-6340.
- Heimes, R. C. 1977. Effects of scene proportions on spectral reflectance in lodgepole pine. Unpublished Master's thesis, Colorado State Univ., Fort Collins, CO.
- Horwitz, H. M., Lewis, J. T., and Pentland, A. P. 1975. Estimating proportions of objects from multispectral scanner data. Final Report, NSAS Contract NAS9-14123, NASA-CR-141862, 108 p.
- Horwitz, H. M., Nalepka, R. F., Hyde, P. D., and Morgenstern, J. P. 1971. Estimating the proportions of objects within a single resolution element of a multispectral scanner. Proc. Seventh Int'l Symp. Remote Sens. Environ., Ann Arbor, MI, p. 1307-1320.
- Huete, A. R. 1986. Separation of soil-plant spectral mixtures by factor analysis. Remote Sens. Environ. 19:237-251.
- Huete, A. R., Jackson, R. D., and Post, D. F. 1985. Spectral response of a plant canopy with different soil backgrounds. Remote Sens. Environ. 17:37-53.
- Jackson, R. D. 1983. Spectral indices in n-space. Remote Sens. Environ. 13:409-421.
- Johnson, P. E., Singer, R. B., Smith, M. O., and Adams, J. B. 1990. Quantitative determination of mineral abundances and particle sizes from reflectance spectra. J. Geophys. Res., *in press*.
- Johnson, P. E., Smith, M. O., Taylor-George, S., and Adams, J. B. 1983. A semiempirical method for analysis of the reflectance spectra of binary mineral mixtures. J. Geophys. Res. 88:3557-3561.
- Kauth, R. L., and Thomas, G. S. 1976. The tasseled cap - a graphic description of the spectral temporal development of agricultural crops as seen by Landsat. Proc. 3rd Symp. Machine Processing of Remote Sens. Data, LARS, Purdue, pp. 4B/41-4B/51.
- Marsh, S. E., Switzer, P., Kowalik, W., and Lyon, R. J. P. 1980. Resolving the percentage of component terrains within single resolution elements. Photogramm. Engr. and Remote Sens. 46:1079-1086.
- Moore, J. G. 1963. Geology of the Mount Pinchot Quadrangle, southern Sierra Nevada, California. U. S. Geol. Survey Bull. 1130, 152 p.
- Mustard, J. F., and Pieters, C. M. 1986. Quantitative abundance estimates from bidirectional reflectance measurements. J. Geophys. Res. pp. E617-E626.
- Mustard, J. F., and Pieters, C. M. 1987. Abundance and distribution of ultramafic microbreccia in Moses Rock dike: Quantitative application of mapping spectroscopy. J. Geophys. Res. 92:10376-10390.

- Nalepka, R. F., and Hyde, P. D. 1972. Classifying unresolved objects from simulated space data. Proc. Eighth Int'l Symp. on Remote Sens. of Environ., Ann Arbor, MI, p. 935-949.
- Nash, D. B., and Conel, J. E. 1974. Spectral reflectance systematics for mixtures of powdered hypersthene, labradorite, and ilmenite. J. Geophys. Res. 79:1615-1621.
- Otterman, J., Ungar, S., Kaufman, Y., Podolak, M. 1980. Atmospheric effects on radiometric imaging from satellites under low optical thickness conditions. Remote Sens Environ. 9:115-129.
- Pace, W. H., and Detechmendy, D. M. 1973. A fast algorithm for the decomposition of multispectral data into mixtures. Remote Sens. Earth Resources, Vol. II., F. Shahrokhi, ed., Tullahoma, TN, p. 831-848.
- Pech, R. P., Graetz, R. D., and Davis, A. W. 1986. Reflectance modelling and the derivation of vegetation indices for an Australian semi-arid shrubland. Intl. J. Remote Sensing 7:389-403.
- Pieters, C. M., Adams, J. B., Mouginis-Mark, P. J., Zisk, S. H., Smith, M. O., Head, J. W., and McCord, T. B. 1985. The nature of crater rays: The Copernicus example. J. Geophys. Res. 90:12392-12413.
- Possolo, A., Adams, J., and Smith, M. 1990. Mixture models for multispectral images. J. Geophys. Res., submitted.
- Ranson, K. J. 1975. Computer assisted classification of mixtures with simulated spectral signatures. Unpublished Master's thesis, Colorado State Univ., Fort Collins, CO.
- Ranson, K. J., and Daugherty, C. S. T. 1987. Scene shadow effects on multispectral response. IEEE Trans. Geosci. and Remote Sens. GE-25(4):502-509.
- Reid, M. J., Gancarz, A. J., and Albee, A. L., 1973. Constrained least-squares analysis of petrologic problems with an application to lunar sample 12040. Earth Planet. Sci. Lett. 17:433-445.
- Richardson, A. J., Wiegand, C. L., Gausman, H. W., Cuellar, J. A., and Gerbermann, A. H., 1975. Plant, soil and shadow reflectance components of row crops. Photogramm. Engr. Remote Sens. 41:1401-1407.
- Roberts, D. A., Adams, J. B., and Smith, M. O. 1990. Distribution of visible and near-infrared radiant flux above and below a transmittant leaf. Remote Sens. Environ., *accepted*.
- Roberts, D. A., Smith, M. O., Adams, J. B., Sabol, D. E., Gillespie, A. R., and Willis, S. C. 1990. Isolating woody plant material and senescent vegetation from green vegetation in AVIRIS data. Proc. Airborne Sci. Workshop: AVIRIS, Jet Propulsion Laboratory, Pasadena, CA., 4-5 June. *This volume*.
- Sabol, D. E., Adams, J. B., and Smith, M. O. 1990. Predicting the spectral detectability of surface materials using spectral mixture analysis. Proc. Int. Geosci. Remote Sens. Symposium '90 (IGARRS '90), 2:967-970.
- Sacco, W. J., 1972. On mixture distributions in pattern recognition. Information Sciences 4:101-120.
- Sasaki, K., Kawata, S., and Minami, S. 1983. Constrained nonlinear method for estimating component spectra from multicomponent mixtures. Appl. Optics 22:3599-3603.
- Shipman, H., and Adams, J. B. 1987. Detectability of minerals on desert alluvial fans using reflectance spectra. J. Geophys. Res. 92:10391-10402.
- Shippert, P., Bradshaw, G., and Willis, S. C. 1988. Washington Image and Spectral Package (WISP): Preliminary Documentation. Remote Sensing Laboratory, AJ-20., Dept. of Geological Sciences, University of Washington, Seattle, WA 98195, 194 pp.
- Singer, R., and McCord, T. B. 1979. Mars: Large scale mixing of bright and dark surface materials and implications for analysis of spectral reflectance. Proc. 10th Lunar Planet. Sci. Conf. p. 1835-148.
- Smith, M. O., and Adams, J. B. 1985a. Strategy for analyzing mixed pixels in remotely sensed imagery. Proc. NASA/JPL Aircraft SAR Workshop JPL Publ. 85-39, p. 47-48.
- Smith, M. O., and Adams, J. B. 1985b. Interpretation of AIS images of Cuprite, Nevada, using constraints of spectral mixtures. Proc. Airborne Imaging Spectrometer Data Analysis Workshop JPL Publ. 85-41, p. 62-68.
- Smith, M. O., Adams, J. B., and Gillespie, A. R. 1988a. Evaluation and calibration of AVIRIS test-flight data: Owens Valley, CA. Final Report NASA CONTRACT No. NAGW 1135, 17 p.

- Smith, M. O., Adams, J. B., and Gillespie, A. R. 1990c. Reference endmembers for spectral mixture analysis. Proc. 5th Australasian Conf. on Remote Sens., Perth, Australia, 8-12 Oct.
- Smith, M. O., Johnson, P. E., and Adams, J. B. 1985. Quantitative determination of mineral types and abundances from reflectance spectra using principal components analysis. Proc. 15th Lunar Planet. Sci. Conf. Part 2. J. Geophys. Res., 90, Suppl., pp. C797-C804.
- Smith, M. O., Roberts, D. A., Shipman, H. M., Adams, J. B., Willis, S. C., and Gillespie, A. R. 1988b. Calibrating AIS images using the surface as reference. Proc. Airborne Imaging Spectrometer Workshop III (June), JPL Publ. 88-30, p 63-69, Jet Propulsion Laboratory, Pasadena, California.
- Smith, M. O., Ustin, S. L., Adams, J. B., and Gillespie, A. R. 1990a. Vegetation in deserts: I. A regional measure of abundance from multispectral images. Remote Sens. Environ. 31:1-26.
- Smith, M. O., Ustin, S. L., Adams, J. B., and Gillespie, A. R. 1990b. Vegetation in deserts: II. Environmental influences on regional abundance. Remote Sens. Environ. 31:27-52.
- Suits, G. H. 1972. The cause of azimuthal variations in directional reflectance of vegetative canopies. Remote Sens. Environ. 22:175-182.
- van den Bosch, J. M., and Alley, R. E. 1990. Application of LOWTRAN 7 as an atmospheric correction to AVIRIS data. Proc. Airborne Sci. Workshop: AVIRIS, Jet Propulsion Laboratory, Pasadena, CA., 4-5 June. *This volume*.
- Vane, G., and Goetz, A. F. H. 1988. Terrestrial imaging spectroscopy. Remote Sens. Environ. 24, 1 -29.

Evolution of the Airborne Visible/Infrared Imaging Spectrometer (AVIRIS) Flight and Ground Data Processing System

Wallace M. Porter, Thomas G. Chrien, Earl G. Hansen, and Charles M. Sarture

Jet Propulsion Laboratory, California Institute of Technology
Pasadena, California 91109

ABSTRACT

The AVIRIS instrument underwent its first flight season in the summer of 1987. Since then, both the instrument and its data processing facility have evolved through a number of changes designed to correct performance and operating deficiencies observed during the first flight season. This paper describes the modifications made to both the instrument and the data processing facility, the reasons for these modifications, and the resulting improvements.

1. INTRODUCTION

During the last three years (1987-89) several problems were noted in the performance of the AVIRIS instrument and corrected. The observed performance deficiencies fell into two major categories. The first concerned instrument stability. The radiometric performance of the instrument showed variations of 0% to 40% between laboratory calibration and ground truth.

The other concern was the instrument noise performance. The Gaussian noise measured in the signal chains was between three and five times higher than predicted in the system model. Other noise problems included fixed-pattern noise in the images, offset drift that would cause occasional signal clipping, and random level shifts in the signal that were manifest as banding along the flight line.

The AVIRIS has produced large volumes of data in each of the last three years, requiring a dedicated ground data processing facility to process and archive this data. Over this time period the data facility has evolved, especially in regard to the software used. The increase in the amount of data to be processed and a need to improve the response time for data requests have necessitated changes in processing techniques and products. Additional changes were made to increase the capability for error detection and to allow for data product quality control procedures.

2. INSTRUMENT STABILITY

Analysis performed at the time that the instrument was built called for each of the spectrometers to be maintained within 5°C of a constant temperature to maintain their optical alignment.¹ This was initially accomplished by means of two strip heaters around each of the spectrometers. These heater pairs were each controlled by a thermostatic switch having a hysteresis of 3°C.

During the initial instrument calibration, it was noted that the thermal transients caused by the cycling of the thermostatic switches produced fluctuations of several percent in the outputs of the spectrometers. Furthermore, data taken during the first flight season, showed temperature-related variations in spectrometer output approaching 40%. To overcome these problems it was decided to fit each spectrometer with a proportional temperature controller and to distribute the heaters more uniformly over the spectrometer structure. Two separate controllers were used on each spectrometer: one on the structure supporting the optics, and the other on the outer shell of the dewar holding the detector. The structure is maintained at 27°C.

The two belt heaters have been replaced by 24 spot heaters positioned empirically over the spectrometer structure, including the grating and collimator mirror housings. Spectrometer thermal gradients under simulated flight conditions were measured to be on the order of a few tenths of a degree C.

An additional radiometric stability problem, discovered prior to the first flight season, had to do with the way the spectrometers were mounted to the instrument frame. The spectrometers, which have a flat base, were simply bolted to two parallel frame rails. Initially, this caused no trouble. But after several flights, differences in spectrometer performance of up to 50% were observed between operation in the instrument and operation on the test bench. This problem was demonstrated to be caused by warpage of the spectrometer structure by the frame rails, which were no longer parallel.

This problem was corrected by fitting the spectrometers with kinematic mounts. Spectrometers A, B, and C are each mounted on a three-point vibration isolation mount, while spectrometer D is mounted on a four-point mount, made necessary by packaging constraints.

A final stability problem had to do with a plastic isolation bushing which supported the dewar/detector assembly in each spectrometer. This bushing would slip under temperature cycling and vibration, allowing the dewar to move. This problem was solved by replacing the plastic bushing with an aluminum bushing.

The modifications described above have resulted in an overall radiometric stability of better than 10%, with stability of only a few percent during a single flight.

3. INSTRUMENT NOISE PERFORMANCE

During the 1987 flight season, signal-to-noise ratio was three to four times lower than it should have been. Laboratory measurements of the detectors and signal chains predicted a noise figure of 1 to 2 DN. Under flight conditions, however, noise was as high as 8 to 9 DN. In addition, random offset changes and noise stripes occurred in the images.

The offset and striping problems were solved by rebuilding the preamplifiers to remove potentiometer adjustments which were vibration sensitive.

Overall noise performance was improved by repackaging the timing circuitry driving the detectors (Fig. 1). Originally, this circuitry was packaged with the data buffers and instrument control circuitry sharing common power supplies. Phase jitter on the detector drive waveforms translated to noise at the output of the signal chains.

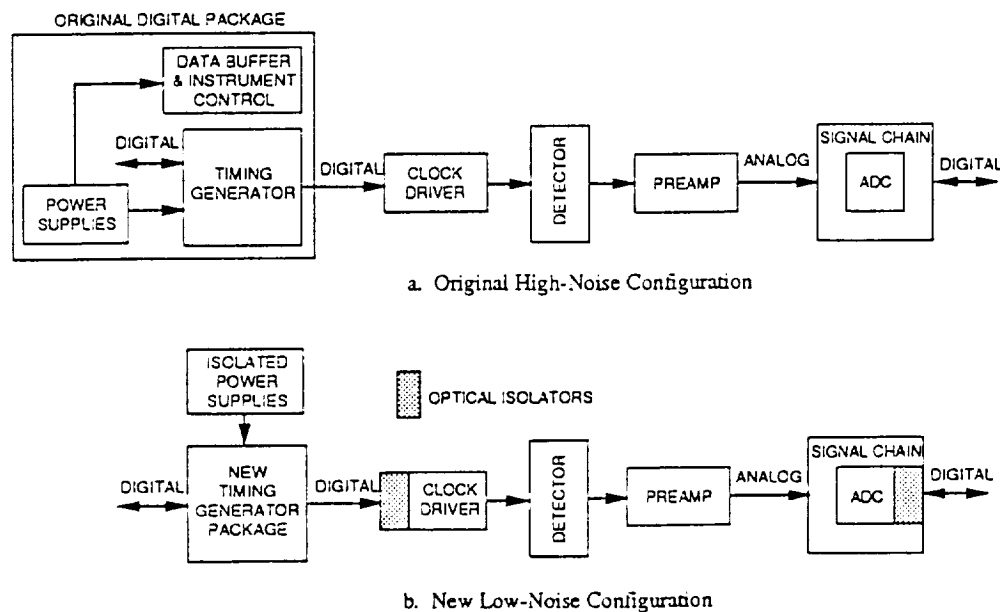


Fig. 1. Digital-to-analog interfacing.

Retirement of NASA's last U2 aircraft allowed AVIRIS (which was at its upper weight limit) to be modified to incorporate a separate package containing detector timing and isolated power supplies. The noise improvement resulting from this repackaging is shown in Fig. 2.

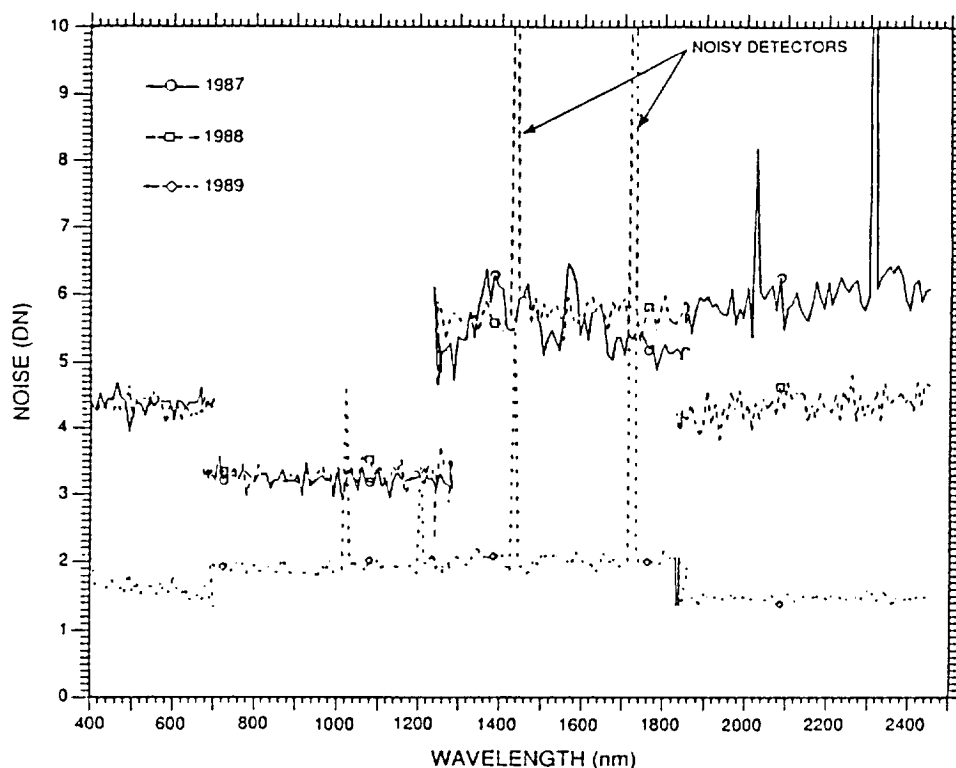


Fig. 2. Noise comparison between 1987, 1988, and 1989.

4. CURRENT INSTRUMENT PERFORMANCE IMPROVEMENTS

In preparation for the 1990 flight season, two performance improvements are under way. The first deals with water damage incurred during the last two flight seasons. Condensation occurring in a high-humidity environment has been damaging the instrument's mirror coatings and has destroyed the IR fibers.

To prevent further damage, the scanner will be sealed behind a window. Air entering the scanner will pass through a desiccant bed. The LN_2 fill system has been modified to vent outboard of the instrument, and fill sensors have been added to prevent overfilling. A dry-air purge system is being purchased to dry and warm the instrument in the aircraft upon return from a flight.

The second improvement is a modification to the onboard calibrator to provide calibration through the data fibers connecting the scanner and foreoptics to the spectrometers.

5. DATA FACILITY OBJECTIVES

The general objectives of the AVIRIS data facility are:

- (1) To provide rapid and automated decommutation and archiving of data.
- (2) To provide the ability to assess the quality of the data and the health of the instrument.

- (3) To provide an automated procedure for applying radiometric corrections to the data.
- (4) To provide responsive processing of data requests from investigators.

These objectives have applied throughout the 3-year lifetime of data production. The alterations to programs and procedures have been instituted to expand the ability of the data facility to accomplish these goals. Previously published details of these objectives¹ have been followed, and goals have been met. The experience gained over this time period, however, indicated that specific changes were needed to meet these objectives in the context of current conditions.

6. HISTORICAL DEVELOPMENT OF DATA SYSTEM

Although the general objectives of the data facility have not changed, many specifics have. The data processing flow is depicted in Fig. 3. Neither the systematic processing flow nor the data processing system has changed over the 3-year period (1987 to 1989), but several requirements have. The quantity of data to be processed has increased, the need for shorter turnaround times for processed data has been expressed, data quality control procedures have become necessary, and an increased role in instrument performance monitoring has developed. All of these factors precipitated changes in the data processing system currently operational and point to additional enhancements needed in the future.

Each of these changes to requirements was addressed by a change to the processing system. The increase in data to be processed was the result of more data being acquired. More and longer flights for more investigators increased the data load by more than 20% from 1987 to 1989, with expectations of further increases in subsequent years. A comparison between the 1987 and 1989 quantities is shown in Table 1. The problem that has occurred as a result of this expanded data load can be seen by noting that the processing times have increased for both archival and retrieval processing. Since the hardware system being used has not changed from the original VAX 11/780,¹ further delays in processing were expected. This became unacceptable, and several software changes were implemented in attempts to handle the processing load.

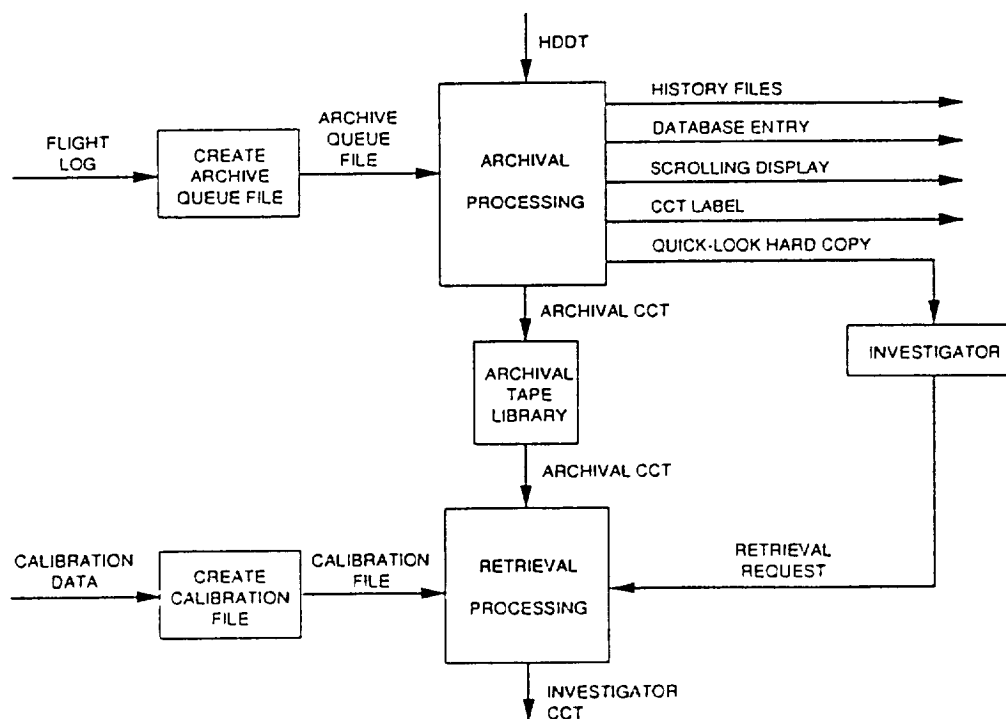


Fig. 3. Systematic processing flow diagram.

Table 1. AVIRIS data processing statistics

	<u>1987</u>	<u>1989</u>
Data quantity collected (high-density data tapes)	33	43
Data quantity archived (computer-created tapes)	795	958
Data quantity archived (gigabytes)	111	134
Data quantity retrieved (computer-created tapes)	339	400
Data quantity retrieved (gigabytes)	47	55
Number of investigators receiving data	58	70
Data processing times (average in weeks):		
From acquisition through archival	6	8
From receipt of request to distribution	3	8

Initially, the retrieval processing system was changed. Retrieval processing consists of several steps that transform archived raw data to the needed form to be sent to the investigator who has requested the data.² This function is process intensive in two ways: it handles large amounts of data in the form of the 140-megabyte image, and it does many floating-point operations on each of the more than 70 million pixels of the image. In the original design, both radiometric and geometric rectification were to be done on the image.² The geometric rectification process was never implemented. The intensive processing needed for this step was prohibitive, and the spatial image from the AVIRIS instrument was found to be acceptable in its raw form.

The radiometric rectification process consisted of two major parts. First the instrument data values were converted into radiance values, and then the spectrum was reconstructed by resampling the data in the spectral direction into bands of uniform spacing. The resampling step was very process intensive and irreversibly altered the data. It was felt that such a data-altering procedure was not within the proper scope of systematic processing, and so this step was discontinued. This decreased the overall processing time, but it needed to be decreased further.

The computing-intensive step of radiometric correction was changed next. Each retrieval of a single 512-line scene was taking 7 hours of processing time. The radiometric correction step was executing 1.4 billion floating-point operations per scene. Since the VAX hardware used has a small floating-point operation capability, changing this step would make a significant impact on the time required to process each scene. Through algorithm changes and intensive code optimization, the number of floating-point operations needed was decreased to 350 million per scene, and the overall run time was decreased to 3 hours per scene. This processing enhancement allowed for a 50% increase in retrieval request throughput for the upcoming 1990 flight season.

Once changes to the retrieval system were completed, the archival system problems were addressed. Decommutating and archiving the raw data is the first step in the data processing flow. All the data acquired by the instrument must go through this process to become usable by the investigator. Thus, although archiving each scene takes only 60 minutes, the aggregate time needed for all the flight data is large. Also, the requirement for this amount of time per scene resulted in backlogs of acquired data waiting to be archived and extended the turnaround time to the investigator. To alleviate this problem, changes were made to the archiving software. Each scene processed is 140 megabytes in size and was read several times in order to decommutate and reformat the data. This process was altered to reduce by half the number of times the data is read and to discontinue some of the reformatting steps. This decreased the run time by one-third, resulting in a projected 30% increase in archival processing throughput.

Both of the software changes described above were implemented to increase throughput and alleviate serious delays

in data request response times. Additional steps will need to be taken for further improvements, including hardware upgrades, as the quantity of data handled continues to increase.

Throughput problems were not the only issues to be addressed in the evolution of the data facility system. Another major area was data product quality control. A procedure was implemented to monitor the quality and correctness of the data being sent out in response to investigator requests. Previously, a randomly conducted manual process was used to determine the quality of the output product of the retrieval system. At randomly selected times the image from the retrieval program was viewed on an image display to see if it appeared reasonable. This was an inadequate quality control method.

A new procedure was implemented which checks every output image in two ways. The retrieval software was expanded to record a one-band 100-line test image and to store a selected spectrum across all bands of the image. The test image is photographically recorded as an audit of the retrieved data and to assure a reasonable spatial image. A hard-copy plot of the spectrum is produced and checked for conformity to expected results. This procedure gives both a means of checking system performance and an audit trail of all products produced for future reference and problem resolution.

An increased role in data quality monitoring at the input stage has also developed. After the instrument records the image and ancillary data on the high-density output tape, the data facility provides the only means of viewing this information. Monitoring both the health of the instrument and the quality of the data recorded must be done at this phase of the process. As the acquisition flights became more frequent and critical, a means to determine the health of the instrument was needed. It was determined that a minimal review of the acquired data was necessary within 24 hours of a flight. Because processing times were so extended, as described above, a limited reviewing system was put in place to respond in the required time. This system processes a small amount of data from selected portions of the high-density data tape to assure that the instrument is imaging from all spectrometers and that specified threshold limits for signal strength and noise are met. By use of this system, instrument failures can be detected and long-term instrument performance trends can be monitored.

In addition to this review process, further error detection means were added to the archival system software. Prior to these changes, data recording errors were minimally processed. Each type of error was detected and flagged as a group, and no detailed information was provided. This was an inadequate means of error tracking and feedback to the engineering team. To rectify this problem, software enhancements were implemented to record each error separately and to present a detailed view of what the erroneous data contains. With this information the possible points of error production can be ascertained, and the engineering team has adequate feedback for use in instrument diagnostic procedures. This additional information has already provided the means to recognize an instrument failure and assist the engineering team in its resolution.

All the changes described have been put in place in preparation for the 1990 flight season. Their implementation should increase the throughput and error detection capabilities of the AVIRIS data processing system. Further changes are envisioned to respond to the continuing increases in data acquired and investigators supported. The retrieval system will be changed to improve the input/output methods. With the large amounts of data handled for each scene processed (more than 140 megabytes), enhancements to this part of the retrieval process should gain another substantial reduction in processing time. In addition to this change, the entire retrieval system is being prototyped for movement onto new hardware, a SUN server system. With this type of system, it is expected that run times for retrieval processing can be reduced to less than one hour per scene. The archival system is also being prototyped onto a SUN system, with the high-density tape processing hardware interfaced to the SUN input/output bus structure. An increase in high-density tape reading speed is expected, which would both decrease processing time for the archival process and improve the data quality through reduction of errors. The movement of the archival processing to this type of hardware system is hoped for in the near future.

The system changes described above have improved the means by which the AVIRIS data is processed and delivered to the science community. Both the responsiveness to data requests and the quality of data provided have been enhanced. The projected future changes should extend these improvements, allowing them to be maintained for larger processing requirements.

7. ACKNOWLEDGEMENTS

The research reported herein was carried out by the Jet Propulsion Laboratory, California Institute of Technology, under a contract with the National Aeronautics and Space Administration. The authors wish to express thanks to the members of the data facility staff, Steve Larson, Steve Carpenter, Manuel Solis, and Ian Novack, for their assistance. The authors also wish to thank the following people for their assistance and support: James S. Bunn, Michael L. Eastwood, John J. Genovsky, Robert O. Green, Charles G. Kurzweil, Robert M. Medina, Donald V. Haffner, Robert W. Hagood, Robert Higgins (NASA/Ames), Stanley R. Jones, J. Colin Mahoney, Mark C. McKelvey, William J. Sleight, Dr. Harold R. Sobel, and Ronald E. Steinkraus.

8. REFERENCES

1. Wallace M. Porter and Harry T. Enmark, "A System Overview of the Airborne Visible/Infrared Imaging Spectrometer (AVIRIS)," *Imaging Spectroscopy II, Proceedings of SPIE*, Vol. 834, pp. 22–31, 1987.
2. John H. Reimer et al., "AVIRIS Ground Data-Processing System," *Imaging Spectroscopy II, Proceedings of SPIE*, Vol. 834, pp. 79–90, 1987.

SLIDE CAPTIONS

<u>Slide No.</u>	<u>Caption</u>	<u>Senior Author</u>
1	A 171-band subset of the 224 AVIRIS bands, consisting of bands outside of major atmospheric adsorption features.	Roberts
2	Simplified geomorphic map of the Kyle Canyon alluvial fan (after Chadwick et al., 1989).	Carrere
3	AVIRIS color composite.	Carrere
4	AVIRIS PC color composite.	Carrere
5	Mineralogy map of the Kyle Canyon fan obtained from combined band ratios.	Carrere
6	Color coded thematic image map showing the distribution of calcite (red) and dolomite (yellow), based upon the relative position of the $\sim 2.3 \mu\text{m}$ absorption feature ($2.32 \mu\text{m}$ for dolomite vs $2.34 \mu\text{m}$ for calcite).	Kruse
7	Color coded thematic image map showing the distribution of sericite, carbonates (calcite and dolomite combined as a group), hematite, goethite, and mixtures of the iron oxides with the other minerals.	Kruse
8	Location of the Salton Sea test site in south-eastern California (inset). MSS image shows orientation and extent of the AVIRIS flight paths over Salton Sea in the Salton Trough, April 18, 1989.	Carrere
9	Left image: three-color composite AVIRIS image of near-shore area (11:05 PST segment) in northwest Imperial Valley. Right image: spatial distribution of atmospheric water vapor (column abundance) derived using CIBR algorithm and 940-nm water band.	Carrere
10	Spatial distribution of atmospheric moisture (column abundance) compared to the distribution of green fields as shown in left image of Figure 8 (Slide 9).	Carrere
11	Spatial distribution of atmospheric water vapor (column abundance) derived by the CIBR algorithm for the 940- and 1130-nm water bands.	Carrere

12	The 10:50 PST segment of AVIRIS data from the NE-SW flight line at Salton Sea, April 18, 1989. Left panel: three-color composite image. Right panel: distribution of water vapor retrieved for the scene using the continuum interpolated band ratio (CIBR) algorithm described in Part I. The points A and B are ends of the water vapor column abundance profile given in Figure 2.	Conel
13	Flash towers at the UNOCAL Unit 3 geothermal power facility, Imperial Valley, CA.	Conel
14	A false-color-infrared composite of the Canon City AVIRIS scene.	Clark
15	A Color-Composite-Band-Depth Image (CCBDI) for Canon City: blue is kaolinite, green is calcite, and red is dolomite.	Clark
16	A Color-Composite-Band-Depth Image (CCBDI) for Canon City: blue is kaolinite, green is montmorillonite, and red is goethite.	Clark
17	A Color-Composite-Band-Depth Image (CCBDI) for Canon City: blue is montmorillonite, green is goethite, and red is hematite.	Clark
18	A Color-Composite-Band-Depth Image (CCBDI) for Canon City: blue is kaolinite, green is illite, and red is montmorillonite.	Clark
19	Calibrated reflectance flight lines were registered together to produce a HIRIS image of 800X800 pixels.	Kierein-Young
20	Color composite image produced from a decorrelation stretch of AVIRIS bands 187 (2088 nm), 192 (2134 nm), and 198 (2217 nm) displayed as red, green, and blue, respectively.	Hook
21	Wavelength and depth of deepest absorption feature in each pixel in hull quotients of log residual AVIRIS data from 2000 to 2350 nm wavelength range displayed as gray scale images. Wavelength - top; depth - bottom.	Hook
22	The T-SPECTRA menu interface showing interactive selection of input image format.	Donoghue
23	The graphics interface showing an albedo image from AVIRIS SWIR data processed with the log residual technique. Spectra from a 3*3 area have been interactively extracted and these correspond closely with the minerals kaolinite and alunite.	Donoghue